PH.D. DISSERTATION

# Robust GNSS Carrier Phase-based Position and Attitude Estimation

## Theory and Applications

AUTHOR: DANIEL ARIAS MEDINA

THESIS ADVISORS:
PROF. JESÚS GARCÍA HERRERO
PROF. JORDI VILÀ-VALLS
DR. RALF ZIEBOLD

DISSERTATION COMMITTEE:
PROF. JOSE MANUEL MOLINA LÓPEZ
PROF. FABIO DOVIS
DR. GABRIELE GIORGI
PROF. DAVID MARTÍN GÓMEZ

A dissertation submitted by in partial fulfillment of the requirements for the degree of Doctor of Philosophy in

*Doctor on Computer Science and Technology*

Berlin, October 2021

Daniel Arias Medina
ariasmedinad@gmail.com
German Aerospace Center (DLR)
Kalkhorstweg 53
17235 Neustrelitz, Germany

*A mis padres, por hacerme persona.*
*A Alejandra, por ser mi brigada.*

# Acknowledgements

“*Dissertations are not finished; they are abandoned*”
Fred Brooks

It results extremely difficult to put an end to the work of five years. Every time I reviewed this manuscript, I would find an opportunity (or excuse) to extend my writing period by adding a new simulation or a discussion. Luckily, I have been surrounded by extraordinary people whose support and encouragement pushed me through the last steps of this work. At last, I can cite my good friend Pau Closas: *Habemus Thesis*.

I am a very fortunate person who has a lot to thank for. Therefore, do not expect the sequel to be short.

First and foremost, I would like to express my eternal gratitude to my three advisors: Jesús, Ralf and Jordi. Despite the distance and the ever-growing duration of this thesis, Jesús, thanks for supervising me throughout my Master and PhD studies. Your patience and enthusiasm made this work possible. Ralf, thank you for your wise guide through all of the stages of my PhD. You have always understood when to give *carte blanche* or to keep a close rein on me (given my easiness in diverging, this was a fundamental skill!) which, among other reasons, makes you an excellent group leader. Jordi, pirata, muchísimas gracias por hacerme sentir ilusión en esto de *la ciencia*. Eres el supervisor que todo estudiante quisiera y que ninguno se merecería, y espero que esto no sea más que el comienzo de muchos años de amistad.

This PhD has become a reality thanks to the amazing work environment that I encountered since my first day at DLR. I would not be able to name you all, but this is my attempt: Gregor, Iván, Pozo, Anja (who teached me all I know [and more that I have forgotten] about RTK!), Filippo, Lars, Niklas, JuanMar, Frank, Christoph, Sandeep, Stefan, Shradha, Astrid, Uwe, Evelin, Paweł, Carsten, Lukas, Omar, Emilio, ... You see, too many incredible people gathered under the same institution! Of course, I could not forget Michailas, the person who light the spark of research on myself, thank you for being my first supervisor and teaching me to work hard, really hard. Last but not least, the best department head that one could think of, Thoralf, thank you for always supporting, trusting and betting on me.

I would also like to thank the beautiful international research network that was somehow born out of the friendship between Pau and Jordi. Pau, eres una máquina, la imagen que todo investigador quisiera encontrar en su espejo, incansable y siempre dispuesto a nuevos desafíos. Thanks again to Jordi for inviting me to ISAE-SUPAERO, Toulouse, where I met individuals of the highest personal quality: Eric (the crazy Eric, the bound maker, the person who came up with a “simple” 15 page-long derivation of a bound after half hour of “*What is RTK?*” introduction), Lorenzo, Paul (otro loco), Gaël and François. *Merci beaucoup!*

To my Berliner friends, now also my family, who have made feel like in my Málaga natal. Lucky me again, you are many and too good: Sara, Jordi Calli, Andrés, Madeleine, Andrea, Tim. Melvin, my man, thank you very much for your dancing skills, for sharing with me the most amazing of the parties and for trusting me even in the day of your wedding. Elmar, you are the best friend, the very best friend that one could not even dream of. I could say nicer things about you, but it would not feel right. So, thanks for being as stupid as you are. La tríada sagrada, el fundamento de mi diversión y los pobres que sufren con mi pobre habilidad padelística: Jonathan, Dani, Iván. ¡Este fin de semana sí que fue el último del doctorado! David, muchas gracias por compartir conmigo tu sensibilidad, tu arte, tu poesía y, aún más especial, por confiarnos a Bowie.

Finalmente llegamos a casa, a mi Málaga. Muchas gracias a mis amigos, por hacer que cada visita fuera especial y que sintiera como si no hubiera pasado el tiempo. Mis amigos del alma, Luis, Marina, Raquel e Irene, no sé vivir sin vosotros. Juanca, Alberto, estáis en mi mente, en mi corazón y ojalá estuvierais conmigo cada final de la jornada. Juanma, mi Vasco querido, no te cabe el corazón en el pecho y no te caben tantas buenas ideas en esa cabeza rubia. Sin ti no tendría siquiera el Grado de Ingeniero y míranos ahora, tú un grandísimo doctor y yo... bueno, en ello estoy. La familia es de la pocas cosas que no se eligen en la vida y es por ello que no concibo cómo han podido alinearse personas tan increíbles en la mía: familia adoptiva Marqués Mazón, tita y segunda madre Mari y titos Ani, Francis y Eduardo, qué suerte de teneros. A mi Cheli, que tanto me sacas de quicio como te quiero (¡imagina cuánto es eso!), nos quedan infinitos viajes y Años Nuevos que disfrutar juntos y eso me hace muy feliz. Papá, mamá, sois las personas que más quiero en el mundo y a las que más echo de menos. Muchas gracias por todo el sacrificio que habéis hecho siempre por nosotros, por darnos la mejor educación y por desviviros por nosotros. Ahora que la losa del doctorado no me pesa, espero poder pasar con vosotros el tiempo que os merecéis. Por último, a la luz de mi vida, Alejandra. No sé cómo agradecerte todo lo que haces por mí cada día, no es ni medio normal la paciencia y comprensión que has tenido conmigo a lo largo de tantas noches y fines de semana frente al ordenador. Definitivamente, sin tu apoyo, inspiración y amor jamás habría podido terminar este trabajo.

Daniel Arias Medina
Berlin, October 18, 2021

# Published and submitted content

All the contributions of this doctoral thesis have been published in journals and conferences. This section enumerates the involved publications and relates them to the main chapters and sections, specifying the way of inclusion.

## Journal Articles

- (July, 2021) Castro-Arvizu, J. M., Medina, D., Ziebold, R., Vilà-Valls, J., Chaumette, E., & Closas, P. "Precision-Aided Partial Ambiguity Resolution Scheme for Instantaneous RTK Positioning." Published in: *Remote Sensing, 13(15), 2904.* Ref. [1].
  DOI: 10.3390/rs13152904
  Impact factor: 4.848 / Q1 (2020)
  Role: second author.
  Statement: the content from this publication is partially included in Chapter 2.

- (March, 2021). Meyer, L., Smíšek, M., Fontan Villacampa, A., Oliva Maza, L., Medina, D., Schuster, M. J., & Triebel, R. "The MADMAX data set for visual-inertial rover navigation on Mars." Published in: *Journal of Field Robotics.* Ref. [2].
  DOI: 10.1002/rob.22016
  Impact factor: 3.767 / Q2 (2020)
  Role: first author.
  Statement: the content from this publication is partially included in Chapter 3.

- (February, 2021) Medina, D., Li, H., Vilà-Valls, J., & Closas, P. "Robust Filtering Techniques for RTK Positioning in Harsh Propagation Environments." Published in: *Sensors, 21(4), 1250.* Ref. [3].
  DOI: 10.3390/s21041250
  Impact factor: 3.576 / Q1 (2020)
  Role: first author.
  Statement: the content from this publication is fully included in Chapter 6.

- (February, 2021) Medina, D., Vilà-Valls, J., Chaumette, E., Vincent, F., & Closas, P. "Cramér-Rao bound for a mixture of real-and integer-valued parameter vectors and its application to the linear regression model." Published in: *Signal Processing, 179, 107792.* Ref. [4].
  DOI: 10.1016/j.sigpro.2020.107792
  Impact factor: 4.662 / Q1 (2020)
  Role: first author.
  Statement: the content from this publication is fully included in Chapter 2.

- (December, 2020) Li, H., Medina, D., Vilà-Valls, J., & Closas, P. "Robust Variational-based Kalman Filter for Outlier Rejection with Correlated Measurements." Published in: *IEEE Transactions on Signal Processing, 69, 357-369.* Ref. [5].
  DOI: 10.1109/tsp.2020.3042944
  Impact factor: 4.931 / Q1 (2020)
  Role: second author.
  Statement: this publication is partially included in Chapter 6 and Appendix D.

- (June, 2020) Heßelbarth, A., Medina, D., Ziebold, R., Sandler, M., Hoppe, M., & Uhlemann, M. "Enabling Assistance Functions for the Safe Navigation of Inland Waterways." Published in: *IEEE Intelligent Transportation Systems Magazine, 12(3), 123-135.* Ref. [6].
  DOI: 10.1109/mits.2020.2994103
  Impact factor: 3.419 / Q2 (2020)
  Role: second author.
  Statement: the content from this publication is partially included in Chapter 2.

- (June, 2020) Ortega, L., Medina, D., Vilà-Valls, J., Vincent, F., & Chaumette, E. "Positioning Performance Limits of GNSS Meta-Signals and HO-BOC Signals." Published in: *Sensors, 20(12), 3586.* Ref. [7].
  DOI: 10.3390/S20123586
  Impact factor: 3.576 / Q1 (2020)
  Role: second author.
  Statement: the content from this publication is partially included in Chapters 1 and 2.

- (June, 2020) Medina, D., Vilà-Valls, J., Heßelbarth, A., Ziebold, R., & García, J. "On the Recursive Joint Position and Attitude Determination in Multi-Antenna GNSS Platforms." Published in: *Remote Sensing, 12(12), 1955.* Ref. [8].
  DOI: 10.3390/rs12121955
  Impact factor: 4.848 / Q1 (2020)
  Role: first author.
  Statement: the content from this publication is fully included in Chapter 4.

- (June, 2020) Medina, D., Ortega, L., Vilà-Valls, J., Closas, P., Vincent, F., & Chaumette, E. "Compact CRB for delay, Doppler, and phase estimationapplication to GNSS SPP and RTK performance characterisation." Published in: *IET Radar, Sonar & Navigation, 14(10), 1537-1549.* Ref. [9].
  DOI: 10.1049/iet-rsn.2020.0168
  Impact factor: 1.955 / Q3 (2020)
  Role: first author.
  Statement: the content from this publication is partially included in Chapters 1 and 2.

- (December, 2019) Medina, D., Li, H., Vilà-Valls, J., & Closas, P. “Robust statistics for GNSS positioning under harsh conditions: A useful tool?.” Published in: *Sensors, 19(24), 5402.* Ref. [10]
  DOI: 10.3390/s19245402
  Impact factor: 3.576 / Q1 (2020)
  Role: first author.
  Statement: the content from this publication is fully included in Chapter 5.

## Conference Articles

- (2021, November) Chauchat, P., Medina, D., Vilà-Valls, J., & Chaumette, E. “Robust Linearly Constrained Filtering for GNSS Position and Attitude Estimation under Antenna Baseline Mismatch.” Accepted in: *2021 24th International Conference on Information Fusion (FUSION). IEEE. (to appear)*. Ref. [11].
  Role: second author.
  Statement: the content from this publication is partially included in Chapter 6.

- (2021, March) Medina, D., Castro-Arvizu, J. M., Vilà-Valls, J., Ziebold, R., & Closas, P. (2021, March). Precision-Driven Partial Ambiguity Resolution Technique for Short to Medium Baseline Positioning. In *2021 IEEE Aerospace Conference* (pp. 1-7). IEEE. Ref. [12].
  DOI: 10.1109/aero50100.2021.9438266
  Role: first author.
  Statement: this publication is partially included in this thesis in Chapter 2.

- (2020, November) Medina, D., Ziebold, R., & García, J. (2020, November). “On the Kalman Filter Design for Quaternion-based GNSS-Inertial Attitude Determination.” Presented in: *2020 European Navigation Conference (ENC), IEEE*. Ref. [13].
  Role: first author.
  Statement: this publication is partially included in this thesis in Chapter 3.

- (2020, December) Ortega, L., Medina, D., Vilà-Valls, J., Vincent, F., & Chaumette, E. “A Compact CRB for the Single Source Conditional Signal Model with Application to Delay-Doppler-Phase Estimation of Band-Limited Signals.” Published in: *2020 59th IEEE Conference on Decision and Control (CDC) (pp. 2906-2911). IEEE.* Ref. [14].
  DOI: 10.1109/cdc42340.2020.9303748
  Role: second author.
  Statement: this publication is partially included in this thesis in Chapter 1.

- (2020, January) Castro-Arvizu, J. M., Medina, D., & Ziebold, R. “Impact of Satellite Elevation Mask in GPS+ Galileo RTK Positioning.” Published in: *Proceedings of the*

*2020 International Technical Meeting of The Institute of Navigation (pp. 487-498). ION.* Ref. [15].
DOI: 10.33012/2020.17157
Role: second author.
Statement: this publication is partially included in this thesis in Chapter 2.

- (2019, October) Medina, D., Li, H., Vilà-Valls, J., & Closas, P. "On Robust Statistics for GNSS Single Point Positioning". Published in: *2019 IEEE Intelligent Transportation Systems Conference (ITSC)* (pp. 3281-3287). IEEE. Ref. [16].
  DOI: 10.1109/itsc.2019.8917484
  Role: second author.
  Statement: this publication is partially included in this thesis in Chapter 5.

- (2019, September) Medina, D., Centrone, V., Ziebold, R., & García, J. "Attitude Determination via GNSS Carrier Phase and Inertial Aiding". Published in: *Proceedings of the 32nd International Technical Meeting of the Satellite Division of The Institute of Navigation (ION GNSS+ 2019) (pp. 2964–2979). ION.* Ref. [17].
  DOI: 10.33012/2019.16963
  Role: second author.
  Statement: this publication is partially included in this thesis in Chapter 3.

- (2019, September) Li, H., Medina, D., Vilà-Valls, J., & Closas, P. "Robust Kalman Filter for RTK Positioning Under Signal-Degraded Scenarios." Published in: *Proceedings of the 32nd International Technical Meeting of the Satellite Division of The Institute of Navigation (ION GNSS+ 2019) (pp. 16–20). ION.* Ref. [18].
  DOI: 10.33012/2019.17021
  Role: second author.
  Statement: this publication is partially included in this thesis in Chapter 4.

- (2019, September) Medina, D., Alvarez-Merino, C., Ziebold. R. "Partial Ambiguity Resolution for Reliable GPS/Galileo Positioning." Presented in: *2019 International Workshop on GNSS Ionosphere (IGWI)*. Ref. [19].
  DOI: 10.3390/s18092954
  Role: second author.
  Statement: this publication is partially included in this thesis in Chapter 2.

- (2018, September) Medina, D., Gibson, K., Ziebold, R., & Closas, P. "Determination of pseudorange error models and multipath characterization under signal-degraded scenarios." Published in: *Proceedings of the 31st International Technical Meeting of the Satellite Division of The Institute of Navigation (ION GNSS+ 2018). ION.* Ref. [20].
  DOI: 10.33012/2018.16094
  Role: second author.

Statement: this publication is partially included in this thesis in Chapter 1 and Appendix B.

- (2018, April) Crespillo, O. G., Medina, D., Skaloud, J.,& Meurer, M. "Tightly coupled GNSS/INS integration based on robust M-estimators." Published in: *2018 IEEE/ION Position, Location and Navigation Symposium (PLANS) (pp. 1554-1561). IEEE.* Ref. [21].
  DOI: 10.1109/plans.2018.8373551
  Role: second author.
  Statement: this publication is partially included in this thesis in Chapter 6.

- (2018, April) Medina, D., Heßelbarth, A., Büscher, R., Ziebold, R., & García, J. "On the Kalman filtering formulation for RTK joint positioning and attitude quaternion determination." Published in: *2018 IEEE/ION Position, Location and Navigation Symposium (PLANS) (pp. 597-604). IEEE.* Ref. [22].
  DOI: 10.1109/plans.2018.8373432
  Role: second author.
  Statement: this publication is partially included in this thesis in Chapter 4.

## Submitted Works

- Singh. S.K., Fowdur, S.J., Gawlikowski, J., Medina, D. (2021). Leveraging Evidential Deep Learning Uncertainties with Graph-based Clustering to Detect Anomalies. *Submitted to IEEE Transactions on Intelligent Transportation Systems (second round of reviews).*

- Fortini, L., Gandarias, J.M., Medina, D., Ajoudani, A. (2021) Deciphering OpenPose: Determination of 3D Position Error Models with RGB-D Cameras. *Submitted to IEEE Sensors Journal.*

- Medina, D., Castro-Arvizu, J. M., Grundhöfer, L., Vilà-Valls, J. (2021). Network RTK: A Collaborative Approach to Precise Positioning in Urban Scenarios. *Submitted to 2022 IEEE Aerospace Conference.*

- Bellés, A., Medina, D., Chauchat, P., Vilà-Valls, J. (2021). Reliable GNSS Joint Position and Attitude Estimation in Harsh Environments through Robust Statistics. *Submitted to 2022 IEEE Aerospace Conference.*

---

*Note: the material from these sources included in this thesis is not singled out with typographic means and references.*

# Other research merits

Along the elaboration of this thesis, a number of contributions were published. At the end of every chapter, the research contributions and the corresponding publications will be listed. Part due to having old good friends pursuing a research career and part due to my inability to decline any chance of collaboration, some of works listed below are not mentioned at the end of the chapters, to not affect the coherence of the thesis. Besides, a list of advised students and other research merits are enumerated.

## Additional Publications

- (November, 2020) Pastor, F., García-González, J., Gandarias, J. M., Medina, D., Closas, P., García-Cerezo, A. J., & Gómez-de-Gabriel, J. M. "Bayesian and Neural Inference on LSTM-Based Object Recognition from Tactile and Kinesthetic Information." Published in: *IEEE Robotics and Automation Letters, 6(1), 231-238.* Ref. [23].
  DOI: 10.1109/lra.2020.3038377
  Impact factor: 3.576 / Q1 (2020)
  Role: fourth author.

- (July, 2020) Vincent, F., Vilà-Valls, J., Besson, O., Medina, D., & Chaumette, E. "Doppler-aided positioning in GNSS receivers-A performance analysis." Published in: *Signal Processing, 176, 107713.* Ref. [24].
  DOI: 10.1016/j.sigpro.2020.107713
  Impact factor: 4.662 / Q1 (2020)
  Role: third author.

- (September, 2018) Ziebold, R., Medina, D., Romanovas, M., Lass, C., & Gewies, S. "Performance characterization of GNSS/IMU/DVL integration under real maritime jamming conditions." Published in: *Sensors, 18(9), 2954.* Ref. [25].
  DOI: 10.3390/s18092954
  Impact factor: 3.576 / Q1 (2020)
  Role: second author.

- (2020, September) Medina, D., Grundhöfer, L., & Hehenkamp, N. "Evaluation of Estimators for Hybrid GNSS-Terrestrial Localization in Collaborative Networks." Published in: *2020 IEEE 23rd International Conference on Intelligent Transportation Systems (ITSC) (pp. 1-7). IEEE.* Ref. [26].
  DOI: 10.1109/ITSC45102.2020.9294750
  Role: first author.

- (2019, September) Medina, D., Lass, C., Marcos, E.P., Ziebold, R., Closas, P. & García, J. “On GNSS Jamming Threat from the Maritime Navigation Perspective.” Published in: *2019 22th International Conference on Information Fusion (FUSION) (pp. 1-7). IEEE.* Ref. [27].
  URL: https://ieeexplore.ieee.org/abstract/document/9011348
  Role: first author.

## Patent

- Grundhoefer, L., Medina, D., (May 2021) Kooperative Navigation unter Nutzung von R-Mode. *In process.*

## Advised Students

- Belles Ferreres, A. “Robust Solutions for GNSS Position and Attitude Estimation under Model Mismatches”. Master Thesis. École Nationale de l’Aviation Civile (ENAC). May 2021 – December 2021.
- Álvarez Merino, C. “Partial Ambiguity Resolution for Multi-GNSS Precise Positioning Applications”. Master Thesis. Escuela Técnica Superior de Ingeniería de Telecomunicación, Universidad de Málaga. March 2019 – September 2019. Grade: *Outstanding* (9/10).
- Dalton. J. “Satellite Navigation for Autonomous Vehicles”. DAAD Scholarship. University of Rochester. May 2019 – August 2019.
- Centrone, V. “Techniques for attitude determination using GNSS carrier phase observations”. Politecnico di Torino. September 2018 – March 2019. Grade: *Cum Laude*.
- Gibson, K. “Stochastic Characterization of GNSS Observations”. Summer internship. Northeastern University Boston. June 2018 – August 2018.

## Other Research Activities

- Vice Chair for the German Chapter of the IEEE ITS Society (2021–Present).
- Secretary for the German Chapter of the IEEE ITS Society (2019–2020).
- 3 Special Sessions on “Navigation and Localization for Intelligent Transport. Systems” - International Conference on Intelligent Transportation Systems, IEEE ITSC 2019, IEEE ITSC 2020 and IEEE ITSC 2021. Role: Co-organizer with Pau Closas and Jordi Vilà-Valls.

- Member of the Technical Program Committee (TPC) for IEEE ITSC'19, IEEE FUSION'20, IEEE ITSC'20, IEEE FUSION'21, IEEE VTC'21 Spring, IEEE ITSC'21.
- Topical Advisory Panel Member for Section Remote Sensors for MDPI Sensors Journal.
- Best Presentation Award for the paper "Determination of pseudorange error models and multipath characterization under signal-degraded scenarios" [20] for the 31st International Technical Meeting of the Satellite Division of The Institute of Navigation (ION GNSS+ 2018).
- Best Paper Award for the paper "Robust Position and Velocity Estimation Methods in Integrated Navigation Systems for Inland Water Applications" [28] for the 2016 IEEE/ION Position, Location and Navigation Symposium (PLANS 2016).
- Award for the DLR internal project on international cooperation under "Robust Estimation for Safe Navigation (RESNav)" – Grant for two weeks of research visit to Prof. Pau closas at Northeastern University, Boston (USA) within the period 2022–2023.
- Invited talk on "Robust Statistics for GNSS Positioning" at the Robust GNSS Workshop, Telecommunications for Space and Aeronautics (TéSA), Toulouse (France), July 2019.
- Invited talk on "Sensor Fusion for Robust Navigation under GNSS Challenging Conditions" at Politecnico di Torino, Torino (Italy), March 2019.

# Abstract

Navigation information is an essential element for the functioning of robotic platforms and intelligent transportation systems. Among the existing technologies, Global Navigation Satellite Systems (GNSS) have established as the cornerstone for outdoor navigation, allowing for all-weather, all-time positioning and timing at a worldwide scale. GNSS is the generic term for referring to a constellation of satellites which transmit radio signals used primarily for ranging information. Therefore, the successful operation and deployment of prospective autonomous systems is subject to our capabilities to support GNSS in the provision of robust and precise navigational estimates.

GNSS signals enable two types of ranging observations: –*code pseudorange*, which is a measure of the time difference between the signal's emission and reception at the satellite and receiver, respectively, scaled by the speed of light; –*carrier phase pseudorange*, which measures the beat of the carrier signal and the number of accumulated full carrier cycles. While code pseudoranges provides an unambiguous measure of the distance between satellites and receiver, with a dm-level precision when disregarding atmospheric delays and clock offsets, carrier phase measurements present a much higher precision, at the cost of being ambiguous by an unknown number of integer cycles, commonly denoted as ambiguities. Thus, the maximum potential of GNSS, in terms of navigational precision, can be reach by the use of carrier phase observations which, in turn, lead to complicated estimation problems.

This thesis deals with the estimation theory behind the provision of carrier phase-based precise navigation for vehicles traversing scenarios with harsh signal propagation conditions. Contributions to such a broad topic are made in three directions. First, the ultimate positioning performance is addressed, by proposing lower bounds on the signal processing realized at the receiver level and for the mixed real- and integer-valued problem related to carrier phase-based positioning. Second, multi-antenna configurations are considered for the computation of a vehicle's orientation, introducing a new model for the joint position and attitude estimation problems and proposing new deterministic and recursive estimators based on Lie Theory. Finally, the framework of robust statistics is explored to propose new solutions to code- and carrier phase-based navigation, able to deal with outlying impulsive noises.

# Resumen

La información de navegación es un elemental fundamental para el funcionamiento de sistemas de transporte inteligentes y plataformas robóticas. Entre las tecnologías existentes, los Sistemas Globales de Navegación por Satélite (GNSS) se han consolidado como la piedra angular para la navegación en exteriores, dando acceso a localización y sincronización temporal a una escala global, irrespectivamente de la condición meteorológica. GNSS es el término genérico que define una constelación de satélites que transmiten señales de radio, usadas primordinalmente para proporcionar información de distancia. Por lo tanto, la operatibilidad y funcionamiento de los futuros sistemas autónomos pende de nuestra capacidad para explotar GNSS y estimar soluciones de navegación robustas y precisas.

Las señales GNSS permiten dos tipos de observaciones de alcance: –*pseudorangos de código*, que miden el tiempo transcurrido entre la emisión de las señales en los satélites y su acquisición en la tierra por parte de un receptor; –*pseudorangos de fase de portadora*, que miden la fase de la onda sinusoide que portan dichas señales y el número acumulado de ciclos completos. Los pseudorangos de código proporcionan una medida inequívoca de la distancia entre los satélites y el receptor, con una precisión de decímetros cuando no se tienen en cuenta los retrasos atmosféricos y los desfases del reloj. En contraposición, las observaciones de la portadora son super precisas, alcanzando el milímetro de exactidud, a expensas de ser ambiguas por un número entero y desconocido de ciclos. Por ende, el alcanzar la máxima precisión con GNSS queda condicionado al uso de las medidas de fase de la portadora, lo cual implica unos problemas de estimación de elevada complejidad.

Esta tesis versa sobre la teoría de estimación relacionada con la provisión de navegación precisa basada en la fase de la portadora, especialmente para vehículos que transitan escenarios donde las señales no se propagan fácilmente, como es el caso de las ciudades. Para ello, primero se aborda la máxima efectividad del problema de localización, proponiendo cotas inferiores para el procesamiento de la señal en el receptor y para el problema de estimación mixto (es decir, cuando las incógnitas pertenecen al espacio de números reales y enteros). En segundo lugar, se consideran las configuraciones multiantena para el cálculo de la orientación

de un vehículo, presentando un nuevo modelo para la estimación conjunta de posición y rumbo, y proponiendo estimadores deterministas y recursivos basados en la teoría de Lie. Por último, se explora el marco de la estadística robusta para proporcionar nuevas soluciones de navegación precisa, capaces de hacer frente a los ruidos atípicos.

# Contents

**Appendices**

# List of Figures

# List of Symbols

## Sets, spaces and manifolds

| | |
|---|---|
| $\mathbb{R}, \mathbb{C}, \mathbb{Z}, \mathbb{H}$ | The sets of Real, Complex and Integer numbers. The set of quaternions. |
| $\mathcal{M}$ | A smooth (usually Riemannian) manifold. |
| $\mathcal{S}^n$ | The unit sphere, $\mathcal{S}^n = \{\mathbf{x} \in \mathbb{R}^{n+1} : \mathbf{x}^\top \mathbf{x} = 1\}$. |
| $\mathcal{SO}(n)$ | Special orthogonal group, $\mathcal{SO}(n) = \{\mathbf{R} \in \mathbb{R}^{n,n} : \mathbf{R}^\top \mathbf{R} = \mathbf{I}_n, \det(\mathbf{R}) = 1\}$. |
| $\mathfrak{so}(n)$ | Lie algebra of $\mathcal{SO}(n)$. |
| $\emptyset$ | The empty set. |
| $\mathbb{R}^+$ | The set of non-negative real numbers. |
| $\mathbb{R}^n$ | The set of real-valued column vectors of size $n$. |
| $\mathbb{R}^{m,n}$ | The space of all $n$-tuples of Real numbers. |

## Matrices and Vectors

| | |
|---|---|
| $a, A$ | A scalar value. |
| $\mathbf{a}$ | A column vector. |
| $\mathbf{A}$ | A matrix. |
| $a_i, [\mathbf{a}]_i$ | The $i$th element for the vector $\mathbf{a}$. |
| $A_{i,j}, [\mathbf{A}]_{i,j}$ | The $i$th row, $j$th column element for the matrix $\mathbf{A}$. |
| $\mathbf{I}_n$ | Identity matrix of dimension $n \times n$ – the subscript may be omitted for notation convenience. |
| $\mathbf{1}_{n,m}$ | Matrix of dimension $n \times m$ whose all elements are equal to 1. |
| $\mathbf{0}_{n,m}$ | Matrix of dimension $n \times m$ whose all elements are equal to 0. |
| $\mathbf{A}^\top$ | Transpose of matrix $\mathbf{A}$. |
| $\mathbf{A}^{-1}$ | Matrix inverse of $\mathbf{A}$ which, for squares matrices, leads to $\mathbf{A}\mathbf{A}^{-1} = \mathbf{I}$. |
| $\mathbf{A}^H$ | Conjugate transpose or Hermitian transpose of matrix $\mathbf{A}$. |
| $\mathbf{A}^\dagger$ | Moore-Penrose pseudo-inverse of matrix $\mathbf{A}$.<br>If $\mathbf{A} \in \mathbb{R}^{n,m}$, with $m \leq n$, then $\mathbf{A}^\dagger = (\mathbf{A}^\top \mathbf{A})^{-1} \mathbf{A}^\top$.<br>If $\mathbf{A} \in \mathbb{R}^{n,m}$, with $n \leq m$, then $\mathbf{A}^\dagger = \mathbf{A}^\top (\mathbf{A}\mathbf{A}^\top)^{-1}$. |
| $\boldsymbol{\Pi}_{\mathbf{A}}$ | Orthogonal projector onto the subspace spanned by the columns of $\mathbf{A}$, such that $\boldsymbol{\Pi}_{\mathbf{A}} = \mathbf{A}\left(\mathbf{A}^\top \mathbf{A}\right)^{-1} \mathbf{A}^\top$ |
| $\boldsymbol{\Pi}_{\mathbf{A}}^{\perp}$ | Orthogonal projector onto the orthogonal complement to the columns of $\mathbf{A}$, such that $\boldsymbol{\Pi}_{\mathbf{A}}^{\perp} = \mathbf{I} - \boldsymbol{\Pi}_{\mathbf{A}}$ |

| | |
|---|---|
| $\mathbf{A} \otimes \mathbf{B}$ | Kronecker product of matrices $\mathbf{A}$ and $\mathbf{B}$. If $\mathbf{A} \in \mathbb{R}^{n,m}$, then $\mathbf{A} \otimes \mathbf{B} = \begin{bmatrix} [\mathbf{A}]_{1,1}\mathbf{B} & \dots & [\mathbf{A}]_{1,m}\mathbf{B} \\ \vdots & \ddots & \vdots \\ [\mathbf{A}]_{n,1}\mathbf{B} & \dots & [\mathbf{A}]_{n,m}\mathbf{B} \end{bmatrix}$ |
| det($\mathbf{A}$) | Determinant of a matrix. |
| tr($\mathbf{A}$) | Trace of a matrix. |
| diag($\mathbf{a}$) | Diagonal matrix whose diagonal entries are given by $\mathbf{x}$. |
| vec($\mathbf{A}$) | Subspace spanned by the columns of $\mathbf{A}$. |

## Random variables and estimation

| | |
|---|---|
| pdf | Abbr. for 'probability density function'. |
| $p_X(\mathbf{x})$ | pdf for the random variable $X$ as a function of the possible values $\mathbf{x}$. |
| $p(\mathbf{x})$ | shortcut for the term above. |
| $\mathbf{x}$ | alternate name for the random variable $X$. |
| $\hat{\mathbf{x}}$ | an estimate for the random variable $\mathbf{x}$. |
| $\mathbf{P}$ | The covariance matrix of $\mathbf{x}$. |
| $\mathcal{N}(\mathbf{x}, \mathbf{P})$ | Multivariate Gausian pdf with $\mathbf{x}$ mean and $\mathbf{P}$ covariance. |
| $\sigma_a$ | Standard deviation of the scalar variable $a$. |
| $\mathbb{E}(\cdot)$ | Statistical expectation. When used with a subindex, it specifies the distribution over which the expectation is taken:<br>$\mathbb{E}_x(\cdot)$ over the distribution of a random variable $x$;<br>$\mathbb{E}_{x,y}(\cdot)$ over the joint distribution of $x$ and $y$, $p(x, y)$;<br>$\mathbb{E}_{x\|y}(\cdot)$ over the joint distribution of $x$ conditioned on $y$, $p(x\|y)$. |
| $\mathbb{D}(\cdot)$ | Dispersion of. |

## Operators and functions

| | |
|---|---|
| Re$\{\cdot\}$, Im$\{\cdot\}$ | Real and imaginary parts, respectively. |
| exp$(\cdot)$ | Exponential function. |
| log$(\cdot)$ | Logarithm function. |
| $\oplus$ | Composition operator. |
| $\|a\|$ | Absolute value for $a$. |
| $\\|\mathbf{a}\\|$ | $\ell_2$ norm for the vector $\mathbf{a}$, such that $\\|\mathbf{a}\\| = \sqrt{\mathbf{x}^\top \mathbf{x}}$. |
| $\\|\mathbf{a}\\|_\mathbf{A}$ | Weighted squared norm of a vector, $\\|\mathbf{a}\\|_\mathbf{A} = \mathbf{a}^\top \mathbf{A}^{-1} \mathbf{a}$. |
| $\arg\max_x f(x)$ | Value that maximizes $f(x)$. |
| $\arg\min_x f(x)$ | Value that minimizes $f(x)$. |

## Observation Notation

| | |
|---|---|
| $\mathbf{y}$ | Generic vector of observations. |
| $\mathbf{\Sigma}$ | Covariance matrix for a generic vector of observations. |
| $\mathbf{h}(\cdot)$ | Generic observation function. |
| $\mathbf{f}(\cdot)$ | Generic dynamical model. |
| $\rho$ | Code pseudorange measurement. |
| $\Phi$ | Carrier phase pseudorange measurement. |
| $\lambda_c$ | Wavelength for a carrier signal of frequency $f_c$. |

# Acronyms

| | |
|---|---|
| **ADC** | Analog-to-Digital Converter. |
| **AltBOC** | Alternative Binary Offset Carrier. |
| **A-PPP** | Array-aided Precise Point Positioning. |
| **AWGN** | Additive White Gaussian Noise. |
| **BPSK** | Binary Phase Shift Keying. |
| **BOC** | Binary Offset Carrier. |
| **CDMA** | Code-Division Multiple Access. |
| **C-LAMBDA** | Constrained Least squares AMBiguity Decorrelation Adjustment. |
| **CN0** | Carrier-to-Noise Density Ratio, $C/N_0$. |
| **CRB** | Cramér-Rao Bound. |
| **DD** | Double-difference. |
| **DGNSS** | Differential Global Navigation Satellite System. |
| **DLL** | Delay Lock Loop. |
| **DPE** | Direct Position Estimation. |
| **DT** | Difference Test. |
| **ECEF** | Earth-Centered Earth-Fixed coordinate system. |
| **EKF** | Extended Kalman Filter. |
| **ENU** | East-North-Up coordinate system. |
| **ESKF** | Error State Kalman Filter. |
| **FAR** | Full Ambiguity Resolution. |
| **FF-RT** | Fixed Failure Rate Test. |
| **FDMA** | Frequency-Division Multiple Access. |

| | |
|---|---|
| **FIM** | Fisher Information Matrix. |
| **GIA** | Generalized Integer Aperture. |
| **GLONASS** | GLObalnaya Navigasionnay Sputnikovaya Sistema. |
| **GMKF** | Generalized M-estimator Kalman Filter. |
| **GN** | Gauss-Newton. |
| **GNSS** | Global Navigation Satellite System. |
| **GPS** | Global Positioning System. |
| **IA** | Integer Aperture. |
| **IAR** | Integer Aperture Resolution. |
| **IB** | Integer Bootstrapping. |
| **IE** | Integer Equivariant. |
| **ILS** | Integer Least Squares. |
| **IMU** | Inertial Measurement Unit. |
| **INS** | Inertial Navigation System. |
| **IR** | Integer Rounding. |
| **IRNSS** | Indian Regional Navigation Satellite System. |
| **ITS** | Intelligent Transportation Systems. |
| **JPA** | Joint Position and Attitude. |
| **KF** | Kalman Filtering. |
| **LAD** | Least Absolute Deviation. |
| **LAMBDA** | Least squares AMBiguity Decorrelation Adjustment. |
| **LB** | Lower Bound. |
| **LNA** | Low-Noise Amplifier. |
| **LOS** | Line-of-sight. |
| **LS** | Least Squares. |
| **MAP** | Maximum a Posteriori. |
| **MC-LAMBDA** | Multivariate-Constrained LAMBDA. |
| **ML** | Maximum Likelihood. |
| **MLE** | Maximum Likelihood Estimator. |
| **MSE** | Mean Squared Error. |
| **NCA** | Near Constant Acceleration. |

| | |
|---|---|
| **NCV** | Near Constant Velocity. |
| **NLOS** | Non-line-of-sight. |
| **PAR** | Partial Ambiguity Resolution. |
| **PD-PAR** | Precision-Driven Partial Ambiguity Resolution. |
| **PLL** | Phase Locked Loop. |
| **PNT** | Position, Navigation and Timing. |
| **PPP** | Precise Point Positioning. |
| **PRN** | Pseudo-Random Noise. |
| **PSD** | Power Spectral Density. |
| **PVT** | Position, Velocity and Timing. |
| **Q-LAMBDA** | Quaternion-based LAMBDA. |
| **QZSS** | Quasi-Zenith Satellite System. |
| **RAIM** | Receiver Autonomous Integrity Monitoring. |
| **RBE** | Recursive Bayesian Estimation. |
| **RF-FE** | Radio-Frequency Front End. |
| **RIF** | Robust Information Filter. |
| **RMSE** | Root Mean Square Error. |
| **RT** | Ratio Test. |
| **RTK** | Real Time Kinematic. |
| **RTN** | Real Time Network. |
| **SNR** | Signal-to-Noise Ratio. |
| **SPKF** | Sigma Point Kalman Filter. |
| **SPP** | Single Point Positioning. |
| **SSM** | State Space Model. |
| **TOW** | Time of Week. |
| **UAV** | Unmanned Aerial Vehicle. |
| **UKF** | Unscented Kalman Filter. |
| **VB** | Variational Bayesian. |
| **VI** | Variational Inference. |
| **VCE** | Variance Component Estimation. |
| **VKF** | Variational Kalman Filter. |
| **WLS** | Weighted Least Squares. |

# Introduction

The umbrella topic of this thesis relates to using Global Navigation Satellite Systems (GNSS) carrier phase measurements for the provision of precise navigation solutions. In particular, the focus lays on recursive positioning and attitude estimates for vehicles traversing outdoor scenarios with harsh signal propagation conditions. Under such environments, the received signals undergo delays due to multipath effects and the performance of satellite-based navigation is strongly jeopardized. It is introduced a collection of lower bounds to characterize the capability of a receiver to track satellite signals and its relationship to precise positioning performance, conditioned on the receiver operation point. Then, multi-antenna configurations are discussed as means of orientation information, the GNSS-based attitude models are revisited and new estimators based on Lie Theory are provided. Finally, robust filtering solutions against outlying observations are proposed and applied to carrier phase-based navigation to maximize the performance of GNSS even in complex scenarios.

## Motivation and Research Questions

Location-based services, alongside with modern intelligent transportation systems (i.e., driverless cars, autonomous shipping, unmanned navigation systems) and other safety-critical applications require reliable, continuous and precise positioning, navigation and timing (PNT) information for their successful operation and implantation in the market. GNSS constitutes the backbone and main information supplier of PNT data, and this dependence can only but grow in the future. Within the GNSS context, two types of ranging measurements can be obtained: 1) code observations, derived from the apparent signal time-of-arrival from the transmitter satellite to the receiver on Earth; 2) carrier phase observations, estimated by aligning a locally generated replica of the incoming signal and counting the cycles (time) elapsed over time.

The use of code observations is the gold standard for most commercial and mass-market receivers, leading to instantaneous positioning solutions of meter-level accuracy. Despite offering a fairly good performance in open sky conditions, the resulting accuracy results insufficient for a plethora of applications that need decimeter- to centimeter-level precision. Lane-awareness for automobiles, docking approaches for unmanned vessels or the operation of autonomous drones and robots are exemplary applications whose deed cannot be reached with conventional code-based localization methods. Therefore, the transition to carrier phase-based positioning techniques is required. GNSS receivers can measure the phase of carrier signals with millimeter accuracy, although such measurement is ambiguous due to the carrier periodicity. Indeed, since only the fractional part is tracked, the integer number of cycles elapsed between the transmitting satellite and the receiver is unknown. Using carrier phase observations results in the so-called mixed estimation problems where real- and integer-valued unknown parameters are to be regressed.

From within and outside the GNSS community, the mixed estimation problem constitutes a recurrent subject of study and a rich literature on the performance of various estimators is readily available. Nevertheless, the road towards resilient and precise carrier phase-based navigation systems is long from paved and relevant matters remain unaddressed. One of them leads to the question, *what is the connection between the signal processing at the receiver and the final PNT?* Chapter 1 addresses the question by relating the quality of the ranging observations with the processing performed at the channels of a receiver for tracking a satellite signal, given a set of "raw" digital samples. To do so, bounds for the problem of parameter estimation for a band-limited signal are derived. Then, provided a set of code and carrier phase observations, one would wonder, *what is the efficiency of estimators at solving the mixed estimation problem?* Chapter 2 sheds some light into the matter by introducing a new lower Cramér-Rao Bound (CRB) for the mixed model parameter vectors, with its application to carrier phase-based precise positioning being discussed. As previously discussed, the use of phase observables drives to the presence of an unknown number of integer ambiguities and the mixed estimation problem. Since an explicit solution to the former remains undiscovered, its estimation requires the decomposition of the same into three successive least-squares (LS) adjustments. Among them, the integer least-squares (ILS) comprises an increased complexity and the study of its performance, both empirically and analytically, has attracted the attention of numerous research works. Nonetheless, to understand what is the ultimate achievable phase-based positioning performance, under a certain satellite geometry and noise level, one shall address the complete mixed model. Thus, the second contribution of this thesis is the proposal of a closed-form lower CRB for the mixture of real- and integer-valued parameter vectors, its application to carrier phase-based positioning and the assessment of the asymptotic efficiency for the associated estimators.

Another well-known application of GNSS carrier phase measurements relates to attitude determination. Attitude estimation is the process of determining the spatial orientation of an object. Orientation information constitutes an important navigation component for vehicles that require attitude aiding, such as spacecraft or drones. GNSS enables resolving the orientation of a vehicle in a precise and absolute manner, by employing a setup of multiple GNSS antennas rigidly mounted onboard the tracked vehicle. The former represents an appealing alternative to magnetomers, gyroscopes or other means of orientation tracking, providing a drift-less absolute attitude solution while posing a fair compromise in terms of cost, weight and precision. While the GNSS compass model has been extensively explored, especially as constrained minimization problems to integrate the geometrical constraints (i.e., the known distance between antennas and their relative orientation), its extension to recursive solutions is not as widespread. The question is, *how can the GNSS attitude problem be recursively estimated with minimal state parametrization?* Chapter 3 provides some hints for such question. A key factor consists on the use of unit quaternions as orientation parametrization. Unlike rotation matrices or Euler angles, quaternions provide minimal state representation while posing no singularity problems. Moreover, the time evolution equations based on quaternions are continuous and continuously derivable, something useful for filtering solutions and integration with other sensors. Thus, Chapter 3 contribution relates to (re-)formulating the GNSS-based attitude problem using Lie Theory principles and the proposal of the Error State Kalman Filter (ESKF) for recursive attitude estimation.

The combination of positioning and attitude information for a certain object provides its complete static characterization, also known as pose of such object. On the other hand, the description of a rigid body kinematics (i.e., the navigation information) also includes the velocity and their evolution over time. Traditionally —and particularly from the focal point of experts on the use of carrier phase observations—, the positioning and attitude determination problems are considered as two independent processes. Even when integrated as part of the same filtering solution, the cross-correlation between the positioning- and attitude-related observations is disregarded. However, this information results very useful, and it strengthens the overall observation model. The question then raises on, *how to optimally approach the joint positioning and attitude estimation problem?* Chapter 4 extends the principles on Lie Theory previously introduced and formalize the concept of joint position and attitude (JPA) based on the exploitation of GNSS carrier phase observables.

Regardless of whether one is concern with positioning and/or attitude estimation, a common challenge for safety-critical applications concerns with the special conditions occurring in urban situations. Urban scenarios are typically affected by multipath and non-line-of-sight (NLOS) propagation conditions. This means that satellite signals arrive to a receiver either as a composite of direct LOS and additional paths due to reflection and refraction (multipath) or as a single reflected signal (NLOS). Such conditions lead to tracking errors in the receiver and subsequently code and phase measurement errors. In result, the noise present on a portion of the observations do not obey the normal-distributed assumption. Conventional estimators, both in the framework of Maximum Likelihood (ML) and Maximum a Posteriori (MAP) estimation cannot cope with outlying observations, up to the point that a single outlier could spoil the estimated solution. The questions to address are *what are robust estimators, how do they work? How to successfully apply robust estimators in the context of carrier phase-based positioning?* These questions are addressed in Chapters 5 and 6, respectively. Chapter 5 presents the basic principles of the Robust Statistics framework and introduces well-known estimators typically applied for linear regression. Instantaneous (memoryless) code-based positioning serves as exemplary application of the aforementioned estimators, showcasing their characteristics in terms of robustness and loss-of-efficiency. Then, Chapter 6 focuses on state-space models involving Gaussian distributions under nominal conditions along with additional outliers under non-nominal conditions. In particular, we are interested in filtering solutions robust against model mismatch and its application to carrier phase-based positioning under challenging scenarios. For such end, the conventional ML-styled mixed model is expressed as a MAP problem, Robust Statistics-based filters are particularized for the MAP mixed model and a Generalized Variational-based KF for outlier rejection is proposed.

In summary, this thesis proposes

- A new CRB for the standard GNSS narrowband signal model. The CRB is expressed in terms of signal samples, making easy to use irrespective of the considered based signal.
- A CRB for the mixed estimation problem, which results key to understand the performance of carrier phase-based positioning. As a particular case of the general bound, a closed-form expression for the Real Time Kinematics (RTK) functional model is derived. A (very) useful property of such CRB expression is its ability to predict the RMSE performance of the MLE.
- Leveraging on the CRB for the signal parameters and for the mixed model, to theoretically assess positioning techniques from the baseband signal model in terms of the CRB and MLE. Important related findings are:

  - Bridging the gap between receiver performance, the quality of the observables and the final positioning performance.
  - Large bandwidth signals, such as Galileo E5 or modern meta-signals, can be exploited for code-based positioning to potentially reach decimeter-level accuracies.

- A new estimator for the attitude mixed model problem, denoted as Q-LAMBDA, which leverages on quaternion parametrization and Lie Theory for solving the orientation-related parameters and on integer reparametrizations and ILS for estimating the carrier ambiguities.

- Exploiting the unit quaternion and its associated Lie Algebra as orientation representation for GNSS-based attitude estimation.

- The joint position and attitude (JPA) model to exploit the cross-correlation between positioning- and attitude-related observations. Deterministic and recursive estimators are proposed, making use of general forms of Q-LAMBDA and ESKF respectively.

- A framework of robust instantaneous and recursive solutions and its application to code- and carrier-phase based navigation.

- A Generalized form of the Variational-based Kalman Filter for outlier rejection with correlated measurements (e.g., the RTK case), and particular cases for independent data with multiple or a single indicators.

## Thesis Structure and Reading Directions

Besides the introductory and concluding chapters, this dissertation is organized in three parts which assess three distinct topics: I) Signal Processing for GNSS, II) Position and Attitude Determination for Multi-Antenna Setups and III) Robust Estimation for Navigation under Harsh Conditions. While each of the topics represents a broad line of research on their own, the use of carrier-phase observations constitutes the leitmotif and the connection thread of these three. A final part has been reserved for the appendices.

This dissertation is devised to provide a comprehensive guide on the use of carrier phase observations for navigation-related problems, while dealing with a recurrent challenge on GNSS, namely treating with multipath and other outlying measurements. Thus, students who read this work shall learn the fundamentals of GNSS-based precise pose estimation and the particulars related to using carrier phase observations.

# Part I

# A Signal Processing Approach to Satellite-based Navigation

# CHAPTER 1

# Fundamentals of Global Navigation Satellite Systems

GLOBAL Navigation Satellite System (GNSS) is the generic term employed to identify radionavigation systems based on a constellation of satellites. Besides the well-known Global Positioning System (GPS), i.e., the American GNSS, the GNSS list includes the European Galileo, the Russian GLONASS and the Chinese BeiDou. These systems share the same working principle, for which an user estimates his or her localization based on the observed distances between the receiver and the tracked satellites. Thus, GNSS satellites continuously transmit radio signals in the L frequency band (between 1.2 and 1.6 GHz). A receiver interprets the ranging codes and navigation data included in such signals, allowing to identify the transmitting satellites and their positions, as well as computing the traveling time through space and the consequent range information. GNSS has become an integral part of our modern society, with billions of users around the globe, and the cornerstone for the provision of Positioning, Navigation and Timing (PNT) information. Besides serving localization data for Intelligent Transportation Systems (ITS)-related applications, there is an evergrowing dependency on GNSS for timing purposes, for which power grid distribution, finances or emergency responses rely on. This chapter introduces the basic notions on GNSS, including a brief historical remark, the general GNSS signal model and how ranging observations are derived from the former.

## Outline

## 1.1 Overview on GNSS Constellations

Information on your current location is now taken for granted by virtually anyone with access to a *smarthphone*. Funnily enough, the vast majority of users are unaware of the enormous effort behind the deployment and operability of a GNSS constellation. To understand the current status of radio-navigation, it is interesting to revisit the development of satellite-based navigation from a historical perspective. In $17th$ July 1995, the American Global Positioning System (GPS) was declared fully operational and, since then, provides positioning and timing for users worldwide regardless of the weather conditions. The deployment of GPS extended for over 20 years and it results partly possible after the lessons learned from its ancestor, Transit, which was the world first satnav system. Interestingly, it was the motivation for tracking the orbit of the Russian Sputnik satellite which inspired the concept of satellite-based navigation and lead to building Transit. More than 30 years later, GNSS technology has undergone substantial development, with GPS currently listing 31 operational satellites. Furthermore, the Russian GLONASS (acronym derived from GLObal'naya NAvigatsionnaya Sputnikovaya Sistema) and the Chinese BeiDou constellations are declared fully operational and (even!) the European Galileo launched its initial services at the end of 2016. The regional Japanese and Indian satellite navigation systems –Quasi-Zenith Satellite System (QZSS) and Indian Regional Navigation Satellite System (IRNSS), respectively– complete the list of constellation deployed for the provision of PNT information. An extensive and truly fascinating historical overview can be found in [29], [30]. Satellite coverage is now rich in terms of both number of satellites and received frequencies. Fig. 1.1 illustrates an overview on the normalized power spectra (on a logarithm scale) for different code-division multiple access (CDMA) GNSS signals (i.e., GLONASS frequency-division multiple access (FDMA) signals are disregarded) and their allocation along the L-band frequency.

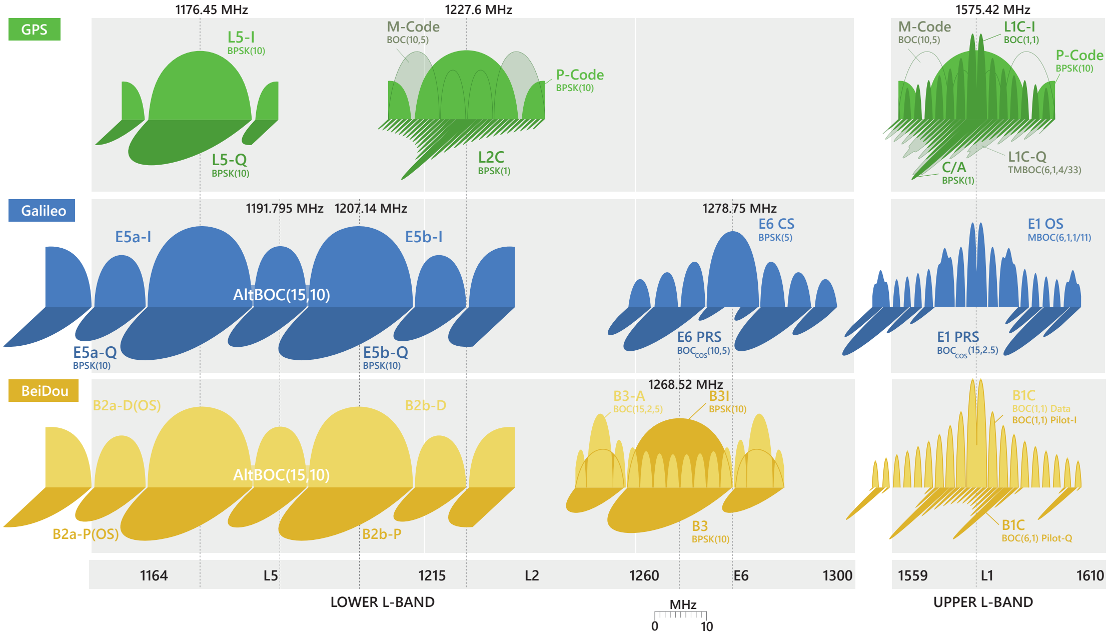

**Figure 1.1:** Overview on the power spectra versus the frequency allocation of GPS, Galileo and Beidou GNSS constellations.

Along with the deployment of the aforementioned GNSS constellations, new frequencies and ranging codes have been incorporated. In comparison with legacy signals, such as GPS coarse/acquisition (C/A), modern GNSS signals include *pilot* (dataless) components, longer codes, wider bandwidth modulations and more content on the navigation data [30, Ch. 7]. Table 1.1 provides an overview on the modern signals for GPS, Galileo and BeiDou, with the fundamental frequency $f_0 = 10.23$ MHz.

**Table 1.1:** Overview on GNSS navigation signals and their characteristics.

| **System** | **Band** | **Carrier freq.** (MHz) | **PRN code** | **Code rate** (Mcps) | **Data rate** (bps) | **Channel** | **Service** |
|---|---|---|---|---|---|---|---|
| GPS | L1 | $154 \cdot f_0$ | C/A | $f_0/10$ | 50 | Data | Open |
| | | | P(Y) | $f_0$ | 50 | Data | Military |
| | | | M | $f_0/2$ | N/A | Data | Military |
| | | | L1C-I | $f_0/10$ | 50 | Data | Open |
| | | | L1C-Q | $f_0/10$ | – | Pilot | Open |
| | L2 | $120 \cdot f_0$ | P | $f_0$ | 50 | Data | Military |
| | | | M | $f_0/10$ | N/A | Data | Military |
| | | | L2C-M | $f_0/10$ | 25 | Data | Open |
| | | | L2C-L | $f_0/10$ | – | Pilot | Open |
| | L5 | $115 \cdot f_0$ | L5C-I | $f_0$ | 50 | Data | Open |
| | | | L5C-Q | | – | Pilot | |
| Galileo | E1 | $154 \cdot f_0$ | E1A | $f_0/4$ | N/A | Data | PRS |
| | | | E1B | $f_0/10$ | 125 | Data | Open, CS |
| | | | E1C | $f_0/10$ | – | Pilot | SoL |
| | E6 | $125 \cdot f_0$ | E6A | $f_0/2$ | N/A | Data | PRS |
| | | | E6B | | 500 | Data | CS |
| | | | E6C | | – | Pilot | CS |
| | E5 | $115 \cdot f_0$ | E5a-I | $f_0$ | 25 | Data | Open |
| | | | E5a-Q | | – | Pilot | Open |
| | | $118 \cdot f_0$ | E5b-I | | 125 | Data | Open, CS |
| | | | E5b-Q | | – | Pilot | SoL |
| BeiBou | B1 | $154 \cdot f_0$ | B1 | $f_0/5$ | 50 | Data | Authorized |
| | | | B1C-I | $f_0/10$ | 50 | Data | Open |
| | | | B1C-Q | $f_0/10$ | – | Pilot | Open |
| | B3 | $124 \cdot f_0$ | B3 | $f_0$ | 500 | Data | Authorized |
| | | | B3A-I | $f_0/4$ | 50 | Data | |
| | | | B3A-Q | $f_0/4$ | – | Pilot | |
| | B2 | $115 \cdot f_0$ | B2a-I | $f_0$ | 25 | Data | Open |
| | | | B2a-Q | | – | Pilot | |
| | | $118 \cdot f_0$ | B2b-I | | 50 | Data | |
| | | | B2b-Q | | – | Pilot | |

Such GNSS signal modernization aims at supporting advanced features, such as improved tracking capabilities under tree foliage or in indoor scenarios, robustness against jamming and spoofing, or enhanced tracking under multipath environments. For instance, Galileo contemplates the offer of distinct services, namely: an Open Service (OS), available to worldwide users free of cost; a Public Regulated Service (PRS), intended for authorities and presenting enhanced modulation and encryption for interference robustness; a Commercial Service (CS), with encrypted signals and higher data rates; a Search and Rescue (SAR) service with a distress signal; and the Safety-of-Life (SoL) service for the aviation community in accordance to the International Civil Aviation Organization (ICAO) standards [31, Ch. 2].

### 1.1.1 A Quick Glance to GNSS Meta-Signals

Besides the formerly described signals, the paradigm of *meta-signals* is rapidly growing in interest. The concept of meta-signals consists of processing two or more GNSS signals, transmitted at different carrier frequencies, in a joint manner as a single signal. At the cost of a more complex receiver design, meta-signals allow for an effective processing strategy in terms of bandwidth exploitation. The latter enables obtaining a better baseband resolution and, therefore, more precise code observables. The main asset relates to obtaining sub-meter positioning in urban scenarios, where the tracking performance of carrier phase observables is jeopardized by the harsh propagation conditions [32].

The idea to process two signals at different frequency bands derives from the Galileo E5 design, proposed by the Galileo Signal Task Force in the early 2000s. Originally, an AltBOC (alternative Binary Offset Carrier) modulation was considered to transmit the E5A and E5B signals using an unique high power amplifier. Following that principle, [33] introduced the meta-signal concept and proposed the combinations of Galileo E5a and E5b with E6. An AltLOC (alternative Linear Offset Carrier) signal can also be exploited to form meta-signals, being equivalent to an AltBOC signal once a transmitter filters the intermodulation products and the harmonics of that AltBOC [34].

To conform a new AltLOC-modulated meta-signal, two independent Pseudo-Random Noise (PRN) codes are multiplexed. To do so, one can build a single side band (SSB) subcarrier and its conjugate, as

$$\begin{aligned} s_{ssb}(t) &= \frac{1}{\sqrt{2}}\left(\cos\left(2\pi f_s t\right) + j\cdot\sin\left(2\pi f_s t\right)\right), \\ s^*_{ssb}(t) &= \frac{1}{\sqrt{2}}\left(\cos\left(2\pi f_s t\right) - j\cdot\sin\left(2\pi f_s t\right)\right), \end{aligned} \tag{1.1}$$

where $f_s$ is the subcarrier frequency. For the combination of two signals, the resulting AltLOC metasignal $s_{ms}(t)$ is defined as

$$\begin{aligned} s_{ms}(t) &= s_a(t)s^*_{ssb}(t) + s_b(t)s_{ssb}(t), \\ &= \left[s_a(t) + s_b(t)\right]\cos\left(2\pi f_s t\right) + j\cdot\left[s_b(t) - s_a(t)\right]\sin\left(2\pi f_s t\right), \end{aligned} \tag{1.2}$$

with $s_a(t)$ and $s_b(t)$ the combined signals sorted in ascending frequency band. An interesting feature is that, the code rate can be different for the $s_a(t)$ and $s_b(t)$ signals. An AltLOC signal is typically described with four parameters, i.e., AltLOC$(p, q, w, b)$, and based on a fundamental frequency $f_0 = 1.023$ MHz. Thus, $p\cdot f_0$ describes the subcarrier frequency, $f_{c,a} = q\cdot f_0$ and $f_{c,a} = q\cdot f_0$ represent the code rate for the signals $a$ and $b$, respectively, and $b\cdot f_0$ is the receiver bandwidth.

Although commercial receivers do not currently feature meta-signal tracking capabilities, the latter will become a key player on defining the performance limits for satellite-based localization. In this thesis, a set of meta-signals is considered and their performance for signal parameter estimation, code- and carrier phase-based positioning analyzed in Sections 1.5.2 and 2.6, respectively. The meta-signals studied include the GPS L5C+L2C, the Galileo E5+E6B and E5a+E6B, as well as the BeiDou B2+B3A and B2a+B3A. Fig. 1.2 illustrates the normalized PSD of the aforementioned meta-signals, as well as their corresponding AltLOC modulation and central frequencies. Notice that, for simplicity, only the pilot components are depicted –e.g., E5 is generated using E5a-Q and E5b-Q, or the GPS meta-signal regards L2C-Q and L2C-L–.

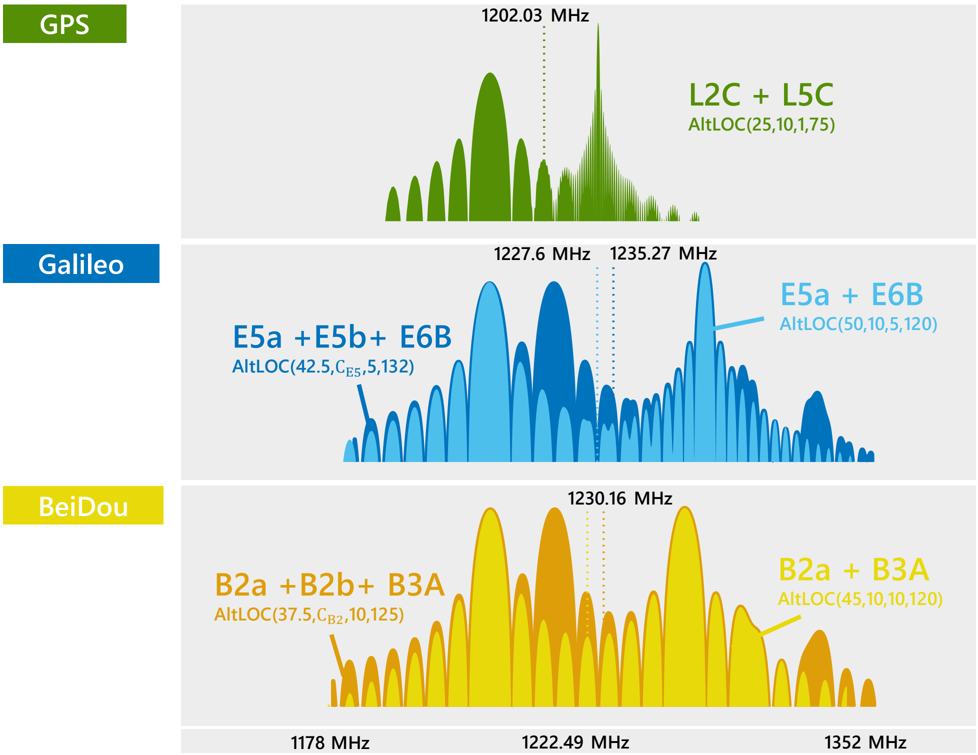

**Figure 1.2:** Power spectral density (PSD) against frequency for different meta-signals.

## 1.2 GNSS Signal Processing

This section examines the main signal processing procedures required for the correct functioning of a generic GNSS receiver. This includes the general GNSS signal model the receiver architecture and the signal parameter estimation. Also, a new form of bound associated with the signal parameter estimation is introduced.

### 1.2.1 Signal Model and Receiver Architecture

A generic signal broadcast by the different satellite constellations relates to a main *carrier* sinusoidal signal, centered at a particular carrier frequency $f_c$, upon which a multiplexing scheme based on phase shift keying is used to code information. The resulting direct-sequence spread-spectrum (DS-SS) signal encodes a multilayer structure formed by: i) the *navigation data* $D(t)$, a low rate stream of binary-coded message with information on satellite orbital parameters, clock biases and health status, as well as a timestamp for the transmission time; ii) the *ranging code* $C(t)$, or PRN code, a sequence of zeros and ones with good autocorrelation and low cross-correlation (i.e., quasi orthogonality) properties which serves as a satellite unique fingerprint. Thus, a signal transmitted by a GNSS satellite in a frequency band is modeled as

$$s(t) = \sqrt{2P(t)}\,\underbrace{D(t)}_{\text{nav}}\,\underbrace{C(t)}_{\text{PRN}}\,\underbrace{\exp\left(j2\pi f_c t\right)}_{\text{carrier}}, \tag{1.3}$$

where $P$ is the signal power and the navigation sequence $D$ shall be either $\pm 1$ or 1 based on whether the signal has a data component (modulated with a binary phase-shift keying (BPSK)) or is a pilot signal. Other coding alternatives, such as BOC, AltBOC or AltLOC would lead to further modifying the ranging code $C(t)$ [30, Ch. 14]. The transmission of multiple signals with different PRNs on the same carrier frequency is commonly referred to as CDMA [35, Ch. 4].

Upon its reception on Earth, the time-delayed signal interpreted by a GNSS receiver for a particular satellite is attenuated in amplitude and its frequency is affected by a Doppler shift effect, leading to the following signal model

$$r_{\mathsf{RF}}(t) = AD\left(t-\tau\right)C\left(t-\tau\right)\exp\left(j2\pi(f_c+f_d)t+\varphi\right)+n_{\mathsf{RF}}(t), \tag{1.4}$$

where $\tau$ is the code delay (s), $f_d$ is the carrier Doppler shift (Hz) due to the transmitter-receptor relative speed, $\varphi$ is the instantaneous carrier phase delay (rad) and $n_{\mathsf{RF}}$ is some complex additive white Gaussian noise (AWGN).

The radio-frequency front end (RF-FE) constitutes the hardware component of a receiver dealing with the analog signal and results key for the subsequent signal processing to be successful. At this stage of the receiver, the very high frequency and low power of GNSS signals would impede digital processors from generating carrier replicas in real time. Thus, a RF-FE generally includes a low-noise amplifier (LNA), a down-conversion of the signal to an intermediate frequency (IF) and a bandpass filter with a given bandwidth $B$ (Hz) to remove image frequencies [36]. Finally, an analog-to-digital converter (ADC) performs the digitization process, i.e., the conversion of continuous time to discrete samples. As a result, (1.4) can be formulated in the IF discrete domain as

$$\begin{aligned} r_{\mathsf{IF}}[k;\mathbf{x}] &= AD\left[T_s k-\tau\right]C\left[T_s k-\tau\right]\exp\left(j2\pi(f_{\mathsf{IF}}+f_d)T_s k+\varphi\right)+n_{\mathsf{IF}}[k], \\ \mathbf{x} &= \left[\tau, f_d, \varphi, A, \sigma^2\right]^\top, n_{\mathsf{IF}}[k]\sim\mathcal{NC}(0,\sigma^2), \end{aligned} \tag{1.5}$$

where $T_s$ is the sampling time interval (s) and $n_{\text{IF}}$ is the corresponding noise at the IF. Finally, one can identify the vector of unknown signal parameters $\mathbf{x}$, whose estimation leads to obtaining the code and carrier phase observations.

Conventional GNSS receivers resolve the complete PVT problem following a well-known two-step procedure, as illustrated in Fig. 1.3. First, the signal parameters $\tau, \varphi, f_d$ in $\mathbf{x}$ are estimated independently at each of the receiver channels using a matched filter w.r.t. a local replica (equivalent to a ML solution). Code and carrier phase pseudorange and pseudorange rate observables are built upon the estimated time delays, carrier offsets and Doppler shifts. Secondly, pseudorange observations are fed to a positioning algorithm to resolve the user location through a trilateration problem. This popular two-step approach is known to be asymptotically equivalent [37] to the denoted Direct Positioning Estimation (DPE), introduced by Closas in his series of works, which is the ML solution directly in the position and velocity domains, preserving the problem geometry, from the IF signal samples [38]–[40]. Despite its optimality, the implementation of DPE into mass-market receivers is jeopardized by its high computational complexity[1], while the two-step procedure is performed by the vast majority (if not all) commercial receivers. Hereinafter, this thesis focuses on the conventional two-step approach.

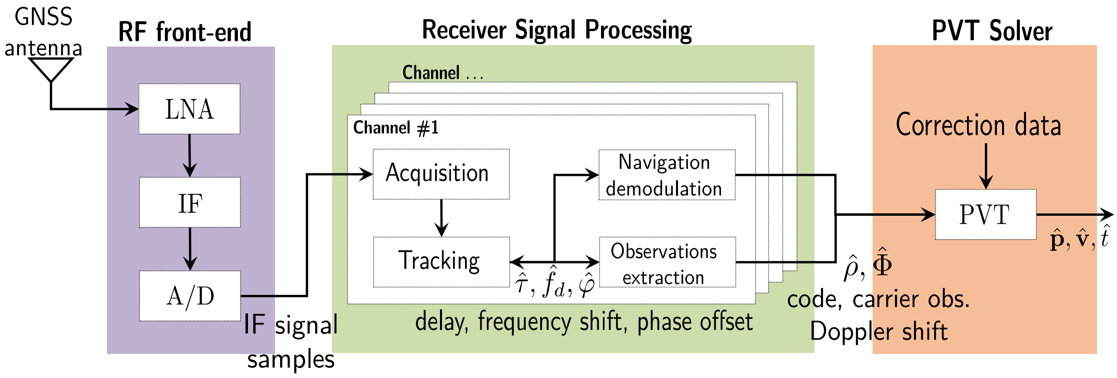

**Figure 1.3:** Block diagram of a generic GNSS receiver architecture and its functional blocks.

### 1.2.2 Signal Parameter Estimation and Associated Bounds

In this subsection, the maximum likelihood estimator (MLE) of the signal parameters is discussed and the compact Cramér-Rao Bound (CRB) associated to such estimation is presented in terms of signal samples. Prior to these notions, terms such as the time delay dilation due to the Doppler effect and the vector of considered signal samples as introduced.

Let us consider that both the transmitter (i.e., the $i$th satellite) and the $j$th receiver move following an uniform linear motion. In this context, the evolution of the propagation delay $\tau_0(t)$ evolves over time due to the relative radial movement between transmitter and receiver and can, during the observation time, be approximated by a first order distance-velocity model

$$\|\mathbf{p}_i\left(t-\tau_0\left(t\right)\right)-\mathbf{p}_j\left(t\right)\| = c\cdot\tau_0\left(t\right) \simeq d + v\cdot t$$
$$\Rightarrow\ \tau_0\left(t\right) \simeq \tau + b\cdot t, \quad \tau = \frac{d}{c},\ b = \frac{v}{c},$$

---

[1] Notice that conventional receivers (two-step procedure) perform a 2-dimensional search of the delay and Doppler shift during the signal acquisition step for each satellite link using 4 to 12 Msamples/s, with this stage being the most time and power consuming of a receiver. Then, the PVT computation rate is, at most, 1 KHz. Instead, DPE requires an 8-dimensional (for 3D position, velocity, clock offset and clock offset rate) grid search for the same 4 to 12 Msamples/s, which leads to a prohibitive computational load for miniaturized platforms.

where $c$ is the speed of light, $d$ is the relative radial distance, $v$ is the relative radial velocity, and $b$ is a delay drift related to the Doppler effect. Thus, the relative uniform radial movement is characterized by the time-delay $(\tau)$ due to the propagation path and the dilation $(1-b)$ induced by the Doppler effect.

Based on the simplification that the relative radial distance remains constant over the observation time, let us consider the acquisition of $N$ signal samples, expressed following the signal model in (1.5), over the sampling time $T_s = 1/F_s$, such that $N_1 \leq N \leq N_2$. Then, the vector of baseband samples $\mathbf{y}$ is given by

$$\mathbf{y} = \mathbf{r}(\mathbf{x}) + \mathbf{n} = A \cdot \mathbf{r} \cdot \exp(j\varphi) + \mathbf{n}, \quad \text{with } A \in \mathbb{R}^+,\ 0 \leq \varphi \leq 2\pi \ , \tag{1.6}$$

$$\mathbf{n} = [n[N_1 T_s], \dots, n[nT_s], \dots, n[N_2 T_s]]^\top \ , \tag{1.7}$$

$$\mathbf{r} = [\dots, D\,[nT_s - \tau]\,C[nT_s - \tau]\exp\left(j\omega_c b(nT_s - \tau)\right), \dots]^\top \ , \ , \tag{1.8}$$

$$\mathbf{c} = [\dots, C[nT_s], \dots]^\top \ , \tag{1.9}$$

where $\omega_c = 2\pi f_c$, $n \in \mathcal{CN}(0, \sigma^2)$ is the noise term and $\mathbf{r}$ is the sampled signal offset by the fractional component of the phase $\exp(j\varphi)$.

Notice that $C[\cdot]$ can be a PRN code with a Binary Phase Shift Keying (BPSK) modulation without a subcarrier, as for GPS L1 C/A, or a subcarrier modulated PRN, as for the modernized GPS L1C or Galileo E1. The subcarrier has a direct impact on the correlation function and, therefore, on the estimation performance. On top of that, the signal may have data bits or not, depending if it belongs to a data component or a pilot component (i.e., $D[\cdot]$ may or not evolve over time). Unless advanced receiver architectures are considered, i.e., long and/or non-coherent integration times as for Assisted GNSS [41], the navigation bit is assumed to not change over the integration time interval. In that case, $\mathbf{r}$ in (1.8) can be further simplified by removing the data component $D[\cdot]$.

Thus, to acquire and track the incoming GNSS signal, the receiver creates a replica signal $\mathbf{a}(\boldsymbol{\theta})$ whose parameters $\boldsymbol{\theta} = [\tau, b]^\top$ comprise the time delay and frequency dilation due to the Doppler effect. The list of unknown parameters to estimate also includes the phase offset, the signal amplitude and the variance of the noise term. The resulting vector of parameters to estimate $\mathbf{x}$ is

$$\mathbf{x} = \left[\tau,\ b,\ \varphi,\ A,\ \sigma^2\right]^\top = \left[\boldsymbol{\theta}^\top,\ \varphi,\ A,\ \sigma^2\right]^\top . \tag{1.10}$$

A basic receiver configuration would only require the estimation of the time delay and the frequency dilation, which suffices for the construction of code pseudorange observables. Else, the estimation of the carrier phase offset enables constructing carrier phase observables and the ratio between amplitude and noise defines measures of the signal strength.

ML estimators for the signal parameters in (1.10) are typically based on the EXtended Invariance Principle (EXIP) [42], for which a re-parametrization simplifies the Maximum Likelihood (ML) criterion to be maximized. Thus, the unknown delay and Doppler are estimated first through a Weighted Least Square (WLS) and then the phase offset estimate follows, as

$$\widehat{\boldsymbol{\theta}} \triangleq \begin{bmatrix} \hat{\tau} \\ \hat{b} \end{bmatrix} = \arg\max_{\boldsymbol{\theta}} \left\{ \left\| \left( \mathbf{a}^H\left(\boldsymbol{\theta}\right) \mathbf{a}\left(\boldsymbol{\theta}\right) \right)^{-1} \mathbf{a}^H\left(\boldsymbol{\theta}\right)\ \mathbf{y} \right\|^2 \right\}, \tag{1.11}$$

$$\widehat{\varphi}\left(\widehat{\boldsymbol{\theta}}\right) = \arg\left\{ \left( \mathbf{a}^H(\widehat{\boldsymbol{\theta}}) \mathbf{a}(\widehat{\boldsymbol{\theta}}) \right)^{-1} \mathbf{a}^H(\widehat{\boldsymbol{\theta}})\ \mathbf{y} \right\} . \tag{1.12}$$

Notice that the phase MLE is given by the argument of the cross-ambiguity function evaluated at the delay and Doppler MLEs. Then, if the estimator for the delay and Doppler reached its asymptotic performance so does the phase estimate. Thus, the MLE of the $\boldsymbol{\theta}$ parameters corresponds to the values for which the power at the output of a matched filter w.r.t. a local replica is maximized [30, Ch. 4]. To do so, a correlator computes the integration of the received signal multiplied with the locally generated replica signal for a certain coherent integration time. In practice, the MLE in (1.11) is performed using a delay locked loop (DLL) during the tracking scheme, which is equivalent to applying a gradient ascent method for such nonlinear regression problem [30, Ch. 14].

Having discussed the estimation process for the GNSS signal model, the CRB associated to the same estimation problem is discussed next. The multi-parameter CRB states that, for any locally unbiased estimate $\hat{\mathbf{x}}$ of a generic, real-valued parameter vector $\mathbf{x}$, the covariance matrix of the estimates is bounded by the reciprocal CRB

$$\mathbf{CRB}_{\mathbf{x}} \leq \mathrm{cov}(\hat{\mathbf{x}}) \triangleq \mathbb{E}_{\mathbf{y},\mathbf{x}}\left\{ (\hat{\mathbf{x}} - \mathbf{x})(\hat{\mathbf{x}} - \mathbf{x})^{\top} \right\}, \tag{1.13}$$

where the matrix inequality $\mathbf{CRB}_{\mathbf{x}} \leq \mathrm{cov}(\hat{\mathbf{x}})$ indicates that the matrix $\mathrm{cov}(\hat{\mathbf{x}}) - \mathbf{CRB}_{\mathbf{x}}$ is positive semidefinite. The first contribution for this chapter relates to the derivation of such a CRB in terms of discrete signal samples.

Then, expressing the CRB with its submatrices:

$$\mathbf{CRB}_{\mathbf{x}} = \begin{bmatrix} \mathbf{CRB}_{\boldsymbol{\theta}} & \mathbf{CRB}_{\boldsymbol{\theta},\varphi} & \mathbf{CRB}_{\boldsymbol{\theta},A} & \mathbf{CRB}_{\boldsymbol{\theta},\sigma^2} \\ \mathbf{CRB}_{\boldsymbol{\theta},\varphi}^{\top} & CRB_{\varphi} & CRB_{\varphi,A} & CRB_{\varphi,\sigma^2} \\ \mathbf{CRB}_{\boldsymbol{\theta},A}^{\top} & CRB_{\varphi,A} & CRB_{A} & CRB_{A,\sigma^2} \\ \mathbf{CRB}_{\boldsymbol{\theta},\sigma^2}^{\top} & CRB_{\varphi,\sigma^2} & CRB_{A,\sigma^2} & CRB_{\sigma^2} \end{bmatrix}, \tag{1.14}$$

the different block matrices are described next. Starting with the diagonal terms, the components of $\mathbf{CRB}_{\mathbf{x}}$ are as follows

$$\mathbf{CRB}_{\boldsymbol{\theta}} = \frac{1}{2\mathsf{SNR}_{\mathsf{out}}}\boldsymbol{\Delta}_{\boldsymbol{\theta}}^{-1} = \frac{1}{2\mathsf{SNR}_{\mathsf{out}}}\begin{bmatrix} [\boldsymbol{\Delta}_{\boldsymbol{\theta}}]_{1,1} & [\boldsymbol{\Delta}_{\boldsymbol{\theta}}]_{1,2} \\ [\boldsymbol{\Delta}_{\boldsymbol{\theta}}]_{2,1} & [\boldsymbol{\Delta}_{\boldsymbol{\theta}}]_{2,2} \end{bmatrix}^{-1}, \tag{1.15}$$

$$[\boldsymbol{\Delta}_{\boldsymbol{\theta}}]_{1,1} = F_s^2\left[\frac{\mathbf{c}^H\mathbf{V}\mathbf{c}}{\mathbf{c}^H\mathbf{c}} - \left\|\frac{\mathbf{c}^H\boldsymbol{\Lambda}\mathbf{c}}{\mathbf{c}^H\mathbf{c}}\right\|^2\right],$$

$$[\boldsymbol{\Delta}_{\boldsymbol{\theta}}]_{2,2} = \frac{\omega_c^2}{F_s^2}\left[\frac{\mathbf{c}^H\mathbf{D}^2\mathbf{c}}{\mathbf{c}^H\mathbf{c}} - \left(\frac{\mathbf{c}^H\mathbf{D}\mathbf{c}}{\mathbf{c}^H\mathbf{c}}\right)^2\right],$$

$$[\boldsymbol{\Delta}_{\boldsymbol{\theta}}]_{1,2} = [\boldsymbol{\Delta}_{\boldsymbol{\theta}}]_{2,1} = \omega_c\,\mathsf{Im}\left\{\frac{\mathbf{c}^H\mathbf{D}\boldsymbol{\Lambda}\mathbf{c}}{\mathbf{c}^H\mathbf{c}} - \frac{\mathbf{c}^H\mathbf{D}\mathbf{c}}{\mathbf{c}^H\mathbf{c}}\frac{\mathbf{c}^H\boldsymbol{\Lambda}\mathbf{c}}{\mathbf{c}^H\mathbf{c}}\right\}$$

where $\mathsf{SNR}_{\mathsf{out}}$ indicates the signal-to-noise ratio (SNR) at the output of the matched filter (i.e., the correlator), which is also linked to the carrier-to-noise density ratio ($C/N_0$) as:

$$\mathsf{SNR}_{\mathsf{out}} = \frac{F_s A^2 \mathbf{c}^H\mathbf{c}}{\sigma^2} = \frac{C}{N_0}T_{\mathsf{PRN}}L_c, \tag{1.16}$$

with SNR and $C/N_0$ related by the coherent integration time $T_I = T_{\mathsf{PRN}}L_c$, i.e., the single code duration $T_{\mathsf{PRN}}$ and $L_c$ the number of codes.

Then, the bound for the phase offset estimate is as follows

$$CRB_{\varphi} = \frac{1}{2\mathsf{SNR}_{\mathsf{out}}} + \begin{bmatrix} F_s\mathsf{Im}\left\{\frac{\mathbf{c}^H\boldsymbol{\Lambda}\mathbf{c}}{\mathbf{c}^H\mathbf{c}}\right\} - b\omega_c \\ \frac{\omega_c}{F_s}\frac{\mathbf{c}^H\mathbf{D}\mathbf{c}}{\mathbf{c}^H\mathbf{c}} \end{bmatrix}^{\top} \mathbf{CRB}_{\boldsymbol{\theta}} \begin{bmatrix} F_s\mathsf{Im}\left\{\frac{\mathbf{c}^H\boldsymbol{\Lambda}\mathbf{c}}{\mathbf{c}^H\mathbf{c}}\right\} - b\omega_c \\ \frac{\omega_c}{F_s}\frac{\mathbf{c}^H\mathbf{D}\mathbf{c}}{\mathbf{c}^H\mathbf{c}} \end{bmatrix}, \tag{1.17}$$

where the estimation performance for the phase offset is manifest to be tightly related to that of the time delay and frequency dilation parameters. However, for real signals the above abound can be simplified to

$$CRB_{\varphi} \underset{\text{real signal}}{=} \frac{1}{2\mathsf{SNR}_{\mathsf{out}}}, \tag{1.18}$$

which implies that the carrier offset depends only on the receiver operation point $\mathsf{SNR}_{\mathsf{out}}$, as oppose to the time delay estimation. Last, the bounds for the amplitude and noise level of the signal are as follows

$$CRB_A = \frac{\sigma^2}{2\mathbf{c}^H\mathbf{c}} + A^2F_s^2 \begin{bmatrix} \mathsf{Re}\left\{\frac{\mathbf{c}^H\mathbf{\Lambda}\mathbf{c}}{\mathbf{c}^H\mathbf{c}}\right\} \\ 0 \end{bmatrix}^{\top} \mathbf{CRB}_{\boldsymbol{\theta}} \begin{bmatrix} \mathsf{Re}\left\{\frac{\mathbf{c}^H\mathbf{\Lambda}\mathbf{c}}{\mathbf{c}^H\mathbf{c}}\right\} \\ 0 \end{bmatrix}, \tag{1.19}$$

$$CRB_{\sigma_n^2} = \frac{1}{N}\left(\sigma_n^2\right)^2. \tag{1.20}$$

The non-diagonals values for $\mathbf{CRB}_{\mathbf{x}}$ are zero in most cases ($\mathbf{CRB}_{\boldsymbol{\theta},A} = \mathbf{CRB}_{\boldsymbol{\theta},\sigma^2} = \mathbf{0}_{2\times 1}$, $CRB_{\varphi,A} = CRB_{\varphi,\sigma^2} = CRB_{A,\sigma^2} = 0$), with the exception of the cross-correlation between $\boldsymbol{\theta}$ and the phase offset, defined as

$$\mathbf{CRB}_{\boldsymbol{\theta},\varphi} = \mathbf{CRB}_{\theta} \begin{bmatrix} F_s\mathsf{Im}\left\{\frac{\mathbf{c}^H\mathbf{\Lambda}\mathbf{c}}{\mathbf{c}^H\mathbf{c}}\right\} - b\omega_c \\ \frac{\omega_c}{F_s}\frac{\mathbf{c}^H\mathbf{D}\mathbf{c}}{\mathbf{c}^H\mathbf{c}} \end{bmatrix}, \tag{1.21}$$

with the undefined submatrix elements equals to zero ($\mathbf{CRB}_{\boldsymbol{\theta},A} = \mathbf{CRB}_{\boldsymbol{\theta},\sigma^2} = \mathbf{0}_{2\times 1}$, $CRB_{\varphi,A} = CRB_{\varphi,\sigma^2} = CRB_{A,\sigma^2} = 0$). Finally, the mixing matrices $\mathbf{D}$, $\mathbf{\Lambda}$ and $\mathbf{V}$ are defined for $N_1 \leq n, n' \leq N_2$ as

$$\mathbf{D} = \mathsf{diag}\left([N_1',\ N_1'+1, \ldots,\ N_2'-1,\ N_2']\right), \tag{1.22}$$

$$(\mathbf{V})_{n,n'} = \left| \begin{array}{l} n' \neq n : (-1)^{|n-n'|}\frac{2}{(n-n')^2} \\ n' = n : \frac{\pi^2}{3} \end{array} \right., (\mathbf{\Lambda})_{n,n'} = \left| \begin{array}{l} n' \neq n : \frac{(-1)^{\left|n-n'\right|}}{(n-n')} \\ n' = n : 0 \end{array} \right., \tag{1.23}$$

The proof for the afore-described CRB can be consulted in Appendix A.1.

An interesting feature of the presented CRB for the joint time delay, Doppler and phase offset is its expression in terms of signal samples (e.g., $\mathbf{c}$). This makes it easily applicable to any other baseband signal under consideration and allows us, for instance, to characterize the tracking performance for various GNSS signals and how this influence the quality of the code and carrier phase range observables.

## 1.3 GNSS Code and Carrier Phase Observables

Code and carrier phase pseudorange observables are constructed based on the signal parameters determined during the digital signal processing on the receiver. In practice, the signal parameter estimation is typically performed in two steps: *acquisition* and *tracking*. First, acquisition consists on a coarse grid search of the Doppler and time delay based on correlations between the incoming and replicated ranging codes. Then, tracking employs control system algorithms to fine search for the unknown parameters. Thus, DLL realized during the tracking measures the time shift within the replicated code chip length. In combination with the number of complete code chips, the time of week (TOW) and the satellite clock offset available from the navigation data, one obtains an unambiguous measure for the time-of-flight of the signal or –when multiplied by the speed of light– the code pseudorange, $\rho$. In a similar fashion, the phase lock loop (PLL) measures the fractional phase shift between the received and replica carrier signals. When the range between user and satellite changes by more than one cycle, the receiver counts the full cycles and thus provides a continuous measurement which, multiplied by the carrier wavelength, constitutes the carrier phase pseudorange, $\Phi$. Along with the code and carrier phase pseudoranges, the Doppler shift is the third observable produced by a GNSS receiver and allows to directly observe a target's speed and, when used for long integration times, aid with positioning procedures [24]. This thesis focuses on range observations and, therefore, the use of Doppler shift observations will not be discussed hereinafter.

Thus, the code and phase pseudorange observations on a particular frequency $f$, from the $i$th satellite and at the $j$th receiver, are formulated as

$$\rho^i_{j,f}(t) = \|\mathbf{p}^i(t-\tau^i) - \mathbf{p}_j(t)\| + c(dt_j(t) - dt^i(t-\tau^i)) + I^i_{j,f} + T^i_j + \varepsilon^i_{j,f}, \tag{1.24}$$

$$\Phi^i_{j,f}(t) = \|\mathbf{p}^i(t-\tau^i) - \mathbf{p}_j(t)\| + c(dt_j(t) - dt^i(t-\tau^i)) - I^i_{j,f} + T^i_j + \lambda_f N^i_{j,f} + \epsilon^i_{j,f}, \tag{1.25}$$

with superscripts make reference to satellites, the subscripts indicate the receiving antenna and frequency, and the terms are

| | |
|---|---|
| $\rho, \Phi$ | code and carrier phase observations [m] |
| $\mathbf{p}^i, \mathbf{p}_j$ | 3D positions of the $i$th satellite and $j$th receiver [m] |
| $I, T$ | ionospheric and tropospheric delays [m] |
| $c$ | speed of light: 299 792 458 [m/s] |
| $dt^i, dt_j$ | satellite and receiver clock offsets [s] |
| $\lambda_f$ | carrier phase wavelength [m] |
| $N^i_{j,f}$ | number of integer ambiguity cycles |
| $\varepsilon^i_{j,f}, \epsilon^i_{j,f}$ | remaining unmodeled code and phase errors [m] |

Notice that tropospheric delays are not frequency dependent and that fractional phase biases are disregarded for $N^i_{j,f}$[2]. It results convenient distinguishing between the "known" and unknown parameters on (1.24) and (1.25). Hence, the $i$th satellite position $\mathbf{p}^i$ and clock offset $dt^i$ are obtained/estimated from the navigation data, while the ionospheric and tropospheric delays are typically derived using models (generally Klobuchar and Saastamonien, respectively) dependent on the user location and some additional parameters also included in the navigation data. Then, the list of unknown parameters include the user position, receiver clock offset and the carrier phase ambiguities.

---

[2] At this stage, $N^i_{j,f}$ is actually not an integer number and a more precise definition corresponds to $N^i_{j,f} = N^i_{\text{int},j,f} + \lambda_f \left(\varphi^i_f(t_0-\tau) + \varphi_{j,f}(t_0)\right)$ where the number of integer numbers $N^i_{\text{int},j,f}$ is complemented with the satellite fractional phase during the signal emission $\varphi_f(t_0-\tau)$ and the receiver fractional phase at the signal tracking $\varphi^i_{j,f}(t_0)$ . However, since this thesis focuses on navigation modes using double-difference observations, the assumption of $N^i_{j,f}$ being integer will not affect any further result.

### 1.3.1 Stochastic Modeling

GNSS stochastic modeling relates to the characterization of the noise present in code and carrier phase observations. Such noises are commonly assumed to be zero-mean, white (time uncorrelated) and normally distributed according to the following covariance matrix

$$\mathbf{\Sigma} = \begin{bmatrix} \mathbf{\Sigma}_{\Phi} & \mathbf{\Sigma}_{\Phi\rho} \\ \mathbf{\Sigma}_{\Phi\rho}^{\top} & \mathbf{\Sigma}_{\rho} \end{bmatrix}, \tag{1.26}$$

with $\mathbf{\Sigma}_{\Phi}$, $\mathbf{\Sigma}_{\rho}$ the covariance matrices for the carrier phase and code observations, and $\mathbf{\Sigma}_{\Phi\rho}$ the cross-correlation between them. A second extended assumption relates to the uncorrelation between each satellite link and between code and carrier measurements. Hence, (1.26) can be further simplified to

$$\mathbf{\Sigma} = \begin{bmatrix} \mathbf{\Sigma}_{\Phi} & \mathbf{0} \\ \mathbf{0} & \mathbf{\Sigma}_{\rho} \end{bmatrix}, \ \mathbf{\Sigma}_{\Phi} = \begin{bmatrix} (\sigma_{\Phi}^{1})^2 & & \\ & \ddots & \\ & & (\sigma_{\Phi}^{n})^2 \end{bmatrix}, \ \mathbf{\Sigma}_{\rho} = \begin{bmatrix} (\sigma_{\rho}^{1})^2 & & \\ & \ddots & \\ & & (\sigma_{\rho}^{n})^2 \end{bmatrix}. \tag{1.27}$$

where $\sigma_{\rho}^{i}$, $\sigma_{\Phi}^{i}$ are the standard deviations for the $i$th satellite code and phase observations and $n$ is the total number of satellites. In a nutshell, code- and phase-related errors are expressed as white zero-mean normal-distributed noise such that, for the $i$th satellite errors

$$\varepsilon^{i} \sim \mathcal{N}\left(0, (\sigma_{\rho}^{i})^2\right), \ \epsilon^{i} \sim \mathcal{N}\left(0, (\sigma_{\Phi}^{i})^2\right). \tag{1.28}$$

Despite the simplicity of the noise model (1.26-1.28), uncertainty characterization constitutes a recurrent field of study for the GNSS community. Accurate estimates of the covariance matrix $\mathbf{\Sigma}$ are key to assure the optimality of positioning algorithms [43] and to obtain tight integrity monitoring indicators [44]–[46]. Thus, weighting schemes are applied to describe observations' variance based on the satellites' elevation or the measured C/N$_0$ as

$$\sigma_{\rho}^{i} = \bar{\sigma}_{\rho}\left(1 + a_{\rho} \cdot \exp\left(-x^{i}/x_0\right)\right), \tag{1.29}$$

$$\sigma_{\Phi}^{i} = \bar{\sigma}_{\Phi}\left(1 + a_{\phi} \cdot \exp\left(-x^{i}/x_0\right)\right), \tag{1.30}$$

with

| | |
|---|---|
| $\bar{\sigma}_{\rho}, \bar{\sigma}_{\rho}$ | code and carrier phase zenith-referenced standard deviations [m] |
| $a_{\rho}, a_{\Phi}$ | model amplification parameter |
| $x^{i}$ | satellite elevation [rad] or measured C/N$_0$ [dB-Hz] |
| $x_0$ | nominal elevation [rad] or nominal C/N$_0$ [dB-Hz] |

where the model parameters (zenith-referenced variances and amplification terms) can be obtained for a specific scenario using model regression [47], [48], least-squares variance component estimation (LS-VCE) [49], or Bayesian conjugate prior analysis [20]. Alternatively, the model amplification parameters $a_{\rho}, a_{\Phi}$ can be dropped and the elevation-dependent model can be expressed as weighting factors and in matrix form as

$$\sigma_{\rho}^{i} = \bar{\sigma}_{\rho} \cdot w^{i}, \ \sigma_{\Phi}^{i} = \bar{\sigma}_{\Phi} \cdot w^{i}, \ w^{i} = 1 + \exp\left(-x^{i}/x_0\right) \tag{1.31}$$

$$\mathbf{W} = \text{diag}\left(w^{1}, \dots, w^{n}\right), \ \mathbf{\Sigma} = \begin{bmatrix} \bar{\sigma}_{\Phi} \cdot \mathbf{W} & \mathbf{0}_{n,n} \\ \mathbf{0}_{n,n} & \bar{\sigma}_{\rho} \cdot \mathbf{W} \end{bmatrix}. \tag{1.32}$$

A practical example on GNSS uncertainty characterization and stochastic modeling via Bayesian conjugate prior analysis is detailed in Appendix B.

## 1.4 Code-based Positioning

The simplest GNSS positioning approach relates to using the single-frequency code pseudoranges received at a particular time instant $t$, disregarding the user dynamics (i.e., in an snapshot/non-recursive manner) and applying the information from the broadcast navigation message to derive satellite positions and atmospheric delays. This strategy is known as single point positioning (SPP) and it constitutes the baseline localization solver for mass-market receivers.

Let us consider $n$ satellites from the same constellation being tracked at time $t$, then a MLE for the SPP problem involves maximizing the probability of the vector of observations, such that

$$\hat{\mathbf{x}} = \arg\max_{\mathbf{x}\in\mathbb{R}^p} p\left(\mathbf{y}|\mathbf{x}\right) \ , \tag{1.33}$$

with the unknowns comprising the position and clock offsets, such that $p = 3+$ the number of GNSS constellations used and $\mathbf{y}$ the vector of code observations whose pdf is described as

$$p\left(\mathbf{y}|\mathbf{x}\right) = \frac{1}{\sqrt{(2\pi)^n \det(\mathbf{\Sigma})}} \exp\left(-\frac{1}{2}\left(\mathbf{y}-\mathbf{h}(\mathbf{x})\right)^\top \mathbf{\Sigma}^{-1}\left(\mathbf{y}-\mathbf{h}(\mathbf{x})\right)\right) \ , \tag{1.34}$$

which leads to the following WLS formulation

$$\hat{\mathbf{x}} = \arg\min_{\mathbf{x}\in\mathbb{R}^p} \|\mathbf{y}-\mathbf{h}(\mathbf{x})\|^2_{\mathbf{\Sigma}} \ , \tag{1.35}$$

given the observation model $h_i(\mathbf{x})$ for the $i$th satellite by (1.24) or, after disregarding the time indexes, by

$$h_i(\mathbf{x}) = \|\mathbf{p}^i - \mathbf{p}\| + c(dt - dt^i) + I^i + T^i + \varepsilon^i \ . \tag{1.36}$$

The overdetermined system of nonlinear equations defined in (1.35) is typically resolved using an iterative Gauss-Newton (GN) approach. Starting with an initial guess $\mathbf{x}^{(0)}$, an iterative procedure over $k = 1, 2, \ldots$ is repeated until convergence, such that

$$\mathbf{x}^{(k)} = \mathbf{x}^{(k-1)} + \left(\mathbf{H}^{(k-1)^\top}\mathbf{\Sigma}^{-1}\mathbf{H}^{(k-1)}\right)^{-1}\mathbf{H}^{(k-1)^\top}\mathbf{\Sigma}^{-1}\left(\mathbf{y}-\mathbf{h}\left(\mathbf{x}^{(k-1)}\right)\right), \tag{1.37}$$

where the superscript $(k)$ indicates the algorithm iteration and $\mathbf{H}^{(k)}$ is the Jacobian matrix given by

$$\mathbf{H}^{(k)} \triangleq \left.\frac{\partial \mathbf{h}}{\partial \mathbf{x}}\right|_{\mathbf{x}^{(k)}} = \begin{bmatrix}\mathbf{G} & \mathbf{1}_{n,1}\end{bmatrix}, \tag{1.38}$$

$$\mathbf{G} = \begin{bmatrix} -\mathbf{u}_1^\top \\ \vdots \\ -\mathbf{u}_n^\top \end{bmatrix} \tag{1.39}$$

where $\mathbf{G} \in \mathbb{R}^{n,3}$ is typically known as the *geometry matrix*, with $n$ the number of tracked satellites, composed by the satellites' steering line-of-sight unit vectors, such that

$$\mathbf{u}_i = \frac{\mathbf{p}^i - \mathbf{p}}{\|\mathbf{p}^i - \mathbf{p}\|} \ . \tag{1.40}$$

Note that the second part of (1.37) corresponds to a weighted least squares (WLS) which, in turn, is the MLE for (1.35) at the Gaussian model. The optimality of the former procedure is discussed more thoughtfully in Section 2.4, while results for non-Gaussian distributions are given in Section 5.3.

## 1.5 From Signal Processing to Code-based Positioning Performance

When considering the generic GNSS receiver architecture, as the one depicted in Fig. 1.3, one rapidly acknowledges that the final PVT performance is conditioned on the digital signal processing realized in parallel in each of the channels of the receiver. In turn, such digital processing depends on the analog operations carried out at the front-end and vary based on the quality of the antenna. Unfortunately, the connection between experts working on these different receiver's blocks is not as tight as one could expect, with the exception being those devoted to studying the DPE problem. For instance, researchers working on PVT estimation tend to overlook the signal processing performed at the receiver level and would solely consider the $C/N_0$ as indicator for the quality of ranging observables.

Only by understanding the performance at signal parameter estimation can the quality of the observables be determined and, in return, the PVT performance characterized. Thus, the second contribution of this thesis relates to bridging the gap between the receiver signal processing and the PVT solver. To do so, the bound derived in Section 1.2.2 serves as analytical tool to assess the theoretical best performance for the channel processing, based on digital signal samples and the receiver operation point (i.e., the SNR at the output of the correlator or $\mathrm{SNR}_{\mathrm{out}}$). This characterizes the noise levels on the code and carrier phase observations and, using the well-known CRB for real values of the SPP, the *ultimate* code-based positioning performance can be addressed. Notice that the "ultimate" term is due to considering only the influence of the receiver processing and disregarding other delays, such as ionospheric and tropospheric factors. In summary, the MLE performance for signal tracking is characterized, which determines the noise levels on the code and carrier phase pseudoranges and the actual code-based performance. Fig. 1.4 illustrates the overall concept and flow diagram.

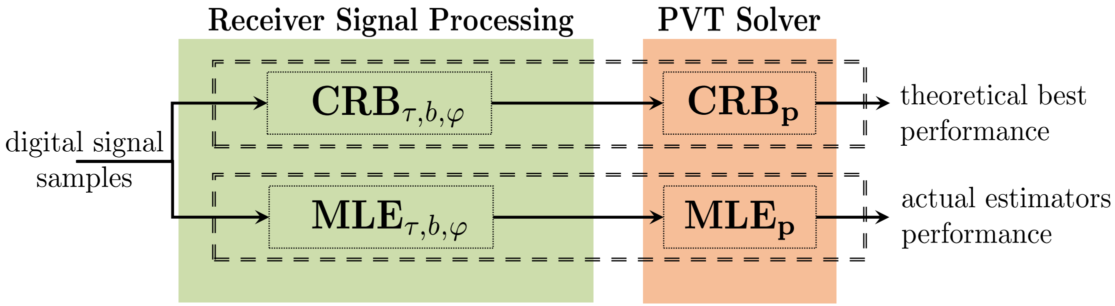

**Figure 1.4:** Flow diagram for the characterization of code-based positioning, based on the performance of the receiver signal tracking, considering digital signals samples as input.

The remaining of the section is, therefore, devoted to characterizing the ultimate SPP performance for representative GNSS signals, as well as for modern GNSS meta-signals. Different sampling frequencies and receiver operating points are considered, making explicit the receiver-to-PVT relationship, and illustrating the performance differences between open sky and harsh propagating scenarios.

### 1.5.1 Performance Analysis for Representative GNSS Signals

It results interesting, assessing the receiver's tracking performance gain from using signals with fast codes, i.e., large bandwidths or equivalently narrow correlation functions. The commonly used GPS L1 C/A signal is considered as the benchmark for the comparison. GPS L5C-I and Galileo E5 are representative large bandwidth signals for both systems. The characteristics for the GPS signals is summarized in Table 1.1, while Galileo E5 results from the combination of the four signal components (E5a-I, E5a-Q, E5b-I and E5b-Q) and is constructed as an AltBOC(15,10). A small summary of the signal characteristics and the autocorrelation function (ACF) properties is given in Table 1.2, while the normalized ACF is graphically illustrated on the left side of Fig. 1.5. To analyze the code-based positioning problem, the receiver is considered to track the satellites for the GPS constellation as observed at the San Fernando IGS station (on UTC time 2020/03/04 10:00), with an elevation mask of five degrees, whose skyplot is depicted on the right side of Fig. 1.5. To segregate the role of geometry and satellite availability across GPS and Galileo from the performance of the studied signals, this work considers the tracked satellites as generic, common to GPS and Galileo.

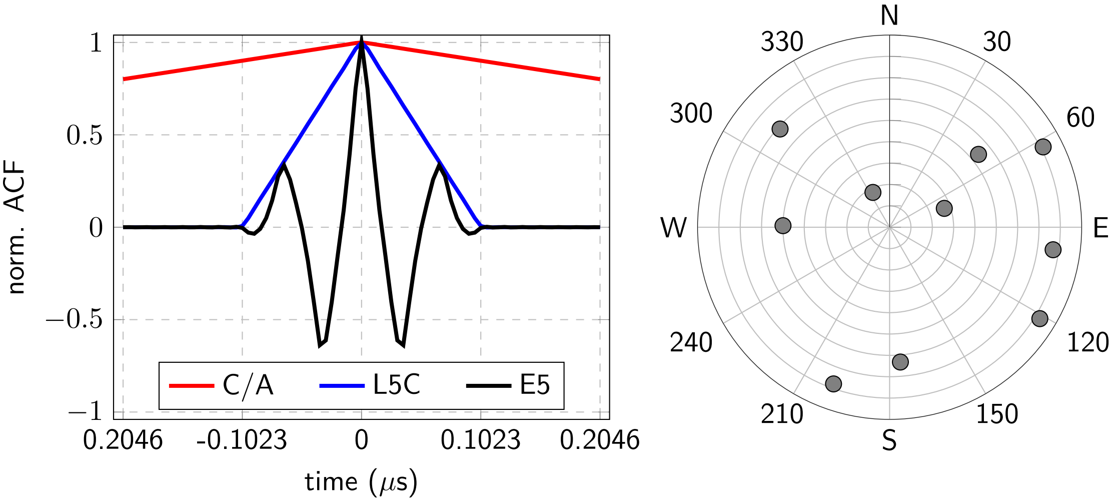

**Figure 1.5:** On the left, the normalized ACF for the following signals: GPS L1 C/A, GPS L5C-I and Galileo E5. On the right, skyplot for the tracked satellites used for the simulated scenario.

The results discussed in this section are given with respect to the $\mathrm{SNR}_{\mathrm{out}} = C/N_0 \cdot T_{\mathrm{PRN}} \cdot L_c$, as described in (1.16). The coherent integration time, $T_I = T_{\mathrm{PRN}} L_c$, corresponds to the time needed to integrate a certain number of codes. Thus, the connection to the typical receiver operation point is clear –lower $\mathrm{SNR}_{\mathrm{out}}$ values can, for instance, be related to harsh propagating conditions–. For each test scenario (i.e., for each signal and receiver operation point), the root mean squared error (RMSE) is estimated via Monte Carlo simulation with $10^4$ runs.

**Table 1.2:** GPS and Galileo signals characteristics. ACF peak refers to the first zero-crossing of the ACF, $T_{\mathrm{PRN}} = 1$ ms.

| Signal | Modulation | $T_{\mathrm{bit}}$ | ACF Peak |
|---|---|---|---|
| GPS L1 C/A | BPSK(1) | 20 ms | $\pm 1.023 \mu s$ |
| GPS L5-I | BPSK(10) | 10 ms | $\pm 0.1023 \mu s$ |
| Galileo E5 | AltBOC(15,10) | 4 ms | $\pm 0.0174 \mu s$ |

### Time-Delay Estimation Performance

First, the time-delay $\tau$ estimation performance is discussed, with the results for different signals depicted in Fig. 1.6. Notice that the MLE asymptotic region threshold (i.e., the operation point where the MLE starts to rapidly deviate from the CRB) is around SNR$_{\text{out}} = 15$ dB. Upon the definition of SNR$_{\text{out}}$ and taking into account that $T_{\text{PRN}} = 1$ ms for the signals considered, this threshold corresponds to a $C/N_0 = 45$ dB-Hz using 1 code ($T_I = 1$ ms), $C/N_0 = 39$ dB-Hz for 4 coherently integrated codes ($T_I = 4$ ms), $C/N_0 = 35$ dB-Hz with 10 coherently integrated codes ($T_I = 10$ ms) and $C/N_0 = 32$ dB-Hz for the L1 C/A $T_{\text{bit}}$ limit of 20 codes ($T_I = 20$ ms).

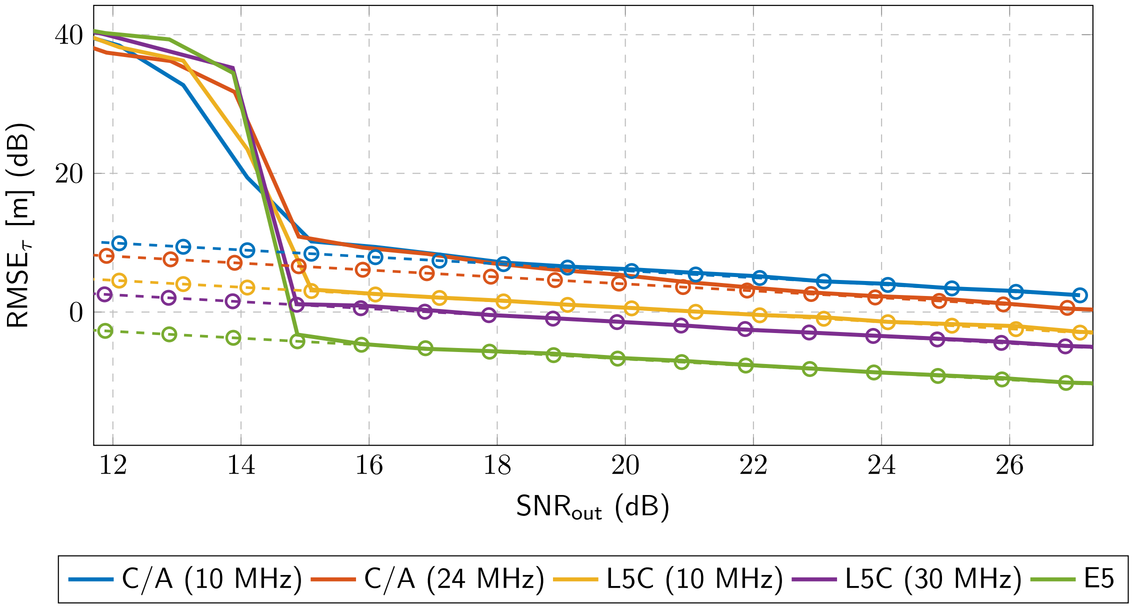

**Figure 1.6:** Root mean squared error (RMSE) for time-delay CRB (dashed lines) and MLE (solid line) for different signals and sampling frequencies: GPS L1 C/A ($F_s = 10, 24$ MHz), GPS L5-I ($F_s = 10, 30$ MHz), and Galileo E5 ($F_s = 60$ MHz).

Next, the relationship between performance and sampling frequency is analyzed. In the case of GPS C/A processing, sampling rates of 10 and 24 MHz are compared, with the latter being the full signal bandwidth. For an operation point SNR$_{\text{out}} = 25$ dB (i.e., a nominal $C/N_0 = 45$ dB-Hz and a standard $T_I = 10$ ms), the time delay deviations are $\sigma_{\tau,L1} = 2.3$ m and $\sigma_{\tau,L1} = 1.5$ m for 10 and 24 MHz, respectively. While exploiting the full signal bandwidth leads to more precise estimates (within the asymptotic regimen of the estimator), the drawback is that the MLE convergence to the CRB is slower. Nevertheless, the standard deviation for a sampling rate of 24 MHz remains lower than that of 10 MHz regardless of the convergence to the bound.

Finally, we can compare these results with larger bandwidth GPS L5 and Galileo E5 signals. Table 1.3 provides an overview on the standard deviation for the time delay, considering an operation point SNR$_{\text{out}} = 25$ dB, for the signals and sampling frequencies considered. The results exposed in Table 1.3 clearly show the considerable improvement on time-delay estimation performance obtained when exploiting large bandwidth signals. For instance, the Galileo E5 AltBOC signal brings a gain factor of 13 and 3 in time-delay standard deviation with respect to the full bandwidth GPS L1 C/A and L5C signals, respectively. Notice that,

**Table 1.3:** Comparison of the standard deviation for the time delay estimates for SNR$_{\text{out}} = 25$ dB accross different signals and sampling frequencies.

| Signal | Sampling frequency $F_s$ (MHz) | Time delay standard deviation $\sigma_\tau$ (m) |
|---|---|---|
| GPS L1 C/A | 10 | 2.20 |
| GPS L1 C/A | 24 | 1.57 |
| GPS L5C | 10 | 0.51 |
| GPS L5C | 30 | 0.41 |
| Galileo E5 | 60 | 0.12 |

in the absence of any additional propagation or ephemeris errors, the standard deviation for the time delay equals that of the code range measurements (i.e., $\sigma_\tau \simeq \sigma_\rho$).

### Phase Offset Estimation Performance

The estimates on phase offset determine the accuracy of the carrier phase observables. To address the bound for phase offset, the simplification in (1.18) for real signals is applied. Also, notice that the standard deviation for the carrier phase observations is derived from the CRB for phase offset estimation and the associated wavelength $\lambda_c$, as

$$\text{CRB}_\Phi = \left(\frac{\lambda_c}{2\pi}\right)^2 \text{CRB}_\varphi. \tag{1.41}$$

As for the time delay estimation case, we are interested in observing the RMSE for the carrier phase observables versus the receiver operation point, as illustrated in Fig. 1.7. For simplicity, the CRB for the E5 has been omitted, since it lays just slightly above that of L5 (gray dashed line). Contrary to the time delay, the accuracy of carrier phase estimates is not driven by the signal bandwidth but by its wavelength instead. Thus, carrier phase observations over L1 frequency result more precise than those in L5/E5. From (1.12), one expects that the ML performance for carrier estimates is driven by the time delay estimation. Therefore, full bandwidth signals abandon the asymptotic regimen faster.

**Table 1.4:** Comparison of the standard deviation for the carrier phase observations (in mm) across the evaluated signals. The comparison is expressed in terms of the SNR$_{\text{out}}$ and the coherent integration time $T_I$ for a $C/N_0 = 45$ dB-Hz.

| SNR$_{\text{out}}$ [dB] | $T_I$ [ms] | $\lambda_{L1}, \sigma_\varphi$ [mm] | $\lambda_{L5}, \sigma_\varphi$ [mm] | $\lambda_{E5}, \sigma_\varphi$ [mm] |
|---|---|---|---|---|
| 15 | 1 | 3.8 | 5.1 | 5.0 |
| 18 | 2 | 2.7 | 3.6 | 3.6 |
| 21 | 4 | 1.9 | 2.6 | 2.5 |
| 25 | 10 | 1.2 | 1.6 | 1.6 |
| 28 | 20 | 0.85 | 1.1 | 1.1 |

Table 1.4 summarizes the standard deviation for carrier phase observations based on the MLE performance at the unknown signal parameters for a nominal $C/N_0$ of 45 dB-Hz. Notice that the obtained standard deviations are in the range of $[1-5]$ mm, in agreement with empirical results obtained applying LS-VCE techniques [50], [51]. Unlike the time delay estimation, exploiting large bandwidths does not lead to more precise carrier phase observations,

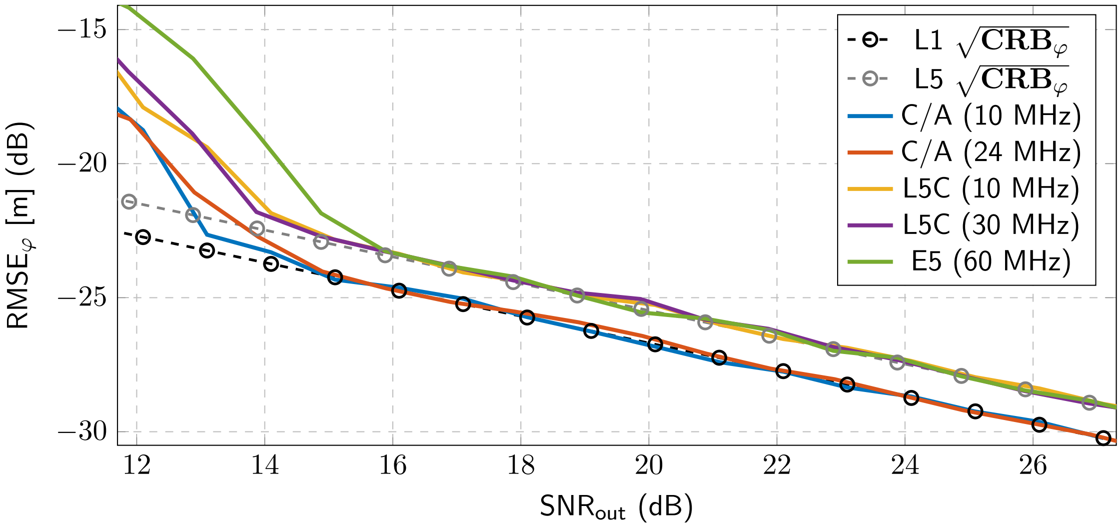

**Figure 1.7:** RMSE for carrier phase observations. The CRB for the E5 is disregarded due to its similarity to the L5C. The CRB (dashed lines) and MLEs' RMSE (solid line) for different signals and sampling frequencies: GPS L1 C/A ($F_s = 10, 24$ MHz), GPS L5-I ($F_s = 10, 30$ MHz), and Galileo E5 ($F_s = 60$ MHz).

as afore-discussed. The same asymptotic behavior is observed, although the carrier phase standard deviations are lower for signals with fast codes, such as Galileo E5.

### Ultimate Code-based Positioning Performance

At last, the code-based positioning (e.g., SPP) problem is analyzed. The SPP estimation bound coincides with the conventional CRB for multidimensional real parameters [52] (i.e., $\text{CRB}_{\mathbf{p}} = (\mathbf{H}^\top \mathbf{\Sigma}_\rho^{-1} \mathbf{H})^{-1}$). As stated on the introductory part of this section, the ionospheric, tropospheric and instrumental delays are disregarded, since it is of our interest to examine the influence of the different signals, integration times and the receiver operation points rather than the model mismatch of the different atmospheric models typically applied.

The CRB and RMSE for the estimates of the SPP problem are depicted in Fig. 1.8. Also, Table 1.5 summarizes the SPP performance with code observations derived using different signals for a nominal case of $\text{SNR}_{\text{out}} = 25$ dB. In analogy with the time delay estimation case, it is evident that using large bandwidth signals has a tremendous impact on the achievable positioning precision. Indeed, in the absence of unmodeled atmospheric residuals or other propagation delays, exploiting the large bandwidth of Galileo E5, decimeter-level positioning accuracy can be obtained for $\text{SNR}_{\text{out}}$ greater than 15 dB.

**Table 1.5:** Comparison of code-based positioning performance for a nominal case $\text{SNR}_{\text{out}} = 25$ dB.

| Signal | Sampling frequency (MHz) | Positioning $\text{RMSE}_{\mathbf{p}}$ (m) |
|---|---|---|
| GPS L1 C/A | 10 | 3.30 |
| GPS L1 C/A | 24 | 2.36 |
| GPS L5C | 10 | 1.00 |
| GPS L5C | 30 | 0.63 |
| Galileo E5 | 60 | 0.19 |

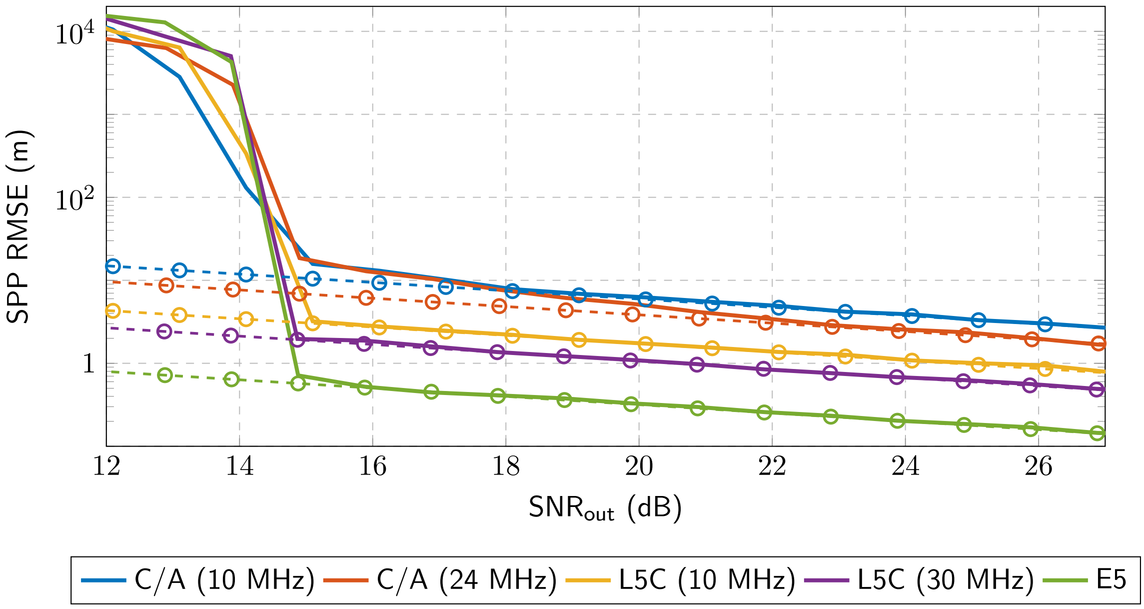

**Figure 1.8:** SPP position CRB (dashed lines) and associated RMSE (solid lines) versus SNR$_{\text{out}}$ for GPS L1 C/A ($F_s = 10, 24$ MHz), GPS L5-I ($F_s = 10, 30$ MHz), and Galileo E5 ($F_s = 60$ MHz).

As closing remark, this subsection showcases the importance of determining the "threshold region" for MLE. That is, the receiver operation point for which an estimator completely deviates from the CRB. It is shown that, regardless of the signal under consideration, the SNR threshold for time-delay and phase offset estimation is around 15 dB. The capability of a receiver at estimating the signal parameters, especially the time delay, plays a role as relevant as satellite geometry, with code-based positioning being strongly degraded whenever time delay estimators abandon their asymptotic regime. Moreover, exploiting signals with large bandwidth leads to a significant positioning precision gain, as for the Galileo E5 case for which an ultimate positioning precision of under 20 centimeters can be reached.

### 1.5.2 Performance Analysis for GNSS Meta-Signals

Having assessed the link between receiver and code-based positioning for "conventional" GNSS signals, such as GPS C/A or Galileo E5, the application of such methodology to meta-signals is of great interest for prospective GNSS receiver configurations. In this subsection, the signals introduced in Section 1.1.1 will be studied:

- GPS L2C + L5C, modulated as an AltLOC(25,10,1,75) and with a central frequency of 1202.03 MHz.
- Galileo E5a + E6B, built with an AltLOC(50,10,5,120) and centered on $f_c = 1227.6$ MHz (coinciding with GPS L2); Galileo E5a+E5b+E6B, or in other words, the complete E5 combined with E6B, and built with an AltLOC(42.5,$C_{\text{E5}}$,5,132) –$C_{\text{E5}}$ represents the full bandwidth E5 signal–, and centered in 1235.27 MHz;
- BeiDou B2a+B3A, generated as an AltLOC(45,10,10,120) and whose central frequency is $1222.49$ MHz; BeiDou B2+B3A, generated through an AltLOC(37.5,$C_{\text{B2}}$,10,125) –$C_{\text{B2}}$ represents the full bandwidth B2 signal– and centered in 1230.16 MHz.

For further reference, Galileo E5 is added for comparison with respect to the meta-signals. In all cases, the sampling frequency coincides with the signal bandwidth (which corresponds to the last number in the AltLOC formulation). The major weakness of large bandwidth signals, as the case for meta-signals, derives from the presence of ACF large secundary peaks close to the main ones. To better illustrate this phenomena, Fig. 1.9. depicts the normalized ACF for a set of meta-signals (L2C+L5C, E5+E6B and B2+B3) along with the Galileo E5 for comparison.

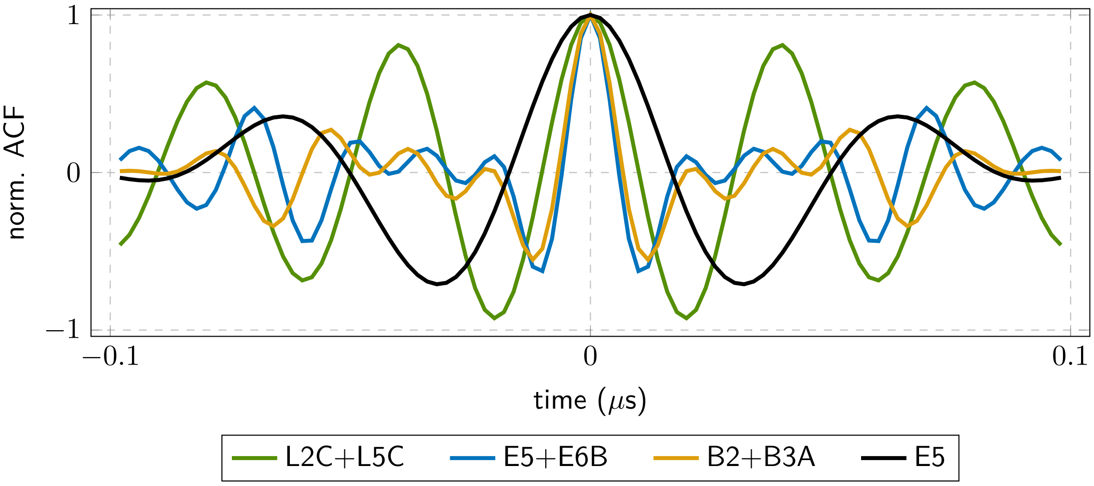

**Figure 1.9:** Comparison of the main normalized ACF peaks for a set of meta-signals: L2C+L5C, E5+E6B and B2+B3. For completeness, Galileo E5 is show in black.

### Time-Delay and Phase Offset Estimation Performance

As for Section 1.5.1 with conventional GNSS signals, the time-delay estimation is first addressed. Fig. 1.10 illustrates the MLEs' performance along the associated bounds against a range of SNR at the output of the correlator. While the use of meta-signals leads to precision gains of around 5 dB compared to the Galileo E5, the MLE convergence becomes strongly degraded. Indeed, narrower ACF main peaks imply an enhancement in the time-delay theoretical precision (i.e., a lower CRB), while larger secondary peaks and closer to the main one leads to poorer convergence and an overall worsen MLE performance. This phenomenon is related to possible false locks, which are more likely to occur at low SNR conditions. For instance, the MLE asymptotic regimen for GPS L2C+L5C and Galileo E5+E6B are abandoned at SNR$_{out}$ values of approximately 21 and 24 dB, respectively. Meanwhile, the Galileo E5 asymptotic behavior extends up to 16 dB, showcasing much better resilience in harsh propagating conditions.

The MLE performance for phase offset, and consequently the carrier phase pseudorange observations, follows the same pattern as for time delay estimates. As shown in (1.12), this relation is due to the phase MLE being given by the argument evaluated at the time delay MLE. Fig. 1.11 illustrates the RMSE for the ML estimators and the associated bound for different values of SNR$_{out}$. In fact, only Galileo E5+E6B and BeiDou B2+B3A offer a performance comparable to Galileo E5, with an asymptotic region that extends up to an SNR of 18 dB. The MLE performance for the remaining meta-signals do not attain the bound for SNR values below 21 dB. Moreover, since the precision of carrier phase observation is linked to the wavelength and these are quite similar among the studied signals, no major improvement is observed (as it can be observed in the detail at SNR$_{\text{out}} = 26$ dB in Fig. 1.11). Although all meta-signals present an slightly lower wavelength, the difference with

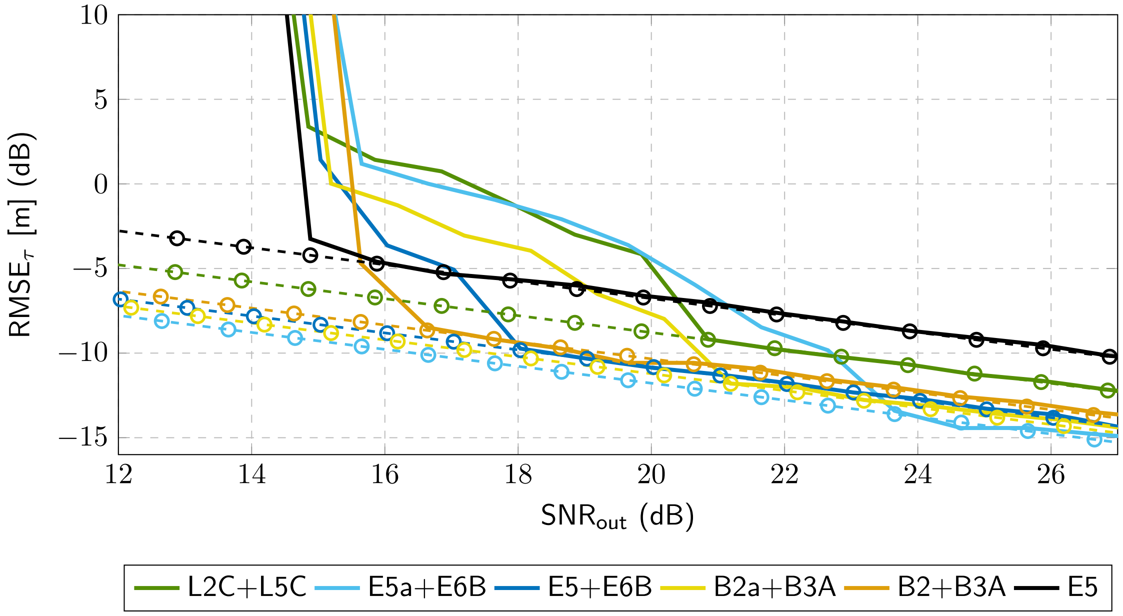

**Figure 1.10:** RMSE for time-delay CRB (dashed lines) and MLE (solid lines) for different meta-signals and Galileo E5.

respect to Galileo E5 is at most of one mm.

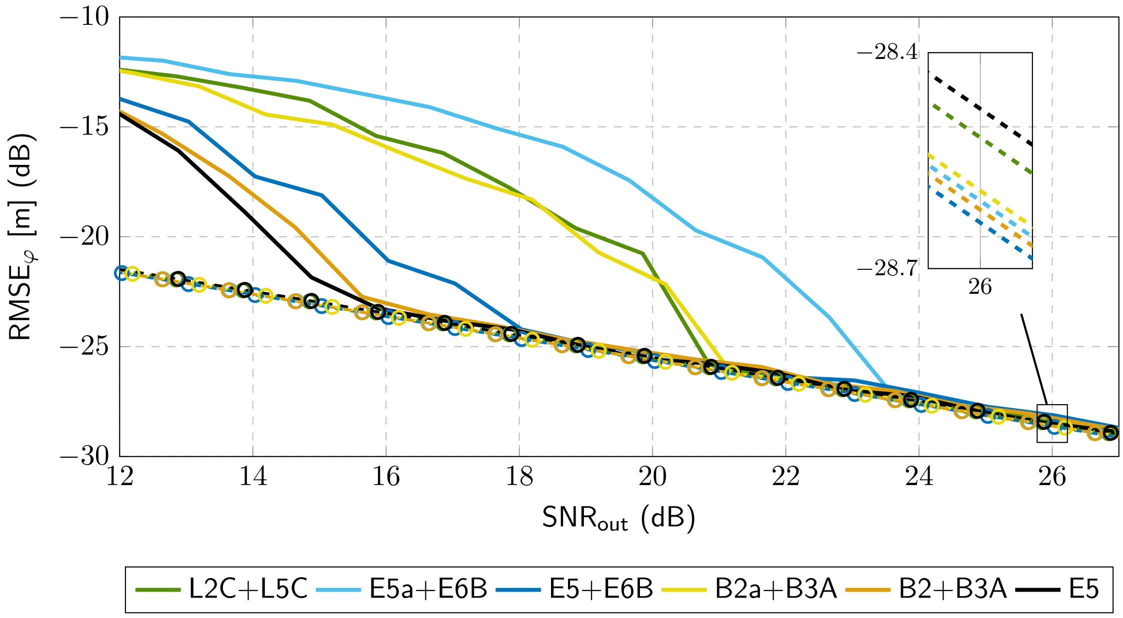

**Figure 1.11:** RMSE for MLE-derived carrier phase observations (solid lines) and associated bounds (dashed lines) for different meta-signals and Galileo E5.

Table 1.6 summarizes the standard deviation for code and carrier phase pseudorange observations for the considered meta-signals at a nominal SNR$_{out}$ of 25 dB, which corresponds to an open sky scenario with good satellite signal reception.

We could conclude that, in terms of robustness (i.e., operability at lower SNR values), the best choice is still Galileo E5, while Galileo E5+E6B and BeiDou B2+B3A meta-

**Table 1.6:** Comparison of the standard deviation for time delay and carrier phase estimates for $\text{SNR}_{\text{out}} = 25$ dB across the considered GNSS meta-signals.

| Signal | Sampling frequency (MHz) | Time delay standard deviation $\sigma_\tau$ (cm) | Phase carrier standard deviation $\sigma_\Phi$ (mm) |
|---|---|---|---|
| GPS L2C+L5C | 75 | 7.5 | 1.7 |
| Galileo E5a+E6B | 120 | 4.2 | 1.6 |
| Galileo E5+E6B | 132 | 4.6 | 1.7 |
| BeiDou B2a+B3A | 120 | 5.4 | 1.5 |
| BeiDou B2+B3A | 125 | 3.7 | 1.6 |
| Galileo E5 | 60 | 12 | 1.6 |

signals are promising contenders. Furthermore, meta-signals may offer very precise code pseudorange observations under open sky conditions, which is key for precise localization even for code-based positioning techniques.

### Ultimate Code-based Positioning Performance

Next, it is assessed how the time-delay estimates derived from meta-signals translate into the position domain using the standard code-based SPP. The satellite geometry is as for Section 1.5.1, with the skyplot depicted in Fig. 1.5 (right). Once again, to separate the constellation geometry from the positioning performance, the satellites are considered as generic and common to GPS, Galileo and BeiDou. The covariance of the code observables noise (i.e., $\sigma_\rho$ in 1.28) was set according to the MLE precision for time-delay estimates (i.e., $\sigma_\tau$ in the previous analyses). Furthermore, the signals from the satellites are assumed to be received with the same power, regardless of their elevation. Fig. 1.12 depicts the SPP performance results against different values of $\text{SNR}_{out}$ for the considered meta-signals –Galileo E5 is added for completeness and comparison–.

Again, considering $\text{SNR}_{out} = 25$ dB as a reference value, the standard deviation for the positioning performance was –following the order in Fig. 1.12– roughly: 11 cm (L2C+L5C), 5.5 cm (E5a+E6B), 7 cm (E5+E6B), 6.5 cm (B2a+B3A), 8 cm (B2+B3A) and 19 cm (E5). Obviously, the limited convergence due to false locks into ACF secondary peaks has a direct translation over the positioning estimates. This fact further supports that, in terms of robustness, Galileo E5 and the meta-signals with full-bandwidth over E5 and B2 are the best option. A relevant factor is the meta-signals' precision gain of one order of magnitude with respect to Galileo E5. Indeed, when properly modeling atmospheric delays and under good propagation conditions, any of the meta-signals could be considered as a precise code-based positioning alternative to carrier phase-based techniques.

In a conclusion similar to analysis to the signal parameter estimation and regardless of the satellite geometry, the best compromise in terms of robustness, performance, and estimator behavior is provided by Galileo E5 and the full-bandwidth E5+E6 and B2+B3 meta-signals. The latter offer an increased precision for time-delay estimates at high SNR at the cost of requiring double bandwidth as Galileo E5.

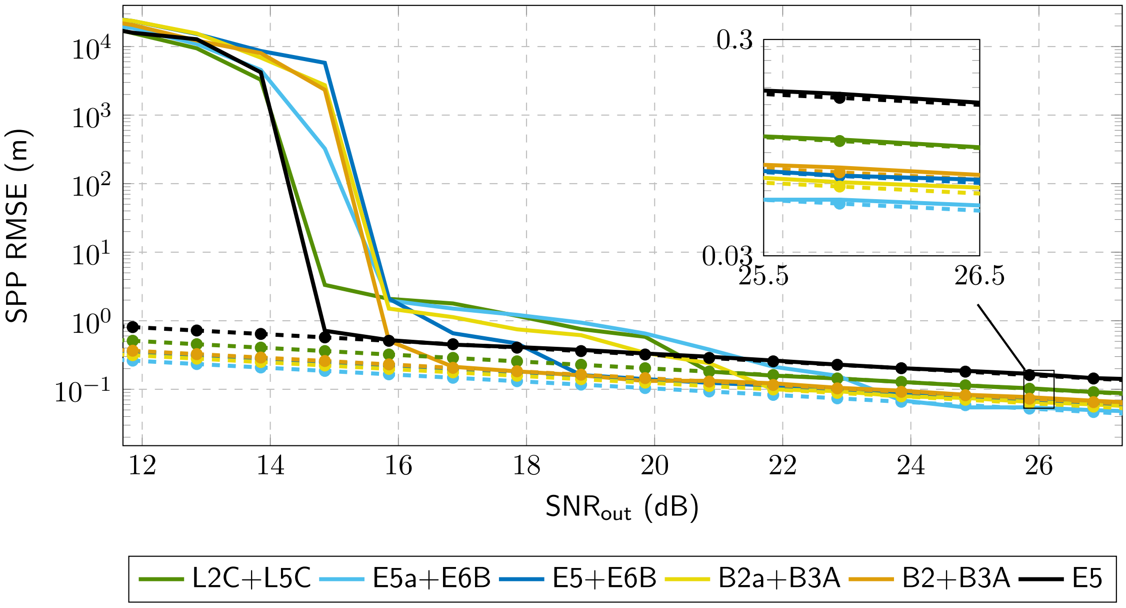

**Figure 1.12:** SPP position CRB (dashed lines) and associated RMSE (solid lines) versus SNR$_{\text{out}}$ for a selection of meta-signals. For completeness, Galileo E5 is show in black.

## 1.6 Summary

This chapter presented the basic working principles of GNSS, a short historical perspective of their development and an oversight to the GNSS signals spectrum and their characteristics. Furthermore, the architecture and functioning of a GNSS receiver is discussed, including the basic signal processing required to track the satellite signals, how the ranging observables are constructed and how the conventional code-based positioning is carried out.

The core contribution of this chapter relates to assessing the relationship between the code-based positioning and the signal processing performed by a conventional GNSS receiver. Doing so requires the formal characterization of the signal parameter estimation realized in each channel of a receiver: i.e., what is the actual estimators performance in comparison to the associated lower bound. Thus, one can assess the quality of the code and phase range observations which, together with the geometrical component, determine the ultimate precision of the positioning procedures.

Section 1.2.2 proposes a compact CRB for the joint estimation of the GNSS signal parameters: time-delay, phase offset, Doppler attenuation, etc. Since the presented CRB is expressed in terms of digital signal samples, it is especially easy to use irrespective of the considered baseband signal. Such a CRB results particularly useful to "bridge the gap" between the digital signal processing realized in parallel in each channel of the receiver and how precise the PVT computation results.

Following that same line of thought, Section 1.5.2 resolves the relationship between the signal parameter estimation and the ultimate code-based positioning performance, via extensive Monte Carlo simulation and the selection of both conventional and modern GNSS signals. Some conclusive points can be deducted from this section:

- Based on the SNR at the output of the matched filter, the behavior of MLEs for the GNSS signal parameters can be described according to the low noise, large noise and the threshold regimes. Only during the low noise the MLEs perform asymptotically and attain the associated CRB. For conventional GNSS signals, the asymptotic regime is generally abandoned for SNRs lower than 15 dB. Those signals exploiting larger bandwidths allow for higher precision at estimating the time-delay, while the precision of carrier phase observables is dictated by the signal's wavelength.

- GNSS meta-signals present significantly lower CRB (higher precision) for the time-delay estimation, when compared to other conventional signals. Indeed, for high SNRs the standard deviation for time delay estimates results of a few centimeters. Unfortunately, the presence of high secondary peaks for the meta-signals' ACF lead to an overall worsen MLE performance and poorer convergence at the CRB.

- When studying the ultimate code-based positioning performance, i.e., disregarding propagation and ephemeris errors, and for high SNR conditions, the use of meta-signals for code-based positioning allows to reach decimeter level precision and can be thought as interesting alternative to carrier phase-based approaches. Otherwise, the Galileo E5 signal exploiting the full bandwidth offers a great compromise in terms of operability at low SNR and precision.

Contributions to this chapter appear partially in:

**Journal articles:**

[9] Medina, D., Ortega, L., Vilà-Valls, J., Closas, P., Vincent, F., & Chaumette, E. (2020). Compact CRB for delay, Doppler, and phase estimationapplication to GNSS SPP and RTK performance characterisation. *IET Radar, Sonar & Navigation*, 14(10), 1537-1549.

[7] Ortega, L., Medina, D., Vilà-Valls, J., Vincent, F., & Chaumette, E. (2020). Positioning Performance Limits of GNSS Meta-Signals and HO-BOC Signals. *Sensors*, 20(12), 3586.

**Conference articles:**

[14] Ortega, L., Medina, D., Vilà-Valls, J., Vincent, F., & Chaumette, E. (2020, December). A Compact CRB for the Single Source Conditional Signal Model with Application to Delay-Doppler-Phase Estimation of Band-Limited Signals. In *2020 59th IEEE Conference on Decision and Control (CDC)* (pp. 2906-2911). IEEE.

[20] Medina, D., Gibson, K., Ziebold, R., & Closas, P. (2018). Determination of pseudorange error models and multipath characterization under signal-degraded scenarios. In *Proceedings of the 31st International Technical Meeting of the Satellite Division of The Institute of Navigation (ION GNSS+ 2018).*

# CHAPTER 2

## GNSS Precise Positioning and its Estimation Bounds

WHILE standard code-based GNSS techniques present a decent performance for most scenarios, they are not compliant with the far more stringent precision requirements of modern safety-critical applications. Instead, the use of carrier phase observations leads to much higher precision, with noise levels two orders of magnitude lower than its code counterpart. This comes at the expense of carrier phase being ambiguous, since a receiver tracks only the fractional phase offset, while the integer number of cycles between the satellite and receiver remains unknown at the start of the phase tracking. This number of integer cycles, so-called ambiguities, must be correctly estimated to grant a high-precision solution. The framework that underpins precise GNSS carrier phase-based ambiguity resolution is the theory of integer aperture (IA) estimation and it is also applied to various other fields. This Chapter presents an overview on the carrier phase-based positioning techniques, describes the mixed real- and integer-valued model, its estimation and associated bounds. Finally, the relationship between the receiver signal processing and the ultimate carrier phase-based positioning is assessed for a selection of GNSS signals.

### Outline

Upon the type of correction data employed and the observations' combination, two carrier phase-based localization techniques are generally distinguished:

**Real Time Kinematics (RTK).** RTK is a differential positioning approach for which the location of the receiver of interest is referred to that of a nearby base station, of known coordinates. The driving idea relates to combining the observations received at both sites to eliminate or diminish the ionospheric and tropospheric delays, alleviate the inaccuracies in the satellites' positions and clock offsets and eliminate the fractional phase biases. From a practical point of view, the performance of RTK is driven by two factors: *i)* the baseline distance to the base station, for which lengths of up to 10 km grant that the differential atmospheric delays are negligible (in principle, one could perform RTK positioning with a baseline distance of at most 100 km, at the cost of estimating the residuals ionospheric delays and a prolonged time to fix the ambiguities); *ii)* a sufficiently broad bandwidth and low-latency communication channel for the transmission of the correction data —the Radio Technical Commission for Maritime Services (RTCM) estimates on 125 bits the volume of data required per satellite and frequency , leading to a minimum bandwidth of 10 Kbits/s with a latency lesser than a second—. Despite the technical challenges present, RTK has become the baseline localization tool for applications in surveying, geodesy, geophysics and modern ITS services, since high-precision positioning can be achieved almost immediately.

**Precise Point Positioning (PPP).** Introduced in 1997 [53], PPP employs undifferenced code and carrier phase pseudorange measurements. Unlike its RTK counterpart, PPP does not require observations from a nearby station and, instead, replaces the broadcast navigation data with precise information on satellite orbits and clocks estimated from a global network of stations. Then, nuisance parameters such as the tropospheric zenith delays (ZTDs), the receiver clock offset and the phase ambiguities and biases are to be recursively estimated. With growing interest on the provision of precise products and worldwide availability [54], PPP constitutes a promising positioning technique and an appealing alternative to RTK. Unlike RTK, PPP provides absolute positioning, which makes it appropriate for geophysical and meteorological applications such as earthquake detection, modeling crustal movements or studying water content . Nonetheless, a major drawback of PPP relates to its long convergence time —i.e., the time needed for reaching certain positioning accuracy and a stable estimate for the other unknown parameters—, ranging from 5 to 20 minutes for static scenarios [55].

Besides PPP and RTK, PPP-RTK is a trending hybridization technique of the former two, for which a conventional PPP algorithm is enhanced with the atmospheric corrections from a Real-Time Network (RTN). Based on the density of the RTN and the proximity to a station, the map of atmospheric corrections is more accurate, leading to faster convergence times for precise positioning. Another advantage is that ionosphere-free data combination would no longer be required [30], and thus dual-frequency users could benefit from a greater data redundancy and single-frequency users could still opt for precise positioning. Since only information on ionospheric and tropospheric delays is provided from the RTN, the communication channel needed for PPP-RTK is considerably less demanding than conventional RTK, both in terms of bandwidth and latency. To serve as overview on the family of GNSS-based positioning algorithms, Table 2.1 summarizes the expected accuracy, convergence time and coverage of the aforementioned code- and carrier phase-based methods.

To illustrate the localization capabilities of carrier phase-based techniques, in relation to that of code-based positioning, an experimental example is introduced next.

**Table 2.1:** Overview on the GNSS positioning algorithms in terms of accuracy, convergence time, coverage area and positioning type (relative or absolute localization).

| Positioning method | | Nominal accuracy | Convergence | Coverage | Type |
|---|---|---|---|---|---|
| **Code-based** | SPP | $< 10$ m | Instantaneous | Global | Absolute |
| | DGNSS | 0.5–2 m | Instantaneous | Regional | Absolute |
| **Phase-based** | RTK | $< 1$ dm | Instantaneous | Local | Relative |
| | PPP | 1–2 dm | $< 10$ min[1] | Global | Absolute |
| | PPP-RTK | $< 1$ dm | 5–20 min[1] | Regional | Absolute |

[1] These time spans have been shown empirically, with a theoretical justification still to be developed.

**Example 1** (Positioning performance for a short baseline)**.** The GNSS observations collected on the IGS stations in San Fernando and San Roque, both located at the South of Spain, and separated by nearly 3 km are fed to code-based (SPP) and carrier phase-based (PPP and RTK) positioning engines. The data corresponds to 04/03/2020 and extends for five hours, with a sampling rate of 30 seconds. Dual constellation (GPS and Galileo) and frequency is employed and the elevation mask is set at 10 degrees. Since both stations are located on the rooftops at their corresponding buildings, this scenario constitutes an ideal case in terms of propagation conditions and separation between base (San Roque) and rover (San Fernando) receivers. In terms of data assimilation, SPP constitutes a snapshot (or memoryless) estimator, PPP and RTK are formulated as recursive estimators. The PPP solution uses final ephemeris and clock products, obtained from the Canadian Geodetic Survey. Fig. 2.1 shows the norm for the three-dimensional positioning error over time. For completeness, both the RTK float and fix solutions are depicted, in yellow and purple color respectively. For the float solution, an additional instance of RTK performs the positioning task without attending to estimate the integer ambiguities. It becomes evident the precision gain from carrier phase-based techniques,

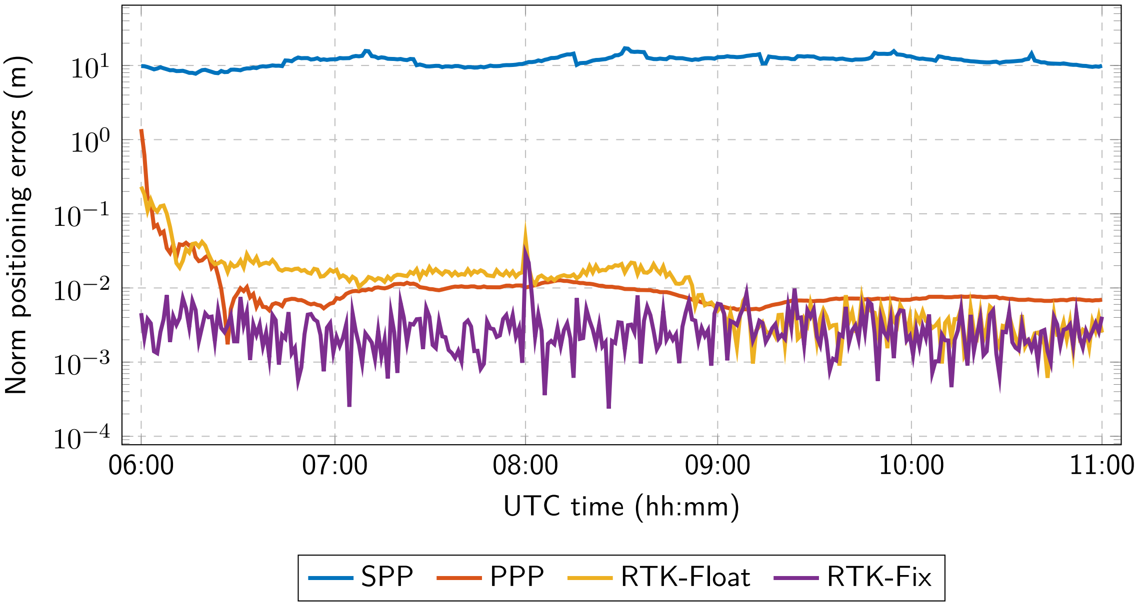

**Figure 2.1:** Root-squared for the 3D-positioning errors over time, based on different code- and carrier phase-based positioning techniques.

the later leading to almost three orders of magnitude higher precision. While the quality of phase observables is responsible for two out of the three orders in precision gain, recursive estimation contributes to an enhanced localization capability. In terms of convergence –here, the time needed to achieve high precision–, RTK manages to instantly estimate the ambiguities and provide accurate positioning, while PPP requires approximately ten minutes for sub-dm precision and over half an hour for cm-level localization. The performance of RTK-float demonstrates that, for a static and short baseline scenario, integer ambiguity estimation shall not be a requisite for high precision, at the cost of long convergence times.

Regardless the algorithm selection, all carrier phase-based positioning methods result in the estimation of the so-called *mixed model*. The mixed model constitutes an estimation problem where a vector of real- and integer-valued unknown parameters is to be estimated. Within the context of GNSS, Teunissen pioneered the study of integer inference and developed the family of estimators for the mixed model: *i)* the class of integer estimators (IE) [56]; *ii)* the class of integer-aperture (IA) estimators [57]; and iii) the class of integer-equivariant (IE) estimators [58]. It is also worth noting that distributional results are available readily [59], [60]. When designing and assessing estimators for a particular problem, it is of great relevance to know the minimum achievable performance, that is, to obtain tight performance lower bounds (LBs). Generally, one is interested in minimal performance bounds in the mean squared error (MSE) sense, which provide the best achievable performance on the estimation of parameters of a signal corrupted by noise. Unfortunately, such type of estimation bound had not been posed for the mixed model, since the discrete distribution of the integer ambiguities impedes the usual formulation of the Fisher Information Matrix (FIM), whose inverse is the Cramér-Rao Bound (CRB) [61]. The lack of LBs for the mixed model ignited the contribution for this chapter.

This dissertation proposes the Cramér-Rao Bound (CRB) for the problem of mixed real- and integer-valued parameter estimation, which results key to understand the ultimate achievable performance of carrier phase-based positioning. For such purpose, a lower bound general CRB formulation, leveraging on the McAulay-Seidman bound, is proposed. As a particular case of the general form of the bound, a closed-form expression for the RTK functional model is derived. One noteworthy point is the assessment of the asymptotic efficiency of the integer estimators for the RTK problem, thus complementing the rather rich literature on that topic. It is shown that the derived CRB expression is able to predict the RMSE performance of the MLE, and that an asymptotically efficient estimator for the mixed model exists for the RTK problem whenever the noise covariance matrix of the observations is known. Insofar, this work focuses on the RTK and relates precise positioning with the former model.

## 2.1 RTK Functional Model

Let us consider $n+1$ GNSS satellites simultaneously tracked over a particular frequency at the $j$ antenna of unknown coordinates $\mathbf{p}_j$ and at a base station of known coordinates $\mathbf{p}_b$. At a particular time, the code and phase observables at the $j$ antenna are

$$\begin{aligned}\rho_j^i &= \|\mathbf{p}^i - \mathbf{p}_j\| + I^i + T^i + c\left(dt_j - dt^i\right) + \varepsilon_j^i,\\ \Phi_j^i &= \|\mathbf{p}^i - \mathbf{p}_j\| - I^i + T^i + c\left(dt_j - dt^i\right) + \lambda N_j^i + \epsilon_j^i.\end{aligned} \tag{2.1}$$

Due to the influence of imprecise ephemeris and atmospheric-related errors, high-precision cannot be achieved directly exploiting the observations on (2.1). Instead, the double-difference (DD) combination formed between two satellites and two receivers is applied to eliminate or minimize nuisance parameters . For the remainder of the section, superscripts refer to a particular satellite ($r$ for the *pivot* and $i = 1, \dots, n$ for the remaining), while subscripts denote a particular receiving antenna ($j$ for the antenna of unknown position and $b$ for the base station), as illustrated in Fig. 2.2. An example of DD code and phase observations is given by

$$\begin{aligned}DD\rho_{b,j}^{i,r} &= \rho_b^i - \rho_j^i - \left(\rho_b^r - \rho_j^r\right),\\ DD\Phi_{b,j}^{i,r} &= \Phi_b^i - \Phi_j^i - \left(\Phi_b^r - \Phi_j^r\right),\end{aligned} \tag{2.2}$$

and the set of positioning DD observations are gathered in the vector $\mathbf{y} \in \mathbb{R}^{2n}$,

$$\mathbf{y} \triangleq \Big[\underbrace{DD\Phi_{b,j}^{1,r}, \cdots, DD\Phi_{b,j}^{n,r}}_{\mathbf{DD\Phi}_{b,j}^{1:n,r\top}}, \underbrace{DD\rho_{b,j}^{1,r}, \cdots, DD\rho_{b,j}^{n,r}}_{\mathbf{DD\rho}_{b,j}^{1:n,r\top}}\Big]^\top \tag{2.3}$$

where the notation $(\cdot)_{b,j}^{i,r}$ refers to the DD observation conformed by the base station and master antennas, pivot and $i$-th satellite, and $(\cdot)_{b,j}^{1:n,r}$ is the corresponding $n$-dimensional vector of DD observations.

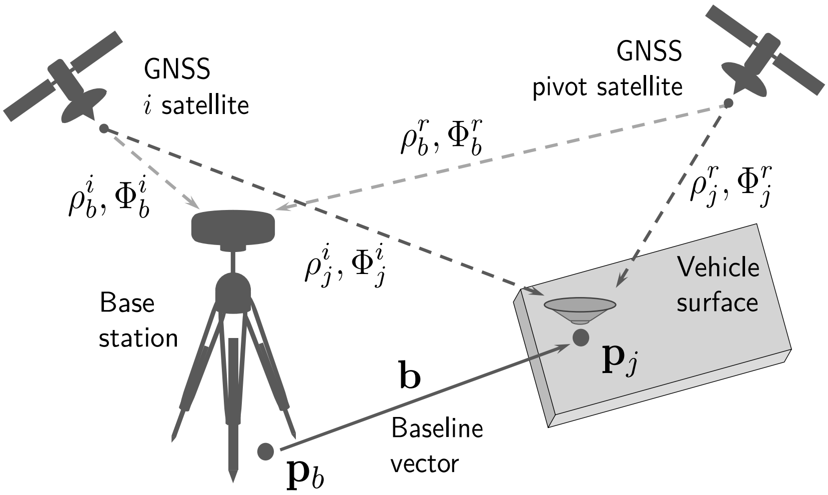

**Figure 2.2:** Depiction of the satellites, base station, and the vehicle equipped with a GNSS antenna to illustrate the RTK working principle.

**Definition 1** (Mixed Model)**.** Let $\mathbf{A}, \mathbf{B}$ be $m \times (n+p)$ full rank matrices and $\boldsymbol{\Sigma}$ an $m \times m$ symmetric and positive semi-definite matrix. Then, the mixed real- and integer-valued model –a.k.a. mixed model– can be cast as

$$\mathbf{y} \sim \mathcal{N}\left(\mathbf{A}\mathbf{a} + \mathbf{B}\mathbf{b}, \boldsymbol{\Sigma}\right), \ \mathbf{a} \in \mathbb{Z}^n, \ \mathbf{b} \in \mathbb{R}^p. \tag{2.4}$$

Within the context of GNSS positioning, the mixed model corresponds to the RTK functional model. This implies that the receiver-satellite ranges in (2.1) are linearized in the receiver-position coordinates [30]. In that case, the dimension $m = 2n$, the vector of observations $\mathbf{y}$ aligns with (2.3) and $\boldsymbol{\Sigma}$ is the observations' covariance matrix. The unknown $\mathbf{a}$ corresponds to the vector of DD ambiguities and $\mathbf{b}$ is the baseline vector between the $j$ antenna and base station positions, such that $p = 3$[1].The system design matrices $\mathbf{A}$ and $\mathbf{B}$ are then defined as follows

$$\mathbf{A} = \begin{bmatrix} \lambda_c \mathbf{I}_n \\ \mathbf{0}_{n,n} \end{bmatrix}, \ \mathbf{B} = \begin{bmatrix} \mathbf{D}\mathbf{G} \\ \mathbf{D}\mathbf{G} \end{bmatrix}, \tag{2.5}$$

where $\lambda_c$ is the carrier wavelength for the signal in use, $\mathbf{G}$ is the geometry matrix composed by the satellite steering line-of-sight vectors, as defined for SPP in (1.40), and the double differencing matrix $\mathbf{D}$ is

$$\mathbf{D} = \begin{bmatrix} -\mathbf{1}_{n,1} & \mathbf{I}_n \end{bmatrix}, \ \mathbf{D} \in \mathbb{R}^{n,n+1}. \tag{2.6}$$

The DD matrix $\mathbf{D}$ also assists when defining the covariance matrix $\boldsymbol{\Sigma}$, since it introduces the noise correlation between the base and the rover, as well as between the pivot and the remaining satellites

$$\boldsymbol{\Sigma} = \begin{bmatrix} \mathbf{D}\boldsymbol{\Sigma}_{\boldsymbol{\Phi}}\mathbf{D}^\top & \\ & \mathbf{D}\boldsymbol{\Sigma}_\rho\mathbf{D}^\top \end{bmatrix}, \tag{2.7}$$

with $\boldsymbol{\Sigma}_{\boldsymbol{\Phi}}$ and $\boldsymbol{\Sigma}_\rho$ the diagonal matrices composed by the variance of the original $n+1$ code and phase observations, respectively

$$\boldsymbol{\Sigma}_{\boldsymbol{\Phi}} = \text{diag}\left(\left(\sigma_\Phi^r\right)^2, \left(\sigma_\Phi^1\right)^2, \ldots, \left(\sigma_\Phi^n\right)^2\right), \ \boldsymbol{\Sigma}_\rho = \text{diag}\left(\left(\sigma_\rho^r\right)^2, \left(\sigma_\rho^1\right)^2, \ldots, \left(\sigma_\rho^n\right)^2\right), \tag{2.8}$$

whose modeling is discussed in 1.3.1.

Notice that resolving the baseline vector $\mathbf{b}$ allows to cast back the position of the rover as $\mathbf{p}_j = \mathbf{p}_b - \mathbf{b}$. Notice as well that, in contrast to (2.1) where the unknown ambiguities include fractional biases, the process of double-differencing eliminate those fractional part and ambiguities become integer.

---

[1] The vector of real parameters $\mathbf{b}$ shall not be limited to the baseline vector between rover and base stations, but it can be extended to include other dynamical parameters such as the velocity of the rover or atmospheric-related parameters. The modification of the former would then require to adapt the system design matrix $\mathbf{B}$ accordingly.

### Dealing with Atmospheric Residuals

As previously described, the delays due to the signals' propagation through the atmosphere are eliminated thanks to the DD combination as long as the distance between base and rover locations is sufficiently small (i.e., below 10 km). However, as the baseline separation grows, the differential biases becomes more prominent. The residuals are due to: *i)* the different line-of-sight vectors towards the satellites from the rover and base; *ii)* the differential tropospheric biases; *iii)* the differential ionospheric delays. While the first two sources can be generally overseen, since their impact on the RTK performance is limited, ionospheric residuals result key for successful differential positioning.

Thus, the baseline distance determines the strategy towards combating differential biases. For medium baselines (i.e., below 50 km), the ionospheric delays can be considered as an additional zero-mean noise term contributing to the covariance matrix $\mathbf{\Sigma}$ [62]. Its variance is expressed as a model dependent on the satellite elevation and the baseline separation, as

$$\sigma_I^i = w^i \cdot \sqrt{2} \cdot 0.4 \, \frac{\text{mm}}{\text{km}}, \tag{2.9}$$

with $w^i$ an elevation weighting function (REF). Thus, the covariance matrix for a short baseline in (2.7) becomes

$$\mathbf{\Sigma} = \begin{bmatrix} \mathbf{D}\mathbf{\Sigma}_{\mathbf{\Phi}}\mathbf{D}^\top & \\ & \mathbf{D}\mathbf{\Sigma}_{\rho}\mathbf{D}^\top \end{bmatrix} + \sigma_I^2 \cdot \mathbf{1}_{2,2} \otimes \mathbf{D}\mathbf{W}\mathbf{D}^\top, \tag{2.10}$$

where $\sigma_I^2$ has been scaled according to the baseline and the elevation weighting factor has been translated to the matrix $\mathbf{W}$ as in (1.32). Notice that a correlation between code and phase DD observations becomes apparent, since the ionospheric residuals affect both. For long baselines (i.e., longer than 50 km), the previous ionospheric model no longer applies and, instead, the DD ionospheric delays are added to the vector of real-valued unknowns $\mathbf{b}$ and estimated recursively.

## 2.2 Estimation Problem for the Mixed Model

The system of observation equations in (2.4) leads to an optimization problem with mixed real and integer parameter estimation. If we consider MLE, the estimates $\check{\mathbf{a}}$ and $\check{\mathbf{b}}$ of $\mathbf{a}$ and $\mathbf{b}$, respectively, are found by maximizing the probability of the observed $\mathbf{y}$ as

$$\begin{bmatrix} \check{\mathbf{a}} \\ \check{\mathbf{b}} \end{bmatrix} = \arg \max_{(\mathbf{a},\mathbf{b}) \in \mathbb{Z}^n \times \mathbb{R}^p} p_{Y|A,B} \left( \mathbf{y} | \mathbf{a}, \mathbf{b} \right), \tag{2.11}$$

where the probability distribution of $\mathbf{y}$ is described by the mixed model in (2.4), or

$$p_{Y|A,B} \left( \mathbf{y} | \mathbf{a}, \mathbf{b} \right) = \frac{1}{\sqrt{(2\pi)^{2n} |\mathbf{\Sigma}|}} \exp \left( -\frac{1}{2} \left\| \mathbf{y} - \mathbf{A}\mathbf{a} - \mathbf{B}\mathbf{b} \right\|_{\mathbf{\Sigma}}^2 \right), \tag{2.12}$$

which leads to the well-known weighted least-squares formulation

$$\begin{bmatrix} \check{\mathbf{a}} \\ \check{\mathbf{b}} \end{bmatrix} = \arg \min_{(\mathbf{a},\mathbf{b}) \in \mathbb{Z}^n \times \mathbb{R}^p} \left\| \mathbf{y} - \mathbf{A}\mathbf{a} - \mathbf{B}\mathbf{b} \right\|_{\mathbf{\Sigma}}^2 . \tag{2.13}$$

Due to the integer nature of $\mathbf{a}$, a closed-form solution to (2.13) is not known. Instead, one typically applies an orthogonal decomposition and expresses the quadratic optimization problem in (2.13) as the sum of three squares [63], as

$$\left\| \mathbf{y} - \mathbf{A}\mathbf{a} - \mathbf{B}\mathbf{b} \right\|_{\mathbf{\Sigma}}^2 = \left\| \hat{\mathbf{e}} \right\|_{\mathbf{\Sigma}}^2 + \left\| \hat{\mathbf{a}} - \mathbf{a} \right\|_{\mathbf{P}_{\hat{\mathbf{a}}\hat{\mathbf{a}}}}^2 + \left\| \hat{\mathbf{b}}(\mathbf{a}) - \mathbf{b} \right\|_{\mathbf{P}_{\hat{\mathbf{b}}(\mathbf{a})}}^2 , \tag{2.14}$$

where $\hat{\mathbf{e}} = \mathbf{y} - \mathbf{A}\hat{\mathbf{a}} - \mathbf{B}\hat{\mathbf{b}}$ is a vector of residuals based on a set of auxiliary variables, $(\hat{\mathbf{a}} \times \hat{\mathbf{b}}) \in \mathbb{R}^n \times \mathbb{R}^p$, commonly referred to as *float estimates*, for which the integer nature of the ambiguities is disregarded. After some trivial matrix operations, the remaining elements in (2.14) are given by

$$\hat{\mathbf{a}} = \left( \bar{\mathbf{A}}^\top \mathbf{\Sigma}^{-1} \bar{\mathbf{A}} \right)^{-1} \bar{\mathbf{A}}^\top \mathbf{\Sigma}^{-1} \mathbf{y} , \qquad \mathbf{P}_{\hat{\mathbf{a}}\hat{\mathbf{a}}} = \left( \bar{\mathbf{A}}^\top \mathbf{\Sigma}^{-1} \bar{\mathbf{A}} \right)^{-1} , \tag{2.15}$$

$$\hat{\mathbf{b}} = \left( \bar{\mathbf{B}}^\top \mathbf{\Sigma}^{-1} \bar{\mathbf{B}} \right)^{-1} \bar{\mathbf{B}}^\top \mathbf{\Sigma}^{-1} \mathbf{y} , \qquad \mathbf{P}_{\hat{\mathbf{b}}\hat{\mathbf{b}}} = \left( \bar{\mathbf{B}}^\top \mathbf{\Sigma}^{-1} \bar{\mathbf{B}} \right)^{-1} , \tag{2.16}$$

$$\hat{\mathbf{b}}(\mathbf{a}) = \left( \bar{\mathbf{B}}^\top \mathbf{\Sigma}^{-1} \bar{\mathbf{B}} \right)^{-1} \bar{\mathbf{B}}^\top \mathbf{\Sigma}^{-1} \left( \mathbf{y} - \mathbf{A}\mathbf{a} \right) , \qquad \mathbf{P}_{\hat{\mathbf{b}}(\mathbf{a})} = \left( \mathbf{B}^\top \mathbf{\Sigma}^{-1} \mathbf{B} \right)^{-1} , \tag{2.17}$$

with $\bar{\mathbf{A}} = \mathbf{\Pi}_{\mathbf{B}}^{\perp} \mathbf{A}$ and $\bar{\mathbf{B}} = \mathbf{\Pi}_{\mathbf{A}}^{\perp} \mathbf{B}$.

Based on the orthogonal decomposition in (2.14), the minimization in (2.13) is formulated as three successive LS adjustments, as

$$\min_{(\mathbf{a},\mathbf{b}) \in \mathbb{Z}^n \times \mathbb{R}^p} \left\| \mathbf{y} - \mathbf{A}\mathbf{a} - \mathbf{B}\mathbf{b} \right\|_{\mathbf{\Sigma}}^2 =$$

$$\left\| \hat{\mathbf{e}} \right\|_{\mathbf{\Sigma}}^2 + \min_{\mathbf{a} \in \mathbb{Z}^n, \mathbf{b} \in \mathbb{R}^p} \left( \left\| \hat{\mathbf{a}} - \mathbf{a} \right\|_{\mathbf{P}_{\hat{\mathbf{a}}\hat{\mathbf{a}}}}^2 + \left\| \hat{\mathbf{b}}(\mathbf{a}) - \mathbf{b} \right\|_{\mathbf{P}_{\hat{\mathbf{b}}(\mathbf{a})}}^2 \right) \tag{2.18}$$

$$\left\| \hat{\mathbf{e}} \right\|_{\mathbf{\Sigma}}^2 + \min_{\mathbf{a} \in \mathbb{Z}^n} \left( \left\| \hat{\mathbf{a}} - \mathbf{a} \right\|_{\mathbf{P}_{\hat{\mathbf{a}}\hat{\mathbf{a}}}}^2 + \min_{\mathbf{b} \in \mathbb{R}^p} \left\| \hat{\mathbf{b}}(\mathbf{a}) - \mathbf{b} \right\|_{\mathbf{P}_{\hat{\mathbf{b}}(\mathbf{a})}}^2 \right) . \tag{2.19}$$

These three estimation processes are graphically illustrated in Fig. and briefly explained in the sequel.

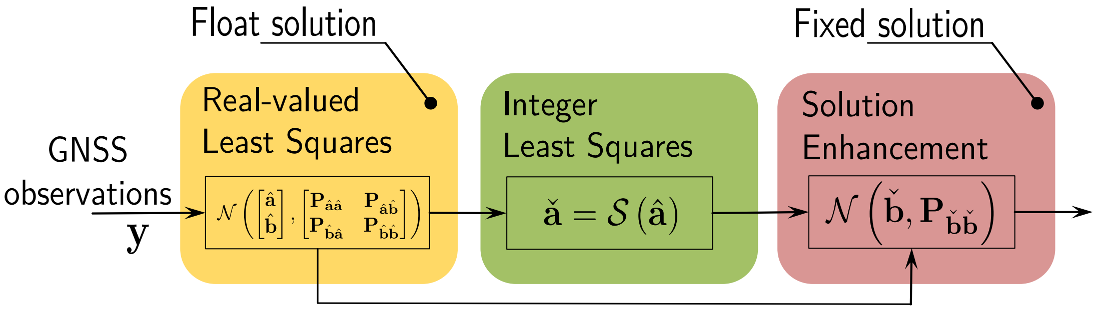

**Figure 2.3:** Diagram flow for the three-step decomposition of the estimation for the mixed model.

**1) Float Solution:** In the first step, the integer nature of the ambiguities is disregarded and a standard LS adjustment is realized. The result of the estimation is the so-called *float solution*, whose name makes reference to "float" numbers i.e., to numbers with decimal precision, whose distribution is

$$\begin{bmatrix}\hat{\mathbf{a}}\\ \hat{\mathbf{b}}\end{bmatrix} \sim \mathcal{N}\left(\begin{bmatrix}\hat{\mathbf{a}}\\ \hat{\mathbf{b}}\end{bmatrix}, \begin{bmatrix}\mathbf{P}_{\hat{\mathbf{a}}\hat{\mathbf{a}}} & \mathbf{P}_{\hat{\mathbf{a}}\hat{\mathbf{a}}}\\ \mathbf{P}_{\hat{\mathbf{b}}\hat{\mathbf{a}}} & \mathbf{P}_{\hat{\mathbf{b}}\hat{\mathbf{b}}}\end{bmatrix}\right), \tag{2.20}$$

where $\mathbf{P}$ is the associated covariance matrix which gather the uncertainty of the estimated $\hat{\mathbf{a}}$, $\hat{\mathbf{b}}$ parameters and their cross-correlation. Notice that, the LS adjustment refers not only to a LS snapshot instance but also to a batch LS estimation or to a KF correction step.

**2) Integer Solution:** The second minimization problem constitutes an Integer Least Squares (ILS) procedure, for which the integer ambiguities are estimated based on the float solution. Thus, the real-to-integer mapping $\mathcal{S} : \mathbb{R}^n \rightarrow \mathbb{Z}^n$ is the process which assigns the float ambiguity vector to an integer one $\check{\mathbf{a}} \in \mathbb{Z}^n$,

$$\check{\mathbf{a}} = \mathcal{S}\left(\hat{\mathbf{a}}\right), \tag{2.21}$$

with the operator $\mathcal{S}$ defined by a particular estimator. In addition, a validation step for the estimated integer solution often accompanies this second step, with estimators of this type belonging to the IA estimation framework. A more profound discussion on integer estimation can be found in Section 2.3.

**3) Fixed Solution:** The third and last minimization problem improves the quality of the real-valued estimates (i.e., the three-dimensional positioning vector) upon the knowledge of the integer ambiguities $\check{\mathbf{a}}$, driving to a high-accurate position solution denoted as *fixed solution*. The mean $\check{\mathbf{b}}$ and covariance $\mathbf{P}_{\check{\mathbf{b}}\check{\mathbf{b}}}$ of the fixed estimate are based on the projection of the estimated integer ambiguities into the position domain as

$$\check{\mathbf{b}} = \hat{\mathbf{b}} - \mathbf{P}_{\hat{\mathbf{b}}\hat{\mathbf{a}}}\mathbf{P}_{\hat{\mathbf{a}}\hat{\mathbf{a}}}^{-1}\left(\hat{\mathbf{a}} - \check{\mathbf{a}}\right), \tag{2.22}$$

$$\mathbf{P}_{\check{\mathbf{b}}\check{\mathbf{b}}} = \mathbf{P}_{\hat{\mathbf{b}}\hat{\mathbf{b}}} - \mathbf{P}_{\hat{\mathbf{b}}\hat{\mathbf{a}}}\mathbf{P}_{\hat{\mathbf{a}}\hat{\mathbf{a}}}^{-1}\mathbf{P}_{\hat{\mathbf{a}}\hat{\mathbf{b}}}. \tag{2.23}$$

A relevant remark is that, whenever the estimated integer ambiguities do not match the true ones, the fixed solution will be biased. This topic will be discussed more thoroughly along this Chapter.

### 2.2.1 Recursive Formulation for the Mixed Model

The purpose of this subsection is twofold: on the one hand, a generic formulation for the recursive estimation of the mixed model is discussed, with the Kalman Filter expression for a constant velocity model being particularized; on the other hand, details on solving such an estimation problem are discussed and a quadratic objective function affine to that of Section 2.2 is presented.

To extend the positioning problem to a recursive estimation for the dynamical parameters of a tracked vehicle –i.e., to exploit the information received from the observations collected over time–, one typically refers to the framework of Recursive Bayesian Estimation (RBE). Among the families of RBE solutions, the Kalman Filter (KF) and its nonlinear extensions –i.e., the Extended and Sigma-Point Gaussian Filters (EKF and SPGF, respectively)– have become the baseline for navigation- and tracking-related applications [64]. Hereinafter, we lay our focus on the KF formulation to solve the navigation problem. Thus, the mixed model can be formulated as the following marginal posterior distribution:

$$p\left(\mathbf{x}_t|\mathbf{y}_{1:t}\right) = \mathcal{N}\left(\mathbf{x}_t; \mathbf{x}_{t|t}, \mathbf{P}_{t|t}\right), \text{ with } \mathbf{x}_t = (\mathbf{a}, \mathbf{b}) \in \mathbb{Z}^n \times \mathbb{R}^p \tag{2.24}$$

with $\mathbf{x}_t$ the random process one aims at estimating, and $\mathbf{x}_{t|t}, \mathbf{P}_{t|t}$ the estimated posterior mean and covariance. The common KF state-space representation allows for modeling both the evolution of the states over time, via the *process model*, and the dependency of those with regards to the measured observations, via the *measurement model* [38, Ch. 3] and leads to the well-known two-step *prediction, correction* recursion.

Hence, the time evolution is dictated by the process function, as

$$\mathbf{x}_t = \mathbf{f}\left(\mathbf{x}_{t-1}, \mathbf{u}_t, \mathbf{w}_t\right), \tag{2.25}$$

where $\mathbf{f}(\cdot)$ is a known, possibly nonlinear, function of the state estimate, $\mathbf{u}_t$ is a control input (e.g., the gyroscope and accelerometer measurements for an inertial navigation system), and $\mathbf{w}_t$ is the process noise that gathers possible disturbances and mismodels within the process function. Typically, the process noise is assumed to be normally-distributed, with zero-mean and known covariance, such that $\mathbf{w}_t \sim \mathcal{N}(\mathbf{0}, \mathbf{Q}_t)$.

Then, the measurement function models the relationship between the state estimate and the observations:

$$\mathbf{y}_t = \mathbf{h}\left(\mathbf{x}_t, +\boldsymbol{\eta}_t\right), \tag{2.26}$$

with $\mathbf{h}(\cdot)$ a known and typically nonlinear function. Similarly to the process noise, the observations' noises $\boldsymbol{\eta}_t$ are generally assumed to follow a Gaussian distribution of known parametrization, such as $\boldsymbol{\eta} \sim \mathcal{N}(\mathbf{0}, \boldsymbol{\Sigma}_t)$.

Upon the choice of the state estimate $\mathbf{x}$, the process function is determined. Taking aside the integer ambiguities and focusing on the dynamical parameters $\mathbf{b}$, in the following some common navigation-related examples are discussed.

- Inertial Navigation System (INS). Whenever the tracked vehicle is equipped with an inertial measurement unit (IMU), the dynamics and subtle accelerations affecting a rigid body can be taken into consideration. For INS, not only are the vehicle's position and the velocity $(\mathbf{v} = \dot{\mathbf{p}})$ relevant, but so is its orientation (expressed, for instance, as unit-quaternion parametrization $\mathbf{q}$). The later allows to transform the accelerations measured at the vehicle local frame to the global or inertial frame and compensate for the gravity accelerations. Also the IMU biases $(\mathbf{b}_\omega, \mathbf{b}_\mathbf{a}$ for gyroscope and accelerometer, respectively) are typically included in the state estimate to compensate for the related drift. Thus, the vector of estimates results as

$$\begin{aligned} \mathbf{b}_{\mathsf{INS}}^{\top} &= \left[\mathbf{p}^{\top}, \mathbf{v}^{\top}, \mathbf{q}^{\top}, \mathbf{b}_{\omega}{}^{\top}, \mathbf{b}_{\mathbf{a}}{}^{\top}\right], \\ \text{with } &(\mathbf{p}, \mathbf{v}, \mathbf{q}, \mathbf{b}_{\omega}, \mathbf{b}_{\mathbf{a}}) \in \mathbb{R}^3 \times \mathbb{R}^3 \times \mathcal{S}^3 \times \mathbb{R}^3 \times \mathbb{R}^3 \end{aligned} \tag{2.27}$$

- Near Constant Acceleration and Velocity Model. Whenever the orientation of a vehicle cannot be estimated or inertial information cannot be captured, a vehicle can be assumed to advance following an accelerated motion –i.e., under the Near Constant Acceleration (NCA) model– or a constant velocity (NCV), with dynamical parameters expressed as

$$\mathbf{b}_{\mathsf{NCA}}^{\top} = \left[\mathbf{p}^{\top}, \mathbf{v}^{\top}, \dot{\mathbf{v}}^{\top}\right], \quad \text{with } (\mathbf{p}, \mathbf{v}, \dot{\mathbf{v}}) \in \mathbb{R}^3 \times \mathbb{R}^3 \times \mathbb{R}^3, \tag{2.28}$$

$$\mathbf{b}_{\mathsf{NCV}}^{\top} = \left[\mathbf{p}^{\top}, \mathbf{v}^{\top}\right], \qquad \text{with } (\mathbf{p}, \mathbf{v}) \in \mathbb{R}^3 \times \mathbb{R}^3. \tag{2.29}$$

The list of choices for a state estimate are, indeed, endless. Notable examples across different domains include: robotics-related applications, such as simultaneous localization and mapping (SLAM), the set of observed landmarks are also included; in PPP, atmospheric-related parameters such as the tropospheric wet content belong to the state estimate; in spacecraft navigation, the position and velocity are often overseen and the attitude and gyroscope biases constitute the unknown parameters.

As illustrative example, the RTK functional model in (2.4) is considered for a target moving according to a NCV model. Thus, the process and measurement models become linear and the noise contribution becomes additive white Gaussian noise (AWGN). Adding the discrete time dependency and the velocity estimation, the KF for the NCV-modeled mixed model becomes

$$\begin{aligned} \mathbf{x}_t &\triangleq \left[\mathbf{b}_{\mathsf{NCV}}{}^{\top} \quad \mathbf{a}_t^{\top}\right]^{\top} = \left[\mathbf{p}_t^{\top} \quad \mathbf{v}_t^{\top} \quad \mathbf{a}_t^{\top}\right]^{\top}, \\ \mathbf{x}_t &= \mathbf{F}_t \mathbf{x}_{t-1} + \mathbf{w}_t, \\ \mathbf{y}_t &= \mathbf{H}_t \mathbf{x}_t + \boldsymbol{\eta}_t = \mathbf{A}_t \mathbf{a}_t + \bar{\mathbf{B}}_t \mathbf{b}_t + \boldsymbol{\eta}_t \end{aligned} \tag{2.30}$$

where the matrices $\mathbf{F}_t$ and $\mathbf{H}_t$ for the prediction and correction steps, respectively, are

$$\mathbf{F}_t = \begin{bmatrix} \mathbf{I}_3 & \Delta t \mathbf{I}_3 & \mathbf{0}_{3,n} \\ \mathbf{0}_{3,3} & \mathbf{I}_3 & \mathbf{0}_{3,n} \\ \mathbf{0}_{n,3} & \mathbf{0}_{n,3} & \mathbf{I}_n \end{bmatrix}, \ \mathbf{H}_t = \begin{bmatrix} \mathbf{B}_t & \mathbf{0}_{2n,3} & \mathbf{A}_t \end{bmatrix}, \ \bar{\mathbf{B}}_t = \begin{bmatrix} \mathbf{B}_t & \mathbf{0}_{2n,3}, \end{bmatrix} \tag{2.31}$$

with $\Delta t$ the time concurred between consecutive prediction steps and $\mathbf{A}, \mathbf{B}$ defined in (2.5).

Let us now discuss the classical KF correction procedure, based on the use of the Kalman gain:

$$\mathbf{K}_t = \mathbf{P}_{t|t-1} \mathbf{H}_t^{\top} \left(\mathbf{H}_t \mathbf{P}_{t|t-1} \mathbf{H}_t^{\top} + \boldsymbol{\Sigma}_t\right)^{-1}, \tag{2.32}$$

$$\mathbf{x}_{t|t} = \mathbf{x}_{t|t-1} + \mathbf{K}_t \left(\mathbf{y}_t - \mathbf{h}(\mathbf{x}_{t|t-1})\right), \tag{2.33}$$

$$\mathbf{P}_{t|t} = \mathbf{P}_{t|t-1} - \mathbf{K}_t \mathbf{H}_t \mathbf{P}_{t|t-1}. \tag{2.34}$$

While the former set of equations are the most common procedure for KFs, its equivalent LS adjustment form [21] results more practical when dealing with the mixed model. Thus, (2.32–2.34) can be expressed as

$$\mathbf{x}_{t|t} = \left(\tilde{\mathbf{H}}_t^{\top} \tilde{\boldsymbol{\Sigma}}_t^{-1} \tilde{\mathbf{H}}_t\right)^{\dagger} \tilde{\mathbf{H}}_t^{\top} \tilde{\boldsymbol{\Sigma}}_t^{-1} \tilde{\mathbf{y}}_t, \tag{2.35}$$

$$\mathbf{P}_{t|t} = \left(\tilde{\mathbf{H}}_t^{\top} \tilde{\boldsymbol{\Sigma}}_t^{-1} \tilde{\mathbf{H}}_t\right)^{\dagger}, \tag{2.36}$$

where the $\sim$ accent indicates an augmented vector or matrix, and $(\cdot)^{\dagger}$ to the Moore-Penrose inverse. Hence, the augmented observation vector $\tilde{\mathbf{y}}_t$ includes the predicted state $\mathbf{x}_{t|t-1}$, and the measurements' covariance matrix and the observation Jacobian matrix $\mathbf{H}_t$ change consequently as:

$$\tilde{\mathbf{y}}_t = \begin{bmatrix} \mathbf{y}_t \\ \mathbf{x}_{t|t-1} \end{bmatrix}, \; \tilde{\mathbf{\Sigma}}_t = \begin{bmatrix} \mathbf{\Sigma}_t & \\ & \mathbf{P}_{t|t-1} \end{bmatrix}, \; \tilde{\mathbf{H}}_t = \begin{bmatrix} \mathbf{H}_t \\ \mathbf{I}_{n+p} \end{bmatrix}, \tag{2.37}$$

with $p = 6$ for the NCV model. The proof for the duality between the Kalman gain and the LS forms of a KF correction step is provided in Appendix A.2.

As aforementioned, the LS form of the KF becomes much more practical than the conventional Kalman gain update. Indeed, (2.35) is identical to (2.4) after replacement of the parameters by their augmented form in (2.37) and leads to

$$\begin{bmatrix} \check{\mathbf{a}}_t \\ \check{\tilde{\mathbf{b}}}_t \end{bmatrix} = \arg \min_{(\mathbf{a}_t, \tilde{\mathbf{b}}_t) \in \mathbb{Z}^n \times \mathbb{R}^p} \left\| \tilde{\mathbf{y}}_t - \mathbf{A}_t \mathbf{a}_t - \tilde{\mathbf{B}}_t \tilde{\mathbf{b}}_t \right\|^2_{\tilde{\mathbf{\Sigma}}_t} . \tag{2.38}$$

The optimization problem (2.38), which now includes the prior knowledge on the state estimate and time recursion, is solved following exactly the same three step decomposition in (2.14), as described in Section 2.2. While still sensitive to wrong integer ambiguity estimation, recursive RTK exploits the knowledge from previously estimated ambiguities and provides an overall better navigation solution as long as the process model is properly design.

## 2.3 Integer Ambiguity Resolution

IAR is the estimation process for which real-to-integer mapping is performed, such that $\mathcal{S} : \mathbb{R}^n \rightarrow \mathbb{Z}^n$. Thus, given an input real vector $\hat{\mathbf{a}} \in \mathbb{R}^n$, integer estimators procure

$$\check{\mathbf{a}} = \mathcal{S}\left(\hat{\mathbf{a}}\right), \; \check{\mathbf{a}} \in \mathbb{Z}^n, \tag{2.39}$$

with the $\mathcal{S}$ being a many-to-one map, since different real-valued vectors will be assigned to the same integer-valued vector. In this context, an estimator is described by its *pull-in region* $\mathcal{P}_{\mathbf{z}} \subset \mathbb{R}^n, \forall \mathbf{z} \in \mathbb{Z}^n$, which denote the set of values for a real vector to be mapped into the same integer via $\mathcal{S}(\cdot)$ [65, Ch. 3]. More formally, the definition of pull-in region is given by

$$\mathcal{P}_{\mathbf{z}} = \left\{ \mathbf{x} \in \mathbb{R}^n \mid \mathbf{z} = \mathcal{S}(\mathbf{x}) \right\}, \; \forall \mathbf{z} \in \mathbb{Z}^n. \tag{2.40}$$

The construction of pull-in regions is subject to three constraints [56], [65], namely

$$\begin{aligned} &i) \quad \bigcup\nolimits_{\mathbf{z} \in \mathbb{Z}^n} \mathcal{P}_{\mathbf{z}} = \mathbb{R}^n, \\ &ii) \quad \mathrm{int}\left(\mathcal{P}_{\mathbf{z}}\right) \bigcap \mathrm{int}\left(\mathcal{P}_{\mathbf{u}}\right) = \emptyset, \quad \forall \mathbf{z}, \mathbf{u} \in \mathbb{Z}^n, \mathbf{z} \neq \mathbf{u}, \\ &iii) \quad \mathcal{P}_{\mathbf{z}} = \mathcal{P}_{\mathbf{0}} + \mathbf{z}, \quad \forall \mathbf{z} \in \mathbb{Z}^n, \end{aligned} \tag{2.41}$$

with the first two conditions implying that pull-in regions cover the whole $\mathbb{R}^n$ space without overlaps –i.e., assuring the uniqueness of an estimated solution–, and the third condition referring to the translational invariance –i.e., when performing the ambiguity search, one can subtract the integer part and concern only about the decimal part of the real vector–. Fig. 2.4 illustrates a two-dimensional example of pull-in regions for three popular IAR estimators: integer rounding (IR), integer bootstrapping (IB) and integer least-squares (ILS).

Pull-in regions result extremely useful to understand the *success rate* $P_s$, i.e., the probability that an estimated integer vector $\check{\mathbf{a}}$ match the true one $P(\check{\mathbf{a}} = \mathbf{a})$. The success rate derives from integrating the PDF of the real vector $\hat{\mathbf{a}}$ over the associated pull-in region:

$$P_s \triangleq P(\check{\mathbf{a}} = \mathbf{a}) = P(\hat{\mathbf{a}} \in \mathcal{P}_{\mathbf{a}}) = \int_{\mathcal{P}_{\mathbf{a}}} p_{\hat{\mathbf{a}}}(\mathbf{x}|\mathbf{a})\,\mathrm{d}\mathbf{x} = \int_{\mathcal{P}_{\mathbf{0}}} p_{\hat{\mathbf{a}}}(\mathbf{x}|\mathbf{0})\,\mathrm{d}\mathbf{x}, \tag{2.42}$$

where the last equality derives from the translational invariance property of pull-in regions, so that $p_{\hat{\mathbf{a}}}(\mathbf{x}+\mathbf{a}|\mathbf{a}) = p_{\hat{\mathbf{a}}}(\mathbf{x}|\mathbf{0})$. Thus, the success rate $P_s$ shall depend only on the pull-in region $\mathcal{P}_0$ and on the $p_{\hat{\mathbf{a}}}(\mathbf{x}|\mathbf{0})$. Therefore, the success rate is determined by the choice of integer estimation and the precision of the float estimates [30, Ch. 23].

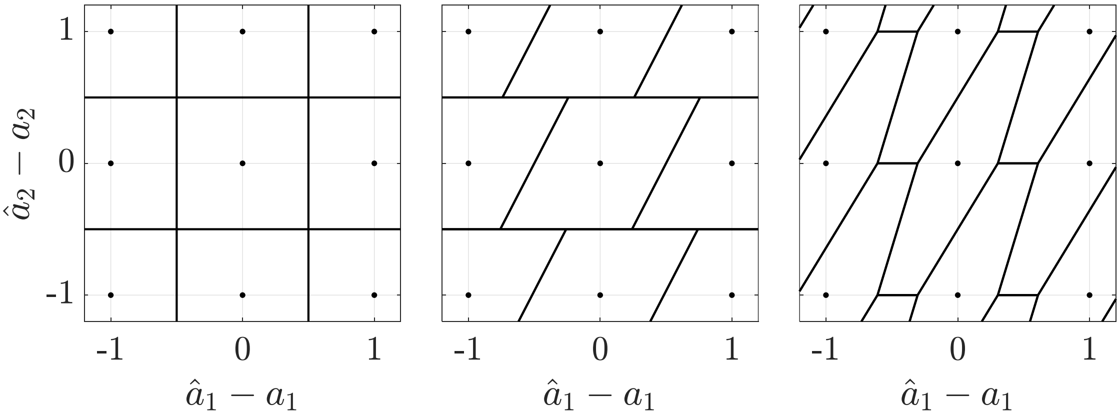

**Figure 2.4:** Pull-in regions $\mathcal{P}_{\mathbf{z}}$ for a two-dimensional example associated with the following integer estimators: integer rounding (left), integer bootstrapping (middle) and integer least-squares (right).

This section provides a brief overview on the most commonly used integer estimators: IR, IB and ILS. For an analytical assessment of the influence of the aforementioned estimators over the mixed model estimation performance, refer to Section 2.5. Also, a short discussion on ambiguity decorrelation and validity tests for estimators of this kind is presented. Finally, it is discussed the framework of Partial Ambiguity Resolution (PAR) and a PAR estimator is introduced.

## 2.3.1 Integer Estimators

### 2.3.1.1 Integer Rounding

The most uncomplicated manner to define the integer mapping $\mathcal{S}(\cdot)$ consists on rounding the elements of the real-valued vector $\hat{\mathbf{a}}$ to the nearest integer values, as

$$\check{\mathbf{a}}_{\mathsf{IR}} = \begin{bmatrix} \lceil \hat{\mathbf{a}}_1 \rfloor \\ \vdots \\ \lceil \hat{\mathbf{a}}_n \rfloor \end{bmatrix}, \tag{2.43}$$

where $\lceil\cdot\rfloor$ denotes rounding to the nearest integer. For IR, the volume of the covariance matrix $\mathbf{P}_{\hat{\mathbf{a}}\hat{\mathbf{a}}}$ and the cross-correlations between ambiguities are completely overseen. The IR pull-in regions $\mathcal{P}_{\mathsf{IR},\mathbf{z}}$ are defined as

$$\mathcal{P}_{\mathbf{z},\mathsf{IR}} = \left\{ \mathbf{x} \in \mathbb{R}^n \mid |x_i - z_i| \leq \frac{1}{2}, i = 1, \dots, n \right\}, \ \forall \mathbf{z} \in \mathbb{Z}^n, \tag{2.44}$$

with a graphical example shown in Fig. 2.4 (left). In terms of success rate, $P_{s,\mathsf{IR}} = P(\check{\mathbf{a}}_{\mathsf{IR}})$, lower and upper bounds are known [66]

$$\prod_{i=1}^{n}\left[2\Phi\left(\frac{1}{2\sigma_{\hat{a}_i}}\right)-1\right] \leq P(\check{\mathbf{a}}_{\mathsf{IR}}) \leq 2\Phi\left(\frac{1}{2\max\limits_{i=1,\ldots,n}\sigma_{\hat{a}_i}}\right), \tag{2.45}$$

with $\sigma_{\hat{a}_i}$ the diagonal values in $\mathbf{P}_{\hat{\mathbf{a}}\hat{\mathbf{a}}}$ and $\Phi(x)$ is the normal distribution function

$$\Phi(x) = \int_{-\infty}^{x}\frac{1}{\sqrt{2\pi}}\exp\left(-\frac{1}{2}v^2\right)\mathrm{d}v. \tag{2.46}$$

These lower and upper bounds for the IR success rate allows to quickly decide whether to use IR as estimator or not. Thus, whenever this lower bound is sufficiently close to 1, one shall not be concerned with using a more complex estimator.

#### 2.3.1.2 Integer Bootstrapping

Integer bootstrapping is a generalization of IR which takes into consideration the correlation between elements of the input real vector. IB proceeds in a sequential manner, starting with simple rounding the first element and correcting the remaining elements by virtue of their correlation. Since the solution depends on the order of the sequential procedure, the real vector $\hat{\mathbf{a}}$ is typically sorted in a decreasing uncertainty for the ambiguities. Then, starting with the $n$th component, the IB solution $\check{\mathbf{a}}_{\mathsf{IB}}$ is given by

$$\begin{aligned}
\check{a}_{n,\mathsf{IB}} &= \lceil \hat{a}_n \rfloor \\
\check{a}_{n-1,\mathsf{IB}} &= \lceil \hat{a}_{n-1|n} \rfloor = \lceil \hat{a}_{n-1} - \sigma_{\hat{a}_{n-1}}\sigma_{\hat{a}_n}^{-2}(\hat{a}_n - \check{a}_{n,\mathsf{IB}}) \rfloor \\
&\vdots \\
\check{a}_{1,\mathsf{IB}} &= \lceil \hat{a}_{1|2,\ldots,n} \rfloor = \lceil \hat{a}_1 - \sum_{i=2}^{n}\sigma_{\hat{a}_1}\sigma_{\hat{a}_{i|I}}^{-2}(\hat{a}_{i|I} - \check{a}_{i,\mathsf{IB}}) \rfloor,
\end{aligned} \tag{2.47}$$

where $\hat{a}_{i|I}$ is the $i$th estimated element of $\hat{\mathbf{a}}$, conditioned on the previously determined $I = i+1,\ldots,n$ elements. The former estimation can also be expressed in a compact vector form as

$$\check{\mathbf{a}}_{\mathsf{IB}} = \lceil \hat{\mathbf{a}} + \left(\mathbf{L}^{-1} - \mathbf{I}_n\right)(\hat{\mathbf{a}} - \check{\mathbf{a}}_{\mathsf{IB}}) \rfloor, \tag{2.48}$$

with $\mathbf{L}$ the unit lower triangular matrix obtained from the decomposition $\mathbf{P}_{\hat{\mathbf{a}}\hat{\mathbf{a}}} = \mathbf{L}^\top\mathbf{P}'_a\mathbf{L}$, and the diagonal matrix $\mathbf{P}'_a$ containing the conditional variances and defined as

$$\mathbf{P}'_a = \mathsf{diag}\left(\sigma^2_{\hat{a}_{1|I}},\ldots,\sigma^2_{\hat{a}_n}\right). \tag{2.49}$$

The IB pull-in region $\mathcal{P}_{\mathbf{z},\mathsf{IB}}$ results as follows

$$\mathcal{P}_{\mathbf{z},\mathsf{IB}} = \left\{\mathbf{x}\in\mathbb{R}^n \mid \left|\mathbf{c}_i^\top\mathbf{L}^{-\top}(\mathbf{x}-\mathbf{z})\right| \leq \frac{1}{2}, i = 1,\ldots,n\right\},\ \forall\mathbf{z}\in\mathbb{Z}^n, \tag{2.50}$$

where $\mathbf{c}_i$ is an unit vector whose $i$th element equals 1. A graphical example for the IB pull-in region is shown in Fig. 2.4 (middle). The IB success rate $P_{s,\mathsf{IB}} = P(\check{\mathbf{a}}_{\mathsf{IB}} = \mathbf{a})$ can be estimated exactly:

$$P_{s,\mathsf{IB}} \triangleq P(\check{\mathbf{a}}_{\mathsf{IB}} = \mathbf{a}) = \prod_{i=1}^{n}\left(2\Phi\left(\frac{1}{2\sigma_{\hat{a}_{i|I}}}\right)-1\right) \tag{2.51}$$

If one compares the success rates of IR and IB in (2.51) and (2.45), respectively, it results apparent that bootstrapping provides a better integer estimation: $P(\check{\mathbf{a}}_{\mathsf{IR}} = \mathbf{a}) \leq P(\check{\mathbf{a}}_{\mathsf{IB}} = \mathbf{a})$.

#### 2.3.1.3 Integer Least-Squares

The ILS considers all cross-correlations existing among elements of the real solution $\hat{\mathbf{a}}$. The ILS estimate $\check{\mathbf{a}}_{\mathsf{ILS}}$ corresponds to the second minimization problem of the three-step decomposition (2.14) of the mixed model estimation, such that

$$\check{\mathbf{a}}_{\mathsf{ILS}} = \arg\min_{\mathbf{z}\in\mathbb{Z}^n} \|\hat{\mathbf{a}} - \mathbf{z}\|^2_{\mathbf{P}_{\hat{\mathbf{a}}\hat{\mathbf{a}}}}. \tag{2.52}$$

The ILS pull-in regions are defined by an ellipsoidal search

$$\mathcal{P}_{\mathbf{z},\mathsf{ILS}} = \left\{\mathbf{x}\in\mathbb{R}^n \mid \|\mathbf{x}-\mathbf{z}\|^2_{\mathbf{P}_{\hat{\mathbf{a}}\hat{\mathbf{a}}}} \leq \|\mathbf{x}-\mathbf{u}\|^2_{\mathbf{P}_{\hat{\mathbf{a}}\hat{\mathbf{a}}}}, \forall \mathbf{u}\in\mathbb{Z}^n\right\},\ \forall \mathbf{z}\in\mathbb{Z}^n, \tag{2.53}$$

with a graphical two-dimensional example shown in Fig. 2.4 (right). While the IR and IB two-dimensional pull-in regions are squares and parallelograms, respectively, the ILS pull-in region is an hexagon. Unlike IR and IB, ILS estimates cannot be solved via integer rounding operations and, instead, requires searching for the optimal vector of integers over the integer grid points of an $n$-dimensional hyper-ellipsoid defined by the covariance matrix $\mathbf{P}_{\hat{\mathbf{a}}\hat{\mathbf{a}}}$ and centered in $\hat{\mathbf{a}}$. The procedure consists on evaluating the loss function $d(\mathbf{z})$ over a search size determined by the parameter $\chi^2$, as

$$d(\mathbf{z}) = (\hat{\mathbf{a}}-\mathbf{z})^\top \mathbf{P}^{-1}_{\hat{\mathbf{a}}\hat{\mathbf{a}}} (\hat{\mathbf{a}}-\mathbf{z}) \leq \chi^2, \tag{2.54}$$

so that the integer vector inside the ellipsoid with a minimum weighted distance $d(\mathbf{z})$ constitutes the ILS estimate $\check{\mathbf{a}}_{\mathsf{ILS}}$. A comprehensive explanation on the ILS search procedure is provided in [65, Ch. 3] and adapted here. Upon the Cholesky decomposition of the ambiguity covariance matrix $\mathbf{P}_{\hat{\mathbf{a}}\hat{\mathbf{a}}} = \tilde{\mathbf{L}}\tilde{\mathbf{L}}^\top$, with $\tilde{\mathbf{L}}$ a left lower triangular matrix, the cost function $d(\mathbf{z})$ is estimated following the recursion

$$d(\mathbf{z}) = \sum_{i=1}^{n}\left(\sum_{j=1}^{l}\tilde{L}_{ji}\left(\hat{a}_j - z_j\right)\right)^2 = \sum_{i=1}^{n} e_i\left(z_i,\ldots,z_n\right), \tag{2.55}$$

where $e_i(\cdot)$ indicates the distance increments dependent on the entries $z_j$, with $j \geq i$. As for IB, the ambiguities are assumed to be sorted such that the $n$th element presents the highest precision. Then, starting with $i = n$, the partial distances $d_i(z_i,\ldots,z_n)$ are expressed as

$$d_i(z_i,\ldots,z_n) = d_{i+1}(z_{i+1},\ldots,z_n) + e_i\left(z_i,\ldots,z_n\right), \tag{2.56}$$

with the initial values for $d_{n+1} = 0$ and the weighted distance $d_1(\mathbf{z})$ coincides with $d(\mathbf{z})$. Since the distance increments are non-negative, the determination of (2.55) corresponds to a tree search problem. Nodes of the tree are the partial squared distances $d_i(\cdot)$ while each of branches corresponds to a different integer value and has assigned a $e_i(\cdot)$ weight. Those nodes whose $d_i(\cdot) > \chi^2$ are disregarded, since they exceed the search space. In the final level of the three (for the first ambiguity), all the integer vector candidates are found, and the one with smallest weighted distance $d_1(\cdot)$ is the ILS solution.

Evaluating the ILS success rate $P_{s,\mathsf{ILS}} = P(\check{\mathbf{a}}_{\mathsf{ILS}} = \mathbf{a})$ results nontrivial, due to the complicated geometry of its pull-in region. While Monte Carlo simulation methods can be used to precisely characterize the success rate [67], sharp lower and upper bounds have been proposed [68], [69] for the ILS success rate:

$$P_{s,\mathsf{IB}} \leq P(\check{\mathbf{a}}_{\mathsf{ILS}} = \mathbf{a}) \leq P\left(\chi^2_{n,0} \leq \frac{c_n}{\mathsf{ADOP}^2}\right), \tag{2.57}$$

with $\chi^2_{n,0}$ a random variable having a central chi-square distribution of $n$ degrees of freedom, and the parameter $c_n$ and the Ambiguity Dilution of Precision (ADOP) defined as

$$c_n = \frac{1}{\pi} \cdot \left(\frac{n}{2}\Gamma\left(\frac{n}{2}\right)\right)^{2/n}, \ \text{ADOP} = \det\left(\mathbf{P}_{\hat{\mathbf{a}}\hat{\mathbf{a}}}\right)^{\frac{1}{2n}}, \tag{2.58}$$

with $\Gamma(x)$ the gamma function. It results clear that ILS is the best among the aforementioned estimators since IB is a better estimator than IR and, likewise, ILS is better than IB.

#### 2.3.1.4 The Role of Ambiguity Decorrelation

Due to the DD combination of the observations and after the float estimation, the covariance matrix for the float ambiguities $\mathbf{P}_{\hat{\mathbf{a}}\hat{\mathbf{a}}}$ becomes fully populated. Therefore, a high correlation between the elements of $\hat{\mathbf{a}}$ exists, as well as some ambiguities presenting a poor precision. As a result, integer estimation may become unreliable –as the case of IR and IB, whose estimation is variant against integer reparametrizations–, or computationally very demanding –as for ILS, whose performance is invariant against reparametrizations, but the number of candidates in the tree search problem is not–. A well-known solution to overcome this limitation relates to the integer reparametrizations, also known as *Z-transformations.* A square matrix $\mathbf{Z}$ may constitute a Z-transformation as long as all their entries and its inverse are integer numbers. The general class $\mathcal{Z}$ of Z-transformations is defined as follows

$$\mathcal{Z} = \left\{\mathbf{Z} \in \mathbb{Z}^{n,n} \mid |\mathbf{Z}| = \pm 1\right\}. \tag{2.59}$$

The $\mathcal{Z}$ class preserves the volume of the transformed matrix, such that $|\mathbf{P}_{\hat{\mathbf{z}}\hat{\mathbf{z}}}| = \left|\mathbf{Z}\mathbf{P}_{\hat{\mathbf{a}}\hat{\mathbf{a}}}\mathbf{Z}^\top\right| = |\mathbf{P}_{\hat{\mathbf{a}}\hat{\mathbf{a}}}|$. Due to the integer constraints over $\mathcal{Z}$, the complete decorrelation of the ambiguities is not possible, although it can be considerably reduced. In [70], several approaches for the construction of a Z-transform are discussed, with the most widely-known solution consisting on a sequence of integer approximated Gauss transformations and permutations. Thus, the integer minimization in (2.19) is typically expressed and resolved in the Z-space, as

$$\check{\mathbf{z}} = \arg\min_{\mathbf{z}\in\mathbb{Z}^n} \|\hat{\mathbf{z}} - \mathbf{z}\|^2_{\mathbf{P}_{\hat{\mathbf{z}}\hat{\mathbf{z}}}}, \quad \text{with } \hat{\mathbf{z}} = \mathbf{Z}\hat{\mathbf{a}}, \ \mathbf{P}_{\hat{\mathbf{z}}\hat{\mathbf{z}}} = \mathbf{Z}\mathbf{P}_{\hat{\mathbf{a}}\hat{\mathbf{a}}}\mathbf{Z}^\top, \tag{2.60}$$

and, afterwards, the original ambiguity space can be reconstructed from $\check{\mathbf{a}} = \mathbf{Z}^{-1}\check{\mathbf{z}}$. At this stage, a reader familiar with carrier phase-based positioning has surely recognized LAMBDA from (2.60). Least-squares AMBiguity Decorrelation Adjustment (LAMBDA) is the well-known process of performing an ILS estimation after Z-transforming the basis of real-valued ambiguities. As aforementioned, the ILS performance is not subject to integer reparametrizations although applying the later leads to search tree pruning and faster computation times. The next illustrative example showcases the relevance of Z-transformations for a two-dimensional example.

**Example 2** (Two-dimensional integer estimation.)**.** To showcase and compare the performance of IR, IB and ILS estimation, a Monte Carlo experiment with 10.000 runs is carried for a toy two-dimensional problem. Over each of these Monte Carlo runs, float ambiguities are randomly sampled from $\hat{\mathbf{a}} \sim \mathcal{N}(\mathbf{a}, \mathbf{P}_{\hat{\mathbf{a}}\hat{\mathbf{a}}})$, with

$$\mathbf{a} = \begin{bmatrix} 0 \\ 0 \end{bmatrix}, \ \mathbf{P}_{\hat{\mathbf{a}}\hat{\mathbf{a}}} = \begin{bmatrix} \sigma^2_{\hat{a}_1} & \rho_a\sigma_{\hat{a}_1}\sigma_{\hat{a}_2} \\ \rho_a\sigma_{\hat{a}_1}\sigma_{\hat{a}_2} & \sigma^2_{\hat{a}_2} \end{bmatrix} = \begin{bmatrix} 0.15 & 0.247 \\ 0.247 & 0.50 \end{bmatrix},$$

with $\rho_a = 0.90$ the correlation coefficient between ambiguities. The Z-transform is estimated following [70] and the transformed ambiguities result:

$$\mathbf{Z} = \begin{bmatrix} 1 & -2 \\ 0 & 1 \end{bmatrix}, \ \mathbf{P}_{\hat{\mathbf{z}}\hat{\mathbf{z}}} = \begin{bmatrix} \sigma^2_{\hat{z}_1} & \rho_z \sigma_{\hat{z}_1} \sigma_{\hat{z}_2} \\ \rho_z \sigma_{\hat{z}_1} \sigma_{\hat{z}_2} & \sigma^2_{\hat{a}_2} \end{bmatrix} = \begin{bmatrix} 0.15 & -0.054 \\ -0.054 & 0.114 \end{bmatrix},$$

with $\rho_z = -0.04$, i.e., the correlation is considerably lower. On the first row, Fig. 2.5 depicts the 10.000 simulated ambiguities in their original space, with estimates drawn in green or red according to whether or not correct estimation was performed, respectively. The second row of Fig. 2.5 shows the estimation performance for the decorrelated space. Estimates from IR, IB and ILS are shown from left to right.

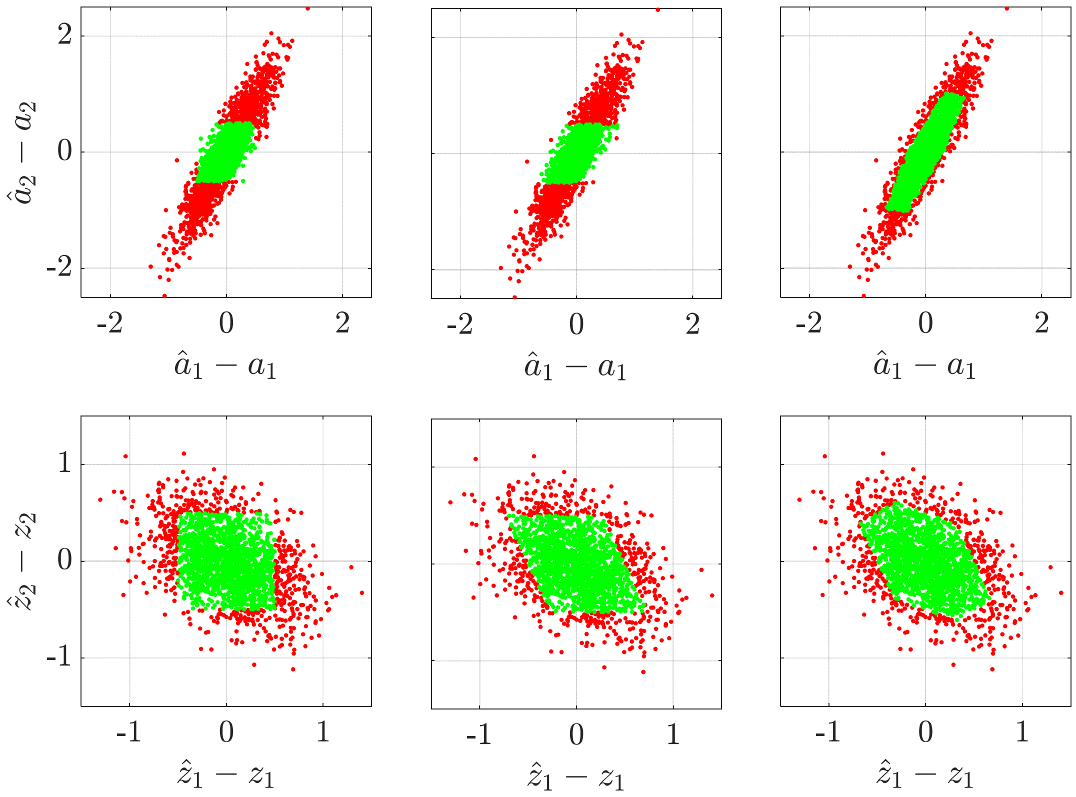

**Figure 2.5:** 2-D integer estimation problem and performance of the estimators. Red dots will pull to wrong integer solutions while green dots will pull correct ones. Original and Z-transformed ambiguities correspond to the first and second row, respectively. From left to right, integer estimation performance for IR, IB and ILS.

The percentage of correctly estimated ambiguities, or experimental success rate, is summarized in Table 2.2. In agreement with the theoretical success rate, the ILS is the best estimators, followed by IB and IR. The performance of ILS remains unaffected by the transformation, while IR and IB significantly improve after the Z-transformation is applied to the ambiguities.

**Table 2.2:** Integer estimators performance, in terms of experimental success rate (%).

| Estimator | Original ambiguities | Z-transformed ambiguities |
|---|---|---|
| IR | 50.59 | 71.12 |
| IB | 51.40 | 72.74 |
| ILS | 73.52 | 73.52 |

### 2.3.2 Validity Tests for Integer Estimation

As explained in Section 2.2, producing a fixed solution leads to an increase accuracy of the dynamical parameters only if the integer estimates are correct. Therefore, when the success rate $P(\check{\mathbf{a}} = \mathbf{a})$ of an estimator is sufficiently close to one, shall the third step in (2.14) be executed and, otherwise, the positioning solution could be biased. Integer estimators which include a validation step belong to the framework of IA estimation [56], [71], [72]. An IA estimator describes the integer mapping $\mathcal{S}(\cdot)$ in a more flexible way, as

$$\mathcal{S}\left(\hat{\mathbf{a}}\right) = \begin{cases} \check{\mathbf{a}} \in \mathbb{Z}^n & \text{if } \mathcal{T}(\cdot) \leq \mu_0, \\ \hat{\mathbf{a}} \in \mathbb{R}^n & \text{otherwise,} \end{cases} \tag{2.61}$$

with $\mathcal{T}(\cdot)$ and $\mu_0$ a generic testing function and threshold value, respectively. The definition for the testing functions leads to *model-* and *data-driven* rules. Model-driven rules are purely based on the "strength" of the model, i.e., dependent on the covariance matrix for the ambiguities $\mathcal{T}(\mathbf{P}_{\hat{\mathbf{a}}\hat{\mathbf{a}}})$, with the operator $\mathcal{S}_{\text{MD}}\left(\cdot\right)$ expressed as

$$\mathcal{S}_{\text{MD}}\left(\hat{\mathbf{a}}\right) = \begin{cases} \check{\mathbf{a}} \in \mathbb{Z}^n & \text{if } \mathcal{T}(\mathbf{P}_{\hat{\mathbf{a}}\hat{\mathbf{a}}}) \leq P_0, \\ \hat{\mathbf{a}} \in \mathbb{R}^n & \text{otherwise,} \end{cases} \tag{2.62}$$

with $\mathcal{T}(\mathbf{P}_{\hat{\mathbf{a}}\hat{\mathbf{a}}}) = P_f$ the failure rate $P_f$ –i.e., the remaining probability of not having a successful integer estimation $P_f = 1 - P_s$– and $P_0$ the target maximum probability of providing a wrong integer estimation. Thus, a model-driven test accepts an integer estimate whenever the success rate is high enough or, in other words, only if the BS success rate (which is an upper bound for the ILS performance) is sufficiently high. Alternatively, data-driven tests consider studies the likelihood for an integer estimation to be correct given its solution, the float estimate for the ambiguities and their covariance matrix. Thus, let us with $\mathcal{S}_{\text{DD}}$ the integer-mapping operator from a data-driven rule, expressed as

$$\mathcal{S}_{\text{DD}}\left(\hat{\mathbf{a}}\right) = \begin{cases} \check{\mathbf{a}} \in \mathbb{Z}^n & \text{if } \mathcal{T}\left(\hat{\mathbf{a}}, \mathbf{P}_{\hat{\mathbf{a}}\hat{\mathbf{a}}}\right) \leq \mu_0, \\ \hat{\mathbf{a}} \in \mathbb{R}^n & \text{otherwise,} \end{cases} \tag{2.63}$$

where one can distinguish, for instance, the ratio and difference tests (RT and DT), whose test functions are given by

$$\mathcal{T}_{\text{RT}} = \frac{\|\hat{\mathbf{a}} - \check{\mathbf{a}}\|^2_{\mathbf{P}_{\hat{\mathbf{a}}\hat{\mathbf{a}}}}}{\|\hat{\mathbf{a}} - \bar{\mathbf{a}}\|^2_{\mathbf{P}_{\hat{\mathbf{a}}\hat{\mathbf{a}}}}} \leq \mu_{\text{RT}}, \quad \mathcal{T}_{\text{DT}} = \|\hat{\mathbf{a}} - \bar{\mathbf{a}}\|^2_{\mathbf{P}_{\hat{\mathbf{a}}\hat{\mathbf{a}}}} - \|\hat{\mathbf{a}} - \check{\mathbf{a}}\|^2_{\mathbf{P}_{\hat{\mathbf{a}}\hat{\mathbf{a}}}} \leq \mu_{\text{DT}}, \tag{2.64}$$

with $\bar{\mathbf{a}}$ the best counter hypothesis to $\check{\mathbf{a}}$, and $\mu_{\text{RT}}$, $\mu_{\text{DT}}$ the threshold values for RT and DT, respectively. The use of data-driven tests leads to pull-in regions different to those presented in Section 2.3 –an detail description of these can be consulted in [65]–, with the $\mu$ threshold determining the size or aperture of such pull-in regions. Taking the RT as example, smaller values of $\mu_{\text{RT}}$ correspond to smaller apertures and, therefore, lower chances for a failure integer estimate. In case $\mu_{\text{RT}} = 1$, the aperture of the RT pull-in region becomes equal to that of the ILS, and integer solutions are always accepted. The underlying challenge relates to choosing the threshold value, given the changing conditions for geometry and receiver operation point. While a variety of values have been proposed based on empirical results, the fixed failure rate test (FF-RT) constitutes the most well-known solution to the afore-described challenge [73], [74]. Based on an extensive sequence of Monte Carlo experiments, a collection of look-up tables provides the user with a critical value $\mu$, based on the choice of failure rate and the strength of the model in question, which makes it very appealing for real-time implementations of carrier phase-based positioning.

The realization of a validity test leads to either a correct or wrong outcome and four possible cases:

**Success:** occurs when an estimator provides an integer solution, and this one is pulled to the true one $\mathcal{S}(\hat{\mathbf{a}}) = \check{\mathbf{a}} = \mathbf{a}$.

**Detection:** when an integer estimator returns a real-valued solution, but this would have been pulled to a wrong integer vector $\mathcal{S}(\hat{\mathbf{a}}) = \hat{\mathbf{a}} \notin \mathcal{P}_{\mathbf{a}}$.

**Failure:** when an estimator outputs an integer solution, with the latter not pulled to the true integer vector $\mathcal{S}(\hat{\mathbf{a}}) = \check{\mathbf{a}} \neq \mathbf{a}$.

**False alarm:** when a real-valued solution is provided, although this belong to the pull-in region of the correct integer solution, $\mathcal{S}(\hat{\mathbf{a}}) = \hat{\mathbf{a}} \in \mathcal{P}_{\mathbf{a}}$.

### 2.3.3 Partial Ambiguity Resolution

The estimation of the complete vector of ambiguities can be a challenging task, provided that a single bias or inaccuracy in a carrier phase pseudorange could potentially spoil the estimation. A representative example of the former relates to medium and long baseline RTK positioning. Furthermore, when observing the success rates for the previously listed estimators, the probability of correctly finding the integer vector of ambiguities tends to decrease with a raise on the number of observations, phenomena known as IAR dimensionality course [75]. The process of determining the complete vector of integer unknowns, as for the configuration of IR, IB and ILS previously described, is denoted as Full Ambiguity Resolution (FAR).

On the contrary, the framework of Partial Ambiguity Resolution (PAR) relaxes the condition of estimating the complete set of integers and so circumvents the aforementioned issues. Instead of mapping integer for all the elements in $\hat{\mathbf{a}}$, PAR identifies the subset of ambiguities to fix in agreement to a certain condition –i.e., maximizing the success rate or minimizing the failure rate–. Let $\mathcal{I}$ be the index of the ambiguities mapped to integer, such that

$$\mathcal{I} \subseteq \{1, \ldots, n\}, \ \mathcal{I} \in \mathfrak{J} \tag{2.65}$$

where $\mathfrak{J}$ denotes the set of possible non-empty index combinations, with cardinality $|\mathfrak{J}| = 2^n - 1$. The complementary set $\bar{\mathcal{I}}$, i.e., the ambiguities to remain real-valued, is given by

$$\mathcal{I} \cap \bar{\mathcal{I}} = \emptyset, \ \mathcal{I} \cup \bar{\mathcal{I}} = \{1, \ldots, n\}. \tag{2.66}$$

The real-to-integer mapping function now becomes $\mathcal{S} : \mathbb{R}^n \to \mathbb{Z}^{|\mathcal{I}|}$, and it is different among estimators. Still, an estimator and its $\mathcal{S}(\cdot)$ is related to a pull-in region, such that

$$\mathcal{P}_{\mathbf{z}} = \left\{ \mathbf{x} \in \mathbb{R}^n \mid \mathbf{z} = \mathcal{S}(\mathbf{x}) \right\}, \ \forall \mathbf{z} \in \mathbb{Z}^{|\mathcal{I}|}, \tag{2.67}$$

with the construction of the pull-in regions obeying similar constraints to those in (2.41), but for the dimension $|\mathcal{I}|$:

$$\begin{aligned} &i) \ \ \textstyle\bigcup_{\mathbf{z} \in \mathbb{Z}^{|\mathcal{I}|}} \mathcal{P}_{\mathbf{z}} = \mathbb{R}^n, \\ &ii) \ \ \mathsf{int}\left(\mathcal{P}_{\mathbf{z}}\right) \bigcap \mathsf{int}\left(\mathcal{P}_{\mathbf{u}}\right) = \emptyset, \quad \forall \mathbf{z}, \mathbf{u} \in \mathbb{Z}^{|\mathcal{I}|}, \mathbf{z} \neq \mathbf{u}, \\ &iii) \ \ \mathcal{P}_{\mathbf{z}} = \mathcal{P}_{\mathbf{0}} + \mathbf{z}, \quad \forall \mathbf{z} \in \mathbb{Z}^n, \end{aligned} \tag{2.68}$$

where the principles of translation invariance and coverage of the $\mathbb{R}^n$ space without overlaps are satisfied. Next, let us re-define the conventional mixed model, allowing a subset of ambiguities to remain real-valued.

**Definition 2** (PAR Mixed Model)**.** Let $\mathbf{A}_{\mathcal{I}}, \mathbf{A}_{\bar{\mathcal{I}}}, \mathbf{B}$ be full rank matrices and $\mathbf{\Sigma}$ an $m \times m$ symmetric and positive semi-definite matrix. Then, the PAR mixed model is as follows

$$\mathbf{y} \sim \mathcal{N}\left(\mathbf{A}_{\mathcal{I}}\mathbf{a}_{\mathcal{I}} + \mathbf{A}_{\bar{\mathcal{I}}}\mathbf{a}_{\bar{\mathcal{I}}} + \mathbf{B}\mathbf{b}, \mathbf{\Sigma}\right), \ \mathbf{a}_{\mathcal{I}} \in \mathbb{Z}^{|\mathcal{I}|}, \ \mathbf{a}_{\bar{\mathcal{I}}} \in \mathbb{R}^{|\bar{\mathcal{I}}|}, \ \mathbf{b} \in \mathbb{R}^p. \tag{2.69}$$

Following the context of carrier phase-based positioning, the dimension $m = 2 \cdot n$, $\mathbf{y}$ is the vector of DD code and carrier phase measurements, $\mathbf{\Sigma}$ is the covariance matrix of the observations and $p = 3$ when estimating the target-base station baseline vector. The design matrices $\mathbf{A}_{\mathcal{I}}, \mathbf{A}_{\bar{\mathcal{I}}}$ are defined as

$$\mathbf{A}_{\mathcal{I}} = \begin{bmatrix} \lambda_c \mathbf{I}_{n,\mathcal{I}} \\ \mathbf{0}_{n,|\mathcal{I}|} \end{bmatrix}, \quad \mathbf{A}_{\mathcal{I}} = \begin{bmatrix} \lambda_c \mathbf{I}_{n,\bar{\mathcal{I}}} \\ \mathbf{0}_{n,|\bar{\mathcal{I}}|} \end{bmatrix} \tag{2.70}$$

where $\mathbf{I}_{n,\mathcal{I}}$ and $\mathbf{I}_{n,\bar{\mathcal{I}}}$ correspond to the $n \times n$ identity matrix where only the $\mathbf{c}_i$ columns are kept ($\mathbf{c}_i$ is the $n$-dimensional unit vector having a 1 as its $i$th entry and zeros otherwise), such that

$$\mathbf{I}_{n,\mathcal{I}} = \Big[\ldots, \mathbf{c}_i, \ldots\Big], \ \mathbf{I}_{n,\mathcal{I}} \in \mathbb{R}^{n,|\mathcal{I}|}, \ i \in \mathcal{I}, \tag{2.71}$$

$$\mathbf{I}_{n,\mathcal{I}} \underset{(n=3,\mathcal{I}=\{1,3\})}{=} \begin{bmatrix} 1 & 0 \\ 0 & 0 \\ 0 & 1 \end{bmatrix}. \tag{2.72}$$

as for the conventional mixed model, the system of equations in (2.69) leads to an optimization problem where both real- and integer-valued parameters are to be estimated:

$$\begin{bmatrix} \check{\mathbf{a}}_{\mathcal{I}} \\ \check{\mathbf{a}}_{\bar{\mathcal{I}}} \\ \check{\mathbf{b}} \end{bmatrix} = \arg \min_{(\mathbf{a}_{\mathcal{I}}, \mathbf{a}_{\bar{\mathcal{I}}}, \mathbf{b}) \in \mathbb{Z}^{|\mathcal{I}|} \times \mathbb{R}^{|\bar{\mathcal{I}}|} \times \mathbb{R}^{p}} \left\| \mathbf{y} - \mathbf{A}_{\mathcal{I}} \mathbf{a}_{\mathcal{I}} - \mathbf{A}_{\bar{\mathcal{I}}} \mathbf{a}_{\bar{\mathcal{I}}} - \mathbf{B}\mathbf{b} \right\|^2_{\boldsymbol{\Sigma}}, \tag{2.73}$$

and only when $\bar{\mathcal{I}} = \emptyset$, (2.73) is equivalent to the original mixed estimation (2.13). While it appears illogical, aiming at solving a suboptimal problem, the PAR mixed model may improve the overall performance of an estimator for the mixed model by increasing the success rate for *some* ambiguities in contrast to *all* of them.

The question now resides on: how can one know the subset of ambiguities to fix? Indeed, the set $\mathcal{I}$ is not known a priori and needs to be determined along with the actual integer estimation process. Following the nomenclature from the validity tests, strategies for the selection of $\mathcal{I}$ are distinguished in model- and data-driven rules. A well-known instance of model-driven PAR employs the IB success rate (2.51), as upper bound for the ILS performance, to determine the subset $\mathcal{I} = \{n', \ldots, n\}$ that assures an estimate with a failure rate lower than a target $P_0$, such that

$$n_{\mathsf{BS}} = \arg \max_{n' \in \{1,\ldots,n\}} P_{f,\mathsf{IB},n'}, \quad \text{s.t. } P_{f,\mathsf{IB},n'} \leq P_0, \tag{2.74}$$

$$\text{with } \ P_{f,\mathsf{IB},n'} = 1 - \prod_{i=n'}^{n} \left( 2\varPhi\left(\frac{1}{2\sigma_{\hat{z}_{i|I}}}\right) - 1 \right), \tag{2.75}$$

and $\sigma^2_{\hat{z}_{i|I}}$ the conditional variance of the $i$th Z-transformed ambiguity (following an LDL decomposition as in (2.49)). The ambiguities are assumed to be sorted such that $\hat{z}_n$ presents the highest precision ($\sigma_{\hat{z}_{n|I}} \leq \sigma_{\hat{z}_{n-1|I}} \leq \sigma_{\hat{z}_{1|I}}$). The realization for this PAR subset selection is straightforward, since after the Z-transformation and LDL composition, one can quickly evaluate whether a subset fulfills the reliability requirement.

For data-driven PAR techniques, the choice of the set $\mathcal{I}$ also depends on result of applying a data-driven validity test. Doing so requires using a test of the like of (2.63) to, at most, the $2^n - 1$ possible subset combinations. Thus, an integer estimator shall sequentially iterate through the combinations of subsets, computing an integer solution and verifying its validity with a data-driven test. While this practice has been shown to perform effectively [76], [77], it can be computationally very demanding, since the number of estimation instances is not known beforehand. The workflow can also be simplified as summarized in Alg. 1, if only the worst (in terms of precision) of the ambiguities is eliminated in each iteration.

An alternative point of view on PAR is constituted within the framework of Generalized Integer Aperture (GIA) estimation, introduced by Brack in his series of works [65], [78]–[80]. GIA extends the concepts on IA estimation for PAR to describe selective pull-in regions and their aperture. Thus, GIA estimators procure a joint subset selection, integer estimation

**Algorithm 1:** Data-Driven PAR

```
Input  : Float estimate: $\hat{\mathbf{a}}, \mathbf{P}_{\hat{\mathbf{a}}\hat{\mathbf{a}}}$; target $P_{f_0}$
Output : PAR integer estimate: $\check{\mathbf{a}}_{\mathcal{I}}$
Apply Z-transform and sorting $(\sigma_{\hat{z}_{n|I}} \leq \sigma_{\hat{z}_{n-1|I}} \leq \sigma_{\hat{z}_{1|I}})$: $\hat{\mathbf{z}} = \mathbf{Z}\hat{\mathbf{a}},\ \mathbf{P}_{\hat{\mathbf{z}}\hat{\mathbf{z}}} = \mathbf{Z}\mathbf{P}_{\hat{\mathbf{a}}\hat{\mathbf{a}}}\mathbf{Z}^{\top}$.
Initialize $i = 1,\ \mathcal{I} = \{i, \ldots, n\}$.
while $i \geq n$ do
    Integer estimation: $\mathcal{S}_{\text{DD}}(\hat{\mathbf{z}}_{\mathcal{I}})$
    if $\mathcal{S}_{DD}(\hat{\mathbf{z}}_{\mathcal{I}}) \in \mathbb{Z}^{|\mathcal{I}|}$ (validity test passed) then
        return $\check{\mathbf{a}}_{\mathcal{I}} = \mathbf{Z}_{\mathcal{I}}^{-\top}\check{\mathbf{z}}_{\mathcal{I}},\ \check{\mathbf{z}}_{\mathcal{I}} = \mathcal{S}_{DD}(\hat{\mathbf{z}}_{\mathcal{I}})$, (subset integer solution)
    else Shrunk subset
        $i = i + 1,\ \mathcal{I} = \{i, \ldots, n\}$
```

and validity testing, upon the aperture of the *decision* regions. To do so, the best counter hypothesis for each of the $n$ ambiguities is tested against the overall best solution. For instance, the GIA difference test (GIA-DT) describes the subset selection as

$$\mathcal{I}_{\text{GIA-DT}} = \left\{ i = 1, \ldots, n \mid \|\hat{\mathbf{a}} - \bar{\mathbf{a}}^{i}\|^2_{\mathbf{P}_{\hat{\mathbf{a}}\hat{\mathbf{a}}}} - \|\hat{\mathbf{a}} - \check{\mathbf{a}}\|^2_{\mathbf{P}_{\hat{\mathbf{a}}\hat{\mathbf{a}}}} \leq \mu_{\text{GIA-DT}} \right\} \tag{2.76}$$

where $\bar{\mathbf{a}}^{i}$ is the best counter hypothesis to $\check{\mathbf{a}}$ for which the $i$-th element is different and $\mu_{\text{GIA-DT}}$ is a threshold value. In analogy to the FF-RT, such a threshold $\mu_{\text{GIA-DT}}$ can be dynamically estimated upon a particular target failure rate [79]. A relevant note when applying conventional PAR approaches, for all model-, data-driven PAR and GIA, is that a subset of ambiguities may be estimated reliably while the gain on the posterior fixed position solution may be minimal (e.g., if only two ambiguities belonging to the same satellite over different frequencies as integer-mapped, the fixed positioning solution would barely improve its precision).

To overcome the aforementioned limitation of the PAR precision, this Chapter introduces Precision-Driven PAR (PD-PAR). PD-PAR is a subset selection criteria based on the projection of the ambiguities into the domain of the fixed positioning estimate. Thus, one aims at finding a reduced number of ambiguities which guarantee certain target positioning precision criteria $\alpha$ for the fixed position solution while retaining a sufficiently low failure rate $P_{f_0}$. Notice that the precision requirement $\alpha$ refers to the minimal positioning precision required by a particular application (e.g., automobile lane detection may require decimeter-level precision [81], while vessel mooring assistance might entail a precision of a few centimeters [6]). For that purpose, the optimization problem in (2.73) is reformulated with the addition of a constraint over the precision of the fixed positioning solution, as

$$\begin{aligned} \begin{bmatrix} \check{\mathbf{a}}_{\mathcal{I}} \\ \check{\mathbf{a}}_{\bar{\mathcal{I}}} \\ \check{\mathbf{b}} \end{bmatrix} &= \arg \min_{(\mathbf{a}_{\mathcal{I}}, \mathbf{a}_{\bar{\mathcal{I}}}, \mathbf{b}) \in \mathbb{Z}^{|\mathcal{I}|} \times \mathbb{R}^{|\bar{\mathcal{I}}|} \times \mathbb{R}^{p}} \|\mathbf{y} - \mathbf{A}_{\mathcal{I}}\mathbf{a}_{\mathcal{I}} - \mathbf{A}_{\bar{\mathcal{I}}}\mathbf{a}_{\bar{\mathcal{I}}} - \mathbf{B}\mathbf{b}\|^2_{\mathbf{\Sigma}}, \\ &\text{s.t. } \operatorname{tr}\left(\mathbf{P}_{\check{\mathbf{b}}\check{\mathbf{b}}}\right) \leq \alpha^2, \end{aligned} \tag{2.77}$$

where $\mathbf{P}_{\check{\mathbf{b}}\check{\mathbf{b}}}$ is the covariance matrix for the fixed positioning solution. Unlike (2.22) and (2.23), the fixed solution for a PAR estimator is expressed in terms of the subset of ambiguities fixed, as

$$\check{\mathbf{b}} = \hat{\mathbf{b}} - \mathbf{P}_{\hat{\mathbf{b}}\hat{\mathbf{a}}_{\mathcal{I}}}\mathbf{P}^{-1}_{\hat{\mathbf{a}}_{\mathcal{I}}}\left(\hat{\mathbf{a}}_{\mathcal{I}} - \check{\mathbf{a}}_{\mathcal{I}}\right), \tag{2.78}$$

$$\mathbf{P}_{\check{\mathbf{b}}\check{\mathbf{b}}} = \mathbf{P}_{\hat{\mathbf{b}}\hat{\mathbf{b}}} - \mathbf{P}_{\hat{\mathbf{b}}\hat{\mathbf{a}}_{\mathcal{I}}}\mathbf{P}^{-1}_{\hat{\mathbf{a}}\hat{\mathbf{a}}_{\mathcal{I}}}\mathbf{P}_{\hat{\mathbf{a}}_{\mathcal{I}}\hat{\mathbf{b}}}, \tag{2.79}$$

and, since $\mathbf{P}_{\hat{\mathbf{b}}\hat{\mathbf{b}}}$ remains invariant with the subset choice, the selection can be realized so that

$$\text{tr}\left(\mathbf{P}_{\hat{\mathbf{b}}\hat{\mathbf{a}}_{\mathcal{I}}}\mathbf{P}^{-1}_{\hat{\mathbf{a}}\hat{\mathbf{a}}_{\mathcal{I}}}\mathbf{P}_{\hat{\mathbf{a}}_{\mathcal{I}}\hat{\mathbf{b}}}\right) \geq \text{tr}\,\left(\mathbf{P}_{\hat{\mathbf{b}}\hat{\mathbf{b}}}\right) - \alpha^2, \tag{2.80}$$

so that one may omit performing integer estimation if the associated positioning precision does not match the target $\alpha$. The procedure to operate PD-PAR consists on recursively finding the subset with best associated precision and whether a reliable integer solution exists (i.e., passing the validity test assures that the success rate is sufficiently high). If the position precision criteria $\alpha$ is not fulfilled, a fixed solution cannot be estimated for the subset $\mathcal{I}$. The subset $\mathcal{I}$ searching is based on (2.80) that follow from (2.79). Instead, if the precision is sufficient but a reliable solution is unavailable, the size of the subset reduces and the recursion is repeated.

**Algorithm 2:** Precision-Driven PAR

```
Input  : Float estimate: $\begin{bmatrix}\hat{\mathbf{a}}\\ \hat{\mathbf{b}}\end{bmatrix}, \begin{bmatrix}\mathbf{P}_{\hat{\mathbf{a}}\hat{\mathbf{a}}} & \mathbf{P}_{\hat{\mathbf{a}}\hat{\mathbf{b}}}\\ \mathbf{P}_{\hat{\mathbf{b}}\hat{\mathbf{a}}} & \mathbf{P}_{\hat{\mathbf{b}}\hat{\mathbf{b}}}\end{bmatrix}$; target $P_{f_0}, \alpha$
Output : PD-PAR fixed solution: $\check{\mathbf{b}}, \check{\mathbf{a}}_{\mathcal{I}}$
Initialize $s = 0$.
while $s \geq n$ do (iterate over subset size)
    List subsets: $\mathcal{I}' \subseteq \{1, \ldots, n\},\ \mathcal{I}' \in \mathfrak{J}',\ |\mathfrak{J}'| = \binom{n}{n-s}$
    Find best subset: $\mathcal{I} = \arg\max_{\mathcal{I}'}\ \text{tr}\left(\mathbf{P}_{\hat{\mathbf{b}}\hat{\mathbf{a}}_{\mathcal{I}'}}\mathbf{P}^{-1}_{\hat{\mathbf{a}}\hat{\mathbf{a}}_{\mathcal{I}'}}\mathbf{P}_{\hat{\mathbf{a}}_{\mathcal{I}'}\hat{\mathbf{b}}}\right)$
    if $tr\left(\mathbf{P}_{\hat{\mathbf{b}}\hat{\mathbf{a}}_{\mathcal{I}'}}\mathbf{P}^{-1}_{\hat{\mathbf{a}}\hat{\mathbf{a}}_{\mathcal{I}'}}\mathbf{P}_{\hat{\mathbf{a}}_{\mathcal{I}'}\hat{\mathbf{b}}}\right) < tr\left(\mathbf{P}_{\hat{\mathbf{b}}\hat{\mathbf{b}}}\right) - \alpha^2$ (precision test not passed) then
        return $\check{\mathbf{a}}_{\mathcal{I}} = \hat{\mathbf{a}}_{\mathcal{I}}$ (fixed solution unavailable)
    else
        Apply Z-transform and sorting ($\sigma_{\hat{z}_{n-s|I}} \leq \cdots \leq \sigma_{\hat{z}_{1|I}}$):
        $\hat{\mathbf{z}}_{\mathcal{I}} = \mathbf{Z}\hat{\mathbf{a}}_{\mathcal{I}},\ \mathbf{P}_{\hat{\mathbf{z}}\hat{\mathbf{z}}_{\mathcal{I}}} = \mathbf{Z}\mathbf{P}_{\hat{\mathbf{a}}\hat{\mathbf{a}}_{\mathcal{I}}}\mathbf{Z}^{\top}$.
        Integer estimation: $\mathcal{S}_{\text{DD}}(\hat{\mathbf{z}}_{\mathcal{I}})$
        if $\mathcal{S}_{DD}(\hat{\mathbf{z}}_{\mathcal{I}}) \in \mathbb{Z}^{|\mathcal{I}|}$ (validity test passed) then
            return $\check{\mathbf{a}}_{\mathcal{I}} = \mathbf{Z}_{\mathcal{I}}^{-\top}\check{\mathbf{u}}_{\mathcal{I}},\ \check{\mathbf{u}}_{\mathcal{I}} = \mathcal{S}_{DD}(\hat{\mathbf{z}}_{\mathcal{I}})$, (subset integer solution)
        else Shrunk subset
            $s = s + 1$
Fixed solution estimation via (2.78),(2.79)
```

Alg. 2 sketches a top-bottom (the number of ambiguities to integer-map decreases with the iterations) workflow for PD-PAR. Notice that, PD-PAR derives from a model-driven PAR estimator, since the ambiguity validity test aligns with the data-driven rules in (2.63). The novelty is that the subset selection is realized based on how good the ambiguities are projected into the positioning domain. Moreover, the Z-transform is estimated for each subset size, which greatly reduces the degree of decorrelation among ambiguities at the cost of a slightly superior computational complexity. As for other data-driven approaches, the number of iterations until a subset can be reliably integer estimated is not known beforehand. However, whenever the satellite geometry is poor or the model is weak, one can rapidly disregards any integer estimation, provided that a potential fixed solution would not comply with the target positioning precision. More details on the computational complexity and the performance comparison of PD-PAR against other PAR solutions may be consulted in [1].

## 2.4 Estimation Bounds for the Mixed Model

The most popular LB is the well-known CRB derived for the real- and complex-valued parameter vector, mostly because of: $i)$ its simplicity of calculation, for instance using the Slepian-Bangs' formula [82]; $ii)$ it is the lowest bound on the MSE of any unbiased estimator ; and $iii)$ it is asymptotically attained by MLEs under certain conditions (i.e., high SNR [83] and/or large number of snapshots [84]), that is, MLEs are asymptotically efficient. Inherent limitations of such CRBs are their inability to: predict the *threshold phenomena*; provide tight bounds in certain cases [85]; and deal with integer-valued parameter estimation, which is the focus of this section.

There are two main categories of LBs, *deterministic* and *Bayesian* [86]. While the former considers that the parameters to be estimated are deterministic and evaluate the *locally best* estimator performance, the latter consider random parameters with a given *a priori* probability and evaluate the *globally best* estimator behavior. Hereinafter, the focus will lay on deterministic parameter estimation. A plethora of deterministic bounds have been proposed in the literature [87]–[95] to provide computable approximations of the Barankin bound (BB) [96], which is the tightest LB for any absolute moment of order greater than 1 of unbiased estimators but does not admit an analytic solution in general.

To obtain a closed-form CRB expression for the mixed model, one leverages on the McAulay-Seidman bound (MSB) [89]. The MSB is the BB approximation obtained from a discretization of the Barankin uniform unbiasedness constraint, using a set of selected values of the parameter vector, so-called *test points*. Thus, a general CRB definition for the mixed model is obtained and it is particularized for the RTK functional model (as example of linear regression problem). Next, a brief introduction to the MSB and the CRB is provided.

### 2.4.1 Background on MSB and CRB for Real Parameters

Let $\mathbf{y}$ be a random real-valued observations vector and $\mathcal{Y} \subset \mathbb{R}^n$ the observation space. Denote by $p(\mathbf{y}; \mathbf{x}) \triangleq p(\mathbf{y}|\mathbf{x})$ the pdf of the observations conditional on an unknown deterministic real-valued parameter vector $\mathbf{x} \in \mathcal{X} \subset \mathbb{R}^K$. Let $\mathcal{L}_2(\mathcal{Y})$ be the real vector space of square integrable functions over $\mathcal{Y}$. If we consider an estimator $\mathbf{g}(\hat{\mathbf{x}}) \in \mathcal{L}_2^n(\mathcal{Y})$ of $\mathbf{g}(\mathbf{x})$, where $\mathbf{x}$ is a selected generic parameter vector and $\mathbf{g}(\mathbf{x}) = [g_1(\mathbf{x}), \ldots, g_n(\mathbf{x})]^\top$ is a real-valued function vector, then the MSE matrix writes,

$$\mathbf{MSE}(\mathbf{g}(\hat{\mathbf{x}})) = \mathbb{E}_{\mathbf{y};\mathbf{x}}\left[(\mathbf{g}(\hat{\mathbf{x}}) - \mathbf{g}(\mathbf{x}))(\mathbf{g}(\hat{\mathbf{x}}) - \mathbf{g}(\mathbf{x}))^\top\right]. \qquad (2.81)$$

The search for a LB on the MSE (2.81) (w.r.t. the Löwner ordering for positive symmetric matrices [97]) can be performed with the minimization of a norm under linear constraints [90], [92], [93]. Thus, to avoid the trivial solution $\mathbf{g}(\hat{\mathbf{x}}) = \mathbf{g}(\mathbf{x})$, [96] introduced the formulation of *uniform unbiasedness*,

$$\mathbb{E}_{\mathbf{y};\mathbf{x}}[\mathbf{g}(\hat{\mathbf{x}})] = \mathbf{g}(\mathbf{x}), \forall \mathbf{x} \in \mathcal{X}, \qquad (2.82)$$

and the consequent Barankin bound (BB) subject to such constraints, as

$$\min_{\mathbf{g}(\hat{\mathbf{x}}) \in \mathcal{L}_2^n(\mathcal{Y})} \{\mathbf{MSE}(\mathbf{g}(\hat{\mathbf{x}}))\} \text{ s.t. } \mathbb{E}_{\mathbf{y};\mathbf{x}}[\mathbf{g}(\mathbf{x})] = \mathbf{g}(\mathbf{x}), \forall \mathbf{x} \in \mathcal{X}, \qquad (2.83)$$

which does not admit an analytic solution in general.

The McAulay-Seidman bound (MSB) is the computable BB approximation obtained from a discretization of the *uniform unbiasedness* constraint (2.82). Let $\{\mathbf{x}\}^L \triangleq \{\mathbf{x}\}^{[1,L]} = \left\{\mathbf{x}^1, \ldots, \mathbf{x}^L\right\} \in \mathcal{X}^L$ be a subset of $L$ selected values of $\mathbf{x}$ (a.k.a. *test points*). Then, any unbiased estimator $\mathbf{g}(\hat{\mathbf{x}})$ verifying (2.82) must comply with the following subset of $L$ LCs,

$$\mathbb{E}_{\mathbf{y};\mathbf{x}^l}\left[\mathbf{g}(\hat{\mathbf{x}})\right] = \mathbf{g}(\mathbf{x}^l), \quad 1 \leq l \leq L, \tag{2.84}$$

which can be recast as

$$\underbrace{\mathbb{E}_{\mathbf{y};\mathbf{x}}\left[\boldsymbol{\upsilon}_{\mathbf{x}}\left(\mathbf{y};\{\mathbf{x}\}^L\right)\left(\mathbf{g}(\hat{\mathbf{x}}) - \mathbf{g}(\mathbf{x})\right)^\top\right]}_{\boldsymbol{\Gamma}} = \underbrace{\begin{bmatrix} \left(\mathbf{g}(\mathbf{x}^1) - \mathbf{g}(\mathbf{x})\right)^\top \\ \vdots \\ \left(\mathbf{g}(\mathbf{x}^L) - \mathbf{g}(\mathbf{x})\right)^\top \end{bmatrix}}_{\mathbf{V}}, \tag{2.85}$$

where $\boldsymbol{\upsilon}_{\mathbf{x}}\left(\mathbf{y};\{\mathbf{x}\}^L\right) = \left[\upsilon_{\mathbf{x}}\left(\mathbf{y};\mathbf{x}^1\right), \ldots, \upsilon_{\mathbf{x}}\left(\mathbf{y};\mathbf{x}^L\right)\right]^\top$ is the vector of likelihood ratios associated to $\{\mathbf{x}\}^L$ such that, for the $l$th test point the likelihood is given by

$$\upsilon_{\mathbf{x}}\left(\mathbf{y};\mathbf{x}^l\right) = \frac{p\left(\mathbf{y};\mathbf{x}^l\right)}{p\left(\mathbf{y};\mathbf{x}\right)}. \tag{2.86}$$

The $L$ linear constraints in (2.85) yields the approximation of (2.83) proposed by McAulay and Seidman [93],

$$\min_{\mathbf{g}(\hat{\mathbf{x}}) \in \mathcal{L}_2^n(\mathcal{Y})} \left\{\mathbf{MSE}\left(\mathbf{g}(\hat{\mathbf{x}})\right)\right\} \text{ s.t. } \boldsymbol{\Gamma} = \mathbf{V}, \tag{2.87}$$

and defines the MSB (Lemma 1 in [98]) [89], [93]

$$\mathbf{MSE}\left(\mathbf{g}(\hat{\mathbf{x}})\right) \geq \boldsymbol{\Delta}_{\mathbf{g}}\left(\mathbf{x},\{\mathbf{x}\}^L\right)\mathbf{R}_{\boldsymbol{\upsilon}_{\mathbf{x}}}^{-1}\boldsymbol{\Delta}_{\mathbf{g}}^\top\left(\mathbf{x},\{\mathbf{x}\}^L\right), \tag{2.88}$$

with

$$\boldsymbol{\Delta}_{\mathbf{g}}\left(\mathbf{x},\{\mathbf{x}\}^L\right) = \left[\begin{array}{ccc} \mathbf{g}\left(\mathbf{x}^1\right) - \mathbf{g}\left(\mathbf{x}\right) & \ldots & \mathbf{g}\left(\mathbf{x}^L\right) - \mathbf{g}\left(\mathbf{x}\right) \end{array}\right], \tag{2.89}$$

$$\mathbf{R}_{\boldsymbol{\upsilon}_{\mathbf{x}}} \triangleq \mathbf{R}_{\boldsymbol{\upsilon}_{\mathbf{x}}}\left(\{\mathbf{x}\}^L\right) = \mathbb{E}_{\mathbf{y};\mathbf{x}}\left[\boldsymbol{\upsilon}_{\mathbf{x}}\left(\mathbf{y};\{\mathbf{x}\}^L\right)\boldsymbol{\upsilon}_{\mathbf{x}}^\top\left(\mathbf{y};\{\mathbf{x}\}^L\right)\right], \tag{2.90}$$

which results the generalization of the Hammersley-Chapman-Robbins bound (HaChRB), introduced previously in [88], [99] for 2 test points $(L = 2)$.

### CRB as a Limiting Form of the MSB

The definition of the CRB as the limiting form of the aforementioned HaChRB —and consequently, also for the MSB—, was first showed in [96], and later extended to the multidimensional real parameter case in [89]. Thus, let us consider the following subset of test points

$$\{\mathbf{x}\}^{1+K} = \{\mathbf{x}, \mathbf{x} + \mathbf{i}_1 dx_1, \ldots, \mathbf{x} + \mathbf{i}_K dx_K\} \text{ under } dx_k \neq 0, \quad 1 \leq k \leq K,$$

where the first test point corresponds to $\mathbf{x}^0$, and $\mathbf{i}_k$ is the $k$th column of the identity matrix $\mathbf{I}_K$. Thus, (2.86) and (2.89) can be reformulated as

$$\boldsymbol{\upsilon}_{\mathbf{x}^0}\left(\mathbf{y}; \{\mathbf{x}\}^{1+K}\right) = \left[\begin{array}{cccc} 1 & \frac{p(\mathbf{y};\mathbf{x}+\mathbf{i}_1 dx1)}{p(\mathbf{y};\mathbf{x})} & \ldots & \frac{p(\mathbf{y};\mathbf{x}+\mathbf{i}_K dx_K)}{p(\mathbf{y};\mathbf{x})} \end{array}\right]^\top,$$

$$\boldsymbol{\Delta}_{\mathbf{g}}\left(\mathbf{x}, \{\mathbf{x}\}^{1+K}\right) = \left[\begin{array}{cccc} \mathbf{0} & \mathbf{g}\left(\mathbf{x} + \mathbf{i}_1 dx_1\right) - \mathbf{g}\left(\mathbf{x}\right) & \ldots & \mathbf{g}\left(\mathbf{x} + \mathbf{i}_K dx_K\right) - \mathbf{g}\left(\mathbf{x}\right) \end{array}\right],$$

and, with $d\mathbf{x} = (dx_1, \ldots, dx_K)^\top$, yields to (see Appendix A.3)

$$\boldsymbol{\Delta}_{\mathbf{g}}\left(\mathbf{x}\right) \mathbf{R}_{\boldsymbol{\upsilon}_{\mathbf{x}}}^{-1} \boldsymbol{\Delta}_{\mathbf{g}}^\top\left(\mathbf{x}\right) = \boldsymbol{\Lambda}_{\mathbf{g}}\left(\mathbf{x}, d\mathbf{x}\right) \widetilde{\mathbf{F}}\left(\mathbf{x}, d\mathbf{x}\right)^{-1} \boldsymbol{\Lambda}_{\mathbf{g}}^\top\left(\mathbf{x}, d\mathbf{x}\right), \tag{2.91}$$

where

$$\widetilde{\mathbf{F}}\left(\mathbf{x}, d\mathbf{x}\right) = \mathbb{E}_{\mathbf{y};\mathbf{x}}\left[\left(\begin{array}{c} \frac{p(\mathbf{y};\mathbf{x}+\mathbf{i}_1 dx_1)-p(\mathbf{y};\mathbf{x})}{dx_1 p(\mathbf{y};\mathbf{x})} \\ \vdots \\ \frac{p(\mathbf{y};\mathbf{x}+\mathbf{i}_K dx_K)-p(\mathbf{y};\mathbf{x})}{dx_K p(\mathbf{y};\mathbf{x})} \end{array}\right)\left(\begin{array}{c} \frac{p(\mathbf{y};\mathbf{x}+\mathbf{i}_1 dx_1)-p(\mathbf{y};\mathbf{x})}{dx_1 p(\mathbf{y};\mathbf{x})} \\ \vdots \\ \frac{p(\mathbf{y};\mathbf{x}+\mathbf{i}_K dx_K)-p(\mathbf{y};\mathbf{x})}{dx_K p(\mathbf{y};\mathbf{x})} \end{array}\right)^\top\right] \tag{2.92}$$

$$\boldsymbol{\Lambda}_{\mathbf{g}}\left(\mathbf{x}, d\mathbf{x}\right) = \left[\begin{array}{ccc} \frac{\mathbf{g}(\mathbf{x}+\mathbf{i}_1 dx_1)-\mathbf{g}(\mathbf{x})}{dx_1} & \ldots & \frac{\mathbf{g}(\mathbf{x}+\mathbf{i}_K dx_K)-\mathbf{g}(\mathbf{x})}{dx_K} \end{array}\right], \tag{2.93}$$

which results in a general definition of the $\mathbf{CRB}\left(\mathbf{g}(\hat{\mathbf{x}})\right)$ as

$$\mathbf{CRB}\left(\mathbf{g}(\hat{\mathbf{x}})\right) = \lim_{\sup\{dx_1 \neq 0, \ldots, dx_K \neq 0\} \to 0} \boldsymbol{\Lambda}_{\mathbf{g}}\left(\mathbf{x}, d\mathbf{x}\right) \widetilde{\mathbf{F}}\left(\mathbf{x}, d\mathbf{x}\right)^{-1} \boldsymbol{\Lambda}_{\mathbf{g}}^\top\left(\mathbf{x}, d\mathbf{x}\right). \tag{2.94a}$$

If $\mathbf{x} \in \mathcal{X} \subset \mathbb{R}^K$ and $\mathbf{g}\left(\mathbf{x}\right)$ and $p\left(\mathbf{y}; \mathbf{x}\right)$ are $C^1$ at $\mathbf{x}$, then (2.94a) yields the well known Fisher Information Matrix (FIM) $\mathbf{F}\left(\mathbf{x}\right)$ and the usual CRB expression

$$\mathbf{F}\left(\mathbf{x}\right) = \mathbb{E}_{\mathbf{y};\mathbf{x}}\left[\frac{\partial \ln p\left(\mathbf{y}; \mathbf{x}\right)}{\partial \mathbf{x}} \frac{\partial \ln p\left(\mathbf{y}; \mathbf{x}\right)}{\partial \mathbf{x}}^\top\right], \tag{2.94b}$$

$$\mathbf{CRB}\left(\mathbf{g}(\hat{\mathbf{x}})\right) = \frac{\partial \mathbf{g}\left(\mathbf{x}\right)}{\partial \mathbf{x}^\top} \mathbf{F}\left(\mathbf{x}\right)^{-1} \left(\frac{\partial \mathbf{g}\left(\mathbf{x}\right)}{\partial \mathbf{x}^\top}\right)^\top. \tag{2.94c}$$

Leveraging the MSB and CRB results presented in this section, a LB for deterministic parameter vector estimation, where such vector presents a mixture of real- and integer-valued parameters, is derived next. A general result is provided and then particularized for the case of linear regression under Gaussian observations, which corresponds to the RTK functional model described in Section 2.1.

### 2.4.2 General CRB for Mixed Parameter Estimation

The main result derived in this section is summarized in the form of Theorem 1. A corollary follows, which simplifies the former for a particular class of models.

**Theorem 1** (General CRB for mixed parameter vectors)**.** *Assume a set of observations* $\mathbf{y} \in \mathcal{Y} \subset \mathbb{R}^n$ *and an unknown deterministic real-valued parameter vector* $\mathbf{x} \in \mathcal{X} \subset \mathbb{R}^K$ *where* $\mathbf{x}^\top = \left[\boldsymbol{\omega}^\top, \mathbf{z}^\top\right]$, $\boldsymbol{\omega} \in \mathbb{R}^{K_\omega}$, $\mathbf{z} \in \mathbb{Z}^{K_z}$, $K_\omega + K_z = K$. *Those quantities are related through a statistical model of the form* $\mathbf{y}|\mathbf{x} \sim p(\mathbf{y}|\mathbf{x})$, *which is available. Then, the MSE of any unbiased estimator of a function* $\mathbf{g}(\hat{\mathbf{x}}) \in \mathcal{L}_2(\mathcal{Y})$ *for a selected value of the parameter* $\mathbf{x}$ *is lower bounded by*

$$\mathbf{CRB}(\mathbf{g}(\hat{\mathbf{x}})) = \boldsymbol{\Lambda}_{\mathbf{g}}(\mathbf{x})\, \overline{\mathbf{F}}(\mathbf{x})^{-1} \boldsymbol{\Lambda}_{\mathbf{g}}^\top(\mathbf{x}), \tag{2.95}$$

*with*

$$\boldsymbol{\Lambda}_{\mathbf{g}}(\mathbf{x}) = \left[\begin{array}{cccc} \frac{\partial \mathbf{g}(\mathbf{x})}{\partial \boldsymbol{\omega}^\top} & \mathbf{g}(\mathbf{x}^1) - \mathbf{g}(\mathbf{x}) & \dots & \mathbf{g}\left(\mathbf{x}^{2K_z}\right) - \mathbf{g}(\mathbf{x}) \end{array}\right] \tag{2.96}$$

$$\overline{\mathbf{F}}(\mathbf{x}) = \left[\begin{array}{cc} \mathbf{F}_{\boldsymbol{\omega}\boldsymbol{\omega}} & \mathbf{F}_{\boldsymbol{\omega}\mathbf{z}} \\ \mathbf{F}_{\boldsymbol{\omega}\mathbf{z}}^\top & \mathbf{F}_{\mathbf{z}\mathbf{z}} \end{array}\right], \tag{2.97}$$

*where the test points* $\{\mathbf{x}\}^{2K_z}$ *are defined as*

$$\mathbf{x}^j = \mathbf{x} + (-1)^{j-1}\, \mathbf{i}_{K_\omega + \left\lfloor \frac{j+1}{2} \right\rfloor}, \quad 1 \le j \le 2K_z, \tag{2.98}$$

*that is,*

$$\left[\mathbf{x}^1, \mathbf{x}^2, \dots, \mathbf{x}^{2K_z - 1}, \mathbf{x}^{2K_z}\right] = \left[\mathbf{x} + \mathbf{i}_{K_\omega+1}, \mathbf{x} - \mathbf{i}_{K_\omega+1}, \dots, \mathbf{x} + \mathbf{i}_K, \mathbf{x} - \mathbf{i}_K\right].$$

*The different terms in* $\overline{\mathbf{F}}(\mathbf{x})$ *are given by*

$$\mathbf{F}_{\boldsymbol{\omega}\boldsymbol{\omega}} = \mathbb{E}_{\mathbf{y};\mathbf{x}}\left[\frac{\partial \ln p(\mathbf{y};\mathbf{x})}{\partial \boldsymbol{\omega}} \frac{\partial \ln p(\mathbf{y};\mathbf{x})}{\partial \boldsymbol{\omega}}^\top\right], \tag{2.99a}$$

$$\mathbf{F}_{\boldsymbol{\omega}\mathbf{z}} = \mathbb{E}_{\mathbf{y};\mathbf{x}}\left[\frac{\partial \ln p(\mathbf{y};\mathbf{x})}{\partial \boldsymbol{\omega}} \mathbf{t}_{2K_z}^\top\right] \tag{2.99b}$$

$$= \left[\begin{array}{cccc} \mathbf{f}(\mathbf{x}, \mathbf{x}^1) & \mathbf{f}(\mathbf{x}, \mathbf{x}^2) & \dots & \mathbf{f}\left(\mathbf{x}, \mathbf{x}^{2K_z}\right) \end{array}\right], \tag{2.99c}$$

$$\mathbf{F}_{\mathbf{z}\mathbf{z}} = \mathbb{E}_{\mathbf{y};\mathbf{x}}\left[\mathbf{t}_{2K_z} \mathbf{t}_{2K_z}^\top\right] - \mathbf{1}_{2K_z} \mathbf{1}_{2K_z}^\top, \tag{2.99d}$$

*where* $\mathbf{t}_{2K_z}$ *is defined as*

$$\mathbf{t}_{2K_z} \triangleq \boldsymbol{\upsilon}_{\mathbf{x}}\left(\mathbf{y}; \{\mathbf{x}\}^{2K_z}\right) = \left(\frac{p(\mathbf{y};\mathbf{x}^1)}{p(\mathbf{y};\mathbf{x})}, \frac{p(\mathbf{y};\mathbf{x}^2)}{p(\mathbf{y};\mathbf{x})}, \dots, \frac{p\left(\mathbf{y};\mathbf{x}^{2K_z}\right)}{p(\mathbf{y};\mathbf{x})}\right)^\top. \tag{2.99e}$$

The proof of Theorem 1 is shown in Appendix A.4.

**Corollary 1.** *If* $\mathbf{g}(\mathbf{x}) = \mathbf{x}$, *matrix* $\boldsymbol{\Lambda}_{\mathbf{g}}(\mathbf{x})$ *in Theorem 1 simplifies to*

$$\begin{aligned} \boldsymbol{\Lambda}_{\mathbf{g}}(\mathbf{x}) &= \left[\begin{array}{ccccccc} \mathbf{i}_1 & \dots & \mathbf{i}_{K_\omega} & \mathbf{i}_{K_\omega+1} & -\mathbf{i}_{K_\omega+1} & \dots & \mathbf{i}_K & -\mathbf{i}_K \end{array}\right] \\ &\underset{(K_z=3)}{=} \left[\begin{array}{ccccccc} \mathbf{I}_{K_\omega} & \mathbf{0} & \mathbf{0} & \mathbf{0} & \mathbf{0} & \mathbf{0} & \mathbf{0} \\ \mathbf{0} & 1 & -1 & 0 & 0 & 0 & 0 \\ \mathbf{0} & 0 & 0 & 1 & -1 & 0 & 0 \\ \mathbf{0} & 0 & 0 & 0 & 0 & 1 & -1 \end{array}\right]. \end{aligned} \tag{2.100}$$

### CRB for the Mixed Model under Gaussian Observations

The CRB introduced in Theorem 1 results valid for deterministic mixed model estimation under any kind of statistical distribution of the observations. Prior to exploring the CRB for the RTK positioning model, it is introduced an expression of the general CRB of the mixed model for the Gaussian observation case.

Let us consider an $n$-dimensional Gaussian real vector $\mathbf{y}$ whose distribution is conditioned on the parameter vector $\mathbf{x}$ as: $\mathbf{y} \sim \mathcal{N}\left(\boldsymbol{\mu}(\mathbf{x}), \boldsymbol{\Sigma}(\mathbf{x})\right)$ and $p\left(\mathbf{y}; \mathbf{x}\right) = p\left(\mathbf{y}; \boldsymbol{\mu}\left(\mathbf{x}\right), \boldsymbol{\Sigma}\left(\mathbf{x}\right)\right)$ such that

$$p\left(\mathbf{y}; \boldsymbol{\mu}\left(\mathbf{x}\right), \boldsymbol{\Sigma}\left(\mathbf{x}\right)\right) = \frac{1}{\sqrt{2\pi}^{n}\sqrt{\left|\boldsymbol{\Sigma}\left(\mathbf{x}\right)\right|}} \exp\left(-\frac{1}{2}\left(\mathbf{y}-\boldsymbol{\mu}\left(\mathbf{x}\right)\right)^{\top}\boldsymbol{\Sigma}^{-1}\left(\mathbf{x}\right)\left(\mathbf{y}-\boldsymbol{\mu}\left(\mathbf{x}\right)\right)\right) . \tag{2.101}$$

Upon defining

$$\boldsymbol{\Sigma}^{ij} = \left[\boldsymbol{\Sigma}\left(\mathbf{x}^{i}\right)^{-1} + \boldsymbol{\Sigma}\left(\mathbf{x}^{j}\right)^{-1} - \boldsymbol{\Sigma}\left(\mathbf{x}\right)^{-1}\right]^{-1}, \tag{2.102a}$$

$$\boldsymbol{\mu}^{ij} = \boldsymbol{\Sigma}\left(\mathbf{x}^{i}\right)^{-1}\boldsymbol{\mu}\left(\mathbf{x}^{i}\right) + \boldsymbol{\Sigma}\left(\mathbf{x}^{j}\right)^{-1}\boldsymbol{\mu}\left(\mathbf{x}^{j}\right) - \boldsymbol{\Sigma}\left(\mathbf{x}\right)^{-1}\boldsymbol{\mu}\left(\mathbf{x}\right), \tag{2.102b}$$

$$\begin{aligned}\delta^{ij} = {} & \boldsymbol{\mu}\left(\mathbf{x}^{i}\right)^{\top}\boldsymbol{\Sigma}\left(\mathbf{x}^{i}\right)^{-1}\boldsymbol{\mu}\left(\mathbf{x}^{i}\right) + \boldsymbol{\mu}\left(\mathbf{x}^{j}\right)^{\top}\boldsymbol{\Sigma}\left(\mathbf{x}^{j}\right)^{-1}\boldsymbol{\mu}\left(\mathbf{x}^{j}\right) \\ & - \boldsymbol{\mu}\left(\mathbf{x}\right)^{\top}\boldsymbol{\Sigma}\left(\mathbf{x}\right)^{-1}\boldsymbol{\mu}\left(\mathbf{x}\right),\end{aligned} \tag{2.102c}$$

then one may obtain the different components required to compute the CRB (2.95) (see A.5 for the detailed derivation of $\mathbf{F}_{\mathbf{zz}}$ and $\mathbf{f}\left(\mathbf{x}, \mathbf{x}^{j}\right))$ as

$$\left[\mathbf{F}_{\mathbf{zz}}\right]_{i,j} = \sqrt{\frac{\left|\boldsymbol{\Sigma}^{ij}\right|\left|\boldsymbol{\Sigma}\left(\mathbf{x}\right)\right|}{\left|\boldsymbol{\Sigma}\left(\mathbf{x}^{i}\right)\right|\left|\boldsymbol{\Sigma}\left(\mathbf{x}^{j}\right)\right|}} e^{\frac{1}{2}\left[\boldsymbol{\mu}^{ij\top}\boldsymbol{\Sigma}^{ij}\boldsymbol{\mu}^{ij}-\delta^{ij}\right]} - 1, \tag{2.102d}$$

$$\left[\mathbf{f}\left(\mathbf{x}, \mathbf{x}^{j}\right)\right]_{k} = \left(\begin{array}{l} \frac{1}{2}tr\left(\frac{\partial\boldsymbol{\Sigma}(\mathbf{x})^{-1}}{\partial\omega_{k}}\left(\boldsymbol{\Sigma}\left(\mathbf{x}\right)-\boldsymbol{\Sigma}\left(\mathbf{x}^{j}\right)\right) - \frac{\partial\boldsymbol{\Sigma}(\mathbf{x})^{-1}}{\partial\omega_{k}}\right. \\ \left.\times\left(\boldsymbol{\mu}\left(\mathbf{x}^{j}\right)-\boldsymbol{\mu}\left(\mathbf{x}\right)\right)\left(\boldsymbol{\mu}\left(\mathbf{x}^{j}\right)-\boldsymbol{\mu}\left(\mathbf{x}\right)\right)^{\top}\right) \\ +\frac{\partial\boldsymbol{\mu}(\mathbf{x})}{\partial\omega_{k}}^{\top}\boldsymbol{\Sigma}\left(\mathbf{x}\right)^{-1}\left(\boldsymbol{\mu}\left(\mathbf{x}^{j}\right)-\boldsymbol{\mu}\left(\mathbf{x}\right)\right) \end{array}\right) \tag{2.102e}$$

$$\begin{aligned}\left[\mathbf{F}_{\omega\omega}\right]_{k,l} = {} & \frac{\partial\boldsymbol{\mu}\left(\mathbf{x}\right)}{\partial\omega_{k}}^{\top}\boldsymbol{\Sigma}^{-1}\left(\mathbf{x}\right)\frac{\partial\boldsymbol{\mu}\left(\mathbf{x}\right)}{\partial\omega_{l}} \\ & + \frac{1}{2}tr\left(\boldsymbol{\Sigma}^{-1}\left(\mathbf{x}\right)\frac{\partial\boldsymbol{\Sigma}\left(\mathbf{x}\right)}{\partial\omega_{k}}\boldsymbol{\Sigma}^{-1}\left(\mathbf{x}\right)\frac{\partial\boldsymbol{\Sigma}\left(\mathbf{x}\right)}{\partial\omega_{l}}\right),\end{aligned} \tag{2.102f}$$

where (2.102f) is the Slepian-Bangs formula [100, p.47].

### 2.4.3 Cramér-Rao Bound for RTK Positioning

Recalling Section 2.2, the RTK estimation problem reads

$$\mathbf{y} = \mathbf{H}\mathbf{x} + \mathbf{n},\ \mathbf{n} \sim \mathcal{N}(\mathbf{0}, \boldsymbol{\Sigma}),\ \mathbf{H} = \begin{bmatrix} \mathbf{B} & \mathbf{A} \end{bmatrix},\ \mathbf{x} = \begin{bmatrix}\mathbf{b}^\top\ \mathbf{a}^\top\end{bmatrix}^\top. \tag{2.103}$$

With $\mathrm{g}(\mathbf{x})$ a linear operator such that $\mathrm{g}(\mathbf{x}) = \mathbf{H}\mathbf{x}$, and recalling Theorem 2.4.2, let us rename $\mathbf{CRB}(\mathrm{g}(\hat{\mathbf{x}}))$ to $\mathbf{CRB}(\check{\mathbf{x}})$, given by

$$\mathbf{CRB}_{\mathsf{mixed}} \triangleq \mathbf{CRB}(\check{\mathbf{x}}) = \boldsymbol{\Lambda}_{\mathbf{g}}(\mathbf{x})\,\overline{\mathbf{F}}(\mathbf{x})^{-1}\boldsymbol{\Lambda}_{\mathbf{g}}^\top(\mathbf{x}), \tag{2.104a}$$

$$\overline{\mathbf{F}}(\mathbf{x}) = \begin{bmatrix} \mathbf{F}_{\omega\omega} & \mathbf{F}_{\omega\mathbf{z}} \\ \mathbf{F}_{\omega\mathbf{z}}^\top & \mathbf{F}_{\mathbf{z}\mathbf{z}} \end{bmatrix}, \tag{2.104b}$$

where $\boldsymbol{\Lambda}_{\mathbf{g}}(\mathbf{x})$ is given by (2.100), and the FIM, $\overline{\mathbf{F}}(\mathbf{x})$, is obtained using the Gaussian model equations given in Section 2.4.2. Notice the notation change $\mathrm{g}(\hat{\mathbf{x}})$ to $\check{\mathbf{x}}$ makes emphasis on the reference to a fixed solution, as described in Section 2.2. Similarly, $\boldsymbol{\omega}$ and $\mathbf{z}$ in $\overline{\mathbf{F}}(\mathbf{x})$ correspond to $\mathbf{b}$ and $\mathbf{a}$.

Since $\boldsymbol{\Sigma}$ is not dependent on the estimate $\mathbf{x}$ and $\boldsymbol{\mu}(\mathbf{x}) = \mathbf{H}\mathbf{x}$, (2.102a-2.102c) simplify to

$$\begin{aligned}
\boldsymbol{\Sigma}^{ij} &= \boldsymbol{\Sigma}, \\
\boldsymbol{\mu}^{ij} &= \boldsymbol{\Sigma}^{-1}\mathbf{H}\left(\mathbf{x}^i + \mathbf{x}^j - \mathbf{x}\right), \\
\delta^{ij} &= {\mathbf{x}^i}^\top\mathbf{H}\boldsymbol{\Sigma}^{-1}\mathbf{H}\mathbf{x}^i + {\mathbf{x}^j}^\top\mathbf{H}\boldsymbol{\Sigma}^{-1}\mathbf{H}\mathbf{x}^j - \mathbf{x}^\top\mathbf{H}\boldsymbol{\Sigma}^{-1}\mathbf{H}\mathbf{x},
\end{aligned}$$

for the test points $\{\mathbf{x}^i, \mathbf{x}^j\}^{i,j\in[0,2K_z]}$, $\mathbf{x}^j = \mathbf{x} + (-1)^{j-1}\mathbf{i}_{K_\omega+\lfloor\frac{j+1}{2}\rfloor}$ and $\mathbf{x}^i = \mathbf{x} + (-1)^{i-1}\mathbf{i}_{K_\omega+\lfloor\frac{i+1}{2}\rfloor}$. Then, (2.102d-2.102f) are further simplified and one can estimate the elements of $\overline{\mathbf{F}}(\mathbf{x})$ in a straight-forward manner. Particularly, computing $\mathbf{F}_{\omega\omega}$ for $1 \leq k, k' \leq K_\omega$ becomes

$$\left[\mathbf{F}_{\omega\omega}\right]_{k,k'} = \frac{\partial\mathbf{H}\mathbf{x}}{\partial\omega_k}^\top\boldsymbol{\Sigma}^{-1}\frac{\partial\mathbf{H}\mathbf{x}}{\partial\omega_{k'}} = \left[\mathbf{B}\right]_{:,k}^\top\boldsymbol{\Sigma}^{-1}\left[\mathbf{B}\right]_{:,k'},$$

such that

$$\mathbf{F}_{\omega\omega} = \mathbf{B}^\top\boldsymbol{\Sigma}^{-1}\mathbf{B}, \tag{2.104c}$$

then the FIM for integer-valued parameters reads

$$[\mathbf{F}_{\mathbf{z}\mathbf{z}}]_{i,j} = \exp\left(\left(\mathbf{x} - \mathbf{x}^i - \mathbf{x}^j\right)^\top\mathbf{H}^\top\boldsymbol{\Sigma}^{-1}\mathbf{H}\mathbf{x} + {\mathbf{x}^i}^\top\mathbf{H}^\top\boldsymbol{\Sigma}^{-1}\mathbf{H}\mathbf{x}^j\right) - 1. \tag{2.104d}$$

Finally, for $1 \leq k \leq K_\omega$, $\mathbf{f}\left(\mathbf{x}, \mathbf{x}^j\right)$ can be expressed as

$$\left[\mathbf{f}\left(\mathbf{x}, \mathbf{x}^j\right)\right]_k = \frac{\partial\mathbf{H}\mathbf{x}}{\partial\omega_k}^\top\boldsymbol{\Sigma}^{-1}\left(\mathbf{H}\mathbf{x}^j - \mathbf{H}\mathbf{x}\right) = \left[\mathbf{B}\right]_{:,k}^\top\boldsymbol{\Sigma}^{-1}\mathbf{H}\left(\mathbf{x}^j - \mathbf{x}\right),$$

which, in matrix form, leads to

$$\mathbf{F}_{\omega\mathbf{z}} = \mathbf{B}^\top\boldsymbol{\Sigma}^{-1}\mathbf{H}\begin{bmatrix} \mathbf{i}_{K_\omega+1} & -\mathbf{i}_{K_\omega+1} & \dots & \mathbf{i}_{K_\omega+K_z} & -\mathbf{i}_{K_\omega+K_z} \end{bmatrix}. \tag{2.104e}$$

It is worth noting that relaxing the condition on the integer-valued part of the parameters' vector, and assuming that both parameters are real-valued, $\boldsymbol{\omega} \in \mathbb{R}^{K_\omega}$, $\mathbf{z} \in \mathbb{R}^{K_z}$, then the standard CRB is given by the inverse of the following FIM,

$$\mathbf{CRB}_{\mathsf{real}} \triangleq \mathbf{CRB}(\hat{\mathbf{x}}) = \mathbf{F}(\hat{\mathbf{x}})^{-1} = \mathbf{H}^\top\boldsymbol{\Sigma}^{-1}\mathbf{H}, \tag{2.105}$$

which corresponds to the estimation bound for the float solution of the RTK positioning model.

## 2.5 Efficiency of Estimators at the RTK Model

This section studies the performance of estimators at the RTK positioning model, with regards to the CRB proposed in Section 2.4.3. For such end, a simulated scenario is studied based on the satellite geometry presented in Section 1.5.1, under a wide range of precision levels for the undifferenced code observations $\sigma_\rho$ –preserving the noise of carrier-phase $\sigma_\Phi$ as two orders of magnitude lower than the code one–. The characterization of the estimators is obtained from $10^4$ Monte Carlo iterations, for which the RMSE of the 3D positioning is regarded as performance metric and compared with the corresponding CRB.

When observing the estimation procedure presented in Section 2.2, one can appreciate that while the float solution estimation performed by a MLE estimation is asymptotically efficient, the fixed positioning solution is conditioned on the performance of integer estimators, whose efficiency have not been addressed. In particular, this work focuses on the performance of the IR, IB and ILS estimators, for which the RMSE for the baseline fix solution is defined as

$$\mathsf{RMSE}_{(\cdot)} \triangleq \mathsf{RMSE}\left(\check{\mathbf{b}}_{(\cdot)}\right) = \sqrt{\mathsf{MSE}\left(\check{\mathbf{b}}_{(\cdot)}\right)} \tag{2.106}$$

$$\mathsf{MSE}\left(\check{\mathbf{b}}_{(\cdot)}\right) = \mathbb{E}\left[\left(\check{\mathbf{b}}_{(\cdot)} - \mathbf{b}\right)^\top \left(\check{\mathbf{b}}_{(\cdot)} - \mathbf{b}\right)\right], \tag{2.107}$$

for $\check{\mathbf{b}}_{(\cdot)}$ the solution conditioned on $(\cdot) = \{\mathsf{IR, IB, ILS}\}$, the estimators compared. It results useful, "looking inside" the CRB matrices (2.104b,2.105) for the RTK fixed and float solutions

$$\mathbf{CRB}_{\mathsf{mixed}} = \begin{bmatrix} \mathbf{CRB}_{\check{\mathbf{b}}} & \mathbf{CRB}_{\check{\mathbf{b}}\check{\mathbf{a}}} \\ \mathbf{CRB}_{\check{\mathbf{b}}\check{\mathbf{a}}}^\top & \mathbf{CRB}_{\check{\mathbf{a}}} \end{bmatrix}, \; \mathbf{CRB}_{\mathsf{real}} = \begin{bmatrix} \mathbf{CRB}_{\hat{\mathbf{b}}} & \mathbf{CRB}_{\hat{\mathbf{b}}\hat{\mathbf{a}}} \\ \mathbf{CRB}_{\hat{\mathbf{b}}\hat{\mathbf{a}}}^\top & \mathbf{CRB}_{\hat{\mathbf{a}}} \end{bmatrix},$$

from which the following metrics are derived and compared with the aforementioned RMSE

$$\mathsf{CRB}_{\mathbf{b},\mathsf{mixed}} = \sqrt{\mathsf{tr}\left(\mathbf{CRB}_{\check{\mathbf{b}}}\right)}, \; \mathsf{CRB}_{\mathbf{b},\mathsf{real}} = \sqrt{\mathsf{tr}\left(\mathbf{CRB}_{\hat{\mathbf{b}}}\right)}, \tag{2.108}$$

and, similarly for the ambiguities

$$\mathsf{CRB}_{\mathbf{a},\mathsf{mixed}} = \sqrt{\mathsf{tr}\left(\mathbf{CRB}_{\check{\mathbf{a}}}\right)}, \; \mathsf{CRB}_{\mathbf{a},\mathsf{real}} = \sqrt{\mathsf{tr}\left(\mathbf{CRB}_{\hat{\mathbf{a}}}\right)}. \tag{2.109}$$

Fig. 2.6 shows the 3D position RMSE on the abscissa axis, while the standard deviation of code observations $\sigma_\rho$ defines the ordinate axis, with a zoom of the low noise region given in Fig. 2.7. Solely by observing the bounds $\mathsf{CRB}_{\mathbf{b},\mathsf{real}}$ and $\mathsf{CRB}_{\mathbf{b},\mathsf{mixed}}$, it becomes obvious the great precision obtained by means of constraining the baseline solution by virtue of the integer ambiguities and justifies the need for powerful integer estimators to do so. As a byproduct, this highlights the importance of the LB proposed in this contribution. Clearly, restricting the set of possible values (integer instead of real) leads to a LB such that $\mathsf{CRB}_{\mathsf{mixed}} \leq \mathsf{CRB}_{\mathsf{real}}$. Focusing on the specifics of the mixed problem, the derived CRB showcases the existence of three zones: *high SNR region* ($\sigma_\rho <$10), for which an estimation shall (in theory) have a high probably to be on the correct peak of the log-likelihood function and present small errors [86]; *threshold region* (10$\leq \sigma_\rho \leq 10^4$), as the SNR decreases, the estimator reaches a threshold for which some estimates would be near the CRB while others are randomly affected by the noise distribution; *no information region* ($\sigma > 10^4$), as SNR continues decreasing, the observations do not shed any useful information and the estimator's outputs would be fully random —in this case, whether ambiguities are estimated would not play any role on the positioning, since

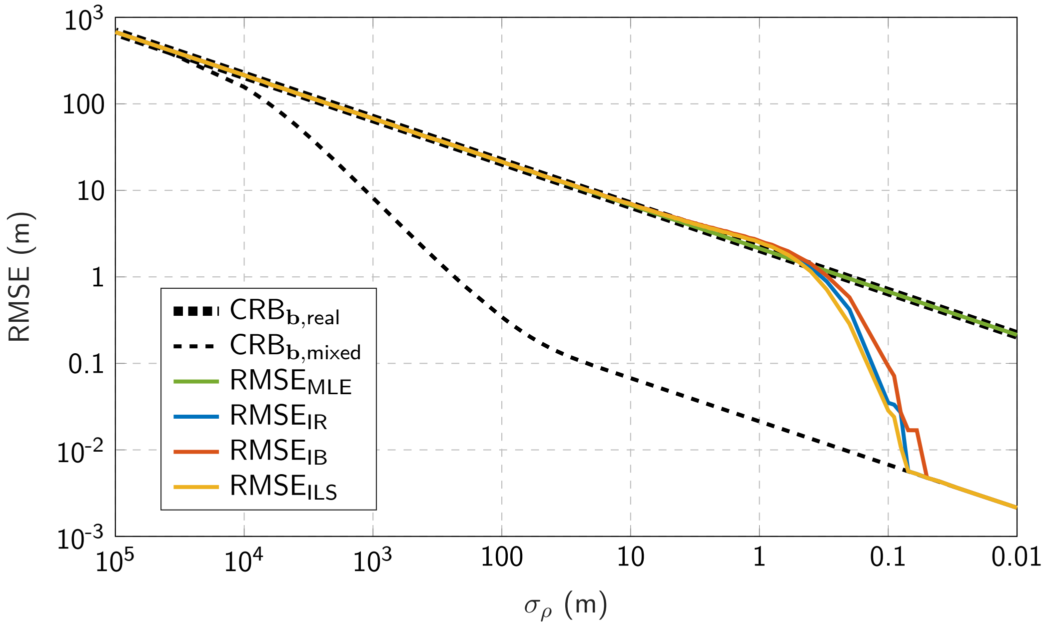

**Figure 2.6:** Positioning RMSE of estimators (solid lines) and square-root of CRBs (dashed lines) as a function of the standard deviation of the undifferenced code observations' noise $\sigma_\rho$.

$\text{CRB}_{\text{mixed}}$ would have aligned with $\text{CRB}_{\text{real}}$.

When observing the performance of the estimators, first notice that the MLE estimate for the float problem (applying a LS adjustment) coincides with the $\text{CRB}_{real}$ for the range of tested $\sigma_\rho$ values, which gives the ultimate achievable performance with both code and phase observables if no integer constraint is imposed. The performance of the fixed solution, conditioned on the integer estimation, clearly varies based on the noise levels. As for the study of the CRB, three regions can be identified:

- Large noise regime: the ILS coincides with the MLE float solution and with $\text{CRB}_{\mathbf{b},\text{fix}}$, which is clear from the ILS success rate shown in Fig. 2.8, where we can see that for $\sigma_\rho > 3$ [m] a correct integer solution is never found. In that case, the fixed solution is as if no integer constraints were imposed.

- Low noise regime: the IAR obtains the correct ambiguity solution with high probability, then the integer estimators coincide with the $\text{CRB}_{\mathbf{b},\text{fix}}$, meaning that they result asymptotically efficient.

- Threshold regime: below the so-called threshold point (in this case, $\sigma_\rho \simeq 0.08$ [m]), the fixed solution RMSE departs from $\text{CRB}_{\mathbf{b},\text{fix}}$ and rises towards the $\text{CRB}_{\mathbf{b},\text{float}}$. This region describes the behaviour of the integer estimators, which abandon the asymptotic efficiency and ambiguous errors occur due to the (partially) wrong estimation of the integer ambiguities. The threshold point depends on the estimators, the satellite geometry, number of observations and observation noises. Therefore, the precise prediction for the transition point remains an open challenge. A remarkable point can be appreciated in Fig. 2.7, for $0.6 \leq \sigma_\rho \leq 5$ [m], for which the fixed solutions present a worsen positioning accuracy than the float one. This is due to wrongly estimated ambiguities inducing a bias in the fixed baseline solution, which highlights the need for

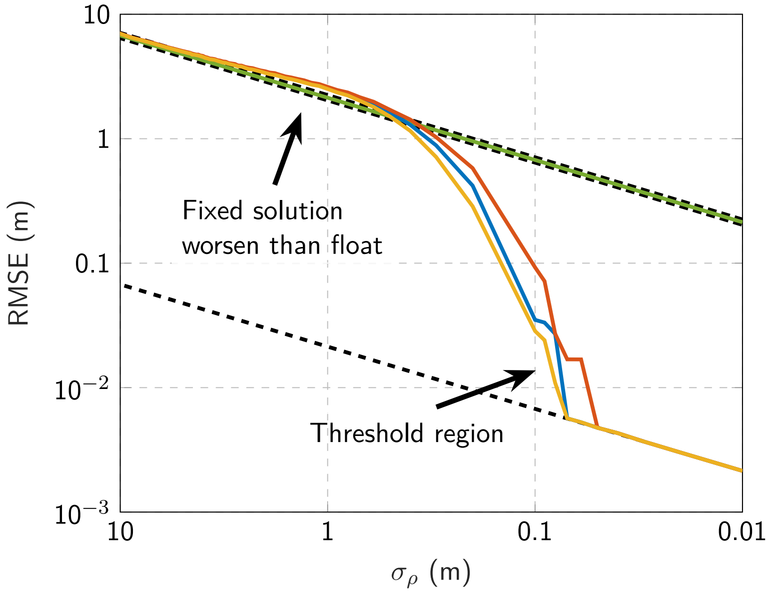

**Figure 2.7:** Detail on the threshold region for the positioning RMSE performance of estimators at the mixed model problem.

IA algorithms (see Section 2.2), i.e., recognizing when a fixed solution shall or not be accepted.

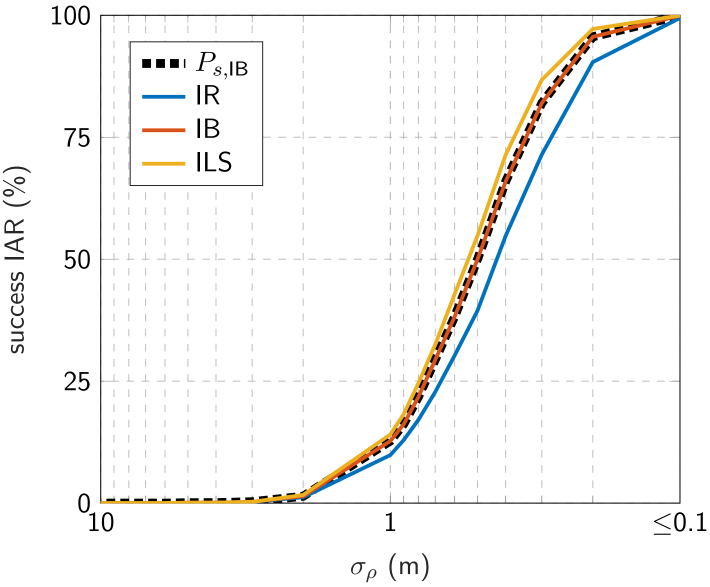

**Figure 2.8:** Experimental success ratio for the integer estimation of the mixed model against the standard deviation of the undifferenced code observations' noise for the low noise and threshold regimes.

Fig. 2.8 depicts the integer ambiguity success rate —i.e., the percentage of experiments for which the complete set of ambiguities are correctly estimated by the pertinent estimator— against the code precision. For low noise, e.g., for $\sigma_\rho \leq 0.1$, the integer estimators perform asymptotically and IR, IB and ILS manage to always correctly estimate the integer ambiguities. As the noise level increases, such percentage rapidly decay for the three estimators of interest, with the best and worst performances brought by ILS and IR respectively. A relevant point relates to the application of the IB estimation bound, which is shown to be a tight bound for the IB [30, Ch. 23] (in Fig. 2.8 denoted as $P_s$ UB) performance and serves as upper bound for ILS estimates —i.e., the performance of ILS shall overpass the IB bound—, as discussed in Section 2.2.

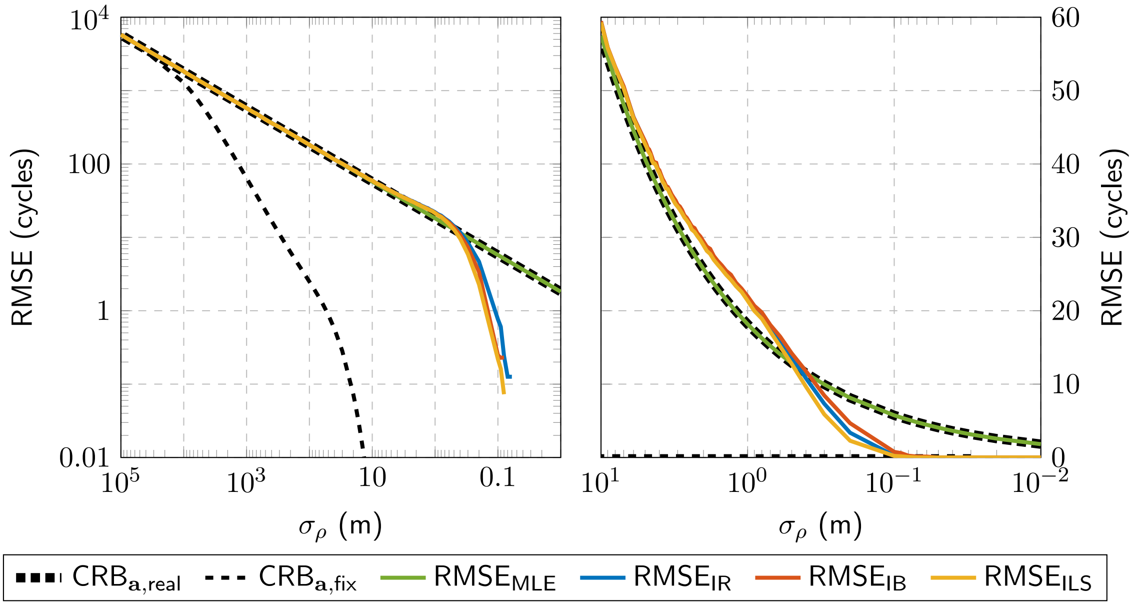

**Figure 2.9:** On the left, ambiguities RMSE of estimators (solid lines) and square-root of CRBs (dashed lines) as a function of the complete range of values for the standard deviation of the undifferenced code observations' noise $\sigma_\rho$. On the right, detail on the ambiguities RMSE for the low noise and threshold regimes.

The performance of the estimators for the integer ambiguities is discussed next. Fig. 2.9 (left) shows the ambiguity RMSE (in cycles), alongside the square-root of the corresponding CRBs, with a zoom of the low noise region given in Fig. 2.9 (right). As for the positioning case, the standard MLE estimates attains the CRB$_{\mathsf{float}}$ regardless of the noise level. Again, the integer estimators present the three same regions of performance (high and low noise, with a threshold region in between). Together with the previous results for the position estimate, this shows the validity and interest of the mixed real/integer bound, and the consistency of the results related to the ambiguity fixing capabilities (i.e., success rate). Overall, the results obtained from the simulation align with the initial hypothesis stated by Teunissen [30], with regards to the relative performance of IR, IB and ILS

$$P\left(\check{\mathbf{a}}_{\mathsf{IR}} = \mathbf{a}\right) \leq P\left(\check{\mathbf{a}}_{\mathsf{IR}} = \mathbf{a}\right) \leq P\left(\check{\mathbf{a}}_{\mathsf{ILS}} = \mathbf{a}\right),$$

and, in the following, some additional considerations on such estimators efficient are presented.

First, let us recall the definition of covariance matrix for the float estimates in (2.20)

$$\mathbf{P}_{\hat{\mathbf{x}}} \triangleq \begin{bmatrix} \mathbf{P}_{\hat{\mathbf{a}}\hat{\mathbf{a}}} & \mathbf{P}_{\hat{\mathbf{a}}\hat{\mathbf{b}}} \\ \mathbf{P}_{\hat{\mathbf{b}}\hat{\mathbf{a}}} & \mathbf{P}_{\hat{\mathbf{b}}\hat{\mathbf{b}}} \end{bmatrix},$$

which, by exploiting the four-blocks matrix inversion expression [97], leads to

$$\begin{aligned} \mathbf{P}_{\hat{\mathbf{b}}(\mathbf{a})} &= \underbrace{\mathbf{P}_{\hat{\mathbf{b}}\hat{\mathbf{b}}} - \mathbf{P}_{\hat{\mathbf{b}}\hat{\mathbf{a}}}\mathbf{P}_{\hat{\mathbf{a}}\hat{\mathbf{a}}}^{-1}\mathbf{P}_{\hat{\mathbf{b}}\hat{\mathbf{a}}}^{\top}}_{\mathbf{P}_{\check{\mathbf{b}}\check{\mathbf{b}}}} \\ &= \left(\mathbf{B}^{\top}\mathbf{\Sigma}^{-1}\mathbf{B}\right)^{-1}, \end{aligned}$$

from which one recognizes that the covariance matrix of the fixed positioning solution (2.23) corresponds to that of an MLE where the ambiguities are ignored and, therefore, the choice of integer estimator does not play a role on the variance of the computed solution.

Secondly, the estimated fixed baseline (2.22) does depend on the integer estimator, as

$$\check{\mathbf{b}} \triangleq \check{\mathbf{b}}\left(\check{\mathbf{a}}\right) = \hat{\mathbf{b}} - \mathbf{P}_{\hat{\mathbf{b}}\hat{\mathbf{a}}}\mathbf{P}_{\hat{\mathbf{b}}\hat{\mathbf{b}}}^{-1}\left(\hat{\mathbf{a}} - \check{\mathbf{a}}\right),$$

where the improvement in accuracy is due to constraining the float solution to the more restrictive class of integer estimators. Since, the estimators of interest (IR, IB and ILS) have been shown to be uniformly unbiased [101] under Gaussian additive noise —i.e., $\mathbb{E}[\check{\mathbf{b}}] = \mathbb{E}[\hat{\mathbf{b}}] = \mathbf{b}$—, then the proposed $\mathbf{CRB}\left(\mathbf{g}(\hat{\mathbf{x}})\right)$, for $\mathbf{x}$ a vector with real- and integer-valued parameters, in (2.95) is a relevant LB for the Gaussian linear conditional signal model (2.4) and

$$\mathbf{P}_{\check{\mathbf{b}}} = \mathbf{P}_{\check{\mathbf{b}}(\check{\mathbf{a}})} \geq \mathbf{CRB}_{\check{\mathbf{b}}},\ \check{\mathbf{a}} \in \{\check{\mathbf{a}}_{\mathsf{IR}}, \check{\mathbf{a}}_{\mathsf{IB}}, \check{\mathbf{a}}_{\mathsf{ILS}}\}.$$

Finally, if one considers [30, (23.23)] $\lim_{\mathsf{tr}(\mathbf{\Sigma})\to\mathbf{0}} P\left(\check{\mathbf{a}}_{\mathsf{IR}} = \mathbf{a}\right) = 1$ as the asymptotic condition, then

$$\lim_{\mathsf{tr}(\mathbf{\Sigma})\to 0} \mathbf{P}_{\check{\mathbf{a}}_{\mathsf{IR}}} = \lim_{\mathsf{tr}(\mathbf{\Sigma})\to 0} \mathbf{P}_{\check{\mathbf{a}}_{\mathsf{IB}}} = \lim_{\mathsf{tr}(\mathbf{\Sigma})\to 0} \mathbf{P}_{\check{\mathbf{a}}_{\mathsf{ILS}}} = \mathbf{0}.$$

Then, for any estimate $\check{\mathbf{a}} \in \{\check{\mathbf{a}}_{\mathsf{IR}}, \check{\mathbf{a}}_{\mathsf{IB}}, \check{\mathbf{a}}_{\mathsf{ILS}}\}$ and considering the formulation of the fixed covariance matrix from [59, (29)]

$$\mathbf{P}_{\hat{\mathbf{b}}(\check{\mathbf{a}})} = \mathbf{P}_{\hat{\mathbf{b}}(\mathbf{a})} + \mathbf{P}_{\hat{\mathbf{b}}\hat{\mathbf{a}}}\mathbf{P}_{\hat{\mathbf{a}}\hat{\mathbf{a}}}^{-1}\mathbf{P}_{\check{\mathbf{a}}}\mathbf{P}_{\hat{\mathbf{a}}\hat{\mathbf{a}}}^{-1}\mathbf{P}_{\hat{\mathbf{b}}\hat{\mathbf{a}}}^{\top},$$

then the following expression is obtained

$$\lim_{tr(\mathbf{\Sigma})\to 0} \mathbf{P}_{\hat{\mathbf{b}}(\check{\mathbf{a}})} = \left(\mathbf{B}^{\top}\mathbf{\Sigma}^{-1}\mathbf{B}\right)^{-1},$$

and, since adding unknown parameters leads to an equal or higher CRB, then

$$\mathbf{P}_{\check{\mathbf{b}}(\check{\mathbf{a}})} \geq \mathbf{CRB}_{\mathbf{b},\mathsf{fix}} \geq \left(\mathbf{B}^{\top}\mathbf{\Sigma}^{-1}\mathbf{B}\right)^{-1}.$$

Thus, for any estimate $\check{\mathbf{a}} \in \{\check{\mathbf{a}}_{\mathsf{IR}}, \check{\mathbf{a}}_{\mathsf{IB}}, \check{\mathbf{a}}_{\mathsf{ILS}}\}$,

$$\lim_{tr(\mathbf{\Sigma})\to 0} \mathbf{P}_{\hat{\mathbf{b}}(\check{\mathbf{a}})} = \lim_{tr(\mathbf{\Sigma})\to 0} \mathbf{CRB}_{\mathbf{b},\mathsf{fix}} = \left(\mathbf{B}^{\top}\mathbf{\Sigma}^{-1}\mathbf{B}\right)^{-1},$$

which proves that all IR, IB and ILS are asymptotically efficient estimators.

### 2.5.1 Insights from the CRB for the PAR Mixed Model

Similarly to the conventional mixed model for RTK positioning –conventional in the sense that it follows the FAR approach, with the complete set of ambiguities being mapped to integer values–, the CRB in 2.4.3 can be easily extended for the PAR mixed model using the corresponding design matrices and vector of unknowns in (2.69). To better showcase the gain from PAR, it results convenient observing a scenario richer in number of observations. Thus, we replicate the previous Monte Carlo experimentation for the skyplot observed at the Potsdam IGS station on March 26th 2019 (DOY 085 12:00 UTC), where a total of 12 GPS satellites are tracked over the L1 and L2 frequencies (i.e., a total of 22 ambiguities are to be resolved). Once again, a wide range of precision levels for the undifferenced observations are considered and $10^4$ Monte Carlo runs compose the experiment. The comparison is realized in terms of positioning RMSE and experimental success ratio, and the estimators evaluated are: *i)* an MLE estimator for the mixed model 1 (conventional FAR RTK positioning) using an ILS as integer estimator; *ii)* an MLE estimator for the PAR mixed model 2, using ILS as integer estimator and using PD-PAR as subset selection criteria[2].

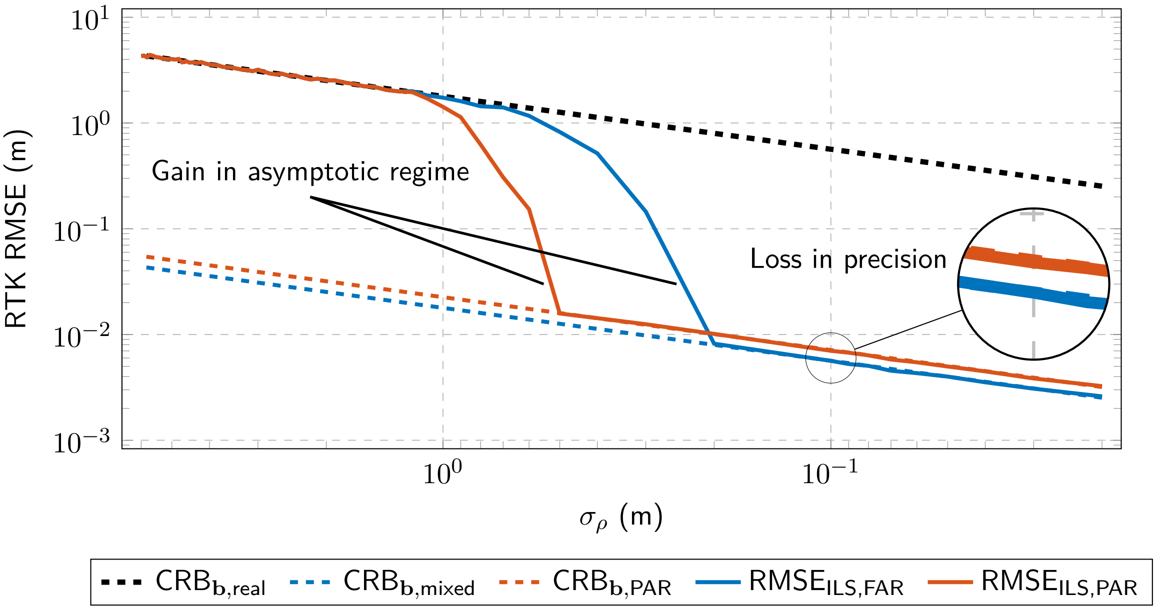

**Figure 2.10:** Three-dimensional positioning RMSE (solid lines) and CRBs (dashed lines) as a function of the undifferenced standard deviation for the code observations, $\sigma_\rho$, for estimators of FAR and PAR mixed model problem. Moreover, a small zoom over the FAR to PAR difference on positioning precision is depicted.

Fig. 2.10 depicts the three-dimensional positioning RMSE against the range of standard deviations for the code observations. The dashed blue and orange lines represent the CRB for the position estimate on the mixed model of FAR and PAR, respectively, while the solid lines with the same color scheme illustrate the performance of the FAR and PAR estimators. The CRB for the real-valued problem is depicted as a black dashed line. Similarly to the previous

---

[2] To properly evaluate the estimator's performance, the validity test for the estimated ambiguities is not carried out and, instead, the integer solution for the subset of ambiguities is always accepted (as for the MLE of the mixed problem). To further simplify the simulation, the PAR estimator consistently discards the four ambiguities whose contribution to the fixed positioning precision is lesser.

analysis, three regions for the estimators' performance can be observed: asymptotic behavior, a threshold region, and the large noise regime where the ambiguities cannot be correctly estimated. Notice that, during the large noise regime, the performance of FAR and PAR align with the CRB for the real-valued problem, since in both cases the integer estimate cannot match the true one. The motivation for using PAR becomes evident when observing the "duration" of the asymptotic behavior: while the threshold region for FAR begins at $\sigma_\rho \simeq 0.2$ m, PAR extends its asymptotic efficiency until $\sigma_\rho \simeq 0.5$ m. This implies that a subset of ambiguities can be mapped into the true vector of integer values, while the complete set of ambiguities cannot, as further illustrated in Fig. 2.11 (notice that the percentage of IAR success for PAR solely considers the subset of integer-mapped ambiguities).

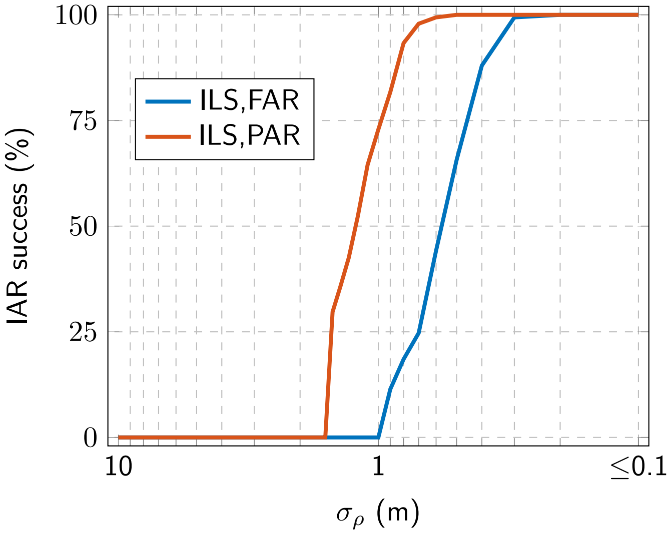

**Figure 2.11:** Experimental success ratio for the FAR and PAR integer estimation against the standard deviation of the undifferenced code observations' noise for the low noise and threshold regimes.

As counterpart, PAR's fixed positioning solution experiments a precision loss with respect to that of FAR. In this particular case, discarding the four least significant ambiguities (in terms of positioning gain) leads to a PAR precision of approx. 0.8 times the one of FAR. Nonetheless, the larger asymptotic performance for PAR compensates for that –for instance, PAR's RMSE at $\sigma_\rho = 0.5$ m is under two cm, while FAR's RMSE is over 80 cm at the same evaluated point–.

## 2.6 From Signal Processing to RTK Positioning Performance

As discussed in Section 1.2.1, code and carrier phase measurements are derived from the estimated parameters (time delay, carrier phase offset, etc.) of the signal model in (1.5). Thus, the quality of the pseudorange observables is conditioned on the operation point of a GNSS receiver (for instance, long integration times and high C/N$_0$ lead to smaller noises in both code and carrier phase observations). Then, addressing the ultimate achievable RTK performance is a two-folded challenge: on the one hand, the receiver capability at estimating the signal parameters defines the observations' noise; on the other hand, RTK positioning is characterized by the tracked satellital geometry and the estimation of the mixed model. Similarly to Section 1.5, where code-based positioning is addressed, the ultimate RTK positioning performance with regards to some GNSS representative signals and meta-signals, considering different sampling rates and receiver operating points.

### Performance Analysis for Representative GNSS Signals

Following the simulated scenario in Section 1.5.1 for the code-based positioning case, the carrier phase-based positioning performance is assessed and the role played by signal type and receiver operation point analyzed. Although it is a common practice for RTK positioning to employ multi-constellation and/or multi-frequency combinations, the focus here lays on observing the performance gain from every individual GNSS signal. Moreover, the characteristics on base and rover receivers may differ in real scenarios, presenting different operation points and/or integration times. For the experimental case at hand, the two receivers are assumed to present the same SNR$_{\text{out}}$.

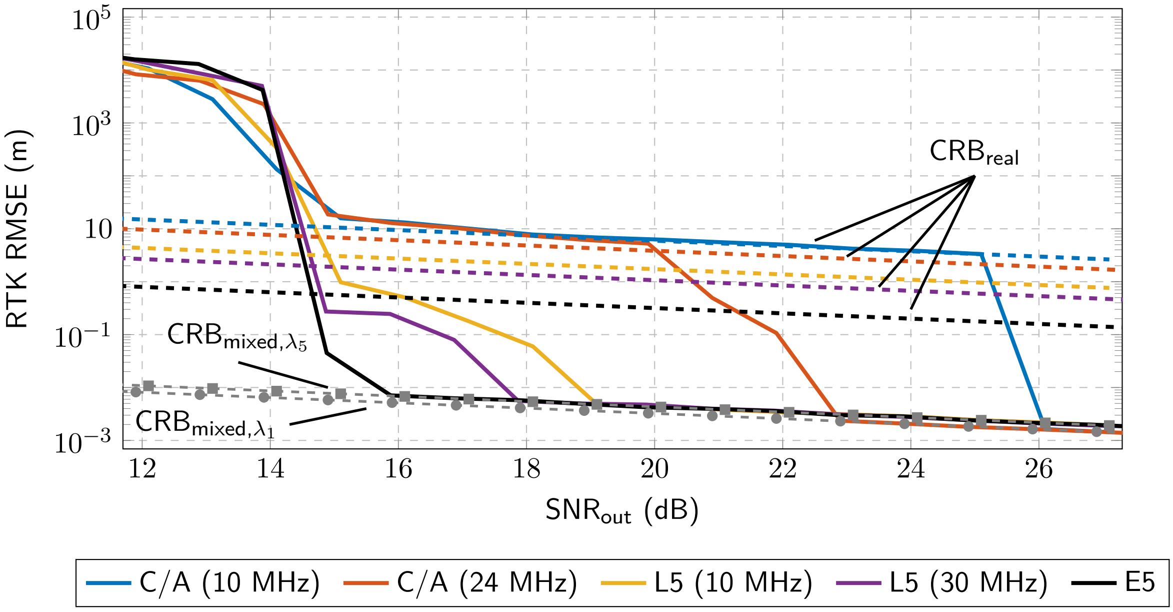

**Figure 2.12:** RTK positioning CRB (dashed lines) and associated RMSE (solid lines) versus SNR$_{\text{out}}$ for a selection of representative GNSS signals. The CRB for the mixed model is shown in gray with circular and squared markers for the L1 and L5 frequencies, respectively.

The position RMSE results are depicted in Fig. 2.12 where, for the sake of simplicity, the wavelength of E5 is assumed identical to L5. Some interesting points of discussion are as follows

- In terms of performance limits, i.e., focusing on the different CRBs, one concludes that:
  - Similarly to code-based positioning, the performance limit of the float solutions (i.e., $\text{CRB}_{\text{real}}$) is purely conditioned on the time-delay estimates and the satellites' geometry. Thus, since the ACF main peaks are clearly distinguished from the secondary ones for the evaluated signals, the time-delay and float positioning performance is driven by the bandwidth of the signals.
  - The performance limit (i.e., $\text{CRB}_{\text{mixed}}$) of the fixed solution is dominated by the carrier phase observables and the geometry. For real signals, the quality of carrier phase pseudoranges is solely based on the $\text{SNR}_{\text{out}}$ (common across signals) and the wavelength (1.41). Hence, the bound for the mixed model is lower for L1 than for L5/E5.
- In terms of estimators' performance, one notices that:
  - The existence of the three previously-discussed regimes still holds, so that the CRB at the mixed model can be attained for high SNR, a transition from the mixed to the real models exists during the threshold regime and the estimator attains the CRB for the real model for low SNR. In addition, the no information regime occurs when the signal parameters cannot be estimated for SNR below 16 dB, as it was formerly discussed in Section 1.5.1.
  - The estimation performance at the mixed model is driven by the quality of the code observables so that, whenever the time-delay estimation is not precise enough, the asymptotic region is immediately abandoned and the real ambiguities cannot be mapped to the correct integer ones.
- In terms of the signal used, one realizes that:
  - If RTK positioning is performed with narrow bandwidth signals, such as the GPS L1 C/A, higher sampling rates shall be preferred. For instance, for L1 C/A signal at $F_s = 10$ MHz, the threshold region starts at $\text{SNR}_{\text{out}} = 26$ dB which, for a coherent integration time $T_I = 20$ ms, corresponds to a $C/N_0 = 43$ dB-Hz (e.g., a nominal $C/N_0$ value in open sky conditions). Note that standard GNSS receiver architectures typically operate in $F_s \in [8 - 12]$ MHz and, therefore, the use of RTK positioning is generally recommended for multi-frequency and/or multi-constellation configurations. A gain of 3 dB in the extent of asymptotic region is obtained, for instance, when exploiting L1 C/A with $F_s = 24$ MHz. A similar conclusion is withdrew from the use of GPS L5, with the threshold regimes starting at 19 and 18 dB for sampling rates of 10 and 30 MHz, respectively.
  - The use of a large bandwidth signal, such as the Galileo E5, leads to a considerable gain in the extent of the asymptotic region. Indeed, with the threshold regime starting at $\text{SNR}_{\text{out}} = 16$ dB, a gain of 10 dB is obtained with respect to GPS L1 C/A at $F_s = 10$ MHz.

In conclusion, there is a clear justification on using fast codes (e.g., E5 and L5 signals) to provide an improved range of RTK operation. Particularly, Galileo E5 could be devised to provide fixed solutions in scenarios with weak signal reception, such as near-indoor environments. Moreover, if a new GNSS signal was specifically designed for precise positioning, the recommendation is to use a carrier frequency as high as possible and a signal modulation with the largest signal bandwidth.

### Performance Analysis for GNSS Metasignals

In accordance to the synthetic scenario described before, the RTK positioning performance is assessed in direct relationship to the receiver capabilities at tracking GNSS metasignals. Recall that Section 1.5.2 discusses the CRBs and the actual estimation performance for the metasignal parameter problem. Fig. 2.13 illustrates the CRB and MLE performance of the studied signals against the receiver operation point. Note that for the sake of visualization the wavelength is assumed to be the same across signals aligned with the one of E5 ($\lambda_{\text{E5}} = 25.17$ cm), and the performance of E5 is added as a reference and for completeness. A detail over $\text{SNR}_{\text{out}} = 26$ is added to showcase the differences in the CRB for the float solution across the different signals.

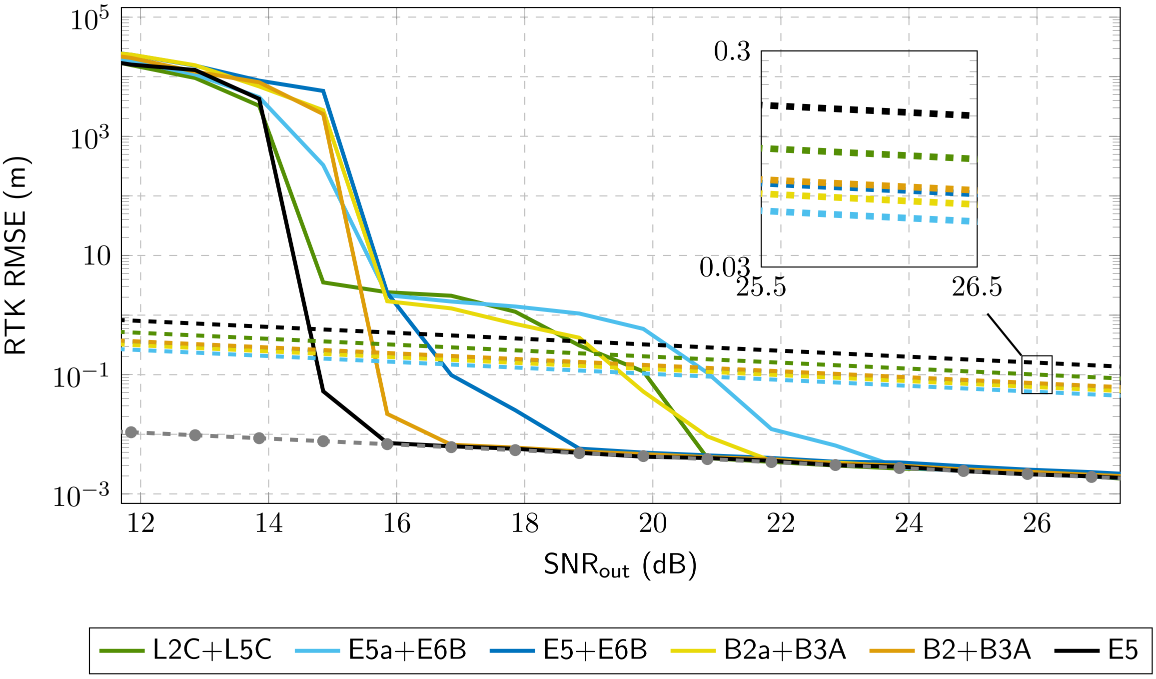

**Figure 2.13:** RTK positioning CRBs (gray and colored dashed lines for the mixed and real models, respectively) and associated RMSE (solid lines) against $\text{SNR}_{\text{out}}$ for a selection of meta-signals. For completeness, Galileo E5 is show in black.

Unlike the other results on RTK positioning with representative signals, one can no longer differentiate the four regimes for the MLE behavior. Instead, there is a rapid transition from the asymptotic performance to the no information region. As a result, the CRB for the real model (i.e., the optimal float solution) is never reached by any of the signals, and one would not benefit from the more precise float solution related to the metasignals. Thus, the MLE for the mixed model abandons the corresponding CRB at the same point as the estimation for the time-delay deviated from its CRB. Notice that such slow convergence is directly link to the false locks due to large secondary peaks present in metasignals. Therefore, a first conclusion was that subcarriers that induced large secondary ACF peaks strongly impacted the achievable RTK performance.

Overall, whenever one's goal is maximizing the operation region for carrier phase-based precise positioning, the best performance is provided by the E5 signal. While metasignals represent a promising alternative to conventional PPP or RTK positioning, unrestrained from augmentation data and differential stations, their use for RTK positioning under nominal conditions is unmeaning. An interesting use case is discussed in [7] for which, under limited or poor satellite visibility, the metasignals E5+E6B and B2+B3A overperform E5 and provide a good trade-off between operability and precision. This is due to the significantly more precise time-delay estimates, which may compensate for the lack of satellites in certain occasions.

## 2.7 Summary

Precise positioning through the use of carrier phase observations is undoubtedly the most relevant use of GNSS for prospective vehicular and autonomous systems applications. This chapter provides a review on carrier phase-based localization, RTK positioning through the mixed real- and integer-valued parameter problem and the intricacies of integer estimation.

Sections 2.1 and 2.2 presents the mixed model for RTK positioning and the procedure for parameter estimation via ML, respectively. Such a MLE for the mixed model consists on a three step decomposition leading to the *float*, integer ambiguities and *fixed* positioning solution. Since the available literature on the former estimation focuses on snapshot or memoryless approaches, Section 2.2.1 introduces its extension to recursive problems, a fundamental key to provide precise navigation estimates via filtering techniques. Section 2.3 provides a short overview on IAR, including relevant integer estimators, ambiguity decorrelation and validity test. Finally, Section 2.3.3 discusses PAR and its importance for situations in which providing an integer solution for the complete vector of ambiguities becomes a challenging task. In addition, a new PAR estimator denoted Precision-Driven PAR is introduced, with the aim of maximizing the accuracy of the fixed localization solution with a minimal number of estimated integer ambiguities.

Section 2.4 constitutes the core contribution of this chapter and proposes a general form CRB for the mixed model. The presented CRB complements the relevant work of Teunissen on upper bounds for integer estimation and provides a tool to assess the best performance, in terms of MSE, of estimators at the mixed model. While the usefulness of the CRB for the mixed model extends to many signal processing, biology or communication problems, this thesis focuses on its particularization for RTK positioning. Thus, a new perspective on estimators for the mixed model is provided in Section 2.5, leading to some interesting conclusions:

- There exist the three regimes for the performance of estimators of the mixed model, conditioned on the satellite geometry and the level of noise on the pseudorange observations.
- Estimators of the mixed model which employ IR, IB or ILS for the real-to-integer mapping procedure are demonstrated to be asymptotically efficient.
- In the asymptotic case, i.e., when the ambiguities can always be correctly mapped to the correct integer vector, the covariance matrix associated with the ambiguities vanishes. In that scenario, the covariance matrix for the fixed solution is equivalent to disregarding the existence of ambiguities.
- The proposed Precision-Driven PAR constitutes an interesting alternative approach to the integer estimation realized for conventional RTK positioning, for which the complete vector of ambiguities is estimated. Indeed, at the cost of an acceptable precision loss, one could obtain a substantial gain in the extent of the asymptotic regime.

The quest towards characterizing the ultimate GNSS-based positioning performance is complete in Section 2.6, where the relationship between the receiver's signal processing and the precision of the fixed localization estimate is addressed. Both representative and modern GNSS signals are analyzed, leading to the conclusion that Galileo E5 currently constitutes the best trade-off between precision and robustness to weak signal reception. While the use of metasignals results promising for code-based positioning, its application to carrier phase-based localization is uninteresting due to the large secondary ACF peaks that complicate the task of the receiver at tracking the signals. A number of open issues are yet to be investigated as will be commented in Chapter 6.5.

The results presented in this chapter were partially published in:

**Journal articles:**

[4] Medina, D., Vilà-Valls, J., Chaumette, E., Vincent, F., & Closas, P. (2021). Cramér-Rao bound for a mixture of real-and integer-valued parameter vectors and its application to the linear regression model. *Signal Processing, 179*, 107792.

[7] Ortega, L., Medina, D., Vilà-Valls, J., Vincent, F., & Chaumette, E. (2020). Positioning Performance Limits of GNSS Meta-Signals and HO-BOC Signals. *Sensors*, 20(12), 3586.

[1] Castro-Arvizu, J. M., Medina, D., Ziebold, R., Vilà-Valls, J., Chaumette, E., & Closas, P. (2021). Precision-Aided Partial Ambiguity Resolution Scheme for Instantaneous RTK Positioning. Remote Sensing, 13(15), 2904.

[6] Heßelbarth, A., Medina, D., Ziebold, R., Sandler, M., Hoppe, M., & Uhlemann, M. (2020). Enabling Assistance Functions for the Safe Navigation of Inland Waterways. *IEEE Intelligent Transportation Systems Magazine*, 12(3), 123-135.

**Conference articles:**

[12] Medina, D., Castro-Arvizu, J. M., Vilà-Valls, J., Ziebold, R., & Closas, P. (2021, March). Precision-Driven Partial Ambiguity Resolution Technique for Short to Medium Baseline Positioning. In *2021 IEEE Aerospace Conference* (pp. 1-7). IEEE.

[15] Castro-Arvizu, J. M., Medina, D., & Ziebold, R. (2020, January). Impact of Satellite Elevation Mask in GPS+ Galileo RTK Positioning. In *Proceedings of the 2020 International Technical Meeting of The Institute of Navigation* (pp. 487-498).

[19] Medina, D., Alvarez-Merino, C., Ziebold. R. (2019, September). Partial Ambiguity Resolution for Reliable GPS/Galileo Positioning. In *2019 International Workshop on GNSS Ionosphere (IGWI).*

# Part II

# On the Position and Attitude Estimation in Multi-Antenna GNSS

## CHAPTER 3

# GNSS-based Attitude Estimation

Attitude determination conforms a navigational element far more relevant than positioning for vehicles with large inertia, such as ships or airplanes. Similarly, orientation information is a fundamental key for the successful realization of spacecraft missions, since satellites and space probes incorporate pointing elements whose control is based upon the attitude knowledge. While inertial sensing and visual odometry constitute consonant sources for relative attitude information, their estimates are prone to rapidly drift and accumulate large errors, especially when the initial orientation is poorly known. The configuration of multiple GNSS antennas on board of a vehicle enables the provision of precise and absolute attitude estimates, at the cost of surveying the distance and relative orientation between these antennas. While limited in precision by the inter-antenna separation, the use of carrier phase-based has been shown to lead to sub-degree orientation determination. This chapter provides an overview on attitude representations and how GNSS-based models can be expressed by virtue of the former. Also, the estimation for GNSS-based attitude is discussed, both for memoryless and recursive forms, as well as examining the expected precision. Finally, synthetic and real experimentation serves to illustrate the performance that can be achieved with multi-antenna configurations for attitude estimation.

## Outline

Let us refer to attitude estimation as the process of finding the relative orientation between two orthogonal frames or, in plain words, as the determination of the spatial orientation of an object. While localization information has been the prior concern for GNSS practitioners, orientation information results key for aiding vehicles which can freely move in a three-dimensional space, such as aircrafts and miniaturized aerial devices. For instance, the information on the pitch of an airplane is as relevant as the height with respect to the ground for driving assistance functions (e.g., automated landing). Similarly, communications and weather satellites present specific pointing requirements, making attitude estimation an indispensable factor on their correct functioning.

From a historical perspective, the need for solving the attitude problem was born and, at the same time, reach its importance peak during the 1960s and 1970s. The reason for such prompt urgency was tightly related to the space race and the development of attitude control systems for the upcoming space missions. During the early years of attitude determination, the first estimators corresponded to geometrical and simplistic LS adjustment solutions (such as TRIAD [102]). It was the formulation of Wahba's problem [103], consisting on the calculation of a proper orthonormal matrix to relate two set of baselines in different frames, which open the door to developing the first optimal memoryless estimators, such as Davenport's $q$ method, or Shuster's Quaternion estimator (QUEST) [104], [105]. A more profound and (very) interesting historical overview to the topic of attitude determination can be found in [106], [107].

In terms of recursive and filtering procedures, attitude estimation poses distinct challenges. On the one hand, the nonlinear constraints that conform a proper rotation are complicated to incorporate to a filter design. On the other hand, the choice of attitude parametrization plays a relevant role and determines whether singularities and/or numerical problems may be encountered on the state (i.e., three-dimensional representations are singular or discontinuous at certain angles, such as the gimbal lock problem in Euler angles) or the covariance estimation (i.e., one might incur in numerical problems whenever the covariance matrix does not represent the uncertainty over the minimal state representation). Both the aerospace and robotics research communities have "pushed" for the development of Kalman Filtering variants that could satisfy the aforementioned challenges. There is a general consensus on the quaternion being the preferred attitude parametrization for the state estimate, since it presents the lowest dimension of any globally non-singular attitude parametrization. Enforcing the unit norm constraint on a quaternion leaves it with the three degrees of freedom consistent with the dimensionality of the rotation group, at the cost of some sort of constrained estimation [108]. The preferred and most acquainted approach represents the orientation with the unit quaternion, while the covariance matrix represents the uncertainty for the three-dimensional component of the attitude errors. This combination is known as the Multiplicative EKF (MEKF), Error-State KF (ESKF) or Indirect KF [108]–[110] within aerospace and robotics practitioners, respectively. While other KF extensions for nonlinear systems (e.g., Unscented or Cubature KFs) can be also applied for attitude estimations, their added complexity does not justify their use and, therefore, they will not be covered within this thesis. The latest contributions on attitude estimation are related to the framework of Invariant Kalman Filtering (IKF), described in the series of work by Barrau and Bonnabel [111]–[113]. The IKF leverages on the geometric structure of Lie groups to provide convergence guarantees for linear systems with group-affine dynamics. While IKF constitutes a promising alternative to MEKF/ESKF, its gain is notable mostly for robotics-related applications (e.g., pre-integration or simultaneous localization and mapping (SLAM)) and, therefore, it is beyond the scope of this thesis.

In regards to sensor modalities providing orientation information, one can distinguish the categories of relative and absolute attitude sensing. Known examples of the former include gyroscopes (i.e., or its combination with accelerometers to conform Inertial Measurement Units (IMU)) and visual odometry, which describes the attitude change over time. The benefits of inertial aiding are clear, since gyroscopes allow for tracking fast and subtle rotations and bridge outages from absolute attitude information. As drawback, relative sensing is subject to rapidly drift and accumulate large errors due to integrating the sensors' noises and biases. The latter category employs external references to estimate the orientation of the tracked vehicle and lists sensors like star trackers, magnetometers or horizon detectors [114, Ch. 1]. Other than for timing and positioning, GNSS signals can be used as absolute attitude information for platforms equipped with a multi-antenna configuration. Indeed, attitude determination was one of the pioneering applications of GNSS, being featured in a low Earth orbit satellite with a dual antenna configuration already in 1976 [115], [116].

Thus, GNSS represents an appealing option for absolute attitude information, providing precise estimates and a fair compromise in terms of expense, weight and energy consumption. Nonetheless, GNSS-based attitude information poses distinct constraints: *i)* at least three non-coplanar antennas are required to sense three-dimensional orientation, with their relative distances being accurately surveyed in the vehicle's body frame; *ii)* the precision of the attitude estimates is directly proportional to the precision on which the inter-antenna baseline vectors can be estimated and inversely proportional to the antenna separation, which limits its use in miniaturized platforms. Since the configuration of the antennas is limited by the dimension of the tracked vehicle, the inherent precision of carrier phase observations becomes a determinant factor to obtain precise attitude estimates. In consequence, the GNSS-based attitude model gathers the complicated inherent constraints on orientation determination with the integer parameter estimation present in every carrier phase-based application.

While the GNSS attitude model has been extensively studied by the works of Teunissen and Giorgi [60], [114], [117]–[119], from which more details are discussed at a later stage in this chapter, the general use of the quaternion parametrization and its extension for recursive and filtering forms have escaped the interest from the GNSS research community. Hence, the formulation of quaternion-focused estimators for the "mixed" model (here, mixed in the sense of mixture of unknowns living in the three-dimensional unit sphere manifold and in the integer space) constitutes the focal point and main contribution of this chapter.

This chapter reviews some notable options for attitude parametrization, with an emphasis on the unit-quaternion form. Then, the different models for GNSS-based attitude information are presented, followed by the introduction of deterministic (memoryless) and recursive estimators. Since estimation bounds for the carrier phase-based attitude problem are not known, due to their extreme complexity in derivation, it is discussed how the precision of related estimates can be approximated using alternative geometrical rules. At last, the performance of estimators for the carrier phase-based attitude model is addressed by means of Monte Carlo characterization, while a real-world experiment serves to illustrate the attitude estimation performance for a recursive solution fusing inertial and GNSS signals.

## 3.1 Attitude Representations

Representing the pose of a rigid body is not as straightforward as one would expect. While there is no ambiguity on the interpretation of a translation or the position for a rigid body, the same cannot be stated with regards to its attitude. The variety of expressions to formulate such orientation information (rotation matrices, Euler angles, rotation vectors, Rodrigues parameters, quaternions, ...) and their convention (only for quaternions: order of the components, handedness, etc.) have created, at least once, frustration and insecurity among most practitioners who encountered dealing with attitude[1]. This section is strongly inspired by the work of Solà [120]–[122], who extensively (and didactically!) discusses matters related to attitude representation and estimation.

Luckily, the relationship of this thesis with regards to attitude is somewhat uncomplicated for two compelling reasons: *i)* there are transformations mostly across two frames; *ii)* only two sensors are considered for the provision of attitude information, namely GNSS signals and gyroscopes. Thus, the kinematic quantities involve the frame whose motion is described, i.e., the body or local vehicle frame denoted with the left subscript $\mathcal{B}$, and the frame with respect to which that motion occurs, i.e., the global or inertial frame denoted with the left subscript $\mathcal{G}$. The body frame is oriented such that the $X-$, $Y-$ and $Z-$axes are aligned with the right, forward and up directions of the vehicle, while the global frame corresponds to the Earth-centered Earth-fixed (ECEF) frame. Fig. 3.1 provides pictorial support for the described frames. While GNSS-related information is expressed on the global frame (i.e., the positions of the satellites or the estimated localization for the tracked platform), the observations from a gyroscope are assumed to be aligned with the body frame. Hereinafter and unless stated otherwise, the rotation operator expresses the orientation of the vehicle $\mathcal{B}$ frame to the global $\mathcal{G}$ frame, massively easing the notation (e.g., one shall avoid notations such as $\mathbf{R}_{\mathcal{G},\mathcal{B}}$ in [123] or $\mathbf{R}^{\mathcal{G}}_{\mathcal{B}}$ in [124] and, instead, directly refer to $\mathbf{R}$).

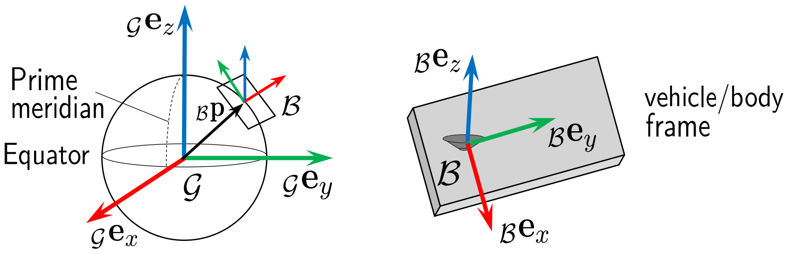

**Figure 3.1:** Depiction for the global and local coordinate frames.

The rotation group, denoted as $SO(3)$ for three-dimensional Euclidean spaces, constitutes the group of rotations under the operation of composition. Rotations are linear transformations preserving vector lengths and relative orientation such that

$$SO(3) : \left\{ r : \mathbb{R}^3 \to \mathbb{R}^3 \mid \forall \mathbf{v}, \mathbf{w} \in \mathbb{R}^3, \|r(\mathbf{v})\| = \|\mathbf{v}\|, r(\mathbf{v}) \times r(\mathbf{w}) = r(\mathbf{v} \times \mathbf{w}) \right\}, \qquad (3.1)$$

with $r : \mathbb{R}^3 \to \mathbb{R}^3$ a generic rotation operator. With multiple ways to represent the

---

[1] A good example of this frustration was made evident during the 2014 International Conference on Robotics and Automation (ICRA). A workshop titled "What Sucks in Robotics and How to Fix It" featured a talk exclusively devoted to the enormous number of combinations one may face when representing a rigid body's orientation and some recommendations and best practices. The talk from Dr. Furgale, titled "Representing Robot Pose: the Good, the Bad, and the Ugly", can be found here and its reading is strongly recommended.

rotation group (i.e., attitude parametrization), the sequel discusses some of these attitude representations along with their advantages and drawbacks for state estimation.

### 3.1.1 Rotation Matrices

Let us consider the two reference frames, $\mathcal{G}$ and $\mathcal{B}$, and a vector expressed in the former as ${}_{\mathcal{B}}\mathbf{v}$. The rotation operator to transform ${}_{\mathcal{B}}\mathbf{v}$ into the global frame can be represented by the matrix $\mathbf{R} \in \mathbb{R}^{3,3}$ as

$$
{}_{\mathcal{G}}\mathbf{v} = r({}_{\mathcal{B}}\mathbf{v}) = \mathbf{R}_{\mathcal{B}}\mathbf{v}, \tag{3.2}
$$

where, in order to preserve vector lengths and their relative orientation (and, therefore belong to $SO(3)$), rotation matrices are such that $\mathbf{R}\mathbf{R}^{\top} = \mathbf{I}$ and $\det(\mathbf{R}) = 1$.

While the rotation matrix results convenient to perform three-dimensional rotations, its direct computation is counter-indicated since its is far from posing a minimal state representation. Thus, while nine parameters are needed to formulate such a matrix, 3D rotations can be specified just with three parameters [120].

### 3.1.2 Euler Angles

Euler angles constitute the most intuitive manner to describe and graphically depict the orientation of a rigid body. Euler angles consists on the composition of three successive rotations, such that the angles describe the rotation that each axis of the reference frame (here, the body frame $\mathcal{B}$) needs to sequentially rotate to align with the target frame (here, the global frame $\mathcal{G}$). Euler angles are typically defined such that they describe the orientation of an aircraft:

- The *roll* angle, $\alpha$, describes the rotation around the X axis (the longitudinal axis), such that a positive value indicates that the right side of the platform sinks.
- The *pitch* angle, $\beta$, describes the rotation around the Y axis (the transversal axis), such that a positive value indicates that the nose of the aircraft sinks.
- The *yaw* or *heading* angle, $\gamma$, describes the rotation around the Z axis (the vertical axis), such that a positive value indicates a left turn.

There are multitude of conventions with regards to the other in which the Euler angles can be performed. For instance, in the Z-Y-X order, one starts rotating the body frame $\mathcal{B}$ around its z-axis by $\gamma$, yielding to a new frame $\mathcal{B}'$. Then, $\mathcal{B}'$ is rotated about its y-axis by $\beta$, yielding to $\mathcal{B}''$. At last, $\mathcal{B}''$ is rotated about its x-axis by an angle $\alpha$ to arrive to the global frame $\mathcal{G}$. The afore-described process for three sequential rotation is illustrated in Figure 3.2.

Since Euler angles do not represent an rotation operator by themselves, instead the formulation of a rotation matrix is required. Thus, given the Euler angles $[\alpha, \beta, \gamma]^{\top}$, and for the Z-Y-X sequence, the rotation matrix is obtained as follows

$$
\mathbf{R} = \begin{bmatrix} \cos\beta\cos\gamma & -\cos\alpha\sin\gamma + \sin\alpha\sin\beta\cos\gamma & \sin\alpha\sin\gamma + \cos\alpha\sin\beta\cos\gamma \\ \cos\beta\sin\gamma & \cos\alpha\cos\gamma + \sin\alpha\sin\beta\sin\gamma & -\sin\alpha\cos\gamma + \cos\alpha\sin\beta\sin\gamma \\ -\sin\beta & \sin\alpha\cos\beta & \cos\alpha\cos\beta \end{bmatrix}. \tag{3.3}
$$

While Euler angles do constitute a minimal attitude representation, they are affected by singularities (also known for its physical effect on gimbal mechanisms, happening when two of the three axes become parallel and, therefore, the rotation degenerates to a two-dimensional space). One might mitigate this shortcoming by limiting the range in which Euler angles can operate.

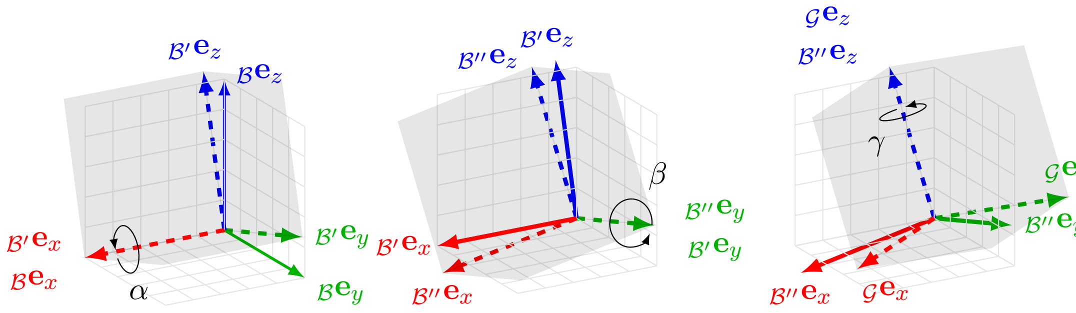

**Figure 3.2:** Sequence of rotations in Z-Y-X order, with $\alpha = 15, \beta = 10, \gamma = 30$ degrees, such that the Euler angles represent a rotation from $\mathcal{B}$ to $\mathcal{G}$. The canvas for the local frame is depicted on the background, while the canvas for each of the rotated frames is depicted on shaded gray.

### 3.1.3 Quaternions

The quaternion is a four dimensional hyper-complex number, first described by Hamilton in 1843 [125], which is often used to represent orientations in 3D spaces under the unit-norm constraint. Despite the attitude quaternion not being intuitive or easy to visualize, its use has been widely adopted in a plethora of applications, including robotics and computer graphics [123], [126]–[128]. The success behind the use of quaternions for attitude representation is motivated by: *a)* presenting the minimal state representation among global non-singular attitude parametrizations (four elements are involved in the estimation process, with only the unit-norm as constraint); *b)* the time evolution or quaternion kinematics can be expressed in linear form.

As for other attitude parametrizations, one could easily get lost in the various forms of representing quaternions. In terms of choice, one shall care for the order (whether the real element appears as the first or last component of the quaternion), handedness (right- or left-handed), function of the rotation operator (passive or active) and direction of the rotation operator (local-to-global or global-to-local). Although there are up to twelve possible combinations for representing quaternions, one may (fortunately) limit his or her options to one of the two principal conventions: Hamilton and JPL. These two conventions are summarized in Table 3.1. While the Hamilton convention is more common within the field of robotics, JPL (Jet Propulsion Laboratory) can be found often for aerospace applications. Interestingly, most "classical" literature on quaternion estimation follows the JPL convention, while most open source software libraries opt for Hamilton convention.

**Table 3.1:** Hamilton and JPL conventions for the representation of quaternions.

| | Hamilton | JPL |
|---|---|---|
| Elements order | real part first:<br>$\mathbf{q}^\top = [q_w, \mathbf{q}_u]$ | Real part last:<br>$\mathbf{q}^\top = [\mathbf{q}_u, q_w]$ |
| Handedness | right-handed<br>$ij = -ji = k$ | left-handed<br>$ji = -ij = k$ |
| Function | Passive | Passive |
| Direction of rotation | Local-to-Global | Global-to-Local |

In this work, the Hamilton convention is adopted (scalar first, right-handed, passive operator and body-to-glocal rotation), such that

$$\mathbf{q} \triangleq \begin{bmatrix} q_w \\ \mathbf{q}_u \end{bmatrix} = \begin{bmatrix} q_w \\ q_x \\ q_y \\ q_z \end{bmatrix} \in \mathbb{H}\,, \tag{3.4}$$

where $q_w$ is the real part, and $\mathbf{q}_v = q_x i + q_y j + q_z k$ is the imaginary vector part (with the complex algebra $i^2 = j^2 = k^2 = ijk = -1$) and $\mathbb{H}$ constitutes the set of quaternions.

Unit quaternions denote those quaternions whose norm is equal to one, such that $\|\mathbf{q}\| \triangleq q_w^2 + \mathbf{q}_u^2 = 1$, and can be used to represent the 3D orientation of a rigid body. Unit quaternions are expressed as

$$\mathbf{q} \triangleq \begin{bmatrix} \cos(\theta/2) \\ \mathbf{u}\sin(\theta/2) \end{bmatrix} \in \mathcal{S}^3\,, \tag{3.5}$$

with $\mathbf{u}$ an unit vector representing the rotation axis and $\theta$ a rotation angle. Unit quaternions are represented by the manifold of 3D unit spheres $\mathcal{S}^3$ and conform a group under the quaternion multiplication. The rotation operator based on the use of unit quaternions is given by

$$r({}_{\mathcal{B}}\mathbf{v}) = \mathbf{q} \circ {}_{\mathcal{B}}\mathbf{v} \circ \mathbf{q}^* = \mathbf{R}_{\mathcal{B}}\mathbf{v}, \tag{3.6}$$

where $\circ$ is the quaternion multiplication and $\mathbf{q}^*$ is the inverse quaternion operation. Details on these operations and other quaternion properties are given in Appendix C. Thus, the transformation of unit quaternion to rotation matrix described by the following homogeneous quadratic function

$$\mathbf{R}\{\mathbf{q}\} = \left(q_w^2 - \mathbf{q}_u^\top \mathbf{q}_u\right)\mathbf{I}_3 + 2\mathbf{q}_u\mathbf{q}_u^\top + 2q_w[\mathbf{q}_u]_\times, \tag{3.7}$$

with $[\cdot]_\times$ the skew operator.

Since $\mathcal{S}^3$ constitutes a smooth manifold, the principles of Lie Theory can be exploited to manipulate quaternions. This results especially useful when estimating quaternions, since one may leverage on the Lie group and algebra to perform unconstrained estimation and still obtain a quaternion of unit norm. Hence, a vector rotation expressed in the Euclidean space for $\boldsymbol{\theta} \in \mathbb{R}^3$ connects to the Lie algebra $\mathbf{u}\theta \in \mathfrak{so}(3)$ (with $\mathbf{u}$ an unit vector of rotation and $\theta$ the rotated angle) with the isomorphism $(\cdot)^\wedge : \mathbb{R}^3 \mapsto \mathfrak{so}(3)$. Then, the Lie algebra connects with $\mathcal{S}^3$ through exponential mapping. The overall procedure is given by

$$\boldsymbol{\theta} \in \mathbb{R}^3 \underset{(\cdot)^\wedge}{\mapsto} \mathbf{u}\theta \in \mathfrak{so}(3) \underset{\exp(\cdot)}{\mapsto} \mathbf{q} \in \mathcal{S}^3\,, \tag{3.8}$$

with

$$(\boldsymbol{\theta})^\wedge \triangleq \begin{cases} \mathbf{u} = \boldsymbol{\theta}/\|\boldsymbol{\theta}\|^2 \\ \theta = \|\boldsymbol{\theta}\| \end{cases}, \quad \exp(\mathbf{e}\theta) \triangleq \begin{bmatrix} \cos(\theta/2) \\ \mathbf{e}\sin(\theta/2) \end{bmatrix}. \tag{3.9}$$

In addition, the formulation $\mathbf{q}\{\boldsymbol{\theta}\}$ will appear repeatedly along this thesis. This refers to the mapping between the Euclidean space and the unit quaternion one via the relationships established in (3.8), such that

$$\mathbf{q}\{\boldsymbol{\theta}\} \triangleq e^{\mathbf{u}\theta/2} = \cos\frac{\theta}{2} + \mathbf{u}\sin\frac{\theta}{2} = \begin{bmatrix} \cos(\theta/2) \\ \mathbf{u}\sin(\theta/2) \end{bmatrix}, \tag{3.10}$$

where $e^{(\cdot)}$ is an extension of the Euler formula, $e^{i\theta} = \cos\theta + i\sin\theta$, for imaginary numbers.

Additional graphical support for the relationship established between the unit quaternion manifold and the Euclidean space is shown in Fig. 3.3. On the left, the $\mathcal{S}^3$ manifold (i.e., the blue sphere) is illustrated along with the hyperplane $\mathbb{R}^3$ (i.e., the red grid). The centre side of Fig. 3.3 shows a side-cut through the sphere and illustrates how real elements are mapped to $\mathcal{S}^3$ with the exponential operator, and viceversa via logarithm mapping.The right side of Fig. 3.3 illustrates the composition operator between two quaternions $\mathbf{q}, \mathbf{p}$, whose connecting arc can be expressed in the tangent space.

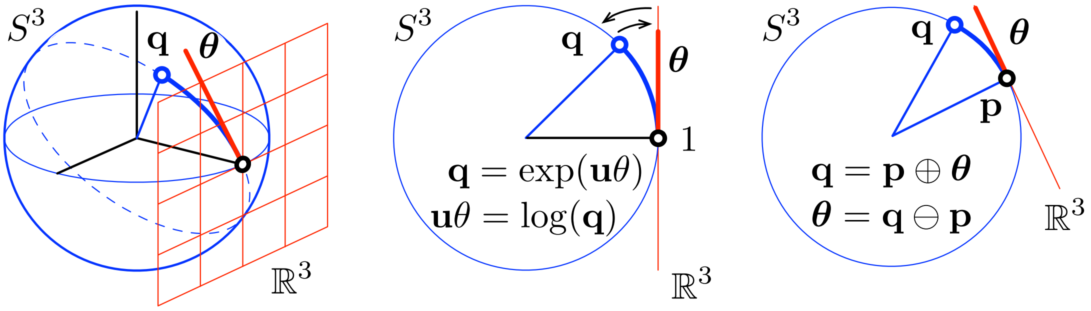

**Figure 3.3:** Relationship between the 3D unit-sphere $\mathcal{S}^3$ manifold and the Euclidean space via its algebra. Image adapted from [122].

The second useful property of quaternions appears in relation with their dynamical model. Considering $\mathbf{q}$ as a time continuous variable, i.e., $\mathbf{q} = \mathbf{q}(t)$, one can develop its time-derivative as follows

$$\begin{aligned}
\dot{\mathbf{q}}(t) &\triangleq \lim_{\Delta t \to 0} \frac{\mathbf{q}(t+\Delta t) - \mathbf{q}(t)}{\Delta t} = \lim_{\Delta t \to 0} \frac{\mathbf{q}(t) \circ \Delta\mathbf{q} - \mathbf{q}(t)}{\Delta t} \\
&= \lim_{\Delta t \to 0} \frac{\mathbf{q}(t) \circ \left( \begin{bmatrix} 1 \\ \Delta\boldsymbol{\theta}/2 \end{bmatrix} - \begin{bmatrix} 1 \\ \mathbf{0} \end{bmatrix} \right)}{\Delta t} \\
&= \lim_{\Delta t \to 0} \frac{\mathbf{q}(t) \circ \begin{bmatrix} 0 \\ \Delta\boldsymbol{\theta}/2 \end{bmatrix}}{\Delta t} \\
&= \frac{1}{2}\mathbf{q}(t) \circ \begin{bmatrix} 0 \\ \boldsymbol{\omega}(t) \end{bmatrix},
\end{aligned} \tag{3.11}$$

where $\boldsymbol{\omega}$ constitutes the vector of angular rate. Extending the former expression to discrete times, let us denote $\mathbf{q}_t = \mathbf{q}(t)$ and $\mathbf{q}_{t+1} = \mathbf{q}(t+\Delta t)$. Then, assuming that the vector of angular rate (measured, for instance with a three-axis gyroscope) $\boldsymbol{\omega}_t = \boldsymbol{\omega}(t)$, remains constant over the period $[t, t+\Delta]$, the Taylor series of $\mathbf{q}(t+\Delta t)$ is as follows

$$\mathbf{q}_{t+1} = \mathbf{q}_t + \dot{\mathbf{q}}_t \Delta t + \frac{1}{2!}\ddot{\mathbf{q}}_t \Delta t^2 + \frac{1}{3!}\dddot{\mathbf{q}}_t \Delta t^3 + \dots \,, \tag{3.12}$$

and, applying a zeroth order integration leads to the following expression for the discrete kinematics of the quaternion

$$\mathbf{q}_{t+1} = \mathbf{q}_t \circ \mathbf{q}\{\boldsymbol{\omega}_t \Delta t\} \,. \tag{3.13}$$

Hereinafter, this thesis makes reference and works only with unit quaternions and, therefore, the notation is simplified such that “quaternions” do actually refer to unit quaternions.

## 3.2 GNSS Attitude Functional Model

In multi-antenna configurations, one of the antennas is treated as *master* and its position considered as the center of the body frame, while the remaining $N$ antennas are denoted *slaves*. Since their positions are surveyed and accurately known within the platform frame, the baseline vectors are known as well. For instance, the vector that relates the positions of the master and $j$th antennas is expressed as

$$ {}_{\mathcal{B}}\mathbf{b}_{j,m} = {}_{\mathcal{B}}\mathbf{p}_j - {}_{\mathcal{B}}\mathbf{p}_m, \tag{3.14} $$

where the left subscript denote the antenna under consideration, with $m$ for the master and $j = 1, \ldots, N$ for the slave antennas, respectively. This notation is illustrated in Fig. 3.4, along with the GNSS code and carrier phase observations.

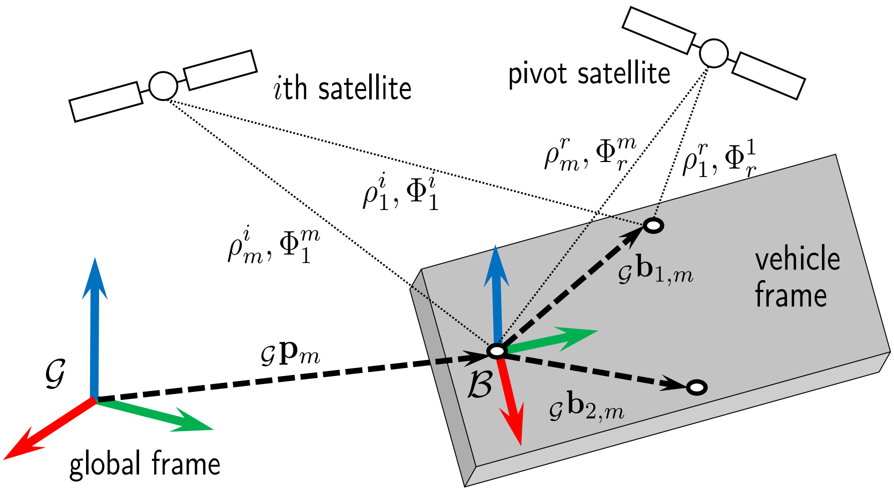

**Figure 3.4:** Diagram for the collection of GNSS data over different GNSS antennas installed on a platform.

Since GNSS ranging signals allows determining the position of these antennas (and, therefore, also of the baseline vectors) in the global frame, the attitude problem can be formulated as finding the rotation matrix that relates both frames. This estimation aligns with the optimization problem formulated by Wahba in 1965 for computing the attitude of a satellite and given by

$$ \sum_{j=1}^{N} w_j \left\| {}_{\mathcal{G}}\mathbf{b}_{j,m} - \mathbf{R}_{\mathcal{B}}\mathbf{b}_{j,m} \right\|^2, \tag{3.15} $$

where $w_j$ is the weight assigned to each of the observations. In principle, one could solve the localization for each of the antennas independently from which the associated baseline vectors in the global frame would be obtained. Given these vectors, one could solve the Wahba's problem in (3.15) to provide attitude estimates. Nonetheless, providing precise localization for each of the antennas is not always possible and, even when it is, the previously described strategy is far from optimal. Instead, one can exploit the fact that all antennas experiment almost the same propagation errors to perform differential "positioning" among pairs of antennas. Thus, one may replicate the RTK positioning procedure and perform double differentiating with respect to the master antenna, instead of the base station.

Let us consider $n+1$ satellites tracked on a single frequency simultaneously at $N+1$ antennas installed on a vehicle. Then, the DD code and carrier observations can be performed as in (2.2) using the master antenna instead of the base station to obtain

$$\begin{aligned} DD\rho_{j,m}^{i,r} &= \rho_j^i - \rho_m^i - \left(\rho_j^r - \rho_m^r\right), \\ DD\Phi_{j,m}^{i,r} &= \Phi_j^i - \Phi_m^i - \left(\Phi_j^r - \Phi_m^r\right) \end{aligned}, \tag{3.16}$$

and the complete set of DD observations is denoted with $\mathbf{y} \in \mathbb{R}^{2nN}$ and expressed as

$$\mathbf{y} \triangleq \text{vec}\left(\mathbf{Y}\right), \quad \text{with } \mathbf{Y} = \left[\mathbf{y}_{1,m}, \ldots, \mathbf{y}_{N,m}\right] , \tag{3.17}$$

and where the observations related to each $j-m$ pair of antennas is

$$\mathbf{y}_{j,m}^{\top} = [\mathbf{DD\Phi}_{j,m}^{1:n,r\top}, \mathbf{DD}\boldsymbol{\rho}_{j,m}^{1:n,r\top}]. \tag{3.18}$$

Similarly to the carrier phase-based positioning case, the GNSS-based attitude model comprises a mixed parameter estimation problem. Unlike the positioning case, there exists multiple forms to express the attitude model, based on whether one is to determine the baseline vectors connecting the antennas in the global frame or the platform attitude *per se*. Moreover, while a general consensus exists for the estimation method of the positioning mixed model (e.g., for memoryless cases, a MLE provides the float and fixed solutions while LAMBDA is generally used for the integer estimation), attitude models can be resolved in different and efficient manners, as discussed later in Section 3.3.

**Definition 3** (Multi-baseline Mixed Model)**.** Let $\mathbf{A}, \mathbf{B}$ be $2n \times (n+p)$ full rank matrices and $\boldsymbol{\Sigma}$ an $M \times M$ symmetric and positive semi-definite matrix. Then, the multi-baseline mixed model can be cast as

$$\mathbf{y} \sim \mathcal{N}\left(\text{vec}(\mathbf{AZ} + \mathbf{BL}), \boldsymbol{\Sigma}\right), \ \mathbf{Z} \in \mathbb{Z}^{n,N}, \ \mathbf{L} \in \mathbb{R}^{3,N} , \tag{3.19}$$

with $p = 3N$ the number of real-valued parameters, $M = 2nN$ the total number of observations, and the matrices holding the unknown parameters, $\mathbf{Z}$ and $\mathbf{L}$, contain the DD ambiguities and the baseline vectors in the global frame as

$$\mathbf{Z} = \left[\mathbf{a}_{1,m}, \ldots, \mathbf{a}_{N,m}\right], \ \mathbf{L} = \left[{}_{\mathcal{G}}\mathbf{b}_{1,m}, \ldots, {}_{\mathcal{G}}\mathbf{b}_{N,m}\right] . \tag{3.20}$$

Notice that estimating the unknowns for the model 3 does not provide with a direct attitude estimation and, instead, one would still have to solve the Wahba's problem in (3.15). Alternatively, one can directly connect the set of observations $\mathbf{y}$ with attitude-related parameters, leading to the following model.

**Definition 4** (Attitude Mixed Model)**.** Let $\mathbf{A}, \mathbf{B}$ be $2n \times (n+p)$ full rank matrices and $\boldsymbol{\Sigma}$ an $M \times M$ symmetric and positive semi-definite matrix. Then, the multi-baseline mixed model can be cast as

$$\mathbf{y} \sim \mathcal{N}\left(\text{vec}\left(\mathbf{AZ} + \mathbf{B}\left[r\left({}_{\mathcal{B}}\mathbf{b}_{1,m}\right), \ldots, r\left({}_{\mathcal{B}}\mathbf{b}_{N,m}\right)\right]\right), \boldsymbol{\Sigma}\right), \ \mathbf{Z} \in \mathbb{Z}^{n,N} , \tag{3.21}$$

with $p$ the number of parameters for a particular attitude parametrization, $M = 2nN$ and $r(\cdot)$ the rotation operator that supports the body-to-global transformation of the inter-antenna baselines in the body frame, given for instance in rotation matrix or quaternion forms as in (3.2), (3.6), respectively.

An important aspect of GNSS-based attitude models relates to the stochastic modeling for the observations. Since the DD combination is performed with respect to the same antenna, additional cross-correlation terms are present. Thus, the covariance matrix $\mathbf{\Sigma}$ can be formulated as

$$\mathbf{\Sigma} = \begin{bmatrix} \bar{\sigma}_{\Phi}^2 \cdot \mathbf{D}_{\text{att}} \otimes \mathbf{D}\mathbf{W}\mathbf{D}^{\top} & \\ & \bar{\sigma}_{\rho}^2 \cdot \mathbf{D}_{\text{att}} \otimes \mathbf{D}\mathbf{W}\mathbf{D}^{\top} \end{bmatrix} , \tag{3.22}$$

where $\bar{\sigma}_{\Phi}, \bar{\sigma}_{\rho}$ are the carrier phase and code zenith referenced variances, $\mathbf{W}$ is a weighting matrix as described in (1.32), $\mathbf{D}$ is the DD matrix defined in (2.6) and $\mathbf{D}_{\text{att}}$ is the matrix that introduces the noise correlation between the master and slaves antennas, as

$$\mathbf{D}_{\text{att}} = \begin{bmatrix} \mathbf{I}_N + \mathbf{1}_{N,N} \end{bmatrix} . \tag{3.23}$$

Also, unlike the stochastic model for RTK positioning in (2.10), additional noise terms due to atmospheric residuals as not required, since the distance between the antennas is minimal.

Another relevant note is that, while the attitude parametrization does not play a role in the correct expression for the attitude model, it takes an important role when it comes to its estimation, as it will be discussed next. In the sequel, the estimation problem for the carrier phase-based attitude models is discussed.

## 3.3 Estimation of GNSS-based Attitude Models

As it occurs with carrier phase-based positioning, the use of these kind of observations for determining attitude information requires solving a mixture of integer and real parameters. In addition, when dealing with the attitude model given in Def. 4, the list of unknowns includes parameters belonging to a manifold. In the following, it is described the ML estimation processes associated with the determination of both, the multi-baseline and the attitude mixed models. Thus, the minimization problem associated with the MLE for the multi-baseline mixed model is given by

$$\begin{bmatrix} \check{\bar{\mathbf{a}}} \\ \check{\bar{\mathbf{b}}} \end{bmatrix} = \arg \min_{\left(\bar{\mathbf{a}},\bar{\mathbf{b}}\right) \in \mathbb{Z}^{nN} \times \mathbb{R}^{3N}} \left\| \mathbf{y} - (\mathbf{I}_N \otimes \mathbf{A})\bar{\mathbf{a}} - (\mathbf{I}_N \otimes \mathbf{B})\bar{\mathbf{b}} \right\|_{\mathbf{\Sigma}}^2 , \tag{3.24}$$

where the unknown parameters have been expressed in vector form such that

$$\bar{\mathbf{a}} = \mathsf{vec}(\mathbf{Z}), \; \bar{\mathbf{b}} = \mathsf{vec}(\mathbf{L}) = \begin{bmatrix} {}_{\mathcal{G}}\mathbf{b}_{1,m} \\ \vdots \\ {}_{\mathcal{G}}\mathbf{b}_{N,m} \end{bmatrix} . \tag{3.25}$$

One quickly realizes the strong similarities between the optimization problems for the conventional mixed model and the multi-baseline mixed model. Indeed, the estimation procedure follows exactly as described in Section 2.2, including the three step decomposition. Thus, the estimation 'simplicity' for the multi-baseline mixed model makes it quite appealing, its use for attitude estimation is still not ideal for two reasons: *i)* the a priori knowledge on the inter-antenna distance and relative orientation is not exploited, leading to a suboptimal solution; *ii)* orientation information is not directly observed and still a posterior estimation of the Wahba's problem is required.

The first steps towards improving the multi-baseline mixed model for better orientation estimations were regarded by the Constrained-LAMBDA (C-LAMBDA) [118], [129], [130]. C-LAMBDA modifies (3.24) by adding a set of constraints on the norm of baselines, which shall correspond to the surveyed baseline lengths in the body frame. Thus, C-LAMBDA expresses the multi-baseline optimization problem as

$$\begin{aligned} \begin{bmatrix} \check{\bar{\mathbf{a}}} \\ \check{\bar{\mathbf{b}}} \end{bmatrix} = \arg & \min_{\left(\bar{\mathbf{a}},\bar{\mathbf{b}}\right) \in \mathbb{Z}^{nN} \times \mathbb{R}^{3N}} \left\| \mathbf{y} - (\mathbf{I}_N \otimes \mathbf{A})\bar{\mathbf{a}} - (\mathbf{I}_N \otimes \mathbf{B})\bar{\mathbf{b}} \right\|_{\mathbf{\Sigma}}^2 , \\ & \text{subject to} \quad \|{}_{\mathcal{G}}\mathbf{b}_{1,m}\| = \|{}_{\mathcal{B}}\mathbf{b}_{1,m}\| \\ & \qquad\qquad\quad \vdots \\ & \qquad\qquad\quad \|{}_{\mathcal{G}}\mathbf{b}_{N,m}\| = \|{}_{\mathcal{B}}\mathbf{b}_{N,m}\| \end{aligned} \tag{3.26}$$

whose resolution, once again, involves a three decomposition given by

$$\begin{gathered} \min_{\left(\bar{\mathbf{a}},\bar{\mathbf{b}}\right) \in \mathbb{Z}^{nN} \times \mathbb{R}^{3N}} \left\| \mathbf{y} - (\mathbf{I}_N \otimes \mathbf{A})\bar{\mathbf{a}} - (\mathbf{I}_N \otimes \mathbf{B})\bar{\mathbf{b}} \right\|_{\mathbf{\Sigma}}^2 , \; \text{s.t. } \|{}_{\mathcal{G}}\mathbf{b}_{j,m}\| = \|{}_{\mathcal{B}}\mathbf{b}_{j,m}\|, \forall j = 1, \ldots, N \rightarrow \\ \|\hat{\mathbf{e}}\|_{\mathbf{\Sigma}}^2 + \min_{\bar{\mathbf{a}} \in \mathbb{Z}^{nN}} \left( \left\| \hat{\bar{\mathbf{a}}} - \bar{\mathbf{a}} \right\|_{\mathbf{P}_{\hat{\mathbf{a}}\hat{\mathbf{a}}}}^2 + \min_{\bar{\mathbf{b}} \in \mathbb{R}^{3N}, \|{}_{\mathcal{G}}\mathbf{b}_{j,m}\| = \|{}_{\mathcal{B}}\mathbf{b}_{j,m}\|} \left\| \hat{\bar{\mathbf{b}}}(\bar{\mathbf{a}}) - \bar{\mathbf{b}} \right\|_{\mathbf{P}_{\hat{\mathbf{b}}|\mathbf{a}}}^2 \right) , \end{gathered} \tag{3.27}$$

where $\hat{\mathbf{e}}$ are the residuals over the float estimates, $\hat{\bar{\mathbf{b}}}$, $\hat{\bar{\mathbf{a}}}$, which are estimated from an unconstrained LS in the space of real numbers. Then, (3.27) couples the IAR process with the (constrained) fixed solution estimation. Thus, instead of estimating the optimal MLE for the integer problem, a set of integer solutions are computed and then these are used for solving the constrained optimization which regards the estimation for the fixed multi-baseline solution. Then, the integer vector that produces the minimal amount of weighted squared residuals over (3.27) is kept.

While C-LAMBDA has been shown to improve the original unconstrained multi-baseline mixed problem in (3.24), it still does not fully utilizes the a priori knowledge on the multi-antenna configuration, with the information on relative orientation being disregarded. Indeed, only the attitude mixed model allows for fully incorporating the information on the antenna configuration. When expressing the estimation problem for the attitude mixed model, the parametrization for the orientation does play a role and defines how one might approach its resolution. For instance, the minimization problem for (3.19) based on the rotation matrix reads

$$\left(\check{\mathbf{Z}}, \check{\mathbf{R}}\right) = \arg \min_{(\mathbf{Z},\mathbf{R}) \in \mathbb{Z}^{n,N} \times SO(3)} \|\mathsf{vec}\,(\mathbf{Y} - \mathbf{AZ} - \mathbf{BRF})\|^2_{\mathbf{\Sigma}}\,, \tag{3.28}$$

with $\mathbf{F}$ the matrix containing the inter-antenna baseline vectors expressed in the body frame as

$$\mathbf{F} = \left[{}_{\mathcal{B}}\mathbf{b}_{1,m}, \ldots, {}_{\mathcal{B}}\mathbf{b}_{N,m}\right]. \tag{3.29}$$

Note that the optimization problem in (3.28) results of a complexity superior to that of (3.24), since one shall deal with integer-valued parameters along with the estimation of a matrix which belongs to the special orthonormal group. In his series of works [119], [131]–[133], Teunissen and Giorgi address this problem with the proposal of the Multivariate Constrained-LAMBDA (MC-LAMBDA). MC-LAMBDA also employs the well-known three step decomposition, given in this case by

$$\begin{aligned}
&\min_{\mathbf{Z}\in\mathbb{Z}^{n,N},\mathbf{R}\in SO(3)} \|\mathsf{vec}\,(\mathbf{Y} - \mathbf{AZ} - \mathbf{BRF})\|^2_{\mathbf{\Sigma}} = \\
&\|\hat{\mathbf{e}}\|^2_{\mathbf{\Sigma}} + \min_{\mathbf{Z}\in\mathbb{Z}^{n,N}} \left( \left\|\mathsf{vec}\left(\hat{\mathbf{Z}} - \mathbf{Z}\right)\right\|^2_{\mathbf{P}_{\hat{\mathbf{Z}}\hat{\mathbf{Z}}}} + \min_{\mathbf{R}\in SO(3)} \left\|\mathsf{vec}\left(\hat{\mathbf{R}}(\mathbf{Z}) - \mathbf{R}\right)\right\|^2_{\mathbf{P}_{\hat{\mathbf{R}}(\mathbf{Z})\hat{\mathbf{R}}(\mathbf{Z})}} \right)\,,
\end{aligned} \tag{3.30}$$

where $\|\hat{\mathbf{e}}\|$ is the LS residuals over the float estimates, $\hat{\mathbf{Z}}$, $\hat{\mathbf{R}}$, which are expressed in the space of the real numbers.

The resolution of the procedure in (3.30) is similar to C-LAMBDA, in the sense that all constraints (both related to the integer nature of the ambiguities or the orthonormal properties for the rotation matrix) are disregarded during the float estimation and, then, a single cost function is evaluated for the estimation of the integer ambiguities and the fixed attitude estimation. Notice that the fixed solution is equivalent to the weighted orthogonal Procrustes problem (OPP)[2], which consists on finding the matrix that fits best to the orthonormality constraints.

While MC-LAMBDA is undoubtedly the most prominent estimator for GNSS-based attitude models, a series of factors limit their implementation: *i)* the rotation matrix is an inefficient way to encode rotations, which involve a loss of redundancy during the float estimation and a posterior complex procedure for solving the OPP in order to incorporate the constraints; *ii)* solving MC-LAMBDA results computationally very demanding, with the OPP being a complex algorithm by itself and it is to be repeated for as many time as vector candidates are

---

[2] The Procrustes problem owns his name to the Greek mythological story on a bandit named Procrustes. Procrustes would torture their victims by lying them into an iron bed and forcing them to fit the dimensions of such bed by stretching or cutting their extremidades.

found during the IAR process; *iii)* the estimated rotation does present actual guarantees for optimality, since the IAR no longer constitutes a MLE –i.e., one could end up providing as fixed solution a biased orientation estimate derived from an incorrect integer solution, only because its associated rotation matrix randomly happens to be similar to an orthogonal matrix.

The first contribution of this chapter consists on the formulation of the quaternion-based attitude mixed model and its estimator, as described next.

### 3.3.1 The Quaternion-based Attitude Mixed Model Estimation

As discussed previously, existing estimators for the GNSS-based attitude model result computationally heavy, do not exploit the minimal rotation representation –and, therefore, lose redundancy of observations–, and are subject to provide biased estimates. Moreover, computing rotation matrices makes complicated their recursive formulation and the fusion with other sensors. This section introduces the optimization problem for the quaternion-based attitude model and details an efficient estimator. Thus, one may express the optimization problem for (3.21) as

$$\left(\check{\mathbf{Z}}, \check{\mathbf{q}}\right) = \arg \min_{(\mathbf{Z},\mathbf{q}) \in \mathbb{Z}^{n,N} \times \mathcal{S}^3} \left\|\mathsf{vec}\left(\mathbf{Y} - \mathbf{A}\mathbf{Z} - \mathbf{B}\mathbf{h}(\mathbf{q})\right)\right\|^2_{\boldsymbol{\Sigma}}\,, \tag{3.31}$$

where $\mathbf{h}(\mathbf{q})$ is the rotation operator based on the quaternion parametrization applied to the baseline vectors in the body frame and expressed as

$$\mathbf{h}(\mathbf{q}) = \left[\mathbf{q} \circ {}_{\mathcal{B}}\mathbf{b}_{1,m} \circ \mathbf{q}^*, \ldots, \mathbf{q} \circ {}_{\mathcal{B}}\mathbf{b}_{N,m} \circ \mathbf{q}^*\right]. \tag{3.32}$$

Once again, one leverages on the three-step decomposition of (3.31), such that

$$\begin{aligned}&\min_{\mathbf{Z} \in \mathbb{Z}^{n,N}, \mathbf{q} \in \mathcal{S}^3} \left\|\mathsf{vec}\left(\mathbf{Y} - \mathbf{A}\mathbf{Z} - \mathbf{B}\mathbf{h}(\mathbf{q})\right)\right\|^2_{\boldsymbol{\Sigma}} = \\ &\|\hat{\mathbf{e}}\|^2_{\boldsymbol{\Sigma}} + \min_{\mathbf{Z} \in \mathbb{Z}^{n,N}} \left( \left\|\mathsf{vec}\left(\hat{\mathbf{Z}} - \mathbf{Z}\right)\right\|^2_{\mathbf{P}_{\hat{\mathbf{Z}}\hat{\mathbf{Z}}}} + \min_{\mathbf{q} \in \mathcal{S}^3} \|\hat{\mathbf{q}}(\mathbf{Z}) - \mathbf{q}\|^2_{\mathbf{P}_{\hat{\mathbf{q}}(\mathbf{Z})}} \right).\end{aligned} \tag{3.33}$$

with $\|\hat{\mathbf{e}}\|^2_{\boldsymbol{\Sigma}}$ the norm of residuals over the auxiliary float estimates $\hat{\mathbf{Z}}$, $\hat{\mathbf{q}}$, which can computed via the following minimization

$$\left(\hat{\mathbf{Z}}, \hat{\mathbf{q}}\right) = \arg \min_{\hat{\mathbf{Z}} \in \mathbb{R}^{n,N}, \hat{\mathbf{q}} \in \mathcal{S}^3} \left\|\mathsf{vec}\left(\mathbf{Y} - \mathbf{A}\hat{\mathbf{Z}} - \mathbf{B}\mathbf{h}(\hat{\mathbf{q}})\right)\right\|^2_{\boldsymbol{\Sigma}}. \tag{3.34}$$

Notice that the unit-norm constraint is respected even during the float solution estimation. Doing so required performing an optimization over the manifold $\mathcal{S}^3$ which, luckily, results in an straightforward procedure thanks to the Lie theory and the relationships between the Euclidean space $\mathbb{R}^3$, the algebra $\mathfrak{so}(3)$ and the manifold $\mathcal{S}^3$ described in Section 3.1.3. Nonetheless, one may concern with the fact that Lie theory constitutes a local search on the tangent plane around the current estimate for the quaternion and, therefore, the initialization for the procedure becomes a relevant matter. Thus, the estimation process for (3.34) is as follows

1. Estimation of an initial solution for the quaternion and ambiguities based on the optimization of the multi-baseline mixed model and the posterior Wahba's problem, such that $\hat{\mathbf{q}}^{(0)}, \hat{\mathbf{Z}}^{(0)}$ is given by (3.15) after solving (3.24).

2. For $k = 1, 2, \ldots$, until the convergence criteria is met, the following LS adjustment for the rotation vector is iteratively performed

$$\hat{\boldsymbol{\theta}}^{(k)} = \left(\mathbf{H}^\top \boldsymbol{\Sigma}^{-1} \mathbf{H}\right)^{-1} \mathbf{H}^\top \boldsymbol{\Sigma}^{-1} \left(\mathsf{vec}\left(\mathbf{Y} - \mathbf{A}\hat{\mathbf{Z}}^{(0)} - \mathbf{B}\mathbf{h}(\hat{\mathbf{q}}^{(k-1)})\right)\right) \tag{3.35}$$

with

$$\mathbf{H} = \begin{bmatrix} \mathbf{B}\mathbf{J}_{\hat{\mathbf{q}}^{(k)}}({}_{\mathcal{B}}\mathbf{b}_{1,m}) \\ \vdots \\ \mathbf{B}\mathbf{J}_{\hat{\mathbf{q}}^{(k)}}({}_{\mathcal{B}}\mathbf{b}_{N,m}) \end{bmatrix} \tag{3.36}$$

and $\mathbf{J}_{\mathbf{q}}(\mathbf{u})$ the Jacobian matrix for the rotation of a vector $\mathbf{u}$ about $\mathbf{q}$, as defined in (A.37). Then, in each iteration the quaternion estimate is updated via $\hat{\mathbf{q}}^{(k)} = \hat{\mathbf{q}}^{(k-1)} \circ \mathbf{q}\{\hat{\boldsymbol{\theta}}^{(k)}\}$.

Once the float solution has converged, the IAR process in (3.33) can be solved using the conventional LAMBDA method to obtain $\check{\mathbf{Z}}$. At last, the fixed solution is solved again via LS adjustment and leverage on Lie theory, such that

$$\check{\boldsymbol{\theta}} = \mathbf{P}_{\hat{\boldsymbol{\theta}}\hat{\boldsymbol{\theta}}} \mathbf{P}^{-1}_{\hat{\mathbf{Z}}\hat{\mathbf{Z}}} \left( \text{vec}\left( \hat{\mathbf{Z}} - \check{\mathbf{Z}} \right) \right) , \tag{3.37}$$

$$\check{\mathbf{q}} = \hat{\mathbf{q}} \circ \mathbf{q}\{\check{\boldsymbol{\theta}}\}^* . \tag{3.38}$$

Hereinafter, the estimation procedure described previously will be referred to as quaternion LAMBDA (Q-LAMBDA), since it leverages on the quaternion-parametrized attitude mixed model and applies conventional LAMBDA to resolve the IAR. Using the proposed Q-LAMBDA for the attitude mixed model results advantageous for different reasons: *a)* the solution constitutes the actual MLE for the optimization in (3.31); *b)* the vector of unknowns presents a minimal representation, meaning that fewer elements are to be estimated and, hence, higher data redundancy is available (the total number of non-ambiguity parameters $p = 4$ for the proposed method, $p = 9$ for the MC-LAMBDA and $p = 3N$ for the multi-baseline mixed model); *c)* the computational complexity becomes much lower, since the iterative on-manifold Gauss-Newton described in (3.35) can be efficiently computed and no OPP estimation is realized. Moreover, since the float estimate can be presumed always better than the float solution for the C- and MC-LAMBDA, the search space for the IAR process will become smaller.

## 3.4 Recursive Formulation for the Attitude Mixed Model

Following the same methodology than the carrier phase-based positioning problem in Section 2.2.1, this subsection provides a formulation for the GNSS-based attitude model, expressed in terms of unit quaternion parametrization. Thus, let us consider the discrete SSM described at time $t$ by

$$\mathbf{x}_t = \begin{bmatrix} \mathbf{a}_t \\ \mathbf{q}_t \\ \mathbf{b}_{\omega,t} \end{bmatrix} , \text{ with } (\mathbf{a}_t, \mathbf{q}_t, \mathbf{b}_{\omega,t}) \in \mathbb{Z}^{nN} \times \mathcal{S}^3 \times \mathbb{R}^3 , \tag{3.39}$$

where $\mathbf{b}_\omega$ denotes the gyroscope biases and $\mathbf{a}$ refers to the complete vector of ambiguities $\mathbf{a} = \text{vec}(\mathbf{Z})$ to simplify the notation. Let us recall the process model in (2.25) and particularize it for the SSM in dispute, such that

$$\mathbf{x}_t = \mathbf{f}\left(\mathbf{x}_{t-1}, \boldsymbol{\omega}_t, \mathbf{w}_t\right) ,$$

where $\boldsymbol{\omega}_t$ is the vector of angular rates, as observed by a gyroscope, and $\mathbf{w}_t$ comprises the white normal process noise vector –in this case, composed by the noise of the gyroscope, the random walk for the biases and the random walk for the ambiguities $\mathbf{Q}_t = \text{diag}(\sigma_a^2 \mathbf{I}_{nN}, \sigma_\omega^2 \mathbf{I}_3, \sigma_{b\omega}^2 \mathbf{I}_3)$–. Taking aside the white noises, the process model is given by

$$\mathbf{f}(\mathbf{x}_{t-1}, \boldsymbol{\omega}_t) = \begin{cases} \mathbf{a}_{t-1} \\ \mathbf{q}_{t-1} \circ \mathbf{q}\{(\boldsymbol{\omega}_t - \mathbf{b}_{\omega,t-1})\Delta t\} \\ \mathbf{b}_{\omega,t-1} \end{cases} , \tag{3.40}$$

where the biases and ambiguities evolve as random processes and the kinematics of the quaternion are given by the integration of the measured angular rate compensating for the estimated gyro biases. Similarly, the observation model is denoted with

$$\mathbf{y}_t = \mathbf{h}(\mathbf{x}_t) + \boldsymbol{\nu}_t, \tag{3.41}$$

with $\mathbf{y}_t$ and $\mathbf{h}(\cdot)$ described from (3.21).

For nonlinear models, such as the one concerning the quaternion-based attitude mixed model, time recursion is generally addressed with any of the nonlinear extensions of the KF, with this thesis focusing solely on the EKF. Recursive attitude estimation shall also consider and respect the inherent non-linear geometric constraints (i.e., the unit norm constraint for the quaternion). This thesis approaches this problem based on the Error State KF (ESKF) –also known as Indirect KF and Multiplicative KF– [109], [134], for which the state estimate $\mathbf{x}$ belongs to a manifold and its perturbations $\delta\mathbf{x}$ "live" in the tangent space of that manifold. Thus, the basic *rationale* behind the ESKF is to consider the nominal-state as the conventional state of a KF (whose process and observation models may be applied with the original nonlinear functions) and the error-state as a small-signal gathering the noises and perturbances of the system. During the prediction step, the nominal state integrates noisy inertial data and, therefore, accumulating errors. These errors are collected within the error-state which incorporates the system noises and perturbations. Since the error-state is conformed by small magnitudes, its evolution function can be expressed as a linear dynamic system. Thus, during the prediction step, the ESKF predicts a Gaussian estimate of the error-state. Then, upon the reception of GNSS data and the realization of the correction step, the filter estimates the errors observable. This correction provides a posterior Gaussian estimate of the error-state which is then injected to the nominal-state and then reset to zero.

In our case, the unknown true state is formulated as the composition of the nominal estimate $\mathbf{x}$ and the error state $\delta\mathbf{x}_t$, noted $\mathbf{x} = \hat{\mathbf{x}} \oplus \delta\mathbf{x}$, with the error state given by

$$\delta\mathbf{x}_t = \begin{bmatrix} \delta\mathbf{a}_t \\ \delta\boldsymbol{\theta}_t \\ \mathbf{b}_{\omega,t} \end{bmatrix}, \text{ with } (\delta\mathbf{a}_t, \delta\boldsymbol{\theta}_t, \delta\mathbf{b}_{\omega,t}) \in \mathbb{Z}^{nN} \times \mathbb{R}^3 \times \mathbb{R}^3, \tag{3.42}$$

where $\delta\boldsymbol{\theta}_t$ describes a rotation vector for the attitude errors. Following the exponential mapping presented in (3.9), the afore-mentioned composition of nominal and error state is as follows

$$\mathbf{x} = \hat{\mathbf{x}} \oplus \delta\mathbf{x} = \left\{ \begin{array}{ccc} \hat{\mathbf{a}}_t & + & \delta\mathbf{a}_t \\ \hat{\mathbf{q}}_t & \circ & \mathbf{q}\{\delta\boldsymbol{\theta}_t\} \\ \hat{\mathbf{b}}_{\omega,t} & + & \delta\mathbf{b}_{\omega,t} \end{array} \right. . \tag{3.43}$$

Thus, the ESKF adapts the EKF framework to a chosen non-linear parametrization, here given by (3.43) to preserve the unit-norm quaternion constraint, while using a minimal parametrization of the covariance matrix (i.e., the covariance matrix $\mathbf{P}_t \in \mathbb{R}^{P,^P}$, with $P = nN + 3 + 3$). That is, it uses the $\oplus$ operator, instead of the standard addition, to linearize and update the system. Then the propagation and update steps of the ESKF are given by

$$\hat{\mathbf{x}}_{t|t-1} = \mathbf{f}(\hat{\mathbf{x}}_{t-1|t-1}, \boldsymbol{\omega}_t)\ , \tag{3.44a}$$

$$\mathbf{P}_{t|t-1} = \mathbf{F}_t \mathbf{P}_{t-1|t-1} \mathbf{F}_t^\top + \mathbf{F}_{q,t} \mathbf{Q}_t \mathbf{F}_{q,t}^\top\ , \tag{3.44b}$$

$$\mathbf{K}_t = \mathbf{P}_{t|t-1} \mathbf{H}_t^\top \left( \mathbf{H}_t \mathbf{P}_{t|t-1} \mathbf{H}_t^\top + \boldsymbol{\Sigma}_t \right)^{-1}\ , \tag{3.44c}$$

$$\hat{\mathbf{x}}_{t|t} = \hat{\mathbf{x}}_{t|t-1} \oplus \mathbf{K}_t \left( \mathbf{y}_t - \mathbf{h}(\hat{\mathbf{x}}_{t|t-1}) \right)\ , \tag{3.44d}$$

$$\mathbf{P}_{t|t} = \mathbf{P}_{t|t-1} - \mathbf{K}_t \mathbf{H}_t \mathbf{P}_{t|t-1}\ . \tag{3.44e}$$

The matrices $\mathbf{F}_{k-1}, \mathbf{H}_t$ are the Jacobians of the process and observation models with respect to the composition of nominal and error states. Applying the chain rule, the Jacobian matrices as expressed as

$$\mathbf{F}_t = \left.\frac{\partial \mathbf{f}(\mathbf{x} \oplus \delta\mathbf{x}, \boldsymbol{\omega}_t)}{\partial \delta\mathbf{x}}\right|_{\hat{\mathbf{x}}_{t-1|t-1}, \boldsymbol{\omega}_t} = \left.\frac{\partial \mathbf{f}}{\partial \mathbf{x}}\right|_{\hat{\mathbf{x}}_{t|t-1}, \boldsymbol{\omega}_t} \left.\frac{\partial \mathbf{x} \oplus \delta\mathbf{x}}{\partial \delta\mathbf{x}}\right|_{\hat{\mathbf{x}}_{t-1|t-1}} \tag{3.45}$$

$$\mathbf{H}_t = \left.\frac{\partial \mathbf{h}(\mathbf{x} \oplus \delta\mathbf{x})}{\partial \delta\mathbf{x}}\right|_{\hat{\mathbf{x}}_{t|t-1}} = \left.\frac{\partial \mathbf{h}}{\partial \mathbf{x}}\right|_{\hat{\mathbf{x}}_{t|t-1}} \left.\frac{\partial \mathbf{x} \oplus \delta\mathbf{x}}{\partial \delta\mathbf{x}}\right|_{\hat{\mathbf{x}}_{t|t-1}}, \tag{3.46}$$

leading to the following Jacobians for the process model:

$$\mathbf{F}_t = \begin{bmatrix} \mathbf{I}_{nN} & \mathbf{0} & \mathbf{0} \\ \mathbf{0} & \mathbf{R}\{\delta\mathbf{q}\}^\top & -\Delta t \mathbf{I}_3 \\ \mathbf{0} & \mathbf{0} & \mathbf{I}_3 \end{bmatrix}, \qquad \mathbf{F}_{q,t} = \begin{bmatrix} \Delta t \mathbf{I}_{nN} & \mathbf{0} & \mathbf{0} \\ \mathbf{0} & \Delta t \mathbf{I}_3 & \mathbf{0} \\ \mathbf{0} & \mathbf{0} & \Delta t \mathbf{I}_3 \end{bmatrix}, \tag{3.47}$$

where $\delta\mathbf{q} = \mathbf{q}\{(\boldsymbol{\omega}_t - \mathbf{b}_{\omega,t-1})\Delta t\}$ is the unit quaternion related to the attitude change measured that time $t$. The Jacobian matrix for the observation model is given by

$$\mathbf{H}_t = \mathbf{H}_{\mathbf{x}} \mathbf{H}_{\delta\mathbf{x}}, \tag{3.48}$$

where $\mathbf{H}_{\mathbf{x}}$ and $\mathbf{H}_{\delta\mathbf{x}}$ correspond to the first and second term in (3.46), respectively, expressed as follows

$$\mathbf{H}_{\mathbf{x}} = \begin{bmatrix} \mathbf{I}_N \otimes \mathbf{A} & \mathbf{H}_{\mathbf{q}_{t|t-1}} & \mathbf{0}_{2nN,3} \end{bmatrix}, \text{ with } \mathbf{H}_{\mathbf{q}_{t|t-1}} = \begin{bmatrix} \mathbf{B}\mathbf{J}_{\mathbf{q}_{t|t-1}}({}_{\mathcal{B}}\mathbf{b}_{1,m}) \\ \vdots \\ \mathbf{B}\mathbf{J}_{\mathbf{q}_{t|t-1}}({}_{\mathcal{B}}\mathbf{b}_{N,m}) \end{bmatrix} \tag{3.49}$$

and $\mathbf{H}_{\delta\mathbf{x}}$ defined as

$$\mathbf{H}_{\delta\mathbf{x}} = \begin{bmatrix} \mathbf{I}_{nN} & \mathbf{0} & \mathbf{0} \\ \mathbf{0} & \mathbf{H}_{\delta\boldsymbol{\theta}} & \mathbf{0} \\ \mathbf{0} & \mathbf{0} & \mathbf{I}_3 \end{bmatrix}, \text{ with } \mathbf{H}_{\delta\boldsymbol{\theta}} = \frac{1}{2}[\mathbf{q}]_L \begin{bmatrix} 0 & 0 & 0 \\ 1 & 0 & 0 \\ 0 & 1 & 0 \\ 0 & 0 & 1 \end{bmatrix} \tag{3.50}$$

where $[\mathbf{q}]_L$ is the left quaternion product matrix defined in (C.16).

Making use of the LS-KF equivalence discussed in Section 2.2.1, recall that the corrected estimate $\mathbf{x}_{t|t}$ does correspond to the float estimate (i.e., $\mathbf{x}_{t|t} = \hat{\mathbf{x}}_t$) and, therefore, the overall procedure still requires the real-to-integer mapping and the posterior fixed solution estimation. Then, the IAR estimation corresponds, as for the deterministic estimator, to the conventional ILS and may be solved via LAMBDA. At last, the fixed solution estimated does still require making use of the Lie algebra properties. Focusing on the non-ambiguity terms –denoted with $\delta\mathbf{b}_t$–,

$$\delta\mathbf{x}_t^\top = [\delta\mathbf{a}_k^\top, \underbrace{\delta\boldsymbol{\theta}_t^\top, \delta\mathbf{b}_{\omega,t}^\top}_{\delta\mathbf{b}_t^\top}], \ \mathbf{P}_t = \begin{bmatrix} \mathbf{P}_{\mathbf{aa}} & \mathbf{P}_{\mathbf{a}\boldsymbol{\theta}} & \mathbf{P}_{\mathbf{a}\mathbf{b}_\omega} \\ \mathbf{P}_{\mathbf{a}\boldsymbol{\theta}}^\top & \mathbf{P}_{\boldsymbol{\theta}\boldsymbol{\theta}} & \mathbf{P}_{\boldsymbol{\theta}\mathbf{b}_\omega} \\ \mathbf{P}_{\mathbf{a}\mathbf{b}_\omega}^\top & \mathbf{P}_{\boldsymbol{\theta}\mathbf{b}_\omega}^\top & \mathbf{P}_{\mathbf{b}_\omega\mathbf{b}_\omega} \end{bmatrix}, \ \mathbf{P}_t = \begin{bmatrix} \mathbf{P}_{\mathbf{aa}} & \mathbf{P}_{\mathbf{ab}} \\ \mathbf{P}_{\mathbf{ab}}^\top & \mathbf{P}_{\mathbf{bb}} \end{bmatrix}, \tag{3.51}$$

then, the error state for these parameters is given by

$$\delta\check{\mathbf{b}}_t^\top = \begin{bmatrix} \delta\check{\boldsymbol{\theta}}_t^\top \\ \delta\check{\mathbf{b}}_{\omega,t}^\top \end{bmatrix} = \mathbf{P}_{\mathbf{bb}_t} \mathbf{P}_{\mathbf{aa}_t}^{-1} (\check{\mathbf{a}}_t - \hat{\mathbf{a}}_t), \tag{3.52}$$

which leads to the final fixed solution with the composition operator $\ominus$, as

$$\check{\mathbf{q}}_t = \hat{\mathbf{q}}_t \circ \mathbf{q}\{\delta\check{\boldsymbol{\theta}}_t\}^*, \tag{3.53}$$

$$\check{\mathbf{b}}_{\omega,t} = \hat{\mathbf{b}}_{\omega,t} - \delta\check{\mathbf{b}}_{\omega,t}. \tag{3.54}$$

## 3.5 Expected Accuracy for Attitude Models

The derivation of lower and upper estimation bounds result a key factor when addressing a particular application, allowing to characterize the feasibility of a problem, i.e., what can we expect when solving such problem? Moreover, estimation bounds serve as benchmark for estimators, so that one may discern between estimators which perform better than others in certain conditions. For instance, an estimator for a particular problem may result efficient and attain the associated lower bound under asymptotic conditions (i.e., when the noise level is low or there is a large number of observations), while a second estimator may not be optimal and still perform better than the first estimator when working with high noise levels or with finite number of observations. A clear example of the former is showcased for carrier phase-based positioning in Section 2.5.1, based on the difference between an estimator for PAR and the MLE for the mixed model.

Thus, the derivation of estimation bounds for the attitude mixed model results fundamental to understand the ultimate performance for an attitude determination problem, while serving as "test" to distinguish whether estimators such as LAMBDA and C-LAMBDA (for the multi-baseline mixed model followed by the Wahba's problem), or MC-LAMBDA and the quaternion-based estimator (for the attitude mixed model) are or not optimal and under which conditions. Unfortunately, the derivation for estimation bounds for models which gather real, integer and on-manifold parameters is not trivial and, indeed, such a bound remains unknown. The aim for this Section is to point out at possible directions which one may follow when pursuing the quest for derivation an estimation bound for carrier phase-based attitude models.

Thus, such bound could leverage on two other well-known bounds: *i)* the CRB for a mixture of integer- and real-valued parameters, introduced in [4] and extensively discussed in Chapter 2; *ii)* the Intrinsic CRB, introduced in [135], [136], for parameters that belong to a smooth (Riemannian) manifold. One of the primary ideas derived from the intrinsic CRB is that a particular parametrization of the manifold does not infer on the information that the model carries. In our words and translated to our problem, the parametrization of the attitude (rotation matrices, quaternions, Rodrigues parameters, etc.) does not play a role on the derivation of a bound for an estimation problem where the rotation group appears. The former statement aligns with the definition for the attitude mixed model in (3.21), while still leaves the door open to the discussion on whether the attitude parametrization does or not affect an estimator. Unfortunately, to answer to the former question, the derivation for a bound for the attitude mixed model and the assessment of the efficiency for estimators that solve the carrier phase-based attitude models escape the scope and extension of this thesis.

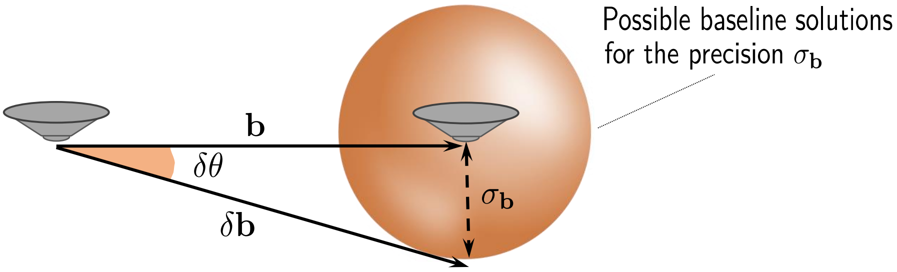

**Figure 3.5:** Coarse prediction for attitude estimates conditioned on the precision of estimated baseline vectors.

Nonetheless, procuring an idea on the expected accuracy for GNSS-based attitude determination remains a valid point. A simplistic and yet effective manner to coarsely describe the precise of attitude estimates leverages on geometric relationships. Let us assume a single baseline of length $\|\mathbf{b}\|$ and express the attitude errors $\delta\theta$ in terms of the precision for the baseline vector $\sigma_{\mathbf{b}}$, as illustrated in Fig. 3.6. For this simple two-dimensional attitude estimation problem, one may express the largest attitude error (i.e., whenever the baseline error is perpendicular to the original baseline) as

$$\sin(\delta\theta) = \frac{\sigma_{\mathbf{b}}}{\|\delta\mathbf{b}\|} = \frac{\sigma_{\mathbf{b}}}{\sqrt{\|\mathbf{b}\| + \|\delta\mathbf{b}\|}}, \tag{3.55}$$

and, considering the error in the estimated baseline is considerably small than its actual length (such that $\|\mathbf{b}\| + \|\delta\mathbf{b}\| \approx \|\mathbf{b}\|$) and under the small angle assumption (i.e., $\sin(\delta\theta) \approx \delta\theta$), leads to the following description on the attitude precision:

$$\sigma_\theta \approx \frac{\sigma_{\mathbf{b}}}{\|\mathbf{b}\|} . \tag{3.56}$$

Now, one may connect the aforementioned precision for the baseline vector with the precision obtained with different code- and carrier phase-based positioning systems. For instance, when performing differential localization for two antennas based on code observations one could expect baseline vector precision on the meter level, with carrier phase-based techniques would improve such precision by two orders of magnitude. Fig. 3.6 showcases the coarse precision for attitude estimates, considering that the individual positions of the antennas were estimated using SPP, PPP or RTK approaches –which are assumed to provide baseline precisions of one meter, 10 cm and 1 cm, respectively–.

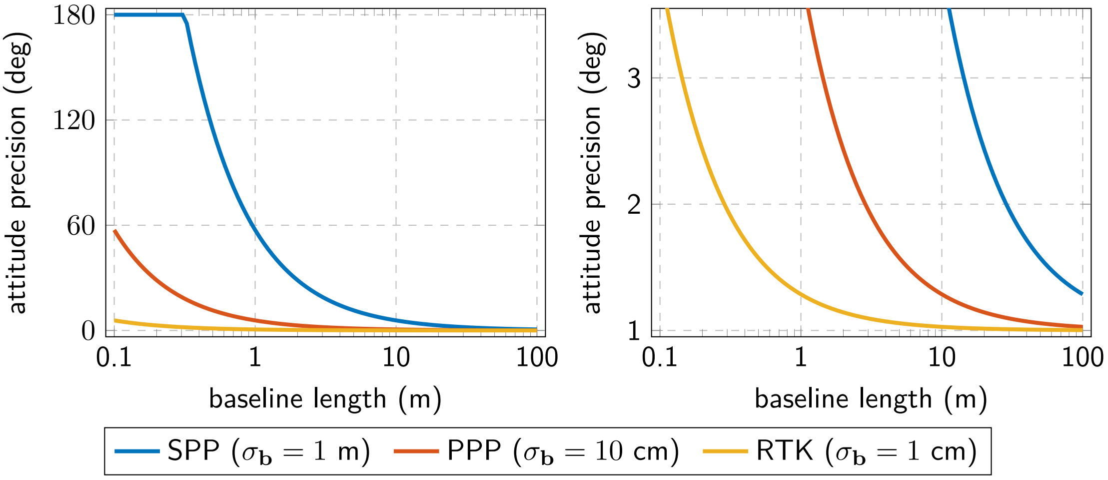

**Figure 3.6:** Geometric approach to address the precision for GNSS-based attitude estimates as function of the baseline length. The vertical axes offers the complete range of precision of the left side, while the right side provides a detail for orientation precision of up to five degrees.

The multi-antenna configuration on board of a platform is limited by the dimensions of the former, meaning that the choice for baseline length is generally not up to the user. Thus, the provision for GNSS-based precise attitude estimates is mostly conditioned on the precision in which the baseline vectors can be estimated. As a result, the use of carrier phase observations and the performance of estimators of the attitude mixed model constitute the key towards obtaining sub-degree precision for attitude solutions.

## 3.6 Performance Characterization for GNSS-based Attitude Estimators

This section assesses the performance of estimators for attitude models based on carrier phase observations, both for deterministic (memoryless) and recursive (via Kalman filtering) estimation. Thus, the experimentation consists on two parts: first, a Monte Carlo simulation serves to illustrate the comparison between the two attitude models (i.e., the multi-baseline mixed model in (3.19) and the attitude mixed model in (3.21)) and the performance of related deterministic estimators; second, a real world experimentation showcases the performance for recursive estimates of the attitude problem, highlighting the importance of sensor fusion and inertial integration for ill-posed orientation configurations of antenna arrays (i.e., when the tracked platform features less than three non-coplanar antennas).

### 3.6.1 Simulation Results: Deterministic Estimators of the Attitude Model

As discussed in Sections 3.2, the carrier phase-based attitude model can be expressed in different manners, based on whether the observations are directly related to a vehicle's orientation (as for the Attitude Mixed Model) or to the inter-antenna baseline vectors (as for the Multi-baseline Mixed Model), with the former requiring an additional computational for solving the Wahba's problem in (3.15). Similarly, different estimators are available to solve either of the former two models. This simulation focuses on expressing the differences between the multi-baseline mixed model, solved via LAMBDA, and the attitude mixed model, resolved by Q-LAMBDA.

The performance characterization is realized based on Monte Carlo simulation, for satellites distributed spatially as described in Table 3.2. The platform of assumed to be equipped with three non-coplanar antennas, which is probably of the most common configuration across vehicles on land, air and water scenarios. The focal point for this simulation lays on assessing the performance of attitude models for scenarios with limited satellite coverage, along with the role played by the inter-antenna baseline lengths and the noise level for the ranging observations. Thus, the number of different tested parameter combinations reaches 180 (for six possible number of tracked satellites, ten baseline lengths and three standard deviations for code observations), with $10^4$ Monte Carlo samples performed for each of them. Figures 3.7 to 3.9 depict the fix rates (i.e., the percentage of Monte Carlo runs in which the vector of integer ambiguities are correctly estimated).

**Table 3.2:** Parameters configuration for the Monte Carlo simulation.

| | |
|---|---|
| | **Scenario setup** |
| UTC time | $15/05/2017\ 09:30$ |
| Location | Koblenz, Germany ($50°21'56''$ N, $7°35'55''$ E) |
| Number of antennas | $N = 3$ |
| Frequency | L1 |
| Number of satellites | $n \in \{10, 9, \ldots, 5\}$ |
| | **Simulation parameters** |
| Code noise (cm) | $\sigma_\rho \in \{30, 15, 5\}$ |
| Phase noise (mm) | $\sigma_\Phi = 3$ |
| Baseline length (m) | $\forall j = 1, \ldots, N, \|\mathbf{b}_j\| \in \{0.1, 0.2, \ldots, 100\}$ |
| Monte Carlo samples | $10^4$ |

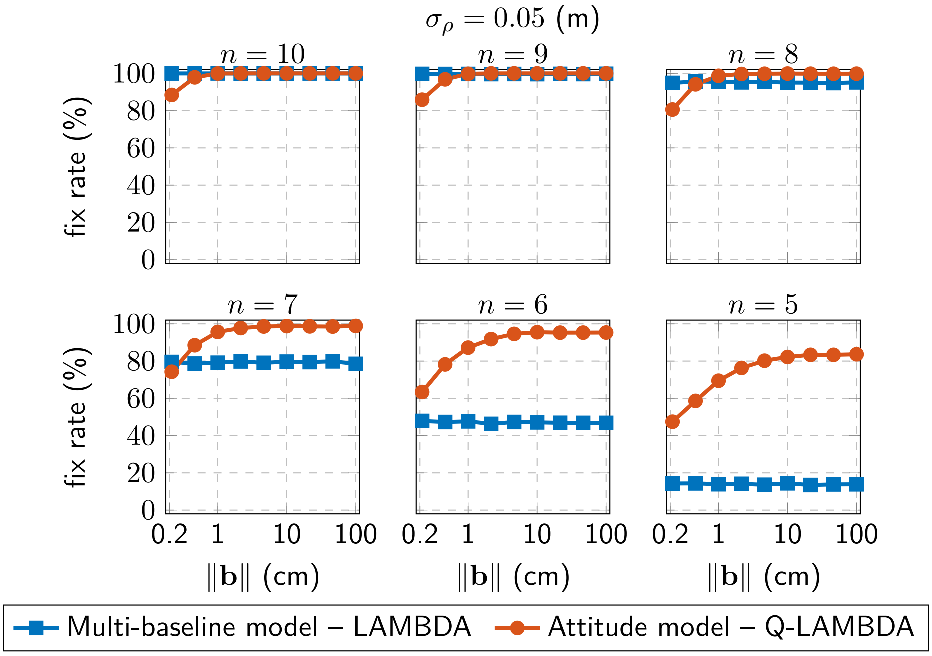

**Figure 3.7:** Fix rate against the baseline length for estimators at the GNSS-based attitude problem. The number of observations employed for each subplot is indicated on its title. The standard deviation for code observations $\sigma_\rho$=5 cm, equivalent to a scenario with high SNR.

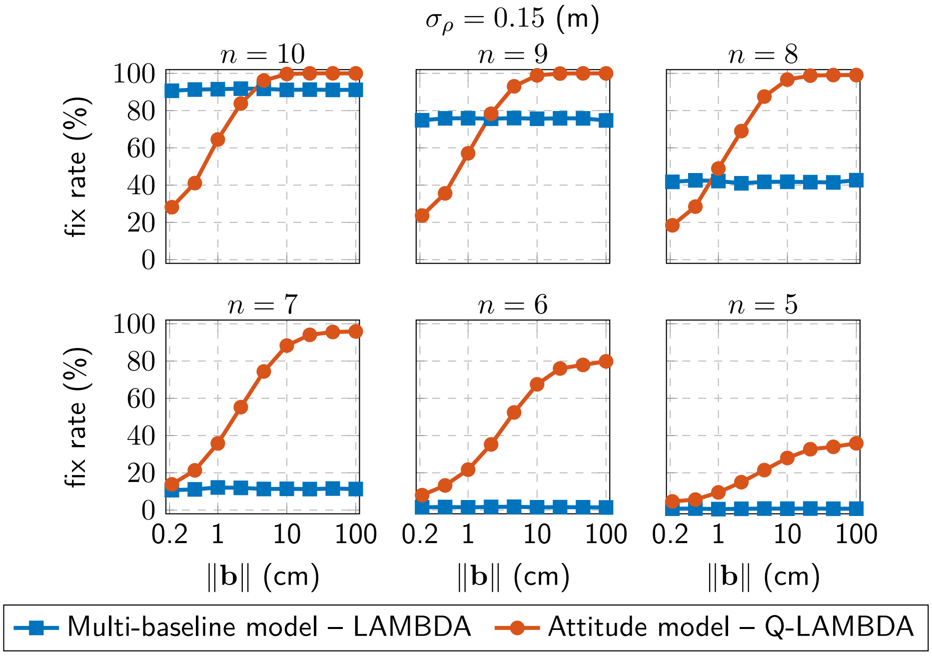

**Figure 3.8:** Fix rate against the baseline length for estimators at the GNSS-based attitude problem. The number of observations employed for each subplot is indicated on its title. The standard deviation for code observations $\sigma_\rho$=15 cm.

Different conclusions can be withdrawn from this simulation:

- The baseline length does not pay any role for the multi-baseline attitude model, since it leads to a linear regression in which only real- and integer-valued parameters are

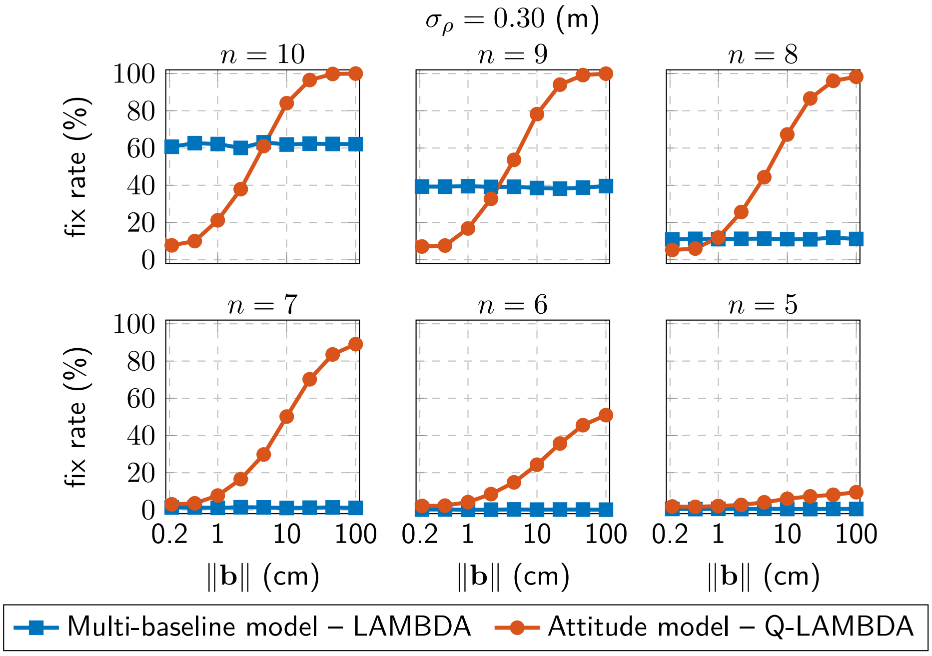

**Figure 3.9:** Fix rate against the baseline length for estimators at the GNSS-based attitude problem. The number of observations employed for each subplot is indicated on its title. The standard deviation for code observations $\sigma_\rho$=30 cm, which may be thought of as a relatively low SNR.

estimated. While the attitude is later resolved by a posterior estimator of the Wahba's problem, the minimization of (3.19) is obviously not affected by it. On the contrary, the performance for the attitude mixed model is strongly influenced by the baseline length, since the noises present on the ranging observations directly affect the optimization in (3.21) and may lead to poor float estimates. As the baseline length increases, the performance of the Q-LAMBDA improves significantly, making the method very attractive for vehicles with medium to large dimensions.

- The multi-baseline attitude model is considerably more sensitive to the 'strength' of the model, with its performance rapidly decaying for both a low number of satellites and high noise. On the other hand, Q-LAMBDA presents a notable fix rate gain with respect to LAMBDA for scenarios with limited satellite availability. This is due to a better exploitation of the data redundancy, since the number of (non ambiguities) parameters with the quaternion-based attitude is four regardless of the number of baselines, while LAMBDA shall estimate a three dimensional vector for each of the baselines.

The general recommendation, in terms of algorithm choice, relates to using Q-LAMBDA for carrier phase-based attitude problems. In comparison to LAMBDA, the performance of the proposed estimator presents a significant gain on the availability of a precise solution, particularly evident for high noise situations, low number of tracked satellites or antenna arrays with more than four elements. The exception to this rule relates to applications where the baseline lengths are lesser than 30 centimeters (for instance, in certain miniaturized aerial vehicles), while platforms of medium to large dimensions (e.g., automobiles, trains or vessels) would greatly benefit from this deterministic method.

### 3.6.2 Attitude Estimation for a Dual Antenna Robotic Platform

This section provides insight into a frequent issue across robotics practitioners, i.e., the need for ground truth attitude information in outdoor scenarios, and illustrates the performance of recursive attitude estimates based on the fusion of inertial and GNSS information, as described in Section . While indoor laboratory setups present high-precision optimal tracking systems, the former are rarely available in outdoor scenarios or are limited to a small experimental area. Rather than providing numerical evaluation or a comparison between methods, this experiment showcases an interesting application for carrier phase-based attitude estimation.

The data collection was performed in the vicinity of Erfoud, in the northern Sahara region on 5th December 2018 (DOY 339, UTC 11:57–12:19) for the SUPER platform[3], illustrated on the left side of Fig. 3.10. Besides the variety of vision systems and an IMU, the SUPER was particularly equipped with a dual GNSS antenna configuration for the purpose of ground truth pose estimation. These two antennas conform a single baseline of 1.28 m length, which limits the orientation observability, leading to the pitch not being observable. The evaluated dataset is a snippet for the more than 30 trajectories recorded in scenarios with different light conditions and terrain typologies. In particular, a zig-zag trajectory of 320 m is performed over a flat area which combines sand and stones at roughly equal parts is studied, as shown on the right side of Fig. 3.10. More details on the Mars-analog data collection and the experimental setup can be consulted in [2].

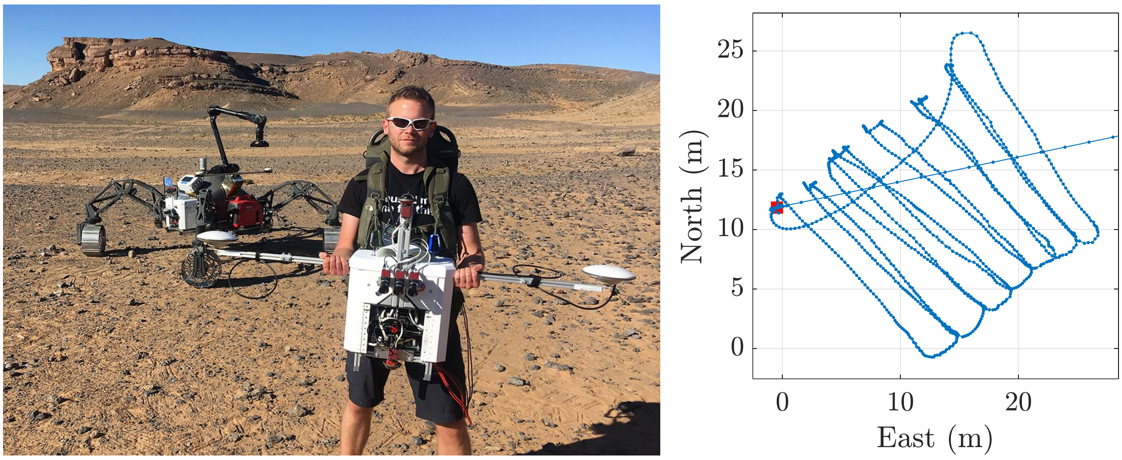

**Figure 3.10:** On the left side, two SUPER modules in the Sahara Desert (the unit on the background is mounted on the SherpaTT rover, while the hand-held unit is carried by a DLR colleague). For the data collection, two GNSS antennas are installed on the sides of SUPER, while the IMU is located directly in the mid-point of the inter-antenna baseline. On the right side, the evaluated zig-zag trajectory.

Fig. 3.11 depicts the time evolution for the estimated Euler angles, with the roll, pitch and yaw corresponding to the top, center and bottom graphs, respectively. The dotted orange line corresponds to the recursive ESKF estimates, which employs solely the GNSS information

---

[3] Planetary rovers strongly rely on vision and inertial systems to perform autonomous navigation and mapping missions. Naturally, testing these systems in their 'natural habit' is not the smartest idea and, instead, data collection of sites analog to the target planet is typically performed. Even in analog sites, the direct experimentation with rovers entails the risk of damaging the robotic platform. The DLR Sensor Unit for Planetary Exploration Rovers (SUPER) constitutes an interesting alternative, consisting on a hand-held human-portable platform that integrates the complete sensor suite for a conventional rover. Thus, data collection for testing VIO or SLAM in planetary analog sites can be performed without the risk of damaging the mechanical parts of the actual rover.

for the two antennas, with is received with an update rate of 1 Hz. The pitch is initialized to zero degrees and, due to the attitude problem resulting ill-posed, its time evolution does not vary. The accuracy of the solution is strongly jeopardized by the lack of observations and the short length of the single baseline, as well as the lack of for a proper time evolution (i.e., the quaternion is assumed to evolve as a random process with a standard deviation of five degrees). Moreover, the low update rate (compared to that of the inertial unit) limits the usability of the solution for subsequent applications requiring orientation guidance. On the other hand, the continuous blue line corresponds to the same ESKF method, with the addition of gyroscope measurements to aid the dynamical process of the attitude estimate. Also, the relationship between the accelerometer readings and the gravity vector serves to provide a more precise initialization for the roll and pitch angles. The resulting sensor fusion-based solution not only presents a much higher update rate (i.e., the inertial unit operates at 100 Hz), capturing the subtle orientation changes occasioned by the movement of the person carrying the SUPER, but also stabilizes the estimates in instances in which GNSS signals present higher noise levels. In summary, the fusion of multi-antenna systems and inertial sensors poses a great synergy, with the GNSS-based providing absolute (and relatively precise) orientation information and gyroscopes allowing for an accurate description of the attitude time evolution.

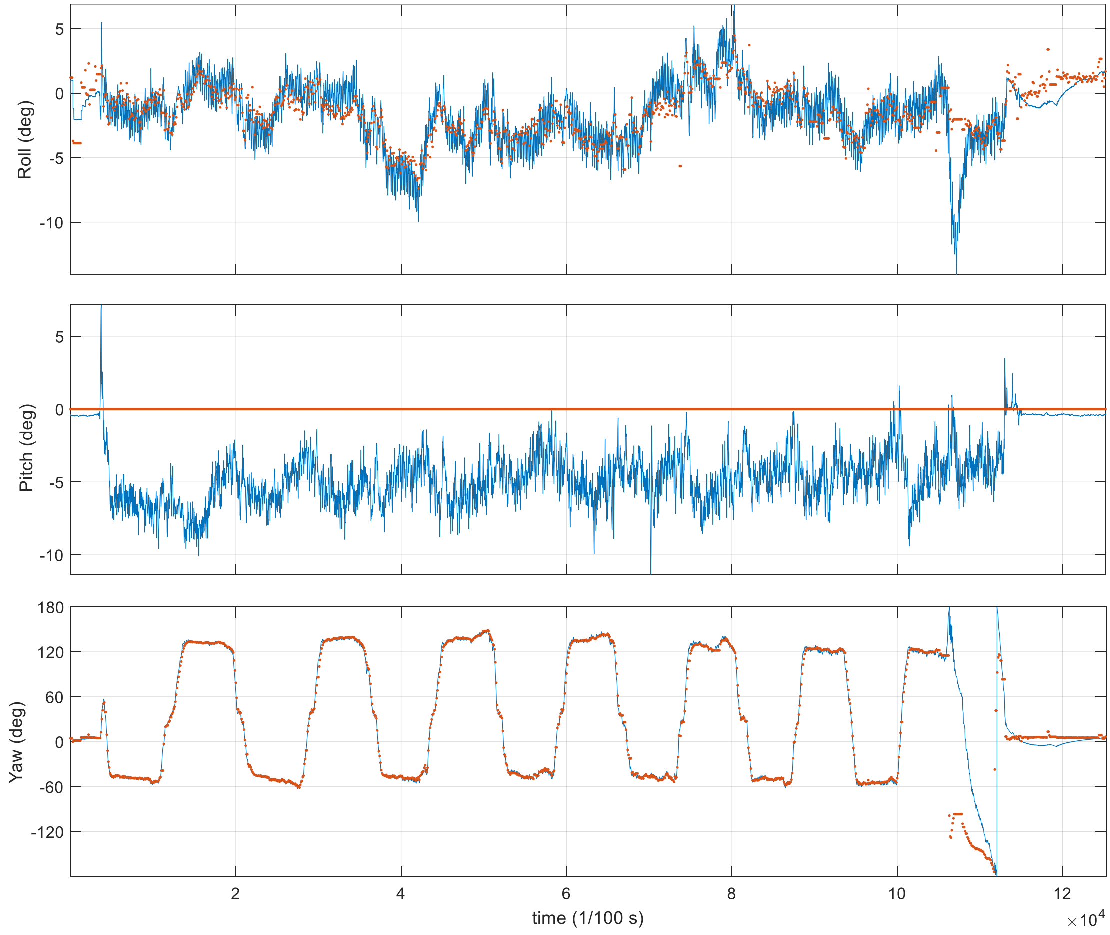

**Figure 3.11:** Time evolution for the attitude estimates, presented in the form of Euler angles, with roll, pitch and yaw solutions depicted on the top, center and bottom graphs. The dotted orange line is computed only from GNSS observations (with the pitch unobservable), while the continuous blue line also incorporates inertial measurements. In both cases, the estimates are based on the ESKF proposed in Section 3.4.

## 3.7 Summary

Undoubtedly, attitude information is a key piece in the navigation puzzle and essential for vehicles requiring orientation guidance. The configuration of multiple antennas on a platform allows for the provision of attitude information and, upon the exploitation of carrier phase observations and the correct estimation of their ambiguities, even sub-degree precision. During its introductory part, this chapter reviews the importance for attitude determination in relation to its primary applications, the challenges associated with the deterministic and recursive attitude estimation and the benefits obtained from using GNSS signals to regress orientation information.

Section 3.1 revisits the myriad options for attitude representation and discusses on the orientation group parametrization based on rotation matrices and quaternions. Special emphasis is put on the latter, discussing their conventions, specifying how this thesis describes them and presenting their dynamics. Also, the trinity of manifold-algebra-Euclidean spaces is discussed, opening the door to some very useful properties in estimators of parameters belonging to a manifold.

Section 3.2 presents the GNSS-based attitude models, namely the multi-baseline mixed model and the attitude mixed model. The first involves an extension of the RTK positioning mixed model, for which the inter-antenna baselines are estimated along with the ambiguities, followed by a posterior estimator to determine the actual attitude information from the relationship between baselines expressed in the local and global frames, respectively. The second directly connects the attitude information with the GNSS observations, which makes the system nonlinear and involves an estimation problem in which the parameters live on the integer and 3D unit-sphere manifold spaces. Then, Section 3.3 reviews the most well-known estimators for both, the multi-baseline mixed and attitude mixed models, such as C-LAMBDA or MC-LAMBDA. Then, the core contribution of this chapter follows, consisting on the proposal of Q-LAMBDA. Q-LAMBDA re-formulates the attitude mixed via quaternion parametrization and leverages on Lie theory to provide a deterministic ML estimation which is both, computationally efficient and maximizes the observation redundancy. Completing the estimation-related topic, Section 3.4 discusses on the recursive formulation of the attitude model. It turns out that certain twists to the conventional Error State/Multiplicative KF may be applied to express Q-LAMBDA as recursive estimator.

Section 3.5 describes the complexity for deriving estimation bounds for the carrier phase-based attitude model. Certain directions for the proposal of bounds at the attitude mixed model are discussed, with their prosecution being arguably the most relevant future line of research for GNSS-based orientation estimation.

At last, Section 3.6 examines the performance of deterministic and recursive estimators at the GNSS-based attitude model. The evaluation consists on a Monte Carlo simulation to address the performance capabilities of the proposed Q-LAMBDA in relation to the multi-baseline attitude model for a variety of scenarios, as well as real data evaluation for an interesting robotic platform with a single baseline configuration. Some closing remarks on the estimators are as follows:

- Q-LAMBDA is a powerful and effective estimator for the carrier phase-based attitude model. Indeed, a significant gain in the fix rate is showcased when compared to conventional LAMBDA estimation. This is achieved by two reasons: *a)* data redundancy is maximized by estimating the minimal number of unknowns; *b)* attitude estimates remain on the manifold during all estimation steps (i.e., the float and fixed estimates shall always constitute a proper rotation). on the negative side, Q-LAMBDA's performance is subject to the separation between antennas, becoming a valuable candidate for platforms which may guarantee at least 30 cm baseline lengths.

- GNSS-based attitude information is a valuable asset for a recurrent problem in robotics, such as the provision of ground truth outdoor information. Since robotic platforms are characterized by their limited dimensions, the configuration of three of more antennas is nearly impossible. Thus, the refinement of filtering solutions to fuse information from GNSS dual antennas, inertial units and vision systems could potentially be the key to bring closer the robotics and radio-navigation research communities.

Contributions to this chapter were partially published in:

**Journal articles:**

[2] Meyer, L., Smíšek, M., Fontan Villacampa, A., Oliva Maza, L., Medina, D., Schuster, M. J., & Triebel, R. (2021). The MADMAX data set for visualinertial rover navigation on Mars. *Journal of Field Robotics.*

**Conference articles:**

[13] Medina, D., Ziebold, R., & García, J. (2020, November). On the Kalman Filter Design for Quaternion-based GNSS-Inertial Attitude Determination. In *2020 European Navigation Conference (ENC)*. IEEE.

[17] Medina, D., Centrone, V., Ziebold, R., & García, J. (2019, September). Attitude Determination via GNSS Carrier Phase and Inertial Aiding. In *Proceedings of the 32nd International Technical Meeting of the Satellite Division of The Institute of Navigation (ION GNSS+ 2019)* (pp. 2964–2979). ION.

CHAPTER 4

# Joint Positioning and Attitude Estimation

ESTIMATING the pose of a rigid body in a three dimensional space combines the positioning and attitude problems, so that the localization and orientation provides the complete static characterization for such rigid body. In addition, the time recursion for pose estimation constitutes the navigation solution for a tracked platform. Along the previous chapters, the value of carrier phase observations for the determination of positioning and attitude estimates has been showcased. Traditionally, GNSS-based localization and orientation are considered as two independent process and, even when integrated within a single filtering solution, the cross-correlation between the observations is disregarded. Nevertheless, this information strengthens the overall observation model and, potentially, comes associated with an improved precision for the estimates and a higher likelihood to correctly resolve the integer ambiguities. This chapter extends the definition of real and on-manifold mixed models to formulate the Joint Positioning and Attitude (JPA) estimation problem. Similarly, the leverage on estimators for the real-, quaternion- and integer-valued parameters allows to propose approximately optimal estimators for the deterministic and recursive forms of JPA. Numerical and experimental evaluations validate the value of JPA with respect to conventional navigation solutions, in which the cross-correlation between positioning- and attitude-related observations is disregarded.

## Outline

Addressing the complete dynamics for a platform implies the estimation of its orientation, velocity and position. Along this thesis, clear arguments in favor of the carrier phase observations use have been exposed, providing precise estimates for both attitude and localization information. It seems evident, the fusion of multi-antenna platforms with base stations communication to comply with the stringent navigational requirements of safety-critical and prospective vehicular applications. While limited to land-based users –or to a lesser extent, low-altitude aerial vehicles and vessels operating in shore sides and inland waterways– which benefit from the differential corrections of a base station, cm- and sub-degree precision for position and orientation solutions can be obtained whenever the integer ambiguities are correctly estimated. Traditionally, the cross-correlations between attitude- and positioning-related observations is neglected during the process of stochastic modeling [137]–[140]. Considering the high complexity for correctly resolving the IAR process, especially in urban scenarios, every dime of information present on the observation models results extremely useful.

Thus, the exploitation for the aforementioned observations' cross-correlations was first posed by Teunissen on his Array-Aided PPP (A-PPP) [141], for which a multi-antenna configuration onboard of a vehicle serves to jointly estimate its positioning and orientation. Since PPP processing requires the estimation of several location-related parameters (i.e., tropospheric wet zenith delays, ionospheric residuals, etc.), the use of an antenna array is not only useful to perform attitude determination, but also to better observe those atmospheric delays common across the antennas. The estimation approach for A-PPP follows that of MC-LAMBDA for attitude determination, consisting on a deterministic estimator for which the IAR and a weighted OPP processes are combined.

The contribution for this chapter formalizes the concept of JPA to perform RTK-like differential positioning and attitude determination, leading to the so-called JPA mixed observation model. As for attitude determination, deterministic and recursive (ESKF-based) estimators are proposed, both of them leveraging on the Lie theory relationships between the $\mathcal{S}^3$ manifold, its algebra and the 3D Euclidean space. Then, a Monte Carlo simulation is employed to characterize the performance of the ESKF for the JPA problem against other filters that deal with attitude- and positioning-related observations in a decoupled manner. Analysis of real data follows, based on a measurement campaign performed for a vessel in an inland waterway scenario. In both cases, the estimator for JPA leads to a significant gain in the availability of the precise positioning solution.

## 4.1 JPA Functional Model

JPA results of the combination of RTK positioning with carrier phase-based attitude determination. Thus, it is assumed that the tracked platform is equipped with multiple GNSS antennas, whose relative location has been accurately surveyed within the local frame, and direct connection to a nearby base station. As in previous chapters, right superscripts and subscripts indicate an observation from a satellite received by an antenna, respectively, while right subscript indicate the frame in which vectors are expressed.

Thus, let us assume that observations from $n+1$ satellites over a particular frequency are simultaneously tracked across a base station, a master antenna and $N$ slave antennas. The center of the body frame (i.e., the reference point whose localization is of interest) is aligned with the position of the master antenna, and the inter-antenna baselines are always expressed with respect to the former. Fig. 4.1 illustrates the elements involved in the JPA model, as well as the global and body/vehicle frames.

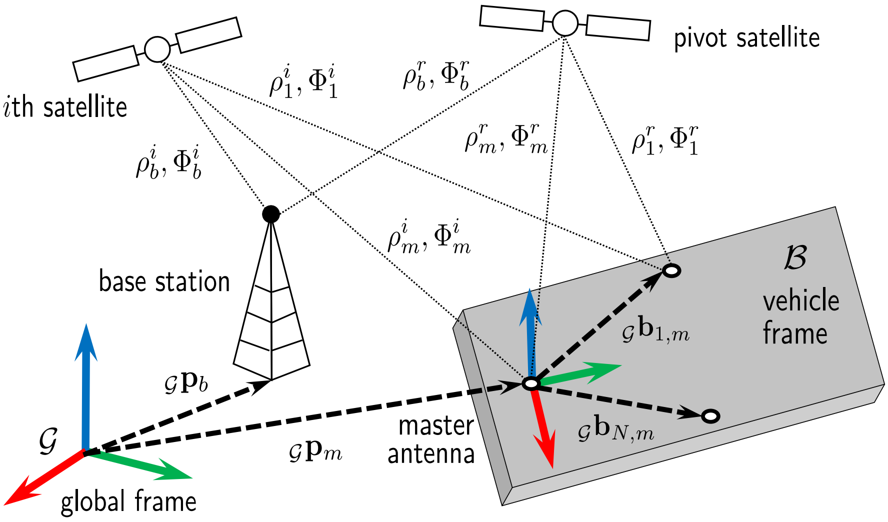

**Figure 4.1:** Illustration for the satellites, base station and multi-antenna configuration involved in the JPA model for a tracked platform.

In line with the carrier phase-based positioning and attitude models, the application of the double-differences combination of observations allows for removing the atmospheric-related delays, receivers and transmitters clock offsets and the errors in the satellite positions. Thus, code and phase measurements across $n$ satellites (all but the reference or pivot) for the base and $N$ slave antennas are double-differenced with respect to the pivot satellite and the master antenna. Let us differentiate between positioning-related (i.e., those DD corresponding to the base station) and orientation-related (i.e., DD performed between the slaves and master antennas) observations, such that

$$\mathbf{y}_{\text{pos}} \triangleq \left[ \left( \mathbf{DD}\boldsymbol{\Phi}_{b,m}^{1:n,r} \right)^\top, \left( \mathbf{DD}\rho_{b,m}^{1:n,r} \right)^\top \right]^\top, \ \mathbf{y}_{\text{pos}} \in \mathbb{R}^{2n}, \tag{4.1}$$

the observations for localization $\mathbf{y}_{\text{pos}}$ coincide with (2.3), and

$$\mathbf{y}_{\text{att}} \triangleq \text{vec}\left(\mathbf{Y}\right), \quad \text{with } \mathbf{Y} = \left[\mathbf{y}_{1,m}, \ldots, \mathbf{y}_{N,m}\right], \ \mathbf{y}_{\text{att}} \in \mathbb{R}^{2nN}, \tag{4.2}$$

such that $\mathbf{y}_{\text{att}}$ corresponds to those in (3.17). Gathering the two types of observations such that $\mathbf{y}^\top = [\mathbf{y}_{\text{pos}}^\top, \mathbf{y}_{\text{att}}^\top]$ or, alternatively in matrix form $\mathbf{Y} = [\mathbf{y}_{\text{pos}}, \mathbf{y}_{1,m}, \ldots, \mathbf{y}_{N,m}]$, the JPA mixed model can be cast as follows.

**Definition 5** (JPA Mixed Model)**.** Let $\mathbf{A}, \mathbf{B}$ be $2n \times (n+p)$ full rank matrices and $\boldsymbol{\Sigma}$ an $M \times M$ symmetric and positive semi-definite matrix. Then, the JPA mixed model can be cast as

$$\mathbf{y} \sim \mathcal{N}\left(\text{vec}\left(\mathbf{AZ} + \mathbf{B}\left[\mathbf{b}, r\left({}_{\mathcal{B}}\mathbf{b}_{1,m}\right), \ldots, r\left({}_{\mathcal{B}}\mathbf{b}_{N,m}\right)\right]\right), \boldsymbol{\Sigma}\right) \ , \tag{4.3}$$

with $p$ the number of non-integer unknowns (three for positioning plus as many as the target attitude parametrization requires), $\mathbf{b} \triangleq {}_{\mathcal{G}}\mathbf{b}_{b,m}$, $\mathbf{b} \in \mathbb{R}^3$ the baseline vector between the base and the platform (i.e., the positioning solution, with ${}_{\mathcal{G}}\mathbf{p}_m = {}_{\mathcal{G}}\mathbf{p}_b - \mathbf{b}$), $\mathbf{Z} \in \mathbb{Z}^{n,N+1}$ the matrix holding the unknown integer ambiguities, and $r(\cdot)$ the operator that supports the body-to-frame rotation. The total number of observations is given by $M = 2n(N+1)$, and the design matrices $\mathbf{A}$ and $\mathbf{B}$ correspond to (2.5).

### 4.1.1 JPA Stochastic Modeling

As described during the introductory part of this chapter, stochastic modeling plays a fundamental role on JPA, making it distinguishable from the independent estimation of positioning and attitude. Since both localization- and attitude-related DD measurements are obtained with respect to the master antenna, cross-correlation between both types of observations becomes apparent. Thus, the covariance matrix $\boldsymbol{\Sigma}$ is expressed as

$$\begin{aligned} \boldsymbol{\Sigma} &= \begin{bmatrix} \boldsymbol{\Sigma}_{\Phi} & \boldsymbol{\Sigma}_{\Phi,\rho} \\ \boldsymbol{\Sigma}_{\Phi,\rho}^{\top} & \boldsymbol{\Sigma}_{\rho} \end{bmatrix} \\ &= \begin{bmatrix} \begin{bmatrix} \boldsymbol{\Sigma}_{\Phi,\text{pos}} & \boldsymbol{\Sigma}_{\Phi,\text{pos,att}} \\ \boldsymbol{\Sigma}_{\Phi,\text{pos,att}}^{\top} & \boldsymbol{\Sigma}_{\Phi,\text{att}} \end{bmatrix} & \boldsymbol{\Sigma}_{\Phi,\rho} \\ \boldsymbol{\Sigma}_{\Phi,\rho}^{\top} & \begin{bmatrix} \boldsymbol{\Sigma}_{\rho,\text{pos}} & \boldsymbol{\Sigma}_{\rho,\text{pos,att}} \\ \boldsymbol{\Sigma}_{\rho,\text{pos,att}}^{\top} & \boldsymbol{\Sigma}_{\rho,\text{att}} \end{bmatrix} \end{bmatrix} \end{aligned} \tag{4.4}$$

with the diagonal elements described by

$$\boldsymbol{\Sigma}_{\Phi} = \left[\bar{\sigma}_{\Phi}^2 \cdot \mathbf{D}_{\text{JPA}} \otimes \mathbf{DWD}^{\top}\right] + \boldsymbol{\Sigma}_I, \tag{4.5}$$

$$\boldsymbol{\Sigma}_{\rho} = \left[\bar{\sigma}_{\rho}^2 \cdot \mathbf{D}_{\text{JPA}} \otimes \mathbf{DWD}^{\top}\right] + \boldsymbol{\Sigma}_I \ , \tag{4.6}$$

where $\bar{\sigma}_{\Phi}^2, \bar{\sigma}_{\rho}^2$ are the carrier phase and code zenith referenced variances, $\mathbf{W}$ is the weighting matrix described in (1.32) and $\mathbf{D}$ is the DD matrix in (2.6). Then, $\mathbf{D}_{\text{JPA}}$ is the mixing matrix that introduces the cross-correlations between the master and the remaining antennas (i.e., the $N$ slave ones on the vehicle and the one on the base station), defined as

$$\mathbf{D}_{\text{JPA}} = \left[\mathbf{I}_{N+1} + \mathbf{1}_{N+1,N+1}\right] . \tag{4.7}$$

At last, $\boldsymbol{\Sigma}_I$ gathers the stochastic model for the atmospheric residuals, the latter affecting solely positioning-related observations –i.e., those in which the base station participates, since the antennas onboard of the vehicle are too close to each other so that any atmospheric residual is present–, and expressed as

$$\boldsymbol{\Sigma}_I = \boldsymbol{\Sigma}_{\Phi,\rho} = \begin{bmatrix} \sigma_I^2 \cdot \mathbf{DWD}^{\top} & \mathbf{0}_{n,nN} \\ \mathbf{0}_{nN,n} & \mathbf{0}_{nN,nN} \end{bmatrix}, \tag{4.8}$$

where $\boldsymbol{\Sigma}_I$ constitutes the ionospheric weighted model described in (2.9) and dependent on the separation between the base and master antennas. Note as well that the cross-correlation terms between code and carrier phase observations is due to the atmospheric residuals present at the positioning DD observations.

To further emphasize the differences between the stochastic models for JPA and the disjoint positioning and attitude estimation, graphical support is provided in Fig. 4.2. This example considers a scenario involving $n = 3 + 1$ tracked satellites across the base station and $N = 2 + 1$ antennas on the target platform. The covariance matrix for code observations $\mathbf{\Sigma}_\rho$ for the JPA model is shown on the right side of Fig. 4.2, while the conventional (independent) positioning-attitude model is depicted on the left side of the same figure, with the colorbar indicating the values for the corresponding standard deviations. It results evident that the additional information gathered by the terms $\mathbf{\Sigma}_\rho$ and $\mathbf{\Sigma}_\Phi$ strength the overall observation model, facilitating the IAR process and, potentially, even increasing the accuracy of the navigational elements.

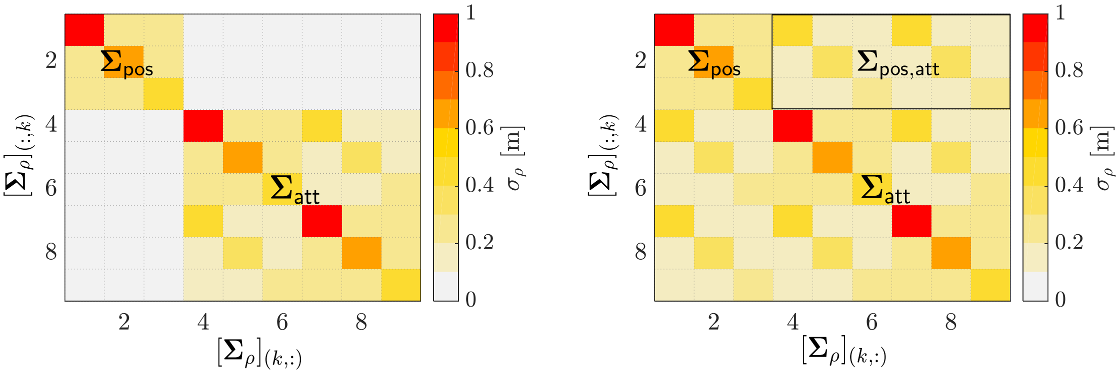

**Figure 4.2:** Pictorial example for the covariance matrix of code observations $\mathbf{\Sigma}_\rho$. On the left, the case for separately solving the positioning and attitude problems. On the right, stochastic characterization for the JPA model.

## 4.2 Estimation Problem for the JPA Mixed Model

In analogy to the estimation problems for the carrier phase-based positioning and attitude models, computing an optimal solution for the JPA involves the following optimization problem

$$\left(\check{\mathbf{Z}}, \check{\mathbf{b}}, \check{\mathbf{q}}\right) = \arg \min_{(\mathbf{Z},\mathbf{b},\mathbf{q})\in\mathbb{Z}^{n,N+1}\times\mathbb{R}^3\times\mathcal{S}^3} \|\text{vec}\left(\mathbf{Y} - \mathbf{A}\mathbf{Z} - \mathbf{B}\left[\mathbf{b},\ \mathbf{h}(\mathbf{q})\right]\right)\|^2_{\mathbf{\Sigma}}, \tag{4.9}$$

with $\mathbf{h}(\mathbf{q})$ defined as in (3.32). Note that the vector of unknown results now a mixture of integer, real and manifold spaces. Note as well that, as for the attitude mixed model, the orientation parametrization plays an important role in maximizing the redundancy of the system. As for the two precedent optimization problems in (2.13), (3.31), a closed form solution for a (4.9) is not known and, instead, one shall take advantage of the well-known three step decomposition:

$$\begin{aligned}
&\min_{\mathbf{Z}\in\mathbb{Z}^{n,N+1},\mathbf{b}\in\mathbb{R}^3,\mathbf{q}\in\mathcal{S}^3} \|\text{vec}\left(\mathbf{Y} - \mathbf{A}\mathbf{Z} - \mathbf{B}\left[\mathbf{b},\ \mathbf{h}(\mathbf{q})\right]\right)\|^2_{\mathbf{\Sigma}} = \\
&= \|\hat{\mathbf{e}}\|^2_{\mathbf{\Sigma}} + \min_{\mathbf{Z}\in\mathbb{Z}^{n,N+1}} \left( \left\|\text{vec}\left(\hat{\mathbf{Z}} - \mathbf{Z}\right)\right\|^2_{\mathbf{P}_{\hat{\mathbf{Z}}\hat{\mathbf{Z}}}} + \min_{\substack{\mathbf{x}^\top=[\mathbf{b}^\top,\mathbf{q}^\top] \\ \mathbf{b}\in\mathbb{R}^3,\mathbf{q}\in\mathcal{S}^3}} \|\hat{\mathbf{x}}(\mathbf{Z}) - \mathbf{x}\|^2_{\mathbf{P}_{\hat{\mathbf{x}}(\mathbf{Z})}} \right).
\end{aligned} \tag{4.10}$$

with $\|\hat{\mathbf{e}}\|^2_{\mathbf{\Sigma}}$ the residuals from a LS adjustment for the auxiliary variables $\hat{\mathbf{Z}}$, $\hat{\mathbf{x}}$, given by

$$\left(\hat{\mathbf{Z}}, \hat{\mathbf{x}}\right) = \arg \min_{\hat{\mathbf{Z}}\in\mathbb{R}^{n,N+1},\hat{\mathbf{b}}\in\mathbb{R}^3,\hat{\mathbf{q}}\in\mathcal{S}^3} \left\|\text{vec}\left(\mathbf{Y} - \mathbf{A}\hat{\mathbf{Z}} - \mathbf{B}\left[\hat{\mathbf{b}},\ \mathbf{h}(\hat{\mathbf{q}})\right]\right)\right\|^2_{\mathbf{\Sigma}}. \tag{4.11}$$

The float step in (4.11) relaxes the integer condition on the ambiguities, while preserving the unit-norm constraint on the quaternion and, so, assuring that a proper rotation is performed. Once again, Lie Theory can be exploited to solve (4.11) through an iterative procedure, at the cost of evaluating the cost function in the surrounding of the last-estimated orientation solution due to the manifold-algebra relationship. Therefore, a proper initialization is as relevant for JPA than for the attitude mixed model in (3.34). The procedure to follow is given by

1. Estimation of the initial solution for the ambiguities, positioning and orientation based on the positioning and multi-baseline mixed models, such that $\hat{\mathbf{Z}}^{(0)}$, $\hat{\mathbf{b}}^{(0)}$, $\hat{\mathbf{q}}^{(0)}$ are given by (2.13), (3.24), (3.15).

2. For $k = 1, 2, \ldots$, until convergence of the solution, perform the following GN adjustment

$$\delta\hat{\mathbf{x}}^{(k)} = \left(\mathbf{H}^\top\mathbf{\Sigma}^{-1}\mathbf{H}\right)^{-1}\mathbf{H}^\top\mathbf{\Sigma}^{-1}\left(\text{vec}\left(\mathbf{Y} - \mathbf{A}\hat{\mathbf{Z}}^{(k-1)} - \mathbf{B}\left[\hat{\mathbf{b}}^{(k-1)},\ \mathbf{h}(\hat{\mathbf{q}}^{(k-1)})\right]\right)\right), \tag{4.12}$$

$$\hat{\mathbf{x}}^{(k)} = \hat{\mathbf{x}}^{(k-1)} \oplus \delta\hat{\mathbf{x}}^{(k)} \tag{4.13}$$

   with $\mathbf{H}$ the Jacobian of the observations with respect to the state estimate evaluated on the latest iteration, given by

$$\mathbf{H} = \begin{bmatrix} \mathbf{I}_{N+1}\otimes\mathbf{A}, & \begin{bmatrix} \mathbf{B} & \mathbf{0} \\ \mathbf{0} & \mathbf{B}\mathbf{J}_{\hat{\mathbf{q}}^{(k-1)}}({}_{\mathcal{B}}\mathbf{b}_{1,m}) \\ \vdots & \vdots \\ \mathbf{0} & \mathbf{B}\mathbf{J}_{\hat{\mathbf{q}}^{(k-1)}}({}_{\mathcal{B}}\mathbf{b}_{N,m}) \end{bmatrix} \end{bmatrix}, \tag{4.14}$$

   and the composition operator updates the float estimates –i.e., the ambiguities and positioning vector are summed with the corresponding sub-vector of $\delta\hat{\mathbf{x}}^{(k)}$, while the quaternion estimate is multiplied with a second quaternion obtained from the sub-vector of $\delta\hat{\mathbf{x}}^{(k)}$ related to the angular error–. Thus, the float solution $\hat{\mathbf{Z}}$, $\hat{\mathbf{q}}$, $\hat{\mathbf{q}}$ corresponds to $\hat{\mathbf{x}}^{(k)}$ once the convergence is reached.

Estimating the next minimization processes, IAR and fixed solution, in (4.10) follows the same principles than for the attitude mixed model in Section 3.3. Thus, the real-to-integer mapping is realized by means of LAMBDA, plus an optimal validation step to verify the correctness of the solution to obtain $\check{\mathbf{Z}}$. Then, the fixed solution estimation leverages on Lie theory, leading to

$$\check{\boldsymbol{\eta}} \triangleq \left[\delta\check{\mathbf{b}}^\top, \quad \delta\check{\boldsymbol{\theta}}^\top\right]^\top = \mathbf{P}_{\hat{\eta}\hat{\eta}}\mathbf{P}^{-1}_{\hat{\mathbf{Z}}\hat{\mathbf{Z}}}\left(\mathrm{vec}\left(\hat{\mathbf{Z}}-\check{\mathbf{Z}}\right)\right) , \tag{4.15}$$

$$\check{\mathbf{b}} = \hat{\mathbf{b}} - \delta\check{\mathbf{b}} , \tag{4.16}$$

$$\check{\mathbf{q}} = \hat{\mathbf{q}} \circ \mathbf{q}^* \left\{\delta\check{\boldsymbol{\theta}}\right\} , \tag{4.17}$$

with $\mathbf{P}_{\hat{\eta}\hat{\eta}}$ the sub-matrix from the covariance matrix of float estimates corresponding to the non-ambiguity parameters. Thus, by virtue of the integer constraints on the ambiguities, positioning and attitude estimates will inherent high precision whenever those ambiguities are correctly resolved.

### 4.2.1 Recursive Formulation for the JPA Mixed Model

For the time recursion and estimation for the JPA problem, one may apply an analog methodology to the attitude mixed model, since handling the unit-quaternion remains the greatest challenge. Thus, let us describe the discrete SSM for an inertial navigation problem at time $t$ by

$$\begin{aligned} \mathbf{x}_t &= \left[\mathbf{a}_t^\top, \quad \mathbf{b}_t^\top, \quad \mathbf{v}_t^\top, \quad \mathbf{q}_t^\top, \quad \mathbf{b}_{\omega,t}^\top, \quad \mathbf{b}_{a,t}^\top\right]^\top , \\ &\text{with } (\mathbf{a}_t, \mathbf{b}_t, \mathbf{v}_t, \mathbf{q}_t, \mathbf{b}_{\omega,t}, \mathbf{b}_{a,t}) \in \mathbb{Z}^{n(N+1)} \times \mathbb{R}^3 \times \mathbb{R}^3 \times \mathcal{S}^3 \times \mathbb{R}^3 \times \mathbb{R}^3 , \end{aligned} \tag{4.18}$$

such that $\mathbf{a}_t = \mathrm{vec}(\mathbf{Z}_t)$ is the vector gathering all the integer ambiguities, $\mathbf{v}_t$ is the linear speed for the platform (expressed in the global frame), and $\mathbf{b}_{\omega,t}$, $\mathbf{b}_{a,t}$ are the gyroscope and accelerometer biases, respectively. In this case, the process model can be expressed as

$$\mathbf{x}_t = \mathbf{f}\left(\mathbf{x}_{t-1}, \mathbf{y}_{\mathsf{INS},t}, \mathbf{w}_t\right) , \tag{4.19}$$

where $\mathbf{y}_{\mathsf{INS},t}$ denotes the vector of angular rates and linear accelerations measured by an IMU, such that $\mathbf{y}_{\mathsf{INS},t} = [\boldsymbol{\omega}_t, \dot{\mathbf{v}}_t]$, and $\mathbf{w}_t$ comprises process model white noises distributed as $\mathbf{w}_t \sim \mathcal{N}(\mathbf{0}, \mathbf{Q}_t)$ and

$$\mathbf{Q}_t = \mathrm{diag}\left(\sigma_a^2\mathbf{I}_{n(N+1)}, \ \sigma_\omega^2\mathbf{I}_3, \ \sigma_{\dot{v}}^2\mathbf{I}_3, \ \sigma_{b\omega}^2\mathbf{I}_3, \ \sigma_{ba}^2\mathbf{I}_3\right) . \tag{4.20}$$

Taking aside the pertinent random walk and denoting as $\mathbf{g}_t$ the gravity vector expressed in the global frame, the process model in (4.19) is formulated as

$$\mathbf{f}\left(\mathbf{x}_{t-1}, \mathbf{y}_{\mathsf{INS},t}\right) = \begin{cases} \mathbf{a}_{t-1} \\ \mathbf{b}_{t-1} + \Delta t \mathbf{v}_{t-1} \\ \mathbf{v}_{t-1} + \Delta t \left(\mathbf{g}_t + \mathbf{R}\{\mathbf{q}_{t-1}\}(\dot{\mathbf{v}}_t - \mathbf{b}_{a,t-1})\right) \\ \mathbf{q}_{t-1} \circ \mathbf{q}\left\{\Delta t(\boldsymbol{\omega}_t - \mathbf{b}_{\omega,t-1})\right\} \\ \mathbf{b}_{\omega,t-1} \\ \mathbf{b}_{a,t-1} \end{cases} , \tag{4.21}$$

where additional inertial factors such as Earth rotation, centrifugal and Coriolis terms are disregarded for simplicity. For further simplification, lever-arm compensation between the IMU and body frame is also neglected necessary (i.e., the gyroscope and accelerometer axis are perfectly aligned with the body frame, and the position of the IMU coincides with the master antenna), and factors such as scaling or cross-coupling errors are not present for the inertial unit. Note that for non-inertial systems, the recursive JPA mixed model follows a very similar formulation by removing the inertial biases from the state estimate and assuming that the velocity and quaternion estimates evolve over time as random processes.

Once again, the ESKF results a powerful filtering alternative to deal with the quaternion-related constraints, while presenting minimal state representation in the estimated covariance matrix (i.e., $\mathbf{P} \in \mathbb{R}^{P,P}$, with the number of minimal state parameters $P = n \cdot (N+1) + 3 \cdot 5$). Similar to the approach derived in Section 3.4 for the attitude model, the state estimate is conformed by the composition of a nominal state vector $\hat{\mathbf{x}}_t$ and the error state $\delta\mathbf{x}_t$, whose uncertainty is represented in the covariance matrix $\mathbf{P}_t$. Such composition is formulated as

$$\mathbf{x} = \hat{\mathbf{x}} \oplus \delta\mathbf{x} = \begin{cases} \hat{\mathbf{a}}_t & + & \delta\mathbf{a}_t \\ \hat{\mathbf{b}}_t & + & \delta\mathbf{b}_t \\ \hat{\mathbf{v}}_t & + & \delta\mathbf{v}_t \\ \hat{\mathbf{q}}_t & \circ & \mathbf{q}\{\delta\boldsymbol{\theta}_t\} \\ \hat{\mathbf{b}}_{\omega,t} & + & \delta\mathbf{b}_{\omega,t} \\ \hat{\mathbf{b}}_{a,t} & + & \delta\mathbf{b}_{a,t} \end{cases} . \tag{4.22}$$

Then, one may use the set of ESKF equations formulated in (3.44) to perform the prediction and correction step for the ESKF-based JPA problem by adapting the process and observation models, as well as the pertinent Jacobian matrices in (3.45)–(3.46), such that

$$\mathbf{F}_t = \begin{bmatrix} \mathbf{I}_{n(N+1)} & \mathbf{0} & \mathbf{0} & \mathbf{0} & \mathbf{0} & \mathbf{0} \\ \mathbf{0} & \mathbf{I}_3 & \Delta t\mathbf{I}_3 & \mathbf{0} & \mathbf{0} & \mathbf{0} \\ \mathbf{0} & \mathbf{0} & \mathbf{I}_3 & -\Delta t\mathbf{R}[\dot{\mathbf{v}}_t - \mathbf{b}_{a,t-1}]_\times & \mathbf{0} & -\Delta t\mathbf{R} \\ \mathbf{0} & \mathbf{0} & \mathbf{0} & \mathbf{R}^\top\{\delta\mathbf{q}\} & -\Delta t\mathbf{I}_3 & \mathbf{0} \\ \mathbf{0} & \mathbf{0} & \mathbf{0} & \mathbf{0} & \mathbf{I}_3 & \mathbf{0} \\ \mathbf{0} & \mathbf{0} & \mathbf{0} & \mathbf{0} & \mathbf{0} & \mathbf{I}_3 \end{bmatrix} , \tag{4.23}$$

where $\mathbf{R}$ is obtained from $\mathbf{q}_{t-1}$, and $\delta\mathbf{q}$ is the quaternion obtained from the integration of the angular rate $\delta\mathbf{q} \triangleq \mathbf{q}\{\Delta t(\boldsymbol{\omega}_t - \mathbf{b}_{\omega,t-1})\}$. Also, the Jacobian matrices for the observation model in(3.49)–(3.50) are expressed as

$$\mathbf{H}_\mathbf{x} = \begin{bmatrix} \mathbf{I}_{N+1} \otimes \mathbf{A}, & \begin{bmatrix} \mathbf{B} & \mathbf{0} \\ \mathbf{0} & \mathbf{B}\mathbf{J}_{\hat{\mathbf{q}}^{(k-1)}}({}_\mathcal{B}\mathbf{b}_{1,m}) \\ \vdots & \vdots \\ \mathbf{0} & \mathbf{B}\mathbf{J}_{\hat{\mathbf{q}}^{(k-1)}}({}_\mathcal{B}\mathbf{b}_{N,m}) \end{bmatrix}, & \mathbf{0}_{2n(N+1),3}, & \mathbf{0}_{2n(N+1),3} \end{bmatrix} , \tag{4.24}$$

$$\mathbf{H}_{\delta\mathbf{x}} = \begin{bmatrix} \mathbf{I}_{n(N+1)+6} & \mathbf{0} & \mathbf{0} \\ \mathbf{0} & \mathbf{H}_{\delta\boldsymbol{\theta}} & \mathbf{0} \\ \mathbf{0} & \mathbf{0} & \mathbf{I}_6 \end{bmatrix} . \tag{4.25}$$

Besides the minimal changes in the state space formulation and those additional ones to re-formulate the Jacobian matrices, the ESKF for the JPA results almost identical to that of the attitude mixed model. The benefits from preserving the geometric constraints over the quaternion along with the minimal uncertainty representation and the linear kinematic model are preserved. Moreover, the IAR and fixed solution processes that come after the float estimation are also realized by means of LAMBDA and the Lie theory-based update.

## 4.3 Performance of Estimators at the JPA Model

In the sequel, the JPA model is compared to that of independently solving for positioning and attitude. Also, the proposed estimator for the recursive estimation of the JPA mixed model is studied and its performance characterized for both synthetic and real data experimentation.

### 4.3.1 Simulation Results

This section serves as analysis for the differences between the JPA mixed model and the "independent" treatment for the positioning and attitude problem. Note that the actual observations and antenna configurations are identical: an antenna array is made available at the platform and has connection to corrections from a nearby base station. Also, the estimation solution is addressed by the same ESKF recursion for both models. This allows to isolate and make evident the pros and cons between exploiting the JPA model defined in 5 or the positioning and attitude models in 1, 4. In other words, this section focuses on assessing the gains from exploiting the stochastic cross-correlations between positioning- and attitude-related observations that conform the JPA model.

Numerical characterization is performed via Monte Carlo experimentation for which, a static GNSS skyplot consisting on eight satellites, as illustrated on the left side of Fig. 4.3, for a multi-antenna configuration conformed of four elements in which the slave antennas are separated by one meter with respect to the master one. The initial distance to the base station is five kilometers. Accelerometer readings are assumed unavailable, so that the time evolution for the orientation is dictated by the gyroscope observations (with $\sigma_\omega = 0.02$ deg/$\sqrt{\text{s}^3}$, and $\sigma_{b\omega} = 2 \cdot 10{-}4$ deg/$\sqrt{s^3}$) and the velocity evolves as a random walk with $\sigma_v = 1$ m/s$^2$. The time evoluation for the 'true' angular rate observations, i.e., free from noises and biases, are shown on the right side of Fig. 4.3. Both prediction and correction steps are sampled at one Hertz, so that $\Delta t = 1$ s. With regards to the GNSS noise distribution, code and carrier phase zenith referenced std, $\bar{\sigma}_\rho$ and $\bar{\sigma}_\Phi$, correspond to 30 cm and 3 mm, respectively. The atmospheric residuals modeled based on the distance to the base, following (2.9). In all cases, the weighting matrix $\mathbf{W}$ corresponds to the elevation-dependent model in (1.32). To make the estimation a bit more challenging and realistic, each satellite link is subject to suffer from the occurrence of a cycle slip, modeled with a 0.5% probability. A total time of 100 seconds are simulated for a total of $10^3$ Monte Carlo runs.

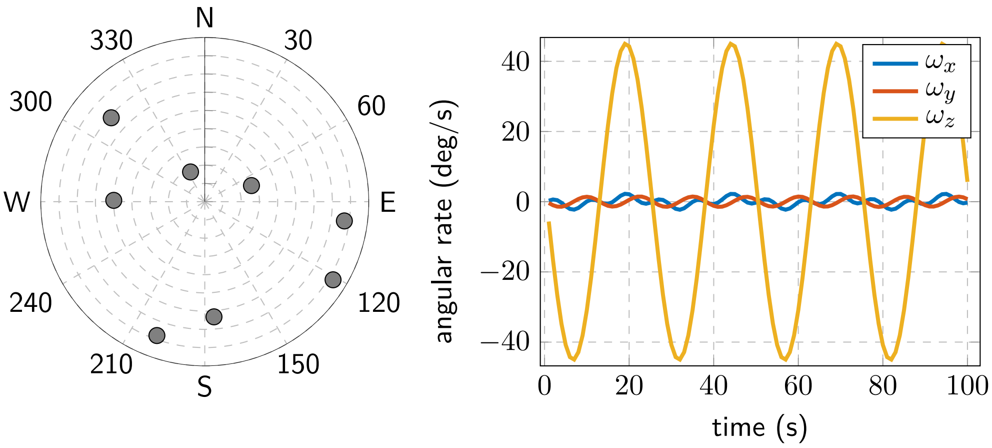

**Figure 4.3:** Skyplot for the JPA problem.

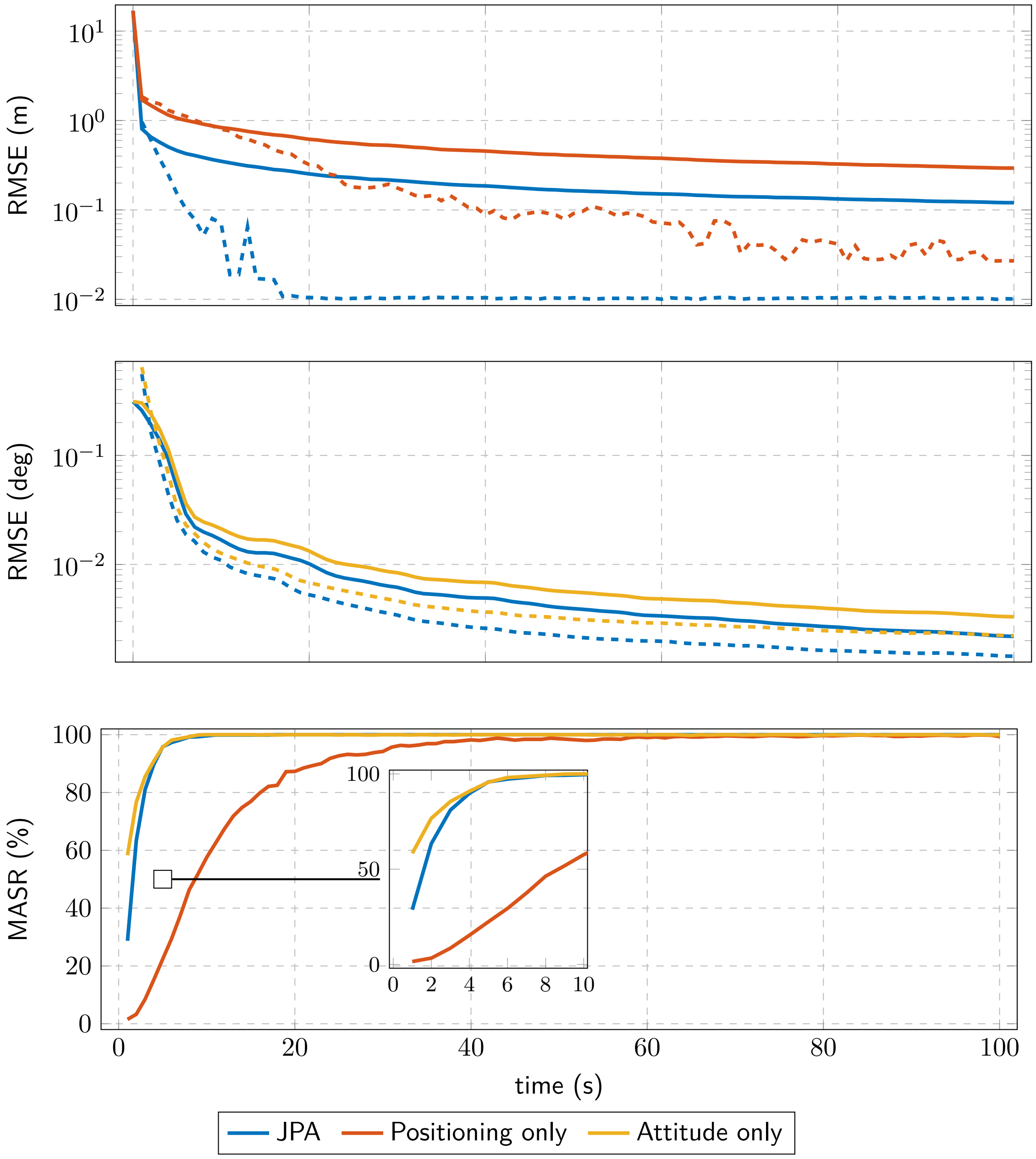

**Figure 4.4:** Performance comparison between the JPA and the independent positioning+attitude mixed models, based on the ESKF recursive estimates. On the top, RMSE for the positioning errors over time, with the continuous and dashed lines indicating the accuracy for float and fixed estimates, respectively. On the center, RMSE for the orientation estimates over time, with the continuous and dashed lines indicating the accuracy for float and fixed estimates, respectively. On the bottom, the mean ambiguity success rate (MASR) over time, with a zoom over the first ten seconds of the trajectory.

Fig. 4.4 collects the results for positioning and attitude RMSE on the top and center graphs, respectively, as well as the mean ambiguity success rate (MASR) –i.e., the percentage of epochs for which the vector of ambiguities is correctly estimated–. For the top and center figures, the float estimates are depicted with solid lines, while the RMSE for fixed solutions are shown with dashed lines. The legend makes reference to JPA, positioning and attitude only, which refers to an ESKF fed with either the JPA observation model or the positioning and attitude models (i.e., disregarding the cross-correlations). Some conclusions can be withdrew:

- In terms of accuracy, JPA leads to a significant improvement with regards to the conventional positioning problem, leading to a gain factor of near 2.5 –e.g., after 100 seconds, the float positioning errors for JPA mixed model-based ESKF stabilize at around 12 cm, while the mixed model-based converge to around 30 cm. Similarly, the accuracy for float orientation estimates of the JPA mixed model is approximately 1.5 times better than that of the attitude mixed model. Note that both these improvements are due to the additional information present on the cross-correlation between positioning- and attitude-related observations, making evident the vast relevance of this factor.
- In terms of availability for precise navigation estimates or, in other words, the chances for correctly estimating the integer ambiguities, positioning becomes the most complicated navigational element. This is due to the lesser observability and higher noise levels due to the atmospheric residuals. An interesting remark is that the attitude mixed model can be resolved in an easier manner than JPA, since the JPA is impeded by the complexity of fixing the positioning-related ambiguities. Nonetheless, the difference is almost minimal, as can be seen on the detail for the bottom graph of Fig. 4.4.

### 4.3.2 JPA Experimental Results

The performance characterization of the proposed ESKF-based JPA problem is addressed for the navigation of a vessel navigation in a inland waterway channel, which is an interesting ITS application. The measurement campaign was conducted in Koblenz (Germany) on 16th May 2017 (DOY 136, UTC 09:00-14:00), being the tracked vehicle the MS Bingen, a multi-purpose research vessel of the German Waterways authorities. The equipment setup listed three navXperience 3G+C GNSS antennas connected to three separate dual frequency Javad Delta receivers, a Fiber Optic Gyroscope (FOG) IMU iMAR and an active reflector under the master antenna. Fig. 4.5 (left) shows the MS Bingen and the location of the GNSS antennas and the reflector, (top right) indicates the configuration of the antennas and the IMU in the body frame, and (bottom right) depicts the number of GPS satellites tracked, as well as the PDOP along the five-hour long campaign.

The trajectory followed and the location of the base station and the total station are illustrated in Fig. 4.6, with the distance between the base and the vessel constitutes a short baseline ranging between 900 m and 2.5 km. The vessel navigates from the port on the right side of Fig. 4.6 up river and then returns back to the point of departure. The reference trajectory of the vessel is obtained based on optical technology, combining a total station on land and an active reflector under the master GNSS antenna for automatic target tracking. This technology assures a precise positioning ground truth solution whose error patterns are independent of GNSS.The integration of the angular rates measured by the high-quality IMU is used as benchmark solution for the attitude estimates.

The ESKF approach is as defined in Section 4.2.1, being either fed with the JPA mixed model in 5 or the positioning and attitude mixed models in 1, 4. Observations for GPS across the L1, L2 frequencies are used, with an elevation mask of 15 degrees and a sampling rate of 1 Hz. IAR is based on LAMBDA, with a posterior FF-RT being applied as validity test. Note that inertial information is not integrated, since the focus is laid on the performance differences between the JPA/independent positioning and attitude models. Instead, inertial integration is used as ground truth for the orientation estimates.

The comparison between JPA and the positioning- and attitude-only models is reported in Table 4.1, in terms of fix ratio over the course of the measurement campaign. The first column

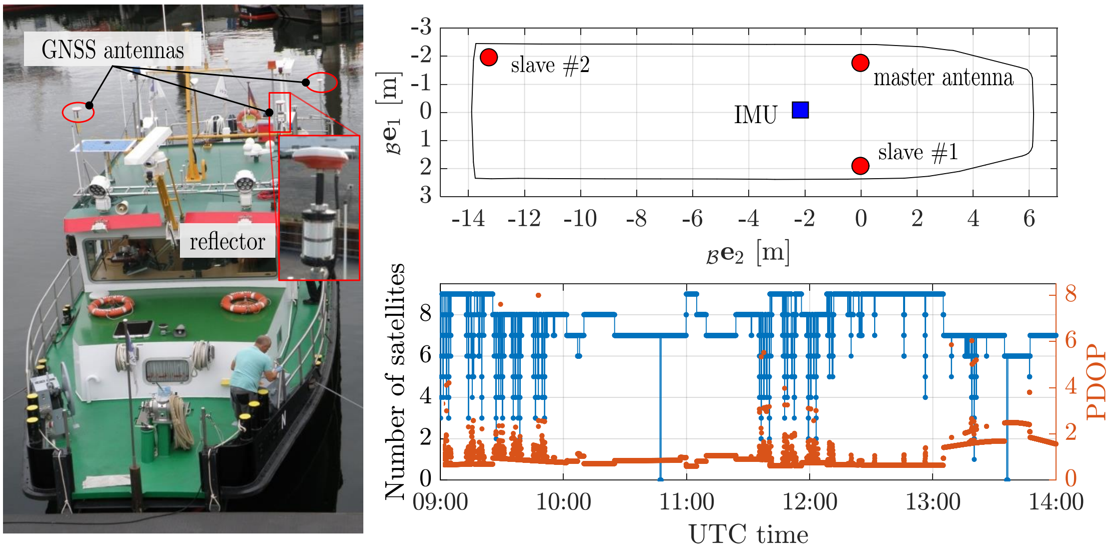

**Figure 4.5:** On the left, the MS Bingen vessel whose navigation solution is estimated. On the top right, the configuration of the antennas in the body/vehicle coordinate frame. On the bottom right, the number of tracked GPS satellites and associated PDOP.

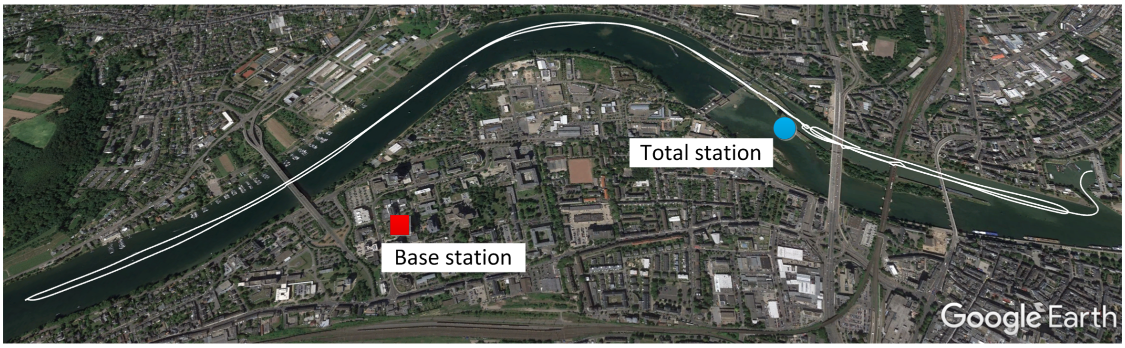

**Figure 4.6:** Trajectory followed by the tracked vessel, whose departure and arrival points coincide with the port on the right hand side. The location of the total station (for optical tracking the vessel) and the base station is marked with a round and a square indicator respectively.

**Table 4.1:** Percentage of fixed solutions (%) depending on the number of locked satellites.

| **Number of satellites / Time** (%) | **Fix ratio** (%) | | | |
|---|---|---|---|---|
| | JPA | Positioning | Attitude | Pos ∩ Attitude |
| 9 (28.68) | 85.94 | 82.30 | 83.25 | 73.10 |
| 8 (27.10) | 83.93 | 54.07 | 78.50 | 49.07 |
| 7 (35.32) | 68.12 | 60.22 | 81.58 | 53.49 |
| 6 (06.51) | 47.78 | 65.27 | 66.89 | 60.24 |
| $\leq$ 5 (2.38) | 01.17 | 02.33 | 02.56 | 01.40 |
| **Total** | 74.60 | 63.84 | 79.35 | 57.11 |

depicts the number of satellites $n+1$ and the corresponding percentage of time for which that number is tracked. The following columns correspond to the fix ratio of the assessed positioning and attitude methods: the second column is for the proposed JPA, the third is for the positioning-only, the fourth is for the attitude-only and the last column is the union of the positioning and attitude (i.e., the simultaneous occurrence of having a fixed solution for the positioning- and attitude-only solution of the third and fourth columns). The first thing to notice is that, generally, the fixing ratio grows with the number of satellites, and the chances of having a fixed solution for five or less satellites is very uncommon. Some conclusions can be drawn from the comparison of JPA against separately estimating positioning and attitude:

i) The attitude model is "stronger" than the positioning one despite the nonlinearities in the observation function. There are two reasons to ground the positioning-attitude difference in performance: on the one hand, small residuals due to the atmospheric propagation delays between the vehicle and the base station might be present despite the short baseline; on the other hand, the data redundancy is higher in the attitude than in the positioning model (i.e., $n(N+1)$ code observations guide the float estimate of the four-dimensional unknown quaternion, while $n$ code measurements support the search of the three-dimensional unknown position).

ii) In average, JPA performs better than the union of separately estimating the position and attitude problems. Thus, the former provides a fixed solution for the $74.60\%$ of time, while the latter is limited to a $57.11\%$ of time —which is a difference in precise navigation availability of over 45 minutes—. This conclusion coincides with the one obtained during the previous numerical experiment, reinforcing the hypothesis that positioning-attitude cross-correlations are of great importance.

iii) The standalone attitude problem presents a higher fix ratio compared to the JPA, as it is unaffected by the residual atmospheric propagation delays present in the positioning problem. Thus, a practical application might be interested in executing in parallel the attitude-only and the JPA filters, leading to a high availability positioning and attitude estimates and a mechanism to monitor the integrity of the algorithms if discrepancies between the estimates occurred.

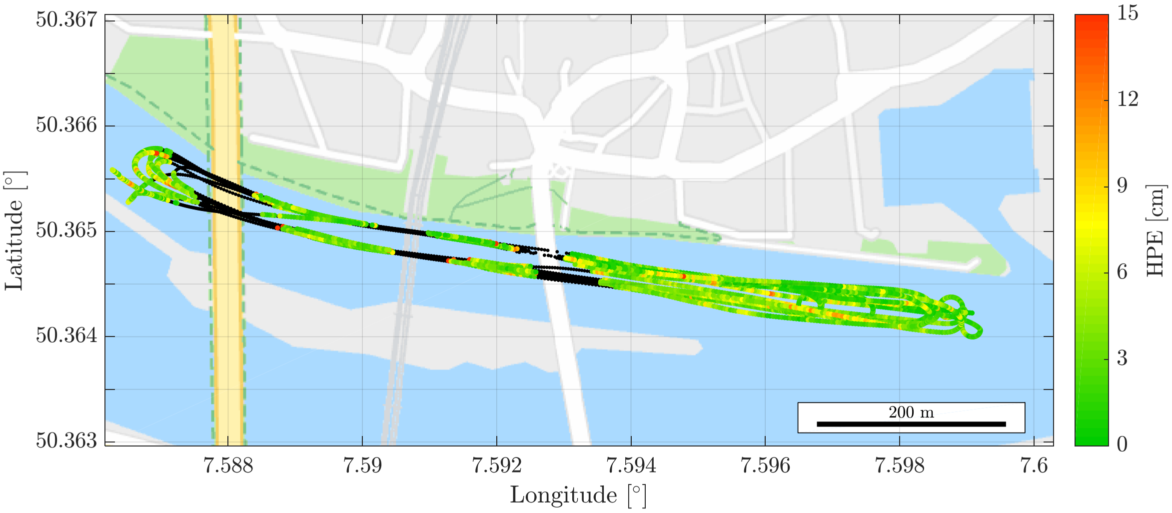

**Figure 4.7:** Positioning performance for the JPA method during bridge passing. The black line is the reference trajectory estimated using laser tracking and the dots correspond to the estimated solution (only fixed estimates) with the horizontal accuracy as indicated on the colorbar.

Next, the positioning performance is analyzed. Besides the higher availability for the JPA against positioning-only estimates, the fixed solutions are very much equivalent up to the mm-regime. As depicted in Fig. 4.7, a GNSS-independent localization ground truth is available, obtained using optical (laser-based) technology. For that, a total station is located in the small island in the center of the river and automatic tracking to the active reflector located below the master antenna is performed. This area is most interesting, since the three bridges induce multipath biases and the track of satellites is often lost. As expected, the chance for having a fixed navigation solution under the bridges results null, although the navigation fix is rapidly recovered. The standard deviation for the fixed position solution is very close to a centimeter, although some few wrong fixes (with horizontal errors of up to 15 cm) occur as well.

Finally, the JPA-based attitude determination performance is examined. As with the positioning case, the fixed attitude solutions are equivalent between attitude-only and JPA estimates. Fig. 4.8 depicts the estimated orientation using the Euler angles. The highest degree of similarity is achieved on the heading estimation, while the pitch and especially the roll are characterized with higher levels of noise. The better heading performance can be explained in relation to the GNSS satellite geometry—offering a higher accuracy on the horizontal plane—, and the antenna configuration onboard the vehicle, as the two front antennas are coplanar with the local horizontal plane of the vehicle. It is noticeable that the IMU allows to track subtle motions, such as the pitch variations due to the small waves in the river, and in general the fusion of IMU and GNSS is recommended. Although the standard deviation for the heading estimates are below the degree, the roll presents some errors of up to 10°, likely due to a wrong fix, since the period of time analyzed (12:00–13:00 UTC) corresponds to the time in which the vessel maneuver around the bridges.

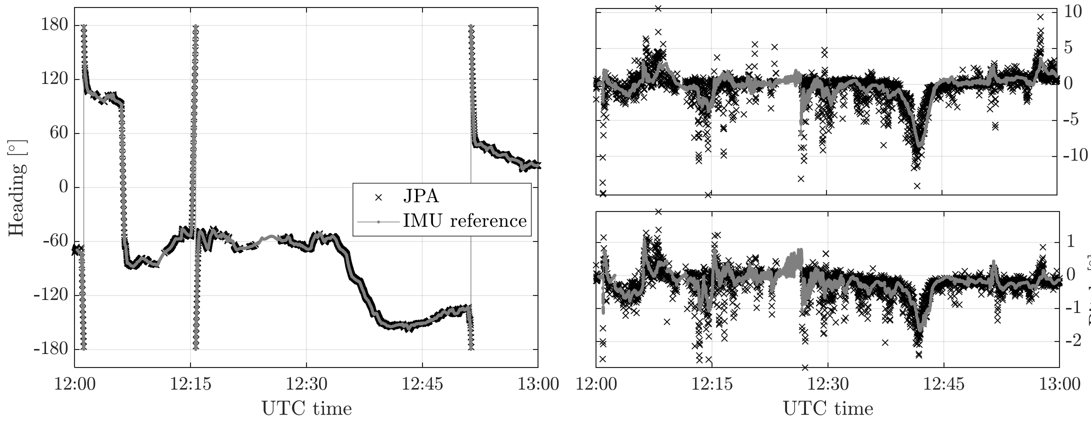

**Figure 4.8:** Attitude estimates over time for an hour of the studied experimentation. The attitude performance of the JPA (in black crosses) is shown against the reference FOG IMU-based estimate (in gray).

## 4.4 Summary

This chapter deals with the topic of pose estimation for a rigid body and, when extended to time recursion, its navigation. The provision of precise navigational solutions constitutes the summit for the exploitation of carrier phase observations, combining RTK-alike differential positioning and attitude estimation for multi-antenna platforms. Thus, this chapter discusses on the pertinent observation models, their estimation and the performance characterization of these via numerical and experimental results.

First, Section 4.1 formalizes the concept of joint position and attitude (JPA) determination, consisting on the fusion of positioning- and attitude-related GNSS measurements under the same observation model. Under this premise, the JPA mixed model is introduced along with the description of its stochastic modeling. The latter is particularly relevant since conventional estimation approaches deal with the positioning and attitude problems as separate manner. Hence, Section 4.1.1 details how the error sources for the JPA model can be modeled, paying special attention to the cross-correlations present due to using the master antenna for the DD combination, as well as the additional atmospheric residuals due to the distance between the base station and the target platform.

Then, Section 4.2 introduces the deterministic and recursive estimators for the JPA mixed model. In this case, the optimization problem gathers a mixture of real, manifold and integer unknown parameters (i.e., the baseline vector for positioning, the quaternion rotation and the carrier ambiguities, respectively). Although an explicit solution to the original optimization problem is not known, the conventional three step decomposition allows to derive MLE which are (approximately) optimal. Moreover, the original ESKF for the attitude mixed model introduced in the previous chapter is now extended to deal with the integration of INS and the JPA observation model. Again, making use of the quaternion parametrization for the rotation operator allows to work with minimal state representations, exploit the Lie algebra relationships and "easily" derive both deterministic and recursive estimators.

Finally, the experimentation based on Monte Carlo simulation and the analysis of real data serves to characterize the performance of the ESKF for the JPA, as well as describing the gain of JPA with respect to modular approaches for the positioning and attitude estimation. The most relevant conclusions derived are as follows:

- The use of JPA provides significant improvements on the accuracy of precise navigation estimates. While such gain may become irrelevant for fixed solutions (they are precise enough already!), the difference for float solutions results key for ITS or robotics applications concerned with availability over precision.

- With regards to availability or, in other words, chances for the integer ambiguities to be correctly estimated, the results are clearly interesting: the attitude mixed model $\geq$ JPA mixed model $\gg$ positioning mixed model. While the differences between the JPA and the mixed model are almost minimal, they are enough to justify the use of a modular approach to execute JPA in parallel with the attitude model. A relevant note is that, JPA does solve the ambiguities for both the positioning and attitude models, leading to a monumental gain in availability for precise positioning compared to conventional RTK-like approaches.

The results presented in this chapter were partially published in:

**Journal articles:**

[8] Medina, D., Vilà-Valls, J., Heßelbarth, A., Ziebold, R., & García, J. (2020). On the Recursive Joint Position and Attitude Determination in Multi-Antenna GNSS Platforms. *Remote Sensing, 12*(12), 1955.

**Conference articles:**

[11] Chauchat, P., Medina, D., Vilà-Valls, J., & Chaumette, E. (2021, November). Robust Linearly Constrained Filtering for GNSS Position and Attitude Estimation under Antenna Baseline Mismatch. In *2021 24th International Conference on Information Fusion (FUSION)*. IEEE.

[22] Medina, D., Heßelbarth, A., Büscher, R., Ziebold, R., & García, J. (2018, April). On the Kalman filtering formulation for RTK joint positioning and attitude quaternion determination. In *2018 IEEE/ION Position, Location and Navigation Symposium (PLANS)* (pp. 597-604). IEEE.

# Part III

# Robust Estimation for Navigation in Harsh Environments

# CHAPTER 5

# Robust Statistics for Code-Based Positioning

CLASSICAL statistical estimators, such as Maximum Likelihood (ML) or Maximum a Posteriori (MAP), are designed and operate optimally under the condition that data is *exactly* normal-distributed. While the Gaussianity assumption is well justified in most occasions, real-world data often features deviations from the assumed distribution. Unfortunately, even slight model mismatches, such as the presence of outliers or contaminated observations, may lead the performance of a classical estimator to strongly decay or even break down. Estimators for GNSS-based positioning are no exception to this rule and, hence, one may experiment gross estimation errors while operating in harsh signal propagation conditions due to multipath and non-line-of-sight effects. Robust Statistics concern with the development of estimators able to perform *nearly* optimally under both, the nominal data distribution and deviations from the model. This Chapter reviews the basic notions on Robust Statistics and the development of deterministic robust estimators for regression. Then, the particulars of applying such methods to the code-based positioning problem are discussed. Finally, theoretical insights and performance characterization for robust positioning methods are provided, including synthetic and experimental analysis.

## Outline

Having become the cornerstone for outdoor localization and navigation, the GNSS community has devoted great efforts towards developing PVT solutions resilient to multipath and other unmodeled propagation effects. Taking aside multi-sensory approaches to compensate for the poor GNSS performance in urban scenarios, PVT resilient approaches typically leverage on solution separation (SS), also denoted consistency-cheking. The former consists on the application of successive statistical tests for the detection and exclusion of potential outliers, i.e., the population of observations is trimmed until only normal-distributed measurements are left. Receiver Autonomous Integrity Monitory (RAIM) [44] and its extensions (e.g., ARAIM [142], [143], CRAIM [144] and others [145], [146]) represent the most well known example of resilient SPP, become the *de facto* positioning method for vertical guidance in the aviation field. Unfortunately, the difficulty of spotting outliers via SS rapidly grows in high dimensionality problems and for an elevated number of observations. Taking into consideration the rapid deployment of GNSS constellations and the abundance of signals across different frequencies, the applicability of SS is limited: its computation constitutes a combinatorial problem which eventually becomes intractable.

The term *robustness* has been used (or misused, to be more precise) in several contexts by the research community. This thesis refers to robustness in the statistical sense, e.g., as described by Huber "*robustness signifies insensivity to small deviations from the assumption*" [147]. The framework of Robust Statistics concern with developing *approximate* parametric estimators. Robust methods are designed in such a way that they behave nearly optimally, if the assumed model is correct, while small deviations from the model assumptions degrade performance only slightly and larger deviations do not cause a catastrophe [147]. The theory of robust statistics was established in the 1960s after the works of Tukey, Huber and Hampel [148]–[150] and, while originally devised for general data analysis, robust estimation has undergone substantial growth and extended to a myriad of fields: signal processing [151]–[153], biomedical [154], [155], power systems [156], etc. For an in-depth analysis of robust statistics, the reader may refer to classical reference textbooks [147], [157], [158], or the more recent [159] for its application to signal processing problems.

Recently, the use of robust statistics has attracted the attention of GNSS practitioners for various purposes. For instance, its application to baseband processing for interference mitigation has been showcased with great success [160], especially with regards to anti-jamming protection [161]–[166]. Nonetheless, computing resilient PVT solutions constitutes the most extended use of robust methods within the context of GNSS, with contributions for code-based positioning in memory-less [47], [167]–[169] and recursive forms [21], [28], [170] being readily available. Unfortunately, a formal discussion on the challenges related to robust estimation for GNSS-based positioning problems has been somewhat overlooked by the GNSS research community. In particular, one may be concern with *i)* GNSS observables not being identical and independent distributed; *ii)* the "fatness" or low redundancy of observations; *iii)* the role of geometry and the nonlinearity of the observation models; *iv)* how robust estimates affects the IAR process when applied to the mixed model.

This thesis addresses the aforementioned challenges and provides theoretical insights and performance characterization for robust estimators applied to the GNSS-based positioning problem. This Chapter focuses on providing a short overview on the fundamentals of Robust Statistics and its application to point estimation for code-based positioning, while Chapter 6 extends the analysis to recursive estimation for carrier phase-based navigation.

## 5.1 Robust Statistics Principles

Conventional statistical estimators, or parametric models, operate under the assumption of perfect knowledge for the data probability distribution. Indeed, ever since the least squares method was introduced [171], data normality constitutes the most widely used model formalization [158]. Such an assumption results very practical, providing a sensible representation of sensors' thermal noise and allowing the derivation of explicit formulae for optimal solvers, such as MLEs. Despite its popularity, the Gaussianity condition does not hold true for multiple real world problems and its justification has often proven wrong. Interestingly, already back in 1904 Poincaré [172] raised concerns on the Gaussian distribution of data:

> *'Everyone believes it: the experimenters imagine that it is a mathematical theorem, and the mathematicians that it is an experimental fact.'*

Indeed, measurements across different fields confirm the presence of heavy-tailed noise [173]–[175], which cause estimators derived from the Gaussian probability model to be biased or even to break down [151]. Robust statistics formalize the concept of *approximate* parametric models and derive methods that produce reliable estimates when data follows certain distribution exactly and/or approximately. Following the descriptions from Muma [176], a robust method shall fulfill three basic requirements:

**Near Optimality:** a robust estimator should perform "reasonably good" (nearly optimal) at the assumed model [147]. Robustness is relative to a nominal model, which is assumed to be approximately valid when: *a)* the bulk of data belongs to the nominal distribution, and some contaminated observations (i.e., the outliers) do not follow the pattern of the majority; *b)* the distribution of the data is within a specific class of neighboring distributions, as measured by some distance measure. Naturally, near-optimality is an imperative requirement, provided that the robust method should be competitive against classical estimators under the nominal noise distribution.

**Qualitative Robustness:** a robust procedure should present stability against infinitesimal perturbations or, in other words, a small change in the data should have a small effect over the estimates. Small changes refer to both changing a small fraction of the data arbitrarily (e.g., under the presence of outliers) or performing a minor change to a large fraction of the data (e.g., rounding the measurements).

**Quantitative Robustness:** a robust estimator should not break down (e.g., when an estimate becomes infinitely biased) even under large deviations from the nominal model. In other words, even under large fraction of contaminated data, the method should provide with a reasonable response.

To illustrate the need for robust estimators, let us leverage on the classical example (showcased, among others, in [158]) for the one-dimensional location and scale estimation problem.

**Example 3** (Location and scale estimation under contaminated data)**.** Consider the following 24 observations for copper content in wholemeal flour (measured in parts per million) [177]:

| | | | | | | | |
|---|---|---|---|---|---|---|---|
| 2.20 | 2.20 | 2.40 | 2.40 | 2.50 | 2.70 | 2.80 | 2.80 |
| 3.03 | 3.03 | 3.10 | 3.37 | 3.40 | 3.40 | 3.40 | 3.50 |
| 3.60 | 3.70 | 3.70 | 3.70 | 3.70 | 3.77 | 5.28 | 28.95 |

One quickly realizes that the measurement 28.95 stands out from the rest of the dataset and could be considered as an outlier. Most likely, such an outstanding value was due to a misplaced decimal point (i.e., 28.95 instead of 2.895). Fig. 5.1 depicts the observations and the location estimates for the mean and median –which correspond to minimizing the $\ell_2$ and $\ell_1$ norms, respectively– with and without the inclusion of the "suspicious" observation.

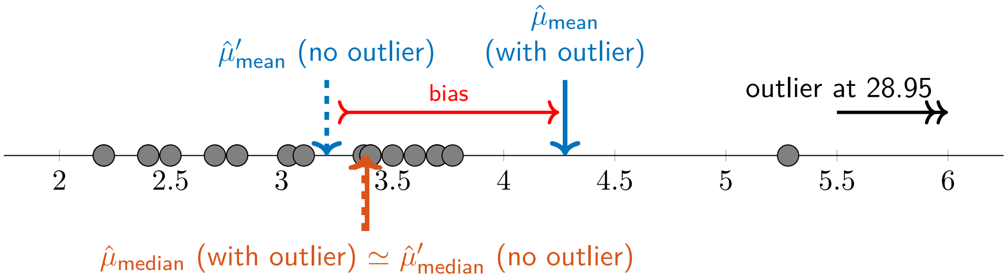

**Figure 5.1:** Copper content in wholemeal flour (in parts per million) and location estimates based on the mean and median, with and without the inclusion of the 28.95 observation.

Due to the influence of the outlier, location and scale estimates based on the MLE at the normal distribution (mean and standard deviation) become highly influenced, with $\hat{\mu}_{\text{mean}} = 4.28$ and $\hat{\sigma}_{\text{std}} = 5.30$. Upon removal of the 28.95 observation, the previous estimates drastically change into $\hat{\mu}'_{\text{mean}} = 3.20$ and $\hat{\sigma}'_{\text{std}} = 0.69$, which constitute a much better fit for the dataset (notice that the superscript '′' refers to estimates for the trimmed distribution). On the other hand, robust estimates for the location and scale, such as the median and the median absolute deviation (MAD), appear nearly unaffected by the outlier and lead to $\hat{\mu}_{\text{median}} = 3.39, \hat{\mu}'_{\text{median}} = 3.37$, $\hat{\sigma}_{\text{MAD}} = 0.53$, $\hat{\sigma}'_{\text{MAD}} = 0.50$. This study case constitutes a nice example for the weakness of the normal model and the need for robust estimators. In the sequel, the basic working principles for robust estimators is explained, followed by a short description of relevant terms for robust statistics.

### 5.1.1 The Intuition Behind Robust Estimation

Let us bring back the one-dimensional location problem from Example 3, where a set of observations $y_i, i = 1, \ldots, n$ are distributed around the location $\mu$ and influenced by some noise $\nu_i$ as

$$y_i = \mu + \nu_i, \quad \text{for } i = 1, \ldots, n, \tag{5.1}$$

where $\mathbf{y}^\top = [y_1, \ldots, y_n]$ is the vector of observations and the errors $\nu_i$ are assumed independent and identical distributed (i.i.d.) and follow a distribution $F_0$. The likelihood function of the observations is given by

$$L\left(y_1, \ldots, y_n | \mu\right) = \prod_{i=1}^{n} f(y_i - \mu), \tag{5.2}$$

with $f(\cdot)$ the probability distribution function (pdf). At this stage, a classical estimator (i.e., MLE) for the location $\mu$ provides an estimate $\hat{\mu}$ based on the maximization of the likelihood, as

$$\hat{\mu} \triangleq \hat{\mu}(\mathbf{y}) = \arg\max_{\mu} L\left(y_1, \ldots, y_n | \mu\right), \tag{5.3}$$

and, if $F_0$ is exactly known, the MLE results optimal in the mean squared error (MSE) sense. The most well-known example relates to the Gaussian model, in which case $F_0 = \mathcal{N}\left(\mu, \sigma^2\right)$

and the pdf for the observations is given by

$$f(y_i|\mu,\sigma^2) = \frac{1}{\sqrt{2\pi\sigma^2}} \exp\left(-\frac{(y_i-\mu)^2}{2\sigma^2}\right). \tag{5.4}$$

Since $L(\mathbf{y}|\mu)$ is always positive, the maximization problem in (5.3) for the Gaussian model is equivalent to the following minimization

$$\hat{\mu}_{\textsf{mean}} = \arg\min_{\mu} \sum_{i=1}^{n} (r_i)^2\,, \tag{5.5}$$

$$\text{with } r_i = y_i - \mu, \tag{5.6}$$

where the residual, $r_i$, describes the difference between the $i$th observation and the estimate, and (5.5) corresponds to the celebrated LS adjustment (i.e., the minimization of the $\ell_2$ norm). Alternatively, if $F_0$ were the Laplace distribution, the pdf for the observation would correspond to

$$f(y_i|\mu,\sigma^2) = \frac{1}{\sqrt{2}\sigma} \exp\left(-\frac{\sqrt{2}\,|y_i-\mu|}{\sigma^2}\right), \tag{5.7}$$

whose MLE involves solving the following minimization

$$\hat{\mu}_{\textsf{median}} = \arg\min_{\mu} \sum_{i=1}^{n} |r_i|\,, \tag{5.8}$$

where (5.8) corresponds to minimizing the $\ell_1$ norm or the least absolute deviation (LAD) adjustment. For the one-dimensional problem, the sample mean (i.e., LS) and median (i.e., LAD) align with the MLEs for the normal and the Laplace distributions, respectively.

While LAD constitutes a robust estimator for the one-dimensional problem, it results evident that the LS adjustment (or the MLE at the normal model) results unbounded against out-of-distribution observations. As we saw in Example 3, a single outlier heavily impacted the estimate. Indeed, if an $k$th observation ($k \subseteq \{1,\ldots,n\}$) sit at a large distance from the distribution, its residual $r_k$ would greatly contribute to the norm $\sum_{i=1}^{n} r_i^2$. The quest for robust estimators resolves around deriving alternative functions $\rho(\cdot)$ for the minimization

$$\hat{\mu}_{\textsf{M}} = \min_{\mu} \sum_{i=1}^{n} \rho\left(\frac{r_i}{\sigma}\right), \tag{5.9}$$

with (5.9) the general form for the M-estimator, as introduced by Huber in his seminal work [149]. Hence, M-estimators result a generalization of MLEs, since one may set $\rho(x) = -\log\left(f(x)\right)$ to fit a particular density function (e.g., $\rho_{\ell_2}(x) = x^2/2$ and $\rho_{\ell_1}(x) = |x|$ are the MLEs at the normal and Laplacian distributions, respectively). Since M-estimators results fundamental to comprehend the overall intuition behind robust estimation –further estimators are presented in Section 5.2–, let us deepen into its working principle.

Provided that $\rho(\cdot)$ is symmetric and differentiable, its score or $\psi$-function is defined as

$$\psi(x) = \frac{d\rho(x)}{dx}, \tag{5.10}$$

and then equations for the M-estimation follow

$$\sum_{i=1}^{n} \psi\left(\frac{y_i-\mu}{\sigma}\right) = 0, \tag{5.11}$$

with $\psi(x)$ a bounded function which penalizes outliers in the observations. In practice, an M-estimator for the location can be thought of as a weighted mean. Assuming that $\psi(0) = 0$ and that $\psi'(0)$ exists, one typically resolves the M-estimation by using an artifact weighting function $w(x)$ defined as

$$w(x) = \begin{cases} \psi(x)/x, & \text{if} \quad x \neq 0 \\ 1, & \text{if} \quad x = 0 \end{cases}, \tag{5.12}$$

and then (5.11) can be reformulated as

$$\sum_{i=1}^{n} w\left(\frac{y_i - \mu}{\sigma}\right) \frac{y_i - \mu}{\sigma} = 0, \tag{5.13}$$

or directly

$$\hat{\mu}_{\mathsf{M}} = \frac{\sum_{i=1}^{n} w_i y_i}{\sum_{i=1}^{n} w_i}, \quad \text{with } w_i = w\left(\frac{y_i - \hat{\mu}_{\mathsf{M}}}{\sigma}\right), \tag{5.14}$$

which formulates the M-estimator as a weighted mean. Notice that the estimate $\hat{\mu}_{\mathsf{M}}$ appears explicitly on the weights and, therefore, the M-estimator constitutes an iterative procedure even for the simple location problem.

M-estimators are typically distinguished based on the shape of their $\psi$-functions as *monotone* and *redescending* M-estimators. The most representative monotone M-estimator is given by the Huber's family of functions

$$\rho_{\mathsf{Hub}}(x) = \begin{cases} x^2/2 & \text{if} \quad |x| \leq c_{\mathsf{Hub}} \\ c_{\mathsf{Hub}}|x| - \frac{1}{2}c_{\mathsf{Hub}}^2 & \text{if} \quad |x| > c_{\mathsf{Hub}} \end{cases}, \tag{5.15}$$

$$\psi_{\mathsf{Hub}}(x) = \begin{cases} x & \text{if} \quad |x| \leq c_{\mathsf{Hub}} \\ c_{\mathsf{Hub}}\mathsf{sign}(x) & \text{if} \quad |x| > c_{\mathsf{Hub}} \end{cases}, \tag{5.16}$$

$$w_{\mathsf{Hub}}(x) = \begin{cases} 1 & \text{if} \quad |x| \leq c_{\mathsf{Hub}} \\ c_{\mathsf{Hub}}/|x| & \text{if} \quad |x| > c_{\mathsf{Hub}} \end{cases}, \tag{5.17}$$

while the family of Tukey's bisquare functions is the most well-known example of redescending M-estimator

$$\rho_{\mathsf{Tuk}}(x) = \begin{cases} \frac{c_{\mathsf{Tuk}}^2}{6}\left(1 - \left(1 - (x/c_{\mathsf{Tuk}})^2\right)^3\right) & \text{if} \quad |x| \leq c_{\mathsf{Tuk}} \\ c_{\mathsf{Tuk}}^2/6 & \text{if} \quad |x| > c_{\mathsf{Tuk}} \end{cases}, \tag{5.18}$$

$$\psi_{\mathsf{Tuk}}(x) = \begin{cases} x\left(1 - (x/c_{\mathsf{Tuk}})^2\right)^2 & \text{if} \quad |x| \leq c_{\mathsf{Tuk}} \\ 0 & \text{if} \quad |x| > c_{\mathsf{Tuk}} \end{cases}, \tag{5.19}$$

$$w_{\mathsf{Tuk}}(x) = \begin{cases} \left(1 - (x/c_{\mathsf{Tuk}})^2\right)^2 & \text{if} \quad |x| \leq c_{\mathsf{Tuk}} \\ 0 & \text{if} \quad |x| > c_{\mathsf{Tuk}} \end{cases}, \tag{5.20}$$

where $c_{\mathsf{Hub}}$ and $c_{\mathsf{Tuk}}$ are control parameters to control the robustness and efficiency. For the limit cases $c_{\mathsf{Hub}}, c_{\mathsf{Tuk}} \to \infty$ and $c_{\mathsf{Hub}}, c_{\mathsf{Tuk}} \to 0$, both estimators correspond to the mean and the median, and otherwise they can be chosen to meet certain efficiency at a distribution model (e.g., $c_{\mathsf{Hub}} = 1.345, c_{\mathsf{Tuk}} = 4.685$ lead to a 95% relative efficiency at the normal model for the location problem).

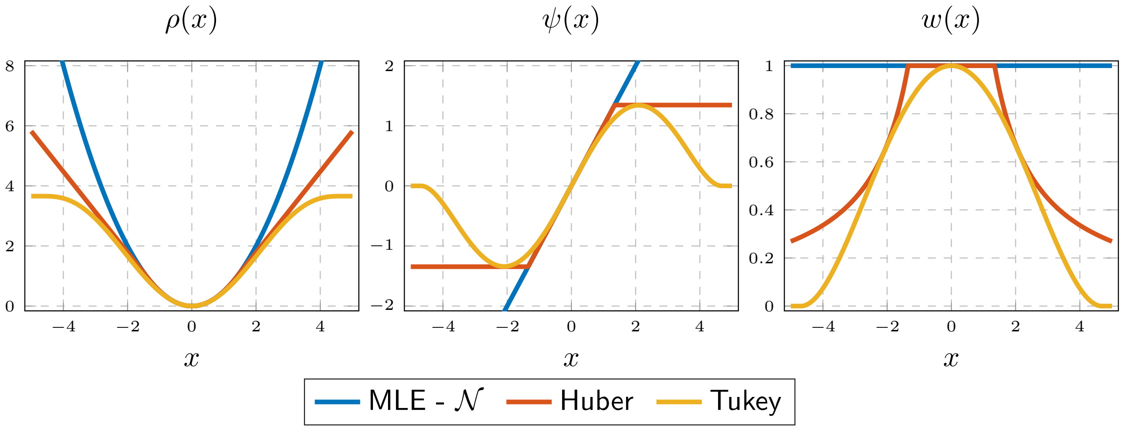

**Figure 5.2:** From left to right, illustration for the loss $\rho(\cdot)$, score $\psi(\cdot)$ and weighting $w(\cdot)$ functions for the MLE at the normal model and M-estimators based on the Huber's and Tukey's families of functions. Here, $c_{\text{Hub}} = 1.345$ and $c_{\text{Tuk}} = 4.685$ for a 95% efficiency at the Gaussian model.

Fig. 5.2 offers pictorial support to the aforementioned Huber and Tukey functions, while the MLE at the normal model is added for completeness. Notice that both M-estimators operate with inliers in a similar manner than the MLE, aiming at providing a near optimality to the normal model. One may rapidly realize that the Huber-based M-estimator is expected to have a higher efficiency at the normal model with respect to the Tukey-based one, since the $\rho, \psi$ and $w$ functions coincide with the LS for healthy measurements. Furthermore, the score $\psi$-function showcases how observations with large residuals affect the MLE in an unbounded manner and, subsequently, the possibility for the estimator to break down would occur given that a single sufficiently large outlier is present. The monotone M-estimator based on Huber would limit the influence of such an outlier, while a redescending M-estimator would nullify its effect. Clearly, monotone and redescending estimators present distinct characteristics: the first leads to convex optimization problems for (5.9) and, therefore, to a solution uniqueness; the second are fully bounded and provide a higher quantitative robustness at the cost of a non-convex optimization for (5.9) and a lower efficiency at the nominal model. Next, a 'dictionary' of terms related to robust estimation is introduced, including a list of metrics to characterize the properties of robust estimators.

### 5.1.2 Dictionary of Robust Statistical Terms

#### Contaminated distribution

As previously discussed, robust methods are yet subject to assumptions over the data distribution. In this context, the concept of approximate normality is essential, and it can be formalized by considering that a proportion $1 - \epsilon$ of the observations follows a normal model, while the complementary $\epsilon$ portion of the data is contaminated by an unknown (potentially) non-Gaussian distribution,

$$F = (1 - \epsilon)\, G + \epsilon H \tag{5.21}$$

where $G = \mathcal{N}(\mu, \sigma^2)$ is the nominal model and $H$ can be any distribution (for instance, another normal with larger variance). The model in (5.21) can be denoted as *contaminated normal distribution*, as the *Tukey-Huber* model after [148] or as *normal mixture* model when both $G$ and $H$ are Gaussians. Alternatively, one may use the so-called *heavy-tailed* or *fat-tailed* distributions, i.e., those whose fails tend to zero at a slower rate than the Gaussian distribution such as the Cauchy, Laplace or the Student-t distributions. Hereinafter, observations distributed according to $G$ will be referred to as *inliers* or healthy measurements, while $G$-distributed data will be denoted as outliers or contaminated observations.

### Relative Efficiency

The relative efficiency is the measure for "near optimality" for an estimator. Such a metric is defined for an exact noise model $F$ and a target estimator $\hat{\theta}(F)$ as the ratio in asymptotic variance between the optimal estimator (i.e., the MLE for the $F$ model) and the target estimator, as

$$\mathsf{Eff}\left(\hat{\theta}(F), F\right) = \frac{\mathsf{var}\left(\hat{\theta}_{\mathsf{MLE}}(F), F\right)}{\mathsf{var}\left(\hat{\theta}(F), F\right)}, \tag{5.22}$$

such that the efficiency is delimited by $0 \leq \mathsf{Eff}\left(\hat{\theta}(F), F\right) \leq 1$. Assuming an unbiased estimator $\hat{\theta}(F)$, the relative efficiency can be used as a measure for the MSE performance loss [178, Ch. 1], since

$$\mathsf{MSE}(\hat{\theta}(F), F) = \left(\mathsf{bias}(\hat{\theta}(F), F)\right)^2 + \mathsf{var}\left(\hat{\theta}_{\mathsf{MLE}}(F), F\right). \tag{5.23}$$

Thus, estimators with a high efficiency involve a small performance loss when the nominal model happens exactly. Unfortunately, explicit expressions for the relative efficiency do not generally exist (exceptions are the Huber-based M-estimator and the LAD for the location problem under normal distributed noise [158, Ch. 2.3]) and its characterization typically requires Monte Carlo approximations.

### Influence Function and Sensitivity Curve

The influence function (IF) constitutes a measure for "qualitative robustness" of an estimator [179]. The IF describes how an infinitesimal contamination $\varepsilon$ at an arbitrary point $z$ impacts an estimate working asymptotically at the model $F$, standardized by the fraction of contamination. The IF is defined as

$$\mathsf{IF}\left(z; \hat{\theta}, F\right) = \lim_{\varepsilon \to 0} \frac{\hat{\theta}_\infty\left((1-\varepsilon)F + \varepsilon\delta_z\right) - \hat{\theta}_\infty(F)}{\varepsilon}, \tag{5.24}$$

with $\hat{\theta}_\infty(F), \hat{\theta}_\infty\left((1-\varepsilon)F + \varepsilon\delta_z\right)$ denotes the asymptotic estimate under the nominal and contaminated distributions, respectively and $\delta_z$ is the point-mass probability at $z$. As graphical example, the $\psi$-functions in Fig. 5.2 for the location problem coincide with the IFs for the same estimators, for $\delta_z = x$ in the plot.

The sensitivity curve (SC) also constitutes a metric for qualitative robustness and can be thought of as the finite sample take on robustness [180]. The SC is defined based on the change experimented by an estimate $\hat{\theta}$ for a set of observations $\mathbf{y} = [y_1, \cdots, y_n]$ when adding an additional observation at $z$ and standardized by the number of observations, as

$$\mathsf{SC}\left(z, \hat{\theta}(\mathbf{y})\right) = (n+1) \cdot \left(\hat{\theta}\left(y_1, \cdots, y_{n-1}, z\right) - \hat{\theta}\left(y_1, \cdots, y_{n-1}\right)\right), \tag{5.25}$$

which is very similar to (5.24) for $\varepsilon = 1/(n+1)$. Indeed, it has been shown [181] that, for the location problem and an M-estimator with bounded and continuous score function, the SC is the limit version of the influence function

$$\text{given } \mathbf{y} \sim F,\ \mathsf{SC}(z, \hat{\theta}(\mathbf{y})) \rightarrow_{a.s.} \mathsf{IF}\left(z; \hat{\theta}, F\right), \tag{5.26}$$

where $a.s.$ denotes almost surely convergence.

### Breakdown Point

The breakdown point (BP) is the metric for quantitative robustness, introduced by Hampel in [182]. The BP of an estimator $\hat{\theta}$ is the largest amount of contamination that a set of data can contain such that $\hat{\theta}$ still provides *some* information about $\theta$ [158]. In plain words, the BP is the smallest percentage of contamination that causes an estimator to break down.

Later, the concept of BP on finite sets was introduced in [183]. Consider a set of $n$ observations $\mathbf{y}$ at the model $F$ and its associated estimate $\hat{\theta}(\mathbf{y})$. The BP on finite sets is defined as the minimal number $m$ of observations that, upon its replacement by arbitrary numbers, from the original $n$ observations lead to an infinite bias on the estimate:

$$\varepsilon_n^*\left(\hat{\theta}(\mathbf{y}), F\right) = \min\left\{\frac{m}{n}; \text{bias}\left(\hat{\theta}(\bar{\mathbf{y}}), F\right) \text{ is infinite}\right\}\ , \tag{5.27}$$

where $\bar{\mathbf{y}}$ is the vector of contaminated observations.

## 5.2 Linear Regression under Contaminated Models

Let us consider a linear regression problem, such that

$$y_i = x_{i,1}\theta_1 + \ldots, x_{i,p}\theta_p + \nu_i, \text{ for } i = 1, \ldots, n, \tag{5.28}$$

where $y_i$ denotes the $i$th observations, $x_{i,1} \ldots, x_{i,p}$ are the explanatory variables (also denoted predictors or covariates) that connect the measurements of the parameters $\theta_j, j = 1, \ldots, p$ and $\nu_1, \ldots, \nu_n$ are i.i.d. noises. Alternatively, in matrix-vector notation

$$\underbrace{\begin{bmatrix} y_1 \\ \vdots \\ y_n \end{bmatrix}}_{\mathbf{y}} = \underbrace{\begin{bmatrix} x_{1,1} & \ldots & x_{1,p} \\ \vdots & & \vdots \\ x_{n,1} & \ldots & x_{n,p} \end{bmatrix}}_{\mathbf{X}} \underbrace{\begin{bmatrix} \theta_1 \\ \vdots \\ \theta_p \end{bmatrix}}_{\boldsymbol{\theta}} + \underbrace{\begin{bmatrix} \nu_1 \\ \vdots \\ \nu_n \end{bmatrix}}_{\boldsymbol{\nu}}, \tag{5.29}$$

and $\mathbf{x}_i = [x_{i,1}, \ldots, x_{i,p}]$ is the vector of predictors for the $i$th observation. Similar to the location problem in Section 5.1.1, the estimation of the parameters $\boldsymbol{\theta}$ involves some type of minimization for the residual vector

$$\mathbf{r} \triangleq \mathbf{r}\left(\hat{\boldsymbol{\theta}}\right) = \mathbf{y} - \mathbf{X}\hat{\boldsymbol{\theta}}, \tag{5.30}$$

such as the well-known sum of squared residuals (or $\ell_2$ norm) or the sum of absolute residuals (or $\ell_1$ norm), both of which coincide with the MLE at the Gaussian and Laplace distributions –again, the LS and LAD estimators–, as

$$\hat{\boldsymbol{\theta}}_{\ell_2} = \arg\min_{\theta} \sum_{i=1}^{n} \left\| y_i - \mathbf{x}_i^\top \boldsymbol{\theta} \right\|^2, \tag{5.31}$$

$$\hat{\boldsymbol{\theta}}_{\ell_1} = \arg\min_{\theta} \sum_{i=1}^{n} \left| y_i - \mathbf{x}_i^\top \boldsymbol{\theta} \right|. \tag{5.32}$$

So far, the scale (or dispersion) $\sigma$ of the noise has been assumed known –as in (5.9)–, or its usefulness was limited for the minimization of the $\ell_1$ and $\ell_2$ norms (since the scale is factored out). Thus, a scale equivariant estimator replaces the assumed know scale in (5.9) with an estimate of it, $\hat{\sigma}$. In principle, one could be tempted on using the sample standard deviation as scale measure

$$\hat{\sigma}^2_{\mathsf{std}} = \frac{1}{n}\sum_{i=1}^{n}\left\|y_i - \mathbf{x}_i^\top \hat{\boldsymbol{\theta}}_{\ell_2}\right\|^2, \tag{5.33}$$

although the former lacks robustness and can be easily affected by outliers (as showcased in Example 3). Instead, one is interested in a *robust* scale estimate such as the normalized mean absolute deviation (MAD), given by

$$\hat{\sigma}_{\mathsf{MAD}} = b \cdot \mathsf{med}\left(|\mathbf{r} - \mathsf{med}(\mathbf{r})|\right), \tag{5.34}$$

where $b$ is a scaling factor to obtain a scale estimate consistent with a target distribution [178] (e.g., for the normal model, $b = 1.4826$).

Unlike the location problem, in linear regression two types of outliers can be distinguished:

- vertical outliers, which are observations whose noise component $\nu$ do not follow the noise distribution,
- leverage points, which correspond to observations whose predictors $\mathbf{x}_i$ lie far away from the bulk of covariates.

Fig. 5.3 depicts two real data examples, replicated from [184, Ch. 2], contaminated with outliers, as well as the LS and LAD estimates for both cases.

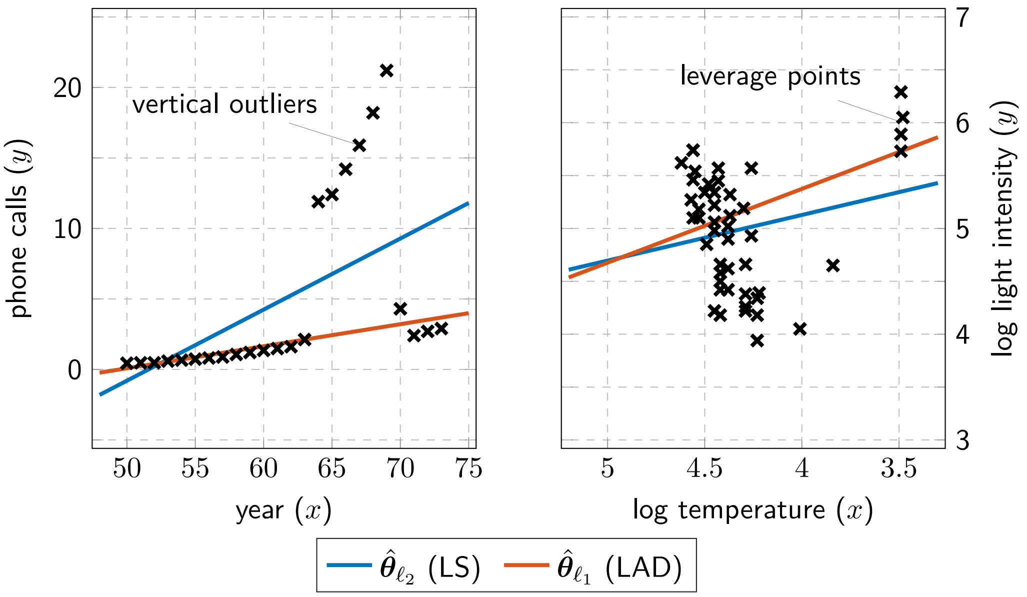

**Figure 5.3:** On the left, example of dataset contaminated with vertical outliers and the estimates for the linear regression based on LS and LAD estimators. On the right, dataset where leverage points are present and the estimates derived LS and LAD adjustments.

On the one hand, Fig. 5.3 left shows the number of international phone calls (in tens of millions) made in Belgium between 1950 and 1973, as published by the Belgian Statistical

Survey. While there was an upward trend over the years, the data collected over the period 1964 to 1969 results very intriguing and is, indeed, due to faulty measurements of the minutes of these calls (the years 1963 and 1970 were also partially affected). These faulty measurements are vertical outliers, since they only affect the measurements *per se*. On the other hand, Fig. 5.3 right illustrates an example from astronomy, containing information for the 47 the cluster CYG OB1. The effective temperature at the surface of the star (in logarithm scale) is shown on the ordinate and the logarithm of its light intensity on the abscissa. While observations for 43 stars lie on the same sequence, the data for the remaining four stars (which are giant stars) constitute leverage points, since their $x$ values (their temperature) lie far away from the bulk of temperatures from the other stars. It results evident that the MLE at the normal model (i.e., the LS solution) lacks robustness against both vertical outliers and leverage points. The MLE at the Laplace model (i.e., the LAD estimate) offers certain robustness against vertical outliers, since the Laplacian distribution presents heavier tails than the Gaussian one, while its performance given the presence of leverage points is as poor as for the LS estimator.

Turning our attention back to GNSS, we are most interested in robust estimators which protect against both vertical outliers and leverage points. The first constitutes the most common cause for contaminated observation within the GNSS context, related to the biases that multipath and NLOS induce into a pseudorange observation. An measurement being a leverage point does not necessarily make it a contaminated one. For instance, a satellite which strongly contributes to the geometry of the solution (e.g., when no other satellite is available around an azimuth direction) is a “good” leverage point as long as its noise follows the assumed underlying distribution. Ideally, a robust estimator should present a high relative efficiency at the normal model while attaining a high breakdown point and a bounded influence function. This section provides an short introduction to some of the most relevant robust estimators: generalized M-estimators, S-estimators and MM-estimators. All of them are scale, regression and affine equivariant, properties defined as

**Definition 6** (Scale Equivariance)**.** Let $\mathbf{X}$ be a $n \times p$ full rank matrix and $a$ a scalar value. Then, an estimate $\hat{\boldsymbol{\theta}}$ is scale equivariant if

$$\hat{\boldsymbol{\theta}}\left(\mathbf{X}, a \cdot \mathbf{y}\right) = a \cdot \hat{\boldsymbol{\theta}}\left(\mathbf{X}, \mathbf{y}\right). \tag{5.35}$$

It implies that the estimate is independent of the choice of measurement unit for the observations or re-scaling these.

**Definition 7** (Regression Equivariance)**.** Let $\mathbf{X}$ be a $n \times p$ full rank matrix and $\mathbf{a}$ a column vector. Then, an estimate $\hat{\boldsymbol{\theta}}$ is regression equivariant if

$$\hat{\boldsymbol{\theta}}\left(\mathbf{X}, \mathbf{y} + \mathbf{X}\mathbf{a}\right) = \hat{\boldsymbol{\theta}}\left(\mathbf{X}, \mathbf{y}\right) + \mathbf{a}. \tag{5.36}$$

Regression and translation invariance are similar concepts, applied to linear regression and multivariate location problems, respectively.

**Definition 8** (Affine Equivariance)**.** Let $\mathbf{X}$ be a $n \times p$ full rank matrix and $\mathbf{A}$ a nonsingular square matrix. Then, an estimate $\hat{\boldsymbol{\theta}}$ is affine equivariant if

$$\hat{\boldsymbol{\theta}}\left(\mathbf{X}\mathbf{A}, \mathbf{y}\right) = \mathbf{A}^{-1}\hat{\boldsymbol{\theta}}\left(\mathbf{X}, \mathbf{y}\right). \tag{5.37}$$

It implies that a linear transformation of the covariates (e.g., a change of basis) should transform the estimator accordingly.

### 5.2.1 Generalized M-Estimator

If one extends the M-estimation in (5.11) to the linear regression problem, one obtains the following minimization over the parameter vector $\boldsymbol{\theta}$

$$\hat{\boldsymbol{\theta}} = \arg \min_{\boldsymbol{\theta} \in \mathbb{R}^p} \sum_{i=1}^{n} \rho \left( \frac{y_i - \mathbf{x}_i^\top \boldsymbol{\theta}}{\hat{\sigma}} \right), \tag{5.38}$$

and making use of the derivative of $\rho(\cdot)$ leads to solving the following system of equations

$$\sum_{i=1}^{n} \psi \left( \frac{y_i - \mathbf{x}_i^\top \boldsymbol{\theta}}{\hat{\sigma}} \right) \mathbf{x}_i^\top = 0, \tag{5.39}$$

with $\hat{\sigma}$ a previously estimated robust scale. Within the scope of this work, we generally make use of the normalized MAD as an auxiliary scale. Whenever the joint regression and scale estimation is considered, the minimization problem is denoted as *Huber's criterion* and expressed as

$$\left\{ \hat{\boldsymbol{\theta}}, \hat{\sigma} \right\} = \arg \min_{\boldsymbol{\theta} \in \mathbb{R}^p, \sigma > 0} \left( 2 \cdot n \cdot \alpha \cdot \sigma + \sum_{i=1}^{n} \rho \left( \frac{y_i - \mathbf{x}_i^\top \boldsymbol{\theta}}{\sigma} \right) \right), \tag{5.40}$$

with $\rho(\cdot)$ assumed to be convex and differentiable and $\alpha$ a scaling factor so that the scale estimate results efficient at a certain distribution model [178, Ch. 2]. The computation of an S-estimate can be realized

Unfortunately, the criterion in (5.39) lacks robustness against leverage points. The generalized M-estimator intends at bounding the influence of outlying predictors $\mathbf{x}_i$ by applying some weighting function on it [185] replace the equations for the M-estimation in (5.39) by

$$\sum_{i=1}^{n} w(\mathbf{x}_i) \psi \left( \frac{r_i}{\hat{\sigma}} \right) \mathbf{x}_i^\top = 0, \tag{5.41}$$

and the choice of a redescending or monotone $\psi$-function and its control parameter allows balancing robustness and efficiency (as discussed earlier in Section 5.1.1). The computation of an M-estimate is generally performed via an Iteratively Reweighted Least Squares (IRLS) procedure. Thus, given the set of observations $\mathbf{y}$ and predictors $\mathbf{X}$, one realizes

1. Estimation of an initial scale invariant robust solution and its associated residuals, for instance via LAD, as: $\hat{\boldsymbol{\theta}}^{(0)} = \hat{\boldsymbol{\theta}}_{\text{LAD}}$, $\mathbf{r}^{(0)} = \mathbf{y} - \mathbf{X}\hat{\boldsymbol{\theta}}^{(0)}$.

2. Estimation of a robust auxiliary scale, for instance the normalized MAD, based on the initial estimate as: $\hat{\sigma} = b \cdot \text{med}\left( \left| \mathbf{r}^{(0)} - \text{med}(\mathbf{r}^{(0)}) \right| \right)$.

3. For $k = 1, 2, \ldots,$ until the convergence criteria is met, compute the weighting matrix $\mathbf{W} = \text{diag}(w_1, \ldots, w_n)$, with $w_i = w(r_i^{(k-1)}/\hat{\sigma})$ and perform a weighted LS adjustment $\hat{\boldsymbol{\theta}}^{(k)} = (\mathbf{X}^\top \mathbf{W} \mathbf{X})^{-1} \mathbf{X}^\top \mathbf{W} \mathbf{y}$.

Unfortunately, the generalized M-estimator is known to offer a low BP –of at most $1/(p+1)$ and without guarantees for this upper bound to be achieved [186]–. Next, estimators with higher breakdown point are discussed.

### 5.2.2 S-Estimator

The class of S-estimators derives from the Least Median of Squares (LMS) and the Least Trimmed Squares (LTS), both proposed by Rousseuw [187], while pursuing affine and scale equivariant estimators with high breakdown point and expressed as

$$\hat{\boldsymbol{\theta}}_{\mathsf{LMS}} = \arg\min_{\boldsymbol{\theta}\in\mathbb{R}^p} \mathsf{med}\left(\mathbf{r}\right), \tag{5.42}$$

$$\hat{\boldsymbol{\theta}}_{\mathsf{LTS}} = \arg\min_{\boldsymbol{\theta}\in\mathbb{R}^p} \sum_{i=1}^{h} \left(r_i\right)^2, \tag{5.43}$$

where the residuals in LTS are sorted such that $r_1^2 \leq \cdots \leq r_n^2$ and $h$ is chosen to attain a high BP (e.g., $h = n/2$ leads to a BP$= 0.5$). In a general form, S-estimators are those based on the minimization of a robust scale estimate for the residuals, as

$$\hat{\boldsymbol{\theta}}_{\mathsf{S}} = \arg\min_{\boldsymbol{\theta}\in\mathbb{R}^p} \hat{\sigma}\left(\mathbf{r}\right), \tag{5.44}$$

with $\hat{\sigma}\left(\mathbf{r}\right)$ a robust scale estimate. When $\hat{\sigma}\left(\mathbf{r}\right)$ is a scale M-estimator, the S-estimator consists on solving the next system of equations

$$\frac{1}{n}\sum_{i=1}^{n} \rho\left(\frac{\mathbf{r}}{\hat{\sigma}(\mathbf{r})}\right) = \delta, \tag{5.45}$$

where $\rho$ is bounded (e.g., Tukey's bisquare in (5.18)) and $\delta$ is a constant that balances consistency at a certain distribution and the BP (i.e., for maximum BP, $\delta = 0.5(1 - n/p)$). In terms of computation, LMS and LTS require drawing $N = \binom{n}{p}$ subsamples of $p$ number of observations and solving for the associated estimates $\hat{\boldsymbol{\theta}}^j$, for $j = 1, \ldots, N$. Then, the LMS and LTS estimates corresponds to the $j$th estimate to minimize (5.42) and (5.43), respectively. Although algorithms for the fast computation of LMS and LTS have been posed [188], the complexity rapidly grows both with $n$ and $p$ –they result as impractical as algorithms for solution separation in GNSS for large number of observations–. Alternatively, an approximate solution for the S-estimation minimization (5.44) can be solved via IRLS, as

1. Estimation of an initial scale invariant robust solution and its associated residuals, for instance via LAD, as: $\hat{\boldsymbol{\theta}}^{(0)} = \hat{\boldsymbol{\theta}}_{\mathsf{LAD}}$, $\mathbf{r}^{(0)} = \mathbf{y} - \mathbf{X}\hat{\boldsymbol{\theta}}^{(0)}$.

2. For $k = 1, 2, \ldots,$ until the convergence criteria is met, compute an M-scale $\hat{\sigma}^{(k)}$ with $\mathbf{r}^{(k-1)}$ via (5.45), the weighting matrix $\mathbf{W} = \mathsf{diag}(w_1, \ldots, w_n)$, with $w_i = w(r_i^{(k-1)}/\hat{\sigma}^{(k)})$ and perform a weighted LS adjustment $\hat{\boldsymbol{\theta}}^{(k)} = (\mathbf{X}^\top\mathbf{W}\mathbf{X})^{-1}\mathbf{X}^\top\mathbf{W}\mathbf{y}$.

where $\rho(\cdot)$ and $w(\cdot)$ belong to a family of redescending $\psi$-functions and the control parameter is set to a small value.

As with M-estimates, a high BP and relative efficiency cannot be achieved simultaneously: the S-estimator presents a BP of up to 50%, while its efficiency at the normal distribution is low. Interestingly, the S-Estimator in (5.44) corresponds to the joint scale and regression of an M-estimator in (5.40), with the difference that S-estimators typically consider the use of redescending score functions.

### 5.2.3 MM-Estimator

The MM-Estimator, introduced in [189], is designed to achieve both high relative efficiency and BP simultaneously. The idea resolves around employing two differently tuned redescending functions, such that $\rho_2 \leq \rho_1$, to minimize

$$\hat{\boldsymbol{\theta}}_{\mathsf{MM}} = \arg \min_{\boldsymbol{\theta} \in \mathbb{R}^p} \sum_{i=1}^{n} \rho_2 \left( \frac{y_i - \mathbf{x}_i^\top \boldsymbol{\theta}}{\hat{\sigma}_1} \right). \tag{5.46}$$

The computation of an MM-estimator can be seen as a two-step estimation:

1. Compute an S-estimate and its scale via (5.44) and (5.45) using $\rho_1$, with $\rho_1$ a redescending function tuned for high BP, to obtain an initial estimate $\hat{\boldsymbol{\theta}}^{(0)} = \hat{\boldsymbol{\theta}}_{\mathsf{S}}$ and $\hat{\sigma}_1$.

2. Compute (5.46) using a IRLS procedure with the previously computed $\hat{\boldsymbol{\theta}}^{(0)}$, $\hat{\sigma}_1$ and using a $\rho_2$ function tuned for high relative efficiency.

## 5.3 Robust Estimation for Code-based Positioning

Let us recall the code-based positioning problem as described in Section 1.4, which leads to the following nonlinear regression problem

$$\hat{\mathbf{x}} = \arg \min_{\mathbf{x} \in \mathbb{R}^p} \left\| \mathbf{y} - \mathbf{h}\left(\mathbf{x}\right) \right\|^2_{\boldsymbol{\Sigma}}, \tag{5.47}$$

with $\mathbf{y}^\top = [y_1, \dots, y_n]$ a vector of code pseudorange observations and $\mathbf{x}^\top = [\mathbf{p}, cdt], p = 4$ the vector of unknown parameters and $h_i(\cdot)$ the observation model in (1.24). The observations are typically assumed to *exactly* follow a Gaussian model, $\mathbf{y} \sim \mathcal{N}(h(\mathbf{x}), \boldsymbol{\Sigma})$, with perfectly known covariance matrix $\boldsymbol{\Sigma}$ and predictors (i.e., the position of the satellites).

Whenever the aforementioned assumptions are fulfilled, a MLE for the normal model provides an optimal solution in the MSE sense. Indeed, all parametric (and Bayesian!) estimators discussed so far in this thesis related to GNSS work under this principle: - the signal parameter estimation (time-delay, carrier phase offset, frequency shift, etc.) performed in parallel at each channel of a receiver in Section 1.2; - the SPP based on code observations in Section 1.4; - the RTK mixed model estimation in Section 2.1; - the GNSS-based attitude model in Section 3.3 and the JPA model in Section 4.2. As discussed during the introductory part of this chapter, it results complicated justifying the *exact* Gaussian distribution of data and the applications of GNSS are no exception: the presence of multipath and NLOS is a clear example of a scenario in which the assumption of normal model is violated. Laying our attention on code-based SPP –applications based on the use of carrier phase observations are discussed in Chapter 6, while robust signal processing at the receiver level is out of the scope of this thesis–, robust estimation faces distinct challenges with respect to the location and linear regression problems, namely

**Nonlinear optimization.** Unlike linear regression, the computation of (5.47) cannot be directly approach via LS adjustment even for the normal model. For nonlinear equations, there can be no solution, any number of solutions or an infinite amount of them [190, Ch. 18]. Fortunately, thanks to the convexity of the GNSS problem and its generally rich geometry, local search procedures such as Gauss-Newton (GN) algorithm allows for solving (5.47) in only a few iterations despite the initial point of search (for instance, the center of the Earth). Combining nonlinear and robust regression involves a concatenated iterative procedure: one would first provide an initial estimate via GN search, then proceed with an GN-IRLS procedure for which a robust regressor estimates a weighting matrix and an estimate is solved applying GN.

**Low-redundant or "fat" datasets.** While the examples typically discussed for robust linear regression present a rather large number of observations and a low amount of unknowns (i.e., a ratio of $n/p$ of at least 10), data redundancy is limited in SPP. Especially when working with a single frequency, one often faces the situation of tracking under a dozen of satellites while estimating four parameters (i.e., a ratio $n/p < 3$). Thus, if outliers are present for such a finite dataset, the performance of robust estimators strongly decay. Notice that scale estimate for fat datasets may require a correction term, as discussed in [191].

**Not independent nor identical noise distributions.** The i.i.d. assumption cannot be employed for GNSS observations since one would expect, for instance, that satellites with higher elevation present smaller errors than those with lower elevation. Therefore, proposing scale invariant estimators requires a double standardization: first, the observations' residuals are normalized based on the covariance matrix $\mathbf{\Sigma}$; second, the normalized residuals are standardized based on a robust estimate of their dispersion or scale $\hat{\sigma}$.

As example, Algorithm 3 describes the computation procedure for an MM-estimator at the SPP problem. Besides the set of observations and associated covariance matrix, it is required a choice of loss functions ($\rho_1$, $\rho_2$ from which the associated weighting functions $w_1$, $w_2$ are derived) and their tuning parameters (in case those loss functions are configured solely on one parameter, as Huber and Tukey, $c_1$ and $c_2$ respectively). Here, GN refers to the iterative local search process described in 1.4.

**Algorithm 3:** Robust SPP via MM-Estimator

```
Input  : Observations $\mathbf{y}, \mathbf{\Sigma}$; MM-estimator configuration $(\rho_1, \rho_2, c_1, c_2, w_1, w_2, \delta)$
Output : Robust estimate $\hat{\mathbf{x}}, \hat{\mathbf{P}}$
Compute an initial estimate $\hat{\mathbf{x}}^{(0)}$ and $\mathbf{H}$, via GN from (1.37),(1.38)
Initialize S-estimate: $\hat{\mathbf{x}}_{\mathsf{S}}^{(0)} = \hat{\mathbf{x}}^{(0)}$
for $k = 1, 2, \ldots$ until convergence do S-estimate via IRLS
    Compute standarized residuals:
    $\bar{\mathbf{r}}^{(k)} = \mathbf{\Sigma}^{-1/2}(\mathbf{y} - \mathbf{h}(\hat{\mathbf{x}}_{\mathsf{S}}^{(k-1)}))$
    Compute M-scale: $\hat{\sigma}_{\mathsf{M}}^{(k)} \leftarrow 1/n \sum_{i=1}^{n} \rho_1(\bar{\mathbf{r}}/\hat{\sigma}_{\mathsf{M}}^{(k)}) = \delta$
    Compute weighting matrix: $\mathbf{W} = \mathrm{diag}(v_1, \ldots, v_n), v_i = w_1(\bar{r}_i^{(k)}/\hat{\sigma}_{\mathsf{M}}^{(k)})$
    Compute estimate: $\hat{\mathbf{x}}_{\mathsf{S}}^{(k)}$ via GN and WLS with $\hat{\mathbf{x}}_{\mathsf{S}}^{(k-1)}, \mathbf{W}$
Initialize MM-estimate with S-estimate: $\hat{\mathbf{x}}_{\mathsf{MM}}^{(0)} = \hat{\mathbf{x}}_{\mathsf{S}}^{(k)}, \hat{\sigma} = \hat{\sigma}_{\mathsf{M}}^{(k)}$
for $k = 1, 2, \ldots$ until convergence do MM-estimate via IRLS
    Compute standarized residuals: $\bar{\mathbf{r}}^{(k)} = \mathbf{\Sigma}^{-1/2}\left(\mathbf{y} - \mathbf{h}(\hat{\mathbf{x}}_{\mathsf{MM}}^{(k-1)})\right)$
    Compute weighting matrix: $\mathbf{W} = \mathrm{diag}(v_1, \ldots, v_n), v_i = w_2(\bar{r}_i^{(k)}/\hat{\sigma})$
    Compute estimate: $\hat{\mathbf{x}}_{\mathsf{MM}}^{(k)}$ via GN and WLS with $\hat{\mathbf{x}}_{\mathsf{MM}}^{(k-1)}, \mathbf{W}$
Return $\hat{\mathbf{x}} = \hat{\mathbf{x}}_{\mathsf{MM}}^{(k)}, \hat{\mathbf{P}} = (\mathbf{H}^{\top}\mathbf{\Sigma}^{-\top/2}\mathbf{W}\mathbf{\Sigma}^{-1/2}\mathbf{H})^{-1}$
```

**Example 4** (MLE and M-estimates for an SPP problem under contamination)**.** Consider the skyplot described in Section 5.4, where ten satellites are tracked ($n = 10$). This example serves to illustrate the importance of convexity in loss functions and whether monotone (convex) or redescending (non-convex) alternatives shall be used. Under the afore-described geometry, nine observations are assumed to follow the nominal Gaussian distribution with a low variance (i.e., observations are i.i.d. and their standard deviation is 0.1 m) while the observation from satellite G17 constitutes an outlier due to an induced bias of 30 meters. In this example, it is compared the performance of the MLE at the normal model (i.e., the LS) with two M-estimators: one uses the monotone Huber family of functions (5.15) with $c_{\mathsf{H}} = 1.345$, and the other employs the redescending Tukey bisquare functions (5.18) with $c_{\mathsf{T}} = 4.685$.

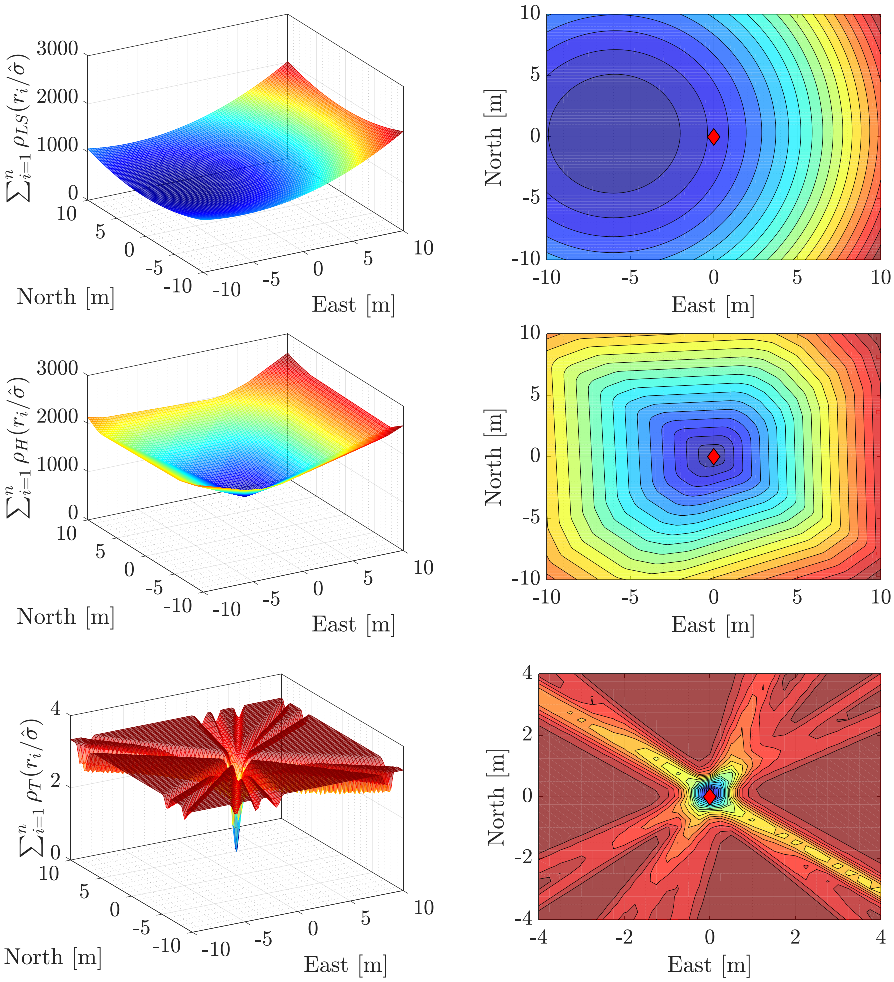

**Figure 5.4:** Surface (left column) and contour (right column) plot of the minimization functions for the SPP problem, projected in the East-North frame. From top to bottom, solutions for the MLE, M-estimate with Huber function ($c = 1.345$) and M-estimate with Tukey function ($c = 4.685$).

Fig. 5.4 depicts the surface (on the left) and the contour (on the right) for the MLE, M-Huber, and M-Tukey minimization functions. While the MLE and M-Huber present a "nice" convex optimization with a single minimum and a guarantee for uniqueness and stability, the M-Tukey clearly depicts the issue of non-convexity optimization with an almost infinite number of possible solutions. In the latter case, one realizes the importance of the initial estimate, since the redescending solver could lead to a biased solution (due to a local minimum) or to a lack of convergence (due to jumps between different local minima). Laying our attention to the right part of Fig. 5.4, one can assess the differences in positioning performance across robust and non-robust estimators, which solutions are marked with a red rhomboid. The MLE showcases how a single bias can drag the estimate towards the wrong direction. On the other hand, both M-estimates manage to mitigate the effect of the outlier and their solution is unaffected. Still, redescending robust estimates are extremely useful, especially for those cases where high percentage of data are contaminated or when the outliers present extremely large biases.

### 5.3.1 Relative Efficiency for Robust SPP Estimators

As we have described through out this Chapter, MLE are optimal whenever the underlying noise distribution is followed exactly, while the need for robust estimators is more than justified due to the constant appearance of outliers in real data. Next, it is described an extension of the relative efficiency presented in Section 5.1.2 for the multi-dimensional point positioning problem.

Since SPP constitutes a real-valued parameter estimation, it is well-known that the MSE for the WLS (i.e., the MLE at the normal model) is given by the estimated covariance matrix, given by

$$\hat{\mathbf{P}}_{\mathcal{N}} = \left(\mathbf{H}^{\top}\boldsymbol{\Sigma}^{-1}\mathbf{H}\right)^{-1}, \tag{5.48}$$

which provides the minimal MSE error for the vector of unknowns $\mathbf{x}$ in (5.47)

$$\mathsf{MSE}\left(\hat{\mathbf{x}}_{\mathcal{N}}\right) = \mathsf{tr}\left(\hat{\mathbf{P}}_{\mathcal{N}}\right), \tag{5.49}$$

since the MLE at (5.47) is unbiased. Thus, for any other suboptimal (robust) estimator $\hat{\mathbf{x}}$ for the distribution $\mathbf{y} \sim \mathcal{N}(\mathbf{h}(\mathbf{x}), \boldsymbol{\Sigma})$, the expression for relative efficiency reads

$$\mathsf{Eff}\left(\hat{\mathbf{x}}, \mathbf{y}\right) = \frac{\mathsf{MSE}\left(\hat{\mathbf{x}}_{\mathcal{N}}\right)}{\mathsf{MSE}\left(\hat{\mathbf{x}}\right)} = \frac{\mathsf{tr}\left(\hat{\mathbf{P}}_{\mathcal{N}}\right)}{\mathsf{tr}\left(\hat{\mathbf{P}}_{\mathcal{N}}\right) + \|\mathsf{bias}\left(\hat{\mathbf{x}}\right)\|^{2}}, \tag{5.50}$$

with $0 \leq \mathsf{Eff}\left(\hat{\mathbf{x}}, \mathbf{y}\right) \leq 1$. While robust estimators are seemingly unbiased and their covariance estimates given by

$$\hat{\mathbf{P}} = (\mathbf{H}^{\top}\boldsymbol{\Sigma}^{-\top/2}\mathbf{W}\boldsymbol{\Sigma}^{-1/2}\mathbf{H})^{-1}, \tag{5.51}$$

the weighting matrix $\mathbf{W}$ is not known beforehand and it is dependent on the initial point estimate. Thus, the denominator terms in (5.50) are unknown and no closed form solution can be obtained, and the efficiency is to be approximated via Monte Carlo sampling.

## 5.4 Results on Robust Estimation for Code-based Positioning

This section address the performance characterization for robust estimators at the SPP problem. Particularly, Section 5.4.1 reports a set of simulated experiments to highlight certain aspects of these estimators and provide further insights on their application to GNSS SPP. Additionally, we provide results with an experimental dataset using real data recorded over harsh propagation conditions in Section 5.4.2.

### 5.4.1 Simulated Environment

The performance of robust estimators is compared to that of an optimal MLE, based on a synthetic experimentation. Two simulation scenarios are considered: a single constellation, single frequency case with ten observations available, and a multi-constellation case for a total of $n = 40$ observations. For the latter, each constellation is considered to have an independent clock offset and thus the number of unknowns $p = 7$. The contaminated normal mixture distribution in (5.21) is used, and it is studied both the fraction of contamination $\varepsilon$ and the magnitude $\alpha$ of such corrupted observations, as indicated in Table 5.1. Overall, a total of 42 experiments are studied, and the performance characterization is obtained via Monte Carlo experimentation with $10^4$ runs. Besides the WLS, the following estimators are considered: *i)* M-estimator based on the Huber; *ii)* S-estimator based on the Tukey function; and *iii)* MM-estimator with Tukey ($\rho_1$) and Huber functions ($\rho_2$). In all cases, the control parameters are chosen so that a 95% efficiency at the normal model is achieved and the M-scale for the S- and MM-estimators target a maximum BP of 40%.

**Table 5.1:** Parameters configuration for the Monte Carlo simulation.

| **Simulation parameters** | |
|---|---|
| Number of satellites | $n \in \{10, 15, \ldots, 40\}$ |
| Percentage of outliers | $\varepsilon \in \{0, 10, 30, 40\}$ |
| Outlier magnitude | $\alpha \in \{1, 3, 6, 10, 30, 60, 100\}$ |
| Robust parameters | $c_{\mathsf{H}} = 1.345, c_{\mathsf{T}} = 4.685, \delta = 0.4 \cdot (1 - p/n)$ |
| **Single-constellation scenario setup** | |
| UTC time | $15/05/2017\ 09:30$ |
| Location | Koblenz, Germany<br>(50°21′56″ N, 7°35′55″ E) |
| PDOP | 1.72 |

The vector of observation errors $\boldsymbol{\nu}$ stacks the errors for the inlier $\boldsymbol{\nu}_{\mathsf{in}}$ and outlier $\boldsymbol{\nu}_{\mathsf{out}}$ observations, which are distributed as follows

$$\boldsymbol{\nu} = \left[\boldsymbol{\nu}_{\mathsf{in}}^{\top}, \boldsymbol{\nu}_{\mathsf{out}}^{\top}\right]^{\top}, \ \boldsymbol{\nu}_{\mathsf{in}} \sim \mathcal{N}\left(0, \sigma^2\right), \ \boldsymbol{\nu}_{\mathsf{out}} \sim \mathcal{N}\left(0, (\alpha \cdot \sigma)^2\right),$$

where the standard deviation of the nominal observations is 2 m. For each Monte Carlo run, the selection of contaminated observations is realized at random. For the scenario with $n = 10$, the geometry of the satellites corresponds to the skyplot of Fig. 5.5. For the multi-GNSS case, ten observations were simulated across four constellations, with the satellites' position obtained from random samples of azimuth, elevation, and satellite-receiver distance (i.e., azimuth $\sim \mathcal{U}(0, 2\pi)$, elevation $\sim \mathcal{U}(0, \pi/4)$, and distance $\sim \mathcal{N}(20.200\,(\mathrm{km}), 2.000\,(\mathrm{km}^2))$).

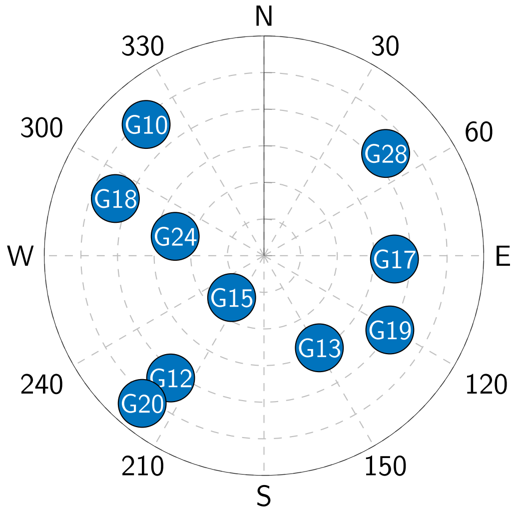

**Figure 5.5:** Skyplot for the single constellation simulation $n = 10$.

Fig. 5.6 depicts the performance of the estimators under evaluation, showing the positioning RMSE on the ordinate axis against the amplification of the outliers' noise. The first and second row in Fig. 5.6 correspond to the single and multi constellation cases, respectively. Moreover, the fraction of contamination $\varepsilon$ increases from 10% to 40% from left to right. A common element across all cases is, the absolute lack of robustness of ML estimates, whose RMSE is dictated by the large errors in the outliers. Laying on the focus on $\varepsilon = 10\%$, all M-, S- and MM-estimators showcase their robustness by neglecting the effects of outliers regardless of their magnitude and number of observations. The latter is interesting, since it appears that, even for $n = 10$, the redundancy is high enough to spot the single outlying observation.

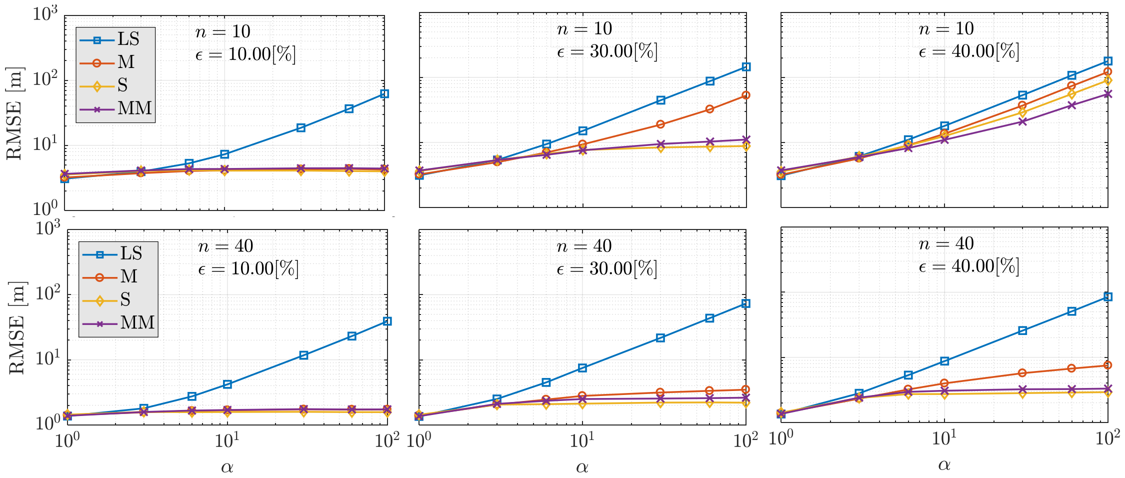

**Figure 5.6:** RMSE positioning error for $\varepsilon \in \{10, 30, 40\}\%$ contamination data (each column) and for $n \in \{10, 40\}$ (single- and multi-constellation cases, respectively) pseudorange observations (each row).

For the second column of images in Fig. 5.6, one starts appreciating differences among the robust estimators, with the S- and MM- solutions remaining nearly unaffected, meaning that their BP is numerically shown to be over 30% for this geometry. On the other hand, the M estimator breaks down for the single constellation case, meaning that its BP is lower than 30%. Finally, let us examine the third column, for a fraction of contamination $\varepsilon = 40\%$. On the one hand, for $n = 10$ all robust methods break down, meaning that the S- and MM-estimators presents a BP which oscillates between the 30 and 40% for such a geometry. On the other hand, for $n = 40$ the S- and MM- estimators are capable of successfully bounding the effects of outliers for the multi-constellation scenario, since the large number of measurements provide with sufficient data redundancy (notice the rate $n/p$, which corresponds to 2.5 and 5.7 for the single- and multi-constellation scenarios, respectively). Insofar, Monte Carlo approximation allows us to withdraw some conclusions over the qualitative and quantitative robustness properties of the M-, S-, and MM-estimators: *a)* all estimators have smooth influence functions (i.e., smooth changes when increasing the location of the outliers) since the random selection of the outlier recreates the SC analysis and, with a total of $42^4$ experiments, one may think of this simulation as a limit case; *b)* redescending S- and MM-estimators present a high BP for the SPP problem, although this BP is strongly conditioned on the redundancy of observations.

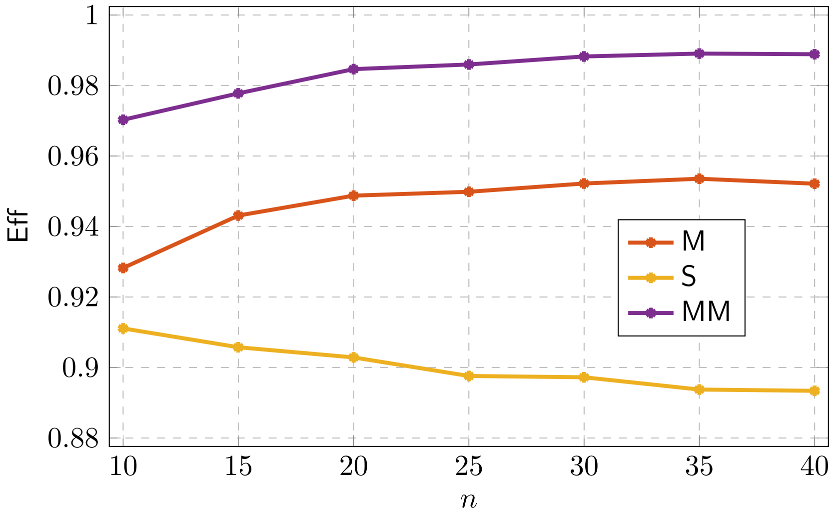

**Figure 5.7:** Relative efficiency of estimators at the normal model as a function of the number of observations.

Next, the focus is laid on the relative efficiency of robust estimators at the nominal Gaussian case—e.g., when no outlying observations are present–. Fig. 5.7 depicts the efficiency of the estimators, as defined in Section 5.3.1. As expected, the S-estimator constitutes the least efficient among the evaluated methods, with its efficiency decreasing as the number of measurements grows. On he contrary, the MM-estimator exhibits the closest performance to the MLE at the normal model and it might be taken as efficient at such model. Note that the MM-estimator's efficiency escalates with the number of observations, making it an appealing option for prospective multi-frequency. multi-constellation scenarios. Overall, one can conclude that the MM-estimator exhibits a great trade-off between robustness (i.e., high breakdown point) and high relative normal efficiency (i.e., similarity to the MLE under Gaussian distributed errors).

It becomes evident that robust methods, especially the MM estimator, represent a promising alternative to traditional ML or LS-based GNSS positioning. Especially for a near future, in which multiple GNSS constellations will be fully deployed and a large number of observations will be made available, robust methods can assure great resilience against satellite faults at a cost of minimal efficiency loss, as shown below.

### 5.4.2 Experimentation under Real Harsh Conditions

After numerical experimentation to characterize the performance of robust estimators for code-based positioning and discussing on their properties, this section provides an analysis under real harsh-propagation conditions. As the MM-estimator was undoubtedly the most promising among the evaluated robust methods and to simplify the discussion, the performance for the MM-estimator is compared against the conventional SPP based on LS adjustments.

The data collection was performed for an automotive scenario. The test vehicle was equipped with a geodetic antenna and receiver (navXperience 3G+C and Javad Delta, respectively), as illustrated on the left side of Fig. 5.8 (left). The experiment was carried out on 15 May 2019 (DOY 135, UTC 10:00–18:00), covering a distance of roughly 800 km from Koblenz to Neustrelitz (Germany), as shown on the right side of Fig. 5.8. Along the path, a wide variety of harsh propagation conditions were encountered: urban navigation, high-speed highways, national roads under forest foliage, bridge passing, etc. Thus, the capability of the MM estimator for dealing with corrupted observations can be consistently evaluated on real multipath and NLOS conditions. The ground truth reference trajectory is estimated upon a dual-frequency GPS+GLONASS PPP solution. Unfortunately, the PPP estimates are unavailable for the most challenging situations (e.g., tunnel or bridge crossing) and, consequently, those epochs are discarded from the study.

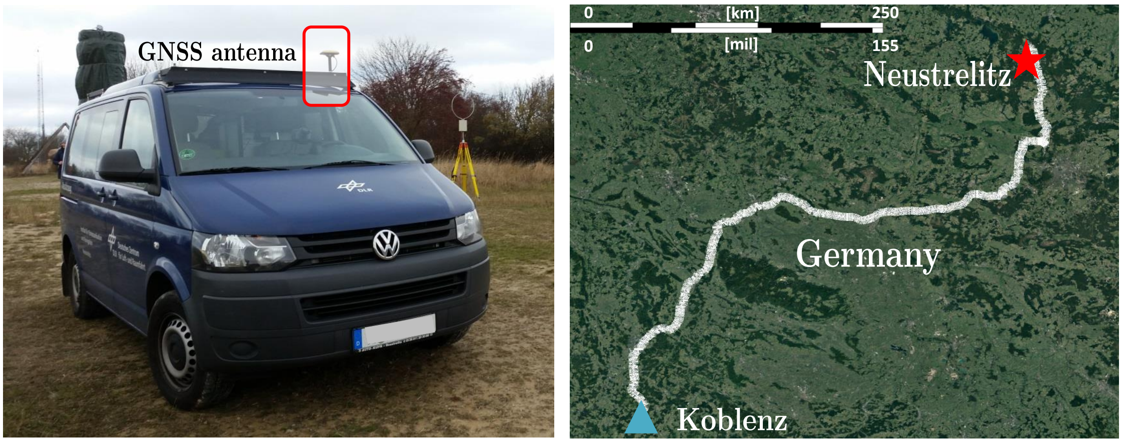

**Figure 5.8:** Experimental setup for the evaluation of robust code-based positioning under real conditions. On the left, the tracked vehicle and a highlight for the position of the antenna. On the right, the route traversed during the data collection, with starting and finish points in the cities of Koblenz and Neustrelitz (Germany), respectively.

The estimation of the code-based positioning is based on GPS and Galileo observations on the L1 frequency, with an elevation mask of $5°$. The time evolution for the number of tracked satellites and the Position Dilution of Precision (PDOP) is shown in Fig.5.9 (bottom left). The combination of GPS and Galileo grants the availability of radio-navigation for around $96.5\%$ of time, with often satellite tracking losses due to signal reflection and blockage.

Fig. 5.9 (top left) depicts the norm of the three-dimensional positioning errors along the duration of the campaign for the LS and MM estimators. For the majority of the studied epochs, in which nominal open-sky conditions for GNSS navigation apply, LS and MM present an equivalent performance, which aligns with the previously-discussed MM-estimator's efficiency at the normal model. This statement is further supported from the results shown on the right side of Fig. 5.9, which illustrates the distribution for the positioning errors. For errors under five meters, which constitute the majority of the results, LS and MM exhibit

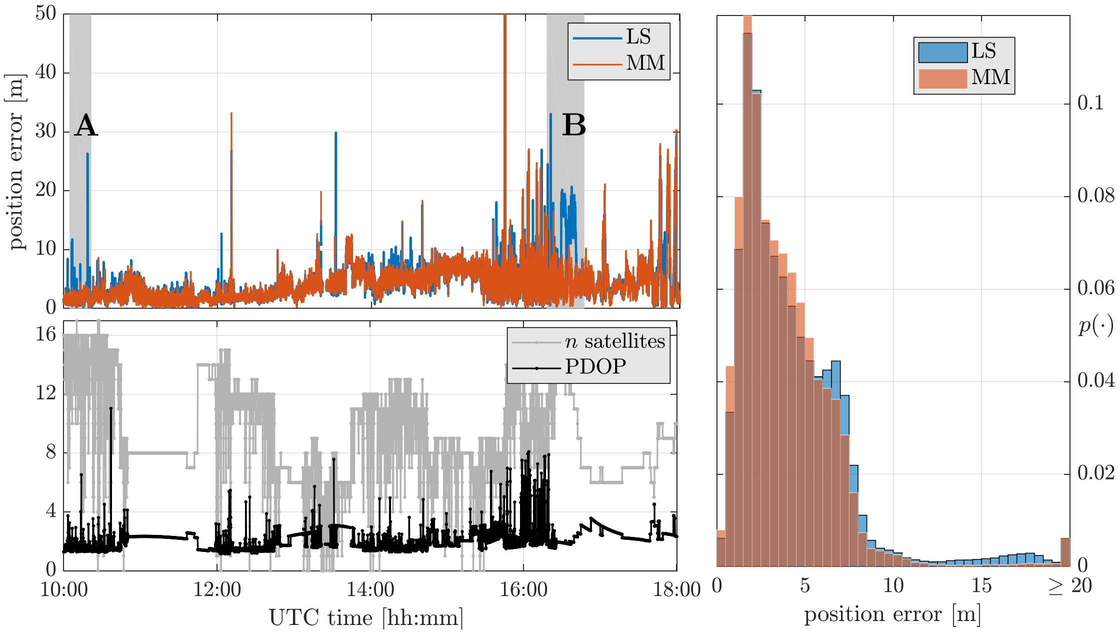

**Figure 5.9:** On the bottom left, number of tracked satellites over GPS and Galileo constellations and the corresponding PDOP. On the top left, norm of the positioning errors for MLE and MM estimators over time, with a gray shadow to emphasize two particular time spans (denoted as A and B). On the right, histogram for the norm of the positioning errors.

a similar performance, with the MM even being slightly better. While the MLE presents a large population of positioning errors between 10 and 20 m, the MM estimator is capable of mitigating the vast majority of these. The largest positioning errors (taking place immediately after 12:00 and around 15:30) cannot be delat with neither by LS or the MM estimators. This is consequence of a rather reduced satellite visibility from which several observations are contaminated with NLOS and multipath effects.

For a better illustration on the robustness of the MM estimator, the two time spans “A” and “B” are highlighted with a grayish area in Fig. 5.9. These periods have a duration of $15$ and $30$ minutes, respectively and are shown with more detail in Fig. 5.10. For greater clarification, pictures taken from the target vehicle during these instances are included. Part A occurs during highway navigation, from which a succession of eight small bridges are present. For this case, the MM-estimator offers robustness and becomes unaffected by multipath and NLOS effects. Then, part B corresponds to a national road surrounded by dense tree foliage, the latter inducing damps on the received satellite signals. Once again, the MM-estimator prevents the outlying effects that, on the other hand, induce positioning errors of over 20 m on the MLE estimator.

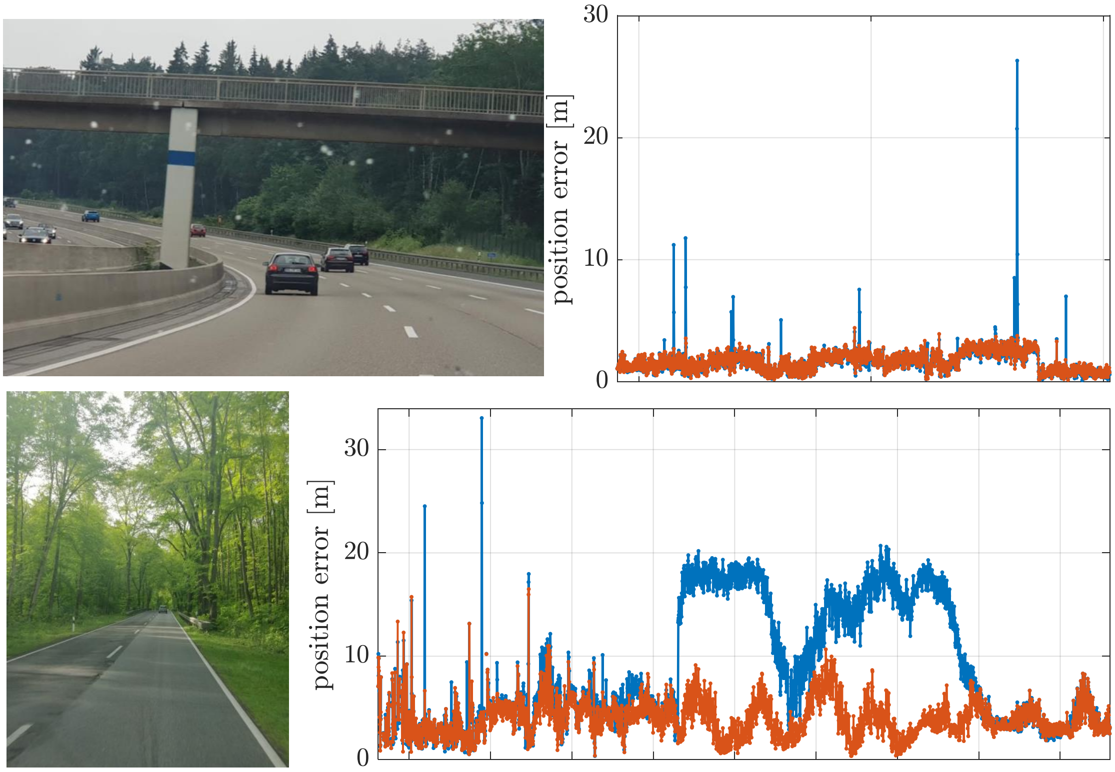

**Figure 5.10:** Detail on the time spans A and B for the measurement campaign. Solid blue and orange lines corresponds to the LS and MM estimators, respectively. The first row (time span A) corresponds to bridge passing during highway navigation, while the second raw (time span B) occurs during national road navigation under tree foliage. The pictures on the left were taken from the vehicle during the measurement campaigns, while the figures on the right depict the norm of positioning errors over time.

## 5.5 Summary

Following the quest of providing precise navigation for intelligent vehicles, it is indispensable using algorithms resilient against adverse signal propagation conditions. This chapter presents the basics of Robust Statistics, a mathematical framework for the development of estimators which are not bounded by exact assumptions on the noise distributions. The weaknesses related to conventional statistical procedures, such as MAP or ML estimation, have been widely recognized across multiple fields of applications, with satellite-based navigation being no exception. Thus, this section presents a short historical remark on the reasoning and development of Robust Statistics, the working principles of robust estimators and their characteristics.

One of the major drawbacks of the aforementioned estimation procedures relates to not knowing the expected performance of estimators beforehand. In other words, one may expect certain relative efficiency or breakdown point from a specific algorithm although its analytical or formal behavior remains uncertain in advance. The contribution of this chapter relates to exploring the performance of robust estimators for non-recursive positioning and their characterization via Monte Carlo experimentation. Thus, Section 5.3 discusses the specific challenges related to using robust estimators for code-based positioning. In particular, the nonlinear form of SPP involves complicated non-convex optimization procedures in which the initialization and choice for score function play a fundamental role. Moreover, the standard use of single frequency and/or constellation implies a low redundancy of observations, which strongly affects the chances for mitigating the effects of contaminated measurements.

Section 5.4 addresses the aforementioned performance characterization for robust estimators for the SPP problem. With a simulated environment and via Monte Carlo experimentation, redescending estimators (S and MM) showcase a breakdown point of up to 30% for a single frequency, single constellation scenario while, for the same study case, the monotone M-estimator breakdown point is only of 10%. For scenarios where data redundancy is much higher, the S- and MM-estimators increase their robustness of up to 40% and offer a bounded sensitivity curve, reason why even extremely large outliers do not impact the resulting estimates. In terms of efficiency at the normal model, the MM-estimator stands out among the other evaluated robust procedures, with an efficiency of over 98% which scales with a growing number of observations.

The results presented in this chapter were partially published in:

**Journal articles:**

[10] Medina, D., Li, H., Vilà-Valls, J., & Closas, P. (2019). Robust statistics for GNSS positioning under harsh conditions: A useful tool?. *Sensors, 19*(24), 5402.

**Conference articles:**

[16] Medina, D., Li, H., Vilà-Valls, J., & Closas, P. (2019, October). On Robust Statistics for GNSS Single Point Positioning. In *2019 IEEE Intelligent Transportation Systems Conference (ITSC)* (pp. 3281-3287). IEEE.

[169] Pozo-Pérez, J. A., Medina, D., Herrera-Pinzón, I., Heßelbarth, A., & Ziebold, R. (2017). Robust Outlier Mitigation in Multi-Constellation GNSS Positioning for Waterborne Applications. In *Proceedings of the International Technical Meeting of The Institute of Navigation (ITM 2017)* (Vol. 64, No. 2, pp. 1330-1343). ION Publications.

CHAPTER 6

# Robust Filtering for Carrier Phase-Based Positioning

STATE estimation is a fundamental task in a plethora of fields, ranging from robotics, guidance and navigation systems, to information fusion or time-series analysis. While the Kalman Filter is well-known for providing an optimal MSE solution for linear dynamic SSMs under normal distributed noises, its performance is conditioned to certain conditions: *known system matrices*, *known noise statistics* and *perfect initialization*. A major problem is the lack of robustness against impulsive, heavy-tailed noises (i.e., outliers), which may lead to infinitely large biases or cause the filter to break down. This chapter advances the previously discussed robust estimation for code-based positioning and extends it to carrier phase-based navigation under the presence of contaminated observations. Thus, alternatives to conventional Gaussian filters for discrete state-space systems are presented in the form of families of KF based on Robust Statistics and Variational Inference. It is discussed the distinct challenges related to the recursive solutions for the mixed model and multi-antenna configurations for JPA estimation under contaminated distributions, with estimators such as the GM-based KF or the Variational-based KF being introduced for this context. The application of the proposed robust filtering solutions to carrier phase-based navigation is of great interest for the deployment of prospective intelligent vehicles, aiming at increasing the availability, accuracy and resilience of navigation solutions in urban and other harsh signal conditions.

## Outline

As discussed during Chapter 5, the presence of multipath and other impulsive noises disrupts the noise assumption of conventional ML and MAP estimators, losing their optimality and strongly degrading their performance. Similarly to point or deterministic regression and beyond the framework of Robust Statistics, the research community has invested monumental efforts for the development of robust filtering solutions for an innumerable number of applications. Thus, the literature on robust filtering is vast and an extensive overview of the former is beyond the scope of this thesis. Interested readers may consult the review works from [192] for an extensive overview for works earlier than 1985, or [159], [193] and therein for more recent approaches.

While the KF constitutes the standard recursive estimator for navigation purposes, providing optimal solutions for linear Gaussian SSMs in the MSE sense, its performance is very sensitive to the presence of outliers. The squared error criterion is overly sensitive to non-Gaussian observations and yields boundlessly large errors as the measurements are pulled further from the mode. Hereinafter, robust filtering alternatives are discussed. Thus, a robust filter shall pose similar characteristics than those of a robust point estimator, in terms of near optimality, qualitative and quantitative robustness: *i)* the errors for the state estimate shall remain bounded even if an outlying observation grows arbitrarily; *ii)* the effect of an outlier shall not spread over time by the SSM dynamics; *iii)* the residual sequence shall remain nearly white when the observations follow the nominal Gaussian distribution except for occasionally occurring outliers. In general, one may distinguish the following filtering perspectives to deal with deviations from the model assumptions:

**Nonparametric methods** — These techniques do not require any assumption on data belonging to a parametric probability distribution. Exemplary methods for nonparametric recursion include the running median filter [194], the myriad filter [195], [196] or the inference via Dirichlet Process Mixtures [197], [198].

**Bayesian methods** — When the noises are assumed to follow a certain family of parametric probability distribution function, such that the estimators can be derived in a Bayesian framework. Thus, latent variables to model such distributions belong to the state estimate, with their prior updated with the incoming observations. Bayesian methods can be further distinguished based on whether the normal assumption is or not considered:

- **Gaussian approaches** — The observations are believed to follow a Gaussian distribution of unknown covariance matrix. Thus, one can resort to innovation-based techniques [199], e.g., Interactive Multiple Models (IMM) [200] or adaptive filtering [201], [202], or variational Bayesian (VB) inference [203]–[205].
- **Non-Gaussian approaches** — The underlying noise distribution is assumed to be heavy-tailed (i.e., the Student $t$-distribution, both for skewed or symmetric cases) and a filtering solution can be obtained via VB approximations [206], [207], or by exploiting a hierarchically Gaussian formulation to obtain approximate Gaussian filtering solutions. For the latter it is possible to use Rao-Blackwellization [208], conjugate prior analysis [209] or for linear systems to resort again to VB approximations [210]–[214].

**Robust Statistical methods** — Also known as *minimax* approaches, these techniques arise from the framework of Robust Statistics and the assumption of contaminated distributions (i.e., a $1-\varepsilon$ portion of data follows the nominal Gaussian distribution, and the remaining $0 \leq \varepsilon \leq 1$ observations are contaminated and follow an unknown distribution). Thus, a filter based on robust statistics shall present a decent performance at the nominal model and against deviations from the same. The conventional way for solving these type of filters consists on reformulating the standard KF as a recursive robust regression problem which can be solved via M-optimization [215]–[217].

**Hypothesis Testing methods** — A simple approach for dealing with outliers consists on their detection via statistical test and the application of a posterior conventional KF over the "cleaned" data. Examples of deletion diagnostics include test derived from robust statistics or the uncomplicated $3\sigma$ rule (i.e., outliers whose residuals exceed three times their associated standard deviations are removed) [218], [219]. Alternatively, a probabilistic outlier rejection method was recently proposed in [220], where the goal is to have a binary indicator to determine whether the vector of observations belongs to the nominal noise distribution.

Within the context of GNSS-based navigation, neither nonparametric nor Bayesian methods are of particular interest and are disregarded in the remaining of this chapter. The justification for discarding these filtering options is clear: *a)* the normal distribution for nominal GNSS observations are well-studied and described precisely (as discussed in Section 1.3.1), making nonparametric and Bayesian methods for unknown Gaussian distributions irrelevant; *b)* the stochastic characterization for pseudorange measurements contaminated with multipath or other outlying errors remains an unexplored research topic, making Bayesian filtering at a particular parametric non-Gaussian distribution a suboptimal, since such noise model is unknown.

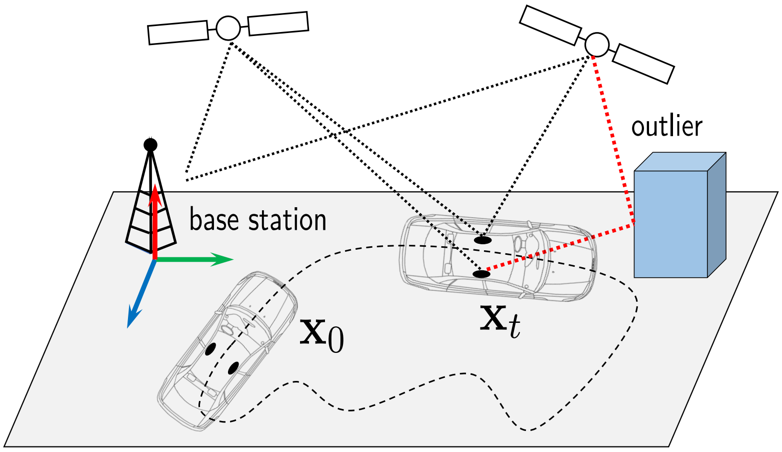

**Figure 6.1:** Graphical representation for the problem addressed in this chapter: GNSS-based precise navigation under multipath or other outlying observations.

In this chapter, the focus is towards the elaboration of filtering solutions based on robust statistical procedures and variational inference (VI) for hypothesis testing approaches. Then, the methodology related to the two aforementioned techniques is particularized both for carrier phase-based positioning and for navigation in multi-antenna configurations, as illustrated in Fig. 6.1. The contribution of this chapter is two-fold: on the one hand, the adaptation of well-known Robust Statistics-based filtering techniques for the mixed estimation problem. On the other hand, a novel Variational-based technique for detecting individual faulty satellite links is introduced. The performance of these two methods is addressed analytically, by means of a Monte Carlo simulation, and with actual data collected on a signal-degraded scenario.

## 6.1 Robust Statistics-based Filtering Approaches

Let us consider the KF update step from the MAP perspective [221], leading to the following optimization procedure

$$\hat{\mathbf{x}}_t = \arg\min_{\mathbf{x}_t} \left( \left\| \mathbf{x}_t - \hat{\mathbf{x}}_{t|t-1} \right\|^2_{\mathbf{P}_{t|t-1}} + \left\| \mathbf{y}_t - \mathbf{h}\left(\mathbf{x}_t\right) \right\|^2_{\mathbf{\Sigma}_t} \right). \tag{6.1}$$

Provided that the observations follow a perfectly known normal distribution and for a linear system (i.e., $\mathbf{h}(\mathbf{x}_t) = \mathbf{H}_t\mathbf{x}_t$), the KF provides with the minimum MSE estimate. While nonlinear systems can be addressed with the extensions of KF, such as EKF or CKF, to provide a quasi-optimal solution, the presence of impulsive non-Gaussian errors could potentially spoil the estimation or lead to large biases.

Let us now focus on the recursive forms for the carrier phase-based models (for positioning, attitude and JPA, respectively),and the MAP to ML equivalence discussed in Section 2.2.1. Thus, estimating parameters belonging to real, integer and manifold spaces requires a three step decomposition, from which only a successful integer estimation grants high precision over the positioning and attitude solutions. Since the existence of robust integer estimators is not known, the key towards carrier phase-based resilient navigation concentrates on the first ML adjustment. In other words, one shall only concern with applying robust filters for the float solution estimation.

The framework of Robust Statistics provides with score functions to mitigate the effect of outliers present in the vector of observations. Thus, the filtering problem in (6.1) can be instead expressed as

$$\hat{\mathbf{x}}_t = \arg\min_{\mathbf{x}_t} \left( \left\| \mathbf{x}_t - \hat{\mathbf{x}}_{t|t-1} \right\|^2_{\mathbf{P}_{t|t-1}} + \left\| \mathbf{y}_t - \mathbf{h}\left(\mathbf{x}_t\right) \right\|^2_{\bar{\mathbf{\Sigma}}_t} \right), \tag{6.2}$$

where $\bar{\mathbf{\Sigma}}_t$ is the estimated covariance matrix of the observations based on certain weighting functions, as

$$\bar{\mathbf{\Sigma}}_t = \mathbf{\Sigma}_t^{1/2}\mathbf{W}^{-1}\mathbf{\Sigma}_t^{\top/2}, \tag{6.3}$$

where $\mathbf{\Sigma}_t^{1/2}$ is obtained from the Cholesky factorization of $\mathbf{\Sigma}_t$ and $\mathbf{W}$ is a weighting matrix given by

$$\mathbf{W} = \text{diag}\left[\mathbf{w}\left(\mathbf{\Sigma}_t^{-1/2}(\mathbf{y}_t - \mathbf{h}(\mathbf{x}_t))\right)\right], \tag{6.4}$$

where $\mathbf{w}(\cdot)$ is a function derived from a robust score function $\psi(\cdot)$, as defined in Section 5.1.1. As afore-discussed, families of score functions can be distinguished as monotone or redescending based on their shape. The basic idea is to mitigate or nullify the effect of observations not fitting the underlying noise model. Fig. 6.2 complements some of the robust functions in Fig. 5.2 by including the Institute of Geodesy and Geoinformation (IGG) [216, Eq. (7)] and the $3\sigma$ rule functions, with the score and weighting functions on the left and right, respectively.

In the context of filtering, one shall distinguish between *innovation outliers*, which affect the state estimate during the prediction step and propagate over time, and *additive outliers*, which are present on the observations at the correction stage. While additive outliers are the most source of disturbances for GNSS-based navigation, occasional mismatches on the dynamical model applied during the filter propagation (i.e., on the prediction) can also be considered as a relevant source of errors. This would happen, for instance, when a vehicle is assumed to move with constant speed while in reality a strong acceleration or deceleration

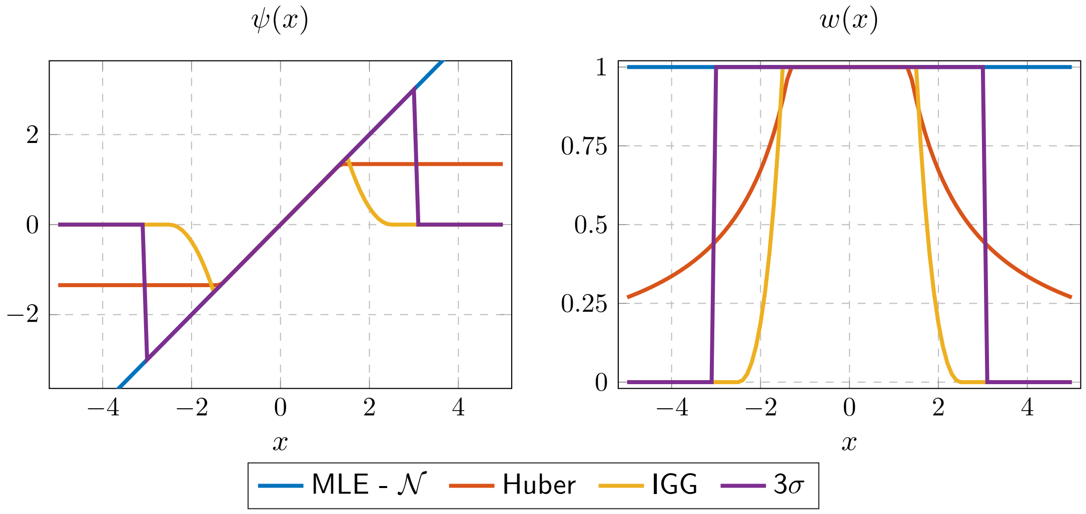

**Figure 6.2:** Robust score $\psi(\cdot)$ and weighting $w(\cdot)$ functions, on the left and right respectively, which are typically applied for robust filtering (in this case, the MLE at the normal model corresponds to the conventional KF update step). The tuning parameters is as follows $c_{\text{Hub}} = 1.345$, $c_{\text{Tuk}} = 4.685$ and $c_{\text{IGG},0} = 1.5$, $c_{\text{IGG},1} = 2.5$.

is taking place. Within the robust statistics-based filtering solutions, one can distinguish between resilience against outliers in the correction step (as for Robust Information Filters) or against outliers in both prediction and correction step (as for Generalized M-estimator KF). Next, these two methods are described.

### 6.1.1 Robust Information Filters

The information filter (IF) is an algebraically equivalent form of the KF, where instead of the state vector and covariance matrix, the filter propagates the so-called information vector, $\mathbf{z}_t = \mathbf{P}_t^{-1}\mathbf{x}_t$, and information matrix, $\mathbf{Z}_t = \mathbf{P}_t^{-1}$. While the IF is primarily used for large-scale and distributed filtering [222], its application to other fields is due to [216], which proposed the RIF as an unified framework for robust filtering based on the M-estimate.

Thus, given a nonlinear filtering problem, the conventional IF update step [223], [224] is adapted for RIF, such that an iterative procedure to down-weight possible additive outliers is performed until certain convergence criteria is reached

$$\mathbf{z}_{t|t} = \mathbf{z}_{t|t-1} + \mathbf{H}_t^\top \boldsymbol{\Sigma}_t^{-\top/2}\ \mathbf{W}\ \boldsymbol{\Sigma}_t^{-1/2} \left(\mathbf{y}_t - \mathbf{h}(\mathbf{x}_{t|t-1}) + \mathbf{H}_t \mathbf{x}_{t|t-1}\right) , \tag{6.5}$$

$$\mathbf{Z}_{t|t} = \mathbf{Z}_{t|t-1} + \mathbf{H}_t^\top \boldsymbol{\Sigma}_t^{-\top/2}\ \mathbf{W}\ \boldsymbol{\Sigma}_t^{-1/2} \mathbf{H}_t. \tag{6.6}$$

This formulation results particularly interesting for robust filters which employ "aggressive" weighting functions. Hence, the use of such redescending functions (where the weights can become zero) may cause numerical issues within the standard robust regression KF, due to matrix inversion. Instead, the RIF formulation makes possible avoiding these numerical issues and still exploit redescending cost functions.

### 6.1.2 Robust Kalman Filter based on Generalized M-estimation

As discussed during in Section 2.2.1, the KF update is equivalent to a LS adjustment. Besides the usefulness of this equality for formulating recursive estimators for the mixed model, such a LS form can be thought of as a regression problem for which one may apply a robust estimators, such as the ones introduced in Section 5.2. Thus, [225] introduces the robust KF based on the generalized M-estimator. Unlike RIFs, the GMKF provides resilience against both innovation and additive outliers, since the predicted state estimate is considered as an additional "observation" for a regression problem, modeled by the predicted covariance matrix.

Let us recall Section 2.2.1 and the definition for the "augmented" vector of observations, defined as

$$\tilde{\mathbf{y}}_t = \begin{bmatrix} \mathbf{y}_t \\ \mathbf{x}_{t|t-1} \end{bmatrix}, \ \tilde{\boldsymbol{\Sigma}}_t = \begin{bmatrix} \boldsymbol{\Sigma}_t & \\ & \mathbf{P}_{t|t-1} \end{bmatrix}, \ \tilde{\mathbf{H}}_t = \begin{bmatrix} \mathbf{H}_t \\ \mathbf{I}_{n+p} \end{bmatrix},$$

with $p$ the dimension of the state estimate, $n$ the total number of ambiguities. Thus, a robust KF update for a linear SSM results in the following regression:

$$\mathbf{x}_{t|t} = \left(\tilde{\mathbf{H}}_t^\top \tilde{\boldsymbol{\Sigma}}_t^{-\top/2} \ \tilde{\mathbf{W}} \tilde{\boldsymbol{\Sigma}}_t^{-1/2} \ \tilde{\mathbf{H}}_t\right)^\dagger \tilde{\mathbf{H}}_t^\top \tilde{\boldsymbol{\Sigma}}_t^{-\top/2} \ \tilde{\mathbf{W}} \tilde{\boldsymbol{\Sigma}}_t^{-1/2} \ \tilde{\mathbf{y}}_t, \tag{6.7}$$

where $\tilde{\mathbf{W}}$ is estimated via (6.4) for the vector of observations $\tilde{\mathbf{y}}$. Once the convergence is reached, the covariance matrix of the associated estimate is as

$$\mathbf{P}_{t|t} = \left(\tilde{\mathbf{H}}_t^\top \tilde{\boldsymbol{\Sigma}}_t^{-\top/2} \ \tilde{\mathbf{W}} \tilde{\boldsymbol{\Sigma}}_t^{-1/2} \ \tilde{\mathbf{H}}_t\right)^\dagger. \tag{6.8}$$

Unfortunately, the recursion in (6.7) is only valid for uncorrelated observations. While that assumption may be justified for certain applications, it definitely does not hold for GNSS-based precise navigation since code and carrier phase observations are highly correlated (due to the double difference operator with respect to the base station and master antennas, for positioning and attitude problems respectively). Instead, one may perform an eigenvalue decomposition and change the basis, such that

$$\breve{\mathbf{y}} = \mathbf{Q}^\top \tilde{\mathbf{y}}, \ \breve{\mathbf{H}} = \mathbf{Q}^\top \tilde{\mathbf{H}}, \text{ with } \tilde{\boldsymbol{\Sigma}} = \mathbf{Q} \boldsymbol{\Lambda} \mathbf{Q}^\top, \tag{6.9}$$

where the accent $\breve{\cdot}$ indicates vectors or matrix in the new basis, $\boldsymbol{\Lambda}$ is a diagonal matrix populated by the eigenvalues and $\mathbf{Q}$ is the orthogonal matrix whose columns correspond to eigenvectors (i.e., $\mathbf{Q}^\top = \mathbf{Q}^{-1}$, since the covariance matrix $\bar{\boldsymbol{\Sigma}}$ is real and symmetric) . Therefore, the GMKF recursion for correlated observations is expressed as

$$\mathbf{x}_{t|t} = \left(\breve{\mathbf{H}}_t^\top \boldsymbol{\Lambda}_t^{-\top/2} \ \breve{\mathbf{W}} \boldsymbol{\Lambda}_t^{-1/2} \ \tilde{\mathbf{H}}_t\right)^\dagger \breve{\mathbf{H}}_t^\top \boldsymbol{\Lambda}_t^{-\top/2} \ \breve{\mathbf{W}} \tilde{\boldsymbol{\Lambda}}_t^{-1/2} \ \breve{\mathbf{y}}_t. \tag{6.10}$$

Unlike RIFs, applying the GMKF involves realizing in operations over the weighting matrix, leading to potential numerical issues whenever redescending functions are used. Moreover, since more "observations" (the actual observations and the predicted state estimate) are being weighted, the search space for the robust mechanism grows and leads to a slight poorer performance for the case when outliers are present only during the correction stage. Nonetheless, the GMKF is able to offer resilience against innovation outliers, which is key for SSMs whose dynamical models are uncertain or require integrating observations which are potentially contaminated (e.g., if an inertial sensor is defect and only returns default messages).

## 6.2 Filtering via Variational Inference Hypothesis Testing

A fundamentally different approach, in comparison to robust statistics-based filtering, consists on the detection and elimination of additive outliers (observations' outliers) via hypothesis testing. Taking aside conventional statistical testing procedures, VB inference techniques [226], [227] constitute a promising line of research to perform outlier detection and deletion. Initially proposed by [220], the VI-based KF consists on estimating the pdf for an auxiliary binary variable that describes the chance for outliers to be present among the vector of observations. This thesis contributes with the generalization of the original work of [220], in which a single indicator would indicate the presence or not of outliers, by introducing a binary indicator per observation [18], and the extension for correlated observations [5].

The underlying idea for robust filters based on hypothesis testing consists on recursively estimating the probability for outliers to be present and then exclude those corrupted observations. The SSM formulation of the problem is as follows:

$$\mathbf{x}_t = \mathbf{f}\left(\mathbf{x}_{t-1}\right) + \mathbf{w}_t \tag{6.11}$$

$$\mathbf{y}_t = \begin{cases} \mathbf{h}\left(\mathbf{x}_t\right) + \boldsymbol{\eta}_t & \text{, under } \mathcal{M}_0 \\ \mathbf{h}\left(\mathbf{x}_t\right) + \boldsymbol{\eta}_t + \mathbf{o}_t & \text{, under } \mathcal{M}_1 \end{cases} \tag{6.12}$$

where $\mathbf{w}$ is the process noise, $\mathbf{w} \sim \mathcal{N}\left(\mathbf{0}, \mathbf{Q}_t\right)$, the vector of observations' noise is $\boldsymbol{\eta}_t \sim \mathcal{N}\left(\mathbf{0}, \boldsymbol{\Sigma}_t\right)$ and $\mathbf{o}_t$ describes the vector of additive outliers whose distribution is unknown. The null hypothesis ($\mathcal{M}_0$) corresponds to the nominal conditions, in which observations' noise are distributed according to a known normal distribution, while the alternative hypothesis ($\mathcal{M}_1$) indicates the presence of one or more outliers.

Let us denote with $\boldsymbol{\zeta}_t$ the vector of binary indicators that determine whether the $i$th observation is an inlier ($\zeta_t^i = 1$) or an outlier ($\zeta_t^i = 0$), formally described as

$$\boldsymbol{\zeta}_t = \left[\zeta_t^{(1)}, \ldots, \zeta_t^{(n)}\right]^\top, \; \boldsymbol{\zeta}_t \in \mathcal{Z} = \{0,1\}^n, \tag{6.13}$$

where note that here $n$ corresponds the total number of observations (not to be confused with the amount of tracked satellites). Thus, instead of approximating the usual posterior distribution $p(\mathbf{x}_t|\mathbf{y}_t)$, one adds the aforementioned vector of indicators and aim at estimating the posterior of $p(\mathbf{x}_t, \boldsymbol{\zeta}_t|\mathbf{y}_t)$, whose approximation is obtained by resorting to VI techniques. Thus, the observation model conditional on the indicators becomes

$$p\left(\mathbf{y}_t|\mathbf{x}_t, \boldsymbol{\zeta}_t\right) = \mathcal{N}\left(\mathbf{h}\left(\mathbf{x}_t\right), \boldsymbol{\Sigma}_t\right)^{\boldsymbol{\zeta}_t}, \tag{6.14}$$

$$= \frac{1}{c\left(\boldsymbol{\zeta}_t\right)} \exp\left(-\frac{1}{2}\left\|\mathbf{y}_t - \mathbf{h}(\mathbf{x}_t)\right\|^2_{\boldsymbol{\Sigma}_t(\boldsymbol{\zeta}_t)}\right), \tag{6.15}$$

where the observations' covariance matrix conditioned on the binary indicators is defined as

$$\boldsymbol{\Sigma}_t\left(\boldsymbol{\zeta}_t\right) = \begin{bmatrix} \sigma^2_{1,1}/\zeta_t^{(1)} & \sigma^2_{1,2} & \cdots & \sigma^2_{1,n} \\ \sigma^2_{2,1} & \sigma^2_{2,2}/\zeta_t^{(2)} & \cdots & \sigma^2_{2,n} \\ \vdots & \vdots & \ddots & \vdots \\ \sigma^2_{n,1} & \sigma^2_{n,2} & \cdots & \sigma^2_{n,n}/\zeta_t^{(n)} \end{bmatrix}, \tag{6.16}$$

which corresponds to dividing the diagonal terms of the original $\boldsymbol{\Sigma}_t$ matrix by the vector of outlier indicators and where the time dependency on the observations' deviations has been omitted for simplicity. Contrarily to what one would expect, the division by zero in (6.14) does not cause numerical issues due to the algorithm operating on the precision matrix. Indeed, the exponent of the likelihood can be equivalently formulated as

$$||\mathbf{y}_t - \mathbf{h}(\mathbf{x_t})||^2_{\boldsymbol{\Sigma}_t^{-1}(\boldsymbol{\zeta}_t)} = ||\mathcal{T}(\mathbf{y}_t - \mathbf{h}(\mathbf{x_t}), \boldsymbol{\zeta}_t)||^2_{\mathbf{C}_t^{-1}(\boldsymbol{\zeta}_t)} \tag{6.17}$$

where $\mathcal{T}(\cdot, \mathbf{z}_t) : \mathbb{R}^n \mapsto \mathbb{R}^{n'}$ is an operator that removes the elements in the input vector corresponding to zero-valued indicators. Similarly, the matrix $\mathbf{C}(\mathbf{z}_t)$ is a transformation of $\boldsymbol{\Sigma}_t(\boldsymbol{\zeta}_t)$ where the rows and columns corresponding to zero values in $\boldsymbol{\zeta}_t$ are removed. Special cases are $i)$ $\mathbf{C}(\mathbf{1}) = \boldsymbol{\Sigma}_t(\mathbf{1}) = \boldsymbol{\Sigma}_t$ (i.e., whenever no outliers are detected and the complete vector of observations is exploited); $ii)$ $\mathbf{C}(\mathbf{0})$, corresponding to the absence of healthy measurements and defined as $\mathbf{C}(\mathbf{0}) = \mathbf{I}$. Therefore, the dimension of the resulting multivariate normal variable $(n')$ is effectively reduced by the amount of outlier indicators: $n' = \sum_{i=1}^{n} \zeta_t^{(i)} \leq n$, with equality when no outliers are detected. Moreover, the proportionality term $c(\mathbf{z}_t)$ in (6.14) will depend on the dimension of the outlier-free vector of observations and their covariance $\mathbf{C}(\mathbf{z}_t)$, as

$$c(\mathbf{z}_t) = \sqrt{(2\pi)^{n'}|\mathbf{C}(\mathbf{z}_t)|}\,. \tag{6.18}$$

Taking into account the aforementioned dimensionality adjusments, the likelihood distribution in (6.14) can also be expressed as

$$\begin{aligned} p\left(\mathbf{y}_t|\mathbf{x}_t, \boldsymbol{\zeta}_t\right) &= \mathcal{N}\left(\mathbf{h}\left(\mathbf{x}_t\right), \boldsymbol{\Sigma}_t\right)^{\boldsymbol{\zeta}_t}, & (6.19)\\ &= \mathcal{N}\Big(\mathcal{T}(\mathbf{y}_t, \boldsymbol{\zeta}_t);\ \mathcal{T}(\mathbf{h}(\mathbf{x}_t), \boldsymbol{\zeta}_t), \mathbf{C}(\boldsymbol{\zeta}_t)\Big). & (6.20) \end{aligned}$$

As a consequence of introducing the vector of binary indicators $\boldsymbol{\zeta}_t$, one needs to estimate these along with the state estimate $\mathbf{x}_t$. To accomplish this task in a Bayesian sense, a beta-Bernoulli hierarchical prior is imposed for each individual indicator as

$$p\left(\zeta_t^{(i)}|\pi_t^{(i)}\right) = \left(\pi_t^{(i)}\right)^{\zeta_t^{(i)}} \left(1 - \pi_t^{(i)}\right)^{1-\zeta_t^{(i)}}, \tag{6.21}$$

where $\pi_t^{(i)}$ is a beta distributed random variable parameterized by the (unknown) hyper-parameters$e_0^{(i)}$ and $f_0^{(i)}$) whose pdf is expressed by[1]

$$p\left(\pi_t^{(i)}\right) = \frac{\left(\pi_t^{(i)}\right)^{e_0^{(i)}-1}\left(1 - \pi_t^{(i)}\right)^{f_0^{(i)}-1}}{\mathrm{B}\left(e_0^{(i)}, f_0^{(i)}\right)}, \tag{6.22}$$

and $\mathrm{B}(\cdot,\cdot)$ is the beta function. Thus, the set of latent unknown variables, denoted by $\boldsymbol{\Theta}_t$, gathers the actual state estimate, the binary indicators and the hyper-parameters that conform the pdf for the former, and is defined as follows

$$\boldsymbol{\Theta}_t = \{\mathbf{x}_t, \boldsymbol{\pi}_t, \boldsymbol{\zeta}_t\}. \tag{6.23}$$

For the estimation of the afore-described set of latent variables, a set of assumptions have been adopted, which hold approximately in many practical situations:

---

[1] Note that a beta distribution is typically expressed as $p(x; \alpha, \gamma) \propto x^{\alpha-1}(1-x)^{\gamma-1}$, where $\alpha$ and $\gamma$ are two shape parameters, while the dependence on $\alpha$ and $\gamma$ is here dropped for simplicity and the term $p(x)$ is used instead.

- **A1:** The dynamics of the SSM can be expressed as a Markovian process, such that

$$p\left(\mathbf{x}_t|\mathbf{x}_{0:t-1}\right) = p\left(\mathbf{x}_t|\mathbf{x}_{t-1}\right), \tag{6.24}$$

$$p\left(\mathbf{x}_t|\mathbf{y}_{1:t}\right) = p\left(\mathbf{x}_t|\mathbf{y}_t\right) p\left(\mathbf{x}_{t-1}\right). \tag{6.25}$$

- **A2:** The binary indicators are assumed to be mutually independent, as well as independent from the observations (since the underlying statistics to model the probability of an outlier occurrence do not depend of the data per se), such that

$$p(\boldsymbol{\zeta}_t, \boldsymbol{\pi}_t) = \prod_{i=1}^{n} p\left(\zeta_t^{(i)}|\pi_t^{(i)}\right) p\left(\pi_t^{(i)}\right). \tag{6.26}$$

- **A3:** The binary indicators present a random time evolution and are, therefore, time uncorrelated such that

$$p\left(\boldsymbol{\zeta}_t|\boldsymbol{\zeta}_{0:t-1}\right) = \prod_{k=0}^{t} p\left(\boldsymbol{\zeta}_k\right). \tag{6.27}$$

These assumptions conform the factor graph depicted in Fig. 6.3, where the known (i.e., the observations) and the a priori information (i.e., the initial state estimate and the hyper-parameters $e_0, f_0$) are encapsulated in circles, while the unknown parameters are inside rectangles.

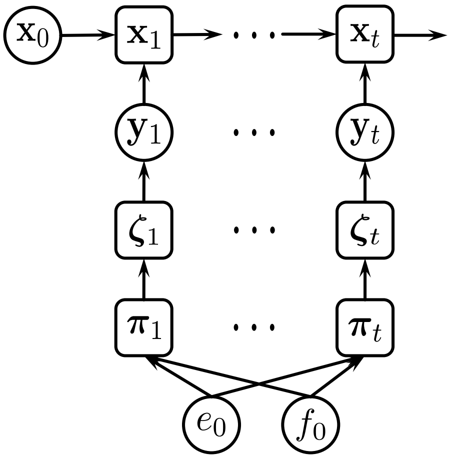

**Figure 6.3:** Graphical model for the sequential estimation of $p\left(\mathbf{x}_{0:t}|\mathbf{y}_{1:t}\right)$ based on the introduced Variational Bayesian inference Kalman Filter.

Following Bayes' law and from assumptions A1-A3, the posterior distribution of the unknown variables conditioned on the observations is given by

$$p\left(\boldsymbol{\Theta}_t|\mathbf{y}_{1:t}\right) = \frac{p\left(\boldsymbol{\Theta}_t, \mathbf{y}_t\right)}{p(\mathbf{y}_t)}, \tag{6.28}$$

which can be approximated using the variational inference principle [228], [229]. In particular, the posterior in (6.28) can be approximated by resorting on the auxiliary distribution $q(\boldsymbol{\Theta}_t)$, such that

$$q(\boldsymbol{\Theta}_t) = q\left(\mathbf{x}_t\right) q\left(\boldsymbol{\pi}_t\right) q\left(\boldsymbol{\zeta}_t\right) \tag{6.29}$$

$$= q\left(\mathbf{x}_t\right) \prod_{i=1}^{n} q\left(\pi_t^{(i)}\right) q\left(\zeta_t^{(i)}\right). \tag{6.30}$$

Thus, the marginal distributions can be factorized and estimated via mean-field approximation [230] applied to the joint distributions

$$p\left(\mathbf{x}_t, \boldsymbol{\pi}_t, \boldsymbol{\zeta}_t, \mathbf{y}_{1:t}\right) \propto p\left(\mathbf{x}|\mathbf{y}_{1:t}\right) p\left(\mathbf{y}_t|\mathbf{x}_t, \boldsymbol{\zeta}_t\right) p\left(\boldsymbol{\zeta}_t, \boldsymbol{\pi}_t\right), \tag{6.31}$$

such that

$$\ln\left[q(\mathbf{x}_t)\right] = \mathbb{E}_{\boldsymbol{\pi}_t, \boldsymbol{\zeta}_t}\{\ln\left[p\left(\mathbf{x}_t, \boldsymbol{\pi}_t, \boldsymbol{\zeta}_t, \mathbf{y}_{1:t}\right)\right]\}\ , \tag{6.32}$$

$$\ln\left[q(\boldsymbol{\pi}_t)\right] = \mathbb{E}_{\mathbf{x}_t, \boldsymbol{\zeta}_t}\{\ln\left[p\left(\mathbf{x}_t, \boldsymbol{\pi}_t, \boldsymbol{\zeta}_t, \mathbf{y}_{1:t}\right)\right]\}\ , \tag{6.33}$$

$$\ln\left[q(\boldsymbol{\zeta}_t)\right] = \mathbb{E}_{\boldsymbol{\pi}_t, \mathbf{x}_t}\{\ln\left[p\left(\mathbf{x}_t, \boldsymbol{\pi}_t, \boldsymbol{\zeta}_t, \mathbf{y}_{1:t}\right)\right]\}\ , \tag{6.34}$$

where the first term $p\left(\mathbf{x}_t|\mathbf{y}_{1:t-1}\right)$ on the right-hand side of (6.32) corresponds to the predicted state of a KF estimate, approximated as $p\left(\mathbf{x}_t|\mathbf{y}_{1:t-1}\right) \approx \mathcal{N}\left(\hat{\mathbf{x}}_{t|t-1}, \mathbf{P}_{t|t-1}\right)$.

In the sequel, it is discussed the estimation procedure of the marginal distributions $q(\mathbf{x}_t)$, $q(\boldsymbol{\pi}_t)$ and $q(\boldsymbol{\zeta}_t)$ which, in turn, leads to solving the unknown parameters in $\boldsymbol{\Theta}_t$. Two particular cases are examined next: the single indicator VB-based robust KF from [220] and the proposed VB-based KF with multiple outlier indicators for uncorrelated observations [18]. For simplicity and to improve the readiness, the following derivations are given for either linear systems or EKF approximations, while the general VB-based KF formulation for nonlinear systems integrating correlated observations is detailed in Appendix D.

### 6.2.1 VB-based Robust Filtering with a Single Outlier Indicator

Let us recall and simplify the likelihood probability in (6.20), such that a single binary indicator is used, leading to

$$p\left(\mathbf{y}_t|\mathbf{x}_t, \zeta_t\right) = \mathcal{N}\Big(\mathcal{T}(\mathbf{y}_t, \zeta_t);\ \mathcal{T}(\mathbf{h}(\mathbf{x}_t), \zeta_t), \mathbf{C}(\zeta_t)\Big)\ , \tag{6.35}$$

$$= \mathcal{N}\left(\mathbf{y}_t; \mathbf{h}(\mathbf{x}_t), \boldsymbol{\Sigma}_t\right)^{\zeta_t}. \tag{6.36}$$

Thus, if an outlier is identified within the vector of observations, the complete set of measurements are disregarded. In other words, if $\zeta_t = 1$, the conventional KF correction step, while for $\zeta_t = 0$ one would skip performing such update stage. Focusing now on the estimation for the marginal distributions, let us start with $q(\mathbf{x}_t)$, which can be expressed as

$$q(\mathbf{x}_t) \propto \exp\left(-\frac{1}{2}\left\|\mathbf{x}_t - \hat{\mathbf{x}}_{t|t-1}\right\|^2_{\mathbf{P}_{t|t-1}} - \frac{\langle\zeta_t\rangle}{2}\left\|\mathbf{y}_t - \mathbf{h}(\mathbf{x}_t)\right\|^2_{\boldsymbol{\Sigma}_t}\right), \tag{6.37}$$

where $\langle\zeta_t\rangle$ is the expectation over $\zeta_t$. It is clear that $q(\mathbf{x}_t)$ corresponds to the Gaussian distribution $\mathcal{N}\left(\hat{\mathbf{x}}_{t|t}, \mathbf{P}_{t|t}\right)$, whose first and second moments can be estimated with the conventional KF with the modified covariance $\bar{\boldsymbol{\Sigma}}_t = \boldsymbol{\Sigma}/\langle\zeta_t\rangle$ as

$$\mathbf{K}_t = \mathbf{P}_{t|t-1}\mathbf{H}_t^\top\left(\mathbf{H}_t\mathbf{P}_{t|t-1}\mathbf{H}_t^\top + \bar{\boldsymbol{\Sigma}}_t\right)^{-1}\ , \tag{6.38}$$

$$\mathbf{x}_{t|t} = \mathbf{x}_{t|t-1} + \mathbf{K}_t\left(\mathbf{y}_t - \mathbf{h}(\mathbf{x}_{t|t-1})\right)\ , \tag{6.39}$$

$$\mathbf{P}_{t|t} = \mathbf{P}_{t|t-1} - \mathbf{K}_t\mathbf{H}_t\mathbf{P}_{t|t-1}, \tag{6.40}$$

which, whenever $\langle\zeta_t\rangle$ is close to 0 (i.e., when the presence of outliers is detected) implies ignoring the observations and updating the marginal distribution of $\mathbf{x}_t$ with the predicted distribution, as

$$q(\mathbf{x}_t) \sim \mathcal{N}\left(\hat{\mathbf{x}}_{t|t}, \mathbf{P}_{t|t}\right) \underset{\langle\zeta_t\rangle\approx 0}{=} \mathcal{N}\left(\hat{\mathbf{x}}_{t|t-1}, \mathbf{P}_{t|t-1}\right). \tag{6.41}$$

Then, the distribution $q(\zeta_t)$ is obtained from

$$q\left(z_t\right) \propto \exp\left(-\frac{1}{2}\zeta_t \operatorname{tr}\left(\boldsymbol{B}_t\boldsymbol{\Sigma}_t^{-1}\right) + \zeta_t\langle\ln(\pi_t)\rangle + \left(1-\zeta_t\right)\langle\ln(1-\pi_t)\rangle\right), \tag{6.42}$$

where $\boldsymbol{B}_t$ is given by

$$\boldsymbol{B}_t = \int \left(\mathbf{y}_t - \mathbf{h}\left(\mathbf{x}_t\right)\right)\left(\mathbf{y}_t - \mathbf{h}\left(\mathbf{x}_t\right)\right)^\top q\left(\mathbf{x}_t\right) d\mathbf{x}_t. \tag{6.43}$$

Moreover, $\zeta_t$ is a Bernoulli parameter whose probability is given by

$$P(\zeta_t = 1) = A \exp\left\langle \ln \pi_t - \frac{1}{2}\operatorname{tr}\left(\boldsymbol{B}_t\boldsymbol{\Sigma}_t^{-1}\right)\right\rangle , \tag{6.44}$$

$$P(\zeta_t = 0) = A \exp\left\langle \ln 1 - \pi_t \right\rangle \tag{6.45}$$

with $A$ a normalizing factor such that $P(\zeta_t = 1) + P(\zeta_t = 0) = 1$ and the expectations over $\pi_t$ given by

$$\langle\ln(\pi_t)\rangle = \Psi(e_t) - \Psi(e_t + f_t) , \tag{6.46}$$

$$\langle\ln(1-\pi_t)\rangle = \Psi(f_t) - \Psi(e_t + f_t), \tag{6.47}$$

where $\Psi(\cdot)$ is the digamma function. Thus, the expectation of $\zeta_t$ is updated from

$$\langle\zeta_t\rangle = \frac{P(\zeta_t = 1)}{P(\zeta_t = 1) + P(\zeta_t = 0)}, \tag{6.48}$$

from which one gets whether an outlier is or not an estimate. Notice that, for the evaluation of 6.48 one would have had previously estimated the hyper-parameters $e_t$ and $f_t$, which depend on the marginal $q(\pi_t)$ distribution. The former can be expressed, after dropping the terms in 6.34 that do not depend on $\pi_t$, as

$$q(\pi_t) \propto \exp\left(e_t \ln(\pi_t) + f_t \ln(1-\pi_t)\right), \tag{6.49}$$

where

$$e_t = e_0 + \langle\zeta_t\rangle , \tag{6.50}$$

$$f_t = f_0 + 1 - \langle\zeta_t\rangle. \tag{6.51}$$

In summary, the realization of a time instance for the VB-based KF with a single outlier implies the following iterative procedure (for $k = 1, 2, \dots$) until convergence:

1. The state estimate $q(\mathbf{x}_t^{(k)})$ is updated via (6.39)-(6.40) or (6.41) depending on $\langle\zeta_t^{(k-1)}\rangle$,
2. The outlier indicator $\zeta_t^{(k)}$ is updated from (6.48),
3. The hyper-parameters $e_t^{(k)}, f_t^{(k)}$ are updated from (6.50)-(6.51).

### 6.2.2 VB-based Robust Filtering with Independent Outlier Indicators

While the filter described in Section 6.2.1 results interesting due to its implementation simplicity, its application should be limited to cases where only a few observations are available or when a constant update on the estimates is not required. This is due to the correction being fully skipped whenever a single outlier is detected which, extrapolated to GNSS-based navigation, implies relying mostly on the dynamical model since outliers are likely to be encountered. This section proposes an extension for the previously described filter, for which VB-based hypothesis testing is performed to the observations individually, allowing to exclude only those which are found contaminated.

Let us assume a set of uncorrelated observations, whose covariance matrix conditional on the binary indicators is expressed by

$$\mathbf{\Sigma}_t(\boldsymbol{\zeta}_t) = \begin{bmatrix} \sigma_{1,1}^2/\zeta_t^{(1)} & 0 & \dots & 0 \\ 0 & \sigma_{2,2}^2/\zeta_t^{(2)} & \dots & 0 \\ \vdots & \vdots & \ddots & \vdots \\ 0 & 0 & \dots & \sigma_{n,n}^2/\zeta_t^{(n)} \end{bmatrix}, \tag{6.52}$$

so that the observation model in (6.20) can be expanded as

$$\begin{aligned} p\left(\mathbf{y}_t|\mathbf{x}_t,\boldsymbol{\zeta}_t\right) &= \prod_{i=1}^{n} \mathcal{N}\Big(\mathcal{T}(y_t^{(i)},\zeta_t^{(i)});\ \mathcal{T}(h^{(i)}(\mathbf{x}_t),\zeta_t^{(i)}),[\mathbf{C}(\zeta_t^{(i)})]_{i,i}\Big)\ , \\ &= \prod_{i=1}^{n} \mathcal{N}\left(y_t^{(i)};\ h^{(i)}(\mathbf{x}_t),[\mathbf{\Sigma}_t]_{i,i}\right)^{\zeta_t^{(i)}}\ . \end{aligned} \tag{6.53}$$

As before, let us now describe the estimation procedure for the different marginal distributions. Starting with $q(\mathbf{x}_t)$:

$$q(\mathbf{x}_t) \propto \exp\left(-\frac{1}{2}\left\|\mathbf{x}_t-\hat{\mathbf{x}}_{t|t-1}\right\|^2_{\mathbf{P}_{t|t-1}} - \frac{\boldsymbol{Z}_t}{2}\left\|\mathbf{y}_t-\mathbf{h}(\mathbf{x}_t)\right\|^2_{\mathbf{\Sigma}_t}\right), \tag{6.54}$$

where $\boldsymbol{Z}_t = \text{diag}[\langle\zeta_t^{(1)}\rangle,\dots,\langle\zeta_t^{(n)}\rangle]$ is a diagonal matrix composed by the expectation over the vector of binary outlier indicators. The estimation of $q(\mathbf{x}_t)$ can be realized following the exact same procedure than for the scalar case with (6.38)-(6.41), with the exception of $\bar{\mathbf{\Sigma}}_t$ now given by (6.52). Then, the update of $q(\zeta_t^{(i)})$ is given by

$$q\left(z_t^{(i)}\right) \propto \exp\left(-\frac{1}{2}\zeta_t^{(i)}b_t^{(i)}/[\mathbf{\Sigma}_t]_{i,i} + \zeta_t^{(i)}\langle\ln(\pi_t^{(i)})\rangle + \left(1-\zeta_t^{(i)}\right)\langle\ln(1-\pi_t^{(i)})\rangle\right), \tag{6.55}$$

and $b_t^{(i)}$ is given by $b_t^{(i)} = \int\left(y_t^{(i)}-h^{(i)}\left(\mathbf{x}_t\right)\right)\left(y_t^{(i)}-h^{(i)}\left(\mathbf{x}_t\right)\right)^\top q\left(\mathbf{x}_t\right)d\mathbf{x}_t,$. Then, the probability of $\zeta_t^{(i)}$ is obtained from

$$P(\zeta_t^{(i)}=1) = A\exp\left(\left\langle\ln\pi_t^{(i)}\right\rangle - \frac{1}{2}b_t^{(i)}/[\mathbf{\Sigma}_t]_{i,i}\right)\ , \tag{6.56}$$

$$P(\zeta_t^{(i)}=0) = A\exp\left\langle\ln 1-\pi_t^{(i)}\right\rangle. \tag{6.57}$$

At this stage, it is clear that one can particularize (6.48)-(6.51) to the $i=1,\dots,n$ indicators' indexes to update the expectation $\langle\boldsymbol{\zeta}_t\rangle$, the marginal $q(\boldsymbol{\pi}_t)$ and the hyper-parameters $e_t^{(i)}$, $f_t^{(i)}$.

## 6.3 Discussion on Robust Filtering for Attitude Estimation

The extension of robust filtering for attitude and JPA determination involves dealing with parameters "living" on a Lie group along with Euclidean and integer spaces. The formulation of the afore-described robust filters requires that the geometrical constraints present on the orientation parametrization are respected, together with posing minimal representation for the second moments (i.e., the covariance matrices for the estimates). Fortunately, Lie Theory provides with a set of algebraic tools that, in combination with the methodology presented along this chapter, allows to provide precise navigational estimates even under the influence of impulsive and other outlying effects.

Thus, the problem of robust filtering over a manifold space is expressed as

$$\hat{\mathbf{x}}_t = \arg \min_{\mathbf{x}_t \in \mathcal{M}} \left( \left\| \mathbf{x}_t \ominus \hat{\mathbf{x}}_{t|t-1} \right\|^2_{\mathbf{P}_{t|t-1}} + \left\| \mathbf{y}_t - \mathbf{h}\left(\mathbf{x}_t\right) \right\|^2_{\bar{\mathbf{\Sigma}}_t} \right) , \tag{6.58}$$

with $\mathcal{M}$ a generic manifold –in our context, the mixture of real numbers and the Lie group–. Let us recall the composition operator for which the nominal state (expressed in a manifold) and the error state (formulated in an Euclidean space), $\mathbf{x} = \hat{\mathbf{x}} \oplus \delta\mathbf{x}$. Thus, adapting robust filters to attitude-related problems primarily deals with converting the filters' innovation vectors to error state vectors.

Taking the RIF as example case, one would provide a robust estimate by expressing the innovation over the information vector in (6.5) as error state, as

$$\mathbf{x}_{t|t} = \widehat{\mathbf{x}}_{t|t} \oplus \delta\mathbf{x}_{t|t}, \tag{6.59}$$

$$\delta\mathbf{x}_{t|t} = \mathbf{P}_{t|t} \delta\mathbf{z}_{t|t} \ , \tag{6.60}$$

where $\delta\mathbf{z}_{t|t}$ is a robust estimate over the change of the information vector. As for other nonlinear problems, such as the robust SPP described in Section 5.3, estimating $\delta\mathbf{z}_{t|t}$ requires two cascaded iterative procedures. Indeed, consider a given fixed weight matrix $\mathbf{W}$. For this weighting, the estimate is obtained recursively, starting from $\hat{\mathbf{x}}^{(0)} = \hat{\mathbf{x}}_{t|t-1}$, and for $i \geq 0$ by

$$\delta\mathbf{z}^{(i+1)} = {\mathbf{H}_t^{(i)}}^\top \mathbf{\Sigma}_t^{-\top/2} \mathbf{W} \mathbf{\Sigma}_t^{-1/2} \left( \mathbf{y}_t - \mathbf{h}(\mathbf{x}^{(i)}) + \mathbf{H}_t \left( \mathbf{Z}^{(i)} \right)^{-1} \delta\mathbf{z}^{(i)} \right) , \tag{6.61}$$

$$\mathbf{Z}^{(i+1)} = \mathbf{Z}_{t|t-1} + {\mathbf{H}_t^{(i)}}^\top \mathbf{\Sigma}_t^{-\top/2} \mathbf{W} \mathbf{\Sigma}_t^{-1/2} \mathbf{H}_t^{(i)} , \tag{6.62}$$

$$\mathbf{x}^{(i+1)} = \mathbf{x}_{t|t-1} \oplus \left( \mathbf{Z}^{(i+1)} \right)^{(-1)} \delta\mathbf{z}^{(i+1)} . \tag{6.63}$$

Note that, in (6.61), $(\mathbf{Z}^{(i+1)})^{-1} \delta\mathbf{z}^{(i+1)} = \delta\mathbf{x}^{(i+1)} = \mathbf{x}_t^{(i+1)} \ominus \hat{\mathbf{x}}_{t|t-1}$. The recursion (6.61) needs to be solved for each value of the weighting matrix, which itself is recomputed afterwards. This double recursion, given in Algorithm 4, forms the iterated robust IF for on-manifold parameters.

Similarly, GM-KF can be adapted to work with Lie groups by transforming the robust LS regression in (6.7) to an error state formulation. Again, let us consider a fixed weighting matrix $\mathbf{W}$. Then, for an initial point $\mathbf{x}^{(0)}$ and for $i = 1, 2, \ldots$ until convergence, it is realized

$$\begin{aligned} \delta\mathbf{x}^{(i)} = & \left( \tilde{\mathbf{H}}^{(i)\top} \tilde{\mathbf{\Sigma}}_t^{-\top/2} \tilde{\mathbf{W}} \tilde{\mathbf{\Sigma}}_t^{-1/2} \tilde{\mathbf{H}}^{(i)} \right)^\dagger \cdot \\ & \tilde{\mathbf{H}}^{(i)\top} \tilde{\mathbf{\Sigma}}_t^{-\top/2} \ \tilde{\mathbf{W}} \tilde{\mathbf{\Sigma}}_t^{-1/2} \left( \tilde{\mathbf{y}}_t - \tilde{\mathbf{h}} \left( \mathbf{x}^{(i-1)} \right) + \tilde{\mathbf{H}}^{(i)} \left( \mathbf{x}^{(i-1)} \ominus \mathbf{x}_{t|t-1} \right) \right) , \end{aligned} \tag{6.64}$$

$$\mathbf{x}^{(i)} = \mathbf{x}^{(i-1)} \oplus \delta\mathbf{x}^{(i)} . \tag{6.65}$$

**Algorithm 4:** Robust IF for parameters on a manifold

```
Input  : Observations: $\mathbf{y}, \boldsymbol{\Sigma}$, robust parameters: $w(\cdot), c$, prediction: $\hat{\mathbf{x}}_{t|t-1}$, $\mathbf{P}_{t|t-1}$
Output : Updated estimate $\hat{\mathbf{x}}_{t|t}$, $\mathbf{P}_{t|t}$
Initialize $\mathbf{W}^{(0)} = \mathbf{I}$, $\hat{\mathbf{x}}^{(0)} = \hat{\mathbf{x}}_{t|t-1}$,
for $p = 1, 2, \dots$ until convergence do solve robust iteration
    Solve (6.58) via iteratively solving (6.61)–(6.63) to obtain $\hat{\mathbf{x}}^{(p)}, \mathbf{Z}^{(p)}$
    Update the weighting matrix:
    $\mathbf{W}^{(p)} = \text{diag}\left(\mathbf{w}\left(\boldsymbol{\Sigma}_k^{-1/2}(\mathbf{y} - \mathbf{h}(\hat{\mathbf{x}}^{(p)}))\right)\right)$
Return: $\hat{\mathbf{x}}_{t|t} = \hat{\mathbf{x}}^{(p)}$, $\mathbf{P}_{t|t} = \left(\mathbf{Z}^{(p)}\right)^{-1}$
```

While the GN procedure described in (6.64) can work under certain scenarios, combining hard-redescending functions with the already nonlinear attitude problem may incur in numerical and convergence problems. Moreover, one may realized that in (6.64) one may combine parameters with “large” magnitudes, such as the position and the ambiguities, with the “small” unit-sphere space of the quaternion. Thus, versions of the GM-KF compatible with Lie groups may consider the use of second-order optimization algorithms on manifolds, e.g., the Riemannian Newton’s method [231, Ch. 6] or penalized step sizes [232].

Robust filtering based on VB-based hypothesis testing provides with an estimation framework naturally design to cope with nonlinear functions. Thus, its adoption to JPA and attitude problems becomes straightforward, only conditioned by the use of the composition operators during the estimation of the marginal conditional probabilities in, for instance, (6.39) or (D.6).

Unfortunately, studying the performance of robust estimators for the carrier phase-based JPA and attitude problems escape the extent of this thesis. Along with the analysis on the converge and uniqueness of second-order optimization (for RIF and GM-KF forms), this constitutes an interesting future research line.

## 6.4 Performance Characterization of Robust Filtering for RTK Positioning

This section provides a profound evaluation of the afore-described robust filtering approaches when applied to the carrier phase-based recursive positioning problem. To achieve that aim, a Monte Carlo experimentation is first carried out for a synthetic scenario so that the relative efficiency at the normal model and the robustness can be assessed under a controlled scenario. Then, the performance of a selection of the best performing filtering solutions are evaluated over real data collected from a measurement campaign where multipath and NLOS effects are present.

### 6.4.1 Simulation Results

The synthetic scenario consists on a static skyplot –the same than for Sections 1.5, 2.5, and as shown on the right side of Fig. 1.5–, for which a rover navigates for a duration of 2000 seconds, with observations being simulated at a 5 Hz rate. In terms of dynamics, such rover moves according to constant velocity model, with the uncertainty about the state transition (i.e., $\mathbf{Q}_t$) is described by a white Gaussian random process $\mathbf{w}_t \sim \mathcal{N}(\mathbf{0}_3, \mathbf{I}_3)$. The observation model corresponds to the mixed model for positioning in (2.4).

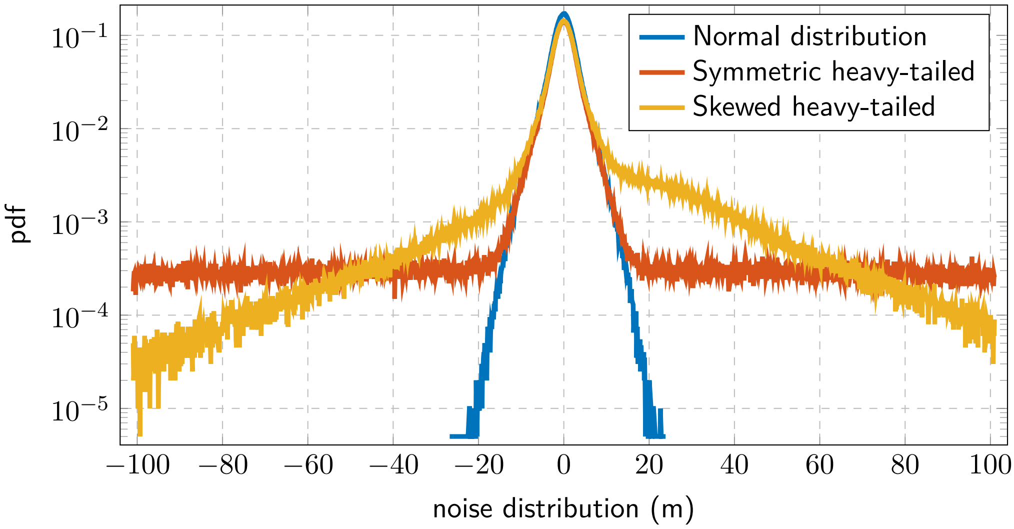

**Figure 6.4:** Skyplot and noise distributions for the different scenarios.

Along the simulation, some time periods incorporate nominal-distributed observations while, for the remaining time instances, measurements are assumed to present the contaminated distribution described in (5.21). The latter occur during the shaded zones in Fig. 6.7 and 6.8. During the “contamination times”, each satellite is randomly sampled to be either healthy or an outlier, with a probability equal to $\epsilon = 0.40$. Whenever a satellite is chosen as outlier, the distribution for its carrier phase pseudorange does not change but it is affected by a cycle slip. Three different scenarios are considered, based on the noise conditions of the observations:

**Case 0: Nominal distribution** – The noise is distributed according to the normal assumptions, such that

$$\nu_\rho^i \sim \mathcal{N}(0, (\sigma_\rho^i)^2),\ \sigma_\rho^i = 0.5 \cdot (1 + 1/\sin(\mathsf{elev}^i)), \tag{6.66}$$

$$\nu_\Phi^i \sim \mathcal{N}(0, (\sigma_\Phi^i)^2),\ \sigma_\Phi^i = \sigma_\rho^i/100 \tag{6.67}$$

with $\nu_\rho^i, \nu_\Phi^i$ the code and carrier phase pseudorange noises for the $i$th satellite and elev$^i$ its elevation.

**Case 1: Symmetric heavy-tailed** – The noise distribution is given by a Gaussian mixture, where the outliers present an $\alpha$-times larger standard deviation and described by

$$\nu_\rho^i \sim (1-\epsilon)\mathcal{N}(0, (\sigma_\rho^i)^2) + \epsilon\mathcal{N}(0, (\alpha \cdot \sigma_\rho^i)^2), \tag{6.68}$$

which corresponds to a symmetric heavy-tailed noise scenario.

**Case 2: Skewed heavy-tailed** – The noise distribution also follows a Gaussian mixture, although the overall distributed is skewed due to the influence of the outliers, such that

$$\nu_\rho^i \sim (1-\epsilon)\mathcal{N}(0, (\sigma_\rho^i)^2) + \epsilon\mathcal{N}(10, (\nu_\rho^i \cdot \sigma_\rho^i)^2), \tag{6.69}$$

which provides an accurate description of the effect of multipath and NLOS over the noise distributions, since their effect typically induce a positive bias on the pseudorange measurements.

The pdf for the noises described in the previous three cases is depicted on the right side of Fig. 6.4.

A total of seven filters are compared, with the former being distinguished in the following categories: *a)* Standard KFs: ideal EKF (i.e., a filter with the information on which observations are or not outliers, and which constitutes the benchmark as the best possible solution) and EKF (i.e., a classical filter heavily affected by the presence of outliers); *b)* Robust statistics-based filters: RIF based on Huber, Tukey, IGG and $3\sigma$ score functions and a GM-KF based on Huber score function; *c)* VB-based filter for hypothesis testing with a single and multiple binary indicators (i.e., corresponding to the filters presented in Sections 6.2.1 and 6.2.2, respectively). Note that the tuning parameters for the robust statistics-based filters are set such that a 95% efficiency at the Gaussian model is achieved (i.e., $c_{\mathsf{Hub}} = 1.345, c_{\mathsf{Tuk}} = 4.685$ and $c_{\mathsf{IGG},0} = 1.5,\ c_{\mathsf{IGG},1} = 2.5$).

To address the performance characterization, different metrics are considered: *i)* the RMSE for the float positioning estimate; *ii)* the mean ambiguity success rate (MASR), i.e., the ratio of Monte Carlo iterations for which a successful integer estimation is performed; *iii)* the cumulative distribution function (CDF) for the positioning errors during the float solution estimation; *iv)* the relative efficiency for the float estimate at the nominal model. The decision of evaluating solely the precision of the float estimate in detriment of the fixed one is motivated by the minimal changes from the former whenever the ambiguities are correctly determined.

### Case 0: Nominal Gaussian Noise Distributions

This first case serves for the characterization of the relative efficiency of the evaluated robust filters under nominal normal noise distributions. Such efficiency is derived following the approach described for code-based positioning in Section 5.3.1, where the optimal solution is provided by the KF (since the model is quasi-linear).

Fig. 6.5 illustrates the results in terms of efficiency, while the RMSE over time is shown in Fig. 6.6. Results on the ratio of successfully-performed ambiguity resolution is showcased in Table 6.1. In general, the complete set of evaluated filters present a good behavior in terms of efficiency and IAR, with two points standing out: first, the two VB-based robust KFs behave optimally, fully recreating the performance of an ideal filter; second, the RIF-IGG and GM-KF performances are slightly degraded with regards to the other options. In any case, all filters manage to have the best possible success at ambiguity fixing which, in turn, grants a high precision for the fixed solution regardless of their efficiency at the float estimates. Nevertheless, having efficient float estimates remains a relevant factor to characterize robust filters, since it will condition the performance under more challenging scenarios.

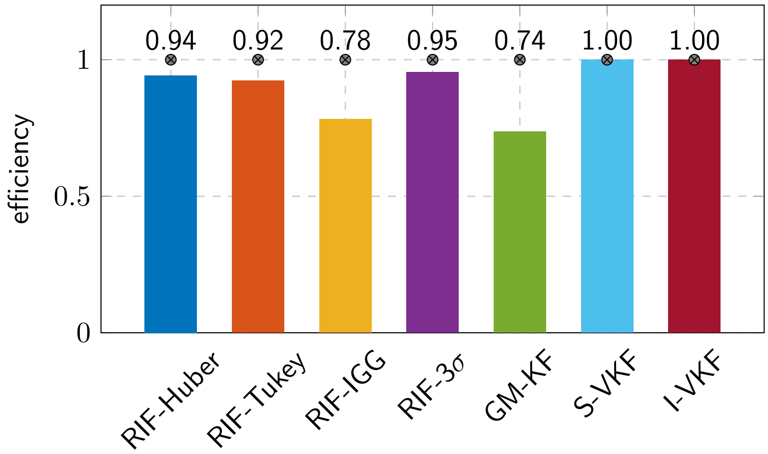

**Figure 6.5:** Efficiency and errors over time for the nominal Gaussian-distributed noise Case 0.

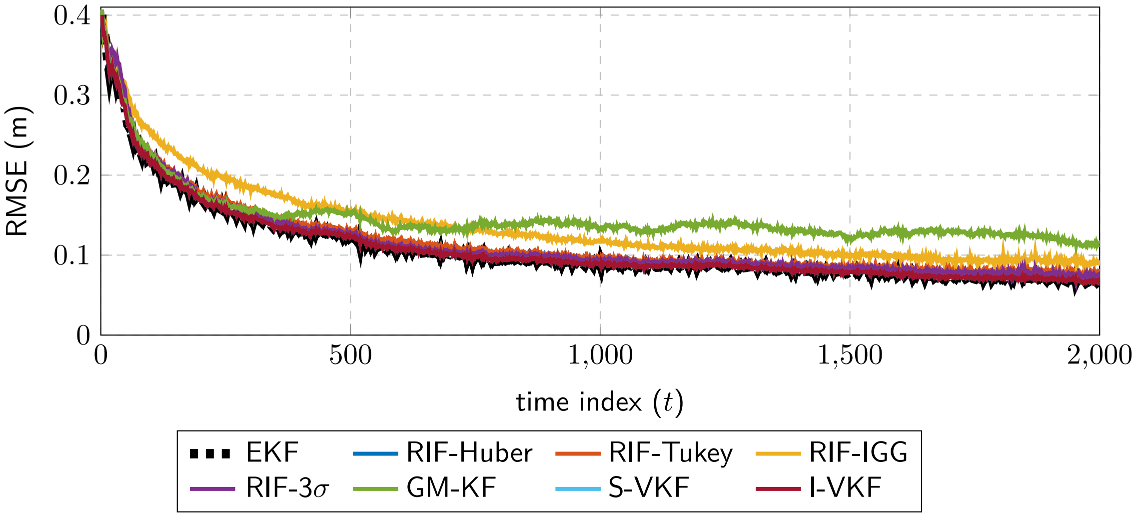

**Figure 6.6:** Skyplot and noise distributions for the different scenarios.

### Cases 1, 2: Heavy-tailed Noise Distributions

Having assessed the performance for the different robust filters under nominal conditions, their behavior under the non-nominal heavy-tailed noise scenarios for the Cases 1 and 2 is analyzed next. First, the RMSE for the positioning float estimates is depicted in Fig. 6.7, with the symmetric and skewed heavy-tailed noise distributions shown on the top and bottom, respectively. The EKF performance becomes clearly degraded when some satellites are affected by outliers, with large biases appearing that impair the IAR process. Also, the S-VKF presents the worst positioning performance among the estimators, due to the correction step not being executed during the time periods with contaminated observations and, thus, the positioning solution is solely based on the dynamical model. Therefore, S-VKF might result interesting solely whenever outliers are expected for occasional and short time spans. On the contrary, the I-VKF allows for an almost perfect solution for outlier detection and removal, with its performance being similar to that of the ideal EKF. This implies that the computational burden for the hyper-parameters estimation based on VB inference does not penalize the overall performance. Indeed, the I-VKF showcases the overall best performance among the robust filters, both in terms of successful IAR and RMSE for the float positioning solutions. For skewed heavy-tailed noises, the performance obtained with the I-VKF is equivalent to the one provided by RIFs based on redescending robust functions, namely RIF-Tukey, RIF-IGG and RIF-3$\sigma$. On the other hand, the exploitation of monotone robust functions, i.e., as for the RIF-Huber and the GM-KF, leads to a slightly worsen performance.

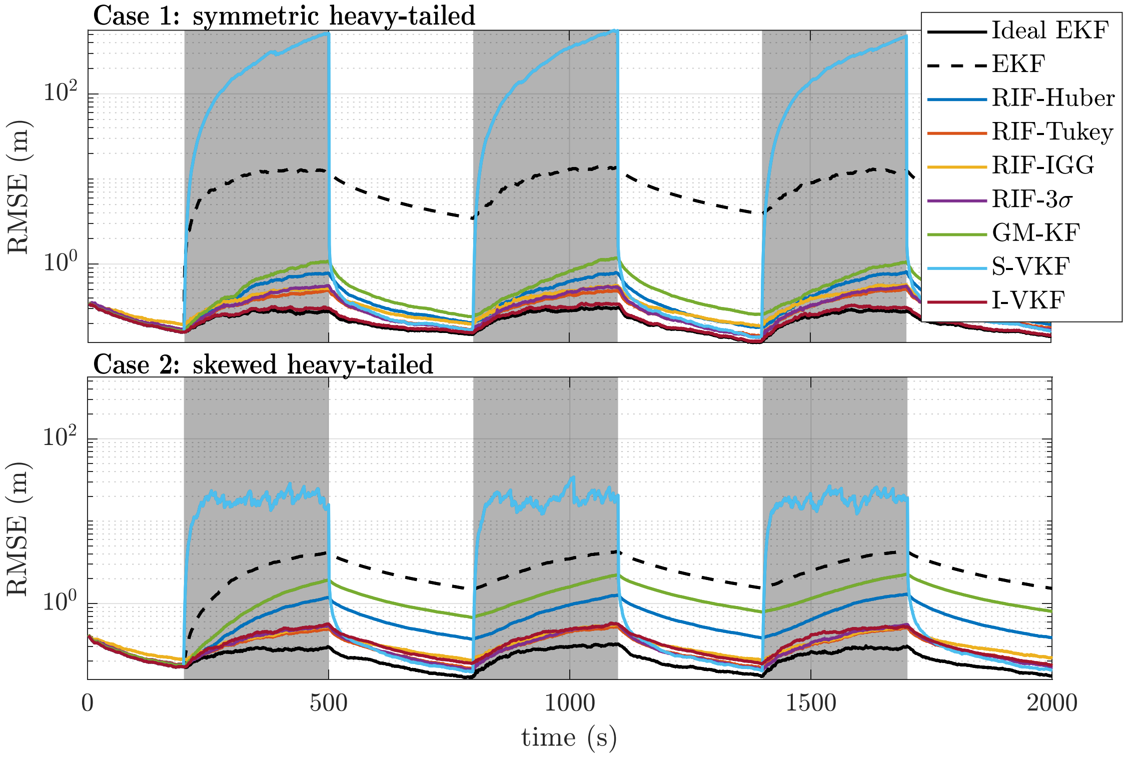

**Figure 6.7:** RMSE for the float positioning results over time for the Cases 1 (top) and 2 (bottom).

These performance results are also backed up by the MASR over time, as shown in Fig. 6.8. It is evident that, as soon as the periods with observation contamination start (i.e., during the shaded gray areas), the EKF is unable to successfully fix its ambiguities. The robust statistics-based filters present a better resilience against such outliers, especially those

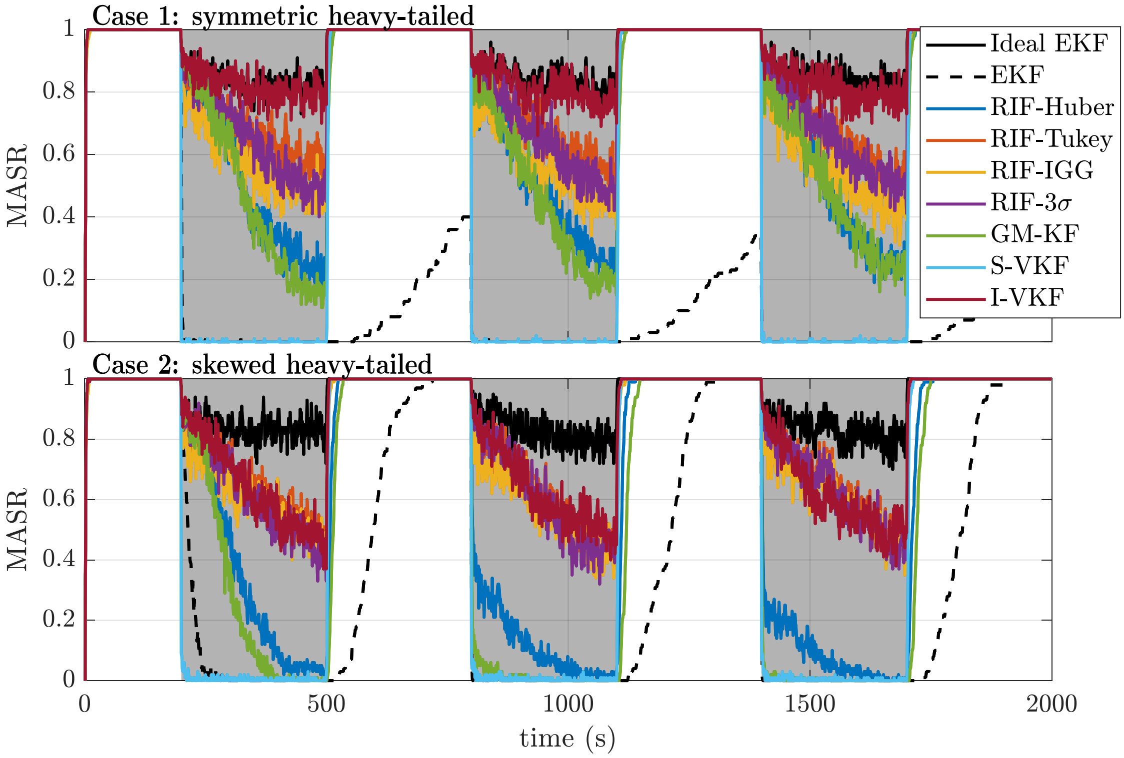

**Figure 6.8:** Mean ambiguity success rate (MASR) over time for the Cases 1 (top) and 2 (bottom).

with redescending functions, since they manage to nullify the biases effect over the estimates. However, the detection capability offered by robust score functions is significantly worse than that of filters equipped with VB-based hypothesis testing. Naturally, the S-VKF results incapable to perform successful integer estimations during the contamination times, since all the observations are rejected. On the other hand, I-VKF offers a performance almost identical to that of the optimal filter for the case of symmetric heavy-tailed noises, while being more sensitive to the skewed noise distributions.

The results are completed with Table 6.1, which depicts the percentage of successfully performed IAR. Again, the best solution both in terms of fix ratio is given by the I-VKF, which from this statistical analysis is the preferred choice. This recommendation needs to be verified with real data in order to see the impact and mitigation capabilities in a real system. This analysis is provided in the sequel. To further complete this evaluation, the empirical CDF for the float solutions is shown Fig. 6.9, while Table 6.1 summarizes the percentage of successfully performed IAR. Again, the best solution both in terms of fix ratio is given by the I-VKF, which from this statistical analysis is the preferred choice. This recommendation needs to be verified with real data in order to see the impact and mitigation capabilities in a real system. This analysis is provided in the sequel.

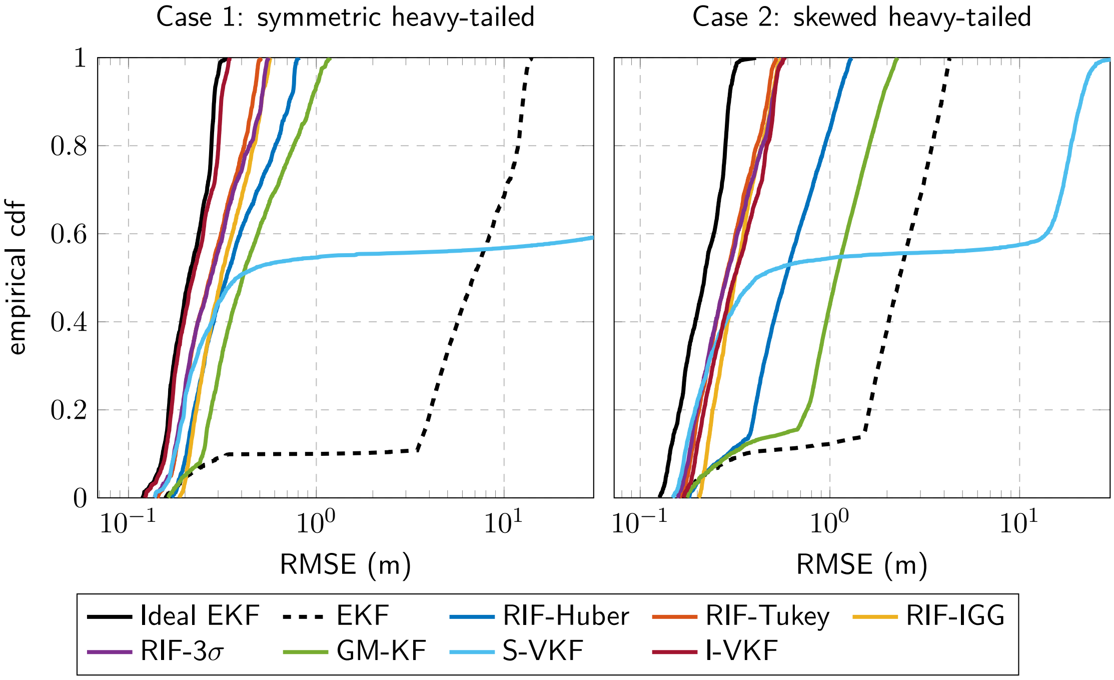

**Figure 6.9:** Empirical CDF of the float positioning errors for the Cases 1 (left) and 2 (right).

**Table 6.1:** Percentage of correctly-estimated integer ambiguities (%).

| **Filtering type** | | **Case 0** | **Case 1** | **Case 2** |
|---|---|---|---|---|
| **Conventional** | Ideal EKF | 99.96 | 92.74 | 92.74 |
| | EKF | 99.96 | 16.20 | 39.89 |
| **Robust Statistics-based** | RIF-Huber | 99.96 | 76.63 | 61.42 |
| | RIF-Tukey | 99.96 | 85.42 | 83.62 |
| | RIF-IGG | 99.96 | 80.41 | 81.47 |
| | RIF-3$\sigma$ | 99.96 | 84.19 | 82.45 |
| | GM-KF | 99.96 | 75.38 | 56.31 |
| **Variational-based** | S-VKF | 99.96 | 54.46 | 54.60 |
| | I-VKF | 99.96 | 91.82 | 83.22 |

### 6.4.2 Real Data Experimentation

This section details the performance characterization for a set of selected robust filters for the recursive RTK positioning problem under real-world harsh signal propagation conditions. To do so, a measurement campaign is conducted on board of a vessel within an inland waterway channel. Such experimentation was carried out in Koblenz (Germany) on 16th May 2017 (DOY 136, UTC 09:00-14:00), with the MS Bingen (a multi-purpose research vessel of the German Waterways authorities) being the tracked vehicle.

As can be seen from the bottom side of Fig. 6.10, multiple passes under three bridges are performed along the five hours of data collection. Thus, strong multipath and NLOS effects were experimented, leading to the GNSS observations presenting large biases and noise distributions which flee the assumption for normal distributions of known parameters. The

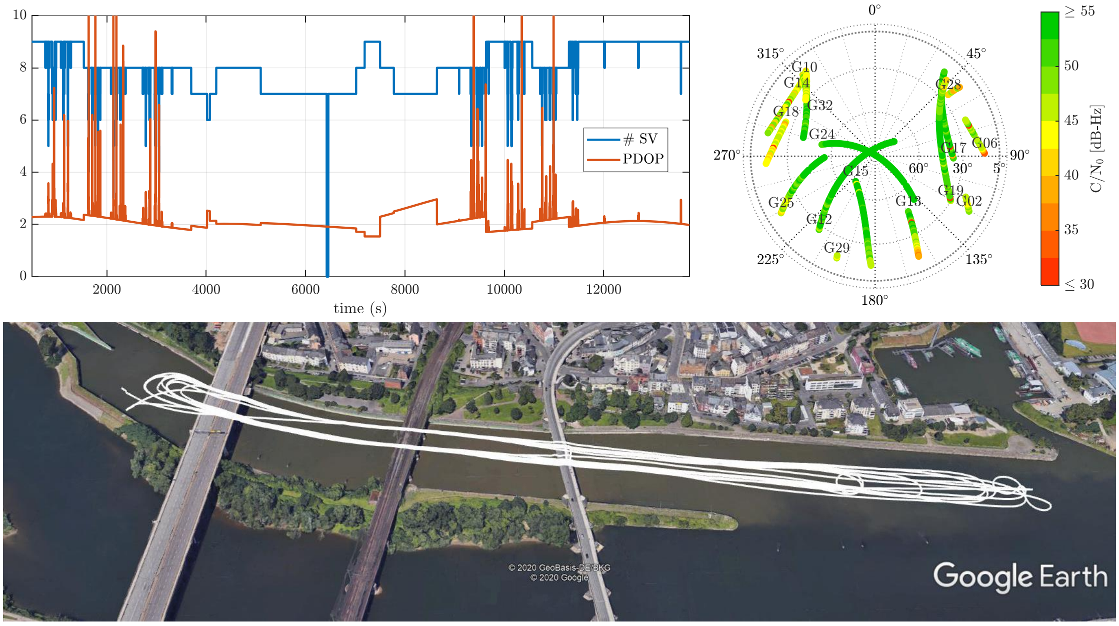

**Figure 6.10:** On the upper left, the number of tracked satellites and associated PDOP. On the upper right, the skyplot of the scenario, with the colorbar indicating the C/N$_0$. In the bottom, the trajectory followed by the tracked vessel during bridge passing, estimated using laser technology.

number of tracked satellites against the time are shown on the top left side of Fig. 6.10 along with the Position Dilution of Precision (PDOP), while the skyplot for the satellites and the associated $C/N_0$ is depicted on the top right side of Fig. 6.10. The ground truth trajectory is estimated based on optical technology, by utilizing a total station on land and an active reflector mounted under the GNSS antenna for automatic target tracking. While conditioned on direct line of sight, the use of this technology leads to an accuracy for the reference positioning solution of around one centimeter and to error patterns independent from GNSS. Moreover, the availability is assured even during the maneuvers realized around the bridges.

For simplicity on the analysis, this section focuses on the performance for four representative filters: the standard EKF, RIF-Tukey, GM-KF and I-VKF. These techniques are either the most promising, as for I-VKF, or provide robustness against innovation errors, as for GM-KF, which is relevant for real-world estimation in which the dynamical models are not perfect. As previously, the performance metrics relate to the accuracy of the float positioning estimates and the percentage of successfully estimated integer ambiguities. Unlike the synthetic scenario, the actual values for the integer ambiguities are not known beforehand and are regressed from the ground truth trajectory. Furthermore, a realistic approach for ambiguity resolution consists on the application of a validity test, as detailed in Section 2.3.2. Thus, the empirical fix ratio is here defined as the percentage of time epochs for which the estimated vector of ambiguities pass a FF-RT test and correspond to the true (regressed) ones.

**Table 6.2:** Percentage of fixed solutions (%).

| | **Estimator** | | | |
|---|---|---|---|---|
| | **EKF** | **RIF-Tukey** | **GM-KF** | **I-VKF** |
| **Fix ratio (%)** | 53.22 | 46.74 | 58.27 | 53.46 |

The norm for the 3D positioning errors associated with the float estimates against the time is depicted on the left side of Fig. 6.11, while the CDF associated with the former is shown on the right side of Fig. 6.11. The aforementioned figures concentrate on a period of slightly over 50 minutes for which several bridge passes occur, with a more extent discussion related to this measurement campaign can be consulted in [3], [6].

Paying attention to the time evolution of the errors, one realizes that filters based on robust statistics and, particularly the RIF-Tukey, present a performance similar to that of a conventional EKF. This is most likely due to the very low amount of observations' redundancy and, therefore, it becomes a complicated problem distinguishing whether observations are or not outliers. Even more, there are particular time instances in which both RIF-Tukey and GM-KF present positioning errors even larger than EKF, as for instance around the 450, 1000 and 2300 times. In general, the recommendation towards using I-VKF agrees with the conclusions derived from the simulation results since, also under real experimentation, the I-VKF overperforms the other robust filtering alternatives. In terms ol empirical fix ratio, the GM-KF is the only method that leads to certain gain in availability for fixed estimates. This is due to the capability of the GM-KF for dealing with innovation outliers or, in this case, addressing imperfect dynamical models. Thus, despite GM-KF not dealing with the presence of strong outliers as good as the I-VKF, GM-KF may improve the overall availability of a high precision positioning solution when tracking vehicles with uncertain kinematic models.

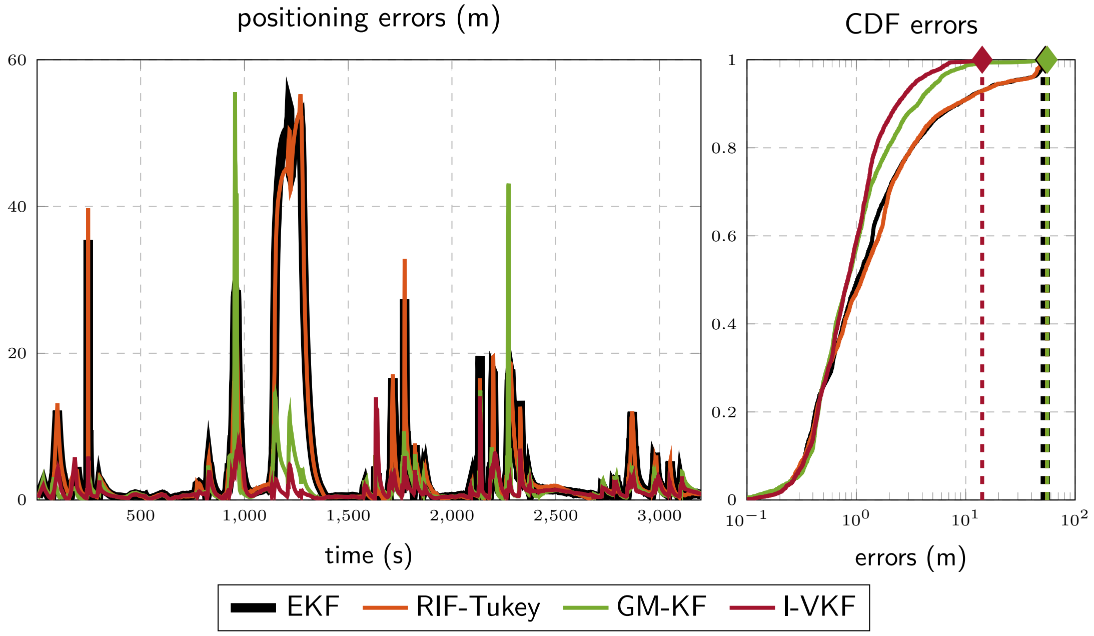

**Figure 6.11:** On the left, norm of the three-dimensional errors for the float positioning estimates for the various filters evaluated. On the right, CDF associated with the norm of the float positioning errors.

## 6.5 Summary

This chapter describes the motivation and need for filtering solutions able to "resist " the influence of outlying observations which do not comply with the assumption of normal-distributed noise. Thus, a short overview on the different robust filtering perspectives is presented, while it is discussed which of these result most convenient for GNSS-based navigation purposes. While the mixture of real and integer spaces is of great relevance for carrier phase-based positioning and attitude estimation problems, this chapter discusses the interesting fact related to robust filters not being directly affected by the mixed model, since the decomposition for the recursive mixed model in Section 2.2.1 allows for the robust estimators to actuate only over real-valued parameters on the float estimation step.

Within the context of this thesis, two distinct strategies for counteracting contaminated distributions are discussed, namely:

- Robust Statistics-based Filtering. This family of methods constitutes the extension of the robust estimators introduced in Chapter 5 to recursive problems. Such methods provide an elegant formalization for filtering under *approximate* distributions, able to provide nearly optimal solutions under both contaminated and clean distributions. Within the general class of robust estimators, the Robust Information Filters (RIFs) and the General M-estimation based Kalman Filter (GM-KF) are discussed and particularized for the GNSS-based navigation problems. On the one hand, RIFs pose as advantages their straightforward implementation and the capability to exploit hard recesdending score functions to nullify the influence of additive outliers. On the other hand, GM-KF provides robustness against both innovation and additive outliers, being able to deal with SSMs whose dynamical models are not perfectly described, at the cost of providing a comparatively poor relative efficiency at the normal model.

- Hypothesis Testing Filters via Variational Bayesian Inference. The driving idea of this class of estimators relates to detecting and discarding possible outliers within the vector of observations and, thus, a conventional filtering method deals solely with data distributed according to the assumed normal distribution. Instead of leveraging on conventional statistical testing, such as the $\chi^2$- or the Wald- tests, this chapter discusses on the use of VB-based inference to perform such task. Thus, one may represent the outlier indicators as random variables distributed according to a Bernoulli distribution, with the hyper-parameters to describe such distributions being estimated along with the remaining parameters of the state estimate. While this novel framework was originally described for a single indicator and under uncorrelated noise distributions, this chapter proposes a generalized form of this filtering technique for which independent outlier indicators can be estimated even under correlated measurements (i.e., crucial for differential carrier phase-based techniques, such as RTK positioning or attitude determination!).

The above-described two strategies for robust filtering are originally described for SSMs whose state estimates comprise solely real-valued parameters. The extension of robust filtering to attitude estimation, both for the GNSS-based attitude and JPA models, is discussed in Section 6.3. Fortunately, major inconveniences for the use of robust filtering on manifold spaces shall not be encountered, with the VB-based hypothesis testing being fully unaffected, while robust statistics-based filters require a couple of minor modifications for their functioning. The actual characterization of robust filters for multi-antenna configurations and attitude determination constitutes one of the prospective research lines of this thesis.

Section 6.4.1 presented a number of simulation results based on Monte Carlo experimentation, while real-world data analysis was performed in Section 6.4.2. In terms of performance characterization for the evaluated methods, the following conclusions were extracted:

- The relative efficiency at the nominal model is shown to be notoriously high, especially when compared to robust estimators for regression problems. For methods derived from robust statistics, this is due to recursive problems having more information and presenting much higher data redundancy. Filters featuring VB-based hypothesis testing were shown to perform optimally, making evident that –probably also due to the observation redundancy– the probability distribution for the indicators was perfectly described and no false alarm was triggered.
- VB-based robust filtering with independent outlier indicators can be recommended with high confidence for GNSS-based navigation under multipath and NLOS conditions. While small finite datasets affect the performance of the former method almost as much as it does for robust statistics-based filters, which could be observed from the real data experimentation, a growing number of observation improves its performance significantly.
- In general, filters derived from the framework of robust estimation do not comply with their expected performance for linear regression problems under large number of observations. While robust filters operate more efficiently (relative to the normal model) and with higher robustness than robust estimators for snapshot code-based positioning, one would expect that filters which employ redescending functions would be able to handle a dataset containing up to 40% of contaminated measurements. Unfortunately, both from the synthetic and real experimentation it was shown that the former expectation cannot be satisfied. It is definitely clear that there is room for improving robust filters, especially when it comes to automatically adapting the tuning parameters (i.e., $c_{\text{Hub}}, c_{\text{Tuk}}, c_{\text{Igg}}$, etc.) for fat datasets.

The research contributions of this chapter were partially published in:

**Journal articles:**

[3] Medina, D., Li, H., Vilà-Valls, J., & Closas, P. (2021). Robust Filtering Techniques for RTK Positioning in Harsh Propagation Environments. *Sensors, 21*(4), 1250.

[5] Li, H., Medina, D., Vilà-Valls, J., & Closas, P. (2020). Robust Variational-based Kalman Filter for Outlier Rejection with Correlated Measurements. IEEE Transactions on Signal Processing, 69, 357-369.

**Conference articles:**

[18] Li, H., Medina, D., Vilà-Valls, J., & Closas, P. (2019, September). Robust Kalman Filter for RTK Positioning Under Signal-Degraded Scenarios. In *Proceedings of the 32nd International Technical Meeting of the Satellite Division of The Institute of Navigation (ION GNSS+ 2019)* (pp. 16–20). ION.

[21] Crespillo, O. G., Medina, D., Skaloud, J.,& Meurer, M. (2018, April). Tightly coupled GNSS/INS integration based on robust M-estimators. In *2018 IEEE/ION Position, Location and Navigation Symposium (PLANS)* (pp. 1554-1561). IEEE.

# Conclusions and Future Research

This thesis addresses the provision of robust solutions for precise position and attitude estimation by exploiting GNSS carrier phase observations. Some contributions are introduced, in relation to the derivation of lower bounds for signal tracking and the mixed integer models, the introduction of estimators for multi-antenna attitude problems and robust solvers for navigation under the presence of unmodeled impulsive noise. The present is a conclusive chapter whose aim is to summarize the objectives, contributions and prospective lines for research arising from each of the topics assessed in the previous chapters.

The first chapter of the dissertation intends at relating the quality of ranging observables with the performance of a receiver at satellite tracking, given a set of "raw" signal samples. Closing the gap between the receiver's signal processing and the actual PVT performance is a twofold issue: first, fundamental bounds for estimating the parameters of a band-limited signal are derived; then, the MLE for such parameters determines the final quality of the code and carrier phase observations. It is shown that signals exploiting larger bandwidths allow for more precise code observables, while the precision on carrier phase measurements is dictated by the signals' frequency. With regards to meta-signals, it results clear their interest as alternative to conventional carrier phase-based positioning techniques, allowing to provide highly accurate code observables for high SNRs. On the other hand, their practicability becomes compromised as SNR decreases, since the presence of multiple secondary peaks close to the main one jeopardize tracking the signal.

Chapter 2 reviews the principles for carrier phase-based positioning and introduces a general lower bound for estimation problems where real- and integer-valued parameters are to be regressed. The particularization of the former bound, in the form of CRB, for linear models under Gaussian distributions allows to define the ultimate best achievable positioning performance and serves as benchmark for estimators at these models. It is shown the existence of asymptotic performance regions for the aforementioned estimators, based on the number and geometry of the tracked satellites and on the noise levels. Thus, a new proof is given for the existence of optimal estimators at the mixed model, typical for RTK positioning applications, which attain the lower bound in asymptotic conditions. More importantly, there exists a threshold region upon which the MLE loses its efficiency due to the vector of ambiguities not being matched to the true one. Immediately after the threshold region, unsuccessful integer estimation leads to positioning errors larger than those of the float solution, which is a sound reason to perform validity tests over the integer estimation. An alternative approach to conventional estimation of the mixed model relates to PAR, the latter relaxing the condition of performing the complete set of ambiguities and, instead, real-to-integer mapping a subset of them. The introduction of a new estimator, PD-PAR, showcases the capability to find a compromise between precision of the positioning solution and a gain in the extent of the asymptotic regime. In other words, one may concern with fixing solely those ambiguities which lead to a relevant precision gain, circumventing the challenge of estimating the complete vector of them. At last, the ultimate achievable positioning precision is shown in relation to the performance of a GNSS receiver, given by the SNR at the output of the matched filter. As for code-based positioning, the use of large bandwidth signals, and particularly Galileo E5, allows attaining the lower bound even under poor propagation conditions. On the contrary, meta-signals are not an appealing option for carrier phase-based applications: their convergence to the bound occurs only for high SNRs while they do not lead to higher precision.

Due to its novelty, different research lines exist whose study is worth exploring:

- The determination of the SNR or observables noise level at which the threshold region starts for estimators at the mixed model.
- Verify the relationship established between the receiver signal processing and the final positioning performance for a real scenario, based on a fully controlled SDR-based GNSS receiver.
- Study the applicability of PD-PAR for multi-antenna configurations, since the redundancy in these cases becomes more evident than for positioning.
- Extend the CRB for the mixed model to a Bayesian CRB which, among other applications, could serve to provide theoretical insight on the performance and convergence time for the PPP problem. For instance, given a set of correction data (e.g., ultra rapid, rapid or final products), a certain geometry and the number of tracked frequencies, one would be able to asses the minimum required time until a particular target precision is reached.

Chapter 3 and Chapter 4 focus on multi-antenna systems for orientation and pose estimation, respectively. Instead of the well-known MC-LAMBDA, this thesis contributes with Q-LAMBDA as alternative to solve the attitude mixed model. Based on the quaternion parametrization of the rotation and a set of actions based on Lie theory, Q-LAMBDA constitutes an approximately optimal (conditioned on the initialization) and computationally efficient estimator for the carrier phase-based attitude model. Moreover, one may conclude that ESKF results the perfect fit for the recursive estimation of multi-antenna problems, since it presents minimal state parametrization, incorporates all the algebra machinery of the Lie theory and allows for straightforward derivations. On another note, the employment of the JPA model may be considered a fundamental piece for pose estimation in land-based vehicles, leading to a vast gain both in accuracy and availability for the precise navigation estimates. The definition of the JPA mixed model, together with its stochastic modeling, is a contribution on itself which has been overlooked by the GNSS research community. An extension of the proposed Q-LAMBDA serves as deterministic estimator for JPA, while the ESKF can be also easily adapted for the same purpose.

At the conclusion of this thesis, there remain certain lines of research related to multi-antenna pose estimation which shall be prosecuted:

- The derivation of lower bounds for the carrier phase-based attitude problem is, arguably, the most interesting and challenging open topic for this thesis. Provided that such bound existed, the performance estimators for the attitude and JPA mixed models could be assessed formally. Moreover, a lower bound of this kind would allow to characterize the precision for attitude estimates without leveraging on simple geometric rules.

- Study the applicability of Invariant Filtering for carrier phase-based attitude estimation is quite promising, given that such type of filter provides convergence guarantees.
- Integrate vision systems as source of attitude information and address their influence over GNSS- and inertial-based solutions.

Chapter 5 and Chapter 6 reviews the principles of robust statistics and its wide family of estimators for regression problems. Within the context of code-based positioning, the challenges associated with the direct application of robust estimators are discussed. Profound details on how resilient estimators shall be formulated for their correct functioning under the nonlinear SPP problem are provided, along with the formulation for their relative efficiency. Unfortunately, the flexibility of robust estimators can also be seen as a major inconvenience: one may never be sure of the actual properties of these estimators, neither in the MLE or the robust sense (i.e., the *near* optimality is complicated to addressed, and so is the breakdown point). Nonetheless, robust estimators are an extremely promising and powerful tool, especially given the perspective in which the data redundancy is high enough. Especially for urban scenarios or safety-critical applications, both which are subject to large multipath effects, it is hard to imagine that conventional MLE could remain an standard. Nonetheless, for the complete implantation of robust methods, certain aspects shall be addressed:

- The choice for the tuning parameter, which controls a robust estimator efficiency, shall be performed in an adaptive manner and based on the current situations. For instance, given a finite number of observations, one could rapidly incur in ill-posed and un-observable estimation problems if too many measurements are discarded.
- Robustness shall not be limited to impulsive noises and violations of the Gaussian conditions. For instance, the development of estimators that handle mis-mismatches on certain model parameters (e.g., in multi-antenna configurations, whenever the inter-antenna distance is vaguely known or slightly erroneous) is indispensable.
- It remains yet to be evaluated the performance of robust filtering solutions at the attitude and JPA mixed model, both in simulated and real-data conditions.

*"Todo lo que somos es el resultado de lo que hemos pensado"*
Gautama Buddha

# Appendices

# APPENDIX A

# Derivations and Proofs

## A.1 Proof of the CRB Expression for the GNSS Signal Model

First notice that

$$\mathbf{CRB}_{\boldsymbol{\theta}} = \frac{\sigma_n^2}{2\rho^2}\boldsymbol{\Phi}_{\eta}^{-1}$$

$$\boldsymbol{\Phi}_{\boldsymbol{\theta}} = \lim_{\left(N_1',N_2'\right)\to(-\infty,+\infty)} \mathsf{Re}\left\{\left(\frac{\partial \mathbf{a}\left(\boldsymbol{\theta}\right)}{\partial \boldsymbol{\theta}^{\top}}\right)^{H} \boldsymbol{\Pi}_{\mathbf{a}(\boldsymbol{\theta})}^{\perp} \frac{\partial \mathbf{a}\left(\boldsymbol{\theta}\right)}{\partial \boldsymbol{\theta}^{\top}}\right\}.$$

The derivative of $a\left(t;\boldsymbol{\theta}\right)$ w.r.t. the parameters of interest reads

$$\frac{\partial a\left(t;\boldsymbol{\theta}\right)}{\partial \boldsymbol{\theta}} = -\mathbf{Q}\boldsymbol{\vartheta}\left(t-\tau\right)\exp\left(-j\omega_c b\left(t-\tau\right)\right),$$

$$\mathbf{Q} = \begin{bmatrix} -j\omega_c b & 0 & 1 \\ 0 & j\omega_c & 0 \end{bmatrix},\ \vartheta\left(t\right) = \begin{pmatrix} c\left(t\right) \\ tc\left(t\right) \\ c^{(1)}\left(t\right) \end{pmatrix}.$$

where $c^{(1)}\left(t\right) = \frac{dc(t)}{dt}$. Then we can write

$$\mathbf{a}^{H}\left(\boldsymbol{\theta}\right)\frac{\partial \mathbf{a}\left(\boldsymbol{\theta}\right)}{\partial \boldsymbol{\theta}^{\top}} = -\left(\mathbf{Q}\sum_{n=N_1'}^{N_2'}\boldsymbol{\vartheta}\left(nT_s-\tau\right)c\left(nT_s-\tau\right)^{*}\right)^{\top},$$

$$\frac{\partial \mathbf{a}\left(\boldsymbol{\theta}\right)}{\partial \eta^{\top}}^{H}\frac{\partial \mathbf{a}\left(\boldsymbol{\theta}\right)}{\partial \boldsymbol{\theta}^{\top}} = \mathbf{Q}^{*}\left(\sum_{n=N_1'}^{N_2'}\boldsymbol{\vartheta}\left(nT_s-\tau\right)\boldsymbol{\vartheta}^{H}\left(nT_s-\tau\right)\right)\mathbf{Q}^{\top}$$

$$\left\|\mathbf{a}\left(\boldsymbol{\theta}\right)\right\|^2 = \sum_{n=N_1'}^{N_2'}\left\|c\left(nT_s-\tau\right)\right\|^2,$$

and

$$\begin{aligned}\lim_{\left(N_1',N_2'\right)\to(-\infty,+\infty)} T_s \sum_{n=N_1'}^{N_2'} \boldsymbol{\vartheta}\left(nT_s-\tau\right) c\left(nT_s-\tau\right)^* &= \int_{-\infty}^{+\infty} \boldsymbol{\vartheta}\left(t-\tau\right) c\left(t-\tau\right)^* dt \\ &= \int_{-\infty}^{+\infty} \vartheta\left(t\right) c\left(t\right)^* dt = \mathbf{w},\end{aligned}$$

$$\begin{aligned}\lim_{\left(N_1',N_2'\right)\to(-\infty,+\infty)} T_s \sum_{n=N_1'}^{N_2'} \boldsymbol{\vartheta}\left(nT_s-\tau\right) \vartheta^H\left(nT_s-\tau\right) &= \int_{-\infty}^{+\infty} \boldsymbol{\vartheta}\left(t-\tau\right) \boldsymbol{\vartheta}\left(t-\tau\right)^H dt \\ &= \int_{-\infty}^{+\infty} \boldsymbol{\vartheta}\left(t\right) \boldsymbol{\vartheta}\left(t\right)^H dt = \mathbf{W}\end{aligned}$$

with

$$\mathbf{w} = \begin{pmatrix} w_1 \\ w_2 \\ w_3 \end{pmatrix}, \quad \mathbf{W} = \begin{bmatrix} w_1 & w_2^* & w_3^* \\ w_2 & W_{2,2} & \varpi^* \\ w_3 & \varpi & W_{3,3} \end{bmatrix},$$

where $\varpi = \int_{-\infty}^{+\infty} tc^{(1)}\left(t\right) c\left(t\right)^* dt$, and $w_1, w_2, W_{2,2}, W_{3,3} \in \mathbb{R}$. From these results, we can write that $\boldsymbol{\Phi}_{\boldsymbol{\theta}}$ is

$$\boldsymbol{\Phi}_{\boldsymbol{\theta}} = F_s \mathsf{Re}\left\{\mathbf{QWQ}^H - \frac{\left(\mathbf{Qw}\right)\left(\mathbf{Qw}\right)^H}{w_1}\right\} = F_s \begin{bmatrix} W_{3,3} - \frac{|w_3|^2}{w_1} & \omega_c \mathsf{Im}\left\{\varpi - \frac{w_2 w_3}{w_1}\right\} \\ \omega_c \mathsf{Im}\left\{\varpi - \frac{w_2 w_3}{w_1}\right\} & \omega_c^2\left(W_{2,2} - \frac{w_2^2}{w_1}\right) \end{bmatrix},$$

where from [233] we already have $w_1$, $w_3$ and $W_{3,3}$,

$$w_1 = \frac{\mathbf{c}^H\mathbf{r}}{F_s},\ w_3 = \mathbf{c}^H\boldsymbol{\Lambda}\mathbf{c},\ W_{3,3} = F_s\mathbf{c}^H\mathbf{V}\mathbf{c},$$

and the remaining terms are computed as

$$
\begin{aligned}
w_2 &= \int_{-\infty}^{+\infty} c\left(t\right)\left(tc\left(t\right)\right)^{*} dt = \int_{-\frac{F_s}{2}}^{\frac{F_s}{2}} c\left(f\right)\left(\frac{j}{2\pi}\frac{dc\left(f\right)}{df}\right)^{*} df \\
&= \frac{1}{F_s^2}\int_{-\frac{1}{2}}^{\frac{1}{2}} \left(\left(\mathbf{D}\mathbf{c}\right)^{H}\boldsymbol{v}\left(f\right)\right)\left(\boldsymbol{v}^{H}\left(f\right)\mathbf{c}\right) df \\
&= \frac{1}{F_s^2}\mathbf{c}^{H}\mathbf{D}^{H}\left(\int_{-\frac{1}{2}}^{\frac{1}{2}} \boldsymbol{v}\left(f\right)\boldsymbol{v}^{H}\left(f\right) df\right)\mathbf{c} = \frac{1}{F_s^2}\mathbf{c}^{H}\mathbf{D}\mathbf{c}, \\
\varpi &= \int_{-\infty}^{+\infty} c^{(1)}\left(t\right)\left(tc\left(t\right)\right)^{*} dt \\
&= \int_{-\frac{F_s}{2}}^{\frac{F_s}{2}} \left(j2\pi f\right) c\left(f\right)\left(\frac{j}{2\pi}\frac{dc\left(f\right)}{df}\right)^{*} df \\
&= \frac{1}{F_s}\int_{-\frac{1}{2}}^{\frac{1}{2}} \left(j2\pi f\right)\left(\boldsymbol{v}^{H}\left(f\right)\mathbf{c}\right)\left(\left(\mathbf{D}\mathbf{c}\right)^{H}\boldsymbol{v}\left(f\right)\right) df \\
&= \frac{1}{F_s}\mathbf{c}^{H}\mathbf{D}^{H}\left(j2\pi\int_{-\frac{1}{2}}^{\frac{1}{2}} f\boldsymbol{v}\left(f\right)\boldsymbol{v}^{H}\left(f\right) df\right)\mathbf{c} = \frac{1}{F_s}\mathbf{c}^{H}\mathbf{D}\boldsymbol{\Lambda}\mathbf{c}, \\
W_{2,2} &= \int_{-\infty}^{+\infty} \left|tc\left(t\right)\right|^{2} dt = \int_{-\frac{F_s}{2}}^{\frac{F_s}{2}} \left|\frac{j}{2\pi}\frac{dc\left(f\right)}{df}\right|^{2} df \\
&= \frac{1}{F_s^3}\int_{-\frac{1}{2}}^{\frac{1}{2}} \left|\boldsymbol{v}^{H}\left(f\right)\left(\mathbf{D}\mathbf{c}\right)\right|^{2} df \\
&= \frac{1}{F_s^3}\mathbf{c}^{H}\mathbf{D}^{H}\left(\int_{-\frac{1}{2}}^{\frac{1}{2}} \boldsymbol{v}\left(f\right)\boldsymbol{v}^{H}\left(f\right) df\right)\mathbf{D}\mathbf{c} = \frac{1}{F_s^3}\mathbf{c}^{H}\mathbf{D}^{2}\mathbf{c}.
\end{aligned}
$$

Finally, the other terms in (1.17)-(1.19) are also computed from $\mathbf{w}$ as follows:

$$
\begin{aligned}
CRB_{\varphi} &= \frac{\sigma_n^2}{2\rho^2}\frac{1}{F_s w_1} + \frac{1}{w_1^2}\begin{pmatrix} \mathsf{Im}\left\{w_3\right\} - b\omega_c w_1 \\ \omega_c w_2 \end{pmatrix}^{\top}\mathbf{CRB}_{\boldsymbol{\theta}}\begin{pmatrix} \mathsf{Im}\left\{w_3\right\} - b\omega_c w_1 \\ \omega_c w_2 \end{pmatrix}, \\
\mathbf{CRB}_{\boldsymbol{\theta},\varphi} &= \mathbf{CRB}_{\boldsymbol{\theta}}\frac{1}{w_1}\begin{pmatrix} \mathsf{Im}\left\{w_3\right\} - b\omega_c w_1 \\ \omega_c w_2 \end{pmatrix}, \\
CRB_{A} &= \frac{\sigma_n^2}{2F_s w_1} + \rho^2\frac{1}{w_1^2}\begin{pmatrix} \mathsf{Re}\left\{w_3\right\} \\ 0 \end{pmatrix}^{\top}\mathbf{CRB}_{\boldsymbol{\theta}}\begin{pmatrix} \mathsf{Re}\left\{w_3\right\} \\ 0 \end{pmatrix}.
\end{aligned}
$$

□

## A.2 Proof for the Equivalence of LS and KF Update

Let us recall the conventional KF representation for the DSS described in Sec. 2.2.1, whose process and observation models are linear, such that

$$\mathbf{x}_t = \mathbf{F}_t \mathbf{x}_t + \mathbf{w}_t, \quad \mathbf{y}_t = \mathbf{H}_t \mathbf{x}_t + \boldsymbol{\eta}_t, \tag{A.1}$$

and the classical KF update procedure expressed using the Kalman gain matrix, as

$$\mathbf{K}_t = \mathbf{P}_{t|t-1} \mathbf{H}_t^\top \left( \mathbf{H}_t \mathbf{P}_{t|t-1} \mathbf{H}_t^\top + \boldsymbol{\Sigma}_t \right)^{-1}, \tag{A.2}$$

$$\mathbf{x}_{t|t} = \mathbf{x}_{t|t-1} + \mathbf{K}_t \left( \mathbf{y}_t - \mathbf{H}_t \mathbf{x}_{t|t-1} \right), \tag{A.3}$$

$$\mathbf{P}_{t|t} = \mathbf{P}_{t|t-1} - \mathbf{K}_t \mathbf{H}_t \mathbf{P}_{t|t-1}. \tag{A.4}$$

Similarly, a LS adjustment for the estimate of $\mathbf{x}_t$ given a set of observations $\mathbf{y}_t$ is as

$$\mathbf{x}_{t|t} = \left( \mathbf{H}_t^\top \boldsymbol{\Sigma}_t^{-1} \mathbf{H}_t \right)^{-1} \mathbf{H}_t^\top \boldsymbol{\Sigma}_t^{-1} \mathbf{y}_t, \tag{A.5}$$

and, in order to consider the a priori information on the state estimate (i.e., from the prediction $\mathbf{x}_{t|t-1}, \mathbf{P}_{t|t-1}$), one would augment the vector of observations as

$$\tilde{\mathbf{y}}_t = \begin{bmatrix} \mathbf{y}_t \\ \mathbf{x}_{t|t-1} \end{bmatrix}, \; \tilde{\boldsymbol{\Sigma}}_t = \begin{bmatrix} \boldsymbol{\Sigma}_t & \mathbf{0} \\ \mathbf{0} & \mathbf{P}_{t|t-1} \end{bmatrix}, \; \tilde{\mathbf{H}}_t = \begin{bmatrix} \mathbf{H}_t \\ \mathbf{I} \end{bmatrix},$$

and, reformulating (A.5) in terms of the augmented observations the following LS is obtained

$$\mathbf{x}_{t|t} = \left( \tilde{\mathbf{H}}_t^\top \tilde{\boldsymbol{\Sigma}}_t^{-1} \tilde{\mathbf{H}}_t \right)^{-1} \tilde{\mathbf{H}}_t^\top \tilde{\boldsymbol{\Sigma}}_t^{-1} \tilde{\mathbf{y}}_t, \tag{A.6}$$

which expands to

$$\mathbf{x}_{t|t} = \left( \begin{bmatrix} \mathbf{H}_t & \mathbf{I} \end{bmatrix} \begin{bmatrix} \boldsymbol{\Sigma}_t^{-1} & \mathbf{0} \\ \mathbf{0} & \mathbf{P}_{t|t-1}^{-1} \end{bmatrix} \begin{bmatrix} \mathbf{H}_t \\ \mathbf{I} \end{bmatrix} \right)^{-1} \begin{bmatrix} \mathbf{H}_t & \mathbf{I} \end{bmatrix} \begin{bmatrix} \boldsymbol{\Sigma}_t^{-1} & \mathbf{0} \\ \mathbf{0} & \mathbf{P}_{t|t-1}^{-1} \end{bmatrix} \begin{bmatrix} \mathbf{y}_t \\ \mathbf{x}_{t|t-1} \end{bmatrix},$$

and, after solving the matrix products, the following expression is obtained

$$\mathbf{x}_{t|t} = \left( \mathbf{H}_t^\top \boldsymbol{\Sigma}_t^{-1} \mathbf{H}_t + \mathbf{P}_{t|t-1}^{-1} \right)^{-1} \left( \mathbf{H}_t^\top \boldsymbol{\Sigma}_t^{-1} \mathbf{y}_t + \mathbf{P}_{t|t-1}^{-1} \mathbf{x}_{t|t-1} \right), \tag{A.7}$$

where the Woodbury identity allows to express the inverse [234] for the first multiplier in (A.7) as

$$\begin{aligned} \mathbf{x}_{t|t-1} = & \left( \mathbf{P}_{t|t-1} - \mathbf{P}_{t|t-1} \mathbf{H}_t^\top \left( \boldsymbol{\Sigma}_t + \mathbf{H}_t \mathbf{P}_{t|t-1} \mathbf{H}_t^\top \right)^{-1} \mathbf{H}_t \mathbf{P}_{t|t-1} \right) \\ & \left( \mathbf{H}_t^\top \boldsymbol{\Sigma}_t^{-1} \mathbf{y}_t + \mathbf{P}_{t|t-1}^{-1} \mathbf{x}_{t|t-1} \right) \end{aligned}$$

and, further developing the product

$$\begin{aligned} \mathbf{x}_{t|t} = & \, \mathbf{P}_{t|t-1} \mathbf{H}_t^\top \boldsymbol{\Sigma}_t^{-1} \mathbf{y}_t \\ & - \mathbf{P}_{t|t-1} \mathbf{H}_t^\top \left( \boldsymbol{\Sigma}_t + \mathbf{H}_t \mathbf{P}_{t|t-1} \mathbf{H}_t^\top \right)^{-1} \mathbf{H}_t \mathbf{P}_{t|t-1} \mathbf{H}_t^\top \boldsymbol{\Sigma}_t^{-1} \mathbf{y}_k \\ & + \mathbf{x}_{t|t-1} - \underbrace{\mathbf{P}_{t|t-1} \mathbf{H}_t^\top \left( \boldsymbol{\Sigma}_t + \mathbf{H}_t \mathbf{P}_{t|t-1} \mathbf{H}_t^\top \right)^{-1}}_{\mathbf{K}_t} \mathbf{H}_t \mathbf{x}_{t|t-1}, \end{aligned}$$

where the Kalman gain in (A.2) can be easily be recognized. Then, the terms multiplying $\mathbf{y}_k$ can be grouped

$$\begin{aligned}\mathbf{x}_{t|t} =& \mathbf{x}_{t|t-1} - \mathbf{K}_t\mathbf{H}_t\mathbf{x}_{t|t-1} \\ &+ \left(\mathbf{P}_{t|t-1}\mathbf{H}_t^\top\mathbf{\Sigma}_t^{-1} - \mathbf{P}_{t|t-1}\mathbf{H}_t^\top\left(\mathbf{\Sigma}_t + \mathbf{H}_t\mathbf{P}_{t|t-1}\mathbf{H}_t^\top\right)^{-1}\mathbf{H}_t\mathbf{P}_{t|t-1}\mathbf{H}_t^\top\mathbf{\Sigma}_t^{-1}\right)\mathbf{y}_t,\end{aligned} \tag{A.8}$$

and, after resorting (A.8) and factoring $\mathbf{P}_{t|t-1}\mathbf{H}_t^\top$ on the left and $\mathbf{\Sigma}_t^{-1}$ on the right, one gets

$$\begin{aligned}\mathbf{x}_{t|t} &= \mathbf{x}_{t|t-1} - \mathbf{K}_t\mathbf{H}_t\mathbf{x}_{t|t-1} \\ &+ \mathbf{P}_{t|t-1}\mathbf{H}_t^\top\underbrace{\left(\mathbf{I} - \left(\mathbf{\Sigma}_t + \mathbf{H}_t\mathbf{P}_{t|t-1}\mathbf{H}_t^\top\right)^{-1}\mathbf{H}_t\mathbf{P}_{t|t-1}\mathbf{H}_t^\top\right)}\mathbf{\Sigma}_t^{-1}\mathbf{y}_t,\end{aligned} \tag{A.9}$$

and operating over the under-braced parenthesis on (A.9), the following simplification can be obtained

$$\begin{aligned}\mathbf{I} - \left(\mathbf{\Sigma}_t + \mathbf{H}_t\mathbf{P}_{t|t-1}\mathbf{H}_t^\top\right)^{-1}\mathbf{H}_t\mathbf{P}_{t|t-1}\mathbf{H}_t^\top &= \mathbf{I} - \frac{\mathbf{H}_k\mathbf{P}_{t|t-1}\mathbf{H}_t^\top}{\left(\mathbf{\Sigma}_t + \mathbf{H}_t\mathbf{P}_{t|t-1}\mathbf{H}_t^\top\right)} \\ &= \frac{\mathbf{\Sigma}_t}{\left(\mathbf{\Sigma}_t + \mathbf{H}_t\mathbf{P}_{t|t-1}\mathbf{H}_t^\top\right)}.\end{aligned} \tag{A.10}$$

Bringing back (A.10) into (A.9) and re-sorting the elements lead to the following expression

$$\begin{aligned}\mathbf{x}_{t|t} &= \mathbf{x}_{t|t-1} - \mathbf{K}_t\mathbf{H}_t\mathbf{x}_{t|t-1} \\ &+ \underbrace{\mathbf{P}_{t|t-1}\mathbf{H}_t^\top\left(\mathbf{\Sigma}_t + \mathbf{H}_t\mathbf{P}_{t|t-1}\mathbf{H}_t^\top\right)^{-1}}_{\mathbf{K}_t}\mathbf{\Sigma}_t\mathbf{\Sigma}_t^{-1}\mathbf{y}_t, \\ &= \mathbf{x}_{t|t-1} + \mathbf{K}_t\left(\mathbf{y}_t - \mathbf{H}_t\mathbf{x}_{t|t-1}\right),\end{aligned}$$

which showcases that the LS adjustment in (A.6) is equivalent to the KF update (A.3). □

## A.3 Proof of (2.91)-(2.93)

Let $\varepsilon_{\mathbf{g}}(\mathbf{y};\mathbf{x}) = \mathbf{g}(\hat{\mathbf{x}}) - \mathbf{g}(\mathbf{x})$. From Lemma 3 in [98], the set of linear constraints

$$\mathbb{E}_{\mathbf{y};\mathbf{x}}\left[\upsilon_{\mathbf{x}}\left(\mathbf{y};\{\mathbf{x}\}^{1+K}\right)\varepsilon_{\mathbf{g}}^{\top}(\mathbf{y};\mathbf{x})\right] = \begin{bmatrix} \mathbf{0}^{\top} \\ \left(\mathbf{g}\left(\mathbf{x}+\mathbf{i}_1 dx_1\right) - \mathbf{g}\left(\mathbf{x}\right)\right)^{\top} \\ \vdots \\ \left(\mathbf{g}\left(\mathbf{x}+\mathbf{i}_K dx_K\right) - \mathbf{g}\left(\mathbf{x}\right)\right)^{\top} \end{bmatrix} = \mathbf{V}, \tag{A.11}$$

are equivalent to

$$\mathbf{T}^{\top}\mathbb{E}_{\mathbf{y};\mathbf{x}}\left[\boldsymbol{\upsilon}_{\mathbf{x}}\left(\mathbf{y};\{\mathbf{x}\}^{1+K}\right)\varepsilon_{\mathbf{g}}^{\top}(\mathbf{y};\mathbf{x})\right] = \mathbf{T}^{\top}\mathbf{V},$$

where (weighted subtraction of the first constraint)

$$\mathbf{T}^{\top} = \begin{bmatrix} 1 & 0 & 0 & \dots & 0 \\ -1/dx_1 & 1/dx_1 & 0 & \dots & 0 \\ -1/dx_2 & 0 & 1/dx_2 & 0 & \vdots \\ \vdots & \vdots & 0 & \ddots & 0 \\ -1/dx_K & 0 & \dots & 0 & 1/dx_K \end{bmatrix},$$

that is

$$\mathbb{E}_{\mathbf{y};\mathbf{x}}\left[\begin{pmatrix} 1 \\ \frac{p(\mathbf{y};\mathbf{x}+\mathbf{i}_1 dx_1)-p(\mathbf{y};\mathbf{x})}{dx_1 p(\mathbf{y};\mathbf{x})} \\ \vdots \\ \frac{p(\mathbf{y};\mathbf{x}+\mathbf{i}_K dx_K)-p(\mathbf{y};\mathbf{x})}{dx_K p(\mathbf{y};\mathbf{x})} \end{pmatrix}\varepsilon_{\mathbf{g}}^{\top}(\mathbf{y};\mathbf{x})\right] = \begin{bmatrix} \mathbf{0}^{\top} \\ \left(\frac{\mathbf{g}(\mathbf{x}+\mathbf{i}_1 dx_1)-\mathbf{g}(\mathbf{x})}{dx_1}\right)^{\top} \\ \vdots \\ \left(\frac{\mathbf{g}(\mathbf{x}+\mathbf{i}_K dx_K)-\mathbf{g}(\mathbf{x})}{dx_K}\right)^{\top} \end{bmatrix}. \tag{A.12}$$

Moreover, since

$$\begin{aligned} \mathbb{E}_{\mathbf{y};\mathbf{x}}\left[1 \times \begin{pmatrix} \frac{p(\mathbf{y};\mathbf{x}+\mathbf{i}_1 dx_1)-p(\mathbf{y};\mathbf{x})}{dx_1 p(\mathbf{y};\mathbf{x})} \\ \vdots \\ \frac{p(\mathbf{y};\mathbf{x}+\mathbf{i}_K dx_K)-p(\mathbf{y};\mathbf{x})}{dx_K p(\mathbf{y};\mathbf{x})} \end{pmatrix}\right] &= \begin{bmatrix} \frac{1}{dx_1}\left(\mathbb{E}_{\mathbf{y};\mathbf{x}}\left[\frac{p(\mathbf{y};\mathbf{x}+\mathbf{i}_1 dx_1)}{p(\mathbf{y};\mathbf{x})}\right] - 1\right) \\ \vdots \\ \frac{1}{dx_K}\left(\mathbb{E}_{\mathbf{y};\mathbf{x}}\left[\frac{p(\mathbf{y};\mathbf{x}+\mathbf{i}_K dx_K)}{p(\mathbf{y};\mathbf{x})}\right] - 1\right) \end{bmatrix} \\ &= \mathbf{0}, \end{aligned}$$

we can apply Lemma 2 in [98] to assert that (A.11) and (A.12) are equivalent to

$$\mathbb{E}_{\mathbf{y};\mathbf{x}}\left[\begin{pmatrix} \frac{p(\mathbf{y};\mathbf{x}+\mathbf{i}_1 dx_1)-p(\mathbf{y};\mathbf{x})}{dx_1 p(\mathbf{y};\mathbf{x})} \\ \vdots \\ \frac{p(\mathbf{y};\mathbf{x}+\mathbf{i}_K dx_K)-p(\mathbf{y};\mathbf{x})}{dx_K p(\mathbf{y};\mathbf{x})} \end{pmatrix}\varepsilon_{\mathbf{g}}^{\top}(\mathbf{y};\mathbf{x})\right] = \begin{bmatrix} \left(\frac{\mathbf{g}(\mathbf{x}+\mathbf{i}_1 dx_1)-\mathbf{g}(\mathbf{x})}{dx_1}\right)^{\top} \\ \vdots \\ \left(\frac{\mathbf{g}(\mathbf{x}+\mathbf{i}_K dx_K)-\mathbf{g}(\mathbf{x})}{dx_K}\right)^{\top} \end{bmatrix}. \square \tag{A.13}$$

## A.4 Proof of Theorem 1

First, notice that in the real-valued parameter case, that is, if $x_k \in \mathbb{R}$, and both $\mathbf{g}(\mathbf{x})$ and $p(\mathbf{y};\mathbf{x})$ are $C^1$ at $x_k$, then, the constraints associated to the following two test points, $\{\mathbf{x} + \mathbf{i}_k dx_k, \mathbf{x} + \mathbf{i}_k(-dx_k)\} = \{\mathbf{x} + \mathbf{i}_k dx_k, \mathbf{x} - \mathbf{i}_k dx_k\}$,

$$\mathbb{E}_{\mathbf{y};\mathbf{x}}\left[\begin{pmatrix} \frac{p(\mathbf{y};\mathbf{x}+\mathbf{i}_k dx_k)-p(\mathbf{y};\mathbf{x})}{dx_k p(\mathbf{y};\mathbf{x})} \\ \frac{p(\mathbf{y};\mathbf{x}-\mathbf{i}_k dx_k)-p(\mathbf{y};\mathbf{x})}{(-dx_k)p(\mathbf{y};\mathbf{x})} \end{pmatrix} (\mathbf{g}(\hat{\mathbf{x}}) - \mathbf{g}(\mathbf{x}))^\top\right] = \begin{bmatrix} \left(\frac{\mathbf{g}(\mathbf{x}+\mathbf{i}_k dx_k)-\mathbf{g}(\mathbf{x})}{dx_k}\right)^\top \\ \left(\frac{\mathbf{g}(\mathbf{x}-\mathbf{i}_k dx_k)-\mathbf{g}(\mathbf{x})}{(-dx_k)}\right)^\top \end{bmatrix} \tag{A.14}$$

aim at the same single constraint in the limiting case where $dx_k \to 0$, $dx_k \neq 0$,

$$\mathbb{E}_{\mathbf{y};\mathbf{x}}\left[\frac{\partial \ln p(\mathbf{y};\mathbf{x})}{\partial x_k} (\mathbf{g}(\hat{\mathbf{x}}) - \mathbf{g}(\mathbf{x}))^\top\right] = \frac{\partial \mathbf{g}(\mathbf{x})}{\partial x_k}^\top. \tag{A.15}$$

However, this phenomenon is *unlikely* to happen if $x_k \in \mathbb{Z}$ in the limiting case where $dx_k \to 0$, $dx_k \neq 0$, since (A.14) then becomes

$$\mathbb{E}_{\mathbf{y};\mathbf{x}}\left[\begin{pmatrix} \frac{p(\mathbf{y};\mathbf{x}+\mathbf{i}_k)-p(\mathbf{y};\mathbf{x})}{p(\mathbf{y};\mathbf{x})} \\ \frac{p(\mathbf{y};\mathbf{x}-\mathbf{i}_k)-p(\mathbf{y};\mathbf{x})}{p(\mathbf{y};\mathbf{x})} \end{pmatrix} (\mathbf{g}(\hat{\mathbf{x}}) - \mathbf{g}(\mathbf{x}))^\top\right] = \begin{bmatrix} (\mathbf{g}(\mathbf{x}+\mathbf{i}_k) - \mathbf{g}(\mathbf{x}))^\top \\ (\mathbf{g}(\mathbf{x}-\mathbf{i}_k) - \mathbf{g}(\mathbf{x}))^\top \end{bmatrix}, \tag{A.16}$$

where $(p(\mathbf{y};\mathbf{x}+\mathbf{i}_k) - p(\mathbf{y};\mathbf{x}))/p(\mathbf{y};\mathbf{x})$ and $(p(\mathbf{y};\mathbf{x}-\mathbf{i}_k) - p(\mathbf{y};\mathbf{x}))/p(\mathbf{y};\mathbf{x})$ are unlikely to be linearly dependent (i.e., notice that $\widetilde{\mathbf{F}}(\mathbf{x}, d\mathbf{x})$ in (2.92) must be invertible to compute the $\mathbf{CRB}(\mathbf{g}(\hat{\mathbf{x}}))$ in (2.94a)). Therefore, *in most cases*, the combination of LCs (A.15) and (A.16) yields, from Lemma 1 in [98], the general definition (2.95) of $\mathbf{CRB}(\mathbf{g}(\hat{\mathbf{x}}))$ where the different terms in $\overline{\mathbf{F}}(\mathbf{x})$ are given by

$$\mathbf{F}_{\boldsymbol{\omega}\boldsymbol{\omega}} = \mathbb{E}_{\mathbf{y};\mathbf{x}}\left[\frac{\partial \ln p(\mathbf{y};\mathbf{x})}{\partial \boldsymbol{\omega}} \frac{\partial \ln p(\mathbf{y};\mathbf{x})}{\partial \boldsymbol{\omega}}^\top\right], \tag{A.17a}$$

$$\mathbf{F}_{\boldsymbol{\omega}\mathbf{z}} = \mathbb{E}_{\mathbf{y};\mathbf{x}}\left[\frac{\partial \ln p(\mathbf{y};\mathbf{x})}{\partial \boldsymbol{\omega}} (\mathbf{t}_{2K_z} - \mathbf{1}_{2K_z})^\top\right], \tag{A.17b}$$

$$\mathbf{F}_{\mathbf{z}\mathbf{z}} = \mathbb{E}_{\mathbf{y};\mathbf{x}}\left[(\mathbf{t}_{2K_z} - \mathbf{1}_{2K_z})(\mathbf{t}_{2K_z} - \mathbf{1}_{2K_z})^\top\right], \tag{A.17c}$$

and where $\mathbf{F}_{\boldsymbol{\omega}\mathbf{z}}$ and $\mathbf{F}_{\mathbf{z}\mathbf{z}}$ can also been expressed as (2.99b) and (2.99d). □

## A.5 Derivation of (2.102a)-(2.102d)

Let us consider an $n$-dimensional Gaussian real vector $\mathbf{y}$ such that $\mathbf{y} \sim \mathcal{N}\left(\boldsymbol{\mu}\left(\mathbf{x}\right), \boldsymbol{\Sigma}\left(\mathbf{x}\right)\right)$ and $p\left(\mathbf{y};\mathbf{x}\right) = p\left(\mathbf{y};\boldsymbol{\mu}\left(\mathbf{x}\right), \boldsymbol{\Sigma}\left(\mathbf{x}\right)\right)$ as in (2.101). The derivation of the components $\mathbf{F}_{\mathbf{zz}}$ and $\mathbf{F}_{\boldsymbol{\omega}\mathbf{z}}$ of the $\mathbf{CRB}\left(\mathbf{g}\left(\hat{\mathbf{x}}\right)\right)$ in (2.95-2.99d) is based on the following factorization property of the Gaussian real pdf,

$$\begin{aligned}
\frac{p\left(\mathbf{y};\mathbf{x}^{i}\right)p\left(\mathbf{y};\mathbf{x}^{j}\right)}{p\left(\mathbf{y};\mathbf{x}\right)} &= \frac{p\left(\mathbf{y};\boldsymbol{\mu}\left(\mathbf{x}^{i}\right), \boldsymbol{\Sigma}\left(\mathbf{x}^{i}\right)\right)p\left(\mathbf{y};\boldsymbol{\mu}\left(\mathbf{x}^{j}\right), \boldsymbol{\Sigma}\left(\mathbf{x}^{j}\right)\right)}{p\left(\mathbf{y};\boldsymbol{\mu}\left(\mathbf{x}\right), \boldsymbol{\Sigma}\left(\mathbf{x}\right)\right)} \\
&= \left[\mathbf{F}_{\mathbf{zz}}\right]_{i,j}\ p\left(\mathbf{y};\boldsymbol{\Sigma}^{ij}\boldsymbol{\mu}^{ij}, \boldsymbol{\Sigma}^{ij}\right), \qquad \text{(A.18)}
\end{aligned}$$

where

$$\begin{aligned}
\boldsymbol{\Sigma}^{ij} &= \left[\boldsymbol{\Sigma}\left(\mathbf{x}^{i}\right)^{-1} + \boldsymbol{\Sigma}\left(\mathbf{x}^{j}\right)^{-1} - \boldsymbol{\Sigma}\left(\mathbf{x}\right)^{-1}\right]^{-1}, \qquad \text{(A.19a)} \\
\boldsymbol{\mu}^{ij} &= \boldsymbol{\Sigma}\left(\mathbf{x}^{i}\right)^{-1}\boldsymbol{\mu}\left(\mathbf{x}^{i}\right) + \boldsymbol{\Sigma}\left(\mathbf{x}^{j}\right)^{-1}\boldsymbol{\mu}\left(\mathbf{x}^{j}\right) - \boldsymbol{\Sigma}\left(\mathbf{x}\right)^{-1}\boldsymbol{\mu}\left(\mathbf{x}\right), \qquad \text{(A.19b)} \\
\delta^{ij} &= \boldsymbol{\mu}\left(\mathbf{x}^{i}\right)^{\top}\boldsymbol{\Sigma}\left(\mathbf{x}^{i}\right)^{-1}\boldsymbol{\mu}\left(\mathbf{x}^{i}\right) + \boldsymbol{\mu}\left(\mathbf{x}^{j}\right)^{\top}\boldsymbol{\Sigma}\left(\mathbf{x}^{j}\right)^{-1}\boldsymbol{\mu}\left(\mathbf{x}^{j}\right) \\
&\quad - \boldsymbol{\mu}\left(\mathbf{x}\right)^{\top}\boldsymbol{\Sigma}\left(\mathbf{x}\right)^{-1}\boldsymbol{\mu}\left(\mathbf{x}\right), \qquad \text{(A.19c)} \\
\left[\mathbf{F}_{\mathbf{zz}}\right]_{i,j} &= \sqrt{\frac{\left|\boldsymbol{\Sigma}^{ij}\right|\left|\boldsymbol{\Sigma}\left(\mathbf{x}\right)\right|}{\left|\boldsymbol{\Sigma}\left(\mathbf{x}^{i}\right)\right|\left|\boldsymbol{\Sigma}\left(\mathbf{x}^{j}\right)\right|}}e^{\frac{1}{2}\left[\left(\boldsymbol{\mu}^{ij}\right)^{\top}\boldsymbol{\Sigma}^{ij}\boldsymbol{\mu}^{ij}-\delta^{ij}\right]}, \qquad \text{(A.19d)}
\end{aligned}$$

which suggests a breakdown into items $\left(\left[\mathbf{F}_{\mathbf{zz}}\right]_{i,j}, \mathbf{f}\left(\mathbf{x},\mathbf{x}^{j}\right)\right)$ depending only on the selected value $\mathbf{x}$ and a couple of test points $\left\{\mathbf{x}^{i},\mathbf{x}^{j}\right\}^{i,j\in[0,2K_Z]}$, as detailed in (2.99b-2.99d). Indeed, denoting

$$\mathbb{E}_{\mathbf{y}}^{ij}\left[g\left(\mathbf{y}\right)\right] = \int g\left(\mathbf{y}\right)p\left(\mathbf{y};\boldsymbol{\Sigma}^{ij}\boldsymbol{\mu}^{ij}, \boldsymbol{\Sigma}^{ij}\right)d\mathbf{y}, \qquad \text{(A.20a)}$$

then

$$\begin{aligned}
\left[\mathbf{F}_{\mathbf{zz}}\right]_{i,j} &= \mathbb{E}_{\mathbf{y};\mathbf{x}}\left[\frac{p\left(\mathbf{y};\mathbf{x}^{i}\right)}{p\left(\mathbf{y};\mathbf{x}\right)}\frac{p\left(\mathbf{y};\mathbf{x}^{j}\right)}{p\left(\mathbf{y};\mathbf{x}\right)}\right] \\
&= \left[\mathbf{F}_{\mathbf{zz}}\right]_{i,j}\int p\left(\mathbf{y};\boldsymbol{\Sigma}^{ij}\boldsymbol{\mu}^{ij}, \boldsymbol{\Sigma}^{ij}\right)d\mathbf{y} \qquad \text{(A.20b)} \\
\mathbf{f}\left(\mathbf{x}^{i},\mathbf{x}^{j}\right) &= \mathbb{E}_{\mathbf{y};\mathbf{x}}\left[\frac{\partial \ln p\left(\mathbf{y};\mathbf{x}^{i}\right)}{\partial \mathbf{x}}\frac{p\left(\mathbf{y};\mathbf{x}^{i}\right)}{p\left(\mathbf{y};\mathbf{x}\right)}\frac{p\left(\mathbf{y};\mathbf{x}^{j}\right)}{p\left(\mathbf{y};\mathbf{x}\right)}\right] \\
&= \left[\mathbf{F}_{\mathbf{zz}}\right]_{i,j}\ \mathbb{E}_{\mathbf{y}}^{ij}\left[\frac{\partial \ln p\left(\mathbf{y};\mathbf{x}^{i}\right)}{\partial \mathbf{x}}\right] \qquad \text{(A.20c)}
\end{aligned}$$

Therefore in the following we consider the representation $\mathbf{y} \sim \mathcal{N}\left(\boldsymbol{\Sigma}^{ij}\boldsymbol{\mu}^{ij}, \boldsymbol{\Sigma}^{ij}\right)$, where $\boldsymbol{\Sigma}^{ij}$, $\boldsymbol{\mu}^{ij}$ are given by (A.19a-A.19d). To compute the missing expectations, let us recall that $p\left(\mathbf{y};\mathbf{x}\right) = e^{-\frac{1}{2}\phi\left(\mathbf{y};\mathbf{x}\right)}/\left(\sqrt{2\pi}^{n}\sqrt{\left|\boldsymbol{\Sigma}\left(\mathbf{x}\right)\right|}\right)$ where $\phi\left(\mathbf{y};\mathbf{x}\right) = tr\left(\boldsymbol{\Sigma}\left(\mathbf{x}\right)^{-1}\boldsymbol{\Sigma}\left(\hat{\mathbf{x}}\right)\right)$ and $\boldsymbol{\Sigma}\left(\hat{\mathbf{x}}\right) = \left(\mathbf{y}-\boldsymbol{\mu}\left(\mathbf{x}\right)\right)\left(\mathbf{y}-\boldsymbol{\mu}\left(\mathbf{x}\right)\right)^{\top}$and that

$$\frac{\partial \boldsymbol{\Sigma}\left(\mathbf{x}\right)^{-1}}{\partial x_k} = -\boldsymbol{\Sigma}\left(\mathbf{x}\right)^{-1}\frac{\partial \boldsymbol{\Sigma}\left(\mathbf{x}\right)}{\partial x_k}\boldsymbol{\Sigma}\left(\mathbf{x}\right)^{-1}, \quad \frac{\partial \ln\left|\boldsymbol{\Sigma}\left(\mathbf{x}\right)\right|}{\partial x_k} = -tr\left(\frac{\partial \boldsymbol{\Sigma}\left(\mathbf{x}\right)^{-1}}{\partial x_k}\boldsymbol{\Sigma}\left(\mathbf{x}\right)\right).$$

Then,

$$\begin{aligned}\frac{\partial \phi\left(\mathbf{y};\mathbf{x}\right)}{\partial x_k} &= -2\frac{\partial \boldsymbol{\mu}\left(\mathbf{x}\right)}{\partial x_k}^{\top}\boldsymbol{\Sigma}\left(\mathbf{x}\right)^{-1}\left(\mathbf{y}-\boldsymbol{\mu}\left(\mathbf{x}\right)\right)+\left(\mathbf{y}-\boldsymbol{\mu}\left(\mathbf{x}\right)\right)^{\top} \\ &\quad \times \frac{\partial \boldsymbol{\Sigma}\left(\mathbf{x}\right)^{-1}}{\partial x_k}\left(\mathbf{y}-\boldsymbol{\mu}\left(\mathbf{x}\right)\right), \qquad \text{(A.21)} \\ \frac{\partial \ln p\left(\mathbf{y};\mathbf{x}\right)}{\partial x_k} &= \frac{1}{2}tr\left(\frac{\partial \boldsymbol{\Sigma}\left(\mathbf{x}\right)^{-1}}{\partial x_k}\left(\boldsymbol{\Sigma}\left(\mathbf{x}\right)-\boldsymbol{\Sigma}\left(\hat{\mathbf{x}}\right)\right)\right) \qquad \text{(A.22)} \\ &\quad + \frac{\partial \boldsymbol{\mu}\left(\mathbf{x}\right)}{\partial x_k}^{\top}\boldsymbol{\Sigma}\left(\mathbf{x}\right)^{-1}\left(\mathbf{y}-\boldsymbol{\mu}\left(\mathbf{x}\right)\right). \qquad \text{(A.23)}\end{aligned}$$

From (A.23), we have that

$$\begin{aligned}\mathbb{E}_{\mathbf{y}}^{ij}\left[\frac{\partial \ln p\left(\mathbf{y};\mathbf{x}\right)}{\partial x_k}\right] &= \frac{1}{2}tr\left(\frac{\partial \boldsymbol{\Sigma}\left(\mathbf{x}\right)^{-1}}{\partial x_k}\left(\boldsymbol{\Sigma}\left(\mathbf{x}\right)-\mathbb{E}_{\mathbf{y}}^{ij}\left[\boldsymbol{\Sigma}\left(\hat{\mathbf{x}}\right)\right]\right)\right) \\ &\quad + \frac{\partial \boldsymbol{\mu}\left(\mathbf{x}\right)}{\partial x_k}^{\top}\boldsymbol{\Sigma}\left(\mathbf{x}\right)^{-1}\left(\mathbb{E}_{\mathbf{y}}^{ij}\left[\mathbf{y}\right]-\boldsymbol{\mu}\left(\mathbf{x}\right)\right), \qquad \text{(A.24)}\end{aligned}$$

where

$$\mathbb{E}_{\mathbf{y}}^{ij}\left[\boldsymbol{\Sigma}\left(\hat{\mathbf{x}}\right)\right] = \boldsymbol{\Sigma}^{ij}+\left(\mathbb{E}_{\mathbf{y}}^{ij}\left[\mathbf{y}\right]-\boldsymbol{\mu}\left(\mathbf{x}\right)\right)\left(\mathbb{E}_{\mathbf{y}}^{ij}\left[\mathbf{y}\right]-\boldsymbol{\mu}\left(\mathbf{x}\right)\right)^{\top}. \qquad \text{(A.25)}$$

Finally,

$$\begin{aligned}\left[\mathbf{F}_{\mathbf{zz}}\right]_{i,j} &= \sqrt{\frac{\left|\boldsymbol{\Sigma}^{ij}\right|\left|\boldsymbol{\Sigma}\left(\mathbf{x}\right)\right|}{\left|\boldsymbol{\Sigma}\left(\mathbf{x}^i\right)\right|\left|\boldsymbol{\Sigma}\left(\mathbf{x}^j\right)\right|}}e^{\frac{1}{2}\left[\left(\boldsymbol{\mu}^{ij}\right)^{\top}\boldsymbol{\Sigma}^{ij}\boldsymbol{\mu}^{ij}-\delta^{ij}\right]}, \qquad \text{(A.26a)} \\ \left[\mathbf{f}\left(\mathbf{x}^i,\mathbf{x}^j\right)\right]_k &= \left[\mathbf{F}_{\mathbf{zz}}\right]_{i,j}\left[\alpha\left(\mathbf{x}^i\right)\right]_k, \qquad \text{(A.26b)}\end{aligned}$$

where

$$\left[\alpha\left(\mathbf{x}^i\right)\right]_k = \left(\begin{array}{l} \frac{1}{2}tr\left(\frac{\partial \boldsymbol{\Sigma}\left(\mathbf{x}^i\right)^{-1}}{\partial x_k}\left(\boldsymbol{\Sigma}\left(\mathbf{x}^i\right)-\boldsymbol{\Sigma}^{ij}\right)-\frac{\partial \boldsymbol{\Sigma}\left(\mathbf{x}^i\right)^{-1}}{\partial x_k}\right. \\ \left.\times\left(\boldsymbol{\Sigma}^{ij}\boldsymbol{\mu}^{ij}-\boldsymbol{\mu}\left(\mathbf{x}^i\right)\right)\left(\boldsymbol{\Sigma}^{ij}\boldsymbol{\mu}^{ij}-\boldsymbol{\mu}\left(\mathbf{x}^i\right)\right)^{\top}\right) \\ +\frac{\partial \boldsymbol{\mu}\left(\mathbf{x}^i\right)}{\partial x_k}^{\top}\boldsymbol{\Sigma}\left(\mathbf{x}^i\right)^{-1}\left(\boldsymbol{\Sigma}^{ij}\boldsymbol{\mu}^{ij}-\boldsymbol{\mu}\left(\mathbf{x}^i\right)\right) \end{array}\right).$$

Moreover, since $\boldsymbol{\Sigma}^{0j}=\boldsymbol{\Sigma}\left(\mathbf{x}^j\right)$, $\boldsymbol{\mu}^{0j}=\boldsymbol{\Sigma}\left(\mathbf{x}^j\right)^{-1}\boldsymbol{\mu}\left(\mathbf{x}^j\right)$, $\boldsymbol{\Sigma}^{0j}\boldsymbol{\mu}^{0j}=\boldsymbol{\mu}\left(\mathbf{x}^j\right)$ and $\delta^{0j}=\boldsymbol{\mu}\left(\mathbf{x}^j\right)^{\top}\boldsymbol{\Sigma}\left(\mathbf{x}^j\right)^{-1}\boldsymbol{\mu}\left(\mathbf{x}^j\right)$, then $\left[\mathbf{F}_{\mathbf{zz}}\right]_{0,j}=1$, and $\mathbf{f}\left(\mathbf{x},\mathbf{x}^j\right)=\alpha\left(\mathbf{x}^i\right)$.

## A.6 Derivation of Jacobian with respect to the Quaternion

This subsection derives the Jacobian matrix $\mathbf{J_q}(\mathbf{v})$ for the rotation of the vector $\mathbf{v}$ with respect to the quaternion $\mathbf{q}$, defined as

$$\mathbf{J_q}(\mathbf{v}) \triangleq \frac{\partial\left(\mathbf{q} \circ \mathbf{v} \circ \mathbf{q}^*\right)}{\partial\, \mathbf{q}}. \tag{A.27}$$

The quaternion multiplication is defined as

$$\mathbf{p} \cdot \mathbf{q} = \begin{bmatrix} p_w q_w - \mathbf{p_u}^\top \mathbf{q_u} \\ p_w \mathbf{q_u} + q_w \mathbf{p_u} + \mathbf{p_u} \times \mathbf{q_u} \end{bmatrix}. \tag{A.28}$$

Then, extending it for the rotation of a vector

$$\begin{aligned} \mathbf{q} \cdot \mathbf{v} \cdot \mathbf{q}^* &= \begin{bmatrix} q_w \\ \mathbf{q_u} \end{bmatrix} \cdot \begin{bmatrix} 0 \\ \mathbf{v} \end{bmatrix} \cdot \begin{bmatrix} q_w \\ -\mathbf{q_u} \end{bmatrix} && \text{(A.29)} \\ &= \begin{bmatrix} -\mathbf{q_u}^\top \mathbf{v} \\ q_w \mathbf{v} + \mathbf{q_u} \times \mathbf{v} \end{bmatrix} \cdot \begin{bmatrix} q_w \\ -\mathbf{q_u} \end{bmatrix}, && \text{(A.30)} \end{aligned}$$

from here, we will pay attention solely to the imaginary part:

$$\begin{aligned} \mathbf{q} \cdot \mathbf{v} \cdot \mathbf{q}^* &= -\mathbf{q_u}^\top \mathbf{v} \left(-\mathbf{q_u}\right) + q_w \left(q_w \mathbf{v} + \mathbf{q_u} \times \mathbf{v}\right) + \left(q_w \mathbf{v} + \mathbf{q_u} \times \mathbf{v}\right) \times \left(-\mathbf{q_u}\right) \\ &= \mathbf{q_u}^\top \mathbf{v}\ \mathbf{q_u} + q_w^2 \mathbf{v} + q_w \mathbf{q_u} \times \mathbf{v} - q_w \mathbf{v} \times \mathbf{q_u} + \left(\mathbf{q_u} \times \mathbf{v}\right) \times \left(-\mathbf{q_u}\right). \end{aligned} \tag{A.31}$$

Considering the vectorial product properties:

$$\mathbf{a} \times \mathbf{b} = -\mathbf{b} \times \mathbf{a} \tag{A.32}$$

$$\mathbf{a} \times \left(\mathbf{b} \times \mathbf{c}\right) = \left(\mathbf{a}^T \mathbf{c}\right) \mathbf{b} - \left(\mathbf{a}^T \mathbf{b}\right) \mathbf{c} \tag{A.33}$$

we can group $q_w \mathbf{q_u} \times \mathbf{v} - q_w \mathbf{v} \times \mathbf{q_u} = -2 q_w \mathbf{v} \times \mathbf{q_u}$. Substituting the vectorial product for the skew operator $[\cdot\times]$, to facilitate the matrix formulation, and applying Eq. A.33, we can reformulate the quaternion operator as:

$$\mathbf{q} \cdot \mathbf{v} \cdot \mathbf{q}^* = q_w^2 \mathbf{v} - 2 q_w [\mathbf{v}\times] \mathbf{q_u} + 2\left(\mathbf{q_u}^\top \mathbf{v}\right) \mathbf{q_u} - \left(\mathbf{q_u}^\top \mathbf{q_u}\right) \mathbf{v}. \tag{A.34}$$

From here, deriving the partial derivatives of the quaternion results uncomplicated:

$$\begin{aligned} \frac{\partial\left(\mathbf{q} \cdot \mathbf{v} \cdot \mathbf{q}^*\right)}{\partial\ q_w} &= 2 q_w \mathbf{v} - 2[\mathbf{v}\times] \mathbf{q_u} && \text{(A.35)} \\ \frac{\partial\left(\mathbf{q} \cdot \mathbf{v} \cdot \mathbf{q}^*\right)}{\partial \mathbf{q_u}} &= -2 q_w [\mathbf{v}\times] + 2\left(\mathbf{q_u}^\top \mathbf{v} I_3 + \mathbf{q_u} \mathbf{v}^\top\right) - 2 \mathbf{v} \mathbf{q_u}^\top, && \text{(A.36)} \end{aligned}$$

obtaining finally

$$\mathbf{J_q}(\mathbf{v}) = 2 \begin{bmatrix} q_w \mathbf{v} - [\mathbf{v}\times] \mathbf{q_u} & -q_w [\mathbf{v}\times] + \mathbf{q_u}^T \mathbf{v} \mathbf{I}_3 + \mathbf{q_u} \mathbf{v}^\top - \mathbf{v} \mathbf{q_u}^\top \end{bmatrix} \quad \in \mathbb{R}^{3,4}. \tag{A.37}$$

## A.7 Computation of $q(\zeta_t^{(i)})$ for Correlated Observations

To preserve $q(\zeta_t^{(i)})$ as a Bernoulli distribution, (D.15) is substituted in (D.20) and so the following equation is derived

$$\begin{aligned}
\ln\left[q(\zeta_t^{(i)})\right] &= \mathbb{E}_{\pi_t^{(i)},\mathbf{x}_t,\zeta_t^{(-i)}}\left\{-\frac{1}{2}\left(\mathbf{y}_t^{(-i)}-\mathbf{h}^{(-i)}\left(\mathbf{x}_t\right)\right)^\top\right.\\
&\times\left(\boldsymbol{\Sigma}_{-i,-i}^{-1}+\frac{\boldsymbol{\Sigma}_{-i,-i}^{-1}\boldsymbol{\Sigma}_{i,-i}\boldsymbol{\Sigma}_{-i,i}\boldsymbol{\Sigma}_{-i,-i}^{-1}}{\frac{\sigma_{i,i}^2}{\zeta_t^{(i)}}-\boldsymbol{\Sigma}_{i,-i}\boldsymbol{\Sigma}_{-i,-i}^{-1}\boldsymbol{\Sigma}_{-i,i}}\right)\\
&\times\left(\mathbf{y}_t^{(-i)}-\mathbf{h}^{(-i)}\left(\mathbf{x}_t\right)\right)-\left(\mathbf{y}_t^{(-i)}-\mathbf{h}^{(-i)}\left(\mathbf{x}_t\right)\right)^\top\\
&\times\left(-\left(\boldsymbol{\Sigma}_{-i,-i}^{-1}+\frac{\boldsymbol{\Sigma}_{-i,-i}^{-1}\boldsymbol{\Sigma}_{i,-i}\boldsymbol{\Sigma}_{-i,i}\boldsymbol{\Sigma}_{-i,-i}^{-1}}{\frac{\sigma_{i,i}^2}{\zeta_t^{(i)}}-\boldsymbol{\Sigma}_{i,-i}\boldsymbol{\Sigma}_{-i,-i}^{-1}\boldsymbol{\Sigma}_{-i,i}}\right)\boldsymbol{\Sigma}_{-i,i}\frac{\zeta_t^{(i)}}{\sigma_{i,i}^2}\right)\\
&\times\left(y_t^{(i)}-h^{(i)}\left(\mathbf{x}_t\right)\right)-\frac{1}{2}\left(y_t^{(i)}-h^{(i)}\left(\mathbf{x}_t\right)\right)^\top\\
&\times\left(\frac{\sigma_{i,i}^2}{\zeta_t^{(i)}}-\boldsymbol{\Sigma}_{i,-i}\boldsymbol{\Sigma}_{-i,-i}^{-1}\boldsymbol{\Sigma}_{-i,i}\right)^{-1}\left(y_t^{(i)}-h^{(i)}\left(\mathbf{x}_t\right)\right)\\
&+\zeta_t^{(i)}\ln[\pi_t^{(i)}]+\left(1-\zeta_t^{(i)}\right)\ln[1-\pi_t^{(i)}]\\
&-\frac{1}{2}\zeta_t^{(i)}\ln|\mathbf{C}([\boldsymbol{\zeta}_t^{(-i)},\zeta_t^{(i)}=1])|\\
&\left.-\frac{1}{2}\zeta_t^{(i)}\ln[2\pi]-\frac{1}{2}(1-\zeta_t^{(i)})\ln|\mathbf{C}([\boldsymbol{\zeta}_t^{(-i)},\zeta_t^{(i)}=0])|+\kappa\right\}.
\end{aligned}\tag{A.38}$$

Following the transform from (D.17) to (D.19), the marginal distribution $q(\zeta_t^{(t)})$ reads

$$\begin{align*}
\ln\left[q(\zeta_t^{(i)})\right] &= \mathbb{E}_{\pi_t^{(i)},\mathbf{x}_t,\zeta_t^{(-i)}}\left\{-\frac{1}{2}\left(\mathbf{y}_t^{(-i)}-\mathbf{h}^{(-i)}\left(\mathbf{x}_t\right)\right)^\top\right.\\
&\times\left(\boldsymbol{\Sigma}_{-i,-i}^{-1}+\frac{\zeta_t^{(i)}\boldsymbol{\Sigma}_{-i,-i}^{-1}\boldsymbol{\Sigma}_{i,-i}\boldsymbol{\Sigma}_{-i,i}\boldsymbol{\Sigma}_{-i,-i}^{-1}}{\sigma_{i,i}^2-\boldsymbol{\Sigma}_{i,-i}\boldsymbol{\Sigma}_{-i,-i}^{-1}\boldsymbol{\Sigma}_{-i,i}}\right)\\
&\times\left(\mathbf{y}_t^{(-i)}-\mathbf{h}^{(-i)}\left(\mathbf{x}_t\right)\right)+\left(\mathbf{y}_t^{(-i)}-\mathbf{h}^{(-i)}\left(\mathbf{x}_t\right)\right)^\top\\
&\times\left(\boldsymbol{\Sigma}_{-i,-i}^{-1}\boldsymbol{\Sigma}_{-i,i}\frac{\zeta_t^{(i)}}{\sigma_{i,i}^2}+\frac{\zeta_t^{(i)}\boldsymbol{\Sigma}_{-i,-i}^{-1}\boldsymbol{\Sigma}_{i,-i}\boldsymbol{\Sigma}_{-i,i}\boldsymbol{\Sigma}_{-i,-i}^{-1}\boldsymbol{\Sigma}_{-i,i}}{\sigma_{i,i}^4-\sigma_{i,i}^2\boldsymbol{\Sigma}_{i,-i}\boldsymbol{\Sigma}_{-i,-i}^{-1}\boldsymbol{\Sigma}_{-i,i}}\right)\\
&\times\left(y_t^{(i)}-h^{(i)}\left(\mathbf{x}_t\right)\right)-\frac{1}{2}\left(y_t^{(i)}-h^{(i)}\left(\mathbf{x}_t\right)\right)^\top\\
&\times\frac{\zeta_t^{(i)}}{\sigma_{i,i}^2-\boldsymbol{\Sigma}_{i,-i}\boldsymbol{\Sigma}_{-i,-i}^{-1}\boldsymbol{\Sigma}_{-i,i}}\left(y_t^{(i)}-h^{(i)}\left(\mathbf{x}_t\right)\right)\\
&+\zeta_t^{(i)}\ln[\pi_t^{(i)}]+\left(1-\zeta_t^{(i)}\right)\ln[1-\pi_t^{(i)}]\\
&-\frac{1}{2}\zeta_t^{(i)}\ln|\mathbf{C}([\boldsymbol{\zeta}_t^{(-i)},\zeta_t^{(i)}=1])| \tag{A.39}\\
&\left.-\frac{1}{2}\zeta_t^{(i)}\ln[2\pi]-\frac{1}{2}(1-\zeta_t^{(i)})\ln|\mathbf{C}([\boldsymbol{\zeta}_t^{(-i)},\zeta_t^{(i)}=0])|+\kappa\right\}. \tag{A.40}
\end{align*}$$

Given the expectation over $\left\{\mathbf{x}_t, \pi_t^{(i)}, \boldsymbol{\zeta}_t^{(-i)}\right\}$, one may express

$$-\frac{1}{2}\left(\mathbf{y}_t^{(-i)} - \mathbf{h}^{(-i)}\left(\mathbf{x}_t\right)\right)^{\top} \boldsymbol{\Sigma}_{-i,-i}^{-1} \left(\mathbf{y}_t^{(-i)} - \mathbf{h}^{(-i)}\left(\mathbf{x}_t\right)\right)$$

in the first term as a normalization term and, hence, remove it from the previous equation to obtain

$$\begin{aligned}
\ln\left[q(\zeta_t^{(i)})\right] &= \mathbb{E}_{\pi_t^{(i)}, \mathbf{x}_t, \boldsymbol{\zeta}_t^{(-i)}} \left\{-\frac{1}{2}\left(\mathbf{y}_t^{(-i)} - \mathbf{h}^{(-i)}\left(\mathbf{x}_t\right)\right)^{\top}\right.\\
&\times \left(\frac{\zeta_t^{(i)} \boldsymbol{\Sigma}_{-i,-i}^{-1} \boldsymbol{\Sigma}_{i,-i} \boldsymbol{\Sigma}_{-i,i} \boldsymbol{\Sigma}_{-i,-i}^{-1}}{\sigma_{i,i}^2 - \boldsymbol{\Sigma}_{i,-i} \boldsymbol{\Sigma}_{-i,-i}^{-1} \boldsymbol{\Sigma}_{-i,i}}\right)\\
&\times \left(\mathbf{y}_t^{(-i)} - \mathbf{h}^{(-i)}\left(\mathbf{x}_t\right)\right) + \left(\mathbf{y}_t^{(-i)} - \mathbf{h}^{(-i)}\left(\mathbf{x}_t\right)\right)^{\top}\\
&\times \left(\boldsymbol{\Sigma}_{-i,-i}^{-1} \boldsymbol{\Sigma}_{-i,i} \frac{\zeta_t^{(i)}}{\sigma_{i,i}^2} + \frac{\zeta_t^{(i)} \boldsymbol{\Sigma}_{-i,-i}^{-1} \boldsymbol{\Sigma}_{i,-i} \boldsymbol{\Sigma}_{-i,i} \boldsymbol{\Sigma}_{-i,-i}^{-1} \boldsymbol{\Sigma}_{-i,i}}{\sigma_{i,i}^4 - \sigma_{i,i}^2 \boldsymbol{\Sigma}_{i,-i} \boldsymbol{\Sigma}_{-i,-i}^{-1} \boldsymbol{\Sigma}_{-i,i}}\right)\\
&\times \left(y_t^{(i)} - h^{(i)}\left(\mathbf{x}_t\right)\right) - \frac{1}{2}\left(y_t^{(i)} - h^{(i)}\left(\mathbf{x}_t\right)\right)^{\top}\\
&\times \frac{\zeta_t^{(i)}}{\sigma_{i,i}^2 - \boldsymbol{\Sigma}_{i,-i} \boldsymbol{\Sigma}_{-i,-i}^{-1} \boldsymbol{\Sigma}_{-i,i}} \left(y_t^{(i)} - h^{(i)}\left(\mathbf{x}_t\right)\right)\\
&+ \zeta_t^{(i)} \ln[\pi_t^{(i)}] + \left(1 - \zeta_t^{(i)}\right) \ln[1 - \pi_t^{(i)}]\\
&- \frac{1}{2}\zeta_t^{(i)} \ln|\mathbf{C}([\boldsymbol{\zeta}_t^{(-i)}, \zeta_t^{(i)} = 1])| - \frac{1}{2}\zeta_t^{(i)} \ln[2\pi]\\
&\left. -\frac{1}{2}(1 - \zeta_t^{(i)}) \ln|\mathbf{C}([\boldsymbol{\zeta}_t^{(-i)}, \zeta_t^{(i)} = 0])| + \kappa\right\}. \qquad \text{(A.41)}
\end{aligned}$$

Benefiting from the properties of the trace of a matrix, the equation above can be further simplified to

$$\begin{aligned}
\ln\left[q(\zeta_t^{(i)})\right] &= \mathbb{E}_{\pi_t^{(i)}, \mathbf{x}_t, \boldsymbol{\zeta}_t^{(-i)}} \left\{-\frac{1}{2}\mathrm{tr}\left[\left(\mathbf{y}_t^{(-i)} - \mathbf{h}^{(-i)}\left(\mathbf{x}_t\right)\right)\right.\right.\\
&\times \left.\left(\mathbf{y}_t^{(-i)} - \mathbf{h}^{(-i)}\left(\mathbf{x}_t\right)\right)^{\top} \left(\frac{\zeta_t^{(i)} \boldsymbol{\Sigma}_{-i,-i}^{-1} \boldsymbol{\Sigma}_{i,-i} \boldsymbol{\Sigma}_{-i,i} \boldsymbol{\Sigma}_{-i,-i}^{-1}}{\sigma_{i,i}^2 - \boldsymbol{\Sigma}_{i,-i} \boldsymbol{\Sigma}_{-i,-i}^{-1} \boldsymbol{\Sigma}_{-i,i}}\right)\right]\\
&+ \mathrm{tr}\left[\left(y_t^{(i)} - h^{(i)}\left(\mathbf{x}_t\right)\right)\left(\mathbf{y}_t^{(-i)} - \mathbf{h}^{(-i)}\left(\mathbf{x}_t\right)\right)^{\top}\right.\\
&\times \left.\left(\boldsymbol{\Sigma}_{-i,-i}^{-1} \boldsymbol{\Sigma}_{-i,i} \frac{\zeta_t^{(i)}}{\sigma_{i,i}^2} + \frac{\zeta_t^{(i)} \boldsymbol{\Sigma}_{-i,-i}^{-1} \boldsymbol{\Sigma}_{i,-i} \boldsymbol{\Sigma}_{-i,i} \boldsymbol{\Sigma}_{-i,-i}^{-1} \boldsymbol{\Sigma}_{-i,i}}{\sigma_{i,i}^4 - \sigma_{i,i}^2 \boldsymbol{\Sigma}_{i,-i} \boldsymbol{\Sigma}_{-i,-i}^{-1} \boldsymbol{\Sigma}_{-i,i}}\right)\right]\\
&- \frac{1}{2}\mathrm{tr}\left[\left(y_t^{(i)} - h^{(i)}\left(\mathbf{x}_t\right)\right)\left(y_t^{(i)} - h^{(i)}\left(\mathbf{x}_t\right)\right)^{\top}\right.\\
&\times \left.\frac{\zeta_t^{(i)}}{\sigma_{i,i}^2 - \boldsymbol{\Sigma}_{i,-i} \boldsymbol{\Sigma}_{-i,-i}^{-1} \boldsymbol{\Sigma}_{-i,i}}\right]\\
&+ \zeta_t^{(i)} \ln[\pi_t^{(i)}] + \left(1 - \zeta_t^{(i)}\right) \ln[1 - \pi_t^{(i)}]\\
&- \frac{1}{2}\zeta_t^{(i)} \ln|\mathbf{C}([\boldsymbol{\zeta}_t^{(-i)}, \zeta_t^{(i)} = 1])| - \frac{1}{2}\zeta_t^{(i)} \ln[2\pi]\\
&\left. -\frac{1}{2}(1 - \zeta_t^{(i)}) \ln|\mathbf{C}([\boldsymbol{\zeta}_t^{(-i)}, \zeta_t^{(i)} = 0])| + \kappa\right\}, \qquad \text{(A.42)}
\end{aligned}$$

and with $\zeta_t^{(i)}$ a scalar, the final expression for $q(\zeta_t^{(i)})$ reads as follows

$$\begin{aligned}
&\ln\left[q(\zeta_t^{(i)})\right] = \mathbb{E}_{\pi_t^{(i)},\mathbf{x}_t,\boldsymbol{\zeta}_t^{(-i)}}\left\{-\frac{1}{2}\zeta_t^{(i)}\right.\\
&\times \mathsf{tr}\left[\left(\mathbf{y}_t^{(-i)} - \mathbf{h}^{(-i)}\left(\mathbf{x}_t\right)\right)\left(\mathbf{y}_t^{(-i)} - \mathbf{h}^{(-i)}\left(\mathbf{x}_t\right)\right)^\top\right.\\
&\left.\times \left(\frac{\boldsymbol{\Sigma}_{-i,-i}^{-1}\boldsymbol{\Sigma}_{i,-i}\boldsymbol{\Sigma}_{-i,i}\boldsymbol{\Sigma}_{-i,-i}^{-1}}{\sigma_{i,i}^2 - \boldsymbol{\Sigma}_{i,-i}\boldsymbol{\Sigma}_{-i,-i}^{-1}\boldsymbol{\Sigma}_{-i,i}}\right)\right]\\
&+ \zeta_t^{(i)}\mathsf{tr}\left[\left(y_t^{(i)} - h^{(i)}\left(\mathbf{x}_t\right)\right)\left(\mathbf{y}_t^{(-i)} - \mathbf{h}^{(-i)}\left(\mathbf{x}_t\right)\right)^\top\right.\\
&\left.\times \left(\boldsymbol{\Sigma}_{-i,-i}^{-1}\boldsymbol{\Sigma}_{-i,i}\frac{1}{\sigma_{i,i}^2} + \frac{\boldsymbol{\Sigma}_{-i,-i}^{-1}\boldsymbol{\Sigma}_{i,-i}\boldsymbol{\Sigma}_{-i,i}\boldsymbol{\Sigma}_{-i,-i}^{-1}\boldsymbol{\Sigma}_{-i,i}}{\sigma_{i,i}^4 - \sigma_{i,i}^2\boldsymbol{\Sigma}_{i,-i}\boldsymbol{\Sigma}_{-i,-i}^{-1}\boldsymbol{\Sigma}_{-i,i}}\right)\right]\\
&- \frac{1}{2}\zeta_t^{(i)}\mathsf{tr}\left[\left(y_t^{(i)} - h^{(i)}\left(\mathbf{x}_t\right)\right)\left(y_t^{(i)} - h^{(i)}\left(\mathbf{x}_t\right)\right)^\top\right.\\
&\left.\times \frac{1}{\sigma_{i,i}^2 - \boldsymbol{\Sigma}_{i,-i}\boldsymbol{\Sigma}_{-i,-i}^{-1}\boldsymbol{\Sigma}_{-i,i}}\right]\\
&+ \zeta_t^{(i)}\ln[\pi_t^{(i)}] + \left(1 - \zeta_t^{(i)}\right)\ln[1 - \pi_t^{(i)}]\\
&- \frac{1}{2}\zeta_t^{(i)}\ln|\mathbf{C}([\boldsymbol{\zeta}_t^{(-i)}, \zeta_t^{(i)} = 1])| - \frac{1}{2}\zeta_t^{(i)}\ln[2\pi]\\
&\left.-\frac{1}{2}(1 - \zeta_t^{(i)})\ln|\mathbf{C}([\boldsymbol{\zeta}_t^{(-i)}, \zeta_t^{(i)} = 0])| + \kappa\right\}.
\end{aligned} \tag{A.43}$$

# APPENDIX B

## Variational Inference for GNSS Stochastic Modeling

Let us recall the code and carrier phase observations introduced in Section 1.3, such that

$$\rho^i_{j,f}(t) = \|\mathbf{p}^i(t-\tau^i) - \mathbf{p}_j(t)\| + c(dt_j(t) - dt^i(t-\tau^i)) + I^i_{j,f} + T^i_j + \varepsilon^i_{j,f}, \tag{B.1}$$

$$\Phi^i_{j,f}(t) = \|\mathbf{p}^i(t-\tau^i) - \mathbf{p}_j(t)\| + c(dt_j(t) - dt^i(t-\tau^i)) - I^i_{j,f} + T^i_j + \lambda_f N^i_{j,f} + \epsilon^i_{j,f}, \tag{B.2}$$

as well as the assumption of normal distribution for the aforementioned observables

$$\varepsilon^i \sim \mathcal{N}\left(0, (\sigma^i_\rho)^2\right),\ \epsilon^i \sim \mathcal{N}\left(0, (\sigma^i_\Phi)^2\right)\ . \tag{B.3}$$

The characterization of the uncertainty present in GNSS signals has been a recurrent topic within the navigation community. Not only this plays a major role in the derivation of efficient estimators, but it is essential for deriving integrity measures over the estimated positioning and timing solutions. This Appendix introduces a method for stochastic modeling based on Bayesian inference, with a particular focus on the characterization of multipath effects.

Thus, besides the well-known stochastic models introduced in Section 1.3.1, another common way to express the standard deviation of the individual links consists on gathering the different error sources –e.g., satellite clocks, ephemeris, ionospheric and tropospheric effects, multipath, etc.– over a particular observation $y_i$, leading to

$$\sigma^2_{y_i} = \sigma^2_{cdt_i} + \sigma^2_{eph_i} + \sigma^2_{I_i} + \sigma^2_{Tr_i} + \sigma^2_{\varepsilon_i}\ , \tag{B.4}$$

where here $\sigma^2_{\varepsilon_i}$ constitutes the remaining unmodeled errors (mainly multipath and the receiver noise due to thermal effects). The multi-frequency code-minus-carrier combination (CMC) is commonly applied for assessing pseudorange multipath. Free of ionospheric and geometric effects, CMC clusters the remaining observables error terms: group-delay variations, carrier-phase ambiguities, receiver noise, and multipath. Thus, given two frequencies $f_A$ and $f_B$, the CMC can be formulated as follows

$$\mathrm{CMC}^i_{f_A} = \rho^i_{f_A} - \Phi^i_{f_A} + \frac{2}{\alpha}\left(\Phi^i_{f_A} - \Phi^i_{f_B}\right), \tag{B.5}$$

$$\mathrm{CMC}^i_{f_A} = \varepsilon^i_{f_A} + \epsilon^i_{f_A} + \frac{2}{\alpha}\left(\epsilon^i_{f_A} + \epsilon^i_{f_B}\right) + \tag{B.6}$$

$$\underbrace{+\lambda_{f_A} N^i + \frac{2}{\alpha}\left(\lambda_{f_A} N^i - \lambda_{f_B} N^i\right)}_{\nu} \tag{B.7}$$

where $\alpha = 1 - (f_A/f_B)^2$ and $\nu$ is a constant factor including carrier phase ambiguities and hardware delay biases [30]. Assuming that multipath and noise of the carrier-phase observations are negligible compared to the corresponding terms of the pseudorange and discarding $\nu$, which remains constant over time, the multipath and receiver noise term $\varepsilon$ for code observations is characterized as:

$$\varepsilon^i_{f_A} \simeq \mathrm{CMC}^i_{f_A} - \nu \ . \tag{B.8}$$

Therefore, given a large dataset, one may attempt at isolating the noise contribution due to multipath effects and characterize it directly at the pseudorange observation level.

## B.1 Probabilistic modeling of the variance

Most of the existing models assume that the variance is an unknown deterministic constant. Alternatively, the variance can be considered as a random variable such that:

$$\sigma^2 \sim p(\sigma^2; \theta, C/N_0) \tag{B.9}$$

represents its probability density function, which depends on elevation and/or C/N$_0$ of the satellite. In a conjugate prior Bayesian analysis, a popular choice for this distribution is the inverse-Gamma distribution. The inverse-Gamma has the desirable feature of having support only over the positive real values such that $\sigma^2 \in \mathbb{R}_+$, which is very appropriate for variances.

Note that, since the distribution of $\sigma^2$ depends on the parameters $\{\theta, C/N_0\}$, its parameterization also does. Therefore, a complete probabilistic characterization would take that into account and write, more precisely, such that a model fitting needs to be done for each $\{\theta, C/N_0\}$ pair, with some granularity. Then, let us consider a set of $N$ i.i.d. code noise samples $\varepsilon_{1:N} \triangleq \{\varepsilon_1, \dots, \varepsilon_N\}$, obtained as in (B.8), for a given $\{\theta, C/N_0\}$ pair. A reasonable modeling of the error is given by

$$\varepsilon_n \sim \mathcal{N}(0, \sigma^2(\theta, C/N_0)) \ . \tag{B.10}$$

At this stage, we are interested in the probabilistic representation of $\sigma^2(\theta, C/N_0)$. To infer such distribution, the conjugate Bayesian analysis was applied to estimate the variance of the sample $\varepsilon_{1:N}$ given a known mean [235].

The conjugate prior of the variances for the likelihood model represented in (B.10) is an inverse Gamma distribution

$$p(\sigma^2) = \mathrm{IG}(\alpha_0, \beta_0) \tag{B.11}$$

with parameters $\alpha_0$ (shape) and $\beta_0$ (scale). For the sake of convenience, the dependence on the $\{\theta, C/N_0\}$ pair was dropped, but it goes without saying that each pair can have different parameters for (B.11). If no prior knowledge is available, a suitable objective prior results by setting $\alpha_0 = 0.001$ and $\beta_0 = 0.001$, such that the prior distribution is *proper* and relatively flat.

The prior is updated with the sample $\varepsilon_{1:N}$, yielding the posterior distribution

$$p(\sigma^2 | \varepsilon_{1:N}) = \mathrm{IG}(\alpha_N, \beta_N) \tag{B.12}$$

where the parameters are computed as

$$\alpha_N = \alpha_0 + \frac{N}{2} \tag{B.13}$$

$$\beta_N = \beta_0 + \frac{1}{2}\sum_{n=1}^{N} \varepsilon_n^2 \ . \tag{B.14}$$

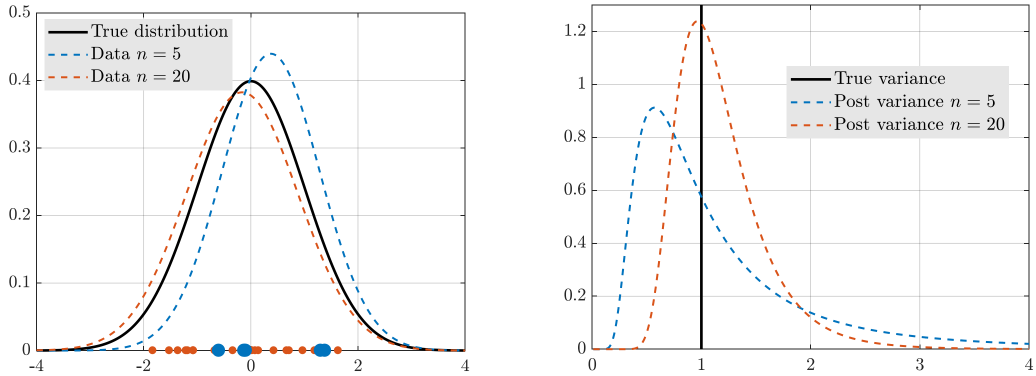

**Figure B.1:** In Bayesian inference, we update the a priori distribution of the unknown parameters with the new data to compute the a posteriori distribution. As a motivating example, when $N$ samples are observed (left) from the Gaussian likelihood in (B.10), they are used to update the parameters in (B.12) to produce a posterior probability distribution (right) for the unknown variance of the likelihood. The accuracy of such distribution improves as more samples are collected.

As a result, a distribution, (B.12), is obtained, which provides all the information available about the variance. In particular, the distribution informs about the uncertainty regarding the variance $\sigma^2$ for the given $\{\theta, C/N_0\}$ pair. Additionally, statistics can be computed from the posterior distribution (B.12) such as the mean:

$$\mathrm{Mean}(\sigma^2|\varepsilon_{1:N}) = \frac{\beta_N}{\alpha_N - 1}\,, \quad \text{for } \alpha_N > 1 \tag{B.15}$$

the mode:

$$\mathrm{Mode}(\sigma^2|\varepsilon_{1:N}) = \frac{\beta_N}{\alpha_N + 1}\,, \tag{B.16}$$

and the variance of $\sigma^2$ given $\varepsilon_{1:N}$:

$$\mathrm{Var}(\sigma^2|\varepsilon_{1:N}) = \frac{\beta_N^2}{(\alpha_N - 1)^2(\alpha_N - 2)}\,, \quad \text{for } \alpha_N > 2\,. \tag{B.17}$$

Notice that the statistics for the a priori distribution in (B.11) can be computed similarly by setting $N = 0$ and thus using the initial parameters $(\alpha_0, \beta_0)$ in (B.15)–(B.17). Summing up, in Bayesian inference the a priori distribution of the unknown parameter given by (B.11) is update using the new data in (B.10) to obtain the posterior distribution in (B.12). In conjugate analysis, both distributions are from the same family and thus only the parameters need to be updated. This process is exemplified in Fig. B.1, where the update of (B.11) to (B.12) is shown for different values of $N$.

## B.2 Regression of variance means

The GNSS community has extensively studied the topic of pseudorange stochastic modeling. For high precision applications, such as Real-Time Kinematic (RTK), satellite elevation dependent models have often been applied [137], [236], [237]. For signal-degraded situations, the signal-to-noise ratio is considered a better quality indicator for GNSS observations. A model based on $C/N_0$ was first introduced in [47], and it has been widely adopted for navigating challenging scenarios [28], [238]. A collection of variance models for pseudorange weighting dependent on either satellite elevation angle, C/N$_0$ or the combination of both is compiled next

- Elevation model

$$\sigma^2 = a + \frac{b}{\sin\theta} \tag{B.18}$$

- CN0-based model

$$\sigma^2 = a + b \cdot 10^{-C/N_0/10} \tag{B.19}$$

- Additive model

$$\sigma^2 = a + \frac{b}{\sin\theta} + c \cdot 10^{-C/N_0/10} \tag{B.20}$$

- Multiplicative model

$$\sigma^2 = a + b \cdot \frac{10^{-C/N_0/10}}{\sin\theta} \tag{B.21}$$

Finding the unknown parameters $a, b, c$ of these models constitute a nonlinear regression problem relating the mean of the estimated Inverse-Gamma distributions (B.15) and the corresponding $\{\theta, C/N_0\}$ pair, conditioned on the respective variance (B.17) for the distribution. Fig. B.2 displays the flow for the described methodology. On the left sub-figure, the estimated multipath error grid is shown according to the corresponding C/N$_0$ values. The middle sub-figure depicts the *pdf* for the inverse-Gamma distribution of each C/N$_0$ division, whose parameters $\alpha$ and $\beta$ are inferred from the data corresponding to each C/N$_0$. In the right sub-figure, the estimated C/N$_0$-dependent variance model regression problem is shown.

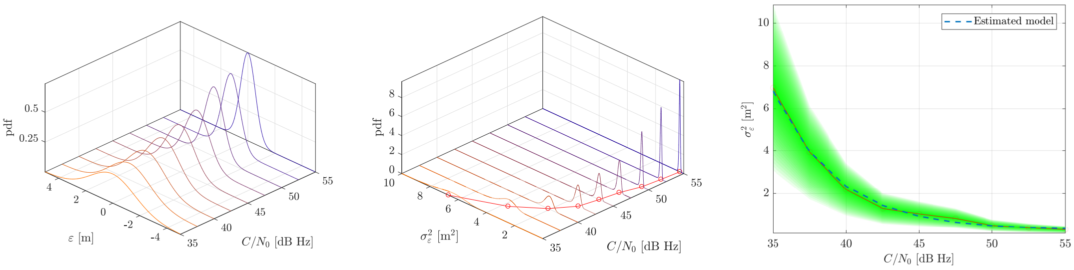

**Figure B.2:** Process flow example for the estimation of the $C/N_0$-based model. In the left plot, the estimated combination of the multipath and receiver noise is gridded for each $C/N_0$ division. In the middle plot, the *pdf* for the inverse-Gamma distributions are shown, whose parameters are inferred from the previously gridded data. In the right plot, the mode of the $\mathrm{IG}$ distributions in red, the corresponding $\mathrm{IG}$ variances in green and in blue the model obtained after the regression.

The framework of conjugate prior analysis applies perfectly to the problem of finding the weighting GNSS observations, as their noise is widely agreed to be zero-mean normally-distributed. The inverse-Gamma distribution results in the conjugate prior for the variance of the observations, and the parameters of the IG distributions estimated from the multipath combination. By determining the pdf of the inverse-Gamma distributions of the GNSS noise for each pair of elevations and signal-to-noise ratios, it is possible to find the unknown parameters of the proposed error models. Following this procedure, the variance models are not only found but also the corresponding confidence bands. It is a challenging and prospective topic to include the uncertainty of the uncertainty into the problem of integrity monitoring, capturing the higher moments of ambiguity into the GNSS positioning problem. A practical example captured onboard of a vessel in a maritime scenario is showcased in Fig. B.3.

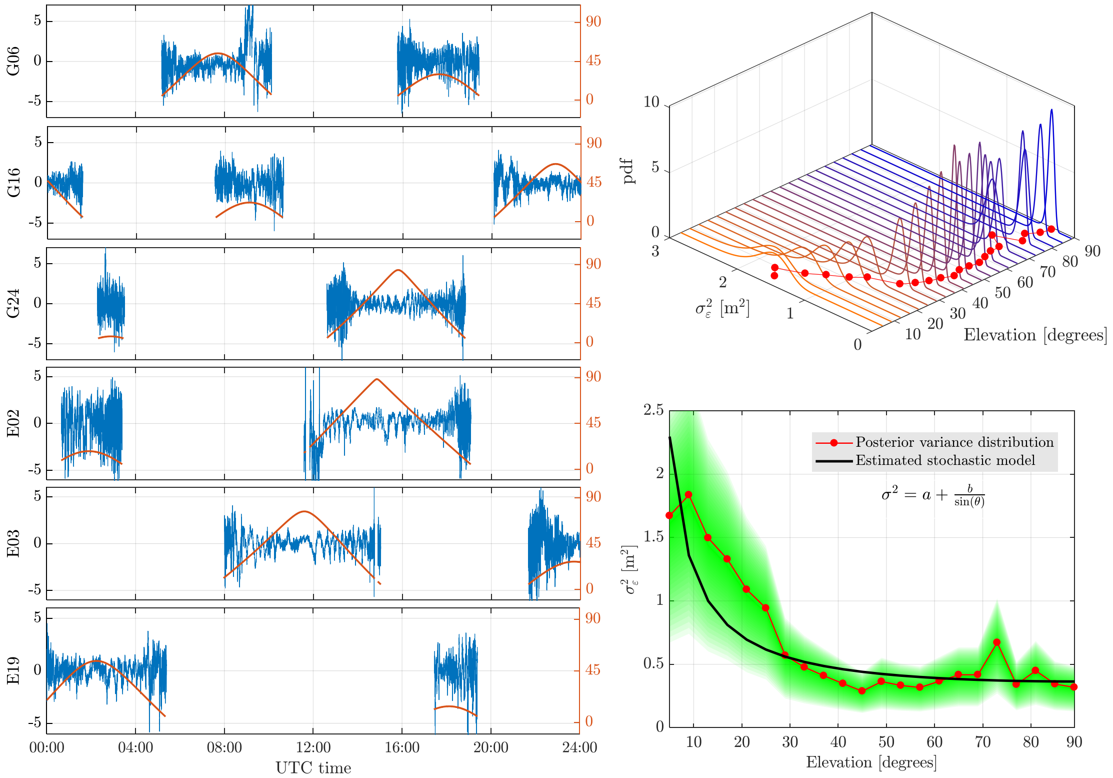

**Figure B.3:** On the left, time series of the CMC combination collected on a maritime scenario at the beginning of 2018. As example, the CMCs on L1/E1 for a total of three GPS and three Galileo satellites are depicted, as well as the corresponding satellite elevation. On the top right, the inferred IG distributions for the noise variance conditioned on the satellite elevation for GPS L1 observations. On the bottom right, the satellite-based stochastic model for the multipath and receiver noise is regressed from the mode of the aforementioned IG distributions.

# APPENDIX C

## Quaternion Operations and Properties

We will use $i, j$, and $k$ to represent the standard orthonormal basis for 3 dimensional space $\mathbb{R}^3$:

$$i = (1,\ 0,\ 0) \tag{C.1}$$
$$j = (0,\ 1,\ 0) \tag{C.2}$$
$$k = (0,\ 0,\ 1) \tag{C.3}$$

which have the following properties:

$$ij = k = -ji \tag{C.4}$$
$$jk = i = -kj \tag{C.5}$$
$$ki = j = -ik \tag{C.6}$$
$$i^2 = j^2 = k^2 = ijk \equiv -1 \tag{C.7}$$

A quaternion is represented is a 4-tuple of real numbers, $q\mathbb{R}^4$. It is formed by a scalar $q_w$ and a vector part $\mathbf{q}_u \in \mathbb{R}^3$ as:

$$\mathbf{q} = (q_w,\ q_x,\ q_y,\ q_z) = q_w + \mathbf{q_u} = q_w + iq_x + jq_y + kq_z \tag{C.8}$$

Next, we will present the basic quaternion arithmetic operations:

**Addition** The sum or difference of two quaternion $\mathbf{q},\ \mathbf{p}$ is another quaternion:

$$\mathbf{q} \pm \mathbf{p} = (q_w + p_w) + i\,(q_x + p_x) + j\,(q_y + p_y) + k\,(q_z + p_z) \tag{C.9}$$

**Conjugate**

$$\mathbf{q}^* = [\ q_w,\ -\mathbf{q_u}\ ] \tag{C.10}$$

**Norm**

$$\|\mathbf{q}\| = \sqrt{q_w^2 + q_x^2 + q_y^2 + q_z^2} = \sqrt{\mathbf{q}^\top \mathbf{q}} \tag{C.11}$$

**Inverse**

$$\mathbf{q}^{-1} = \frac{\mathbf{q}^*}{\|\mathbf{q}\|} \tag{C.12}$$

**Identity** When involving multiplication is $[1,\ (0,\ 0,\ 0)]$, and when involving addition/subtraction $[0,\ (0,\ 0,\ 0)]$

**Multiplication** The quaternion product[1] $\circ$ is non-commutative, associative and distributive over the sum:

$$\mathbf{q} \circ \mathbf{p} = \begin{bmatrix} q_w & -q_x & -q_y & -q_z \\ q_x & q_w & -q_z & q_y \\ q_y & q_z & q_w & -q_x \\ q_y & -q_2 & q_x & q_w \end{bmatrix} \begin{bmatrix} p_w \\ p_x \\ p_y \\ p_z \end{bmatrix} , \tag{C.13}$$

or, in a simplified matrix manner as

$$\mathbf{p} \circ \mathbf{q} = \begin{bmatrix} p_w q_w - \mathbf{p_u}^\top \mathbf{q_u} \\ p_w \mathbf{q_u} + q_w \mathbf{p_u} + \mathbf{p_u} \times \mathbf{q_u} \end{bmatrix} , \tag{C.14}$$

In addition, the composition of quaternions is bilinear and can be expressed as two matrix products:

$$\mathbf{q_1} \circ \mathbf{q_2} = [\mathbf{q_1}]_L \mathbf{q_2} \qquad \mathbf{q_1} \circ \mathbf{q_2} = [\mathbf{q_2}]_R \mathbf{q_1}, \tag{C.15}$$

with $[\mathbf{q}]_L$ and $[\mathbf{q}]_R$ are the left and right quaternion product matrices, respectively. These product matrices are given by:

$$[\mathbf{q}]_L = q_0 \mathbf{I}_4 + \begin{bmatrix} 0 & -\mathbf{q_u}^\top \\ \mathbf{q_u} & [\mathbf{q_u} \times] \end{bmatrix} , \quad [\mathbf{q}]_R = q_0 \mathbf{I}_4 + \begin{bmatrix} 0 & -\mathbf{q_u}^\top \\ \mathbf{q_u} & -[\mathbf{q_u} \times] \end{bmatrix} . \tag{C.16}$$

---

[1] The quaternion product is generally denoted as $\otimes$. However, this work reserves $\otimes$ for the representation of the Kronecker product.

# APPENDIX D

## Variational Bayesian-based Robust Filtering for Correlated Measurements

Let us recall the SSM formulation in (6.11)-(6.12), given by

$$\mathbf{x}_t = \mathbf{f}\left(\mathbf{x}_{t-1}\right) + \mathbf{w}_t$$
$$\mathbf{y}_t = \begin{cases} \mathbf{h}\left(\mathbf{x}_t\right) + \boldsymbol{\eta}_t & \text{, under } \mathcal{M}_0 \\ \mathbf{h}\left(\mathbf{x}_t\right) + \boldsymbol{\eta}_t + \mathbf{o}_t & \text{, under } \mathcal{M}_1 \end{cases}$$

and from (6.16) covariance matrix conditioned on the vector of outlier indicators $\boldsymbol{\zeta}_t$ as

$$\boldsymbol{\Sigma}_t\left(\boldsymbol{\zeta}_t\right) = \begin{bmatrix} \sigma_{1,1}^2/\zeta_t^{(1)} & \sigma_{1,2}^2 & \cdots & \sigma_{1,n}^2 \\ \sigma_{2,1}^2 & \sigma_{2,2}^2/\zeta_t^{(2)} & \cdots & \sigma_{2,n}^2 \\ \vdots & \vdots & \ddots & \vdots \\ \sigma_{n,1}^2 & \sigma_{n,2}^2 & \cdots & \sigma_{n,n}^2/\zeta_t^{(n)} \end{bmatrix},$$

which leads to the likelihood distribution

$$p\left(\mathbf{y}_t|\mathbf{x}_t, \boldsymbol{\zeta}_t\right) = \mathcal{N}\Big(\mathcal{T}(\mathbf{y}_t, \boldsymbol{\zeta}_t);\ \mathcal{T}(\mathbf{h}(\mathbf{x}_t), \boldsymbol{\zeta}_t), \mathbf{C}(\boldsymbol{\zeta}_t)\Big)\ .$$

This appendix details the estimation for the marginal distributions $q(\mathbf{x}_t)$, $q(\boldsymbol{\pi}_t)$ and $q(\boldsymbol{\zeta}_t)$ in (6.32)-(6.34) for a general nonlinear system under correlated observations, given the assumptions derived from the graphical model in Fig. 6.3.

### Update for $q(\mathbf{x}_t)$

According to the mean-field VI method, $q\left(\mathbf{x}_t\right)$ is obtained from (6.32) as

$$\ln(q(\mathbf{x}_t)) = -\frac{1}{2}\left\|\mathbf{x}_t - \hat{\mathbf{x}}_{t|t-1}\right\|^2_{\mathbf{P}_{t|t-1}} - \frac{1}{2}\sum_{\boldsymbol{\zeta}\in\mathcal{Z}} q(\boldsymbol{\zeta}_t = \boldsymbol{\zeta})\ \left\|\mathbf{y}_t - \mathbf{h}(\mathbf{x}_t)\right\|^2_{\boldsymbol{\Sigma}_t^{-1}(\boldsymbol{\zeta}_t)} + \kappa \tag{D.1}$$

$$= -\frac{1}{2}\left\|\mathbf{x}_t - \hat{\mathbf{x}}_{t|t-1}\right\|^2_{\mathbf{P}_{t|t-1}} - \frac{1}{2}\left(\mathbf{y}_t - \mathbf{h}(\mathbf{x}_t)\right)^\top \langle\boldsymbol{\Sigma}_t(\boldsymbol{\zeta}_t)\rangle(\mathbf{y}_t - \mathbf{h}(\mathbf{x}_t)) + \kappa, \tag{D.2}$$

where the term $\kappa$ gathers the logarithm of the constant factors, and $\boldsymbol{\zeta}$ represents one of the $2^n$ possible combinations of $\{\zeta_t^{(i)}\}_{i=1}^n$ binary values; the set of all those possible values is given by $\mathcal{Z} = \{0,1\}^n$ such that $|\mathcal{Z}| = 2^n$; The expectation of $\mathbf{\Sigma}_t(\boldsymbol{\zeta}_t)$ with respect to $q(\boldsymbol{\zeta}_t)$ is defined as

$$\langle \mathbf{\Sigma}_t(\boldsymbol{\zeta}_t) \rangle = \sum_{\boldsymbol{\zeta} \in \mathcal{Z}} \mathbf{\Sigma}_t(\boldsymbol{\zeta}) \, q(\boldsymbol{\zeta}_t = \boldsymbol{\zeta}) \, , \tag{D.3}$$

and $q(\boldsymbol{\zeta}_t = \boldsymbol{\zeta}) = \prod_{i=1}^{n} q(\zeta_t^{(i)} = \zeta^{(i)})$.

Thus, the estimation of $q(\mathbf{x}_t)$ is given by

$$q(\mathbf{x}_t) \propto \exp\left( -\frac{1}{2} \left\| \mathbf{x}_t - \hat{\mathbf{x}}_{t|t-1} \right\|^2_{\mathbf{P}_{t|t-1}} - \frac{1}{2} \left\| \mathbf{y}_t - \mathbf{h}(\mathbf{x}_t) \right\|^2_{\langle \mathbf{\Sigma}_t(\boldsymbol{\zeta}_t) \rangle} \right) \, , \tag{D.4}$$

from which one identifies $q(\mathbf{x}_t) \approx \mathcal{N}\left(\hat{\mathbf{x}}_{t|t}, \mathbf{P}_{t|t}\right)$, with

$$\mathbf{K}_t = \mathbf{C}_t \left( \mathbf{S}_t + \langle \mathbf{\Sigma}_t^{-1}(\boldsymbol{\zeta}_t) \rangle^{-1} \right)^{-1} , \tag{D.5}$$

$$\hat{\mathbf{x}}_{t|t} = \hat{\mathbf{x}}_{t|t-1} + \mathbf{K}_t \left( \mathbf{y}_t - \hat{\mathbf{y}}_{t|t-1} \right) , \tag{D.6}$$

$$\mathbf{P}_{t|t} = \mathbf{P}_{t|t-1} - \mathbf{K}_t \left( \mathbf{S}_t + \langle \mathbf{\Sigma}_t^{-1}(\boldsymbol{\zeta}_t) \rangle^{-1} \right) \mathbf{K}_t^\top , \tag{D.7}$$

$$\tag{D.8}$$

with

$$\hat{\mathbf{y}}_{t|t-1} = \int \mathbf{h}(\mathbf{x}_t) \, p(\mathbf{x}_t | \mathbf{y}_{1:t-1}) \, d\mathbf{x}_t \, , \tag{D.9}$$

$$\mathbf{S}_t = \int \left( \mathbf{h}(\mathbf{x}_t) - \hat{\mathbf{y}}_{t|t-1} \right) \left( \mathbf{h}(\mathbf{x}_t) - \hat{\mathbf{y}}_{t|t-1} \right)^\top p(\mathbf{x}_t | \mathbf{y}_{1:t-1}) \, d\mathbf{x}_t \, , \tag{D.10}$$

$$\mathbf{C}_t = \int \left( \mathbf{x}_t - \hat{\mathbf{x}}_{t|t-1} \right) \left( \mathbf{h}(\mathbf{x}_t) - \mathbf{y}_{t|t-1} \right)^\top p(\mathbf{x}_t | \mathbf{y}_{1:t-1}) \, d\mathbf{x}_t \, , \tag{D.11}$$

where the integrals can be solved analytically in linear systems or, for nonlinear models, approximated based on the first-order Taylor expansion (i.e., using EKF approximations) or through numerical integration for higher order of expansions (i.e., as for sigma point and cubature KFs).

## Update for $q(\boldsymbol{\zeta}_t)$

Recalling the assumption A3, on the indicators being mutually independent, one may operate on the marginal distributions $q(\zeta_t^{(i)})$ for each indicator. Then, following (6.34) one obtains

$$\ln\left[ q(\zeta_t^{(i)}) \right] = \mathbb{E}_{\pi_t^{(i)}, \mathbf{x}_t, \zeta_t^{(-i)}} \left\{ \ln\left[ p(\mathbf{x}_t, \boldsymbol{\pi}_t, \boldsymbol{\zeta}_t, \mathbf{y}_{1:t}) \right] \right\} , \tag{D.12}$$

where the expectation is over $\{\pi_t^{(i)}, \mathbf{x}_t, \boldsymbol{\zeta}_t^{(-i)}\}$. For the sake of convenience, the vector of observations is re-arranged such that the $i$-th element is swapped to the last position, as

$$\mathbf{y}_{t,i} = \begin{pmatrix} \mathbf{y}_t^{(-i)} \\ y_t^{(i)} \end{pmatrix} \, , \quad \mathbf{h}_i(\mathbf{x}_t) = \begin{pmatrix} \mathbf{h}^{(-i)}(\mathbf{x}_t) \\ h^{(i)}(\mathbf{x}_t) \end{pmatrix} \, , \tag{D.13}$$

where $\mathbf{a}^{(-i)}$ is the vector of all elements in a generic vector $\mathbf{a}$ except for $a^{(i)}$, while $[\mathbf{A}]_{-i,-j}$ re-define a generic matrix $\mathbf{A}$ by removing all its elements except for the $i$th row and $j$th column. Hence, the covariance matrix (6.16) is then reorganized to meet the order in D.13, as

$$\mathbf{\Sigma}_{t,i}(\boldsymbol{\zeta}_t) = \begin{bmatrix} \mathbf{\Sigma}_{-i,-i} & \mathbf{\Sigma}_{-i,i} \\ \mathbf{\Sigma}_{i,-i} & \sigma_{i,i}^2 / \zeta_t^{(i)} \end{bmatrix} \, , \tag{D.14}$$

and, operating on the precision matrix $\boldsymbol{\Lambda}_{t,i} = \boldsymbol{\Sigma}_{t,i}(\boldsymbol{\zeta}_t)^{-1}$ and leveraging on the Schur complement, the former can be expressed as

$$\boldsymbol{\Lambda}_{t,i} = \begin{bmatrix} \boldsymbol{\Lambda}_{-i,-i} & \boldsymbol{\Lambda}_{-i,i} \\ \boldsymbol{\Lambda}_{i,-i} & \lambda_{i,i} \end{bmatrix} = \begin{bmatrix} \boldsymbol{M}_{-i} & -\zeta_t^{(i)}/\sigma_{i,i}^2 \boldsymbol{M}_{-i} \boldsymbol{\Sigma}_{-i,i} \\ -\zeta_t^{(i)}/\sigma_{i,i}^2 \boldsymbol{\Sigma}_{i,-i} \boldsymbol{M}_{-i} & M_i \end{bmatrix} \tag{D.15}$$

with

$$\boldsymbol{M}_{-i} = \left(\boldsymbol{\Sigma}_{-i,-i} - \zeta_t^{(i)}/\sigma_{i,i}^2 \boldsymbol{\Sigma}_{-i,i} \boldsymbol{\Sigma}_{i,-i}\right)^{-1}, \tag{D.16}$$

$$M_i = \left(\sigma_{i,i}^2/\zeta_t^{(i)} - \boldsymbol{\Sigma}_{i,-i} \boldsymbol{\Sigma}_{-i,-i}^{-1} \boldsymbol{\Sigma}_{-i,i}\right)^{-1}. \tag{D.17}$$

Then, one can further extend (D.16) by applying the matrix inversion lemma, leading to

$$\boldsymbol{M}_{-i} = \boldsymbol{\Sigma}_{-i,-i}^{-1} + \frac{\boldsymbol{\Sigma}_{-i,-i}^{-1} \boldsymbol{\Sigma}_{i,-i} \boldsymbol{\Sigma}_{-i,i} \boldsymbol{\Sigma}_{-i,-i}^{-1}}{\sigma_{i,i}^2/\zeta_t^{(i)} - \boldsymbol{\Sigma}_{i,-i} \boldsymbol{\Sigma}_{-i,-i}^{-1} \boldsymbol{\Sigma}_{-i,i}} \,. \tag{D.18}$$

Note that for independently-distributed observations, the cross-covariance in $\boldsymbol{\Sigma}_t(\boldsymbol{\zeta}_t)$ is zero and $M_i = \zeta_t^{(i)}/\sigma_{i,i}^2$. For correlated data, $\zeta_t^{(i)}$ is part of a fraction which would make it tedious in terms of computing the Bernoulli probabilities for the indicator. Fortunately, $\zeta_t^{(i)}$ is a binary variable $\zeta_t^{(i)} = \{0, 1\}$ which allows the following equivalent expression

$$M_i = \frac{\zeta_t^{(i)}}{\sigma_{i,i}^2 - \boldsymbol{\Sigma}_{i,-i} \boldsymbol{\Sigma}_{-i,-i}^{-1} \boldsymbol{\Sigma}_{-i,i}} \,, \tag{D.19}$$

which yields to identical result as in (D.17) regardless of the $\zeta_t^{(i)}$ value. Thus, if $\boldsymbol{\zeta}_t = 1$, the original covariance matrix is preserved and the conventional correction step performed; if $\zeta_t^{(i)} = 0$, the corresponding elements in the precision matrix would be zero, meaning that the influence of contaminated observations is eliminated, while the inliers constitute a multivariate normal distribution of reduced dimension $n' \leq n$.

In order to model $q(\zeta_t^{(i)})$ in the form of a Bernoulli distribution, we use

$$\begin{aligned} \ln\left[q(\zeta_t^{(i)})\right] &= \mathbb{E}_{\pi_t^{(i)}, \mathbf{x}_t, \boldsymbol{\zeta}_t^{(-i)}} \left\{\ln\left[p\left(\mathbf{x}_t, \boldsymbol{\pi}_t, \boldsymbol{\zeta}_t, \mathbf{y}_{1:t}\right)\right]\right\} \\ &= \mathbb{E}_{\pi_t^{(i)}, \mathbf{x}_t, \boldsymbol{\zeta}_t^{(-i)}} \Big\{ -\frac{1}{2} \left\|\mathbf{y}_t^{(-i)} - \mathbf{h}^{(-i)}\left(\mathbf{x}_t\right)\right\|_{\boldsymbol{\Lambda}_{-i,-i}}^2 \\ &- \left(\mathbf{y}_t^{(-i)} - \mathbf{h}^{(-i)}\left(\mathbf{x}_t\right)\right)^\top \boldsymbol{\Lambda}_{-i,i} \left(y_t^{(i)} - h^{(i)}\left(\mathbf{x}_t\right)\right) \\ &- \frac{1}{2} || y_t^{(i)} - h^{(i)}\left(\mathbf{x}_t\right) ||_{\lambda_{i,i}}^2 + \zeta_t^{(i)} \ln[\pi_t^{(i)}] \\ &+ \left(1 - \zeta_t^{(i)}\right) \ln[1 - \pi_t^{(i)}] - \frac{1}{2} \zeta_t^{(i)} \ln[2\pi] \\ &- \frac{1}{2} \zeta_t^{(i)} \ln|\mathbf{C}([\boldsymbol{\zeta}_t^{(-i)}, \zeta_t^{(i)} = 1])| \\ &- \frac{1}{2}(1 - \zeta_t^{(i)}) \ln\left|\mathbf{C}([\boldsymbol{\zeta}_t^{(-i)}, \zeta_t^{(i)} = 0])\right| + \kappa \Big\} \end{aligned} \tag{D.20}$$

where, by expanding the terms due to the normalizing constant (6.18), the determinant of $\mathbf{C}(\boldsymbol{\zeta}_t)$ is factorized as

$$|\mathbf{C}(\boldsymbol{\zeta}_t)| = |\mathbf{C}([\boldsymbol{\zeta}_t^{(-i)}, \zeta_t^{(i)} = 1])|^{\zeta_t^{(i)}} |\mathbf{C}([\boldsymbol{\zeta}_t^{(-i)}, \zeta_t^{(i)} = 0])|^{(1-\zeta_t^{(i)})} \,, \tag{D.21}$$

and after some tedious matrix manipulations (see Appendix A.7), the following expression is obtained

$$
\begin{aligned}
q\left(\zeta_t^{(i)}\right) = \exp\{ & -\frac{1}{2}\zeta_t^{(i)} \operatorname{tr}\left(\boldsymbol{B}_{-i,-i}\langle\boldsymbol{\Lambda}_{t1}\rangle\right) \\
& -\frac{1}{2}\zeta_t^{(i)} \operatorname{tr}\left(-\boldsymbol{B}_{i,-i}\langle\boldsymbol{\Lambda}_{t2}\rangle\right) \\
& -\frac{1}{2}\zeta_t^{(i)} \operatorname{tr}\left(-\boldsymbol{B}_{i,-i}\langle\boldsymbol{\Lambda}_{t3}\rangle\right) - \frac{1}{2}\zeta_t^{(i)} \operatorname{tr}\left(b_{i,i}\langle\lambda_{t4}\rangle\right) \\
& + \zeta_t^{(i)}\langle\ln[\pi_t^{(i)}]\rangle + \left(1-\zeta_t^{(i)}\right)\langle\ln[1-\pi_t^{(i)}]\rangle \\
& -\frac{1}{2}\zeta_t^{(i)}\ln[2\pi] \\
& -\frac{1}{2}\zeta_t^{(i)}\langle\ln|\mathbf{C}([\boldsymbol{\zeta}_t^{(-i)},\zeta_t^{(i)}=1])|\rangle \\
& -\frac{1}{2}(1-\zeta_t^{(i)})\langle\ln|\mathbf{C}([\boldsymbol{\zeta}_t^{(-i)},\zeta_t^{(i)}=0])|\rangle + \kappa\}
\end{aligned}
\tag{D.22}
$$

where $\boldsymbol{B}_{-i,-i}$, $\boldsymbol{B}_{i,-i}$, and $b_{i,i}$ are given by

$$
\boldsymbol{B}_{-i,-i} = \int\left(\mathbf{y}_t^{(-i)} - \mathbf{h}^{(-i)}(\mathbf{x}_t)\right)\left(\mathbf{y}_t^{(-i)} - \mathbf{h}^{(-i)}(\mathbf{x}_t)\right)^\top q(\mathbf{x}_t)\, d\mathbf{x}_t, \tag{D.23}
$$

$$
\boldsymbol{B}_{i,-i} = \int\left(y_t^{(i)} - h^{(i)}(\mathbf{x}_t)\right)\left(\mathbf{y}_t^{(-i)} - \mathbf{h}^{(-i)}(\mathbf{x}_t)\right)^\top q(\mathbf{x}_t)\, d\mathbf{x}_t, \tag{D.24}
$$

$$
b_{i,i} = \int\left(y_t^{(i)} - h^{(i)}(\mathbf{x}_t)\right)\left(y_t^{(i)} - h^{(i)}(\mathbf{x}_t)\right)^\top q(\mathbf{x}_t)\, d\mathbf{x}_t, \tag{D.25}
$$

and the expectations with respect to $q(\boldsymbol{\zeta}_t^{(-i)})$ read

$$
\langle\boldsymbol{\Lambda}_{t1}\rangle = \sum_{\boldsymbol{\zeta}^{(-i)}\in\mathcal{Z}_{-i}} \frac{\boldsymbol{\Sigma}_{-i,-i}^{-1}\boldsymbol{\Sigma}_{-i,i}\boldsymbol{\Sigma}_{i,-i}\boldsymbol{\Sigma}_{-i,-i}^{-1}}{\sigma_{i,i}^2 - \boldsymbol{\Sigma}_{i,-i}\boldsymbol{\Sigma}_{-i,-i}^{-1}\boldsymbol{\Sigma}_{-i,i}} q(\boldsymbol{\zeta}_t^{(-i)} = \boldsymbol{\zeta}^{(-i)}) \tag{D.26}
$$

$$
\langle\boldsymbol{\Lambda}_{t2}\rangle = \frac{2}{\sigma_{i,i}^2}\sum_{\boldsymbol{\zeta}^{(-i)}\in\mathcal{Z}_{-i}} \boldsymbol{\Sigma}_{-i,-i}^{-1}\boldsymbol{\Sigma}_{-i,i} q(\boldsymbol{\zeta}_t^{(-i)} = \boldsymbol{\zeta}^{(-i)}) \tag{D.27}
$$

$$
\langle\boldsymbol{\Lambda}_{t3}\rangle = \sum_{\boldsymbol{\zeta}^{(-i)}\in\mathcal{Z}_{-i}} \frac{2\boldsymbol{\Sigma}_{-i,-i}^{-1}\boldsymbol{\Sigma}_{-i,i}\boldsymbol{\Sigma}_{i,-i}\boldsymbol{\Sigma}_{-i,-i}^{-1}\boldsymbol{\Sigma}_{-i,i}}{\sigma_{i,i}^4 - \sigma_{i,i}^2\boldsymbol{\Sigma}_{i,-i}\boldsymbol{\Sigma}_{-i,-i}^{-1}\boldsymbol{\Sigma}_{-i,i}} q(\boldsymbol{\zeta}_t^{(-i)} = \boldsymbol{\zeta}^{(-i)}) \tag{D.28}
$$

$$
\langle\lambda_{t4}\rangle = \sum_{\boldsymbol{\zeta}^{(-i)}\in\mathcal{Z}_{-i}} \frac{1}{\sigma_{i,i}^2 - \boldsymbol{\Sigma}_{i,-i}\boldsymbol{\Sigma}_{-i,-i}^{-1}\boldsymbol{\Sigma}_{-i,i}} q(\boldsymbol{\zeta}_t^{(-i)} = \boldsymbol{\zeta}^{(-i)}) \tag{D.29}
$$

where the sum over $\boldsymbol{\zeta}^{(-i)}$ comprises the sum over all possible $2^{n-1}$ values for $\boldsymbol{\zeta}^{(-i)}$, whose probability is $q(\boldsymbol{\zeta}_t^{(-i)} = \boldsymbol{\zeta}^{(-i)})$. Note that $\boldsymbol{\zeta}_t^{(-i)}$ appears in the diagonal elements of $\boldsymbol{\Sigma}_{-i,-i}$, dependence which is omitted to improve the readiness.

Finally, one can recognize $\zeta_t^{(i)}$ as Bernoulli-distributed variable, whose pdf is characterized by

$$\begin{aligned} p\left(\zeta_t^{(i)}=1\right) \propto \exp\{ & -\frac{1}{2}\operatorname{tr}\left(\boldsymbol{B}_{-i,-i}\langle\boldsymbol{\Lambda}_{t1}\rangle\right) \\ & -\frac{1}{2}\operatorname{tr}\left(\boldsymbol{B}_{i,-i}\langle\boldsymbol{\Lambda}_{t2}\rangle\right)-\frac{1}{2}\operatorname{tr}\left(\boldsymbol{B}_{i,-i}\langle\boldsymbol{\Lambda}_{t3}\rangle\right) \\ & -\frac{1}{2}\operatorname{tr}\left(b_{i,i}\langle\lambda_{t4}\rangle\right)+\langle\ln[\pi_t^{(i)}]\rangle-\frac{1}{2}\ln[2\pi] \\ & -\frac{1}{2}\langle\ln|\mathbf{C}([\boldsymbol{\zeta}_t^{(-i)},\zeta_t^{(i)}=1])|\rangle\} \end{aligned} \tag{D.30}$$

$$\begin{aligned} p\left(\zeta_t^{(i)}=0\right) \propto \exp\{ & \langle\ln[1-\pi_t^{(i)}]\rangle \\ & -\frac{1}{2}\langle\ln|\mathbf{C}([\boldsymbol{\zeta}_t^{(-i)},\zeta_t^{(i)}=0])|\rangle\}\;. \end{aligned} \tag{D.31}$$

Thus, the expectation of a Bernoulli $\zeta_t^{(i)}$ can estimated from

$$\langle\zeta_t^{(i)}\rangle=\frac{p\left(\zeta_t^{(i)}=1\right)}{p\left(\zeta_t^{(i)}=1\right)+p\left(\zeta_t^{(i)}=0\right)}\;, \tag{D.32}$$

a quantity required for the update of $q\left(\pi_t^{(i)}\right)$, which is discussed next.

### Update for $q\left(\pi_t^{(i)}\right)$

Similar to the derivation discussed in Section 6.2, $q\left(\pi_t^{(i)}\right)$ can be updated for each indicator as

$$q\left(\pi_t^{(i)}\right) \propto \exp\left(e_t^{(i)}\ln[\pi_t^{(i)}]+f_t^{(i)}\ln[1-\pi_t^{(i)}]\right) \tag{D.33}$$

where

$$e_t^{(i)}=e_0+\langle\zeta_t^{(i)}\rangle \tag{D.34}$$

$$f_t^{(i)}=f_0+1-\langle\zeta_t^{(i)}\rangle \tag{D.35}$$

such that $f_0$ and $e_0$ constitute the prior over the hyper-parameters of the distribution $\pi_t^{(i)}$, assumed the same for all $i$.

# Bibliography

[1] Juan Manuel Castro-Arvizu, Daniel Medina, Ralf Ziebold, et al. "Precision-Aided Partial Ambiguity Resolution Scheme for Instantaneous RTK Positioning". In: *Remote Sensing* 13.15 (2021), p. 2904.

[2] Lukas Meyer, Michal Smíšek, Alejandro Fontan Villacampa, et al. "The MADMAX data set for visual-inertial rover navigation on Mars". In: *Journal of Field Robotics* (2021).

[3] Daniel Medina, Haoqing Li, Jordi Vilà-Valls, et al. "Robust Filtering Techniques for RTK Positioning in Harsh Propagation Environments". In: *Sensors* 21.4 (2021), p. 1250.

[4] Daniel Medina, Jordi Vilà-Valls, Eric Chaumette, et al. "Cramér-Rao bound for a mixture of real-and integer-valued parameter vectors and its application to the linear regression model". In: *Signal Processing* 179 (2021), p. 107792.

[5] Haoqing Li, Daniel Medina, Jordi Vilà-Valls, et al. "Robust Variational-based Kalman Filter for Outlier Rejection with Correlated Measurements". In: *IEEE Transactions on Signal Processing* 69 (2020), pp. 357–369.

[6] Anja Hesselbarth, Daniel Medina, Ralf Ziebold, et al. "Enabling Assistance Functions for the Safe Navigation of Inland Waterways". In: *IEEE Intelligent Transportation Systems Magazine* 12.3 (2020), pp. 123–135.

[7] Lorenzo Ortega, Daniel Medina, Jordi Vilà-Valls, et al. "Positioning Performance Limits of GNSS Meta-Signals and HO-BOC Signals". In: *Sensors* 20.12 (2020), p. 3586.

[8] Daniel Medina, Jordi Vilà-Valls, Anja Hesselbarth, et al. "On the Recursive Joint Position and Attitude Determination in Multi-Antenna GNSS Platforms". In: *Remote Sensing* 12.12 (2020), p. 1955.

[9] D. Medina, L. Ortega, J. Vilà-Valls, et al. "Compact CRB for Delay, Doppler and Phase Estimation - Application to GNSS SPP & RTK Performance Characterization". In: *IET Radar, Sonar & Navigation* 14.10 (2020), pp. 1537–1549.

[10] Daniel Medina, Haoqing Li, Jordi Vilà-Valls, et al. "Robust Statistics for GNSS Positioning under Harsh Conditions: A Useful Tool?" In: *Sensors* 19.24 (2019), p. 5402.

[11] Paul Chauchat, Daniel Medina, Jordi Vilà-Valls, et al. "Robust Linearly Constrained Filtering for GNSS Position and Attitude Estimation under Antenna Baseline Mismatch". In: *2021 24th International Conference on Information Fusion (FUSION)*. IEEE. 2021.

[12] Daniel Medina, J Manuel Castro-Arvizu, Jordi Vilà-Valls, et al. "Precision-Driven Partial Ambiguity Resolution Technique for Short to Medium Baseline Positioning". In: *2021 IEEE Aerospace Conference*. IEEE. 2021, pp. 1–7.

[13] Daniel Medina, Ralf Ziebold, and Jesús García. "On the Kalman Filter Design for Quaternion-based GNSS-Inertial Attitude Determination". In: *2020 European Navigation Conference (ENC)*. IEEE. 2020.

[14] Lorenzo Ortega, Daniel Medina, Jordi Vilà-Valls, et al. "A Compact CRB for the Single Source Conditional Signal Model with Application to Delay-Doppler-Phase Estimation of Band-Limited Signals". In: *2020 59th IEEE Conference on Decision and Control (CDC)*. IEEE. 2020, pp. 2906–2911.

[15] J Manuel Castro-Arvizu, Daniel Medina, and Ralf Ziebold. "Impact of Satellite Elevation Mask in GPS+Galileo RTK Positioning". In: *Proceedings of the 2020 International Technical Meeting of The Institute of Navigation*. 2020, pp. 487–498.

[16] Daniel Medina, Haoqing Li, Jordi Vilà-Valls, et al. "On Robust Statistics for GNSS Single Point Positioning". In: *2019 22nd International Conference on Intelligent Transportation Systems (ITSC)*. IEEE. 2019.

[17] Daniel Medina, Vincenzo Centrone, Ralf Ziebold, et al. "Attitude determination via GNSS carrier phase and inertial aiding". In: *Proceedings of the 32nd International Technical Meeting of the Satellite Division of The Institute of Navigation (ION GNSS+ 2019)*. 2019, pp. 2964–2979.

[18] Haoqing Li, Daniel Medina, Jordi Vilà-Valls, et al. "Robust Kalman Filter for RTK Positioning Under Signal-Degraded Scenarios". In:

[19] Daniel Medina, Carlos S. Alvarez-Merino, and Ralf Ziebold. "Partial Ambiguity Resolution for Reliable GPS/Galileo Positioning". In: *2019 International Workshop on GNSS Ionosphere (IGWI)*. Sept. 2019.

[20] Daniel Medina, Kasia Gibson, Ralf Ziebold, et al. "Determination of Pseudorange Error Models and Multipath Characterization under Signal-Degraded Scenarios". In: *Proceedings of the 31st International Technical Meeting of the Satellite Division of The Institute of Navigation (ION GNSS+ 2018),* Institute of Navigation. 2018, pp. 3446–3456.

[21] Omar Garcia Crespillo, Daniel Medina, Jan Skaloud, et al. "Tightly coupled GNSS/INS integration based on robust M-estimators". In: *2018 IEEE/ION Position, Location and Navigation Symposium (PLANS)*. IEEE. 2018, pp. 1554–1561.

[22] Daniel Medina, Anja Heßelbarth, Rauno Büscher, et al. "On the Kalman filtering formulation for RTK joint positioning and attitude quaternion determination". In: *2018 IEEE/ION Position, Location and Navigation Symposium (PLANS)*. IEEE. 2018, pp. 597–604.

[23] Francisco Pastor, Jorge García-González, Juan M Gandarias, et al. "Bayesian and Neural Inference on LSTM-Based Object Recognition from Tactile and Kinesthetic Information". In: *IEEE Robotics and Automation Letters* 6.1 (2020), pp. 231–238.

[24] François Vincent, Jordi Vilà-Valls, Olivier Besson, et al. "Doppler-aided positioning in GNSS receivers-A performance analysis". In: *Signal Processing* 176 (2020), p. 107713.

[25] Ralf Ziebold, Daniel Medina, Michailas Romanovas, et al. "Performance Characterization of GNSS/IMU/DVL Integration under Real Maritime Jamming Conditions". In: *Sensors* 18.9 (2018), p. 2954.

[26] Daniel Medina, Lars Grundhöfer, and Niklas Hehenkamp. "Evaluation of Estimators for Hybrid GNSS-Terrestrial Localization in Collaborative Networks". In: *2020 IEEE 23rd International Conference on Intelligent Transportation Systems (ITSC)*. IEEE. 2020, pp. 1–7.

[27] Daniel Medina, Christoph Lass, Emilio Pérez Marcos, et al. "On GNSS Jamming Threat from the Maritime Navigation Perspective". In: *2019 22th International Conference on Information Fusion (FUSION)*. IEEE. 2019, pp. 1–7.

[28] Daniel Arias Medina, Michailas Romanovas, Iván Herrera-Pinzón, et al. "Robust position and velocity estimation methods in integrated navigation systems for inland water applications". In: *Position, Location and Navigation Symposium (PLANS), 2016 IEEE/ION*. IEEE. 2016, pp. 491–501.

[29] Y Jade Morton, Frank van Diggelen, James J Spilker Jr, et al. *Position, Navigation, and Timing Technologies in the 21st Century: Integrated Satellite Navigation, Sensor Systems, and Civil Applications*. John Wiley & Sons, 2021.

[30] P. J. G. Teunissen and O. Montenbruck, eds. *Handbook of Global Navigation Satellite Systems*. Switzerland: Springer, 2017.

[31] Jaime Sanz Subirana, Manuel Hernandez-Pajares, and José Miguel Juan Zornoza. *GNSS Data Processing: Fundamentals and Algorithms*. European Space Agency, 2013.

[32] Priyanka Das, Lorenzo Ortega, Jordi Vilà-Valls, et al. "Performance Limits of GNSS Code-Based Precise Positioning: GPS, Galileo & Meta-Signals". In: *Sensors* 20.8 (2020), p. 2196.

[33] J. Issler, M. Paonni, and B. Eissfeller. "Toward centimetric positioning thanks to L- and S-Band GNSS and to meta-GNSS signals". In: *2010 5th ESA Workshop on Satellite Navigation Technologies and European Workshop on GNSS Signals and Signal Processing (NAVITEC)*. 2010, pp. 1–8.

[34] Laurent Lestarquit, Géraldine Artaud, and Jean-Luc Issler. "AltBOC for dummies or everything you always wanted to know about AltBOC". In: *ION GNSS*. 2008, pp. 961–970.

[35] Elliott Kaplan and Christopher Hegarty. *Understanding GPS: principles and applications*. Artech house, 2005.

[36] Fabio Dovis. *GNSS interference threats and countermeasures*. Artech House, 2015.

[37] F. Vincent, E. Chaumette, C. Charbonnieras, et al. "Asymptotically Efficient GNSS Trilateration". In: *Signal Processing* 133 (2017), pp. 270–277.

[38] Pau Closas Gómez. *Bayesian signal processing techniques for GNSS receivers: from multipath mitigation to positioning*. Universitat Politècnica de Catalunya, 2009.

[39] P. Closas, C. Fernández-Prades, and J. A. Fernández-Rubio. "Maximum likelihood estimation of position in GNSS". In: *IEEE Signal Processing letters* 14.5 (2007), pp. 359–362.

[40] Pau Closas and Adria Gusi-Amigó. "Direct position estimation of GNSS receivers: Analyzing main results, architectures, enhancements, and challenges". In: *IEEE Signal Processing Magazine* 34.5 (2017), pp. 72–84.

[41] Frank Stephen Tromp Van Diggelen. *A-GPS: Assisted GPS, GNSS, and SBAS*. Artech house, 2009.

[42] Petre Stoica and Torsten Söderström. "On reparametrization of loss functions used in estimation and the invariance principle". In: *Signal processing* 17.4 (1989), pp. 383–387.

[43] Jindřich Duník, Ondřej Straka, Oliver Kost, et al. "Noise covariance matrices in state-space models: A survey and comparison of estimation methodsPart I". In: *International Journal of Adaptive Control and Signal Processing* 31.11 (2017), pp. 1505–1543.

[44] Todd Walter and Per Enge. "Weighted RAIM for precision approach". In: *PROCEEDINGS OF ION GPS*. Vol. 8. Institute of Navigation. 1995, pp. 1995–2004.

[45] Steve Hewitson and Jinling Wang. "GNSS receiver autonomous integrity monitoring (RAIM) performance analysis". In: *Gps Solutions* 10.3 (2006), pp. 155–170.

[46] Ni Zhu, Juliette Marais, David Bétaille, et al. "GNSS position integrity in urban environments: A review of literature". In: *IEEE Transactions on Intelligent Transportation Systems* 19.9 (2018), pp. 2762–2778.

[47] Heidi Kuusniemi, Andreas Wieser, Gerard Lachapelle, et al. "User-level reliability monitoring in urban personal satellite-navigation". In: *IEEE Transactions on Aerospace and Electronic Systems* 43.4 (2007), pp. 1305–1318.

[48] Mihaela-Simona Circiu, Michael Meurer, Michael Felux, et al. “Evaluation of GPS L5 and Galileo E1 and E5a performance for future multifrequency and multiconstellation GBAS”. In: *Navigation: Journal of The Institute of Navigation* 64.1 (2017), pp. 149–163.

[49] Peter JG Teunissen and AR Amiri-Simkooei. “Least-squares variance component estimation”. In: *Journal of geodesy* 82.2 (2008), pp. 65–82.

[50] R Odolinski, PJG Teunissen, and Dennis Odijk. “Combined GPS+ BDS for short to long baseline RTK positioning”. In: *Measurement Science and Technology* 26.4 (2015), p. 045801.

[51] Robert Odolinski and Peter JG Teunissen. “Single-frequency, dual-GNSS versus dual-frequency, single-GNSS: a low-cost and high-grade receivers GPS-BDS RTK analysis”. In: *Journal of geodesy* 90.11 (2016), pp. 1255–1278.

[52] Daniel Medina, Lorenzo Ortega, Jordi Vilà-Valls, et al. “A New Compact CRB for Delay, Doppler and Phase Estimation - Application to GNSS SPP & RTK Performance Characterization”. In: *Submitted to IET Radar, Sonar & Navigation* (2020).

[53] J. F. Zumberge, M. B. Heflin, D. C. Jefferson, et al. “Precise point positioning for the efficient and robust analysis of GPS data from large networks”. In: *Journal of Geophysical Research: Solid Earth* 102.B3 (1997), pp. 5005–5017.

[54] Jan Kouba and Pierre Héroux. “Precise point positioning using IGS orbit and clock products”. In: *GPS solutions* 5.2 (2001), pp. 12–28.

[55] Liang Wang, Zishen Li, Maorong Ge, et al. “Validation and assessment of multi-gnss real-time precise point positioning in simulated kinematic mode using igs real-time service”. In: *Remote Sensing* 10.2 (2018), p. 337.

[56] Peter JG Teunissen. “An optimality property of the integer least-squares estimator”. In: *Journal of geodesy* 73.11 (1999), pp. 587–593.

[57] P. J. G. Teunissen. “Penalized GNSS ambiguity resolution”. In: *Journal of Geodesy* 78.4-5 (2004), pp. 235–244.

[58] P. J. G. Teunissen. “Theory of integer equivariant estimation with application to GNSS”. In: *Journal of Geodesy* 77.7-8 (2003), pp. 402–410.

[59] P. J. G. Teunissen. “The probability distribution of the GPS baseline for a class of integer ambiguity estimators”. In: *Journal of Geodesy* 73.5 (1999), pp. 275–284.

[60] S. Verhagen and P.J.G. Teunissen. “The LAMBDA method for the GNSS compass”. In: *GPS Solutions* 10.1 (2006), pp. 21–28.

[61] Louis L Scharf and Cédric Demeure. *Statistical signal processing: detection, estimation, and time series analysis*. Prentice Hall, 1991.

[62] Dennis Odijk. “Weighting ionospheric corrections to improve fast GPS positioning over medium distances”. In: *ION GPS*. 2000, pp. 1113–1123.

[63] Peter JG Teunissen. “The least-squares ambiguity decorrelation adjustment: a method for fast GPS integer ambiguity estimation”. In: *Journal of geodesy* 70.1-2 (1995), pp. 65–82.

[64] J. Dunik, S. K. Biswas, A. G. Dempster, et al. “State Estimation Methods: Overview and Application in Navigation”. In: *IEEE Aerospace and Electronic Systems Magazine* (2020).

[65] Andreas Brack. “Partial carrier-phase integer ambiguity resolution for high accuracy GNSS positioning”. PhD thesis. Technical University Munich, 2019.

[66] Peter JG Teunissen. “ADOP based upper bounds for the boostrapped and the least-squares ambiguity success-rates”. In: *Artificial Satellites* 35.4 (2000), pp. 171–179.

[67] Sandra Verhagen, Bofeng Li, and Peter JG Teunissen. “Ps-LAMBDA: ambiguity success rate evaluation software for interferometric applications”. In: *Computers & Geosciences* 54 (2013), pp. 361–376.

[68] Arash Hassibi and Stephen Boyd. “Integer parameter estimation in linear models with applications to GPS”. In: *IEEE Transactions on signal processing* 46.11 (1998), pp. 2938–2952.

[69] Peter JG Teunissen. “Success probability of integer GPS ambiguity rounding and bootstrapping”. In: *Journal of Geodesy* 72.10 (1998), pp. 606–612.

[70] Paul De Jonge, CCJM Tiberius, et al. “The LAMBDA method for integer ambiguity estimation: implementation aspects”. In: *Publications of the Delft Computing Centre, LGR-Series* 12.12 (1996), pp. 1–47.

[71] Peter Teunissen. “Integer aperture GNSS ambiguity resolution”. In: *Artificial Satellites* 38.3 (2003), pp. 79–88.

[72] Peter JG Teunissen and Sandra Verhagen. “The GNSS ambiguity ratio-test revisited: a better way of using it”. In: *Survey Review* 41.312 (2009), pp. 138–151.

[73] Sandra Verhagen and Peter JG Teunissen. “The ratio test for future GNSS ambiguity resolution”. In: *GPS solutions* 17.4 (2013), pp. 535–548.

[74] Lei Wang and Sandra Verhagen. “A new ambiguity acceptance test threshold determination method with controllable failure rate”. In: *Journal of geodesy* 89.4 (2015), pp. 361–375.

[75] Sandra Verhagen. “Integer ambiguity validation: An open problem?” In: *GPS solutions* 8.1 (2004), pp. 36–43.

[76] Sandra Verhagen, Peter JG Teunissen, Hans van der Marel, et al. “GNSS ambiguity resolution: which subset to fix”. In: *IGNSS Symposium*. 2011, pp. 15–17.

[77] Dennis Odijk, Balwinder S Arora, and Peter JG Teunissen. “Predicting the success rate of long-baseline GPS+ Galileo (partial) ambiguity resolution”. In: *The Journal of Navigation* 67.3 (2014), pp. 385–401.

[78] Andreas Brack and Christoph Günther. “Generalized integer aperture estimation for partial GNSS ambiguity fixing”. In: *Journal of geodesy* 88.5 (2014), pp. 479–490.

[79] Andreas Brack. “On reliable data-driven partial GNSS ambiguity resolution”. In: *GPS solutions* 19.3 (2015), pp. 411–422.

[80] Andreas Brack. “Partial ambiguity resolution for reliable GNSS positioningA useful tool?” In: *Aerospace Conference, 2016 IEEE*. IEEE. 2016, pp. 1–7.

[81] Ignacio Fernandez-Hernandez, Tommaso Senni, David Calle, et al. “Analysis of High-Accuracy Satellite Messages for Road Applications”. In: *IEEE Intelligent Transportation Systems Magazine* 12.3 (2020), pp. 92–108.

[82] H. L. Van Trees. *Optimum Array Processing*. New York, NY, USA: Wiley-Interscience, 2002.

[83] A. Renaux, P. Forster, E. Chaumette, et al. “On the High-SNR Conditional Maximum-Likelihood Estimator Full Statistical Characterization”. In: *IEEE Trans. Signal Process.* 54.12 (2006), pp. 4840 –4843.

[84] H. Cramér, ed. *Mathematical Methods of Statistics*. Vol. 12. NJ, USA: Princeton Univ. Press, 1946.

[85] A. Renaux, P. Forster, E. Boyer, et al. “Unconditional Maximum Likelihood Performance at Finite Number of Samples and High Signal-to-Noise Ratio”. In: *IEEE Trans. Signal Process.* 55.5 (2007), pp. 2358–2364.

[86] H. L. Van Trees and K. L. Bell, eds. *Bayesian Bounds for Parameter Estimation and Nonlinear Filtering/Tracking*. New-York, NY, USA: Wiley/IEEE Press, 2007.

[87] J. M. Hammersley. “On estimating restricted parameters”. In: *Annals of the Royal Statistics Society (Series B)* 12 (1950), pp. 192–240.

[88] D. G. Chapman and H. Robbins. “Minimum variance estimation without regularity assumptions”. In: *Ann. Math. Stat.* 22.4 (1951), pp. 581–586.

[89] R. McAulay and L. P. Seidman. “A useful form of the Barankin lower bound and its application to PPM threshold analysis”. In: *IEEE Trans. Inf. Theory* 15.2 (1969), pp. 273–279.

[90] F. E. Glave. “A new look at the Barankin lower bound”. In: *IEEE Trans. Inf. Theory* 18 (1972), pp. 349–356.

[91] J. S. Abel. “A bound on mean-square-estimate error”. In: *IEEE Trans. on Information Theory* 39.5 (1993), pp. 1675–1680.

[92] P. Forster and P. Larzabal. “On lower bounds for deterministic parameter estimation”. In: *Proc. of the IEEE ICASSP*. 2002.

[93] E. Chaumette, J. Galy, A. Quinlan, et al. “A New Barankin Bound Approximation for the Prediction of the Threshold Region Performance of Maximum-Likelihood Estimators”. In: *IEEE Trans. Signal Process.* 56.11 (2008), pp. 5319–5333.

[94] K. Todros and J. Tabrikian. “General Classes of Performance Lower Bounds for Parameter Estimation-Part I: Non-Bayesian Bounds for Unbiased Estimators”. In: *IEEE Trans. Inf. Theory* 56.10 (2010), pp. 5045–5063.

[95] K. Todros and J. Tabrikian. “Uniformly Best Biased Estimators in Non-Bayesian Parameter Estimation”. In: *IEEE Trans. Inf. Theory* 57.11 (2011), pp. 7635–7647.

[96] E. W. Barankin. “Locally best unbiased estimates”. In: *Ann. Math. Stat.* 20.4 (1949), pp. 477–501.

[97] R. A. Horn and C. R. Johnson. *Matrix Analysis*. Cambridge University Press, 1999.

[98] T. Menni, E. Chaumette, P. Larzabal, et al. “New results on Deterministic Cramér-Rao bounds for real and complex parameters”. In: *IEEE Trans. Signal Process.* 60.3 (2012), pp. 1032–1049.

[99] J. M. Hammersley. “Estimating Restricted Parameters”. In: *Journal of Roy. Stat. Soc.* 12.2 (), pp. 192–240.

[100] S. M. Kay. *Fundamentals of Statistical Signal Processing: Estimation Theory*. Englewood Cliffs, New Jersey, USA: Prentice-Hall, 1993.

[101] P. J. G. Teunissen. “A class of unbiased integer GPS ambiguity estimators”. In: *Artificial Satellites* 33.1 (1998), pp. 3–10.

[102] Malcolm David Shuster and S D_ Oh. “Three-axis Attitude Determination from Vector Observations”. In: *Journal of guidance and Control* 4.1 (1981), pp. 70–77.

[103] Grace Wahba. “A Least Squares Estimate of Satellite Attitude”. In: *SIAM Review* 7.3 (1965), pp. 409–409.

[104] M Shuster. “Approximate Algorithms for Fast Optimal Attitude Computation”. In: *Guidance and Control Conference*. 1978, p. 1249.

[105] James R Wertz. *Spacecraft Attitude Determination and Control*. Vol. 73. Springer Science & Business Media, 2012.

[106] Malcolm D Shuster. “The Quest for Better Attitudes”. In: *The Journal of the Astronautical Sciences* 54.3 (2006), pp. 657–683.

[107] F Landis Markley and John L Crassidis. *Fundamentals of Spacecraft Attitude Determination and Control*. Springer, 2014.

[108] F. Landis Markley. “Attitude Error Representations for Kalman Filtering”. In: *Journal of Guidance, Control, and Dynamics* 26.2 (2003), pp. 311–317.

[109] Nikolas Trawny and Stergios I Roumeliotis. “Indirect Kalman filter for 3D attitude estimation”. In: *University of Minnesota, Dept. of Comp. Sci. & Eng., Tech. Rep* 2 (2005), p. 2005.

[110] Venkatesh Madyastha, Vishal Ravindra, Srinath Mallikarjunan, et al. “Extended Kalman filter vs. Error State Kalman filter for Aircraft Attitude Estimation”. In: *AIAA Guidance, Navigation, and Control Conference*. 2011, p. 6615.

[111] Axel Barrau and Silvere Bonnabel. “Intrinsic Liltering on Lie Groups with Applications to Attitude Estimation”. In: *IEEE Transactions on Automatic Control* 60.2 (2014), pp. 436–449.

[112] Axel Barrau and Silvère Bonnabel. “The Invariant Extended Kalman filter as a Stable Observer”. In: *IEEE Transactions on Automatic Control* 62.4 (2016), pp. 1797–1812.

[113] Axel Barrau and Silvere Bonnabel. “Invariant Kalman Filtering”. In: *Annual Review of Control, Robotics, and Autonomous Systems* 1 (2018), pp. 237–257.

[114] Gabriele Giorgi. “GNSS Carrier Phase-based Attitude Determination: Estimation and Applications”. PhD thesis. TU Delft, 2011.

[115] Penina Axelrad and Charles P Behre. “Satellite Attitude Determination based on GPS Signal-to-Noise Ratio”. In: *Proceedings of the IEEE* 87.1 (1999), pp. 133–144.

[116] VW Spinney. “Applications of the Global Positioning System as an Attitude Reference for Near Earth Users”. In: *Journal of the Institute of Navigation, Spring* (1976).

[117] Peter Teunissen. “A general multivariate formulation of the multi-antenna GNSS attitude determination problem”. In: *Artificial Satellites* 42.2 (2007), pp. 97–111.

[118] Peter JG Teunissen, Gabriele Giorgi, and Peter J Buist. “Testing of a new single-frequency GNSS carrier phase attitude determination method: land, ship and aircraft experiments”. In: *GPS solutions* 15.1 (2011), pp. 15–28.

[119] Gabriele Giorgi and Peter JG Teunissen. “Multivariate GNSS Attitude Integrity: The Role of Affine Constraints”. In: *VIII Hotine-Marussi Symposium on Mathematical Geodesy*. Springer. 2015, pp. 309–315.

[120] Joan Sola. “Towards Visual Localization, Mapping and Moving Objects Tracking by a Mobile Robot: a Geometric and Probabilistic Approach”. PhD thesis. Institut National Politechnique de Toulouse, 2007.

[121] Joan Solà. “Quaternion kinematics for the error-state Kalman filter”. In: *CoRR* abs/1711.02508 (2017).

[122] Joan Sola, Jeremie Deray, and Dinesh Atchuthan. “A micro Lie theory for state estimation in robotics”. In: *arXiv preprint arXiv:1812.01537* (2018).

[123] Timothy D Barfoot. *State Estimation for Robotics*. Cambridge University Press, 2017.

[124] Paul D Groves. “Principles of GNSS, inertial, and multisensor integrated navigation systems, [Book review]”. In: *IEEE Aerospace and Electronic Systems Magazine* 30.2 (2015), pp. 26–27.

[125] William Rowan Hamilton. “On a New Species of Imaginary Quantities, Connected with the Theory of Quaternions”. In: *Proceedings of the Royal Irish Academy (1836-1869)* 2 (1840), pp. 424–434.

[126] Christoph Hertzberg, René Wagner, Udo Frese, et al. “Integrating generic sensor fusion algorithms with sound state representations through encapsulation of manifolds”. In: *Information Fusion* 14.1 (2013), pp. 57–77.

[127] Christian Forster, Luca Carlone, Frank Dellaert, et al. “On-Manifold Preintegration for Real-Time Visual–Inertial Odometry”. In: *IEEE Transactions on Robotics* 33.1 (2016), pp. 1–21.

[128] Stefan Leutenegger, Simon Lynen, Michael Bosse, et al. “Keyframe-based Visual–Inertial Odometry Using Nonlinear Optimization”. In: *The International Journal of Robotics Research* 34.3 (2015), pp. 314–334.

[129] PJG Teunissen and G Giorgi. “To what extent can standard GNSS ambiguity resolution methods be used for single-frequency epoch-by-epoch attitude determination?” In: *Proc. of the 22nd ION GNSS* (2009), pp. 235–242.

[130] Nandakumaran Nadarajah, Peter JG Teunissen, Peter J Buist, et al. “First results of instantaneous GPS/Galileo/COMPASS attitude determination”. In: *2012 6th ESA Workshop on Satellite Navigation Technologies (Navitec 2012) & European Workshop on GNSS Signals and Signal Processing*. IEEE. 2012, pp. 1–8.

[131] Gabriele Giorgi and Peter JG Teunissen. “Carrier phase GNSS attitude determination with the multivariate constrained LAMBDA method”. In: *2010 IEEE Aerospace Conference*. IEEE. 2010, pp. 1–12.

[132] Gabriele Giorgi and Peter Teunissen. “GNSS carrier phase-based attitude determination”. In: *Recent advances in aircraft technology*. InTech, 2012, pp. 193–220.

[133] G Giorgi, PJG Teunissen, S Verhagen, et al. “Improving the GNSS attitude ambiguity success rate with the multivariate constrained LAMBDA method”. In: *Geodesy for Planet Earth*. Springer, 2012, pp. 941–948.

[134] Stergios I Roumeliotis, Gaurav S Sukhatme, and George A Bekey. “Circumventing dynamic modeling: Evaluation of the error-state Kalman filter applied to mobile robot localization”. In: *Proceedings 1999 IEEE International Conference on Robotics and Automation (Cat. No. 99CH36288C)*. Vol. 2. IEEE. 1999, pp. 1656–1663.

[135] S. T. Smith. “Covariance, Subspace, and Intrinsic Cramér-Rao Bounds”. In: *IEEE Transactions on Signal Processing* 53.5 (2005), pp. 1610–1629.

[136] Xavier Pennec. “Intrinsic Statistics on Riemannian Manifolds: Basic Tools for Geometric Measurements”. In: *Journal of Mathematical Imaging and Vision* 25.1 (2006), pp. 127–154.

[137] Christian Eling, Lasse Klingbeil, and Heiner Kuhlmann. “Real-time single-frequency GPS/MEMS-IMU attitude determination of lightweight UAVs”. In: *Sensors* 15.10 (2015), pp. 26212–26235.

[138] Patrick Henkel, Michele Iafrancesco, and Andreas Sperl. “Precise point positioning with multipath estimation”. In: *Position, Location and Navigation Symposium (PLANS), 2016 IEEE/ION*. IEEE. 2016, pp. 144–149.

[139] Gianluca Falco, Marco Pini, and Gianluca Marucco. “Loose and Tight GNSS/INS Integrations: Comparison of Performance Assessed in Real Urban Scenarios”. In: *Sensors* 17.2 (2017), p. 255.

[140] Peirong Fan, Wenyi Li, Xiaowei Cui, et al. “Precise and Robust RTK-GNSS Positioning in Urban Environments with Dual-Antenna Configuration”. In: *Sensors* 19.16 (2019), p. 3586.

[141] Peter JG Teunissen. “A-PPP: Array-Aided Precise Point Positioning with Global Navigation Satellite Systems”. In: *IEEE Transactions on Signal Processing* 60.6 (2012), pp. 2870–2881.

[142] Juan Blanch, Todd Walter, Per Enge, et al. “Advanced RAIM user algorithm description: integrity support message processing, fault detection, exclusion, and protection level calculation”. In: *Proceedings of the 25th International Technical Meeting of The Satellite Division of the Institute of Navigation (ION GNSS 2012)*. 2012, pp. 2828–2849.

[143] Mathieu Joerger and Boris Pervan. “Fault detection and exclusion using solution separation and chi-squared ARAIM”. In: *IEEE Transactions on Aerospace and electronic systems* 52.2 (2016), pp. 726–742.

[144] Shaojun Feng, Washington Ochieng, Terry Moore, et al. “Carrier phase-based integrity monitoring for high-accuracy positioning”. In: *GPS solutions* 13.1 (2009), pp. 13–22.

[145] Young C Lee. “A position domain relative RAIM method”. In: *IEEE Transactions on Aerospace and Electronic Systems* 47.1 (2011), pp. 85–97.

[146] Boris S Pervan, Samuel P Pullen, and Jock R Christie. “A multiple hypothesis approach to satellite navigation integrity”. In: *Navigation* 45.1 (1998), pp. 61–71.

[147] P. J. Huber and E. M. Ronchetti. *Robust Statistics*. 2nd ed. Wiley, 2009.

[148] J.W. Tukey. “Contributions to Probability and Statistics”. In: Stanford University Press, 1960. Chap. A survey of sampling from contaminated distributions.

[149] Peter J Huber et al. “Robust estimation of a location parameter”. In: *The annals of mathematical statistics* 35.1 (1964), pp. 73–101.

[150] Frank R Hampel. “A general qualitative definition of robustness”. In: *The Annals of Mathematical Statistics* (1971), pp. 1887–1896.

[151] Abdelhak M Zoubir, Visa Koivunen, Yacine Chakhchoukh, et al. “Robust estimation in signal processing: A tutorial-style treatment of fundamental concepts”. In: *IEEE Signal Processing Magazine* 29.4 (2012), pp. 61–80.

[152] Zhengyou Zhang. “Determining the epipolar geometry and its uncertainty: A review”. In: *International journal of computer vision* 27.2 (1998), pp. 161–195.

[153] Ezio Malis and Eric Marchand. “Experiments with robust estimation techniques in real-time robot vision”. In: *2006 IEEE/RSJ International Conference on Intelligent Robots and Systems*. IEEE. 2006, pp. 223–228.

[154] Jacek M Leski. “Robust weighted averaging [of biomedical signals]”. In: *IEEE Transactions on Biomedical Engineering* 49.8 (2002), pp. 796–804.

[155] Michael Muma and Abdelhak M Zoubir. “Robust model order selection for corneal height data based on $\tau$ estimation”. In: *2011 IEEE International Conference on Acoustics, Speech and Signal Processing (ICASSP)*. IEEE. 2011, pp. 4096–4099.

[156] Lamine Mili, Michael G Cheniae, and Peter J Rousseeuw. “Robust state estimation of electric power systems”. In: *IEEE Transactions on Circuits and Systems I: Fundamental Theory and Applications* 41.5 (1994), pp. 349–358.

[157] F. R. Hampel et al. *Robust Statistics: The Approach Based on Influence Functions*. John Wiley & Sons, 2011.

[158] Ricardo A Maronna, R Douglas Martin, Victor J Yohai, et al. *Robust statistics: theory and methods (with R)*. Wiley, 2018.

[159] A. M. Zoubir, V. Koivunen, E. Ollila, et al. *Robust Statistics for Signal Processing*. Cambridge University Press, 2018.

[160] Daniele Borio and Pau Closas. “A fresh look at GNSS anti-jamming”. In: *Inside GNSS* 12 (2017), pp. 54–61.

[161] D. Borio. “Robust signal processing for GNSS”. In: *Proc. of the 2017 European Navigation Conference (ENC)*. Lousanne, Switzerland, May 2017, pp. 150–158.

[162] D. Borio. “Myriad Non-Linearity for GNSS Robust Signal Processing”. In: *IET Radar Sonar and Navigation* 11.10 (Oct. 2017), pp. 1467–1476.

[163] D. Borio and Pau Closas. “Complex Signum Non-Linearity for Robust GNSS Signal Mitigation”. In: *IET Radar Sonar and Navigation* (Apr. 2018), pp. 1–10.

[164] D. Borio, H. Li, and P. Closas. “Huber’s Non-Linearity for GNSS Interference Mitigation”. In: *Sensors* 18.7 (2018), p. 2217.

[165] D. Borio and Pau Closas. “Robust Transform Domain Signal Processing for GNSS”. In: *Navigation* 0.0 (2019).

[166] Haoqing Li, Daniele Borio, and Pau Closas. “Dual-Domain Robust GNSS Interference Mitigation”. In: *ION GNSS+, The International Technical Meeting of the Satellite Division of The Institute of Navigation, Miami, FL*. Sep 2019.

[167] Nathan L Knight and Jinling Wang. “A comparison of outlier detection procedures and robust estimation methods in GPS positioning”. In: *The Journal of Navigation* 62.4 (2009), pp. 699–709.

[168] Kia Fallahi, Chi-Tsun Cheng, and Michel Fattouche. “Robust positioning systems in the presence of outliers under weak GPS signal conditions”. In: *IEEE Systems Journal* 6.3 (2012), pp. 401–413.

[169] José A. Pozo-Pérez, Daniel Medina, Iván Herrera-Pinzón, et al. “Robust Outlier Mitigation in Multi-Constellation GNSS-based Positioning for Waterborne Applications,” in: *Proceedings of the 2017 International Technical Meeting of The Institute of Navigation,* Institute of Navigation. 2017, pp. 1330–1343.

[170] Henri Pesonen. “Robust estimation techniques for GNSS positioning”. In: *Proceedings of NAV07-The Navigation Conference and Exhibition, 31.10.-1.11. 2007, London, England*. 2007.

[171] Carl Friedrich Gauss. *Theoria Motus Corporum Coelestium*. Perthes et Besser, 1809.

[172] Henri Poincaré. “Létat actuel et lavenir de la physique mathématique”. In: *Bulletin des sciences mathématiques* 28.2 (1904), pp. 302–324.

[173] T Keith Blankenship, DM Kriztman, and Theodore S Rappaport. “Measurements and simulation of radio frequency impulsive noise in hospitals and clinics”. In: *1997 IEEE 47th Vehicular Technology Conference. Technology in Motion*. Vol. 3. IEEE. 1997, pp. 1942–1946.

[174] David Middleton. “Non-Gaussian noise models in signal processing for telecommunications: new methods an results for class A and class B noise models”. In: *IEEE Transactions on Information Theory* 45.4 (1999), pp. 1129–1149.

[175] Paul C Etter. *Underwater acoustic modeling and simulation*. CRC press, 2018.

[176] Michael E Muma. “Robust Estimation and Model Order Selection for Signal Processing”. PhD thesis. Universitäts-und Landesbibliothek Darmstadt, 2014.

[177] Analytical Methods Committee. “Robust statistics How not to reject outliers”. In: *Analyst* 114 (1989), pp. 1693–1702.

[178] Abdelhak M Zoubir, Visa Koivunen, Esa Ollila, et al. *Robust Statistics for Signal Processing*. Cambridge University Press, 2018.

[179] Frank R Hampel. “The influence curve and its role in robust estimation”. In: *The Annals of Mathematical Statistics* (1974), pp. 383–393.

[180] J.W. Tukey. *Exploratory Data Analysis*. Addison-Wisley, 1977.

[181] C Croux. “Limit behaviour of the empirical influence function of the median”. In: *Statistics and Probability Letters* 37 (1998), pp. 331–340.

[182] Frank R Hampel. “Contributions to the theory of robust estimation”. PhD thesis. University of California, Berkley, 1968.

[183] Peter Rousseeuw and Victor Yohai. “Robust regression by means of S-estimators”. In: *Robust and nonlinear time series analysis*. Springer, 1984, pp. 256–272.

[184] Peter J. Rousseuw. *Robust Regression and Outlier Detection*. John Wiley & Sons, 1987.

[185] C.L. Mallows. *On Some Topics in Robustness*. Vol. unpublished memorandum. Murray Hill, 1975.

[186] R.A. Maronna, O. Bustos, and V. Yohai. “Smoothing Techniques for Curve Estimation”. In: ed. by T. Gasser and M. Rosenblatt. Springer Verlag, 1979. Chap. Bias- and Efficiency-Robustness of General M-estimators for Regression with Random Carriers, pp. 91–116.

[187] Peter J Rousseeuw. “Least Median of Squares Regression”. In: *Journal of the American statistical association* 79.388 (1984), pp. 871–880.

[188] Matías Salibian-Barrera and Víctor J Yohai. “A Fast Algorithm for S-Regression Estimates”. In: *Journal of computational and Graphical Statistics* 15.2 (2006), pp. 414–427.

[189] Victor J Yohai. “High Breakdown-Point and High Efficiency Robust Estimates for Regression”. In: *The Annals of statistics* (1987), pp. 642–656.

[190] Stephen Boyd and Lieven Vandenberghe. *Introduction to Applied Linear Algebra: Vectors, Matrices, and Least Squares*. Cambridge university press, 2018.

[191] Ricardo A Maronna and Victor J Yohai. “Correcting MM estimates for fat data sets”. In: *Computational Statistics & Data Analysis* 54.12 (2010), pp. 3168–3173.

[192] Saleem A Kassam and H Vincent Poor. “Robust techniques for signal processing: A survey”. In: *Proceedings of the IEEE* 73.3 (1985), pp. 433–481.

[193] Laurent E Calvet, Veronika Czellar, and Elvezio Ronchetti. “Robust filtering”. In: *Journal of the American Statistical Association* 110.512 (2015), pp. 1591–1606.

[194] Yong Lee and S Kassam. “Generalized Median Filtering and Related Nonlinear Filtering Techniques”. In: *IEEE Transactions on Acoustics, Speech, and Signal Processing* 33.3 (1985), pp. 672–683.

[195] Juan G Gonzalez and Gonzalo R Arce. “Optimality of the Myriad Filter in Practical Impulsive-Noise Environments”. In: *IEEE Transactions on Signal Processing* 49.2 (2001), pp. 438–441.

[196] Tuncer Can Aysal and Kenneth E Barner. “Meridian Filtering for Robust Signal Processing”. In: *IEEE Transactions on Signal Processing* 55.8 (2007), pp. 3949–3962.

[197] Radford M Neal. “Markov chain sampling methods for Dirichlet process mixture models”. In: *Journal of computational and graphical statistics* 9.2 (2000), pp. 249–265.

[198] F. Caron, M. Davy, A. Doucet, et al. “Bayesian inference for linear dynamic models with Dirichlet process mixtures”. In: *IEEE Trans. Signal Process.* 56.1 (2008), pp. 71–84.

[199] J. Dunik, O. Straka, O. Kost, et al. “Noise Covariance Matrices in State-Space Models: A Survey and Comparison of Estimation Methods - Part I”. In: *Intl. J. of Adaptive Control and Signal Process.* 31 (2017), pp. 1505–1543.

[200] X Rong Li and Yaakov Bar-Shalom. “A Recursive Multiple Model Approach to Noise Identification”. In: *IEEE Transactions on Aerospace and Electronic Systems* 30.3 (1994), pp. 671–684.

[201] Demetrios Lainiotis. “Optimal Adaptive Estimation: Structure and Parameter Adaption”. In: *IEEE Transactions on Automatic Control* 16.2 (1971), pp. 160–170.

[202] Raman Mehra. “Approaches to Adaptive Filtering”. In: *IEEE Transactions on automatic control* 17.5 (1972), pp. 693–698.

[203] S. Särkkä and A. Nummenamaa. “Recursive noise adaptive Kalman filtering by variational Bayesian approximations”. In: *IEEE Trans. on Automatic Control* 54.3 (2009), pp. 596–600.

[204] T. Ardeshiri, E. Ozkan, U. Orguner, et al. “Approximate Bayesian smoothing with unknown process and measurement noise covariances”. In: *IEEE Signal Process. Lett.* 22.12 (2015), pp. 2450–2454.

[205] Y. Huang, Y. Zhang, Z. Wu, et al. “A novel adaptive Kalman filter with inaccurate process and measurement noise covariance matrics”. In: *IEEE Trans. Automatic Control* 63.2 (2018), pp. 594–601.

[206] G. Agamennoni, J. I. Nieto, and E. M. Nebot. “Approximate Inference in State-Space Models With Heavy-Tailed Noise”. In: *IEEE Trans. Sig. Process* 60.10 (2012).

[207] G. Agamennoni and E. Nebot. “Robust estimation in non-linear state-space models with state-dependent noise”. In: *IEEE Trans. Signal Process.* 62.8 (2014), pp. 2165–2175.

[208] S. Saha. *Noise Robust Online Inference for Linear Dynamic Systems*. 2015.

[209] J. Vilà-Valls and P. Closas. “NLOS Mitigation in Indoor Localization by Marginalized Monte Carlo Gaussian Smoothing”. In: *EURASIP Journal on Adv. in Sig. Process.* 62 (2017).

[210] H. Nurminen, T. Ardeshiri, R. Piché, et al. “Robust Inference for State-Space Models with Skewed Measurement Noise”. In: *IEEE Signal Process. Lett.* 22.11 (2015), pp. 1898–1902.

[211] Y. Huang, N. Li Y. Zhang, and J.A. Chambers. “A novel robust Student’s t based Kalman filter”. In: *IEEE Trans. Aerospace Elec. Syst.* 53.3 (2017), pp. 1545–1554.

[212] H. Nurminen, T. Ardeshiri, R. Piché, et al. “Skew-t Filter and Smoother With Improved Covariance Matrix Approximation”. In: *IEEE Trans. Signal Process.* 66.21 (2018), pp. 5618–5633.

[213] Y. Huang, Y. Zhang, P. Shi, et al. “Robust Kalman Filters Based on Gaussian Scale Mixture Distribution with Application to Target Tracking”. In: *IEEE Trans. Systems, Man. And Cybernetics* 49.10 (2019), pp. 2082–2096.

[214] Y. Huang, Y. Zhang, Y.Zhao, et al. “A novel robust Gaussian-Student’s t mixture distribution based Kalman filter”. In: *IEEE Trans. Signal Process.* 67.13 (2019), pp. 3606–3620.

[215] M. A. Gandhi and L. Mili. “Robust Kalman filter based on a generalized maximum-likelihood-type estimator”. In: *IEEE Trans. Signal Process.* 58.5 (2010), pp. 25092520.

[216] L. Chang and K. Li. “Unified form for the robust Gaussian information filtering based on M-estimate”. In: *IEEE Signal Process. Lett.* 24.4 (2017), pp. 412–416.

[217] H. Wang, H. Li, W. Zhang, et al. “A unified framework for M-estimation based robust Kalman smoothing”. In: *Signal Processing* 158 (2019), pp. 61–65.

[218] R Douglas Martin and David J Thomson. “Robust-Resistant Spectrum Estimation”. In: *Proceedings of the IEEE* 70.9 (1982), pp. 1097–1115.

[219] Ronald K Pearson. “Outliers in Process Modeling and Identification”. In: *IEEE Transactions on control systems technology* 10.1 (2002), pp. 55–63.

[220] Hongwei Wang, Hongbin Li, Jun Fang, et al. “Robust Gaussian Kalman Filter With Outlier Detection”. In: *IEEE Signal Processing Letters* 25.8 (2018), pp. 1236–1240.

[221] Rudolph Van Der Merwe et al. “Sigma-point Kalman filters for probabilistic inference in dynamic state-space models”. PhD thesis. OGI School of Science & Engineering at OHSU, 2004.

[222] Paul Chauchat, Jordi Vilà-Valls, and Eric Chaumette. “Robust Information Filtering under Model Mismatch for Large-Scale Dynamic Systems”. In: *IEEE Control Systems Letters* (2021).

[223] T. Vercauteren and X. Wang. “Decentralized Sigma-Point Information Filters for Target Tracking in Collaborative Sensor Networks”. In: *IEEE Trans. on Sig. Process.* 53.8 (2005), pp. 2997–3009.

[224] I. Arasaratnam and K.P.B. Chandra. “Multisensor Data Fusion: From Algorithm and Architecture Design to Applications”. In: CRC Press, 2015. Chap. Cubature Information Filters: Theory and Applications to Multisensor Fusion.

[225] Mital A Gandhi and Lamine Mili. “Robust Kalman filter based on a Generalized Maximum-Likelihood-Type Estimator”. In: *IEEE Transactions on Signal Processing* 58.5 (2009), pp. 2509–2520.

[226] Matthew D Hoffman, David M Blei, Chong Wang, et al. “Stochastic Variational Inference”. In: *Journal of Machine Learning Research* 14.5 (2013).

[227] Andrew Gelman, John B Carlin, Hal S Stern, et al. *Bayesian data analysis*. CRC press, 2013.

[228] V. Šmídl and A. Quinn. *The Variational Bayes Method in Signal Processing*. New York: Springer-Verlag, 2005.

[229] Christopher M. Bishop. *Pattern Recognition and Machine Learning*. Springer, 2006.

[230] Dimitris G Tzikas, Aristidis C Likas, and Nikolaos P Galatsanos. “The Variational Approximation for Bayesian Inference”. In: *IEEE Signal Processing Magazine* 25.6 (2008), pp. 131–146.

[231] P-A Absil, Robert Mahony, and Rodolphe Sepulchre. *Optimization algorithms on matrix manifolds*. Princeton University Press, 2009.

[232] Nicolas Boumal. “An Introduction to Optimization on Smooth Manifolds”. In: *Available online, Aug* (2020).

[233] P. Das, J. Vilà-Valls, E. Chaumette, et al. “On the Accuracy Limit of Time-delay Estimation with a Band-limited Signal”. In: *Proc. of the IEEE Intl. Conf. on Acoustics, Speech and Signal Processing (ICASSP)*. Brighton, UK, 2019.

[234] K. B. Petersen and M. S. Pedersen. *The Matrix Cookbook*. Technical University of Denmark, Oct. 2008.

[235] José M Bernardo and Adrian FM Smith. *Bayesian Theory*. Vol. 405. John Wiley & Sons, 2009.

[236] Bofeng Li. “Stochastic modeling of triple-frequency BeiDou signals: estimation, assessment and impact analysis”. In: *Journal of Geodesy* 90.7 (2016), pp. 593–610.

[237] Robert Odolinski and Peter JG Teunissen. “Low-cost, high-precision, single-frequency GPS–BDS RTK positioning”. In: *GPS solutions* 21.3 (2017), pp. 1315–1330.

[238] Antonio Angrisano, Ciro Gioia, Salvatore Gaglione, et al. “GNSS reliability testing in signal-degraded scenario”. In: *International Journal of Navigation and Observation* 2013 (2013).